



UNIVERSITÀ  
DEGLI STUDI  
DI PADOVA

UNIVERSITA' DEGLI STUDI DI PADOVA  
**Dipartimento di Ingegneria Industriale DII**

Tesi di Laurea Magistrale in Ingegneria Meccanica

**Topology optimisation for structural strength and  
durability of 3D printed curved beams made of polymer  
and metal materials**

Relatore: Prof. Giovanni Meneghetti

Correlatore: Prof. Jernej Klemenc (Università di Lubiana)

Laureando: Guido Sacchetti

Matricola: 1179825

Anno Accademico 2019/2020



# Acknowledgments

I want to thank Prof. Meneghetti for his availability, the trust he has placed in me and the precious support, not only for the development of this thesis, but also throughout my university education.

I want to thank Prof. Klemenc for the welcome and the fruitful collaboration that took place in carrying out most of this thesis, on Erasmus, in the Mechanical Engineering Department of the University of Ljubljana.

I want to thank the Prof. Klemenc's PhD students and the technicians of the Machine Design laboratory of the Faculty of Mechanical Engineering of the Ljubljana's University for the technical and practical support they have provided me.

Finally, a last but not least big thank you to my family and my friends for supporting me throughout my studies. Without them it would have been impossible to achieve this very important goal.





# Abstract

The main objective of this master thesis was the development of an optimized inner support structure for a hollow curved beam made by additive manufacturing technology.

A simple curve beam geometry to work with has been defined and different load cases have been taken in account.

Have been followed two different approaches for the development of the inner support structure; the first one was the iterative-intuitive optimization, the second one was the mathematical design optimization, which comprehends the topology optimization and the variable density lattice optimization approaches.

F.E.M. analyses have been performed to compare the performances of the different inner structural supports developed.

Different curved beam specimens with different structural inner supports have been printed with SLS (PA12 material) and SLM (Maraging steel material) technologies; static and fatigue tests have been then performed.

Have been done also a complete characterization of the PA12 material used, taking in account the three typical print orientations: 0°, 45°, 90°. The idea was to know deeply the material's characteristics to be able to perform static estimations and fatigue life estimations of components made by PA12 material and produced by SLS technology.

Have been done tensile tests of plain specimens, have been done fatigue tests of plain specimens and of two types of V-notch specimens: the first one with a rounded V-notch and the second one with a sharp V-notch.

Since have been decided to use the *Strain Energy Density* (SED) local approach [29] to estimate the fatigue life of PA12, SLS 3D printed, components with sharp and rounded V-notches, have been used the plain specimen's fatigue tests results and the sharp V-notch specimen's fatigue tests results to calibrate the control radius  $R_c$  of the control volume of the PA12 material. Have been then built the  $\Delta W-N$  charts for the PA12 material, using the results above mentioned.

In the end, have been applied the SED local approach to the rounded V-notch specimens, using their tests results to validate the  $\Delta W-N$  charts previously developed.

*L'obiettivo principale di questa tesi di laurea è stato lo sviluppo di una struttura di supporto interna ottimizzata per una trave curva cava realizzata mediante tecnologia di produzione additiva.*

*È stata definita una semplice geometria di trave curva con cui lavorare e sono stati presi in considerazione diversi casi di carico.*

*Sono stati seguiti due diversi approcci per lo sviluppo della struttura di supporto interna; il primo è stato l'ottimizzazione iterativa-intuitiva, il secondo è stato l'ottimizzazione matematica, che comprende gli approcci di ottimizzazione topologica e di ottimizzazione lattice.*

*Sono state eseguite analisi F.E.M. per confrontare le prestazioni dei diversi supporti interni strutturali sviluppati.*

*Diversi provini di trave curva con differenti supporti interni strutturali sono stati stampati con le tecnologie SLS (materiale PA12) e SLM (materiale acciaio Maraging); sono state poi eseguite prove statiche e di fatica.*

*È stata eseguita anche una caratterizzazione completa del materiale PA12 utilizzato, tenendo conto dei tre orientamenti tipici di stampa: 0°, 45°, 90°. L'idea è stata quella di conoscere a fondo le caratteristiche del materiale per essere in grado di eseguire stime statiche e stime della vita a fatica di componenti realizzati con materiale PA12 e prodotti con tecnologia SLS.*

*Sono state eseguite prove di trazione di provini lisci, prove di fatica di provini lisci e di due tipi di provini con intaglio a V: il primo con intaglio a V raccordato e il secondo con intaglio a V a spigolo vivo.*

*Dato che è stato deciso di utilizzare l'approccio locale "Strain Energy Density" (SED) [29] per stimare la vita a fatica di componenti in PA12, stampati 3D con tecnologia SLS, aventi intagli a V sia raccordati sia a spigolo vivo, sono stati utilizzati i risultati dei test di fatica dei provini lisci e i risultati dei test di fatica dei provini con intaglio a V a spigolo vivo per calibrare il raggio di controllo  $R_c$  del volume di controllo del materiale PA12. Sono stati poi anche costruiti i grafici  $\Delta W-N$  per il materiale PA12, utilizzando sempre i risultati dei test sopra citati.*

*Alla fine, è stato applicato l'approccio locale SED ai campioni con intaglio a V raccordato, utilizzando i risultati dei loro test per validare i grafici  $\Delta W-N$  precedentemente sviluppati.*



# Table of contents

Introduction.....	1
<b>CHAPTER 1: The Additive Manufacturing .....</b>	<b>2</b>
1.1 Technology overview and comparison with traditional technologies .....	2
1.2 Comparison between SLS and SLM technologies .....	6
1.3 From the 3D CAD model to the 3D print.....	12
<b>CHAPTER 2: Structural inner support development for hollow curved beams .....</b>	<b>14</b>
2.1 Problems in hollow curved beams made by additive manufacturing .....	14
2.2 Hollow curved beam geometry definition and developing methods for a structural inner support.....	16
2.2.1 Hollow curved beam outer geometry definition .....	16
2.2.2 Developing methods for a structural inner support.....	17
2.3 Load Cases definition .....	19
2.3.1 Load Case 1 .....	20
2.3.2 Load Case 2 .....	21
2.3.3 Load Case 3 .....	22
2.3.4 Load Case 4 .....	23
2.3.5 Load Case 5 .....	24
2.3.6 Load Case 6 .....	25
2.4 Iterative - intuitive optimization .....	26
2.4.1 Load Case 1: Inner support design with iterative - intuitive optimization .....	26
2.4.2 Load Case 1: F.E.M. Analyses .....	30
2.5 Mathematical design optimization: Topology optimization .....	34
2.5.1 Topology Optimization background .....	34
2.5.2 Topology Optimization with Ansys Workbench .....	36
2.5.3 Load Case 1: Inner support design with Topology Optimization .....	42
2.5.4 Load Case 1: F.E.M. Analyses .....	47
2.5.5 Load Case 2: Topology Optimization.....	49
2.5.6 Load Case 3: Topology Optimization.....	51
2.5.7 Load Cases 1+2+3: Inner support design upgrade .....	53
2.5.8 Load Cases 1+2+3: F.E.M. Analyses .....	56
2.5.9 Load Case 4: Topology Optimization.....	63
2.5.10 Load Case 5: Topology Optimization.....	66
2.5.11 Load Case 6: Topology Optimization.....	69
2.5.12 Load Cases 4+5+6: Inner support design upgrade .....	72
2.5.13 Load Cases 4+5+6: F.E.M. Analyses .....	75
2.6 Mathematical design optimization: Topology optimization with overhang constraint ..	79
2.6.1 Load Case 2: Inner support design with Topology Optimization .....	79
2.6.2 Load Case 2: F.E.M. Analysis .....	82
2.6.3 Load Case 3: Inner support design with Topology Optimization .....	83
2.6.4 Load Case 3: F.E.M. Analysis .....	85

2.7 Mathematical design optimization: Lattice Optimization .....	87
2.7.1 Variable density Lattice Optimization with Ansys Workbench .....	87
2.7.2 Load Case 2: Inner support design with Lattice Optimization .....	90
2.7.3 Load Case 2: F.E.M. Analysis .....	95
CHAPTER 3: Laboratory tests of developed curved beams .....	98
3.1 Clamps design and realization .....	98
3.1.1 Clamping system F.E.M. analyses .....	102
3.1.2 Clamping system realization .....	110
3.2 Static tests .....	114
3.2.1 Maraging steel specimens and PA12 specimens .....	114
3.2.2 Tests set-up description .....	117
3.2.3 Test results .....	119
3.3 Fatigue tests .....	123
3.3.1 Maraging steel specimens and PA12 specimens .....	123
3.3.2 Tests set-up description .....	123
3.3.3 Test results .....	124
CHAPTER 4: Characterization of the PA12 material 3D printed with SLS technology .....	128
4.1 Specimens production .....	128
4.2 Tensile tests of plain specimens .....	131
4.2.1 Specimens dimensions .....	131
4.2.2 Tests set-up description .....	132
4.2.3 Tests results .....	133
4.3 Fatigue tests of plain specimens .....	140
4.3.1 Specimens dimensions .....	140
4.3.2 Tests set-up description .....	141
4.3.3 Tests results .....	143
4.4 Fatigue tests of rounded V-notch specimens .....	148
4.4.1 Specimens dimensions and preparation .....	148
4.4.2 Tests set-up description .....	153
4.4.3 Tests results .....	154
4.5 Fatigue tests of sharp V-notch specimens .....	159
4.5.1 Specimens dimensions and preparation .....	159
4.5.2 Tests set-up description .....	160
4.5.3 Tests results .....	161
4.6 S-N charts of all the tested specimens grouped by orientations: 0°, 45°, 90° .....	166
4.7 Calibration of the control radius $R_c$ for the PA12 material .....	168
4.7.1 Calculation of the NSIF $K_1$ for the PA12 sharp V-notch specimen's geometry .....	168
4.7.2 Calculation of the control radius $R_c$ for the PA12 material .....	175
4.8 SED approach for fatigue design of components made by PA12 material .....	177
4.8.1 Creation of the $\Delta W$ -N charts for the PA12 material .....	177
4.8.2 Application of the SED approach to the rounded V-notch specimens .....	182

<b>4.9 Upgrade of the results of Subchapter 4.7 and Subchapter 4.8 with a more realistic specimen's F.E.M. analyses constraints .....</b>	<b>190</b>
<b>Conclusion .....</b>	<b>205</b>
<b>References .....</b>	<b>207</b>
<b>Annex A: Ansys finite elements SOLID186 and SOLID187 comparison .....</b>	<b>208</b>
<b>Annex B: Linear elastic buckling F.E.M. analysis of a slender column and comparison with the Euler's theory .....</b>	<b>212</b>
<b>Annex C: Technical 2D drawings of the curved beam clamp system components .....</b>	<b>215</b>
<b>Annex D: Geometry of the PA12 and Maraging steel curved beams with the notches .....</b>	<b>224</b>
<b>Annex E: Tensile tests Stress - Strain charts of the PA12 plain specimens .....</b>	<b>228</b>
<b>Annex F: Measurements of the fillet radii of the rounded V-notch specimens .....</b>	<b>237</b>
<b>Annex G: Measurements of net widths of the sharp V-notch specimens .....</b>	<b>256</b>

# Introduction

This Master Thesis has been developed for most during an Erasmus program at the Faculty of Mechanical Engineering of Ljubljana's University.

The main objective of this master thesis was the development of an optimized inner support structure for a hollow curved beam made by additive manufacturing technology.

Have been done also a complete characterization of the PA12 material used, taking in account the three typical print orientations: 0°, 45°, 90°. The idea was to know deeply the material's characteristics to be able to perform static estimations and fatigue life estimations of components made by PA12 material and produced by Additive Manufacturing SLS technology.

## CHAPTER 1:

The additive manufacturing technology has been presented. The working principle has been explained and the advantages and disadvantages of using this technology have been illustrated. A continuous comparison with the traditional technologies has been done.

Furthermore, a complete comparison between the SLS and SLM technologies has been presented. These two technologies are the ones used to print the specimens developed in this thesis work. Has been done also a summary of the main constraints to pay attention while designing a component to be printed with these technologies.

In the end, have been explained, with an example, the most two critical phases to prepare a 3D CAD object into a file ready to be sent to a 3D printer to be printed.

## CHAPTER 2:

The main problem about realizing a hollow curved beam by additive manufacturing technology have been explained and has been presented the idea developed to solve it.

Has been defined a hollow curved beam geometry to work with and have been presented the different approaches that have been used to design the structural inner supports.

Have been designed the structural inner supports taking in account different load cases applied to the curved beam and F.E.M. analyses have been done to compare the different structural inner supports designed.

## CHAPTER 3:

Have been designed and realized a clamps system to be able of testing the curved beams developed.

Have been printed the most promising curved beams specimens designed and have been performed static and fatigue tests.

## CHAPTER 4:

Has been characterized completely the PA12 material. Have been performed tensile tests of PA12 plain specimens, have been performed fatigue tests of PA12 plain specimens, have been performed fatigue tests of PA12 specimens with a rounded V-Notch and have been performed fatigue tests of PA12 specimens with a sharp V-Notch.

Has been used the results of the fatigue tests of the PA12 plain specimens and of the PA12 specimens with a sharp V-Notch, to calibrate the control radius  $R_c$  of the PA12 material and to build the  $\Delta W-N$  charts for the PA12 material to be used to estimate the fatigue life of a component with the *Strain Energy Density* (SED) local approach [29].

Have been then applied the SED approach to the rounded V-notch specimens to validate the  $\Delta W-N$  charts developed, thanks to the data of the fatigue tests of the rounded V-notch specimens that have been performed.

# CHAPTER 1: The Additive Manufacturing

## 1.1 Technology overview and comparison with traditional technologies

In this subchapter the additive manufacturing technology has been presented. The working principle has been explained and the advantages and disadvantages of using this technology have been illustrated. A continuous comparison with the traditional technologies has been done since nowadays the materials that can be used in AM are comparable with the ones that can be used in traditional technologies.

*“Innovative and complex product design needs prototyping”.*

(Tony Fadell, creator of the iPod and founder of Nest [1])

The additive manufacturing technology was born and has been developed to produce prototypes because a component made by additive manufacturing is not constrained by the technical and economic limitations of traditional technologies.

The subtractive manufacturing technologies (Figure 1.1.1), like CNC machining, have several limitations regarding the complexity of an object's shape. A CNC machining operation requires for example accessibility for the tool to work the material, accessibility that it is not required by an AM technology. With AM technology it is possible to build objects inside objects at once, undercuts and internal features can be easily built without specific process planning.

The forming technologies (Figure 1.1.1), like injection molding, have in addition to objects' complexity limitations the problem that they are suitable only for high - volume production due to the very high initial cost of the molds production. It is possible to see in Figure 1.1.2 that the cost per parts of the AM technology is constant with respect to the number of parts manufactured. This is a very positive aspect if the number of parts to be manufactured is low mostly because of the higher initial investments that should be done with the forming or subtractive technologies. However, the constancy of the cost per parts become a negative aspect with the increasing of the number of parts to be manufactured, situation in which the forming and the subtractive technologies become very more competitive.

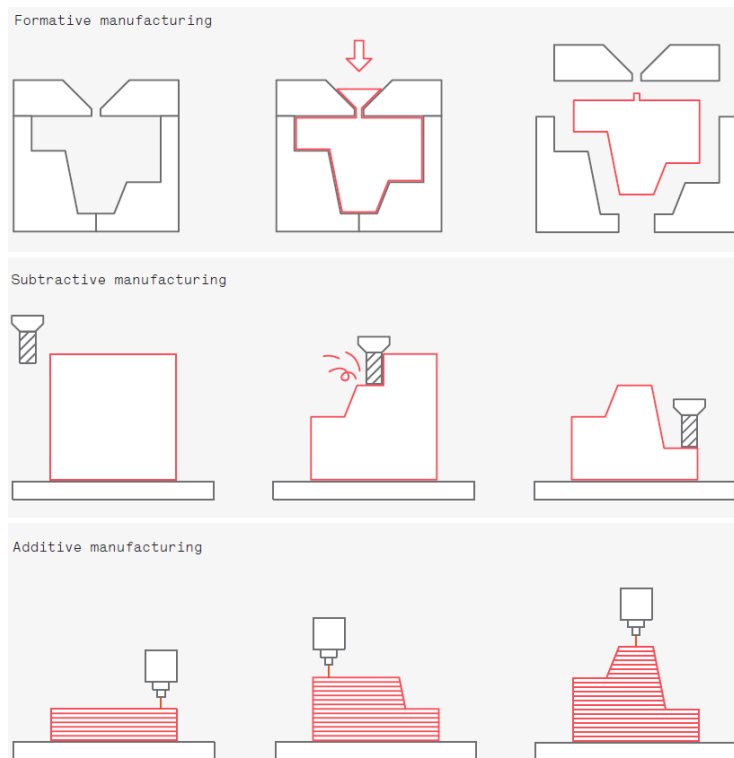


Figure 1.1.1: Schematic representation of the three main manufacturing technologies [1].

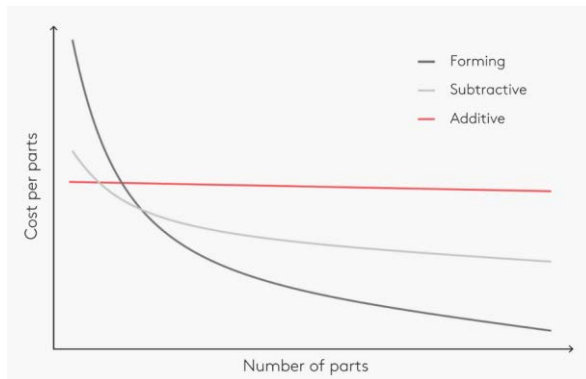


Figure 1.1.2: Economic comparison between the three main manufacturing technologies [2].

In the additive manufacturing technology not only the number of parts doesn't affect the cost per part, as said before in a positive or also in a negative way, but also "Complexity is for free" is a sentence that summarizes the fact that the complexity of an object doesn't impact the production cost and the production time if the AM technology is used as it would on the contrary do if other manufacturing technologies are used.

A very high complex geometry can be built with AM technology because of its general working principle. In opposition to the subtractive manufacturing technology, with AM technology an object is manufactured starting from zero material volume and adding material layer by layer until the entire object has been built (Figure 1.1.1). The amount of the material used is exactly the needed material for each layer to be manufactured (excluding the possible need of supports for printing the object (Figure 1.3.4). Supports to be removed after the object has been printed).

To be able to do that the 3D CAD of the object that has to be built, has to be transformed in an .STL file (the most common file type used in additive manufacturing process) and then sliced in several slices with an appropriate software. Each slice represents one layer and all the layers together shape the object. Deeper information with example images has been provided in the subchapter "1.3 From 3D CAD model to 3D printing". Furthermore, since this process from 3D CAD to AM production is not so time consuming and is not so difficult, thanks to the software that can help a lot the user, it is possible to say that with AM that "What You See Is What You Build (WYSIWYB)" [7]. This means that a proper 3D CAD design can be produced with AM technology very easily and quickly.

In the (Figure 1.1.3) it is possible to see a graphic summary of the considerations that have been done so far:

- AM is the best technology for high complex components and for low quantities even if the complexity of the components is low.
- If it is possible to realize the components with a CNC machine, this is the best choice when quantities become moderate (less than 250/500 pieces [2]) and it could be also a good choice for metal components even if the quantities are low.
- If it is possible to realize the components with forming technology this is in absolute the best choice when quantities become high (more than 250/500 pieces [2]).

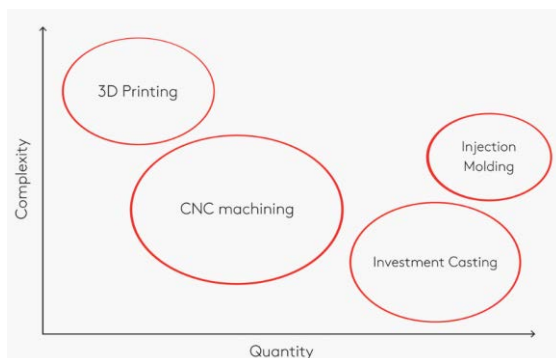


Figure 1.1.3: Graphic guide for the choice of the right manufacturing technology [2].



About disadvantages of AM technology, it is important to consider for example the lower dimensional accuracy compared to the CNC machining technology, this last one can indeed achieve at least one order of magnitude higher dimensional accuracy than AM technology [2]. For achieving very high dimensional accuracy, and/or a desired surface finish, the AM process should be combined with a conventional machining post-processing.

Another disadvantage of additive manufacturing technology is that, due to the lower resolution, lower detail capability is achieved with respect to the subtractive manufacturing technologies. The resolution of an AM machine can also vary among the three space directions X, Y, Z: the vertical build axis (Z) resolution corresponds to the layer thickness and this is typically lower with respect to the resolution of the two axes in the build plane (X, Y) [7].

In the following image it is possible to see a table with the pros and cons of AM technology well summarized (Figure 1.1.5):

PROS	CONS
<b>Part complexity</b>  Being a layer-by-layer fabrication process, this technology is capable of rendering geometries of great complexity, with cavities and forms not possible to obtain with traditional technologies.	<b>Detail/Precision</b>  Traditional technologies such as subtractive manufacturing have significantly more accuracy than additive manufacturing technologies. In general, it is $\pm 0.X00$ mm (AM) vs $0.XX0$ mm (Subtractive).
<b>Lead time (First part/short series)</b>  The ability to generate a part simply from a 3D file makes these technologies unbeatable when manufacturing a first part, since it eliminates the need for other technologies, such as tools or moulds.	<b>Long batches</b>  Although aspects such as speed and raw material costs are being continuously improved, when aiming to produce large amounts of parts/products, these technologies tend to be slower and more expensive than traditional ones.
<b>Customization</b>  Since no additional tooling is required, the manufacture of a modified part is as straightforward as the manufacture of the original design.	<b>Range of available materials</b>  Although the range of available materials is continuously improving (especially in the area of plastics and metals and, more recently, ceramics), it is still limited compared with the materials available for other technologies.
<b>Lower fixed costs for product development and first product series</b>  As no additional investments are required (tooling, moulds, etc.), it is possible to considerably lower the initial cost of producing prototypes and first series of products.	<b>Quality and certification</b>  As a relatively new technology, there are still some uncertainties and a lack of standards for assuring the long-term quality of the manufactured parts.

Figure 1.1.5: Table that summarize the pros and cons of AM technology [14].

There are several AM technologies distinguished by the phenomena they are based on and materials they are utilising (Figure 1.1.6, Figure 1.1.7, Figure 1.1.8, Figure 1.1.9):

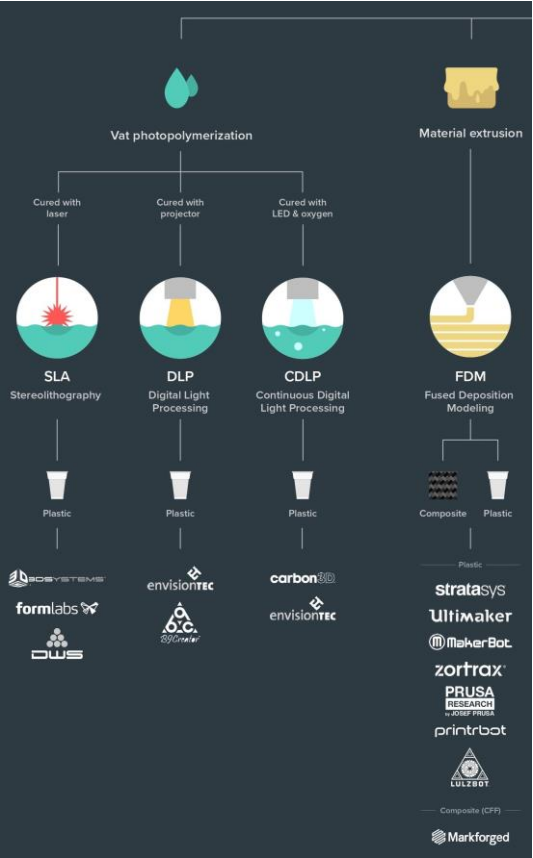


Figure 1.1.6: AM technologies [3].

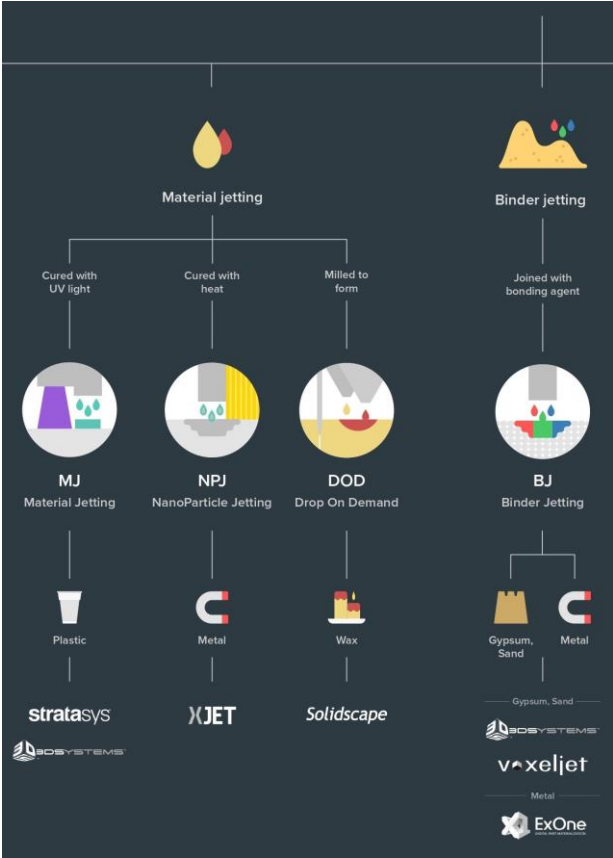


Figure 1.1.7: AM technologies [3].

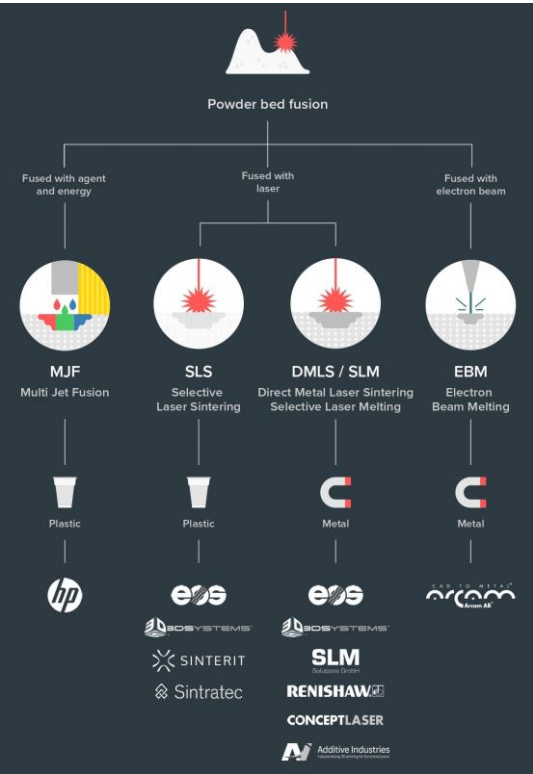


Figure 1.1.8: AM technologies [3].

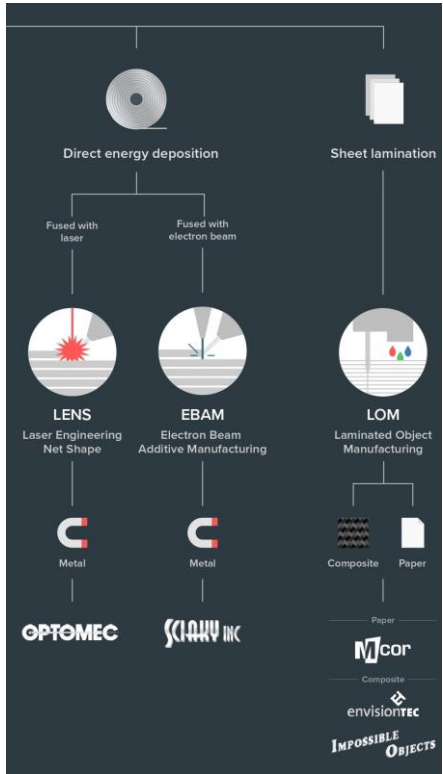


Figure 1.1.9: AM technologies [3].

## 1.2 Comparison between SLS and SLM technologies

In this subchapter a complete comparison between the SLS and SLM technologies has been presented. These two technologies are the ones used to print the specimens developed in this thesis work. The working principle of the two technologies has been explained and a focus in the differences between the materials used by the two technologies and in the performed material treatment has been done. Has been done also a summary of the main constraints to pay attention while designing a component to be printed with these technologies.

The SLS (Selective Laser Sintering) technology (Figure 1.2.1) and the SLM (Selective Laser Melting) technology (Figure 1.2.2) are very similar in terms of how the printer works to build layer by layer the desired object. They are both under the same category of PBF (Powder Bed Fusion) technologies indeed (Figure 1.1.8).

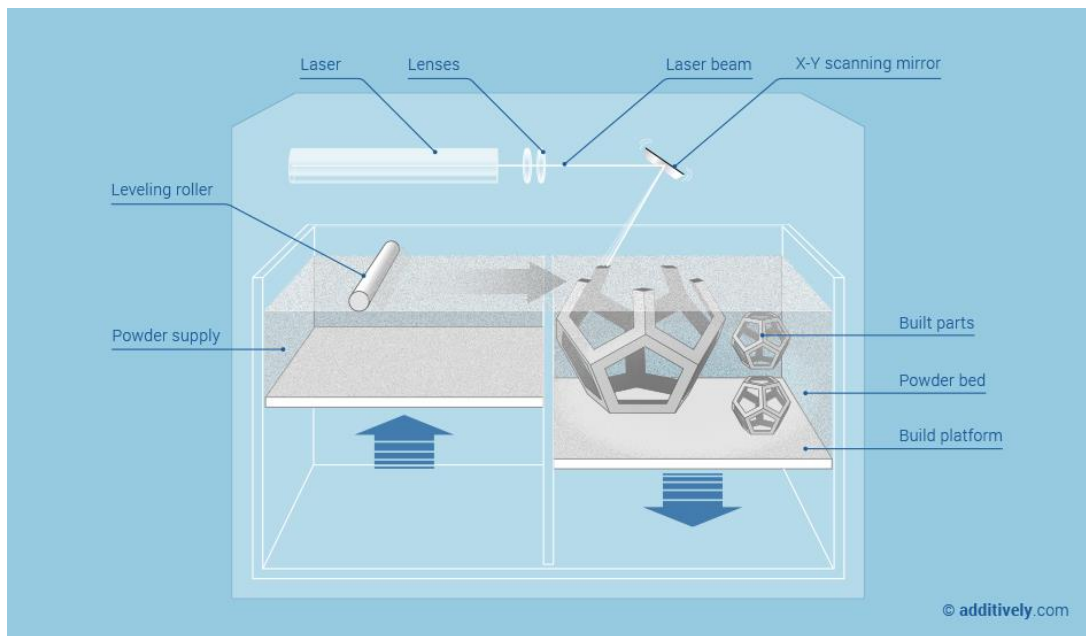


Figure 1.2.1: Schematic representation of an SLS technology 3D printer [4].

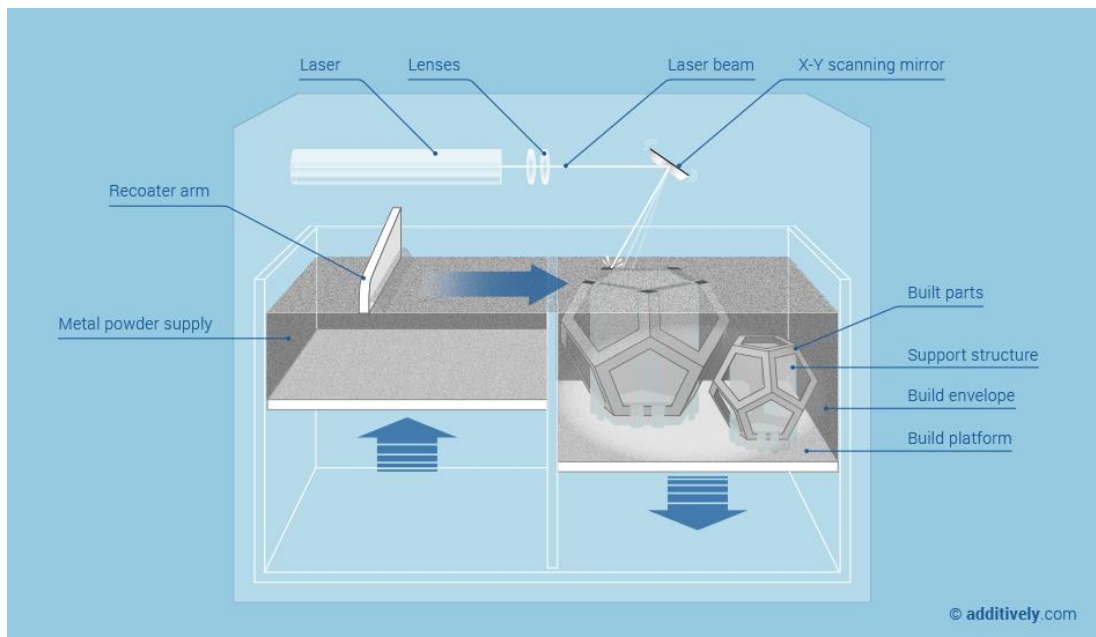


Figure 1.2.2: Schematic representation of an SLM technology 3D printer [5].

In Both the technologies there is a supply powder chamber that goes up by one layer thickness after a layer has been built and there is a roller/arm that transports the fresh powder from the supply chamber to the actual process chamber, chamber that goes down by one layer thickness after a layer has been built. The object is built layer by layer in the process chamber thanks to a laser beam that selectively treat each object's layer, one per time. The main differences between the two processes are the materials that can be produced, the aim of the laser beam treatment and the conditions of the process chamber.

Before going on with the technology's comparison, it is important to distinguish and clarify the powder fusion mechanisms that can be used in a PBF process:

- Solid-State Sintering (Figure 1.2.4): the powder particles fuse together in a solid state, without melting. This occurs at elevate temperature between one half of the absolute melting temperature and the melting temperature. With this mechanism the powder's particles link themselves by forming a "neck" that increase with the increasing of sintering time, sintering temperature and eventually isostatic sintering pressure. Smaller particles sinter more rapidly and initiate sintering at lower temperature than larger particles [7].

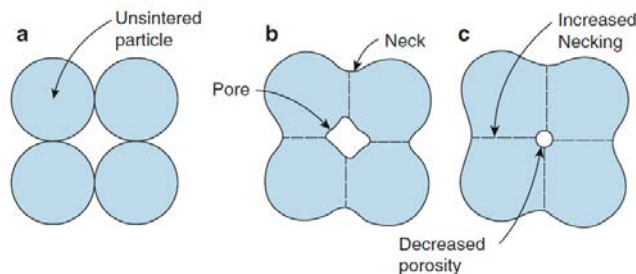


Figure 1.2.4: Representation of the three phases of the Solid-State Sintering [7].

- Chemically Induced Sintering: the powder particles are bonded together by a product that has been formed with thermally activated chemical reactions that can happen between two types of powders or between the powders and the atmospheric gases. This mechanism is primarily utilized for ceramic materials [7].
- Liquid Phase Sintering (LPS): some powder particles remain solid (powder particles of the high temperature material) and some powder particles become molten (powders particles of the lower-melting-point constituents), the molten particles act as a glue that bonds together the other solid particles. The big advantage is that it is possible to bond together particles of high temperature materials without sintering or melting them directly [7].
- Full Melting: the powder particles are fully melted and, if the laser is enough powerful to melt a little bit also the previous layer of material, the result is a fully dense and homogeneous component [7].

*“Regardless of whether a technology is known as “Selective Laser Sintering,” “Selective Laser Melting,” “Direct Metal Laser Sintering,” “Laser Cusing,” “Electron Beam Melting,” or some other name, it is possible for any of these mechanisms to be utilized (and, in fact, often more than one is present) depending upon the powder particle combinations, and energy input utilized to form a part.”* [7].

With this sentence in mind in the following part of the subchapter the main differences between SLS and SLM technologies will be explained but it is important to not focus too much on the name of the technology but to focus instead on the particular material that has to be printed.

The SLS process is especially suitable for producing objects from thermoplastic polymers powders, the most used is the polyamide (polyamide 11 and polyamide 12 are commercial available): it is a semi-crystallin material, so, in opposition to an amorphous material, it has a defined glass transition temperature, a defined crystallization temperature and a defined melting temperature (Figure 1.2.3). Knowing this material thermal behaviour is very important for being able to set-up a proper and

reliable AM process: the sintering temperature window is around the glass transition temperature ( $T_g$ ) for an amorphous material and it is between the crystallization temperature ( $T_c$ ) and the melting temperature ( $T_m$ ) for a semi-crystalline material.

For a semi-crystalline material If during the print process the temperature is too close to the crystallization temperature a distortion of the printed object can occur, if the temperature is too close to the melting temperature a definition loss of object's parts can occur. For this last reason the full melting condition, even if it would be the best option for having the strongest components possible, is avoided. So, the laser, usually a CO<sub>2</sub> one, melts smaller powder particles and the outer regions of larger powder particles without melting the entire structure (Figure 1.2.4). To label this phenomenon LPS or just "partial melting" is a matter of debate [7].

In the SLS technology the process chamber is uniformly preheated to a temperature just below the  $T_g$  for an amorphous material and to a temperature just below  $T_m$  for a semi-crystalline material, this is necessary to minimize the laser power requirements for the powder's treatment process and to prevent warping of the part during the build due to nonuniform thermal expansion and contraction [7]. Another consequence of the preheating of the powders in the process chamber is that some small particles begin to sinter together with Solid-State Sintering mechanism and for this reason is not possible to recycle all the unused powders. It is possible to mix them in a certain % with fresh powders to obtain a powder mix with good maintained forming characteristics [7].

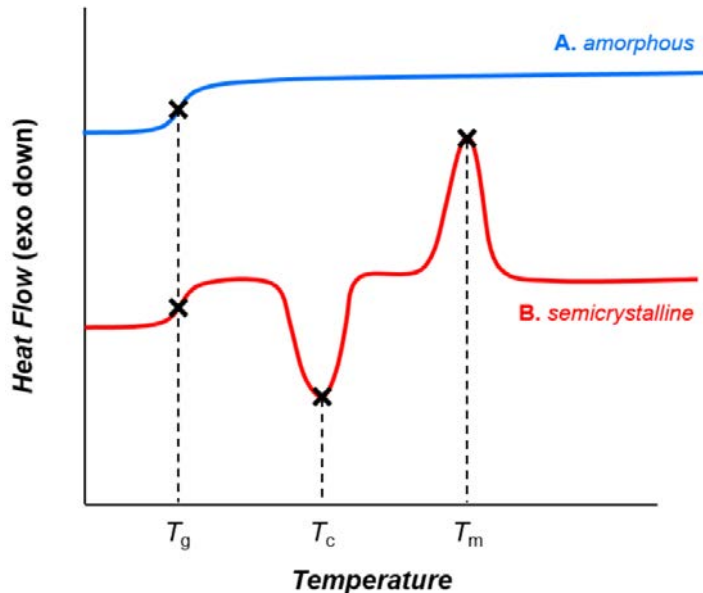


Figure 1.2.3: Essential phase transitions of an amorphous and crystalline polymer [6].

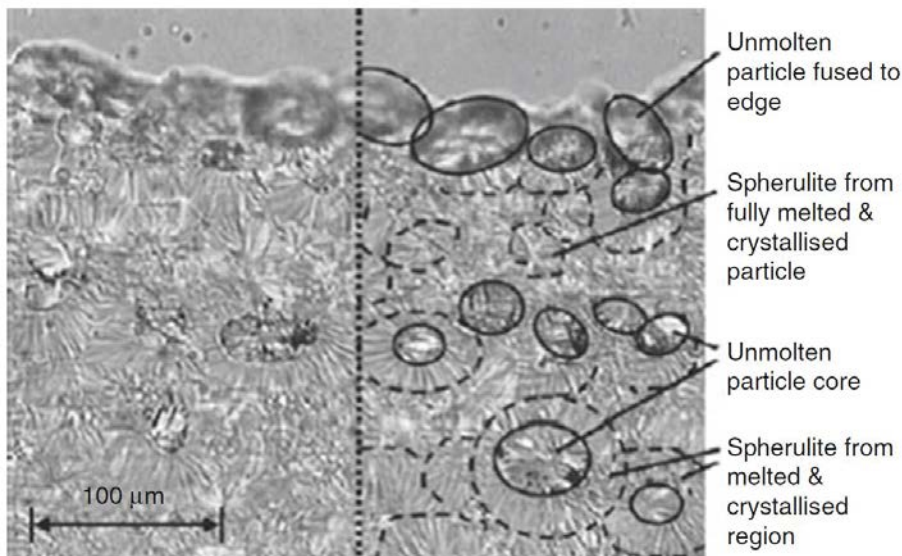


Figure 1.2.4: Typical microstructure of polyamide material 3D printed with SLS technology [7].



For the SLS process the post-processing treatments are:

- Cleaning the object from the untreated powders that can still be weakly attached to the object.
- Using traditional machining processes to achieve desired surface finish or tolerances.

The SLM process is suitable for producing objects from the powders of any metal that can be welded, like for example stainless and tool steels, titanium and its alloys, nickel-base alloys, some aluminium alloys, and cobalt-chrome [7].

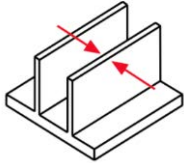
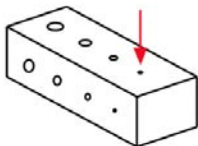
In the SLM process the laser beam selectively heats the powder layer to reach the condition of Full Melting, the metal powders are so welded together. The result is a homogeneous full dense component. The components produced by SLM usually don't have unexpected failure problems due to the almost absence of internal porosity.

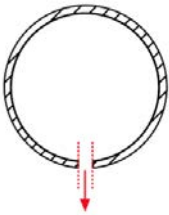
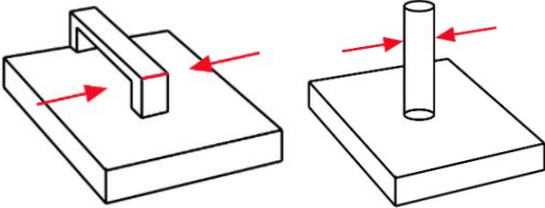
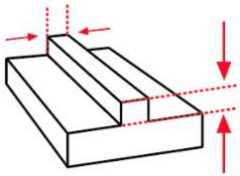
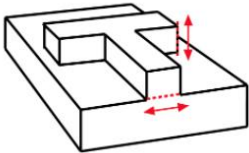
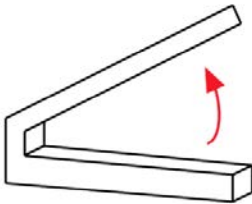
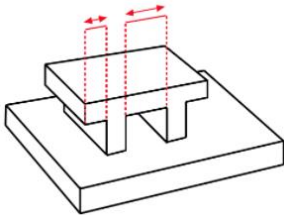
In the SLM technology the process chamber is uniformly preheated to a temperature just below the  $T_m$  of the metal material to be printed, this is necessary to minimize the laser power requirements for the powder's treatment process and it can lead to lower thermal tensions on the parts [14]. Another consequence of the preheating of the powders in the process chamber is that since all the powders achieve a pre-melting stage it is not possible to recycle all the unused powders. It is possible to mix them in a certain % with fresh powders to obtain a powder mix with good maintained forming characteristics. Furthermore, the process chamber of an SLM 3D printer is in a controlled atmosphere of inert gas in a low oxygen environment (less than 500 parts per million) [14]. This is because, as in a traditional welding process, the inert gas prevents oxidation of the material when it is in the fuse state.

For the SLM process the post-processing treatments are:

- Cleaning the object attached to the build platform from the untreated powders that can still be weakly attached to the object.
- Performing a thermal treatment of the object attached to the build platform to release the residual stresses that are consequences of the printing.
- Using traditional machining processes to separate the object from the build platform removing all the created supports.
- Using traditional machining processes to achieve desired surface finish or tolerances.

In the table below it is possible to see all the main constraints to pay attention while designing a component to be printed with SLS or SLM technology (Table 1.2.1):

	<b>SLS</b>	<b>SLM</b>
<p>Minimum wall thickness</p> 	0.7 mm (PA12)	0.4 mm
<p>Minimum hole diameter</p> 	1.5 mm	0.5 mm

<p>Minimum diameter for powder escape holes</p> 	3.5 mm	2-5 mm recommended
<p>Minimum feature size (Pins, protruding features, etc.)</p> 	0.8 mm	1 mm
<p>Embossed and engraved details</p> 	<p>Minimum depth of engraving 1 mm.</p> <p>Minimum height of embossing 1 mm.</p>	/
<p>Text</p> 	<p>Minimum font height of 2 mm (font size 14) suitable for every direction.</p> <p>Sans serif font is recommended for readability.</p>	/
<p>Overhanging support required</p> 	NO supports needed	Angle < 45° relative to the horizontal
<p>Maximum length of unsupported edges</p> 	NO supports needed	<p>0.5 mm for "cantilever" structure</p> <p>1 mm for "simple beam" structure</p>

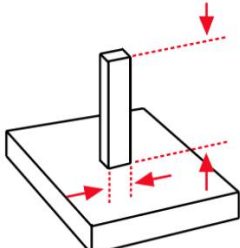
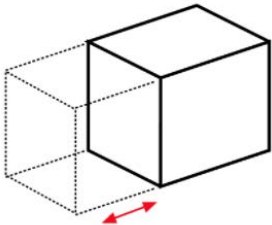
Maximum aspect ratio (height / section width) 	/	8:1
Tolerances 	The greater between $\pm 0,3$ mm and $\pm 0,05$ mm/mm	In the print direction, Z, is $\pm 1$ layer thickness In the XY plane is $\pm 0,127$ mm
Minimum layer thickness	0,1 mm	0,02 mm
Change of mechanical properties of parts printed with different directions	Almost isotropic behaviour of parts printed with different directions	Almost isotropic behaviour of parts printed with different directions

Table 1.2.1: Main constraints to pay attention while designing a component to be printed with SLS or SLM technology [8], [9].

It is important to know that all the constraints that are illustrated in the table above (Table 1.2.1) are a general rule of thumb to not make big mistakes while designing a component to be printed with the two technologies taken in account. Since the knowledge of 3D printing still developing very fast that constraints can vary company to company because a different 3D printing machine with different settings can achieve very better, or worst, results than another one.

About the minimum length of unsupported edges, has been found for example in [12] that it is possible to achieve 2 mm of "simple beam" unsupported structure with SLM technology instead of the 0,5 mm claimed by the table above (Table 1.2.1).



### 1.3 From the 3D CAD model to the 3D print

In this subchapter have been explained, with an example, the most two critical phases to prepare a 3D CAD object into a file ready to be sent to a 3D printer to be printed. These two main phases are always to be done regardless from the AM technology that will be used to print the object then. The phases are:

- Conversion of the 3D CAD model into an STL (Standard Triangulation Language) geometry.
- Slicing the STL geometry to divide it in slices that will be the layers that the printer will print, one per time.

The first critical phase for achieving a good quality product is the transformation of the 3D CAD model of the object in to an STL geometry. During the transformation the key factor is the approximation of all the surfaces of the original CAD object in surfaces made by triangles: more is the number of triangles that compose the STL mesh and better is the geometric accuracy of the object when the surfaces are not plane (Figure 1.3.1). So, to set the appropriate triangles number / dimension is very important especially when the object has curvature and/or small features.

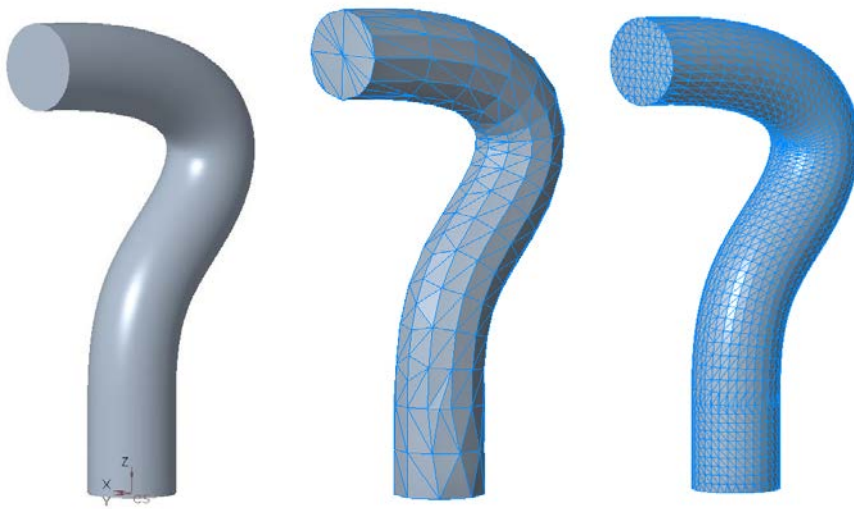


Figure 1.3.1: On the left is represented the 3D CAD model, in the middle is represented an STL conversion with a rough mesh and on the right is represented an STL conversion with a finer mesh.

Moving on to the second phase, the slicing process, it consists in dividing the obtained STL geometry into slices. Every slice corresponds at one layer that will be printed by the printer. The number of slices and so the number of layers and so the layer thickness is a very important parameter that must be set properly to obtain the desired geometric accuracy of the component. Thinner the layer better the surface finish of the object and better the curvatures and/or small features of the object (Figure 1.3.2, Figure 1.3.3). Thinner the layer bigger the print time. The layer thickness range is a property of the 3D printing technology and material that will be used to print the object. For example, for the SLS technology the layer thickness range is: 0,1 – 0,3 mm.

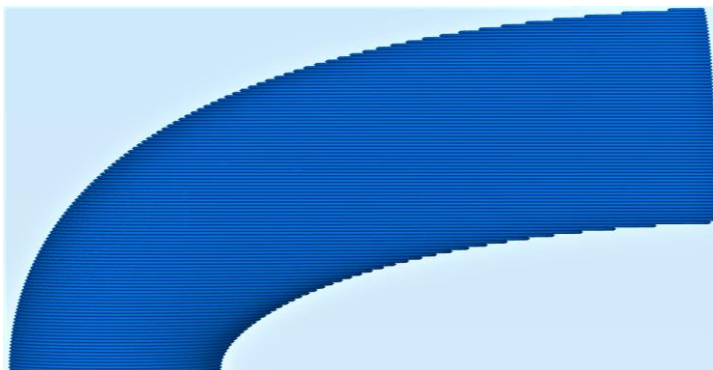


Figure 1.3.2: Slicing process with a 0,3 mm layer thickness.

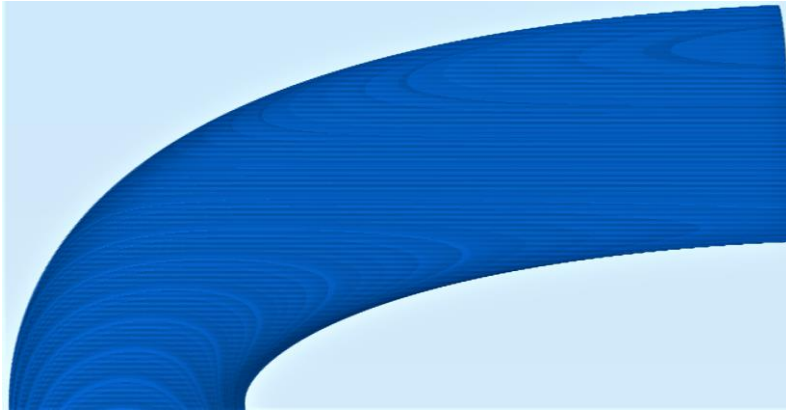


Figure 1.3.3: Slicing process with a 0,1 mm layer thickness.

During the slicing process, not only the object is divided in slices but also support structures are created to sustain the object's zones that are in an overhang condition (Figure 1.3.4). An overhang condition of some object's zones means that the angle between the object's zones and the vertical print direction is greater than a certain limit value. The angle limit value is a property of the 3D printing technology and material that will be used to print the object. A typical angle limit value is  $45^\circ$ . For example, if the technology that will be used is the SLS no supports at all are needed (Table 1.2.1), if the technology that will be used is the SLM the angle limit value is indeed  $45^\circ$  (Table 1.2.1).

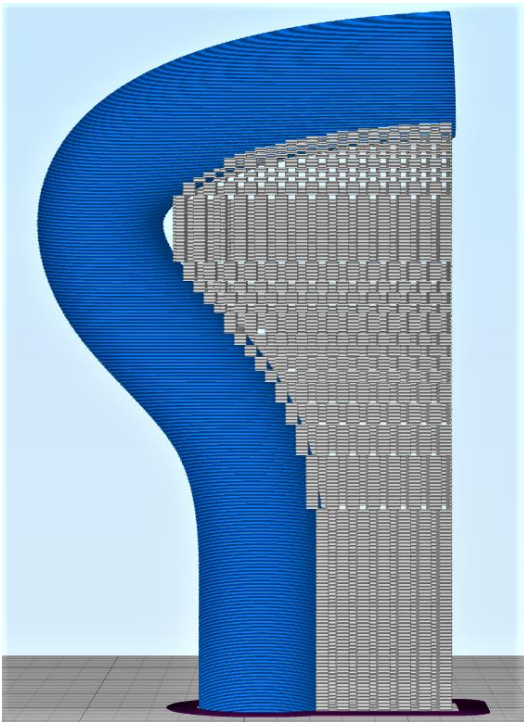


Figure 1.3.4: Sliced object in blue and needed supports in grey ready to be printed.

In the end, during the slicing process it is very important also to orient the object smartly: different orientations of the object can lead to very different supports needing (A simple example of this idea is shown in Subchapter 2.2.1.) and very different quality result of the printed object, usually quality of surface finishing. Furthermore, the orientation of the object during the slicing process can impact a lot on the mechanical characteristics of the printed one if the printing technology is an anisotropy one, like for example the FDM (Fused Deposition Material). If anisotropy technology is used, a good rule of thumb is to orient the object to be sliced in the way that the forces that will be applied to the real printed object will not be perpendicular to the sliced layers. The reason of this is that usually the biggest problem of a printed object with an anisotropy technology is the not perfect adhesion between the layers.

## CHAPTER 2: Structural inner support development for hollow curved beams

### 2.1 Problems in hollow curved beams made by additive manufacturing

The main problem about realizing a hollow curved beam by additive manufacturing technology is that if an inner support is required and if the beam has a complex shape then it is difficult or almost impossible to remove the inner support structure with conventional post-processing machining.

To solve this problem the idea developed in this thesis is that if the inner support is necessary for the successful printing of the hollow curved beam, why not to design it not only with material sustain capabilities but also design it to be part of the complete beam structure itself. The inner support structure should be light weight and it should be able to carry, at least partially, the load applied to the curved beam. Following this idea, the design phase of the inner support structure is no more done after the design of the component, but it is done in the design phase of the component.

An example of a practical application of a hollow curved beam structure are the structures of an automotive suspension system. In Figure 2.1.1 it is possible to see an example of Alfa Romeo suspension system and it is possible also to see that there are hollow curved beam type structures. For rapid prototyping such structures during the first testing phase a lightweight structural inner support would be very useful.

1. An upper control arm;
2. Two decoupled lower links (handling and comfort link);
3. A tie-rod steering arm;
4. A co-axial spring and shock absorber group;
5. A hollow aluminium knuckle.

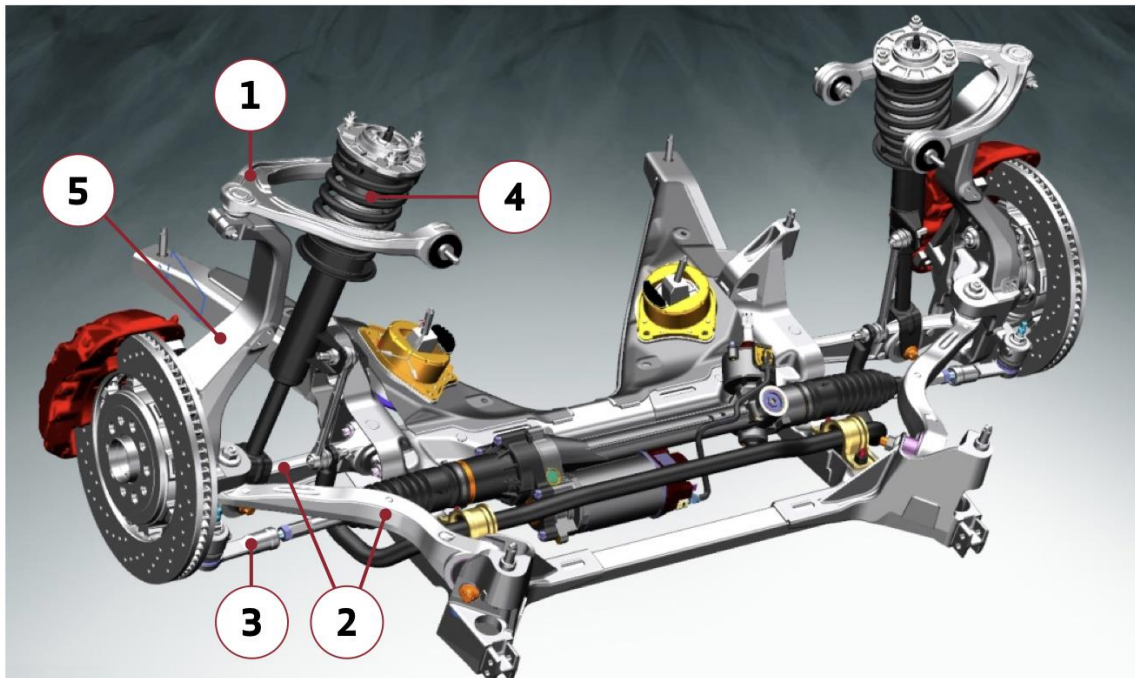
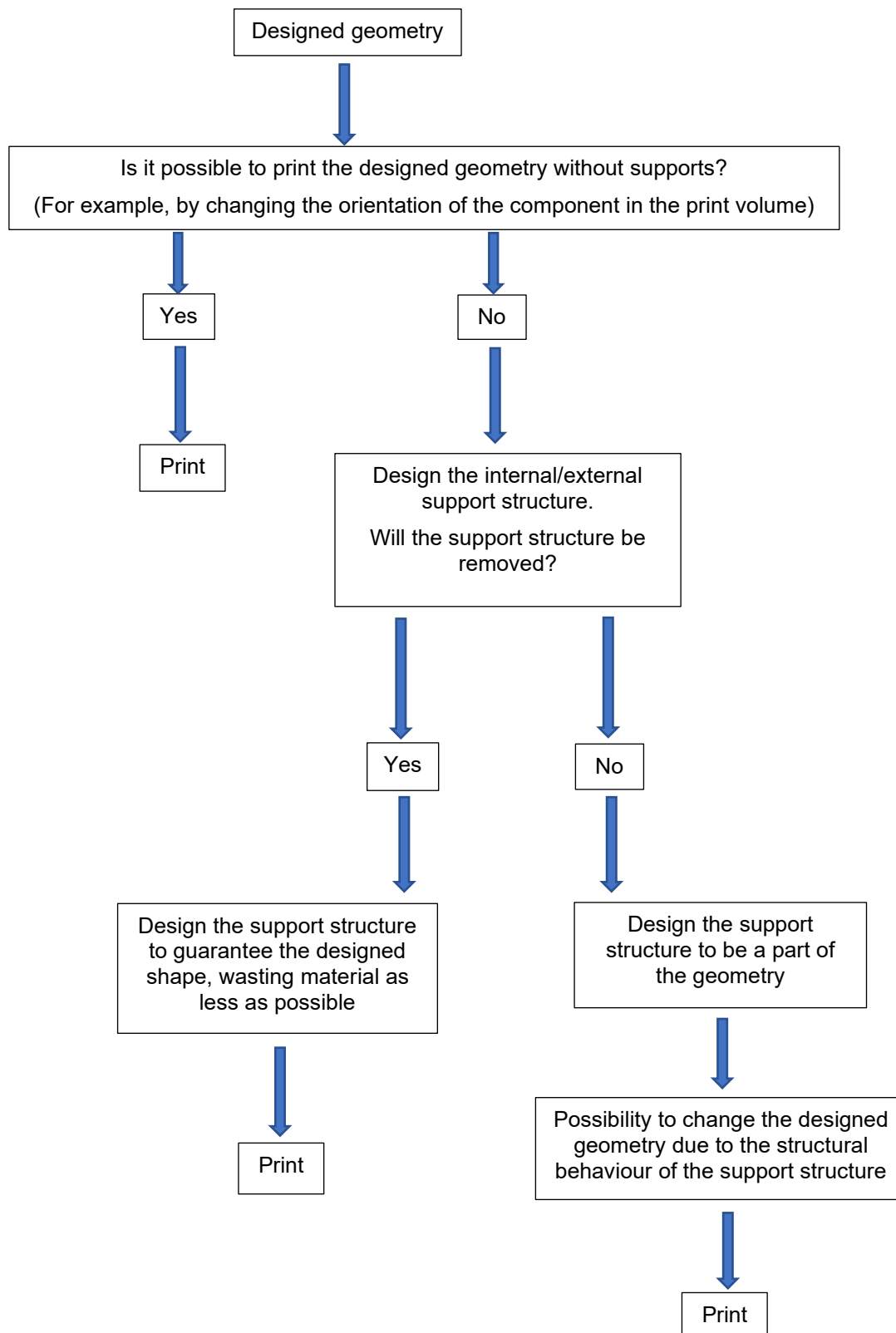


Figure 2.1.1: Alfa Romeo Giulia front suspension system [13].

In the following flow chart have been schematized the concepts expressed above, have been presented the steps to follow for approaching a supports design problem for additive manufacturing:



## 2.2 Hollow curved beam geometry definition and developing methods for a structural inner support

### 2.2.1 Hollow curved beam outer geometry definition

Has been decided to design a single curvature curved beam (Figure 2.2.1.2) with a hollow square section (Figure 2.2.1.1).

At both ends of the curved beam have been left straight two zones 20 mm length for being able of clamping the beam during the laboratory tests (Figure 2.2.1.2).

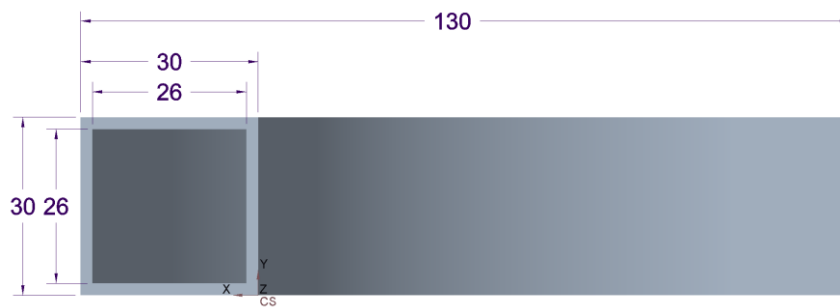


Figure 2.2.1.1: XY-plane view of the hollow curved beam (mm).

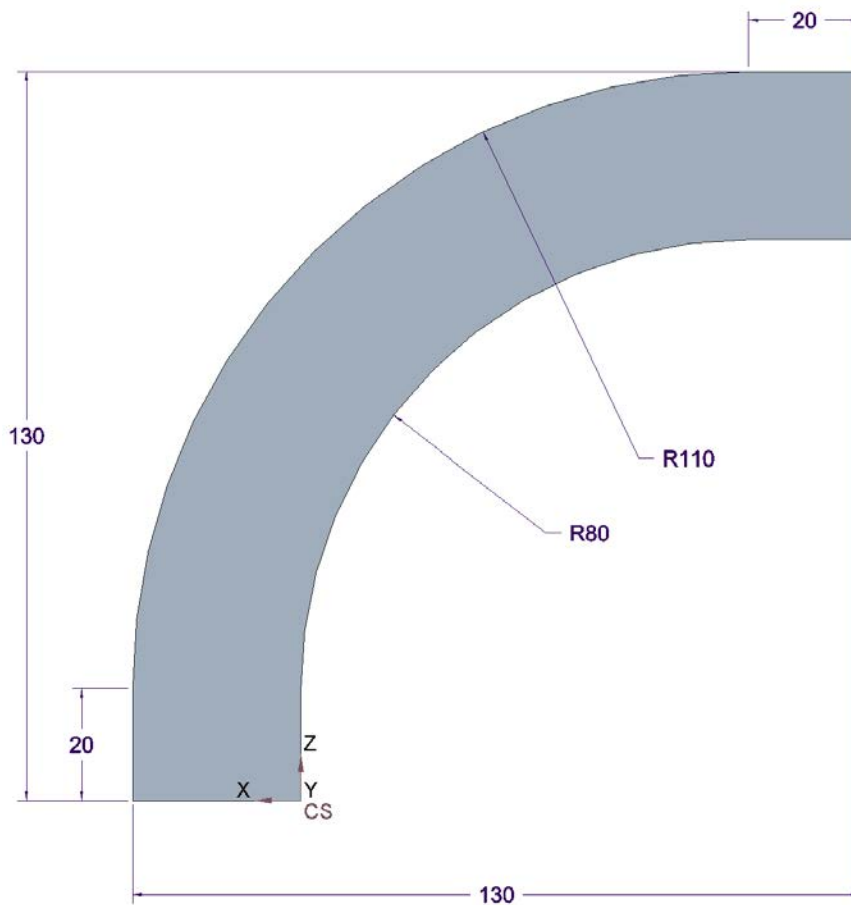


Figure 2.2.1.2: XZ-plane view of the hollow curved beam (mm).

## 2.2.2 Developing methods for a structural inner support

Taking in account the curved beam geometry showed in the previous Subchapter 2.2.1, the supports needed for a successful printing of the curved beam are related to the print direction and to the position of the object in the print volume (Figure 2.2.1.3):

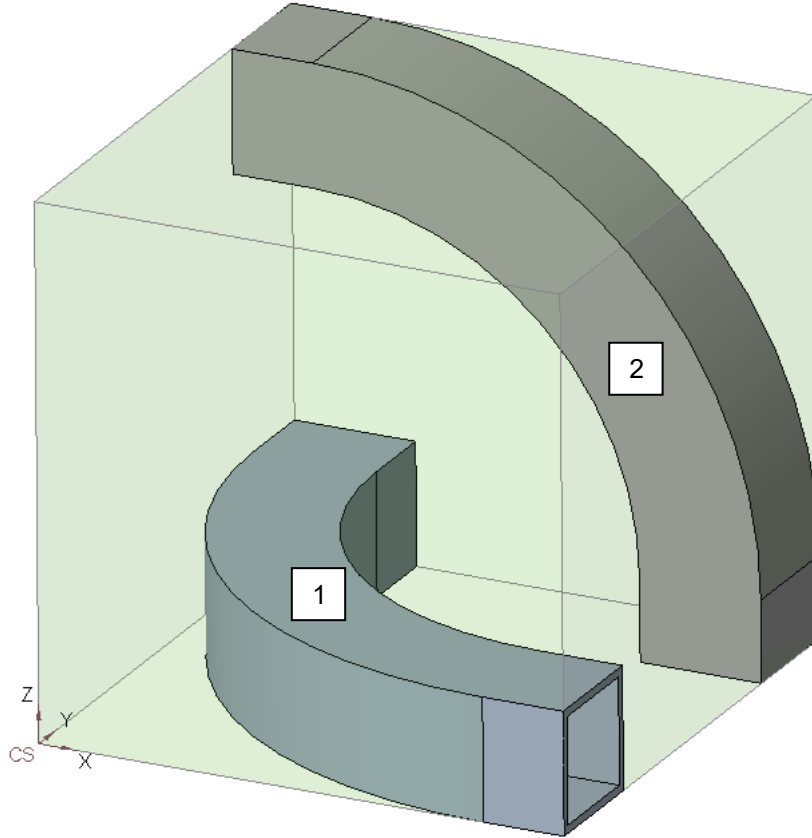


Figure 2.2.1.3: Two different placements of the hollow curved beam in the print volume.

For example, if the print direction is fixed as the Z axis:

- The light grey beam (1) needs no external support structure, but it needs an internal support structure along all the beam because the angle between the inner upper surface and the printing Z axis is  $90^\circ > 45^\circ$ .
- The dark grey beam (2) needs both external and internal support but only along the portion of the beam where the angles between the surfaces and the printing Z axis are greater than  $45^\circ$ .

Have been showed the most two intuitive possibilities to orient the beam in the print volume. With the idea in mind that it is possible to translate and rotate the object of interest in a 3D space (the print volume), an infinite number of orientations would be possible and it would be possible also to find the optimum one, with a mathematical approach after some constraints have been defined. In this thesis work the print orientations of the curved beam have been always defined by following some mathematical suggestions, that vary by the approach used to build the inner support structure, but has not be developed/used a mathematical tool made for the decision of the optimal print orientation.

Have been instead developed some guidelines that include the main steps to follow for the successful design of a structural inner support, depending on the approach that the designer wants to follow. The four different approaches (A, B, C, D) that have been used in this thesis work are now presented, the approaches have been focused in the developing of a structural inner support for a hollow curved beam but it would be possible also to apply them in other contexts of structural supports developing.

- A) Iterative - intuitive optimization (Subchapter 2.4): Design a support pattern made of self-supporting structure.

The steps to follow are:

- 1) To know the outer geometry of the beam.
- 2) To know the boundary conditions (Loads and Constraints).
- 3) To make a F.E.M. analysis of the beam full of material and to look at maximum principal stress, minimum principal stress, maximum shear stress.
- 4) To take in account the isotropic/anisotropic nature of the print technology used.
- 5) To orient the beam into the print volume to be able to design the structural inner support adding material where the principal stresses are higher.
- 6) To design the pattern of the self-supporting structural inner support.

- B) Mathematical design optimization (Subchapter 2.5): Topology optimization of the beam full of material, fixing the outer geometry as non-design space and using the result to decide how to place the beam in the print volume to be able to design an optimized self-supporting inner structure.

The steps to follow are:

- 1) To know the outer geometry of the beam.
- 2) To know the boundary conditions (Loads and Constraints).
- 3) To make a topology optimization of the beam full of material fixing the outer geometry as non-design space and to see the result of the retained material placement.
- 4) To take in account the isotropic/anisotropic nature of the print technology used.
- 5) To orient the beam into the print volume to be able to design the structural inner support adding material where the topology optimization placed the retained material.
- 6) To design the self-supporting structural inner support taking in account the placement of the retained material of the topology optimization.

- C) Mathematical design optimization (Subchapter 2.6): Topology optimization of the beam full of material fixing the outer geometry as non-design space and specifying an *overhang constraint* related to the print direction to obtain a component ready to print directly from the topology optimization.

The steps to follow are:

- 1) To know the outer geometry of the beam.
- 2) To know the boundary conditions (Loads and Constraints).
- 3) To take in account the isotropic/anisotropic nature of the print technology used.
- 4) To make a topology optimization of the beam full of material fixing the outer geometry as non-design space and specifying an overhang constraint related to the print direction.
- 5) To take the topology optimized geometry.

- D) Mathematical design optimization (Subchapter 2.7): Lattice optimization of the beam full of material.

The steps to follow are:

- 1) To know the outer geometry of the beam.
- 2) To know the boundary conditions (Loads and Constraints).
- 3) To take in account the isotropic/anisotropic nature of the print technology used.
- 4) To make a variable density lattice optimization of the beam full of material, choosing a proper lattice type together with the orientation of the curved beam into the print volume, to being able of using the lattice structure as a structural inner support.
- 5) To build the optimized lattice structural inner support.

## 2.3 Load Cases definition

In this thesis work have been taken in account different load cases with the common aim of making the curved beam working with bending and torsional stresses. In the following subchapters have been presented all the load cases that have been used in this thesis work for developing the structural inner supports for the hollow curved beam. For each load case, first have been presented the boundary conditions and then has been presented the Von Mises equivalent stress, result of a F.E.M. analysis of the beam full of material. The Von Mises equivalent stress of the beam full of material has been presented because the arrangement of the stresses in the beam full of material has been the starting point of every four different methods (Subchapter 2.2.2) that have been used for the developing of the structural inner support.

For every F.E.M. analysis, topology optimization and lattice optimization that are described in Chapter 2, has been used as material the Ansys default Structural Steel. The useful properties of this material are presented in the table below (Table 2.3.1):

Density [kg/m <sup>3</sup> ]	7850
Young's Modulus [MPa]	200000
Poisson's Ratio [/]	0,3
Tensile Yield Strength [MPa]	250
Tensile Ultimate Strength [MPa]	460

Table 2.3.1: Main properties of Ansys default Structural Steel material used in chapter 2.

About the Von Mises equivalent stress results presented in Subchapter 2.3, have been performed static structural F.E.M. analyses of the beam full of material with the main parameters presented in the table below (Table 2.3.2):

Material	Ansys default Structural Steel (Table 2.3.1)
Mesh Element Type	SOLID186
Mesh Element Order	Quadratic
Mesh Global Size	1 mm
Mesh Target Quality	0,6

Table 2.3.2: Main parameters of the static structural F.E.M. analyses performed in Subchapter 2.3.



### 2.3.1 Load Case 1

The Load Case 1 is the simplest load case that has been developed, it consists in a fixed support applied in the face at one end of the beam and in a single force of - 800 N directed along the Y-axis applied in the face at the other end of the beam (Figure 2.3.1.1).

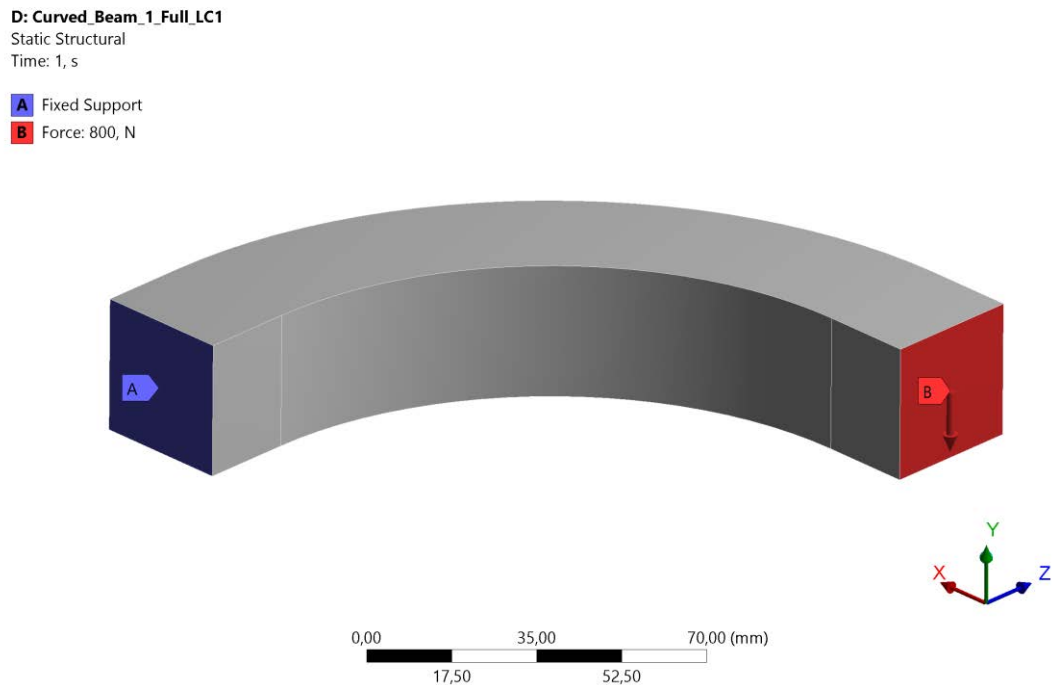


Figure 2.3.1.1: Boundary conditions of Load Case 1.

In the image below it is possible to see the Von Mises equivalent stress of the beam full of material with the Load Case 1 applied (Figure 2.3.1.2):

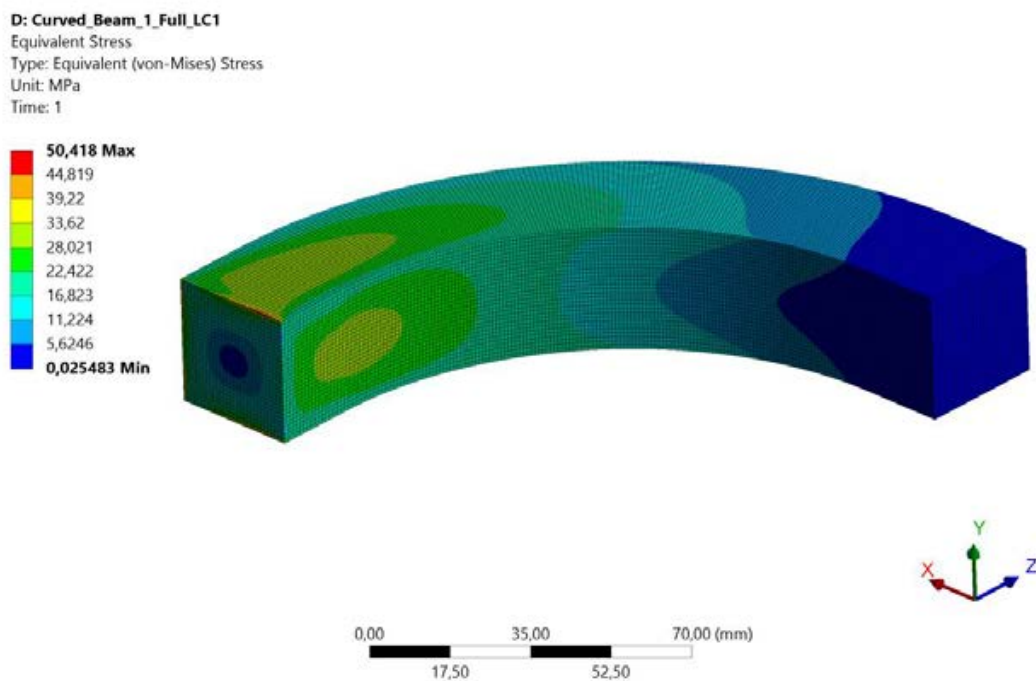


Figure 2.3.1.2: Von Mises equivalent stress of the curved beam full of material with Load Case 1 applied.

### 2.3.2 Load Case 2

The Load Case 2 is a more complicated load case with respect to the Load Case 1. In this load case there is a fixed support applied in the face at one end of the beam and there are two different loads applied in the face at the other end of the beam: the first load is a  $-800\text{ N}$  force directed along the Y-axis and the second load is a  $+80\text{ Nm}$  moment direct along the X-axis (Figure 2.3.2.1).

E: Curved\_Beam\_1\_Full\_LC2

Static Structural

Time: 1, s

- A** Fixed Support
- B** Force: 800, N
- C** Moment: 80000 N-mm

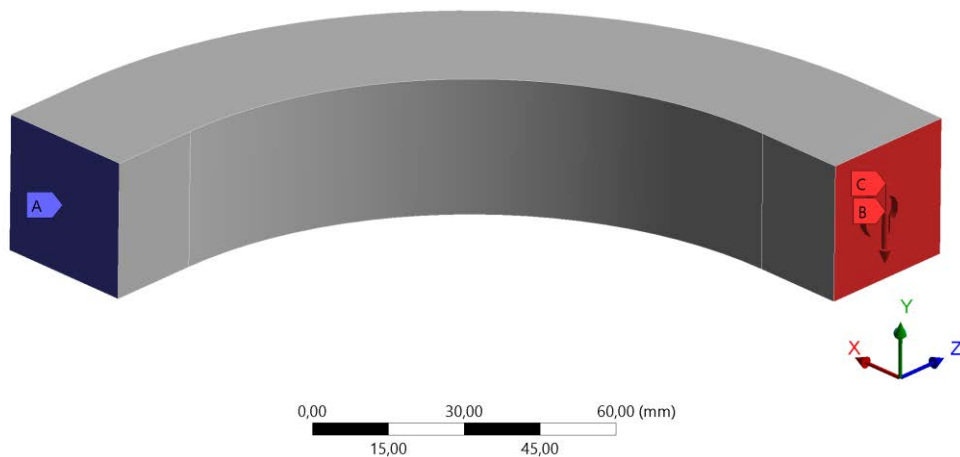


Figure 2.3.2.1: Boundary conditions of Load Case 2.

In the image below it is possible to see the Von Mises equivalent stress of the beam full of material with the Load Case 2 applied (Figure 2.3.2.2):

E: Curved\_Beam\_1\_Full\_LC2

Equivalent Stress

Type: Equivalent (von-Mises) Stress

Unit: MPa

Time: 1

- 80,108 Max
- 71,21
- 62,311
- 53,412
- 44,513
- 35,614
- 26,715
- 17,816
- 8,917
- 0,018035 Min

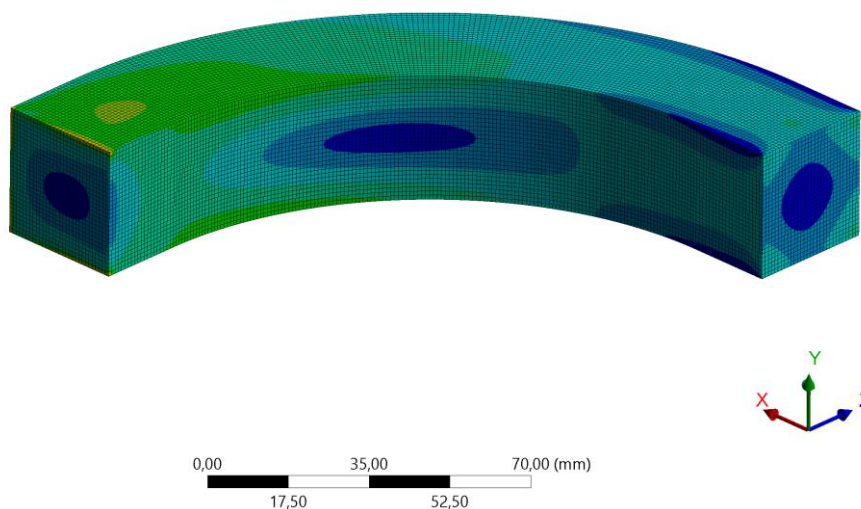


Figure 2.3.2.2: Von Mises equivalent stress of the curved beam full of material with Load Case 2 applied.

### 2.3.3 Load Case 3

The Load Case 3 is very similar to the Load Case 2, but the applied moment is now a – 80 Nm moment directed along the X-axis (Figure 2.3.3.1).

#### E: Curved\_Beam\_1\_Full\_LC3

Static Structural

Time: 1, s

**A** Fixed Support

**B** Force: 800, N

**C** Moment: 80000 N-mm

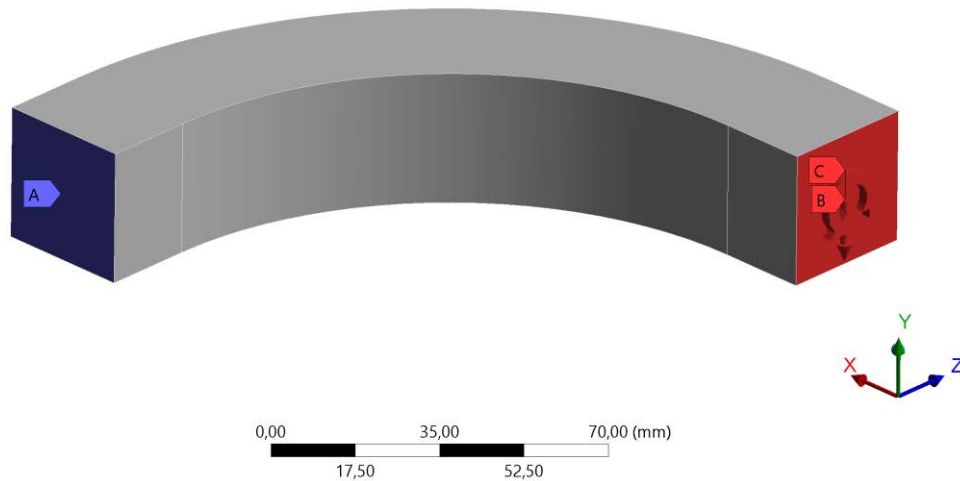


Figure 2.3.3.1: Boundary conditions of Load Case 3.

In the image below it is possible to see the Von Mises equivalent stress of the beam full of material with the Load Case 3 applied (Figure 2.3.3.2):

#### E: Curved\_Beam\_1\_Full\_LC3

Equivalent Stress

Type: Equivalent (von-Mises) Stress

Unit: MPa

Time: 1

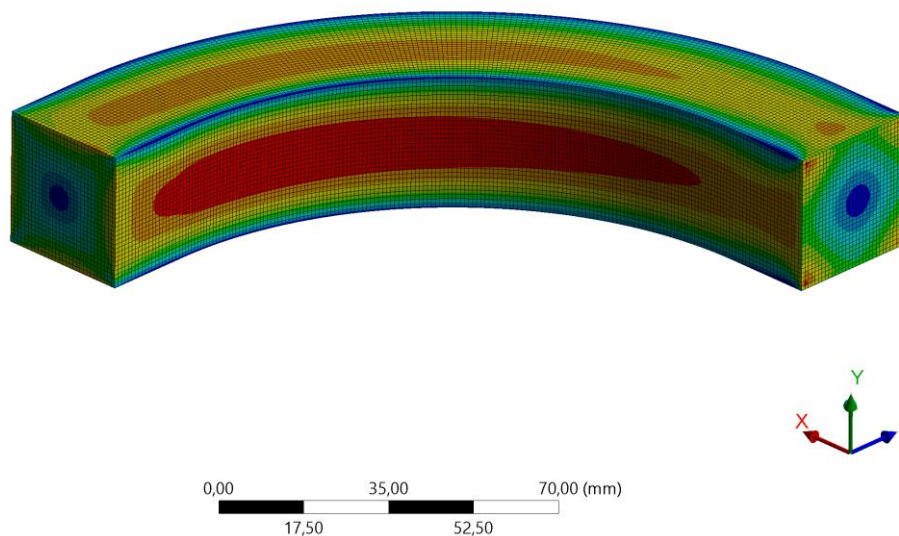
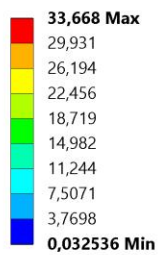


Figure 2.3.3.2: Von Mises equivalent stress of the curved beam full of material with Load Case 3 applied.

### 2.3.4 Load Case 4

The Load Case 4 is very similar to the load case 1, there is as usual a fixed support applied in the face at one end of the beam and there is a single force of 800 N, this time directed along the Z-axis, applied in the face at the other end of the beam (Figure 2.3.4.1).

**F: Curved\_Beam\_1\_Full\_LC4**

Static Structural

Time: 1, s

**A** Fixed Support

**B** Force: 800, N

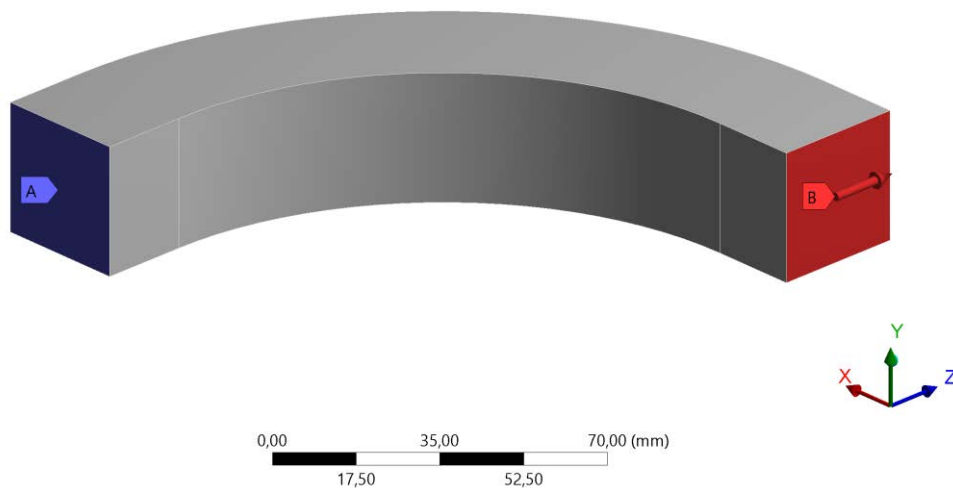


Figure 2.3.4.1: Boundary conditions of Load Case 4.

In the image below it is possible to see the Von Mises equivalent stress of the beam full of material with the Load Case 4 applied (Figure 2.3.4.2):

**F: Curved\_Beam\_1\_Full\_LC4**

Equivalent Stress

Type: Equivalent (von-Mises) Stress

Unit: MPa

Time: 1

44,377 Max  
39,47  
34,563  
29,656  
24,749  
19,842  
14,935  
10,028  
5,121  
0,21401 Min

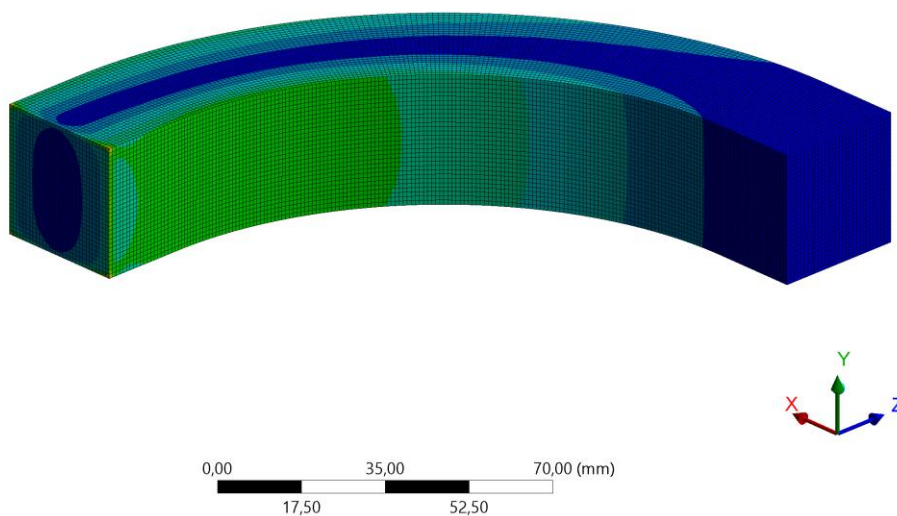


Figure 2.3.4.2: Von Mises equivalent stress of the curved beam full of material with Load Case 4 applied.

### 2.3.5 Load Case 5

In the Load Case 5 there is a fixed support applied in the face at one end of the beam and there are two different loads applied in the face at the other end of the beam: the first load is a 800 N force directed along the Z-axis and the second load is a + 80 Nm moment direct along the X-axis (Figure 2.3.5.1).

**F: Curved\_Beam\_1\_Full\_LC5**  
Static Structural  
Time: 1, s

- A** Fixed Support
- B** Force: 800, N
- C** Moment: 80000 N-mm

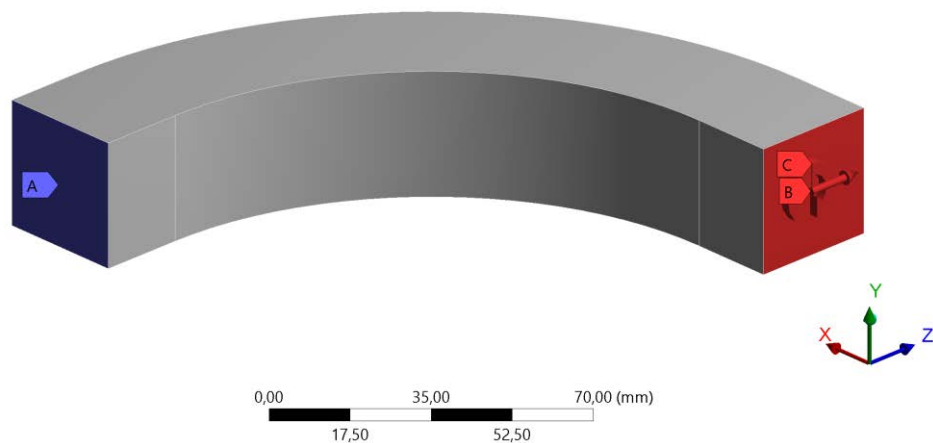


Figure 2.3.5.1: Boundary conditions of Load Case 5.

In the image below it is possible to see the Von Mises equivalent stress of the beam full of material with the Load Case 5 applied (Figure 2.3.5.2):

**F: Curved\_Beam\_1\_Full\_LC5**  
Equivalent Stress  
Type: Equivalent (von-Mises) Stress  
Unit: MPa  
Time: 1

80,741 Max  
71,781  
62,82  
53,86  
44,899  
35,938  
26,978  
18,017  
9,0565  
0,09584 Min

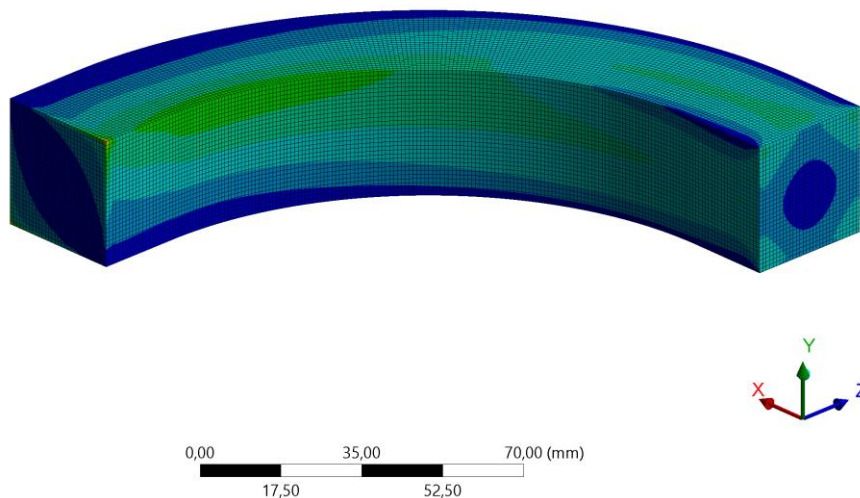


Figure 2.3.5.2: Von Mises equivalent stress of the curved beam full of material with Load Case 5 applied.

### 2.3.6 Load Case 6

The Load Case 6 is very similar to the Load Case 5, but the moment applied is now a – 80 Nm moment directed along the X-axis (Figure 2.3.6.1).

**F: Curved\_Beam\_1\_Full\_LC6**

Static Structural

Time: 1, s

**A** Fixed Support

**B** Force: 800, N

**C** Moment: 80000 N-mm

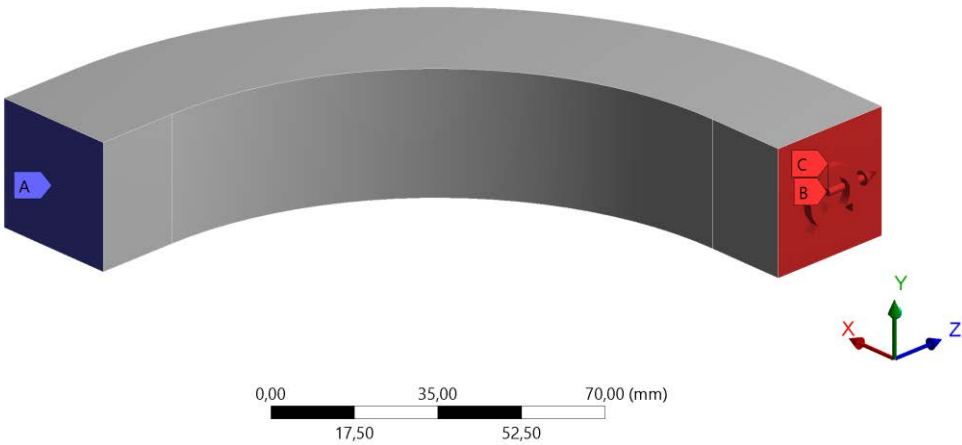


Figure 2.3.6.1: Boundary conditions of Load Case 6.

In the image below it is possible to see the Von Mises equivalent stress of the beam full of material with the Load Case 6 applied (Figure 2.3.6.2):

**F: Curved\_Beam\_1\_Full\_LC6**

Equivalent Stress

Type: Equivalent (von-Mises) Stress

Unit: MPa

Time: 1

80,741 Max  
71,781  
62,82  
53,86  
44,899  
35,938  
26,978  
18,017  
9,0565  
0,09584 Min

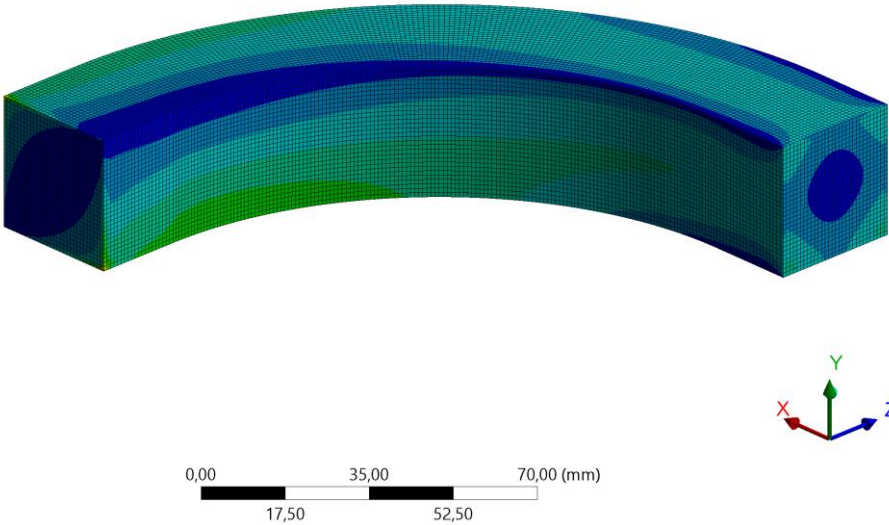


Figure 2.3.6.2: Von Mises equivalent stress of the curved beam full of material with Load Case 6 applied.



## 2.4 Iterative - intuitive optimization

### 2.4.1 Load Case 1: Inner support design with iterative - intuitive optimization

The goal of this first method that has been used is to develop an inner support structure for the hollow curved beam using only a linear elastic F.E.M. analysis tool, leaving to the designer all the effort for building a good geometry for the structural inner support.

In the Subchapter 2.2.2 have been summarized all the steps that the designer should follow for a successful design of a structural inner support. That steps have been followed during this work:

1) To know the outer geometry of the beam.

The outer geometry of the beam that has been used is the one described in the Subchapter 2.2.1

2) To know the boundary conditions (Loads and Constraints).

The boundary conditions that have been used are the ones of the Load Case 1 described in the Subchapter 2.3.1.

3) To make a F.E.M. analysis of the beam full of material and to look at maximum principal stress, minimum principal stress, maximum shear stress.

The F.E.M. analysis has been done with the main parameters showed in the table below (Table 2.4.1.1):

Material	Ansys default Structural Steel (Table 2.3.1)
Mesh Element Type	SOLID186
Mesh Element Order	Quadratic
Mesh Global Size	1 mm
Mesh Target Quality	0,6

Table 2.4.1.1: Main parameters of the F.E.M. analysis of the beam full of material with Load Case 1 applied.

In the images below are showed the results of the maximum principal stress (Figure 2.4.1.1), the minimum principal stress (Figure 2.4.1.2) and the maximum shear stress (Figure 2.4.1.3):

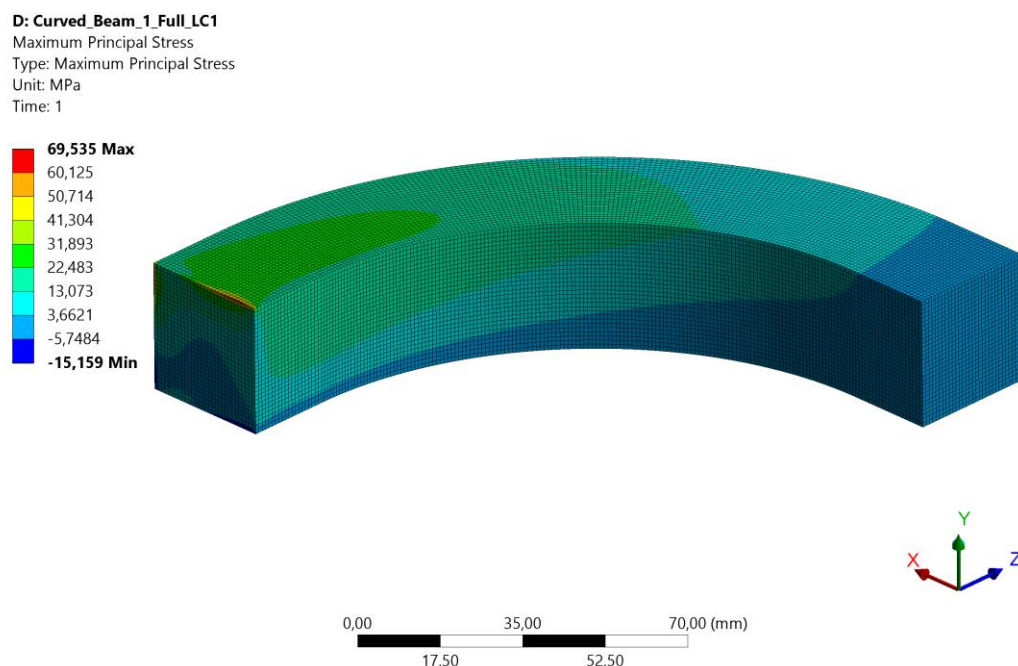


Figure 2.4.1.1: Maximum principal stress of the beam full of material with the Load Case 1 applied.

**D: Curved\_Beam\_1\_Full\_LC1**

Minimum Principal Stress

Type: Minimum Principal Stress

Unit: MPa

Time: 1

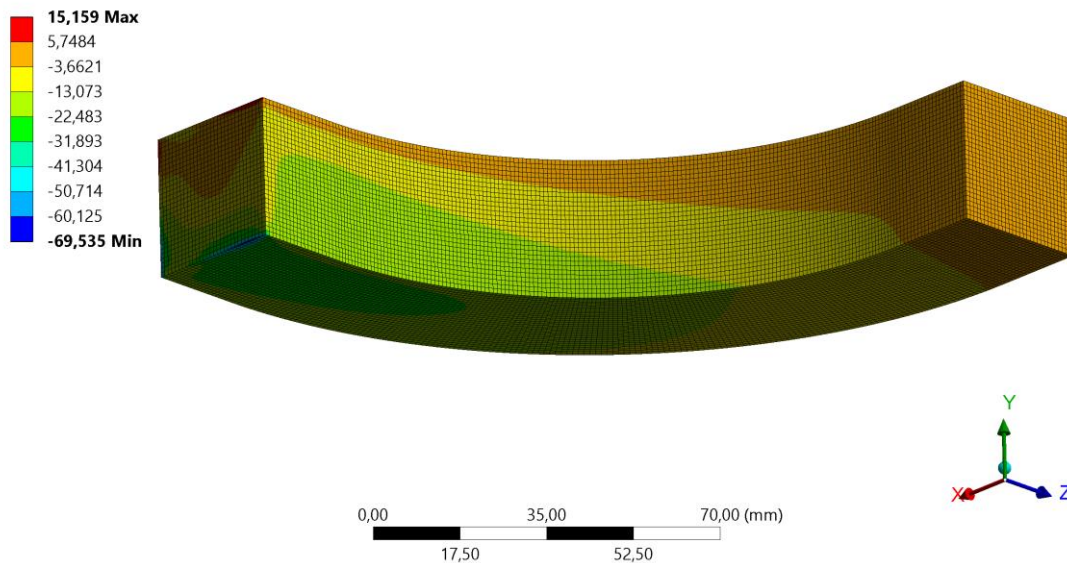


Figure 2.4.1.2: Minimum principal stress of the beam full of material with the Load Case 1 applied.

**D: Curved\_Beam\_1\_Full\_LC1**

Maximum Shear Stress

Type: Maximum Shear Stress

Unit: MPa

Time: 1

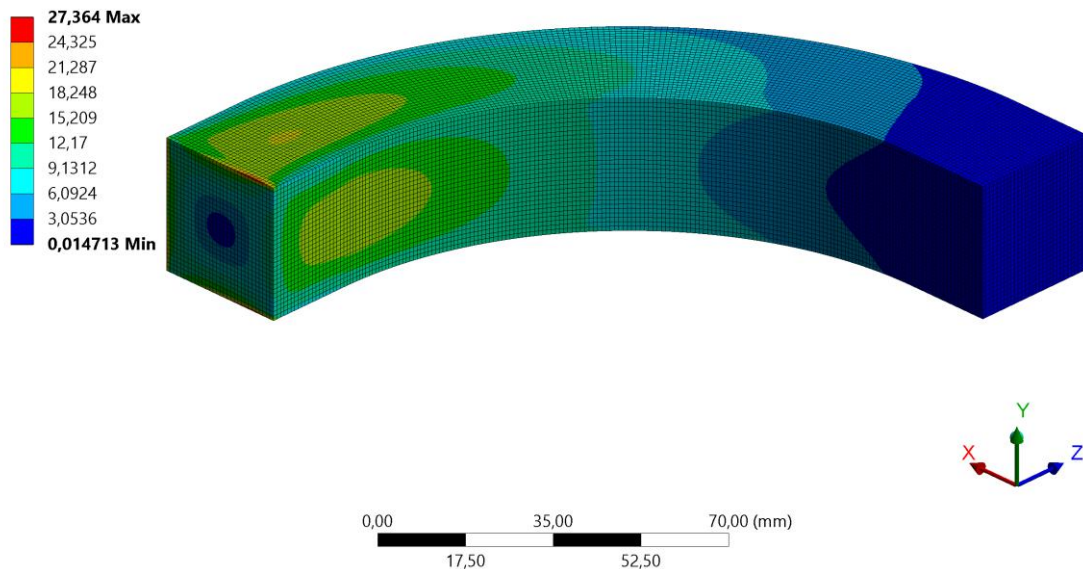


Figure 2.4.1.3: Maximum shear stress of the beam full of material with the Load Case 1 applied.

4) To take in account the isotropic/anisotropic nature of the print technology used.

The print technologies that have been used in this thesis work are the SLS and the SLM, both of them are almost isotropic technologies: the mechanical properties (at least in the elastic regime) of an object printed with one of these technologies do not vary with respect to the orientation of the object in the print volume. On the other hand, an example of an anisotropy technology is the FDM (Fused Deposition Material) one.



5) To place the beam into the print volume to be able to design the structural inner support adding material where the principal stresses are higher.

To place the beam in the print volume have been taken in account the results of the principal stresses showed in the images above. In this case, due to the higher values of the maximum principal stress on the upper surface of the beam and due to the symmetric lower values of the minimum principal stress on the lower surface of the beam, has been decided to place the beam in the print volume as shown below (Figure 2.4.1.4):

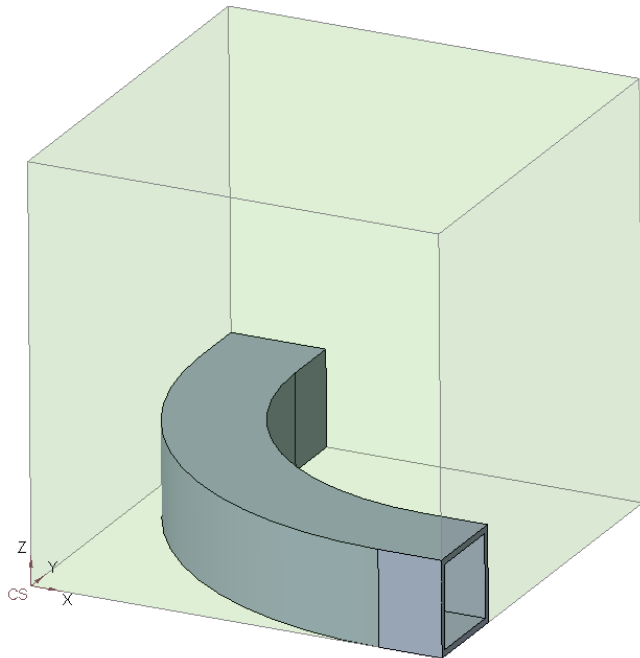


Figure 2.4.1.4: Hollow curved beam placement in the print volume (Z-axis is the print direction).

The upper wall of the curved beam and the lower wall of the curved beam will increase in thickness due to the self-supporting structural inner support that will be built.

Another advantage of this placement of the curved beam is that no external supports are required for printing it so there is no waste of material.

6) To design the pattern of the self-supporting structural inner support.

Three different patterns have been developed: Pattern 1 (Figure 2.4.1.5), Pattern 2 (Figure 2.4.1.6) and Pattern 3 (Figure 2.4.1.7).

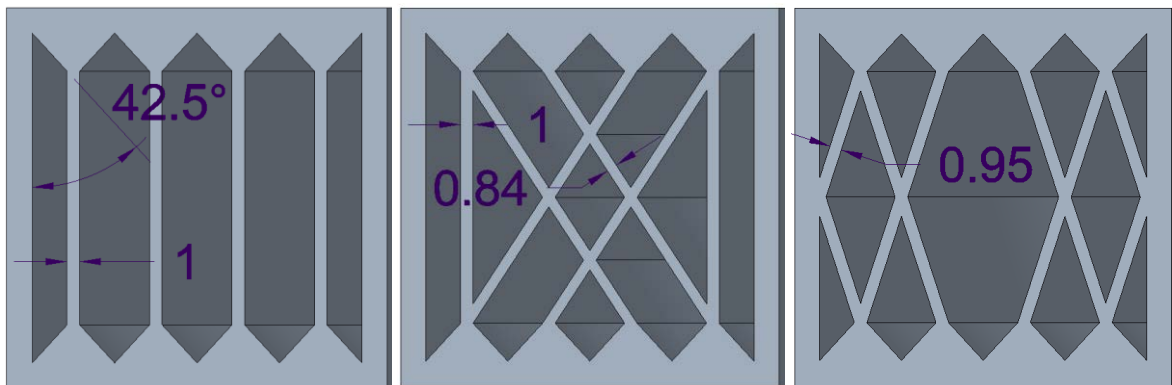


Figure 2.4.1.5: Pattern 1 (mm). Figure 2.4.1.6: Pattern 2 (mm). Figure 2.4.1.7: Pattern 3 (mm).

All the three patterns developed have been designed following the SLS and SLM constraints summarized in the Table 1.2.1.

In particular it have been paid attention to:

- The angle between the structure and the print direction should be  $< 45^\circ$  to avoid the overhang condition for the SLM technology.
- The thickness of the walls should be  $> 0,7$  mm. 0,7 mm is the minimum wall thickenss for SLS technology.

The Pattern 1 is the simplest one, it links with vertical walls the self-supporting triangle shape elements that increase the thickness of the upper and the lower horizontal walls of the curved beam.

The Pattern 2 is a further development of the Pattern 1, the linking walls are not only vertical anymore. They are also inclined near to the  $45^\circ$  direction to be able to carry as best as possible the torsional stresses.

The Pattern 3 is the last development, the walls in the centre zone of the curved beam have been removed because near the neutral axis of the curved beam the stresses to carry are near to zero.

To build the entire structural inner support, for each of the three patterns developed, a single sweep of the 2D pattern has been performed along all the curved beam geometry. The result is a 3D structure that supports the beam all along its length. This approach of designing first a 2D structural inner support pattern and then extend the designed geometry to a 3D domain is meant to be an effective, simple and fast approach.

Below are shown three images of the curved beam with the structural inner supports developed for the Load Case 1: Pattern 1 (Figure 2.4.1.8), Pattern 2 (Figure 2.4.1.9) and Pattern 3 (Figure 2.4.1.10)

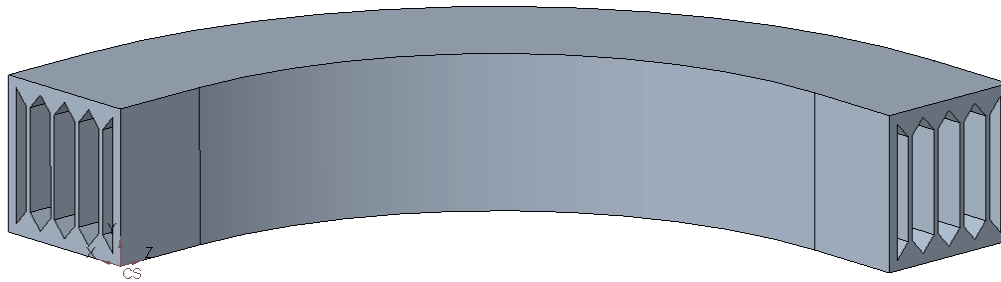


Figure 2.4.1.8: Curved beam with the Pattern 1 structural inner support.

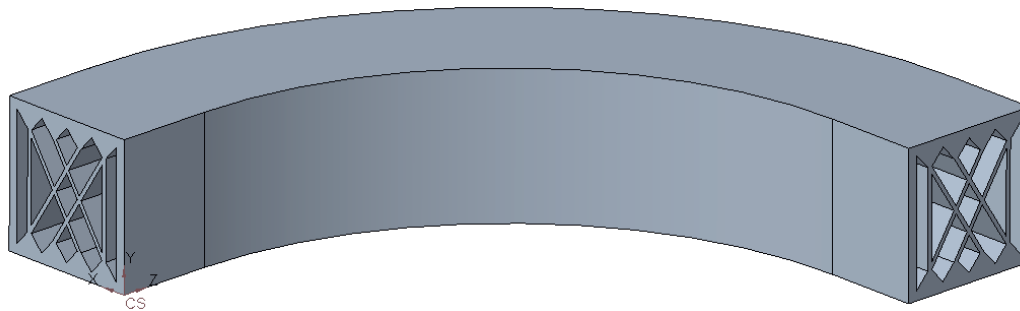


Figure 2.4.1.9: Curved beam with the Pattern 2 structural inner support.

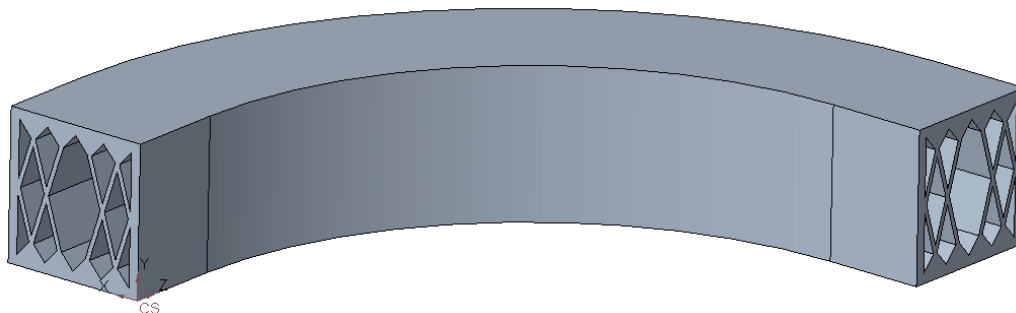


Figure 2.4.1.10: Curved beam with the Pattern 3 structural inner support.

### 2.4.2 Load Case 1: F.E.M. Analyses

The static structural F.E.M. analyses have been performed applying the Load Case 1 (Subchapter 2.3.1) and with the main parameters showed in the table below (Table 2.4.2.1):

Material	Ansys default Structural Steel (Table 2.3.1)
Mesh Element Type	SOLID186
Mesh Element Order	Quadratic
Mesh Global Size	1 mm
Mesh Target Quality	0,6

Table 2.4.2.1: Main parameters of the static structural F.E.M. analyses.

The F.E.M analysis of the curved beam full of material has been already done in the step 3) of the Subchapter 2.4.1. The result of Von Mises equivalent stress is showed in the image below (Figure 2.4.2.1):

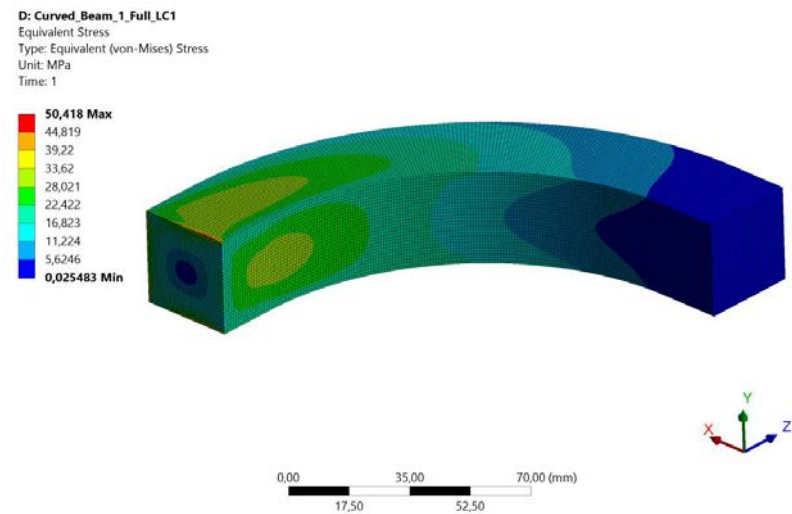


Figure 2.4.2.1: Von Mises equivalent stress of the curved beam full of material with Load Case 1 applied.

Has been also performed a F.E.M. analysis of the hollow curved beam without any inner support to be able of making a complete comparison, not only between the different structural inner supports developed. The Von mises equivalent stress is shown in the image below (Figure 2.4.2.2):

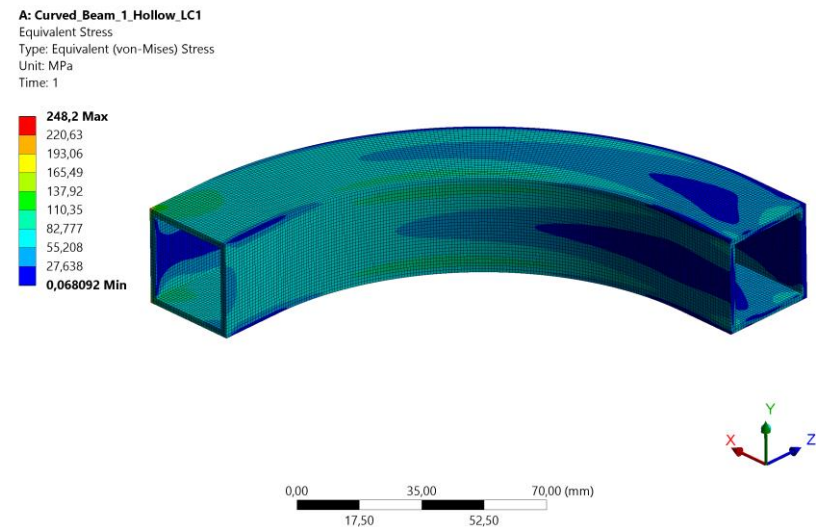


Figure 2.4.2.2: Von Mises equivalent stress of the hollow curved beam with Load Case 1 applied.

The Von Mises equivalent stress results of the curved beam with the developed structural inner supports with Pattern 1 (Figure 2.4.2.3), Pattern 2 (Figure 2.4.2.4) and Pattern 3 (Figure 2.4.2.5) are showed in the images below:

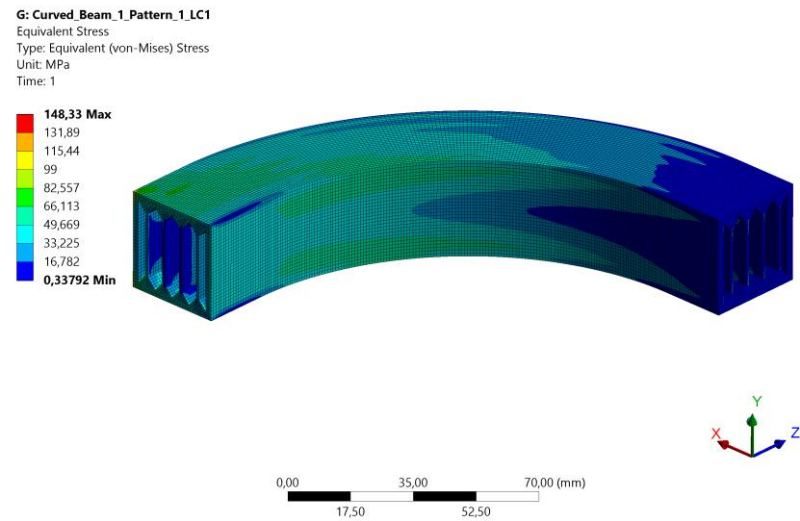


Figure 2.4.2.3: Von Mises equivalent stress of the Pattern 1 curved beam and Load Case 1 applied.

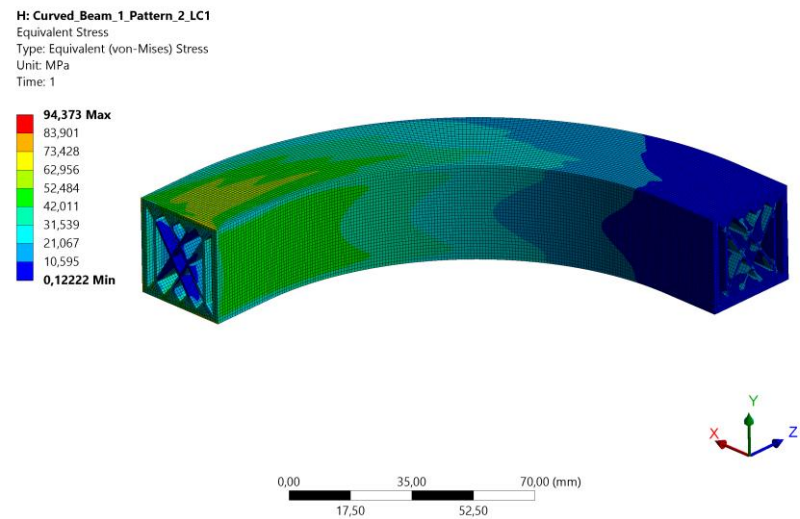


Figure 2.4.2.4: Von Mises equivalent stress of the Pattern 2 curved beam with Load Case 1 applied.

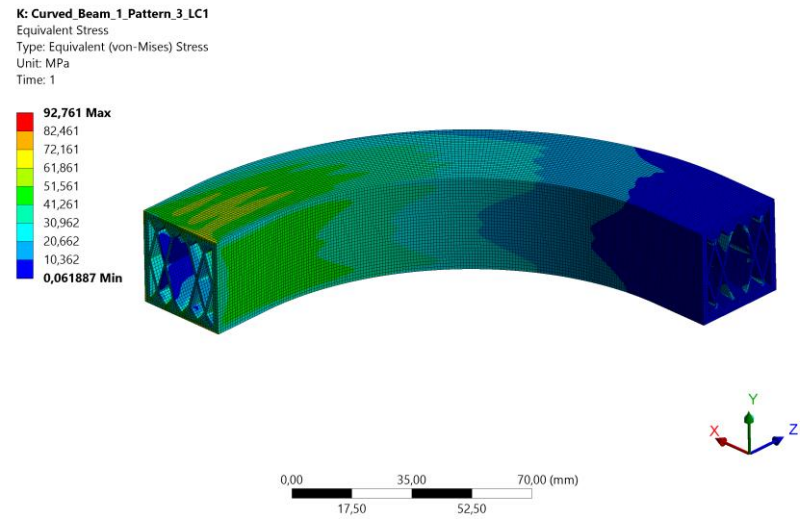


Figure 2.4.2.5: Von Mises equivalent stress of the Pattern 3 curved beam with Load Case 1 applied.

The F.E.M. analyses show how it is possible to reduce the stresses of the hollow curved beam with a structural inner support: the upper and the lower triangle shape elements help to decrease the stresses of the upper and lower surfaces were, respectively, the maximum principal stress was higher and the minimum principal stress was lower in the beam full of material. The inner walls of the patterns help to carry the stresses by linking the more stressed external walls of the original hollow beam.

The results are summarized in the table below (Table 2.4.2.2):

	Full	Hollow	Pattern 1	Pattern 2	Pattern 3
Weight [g]	1337	333	585	636	633
Y Displacement Max  [mm]	0,142	0,562	0,356	0,251	0,242
Stiffness [N/mm]	5634	1424	2247	3187	3306
Stiffness/Weight (Maximum is better)	<b>4,21</b>	<b>4,28</b>	<b>3,84</b>	<b>5,01</b>	<b>5,22</b>

Table 2.4.2.2: Results comparison between the different curved beams.

The table shows that the best configuration among the analysed ones is the Pattern 3: it is the stiffest structural inner support and it is the configuration that has the highest stiffness/weight ratio. Has been decided to stop now the development of the iterative - intuitive optimization process because it would have been more interesting to see what could be done with the topology optimization tool.

A problem that may occur with a design made, as in this case, of thin walls is buckling of the walls themselves.

To analyse the problem, an elastic buckling analysis of the curved beam with the best developed Pattern 3 structural inner support has been done. This analysis is useful to have an idea of the ideal load that must be applied to the structure for buckling to happen. This method matches the classical Euler's solution for the buckling problem of a slender column. (An elastic buckling analysis of a slender column has been done with the same mesh settings of the curved beam buckling analysis. A comparison with the analytical result applying the Euler's formula has also been done and the error between the F.E.M analysis and the Euler's theory is about 0,1 %. The details of this analysis can be found in Annex B.)

However, to get a result of the real buckling load of a real structure with imperfections and nonlinearities a more complex nonlinear buckling analysis should be performed.

For this buckling analysis, due to the 16gb of RAM of the computer used, a 1,5 mm mesh has been used instead of the 1mm mesh used for the static structural analysis that have been done before. The element used was no more the SOLID186 but was the SOLID187 because it was necessary to maintain the quality target of the mesh due to the bigger dimension of the mesh elements (Table 2.4.2.3).

Material	Ansys default Structural Steel (Table 2.3.1)
Mesh Element Type	SOLID187
Mesh Element Order	Quadratic
Mesh Global Size	1,5 mm
Mesh Target Quality	0,6

Table 2.4.2.3: Main parameters of the linear elastic buckling F.E.M. analysis.

A load of 1 N has been applied, using the same boundary conditions scheme of the Load Case 1, to get as a result of the analysis the load multiplier that is exactly the load that must be applied to the structure for buckling to happen.

In the image below (Figure 2.4.2.6) are shown the first six modes of the eigenvalue problem, the most dangerous one is the minimum one taken in absolute value, the number 3. The minus sign of the first two modes means that the buckling would happen if a load equal to the load multiplier (vertical axis of the graph) is applied in opposite direction w.r.t. the direction of the load that has been effectively applied to the curved beam.

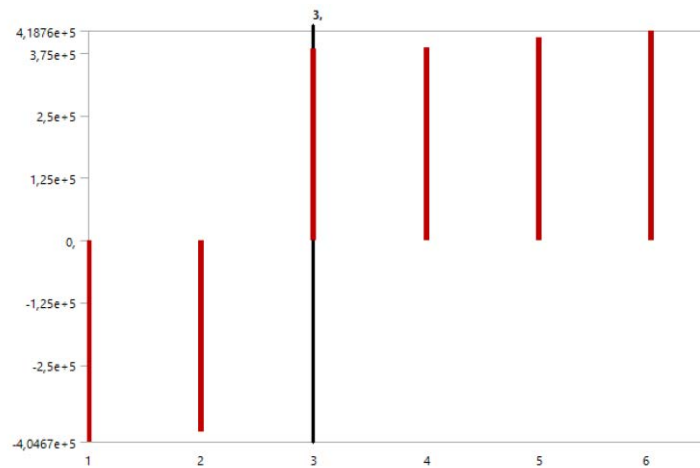


Figure 2.4.2.6: First six modes resulting from the solution of the buckling eigenvalue problem.

The mode number 3 shows that the minimum ideal load that should be applied to the structure for buckling to happen is 383060 N, this value is way higher than the maximum working loads that are expected the curved beam to work with.

In the images below (Figure 2.4.2.7, Figure 2.4.2.8) are highlighted the zones of the curved beam where the buckling should happen:

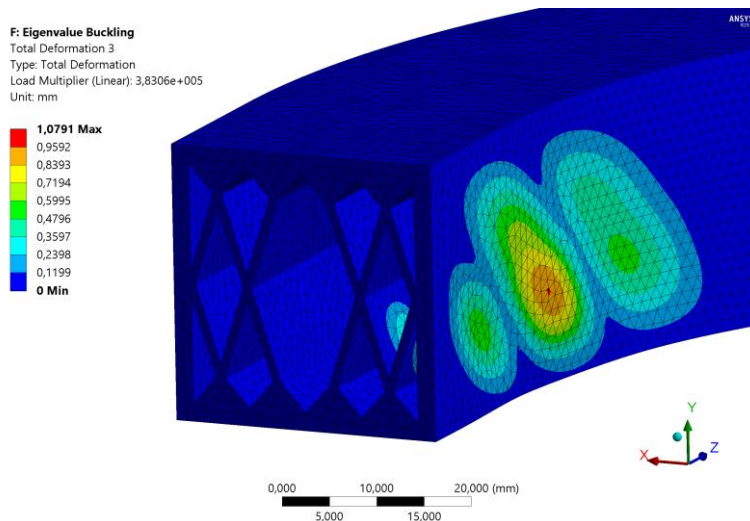


Figure 2.4.2.7: Displacement shape of the curved beam zones where the buckling should happen.

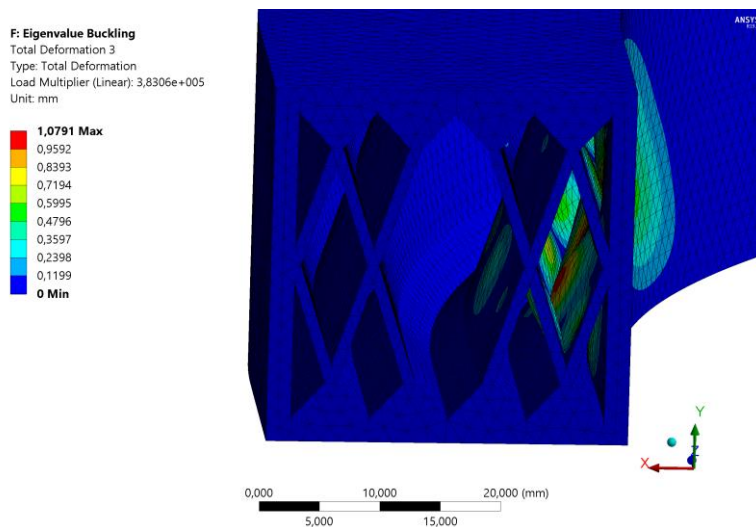


Figure 2.4.2.8: Displacement shape of the curved beam zones where the buckling should happen

## 2.5 Mathematical design optimization: Topology optimization

### 2.5.1 Topology Optimization background

The aim of this subchapter is to present the basic theory background of the topology optimization for understanding the principles that a topology optimization software uses when a topology optimization is performed. The topology optimization is the most general type of structural optimization and it belongs to the *mathematical design optimization* group. The main characteristic of this group is that: “...the concept “as good as possible” is given precise mathematical form” [15].

In a structural optimization problem are always present the following function and variables [15]:

- **Objective function ( $f$ ):** This is a function that quantifies the quality of the design. Usually a function to minimize is wanted. This function usually measures a specific quantity that should be minimized like for example the mass of the component or the displacement in a specific direction. Finding the minimum value of this function is the purpose of the optimization algorithm.
- **Design variable ( $x$ ):** This is a function or a vector that describe the design. It is a characteristic of the component that can change during the optimization process to find the optimum value of  $f$ .
- **State variable ( $y$ ):** This is a function or a vector that represents the response of the structure for every design described by the design variable  $x$ . For mechanical structures the possible responses are forces, displacements, stresses and strains.

The general formulation of the structural optimization problem is [15]:

$$\text{Minimize } f(x, y) \text{ w.r.t. } x \text{ and } y \quad (\text{Eq. 2.5.1.1})$$

Subject to:

- Behavioural constraints on  $y$ , usually written as:  $g(y) \leq 0$  (Eq. 2.5.1.2)
  - Design constraints on  $x$ , usually written as:  $g(x) \leq 0$  (Eq. 2.5.1.3)
  - Equilibrium constraint:  $K(x) \cdot U = F(x)$  (For a discretized linear problem) (Eq. 2.5.1.4)
- where:
- $K(x)$  is the stiffness matrix, which generally is a function of the design variable  $x$
  - $U$  is the displacements vector
  - $F(x)$  is the forces vector, which may also depend on the design variable  $x$ .

If an optimization problem has multiple objective functions  $f_i$  to minimize, probably all the functions wouldn't be minimized w.r.t. the same  $x$  and  $y$ . The solution is to achieve the *Pareto optimality*: to find the only  $(x^*, y^*)$  couple that satisfies in the best way all the objective functions  $f_i$ . To find the Pareto optimal point a common technique is to build a scalar objective function by summing all the single objective functions  $f_i$  pre-multiplied by a weight factor  $w_i \geq 0$  [15]:

$$\sum_{i=1}^n (w_i \cdot f_i(x, y)) \quad (\text{Eq. 2.5.1.5})$$

and

$$\sum_{i=1}^n w_i = 1 \quad (\text{Eq. 2.5.1.6})$$

The Pareto optimal point varies by varying the  $w_i$ .

For a topology optimization problem usually, a *density based method* is used. With this method the design variable  $x$  become a vector that contains all the pseudo density values  $\rho_i$  of all the finite elements of the model. The pseudo density values are dimensionless, the values domain is the interval  $[0, 1]$ . During the topology optimization, at each iteration, the algorithm assigns to the finite elements that have low stress a low value of pseudo density. When the optimization process finishes the result is a geometry that has some finite elements with pseudo density equal to 1, that means material presence in that finite elements, some finite elements with pseudo density equal to 0, that means material void in that finite elements, and some finite elements with a pseudo density value between 0 and 1. The pseudo density threshold value for retaining or not the material, with a pseudo density value between 0 and 1, of the optimized component is usually a choice that the designer makes.

To force the pseudo density values of all the finite elements to approach 0 or 1, rather than varying continuously, a common technique that is used is the *Solid Isotropic Material with Penalization (SIMP)*.

The dimensionless pseudo density can be considered in the finite element calculations by pre-multiplying the Young's modulus by it.

Focusing on the SIMP technique, it is possible to define the “effective” Young's modulus  $E^*$  as:

$$E^* = \rho^q \cdot E \quad (\text{Eq. 2.5.1.7})$$

$E^*$  is function of the Young's modulus  $E$  and of the pseudo density  $\rho$  powered by a coefficient named  $q$ . The coefficient  $q$  is the penalty factor of the SIMP technique: if  $q = 1$  there is a linear proportionality between  $E^*$  and  $\rho$ . If  $q > 1$ ,  $q = 3$  for example as showed in the image below (Figure 2.5.1.1), ideally lowering the  $\rho$  values from 1 to 0 in a linear way it is possible to see that  $E^*$  lowers faster as the  $q$  value increases. For this reason, this method makes simpler to select the low stiffness elements (low  $\rho$  and so very low  $E^*$ ) to be avoided in the optimal solution: they do not represent an economical use of material [15].

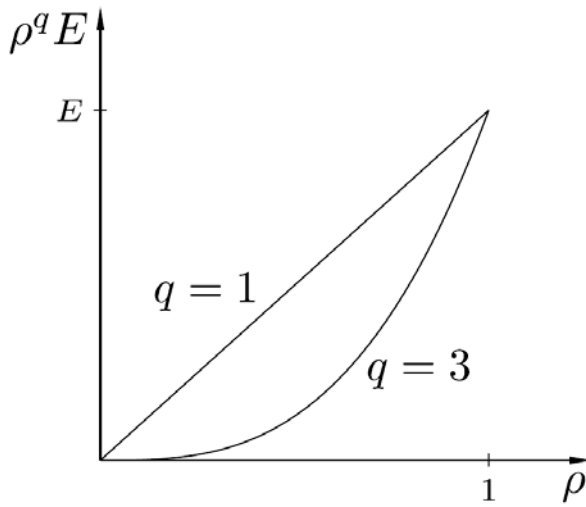


Figure 2.5.1.1: The “effective” Young's modulus as a function of  $\rho$  for different values of  $q$  [15].

In the end, for being precise, having  $\rho = 0$  produces finite elements with zero stiffness giving state problems that are singular and not uniquely solvable. Therefore, a standard procedure is to let  $\rho = \varepsilon$ , where  $\varepsilon$  is a small positive value, but still interpreting regions where the optimal  $\rho = \varepsilon$  as void of material. On the other hand,  $\rho = 1$  represents, as already said, solid regions with a prescribed Young's modulus  $E$  [15].



## 2.5.2 Topology Optimization with Ansys Workbench

To perform a successful topology optimization with Ansys Workbench the step to follow are:

- 1) To perform a *Static Structural* F.E.M. analysis of the component that is wanted to be optimized.

The geometry of the component should comprehend also the chosen design space, the design space is necessary to be present because the topology optimization algorithm will remove material from it during the further optimization process.

The boundary conditions must be the ones that are wanted for the topology optimization.

The mesh global size shouldn't be coarse to avoid coarse results in the further topology optimization. On the other hand, if the mesh global size is too fine the further topology optimization would be very time consuming and not always with better results. The right mesh global size should be the one that gives a fine enough topology optimized shape in a reasonable amount of time.

- 2) To link a new *Topology Optimization* to the *Static Structural* F.E.M. analysis performed before (Figure 2.5.2.1).

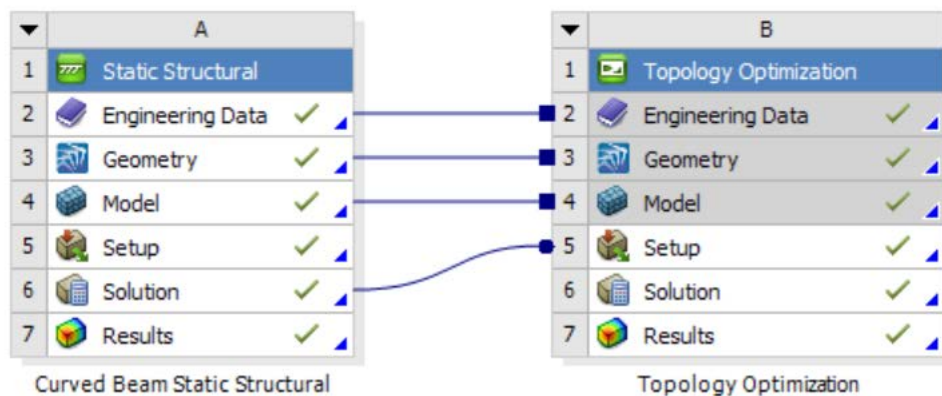


Figure 2.5.2.1: *Topology Optimization* linked to the *Static Structural* analysis in Ansys Workbench Project Schematic.

- 3) To set-up and to run the topology optimization, the general settings menu of a *Topology Optimization* is shown in the image below (Figure 2.5.2.2):

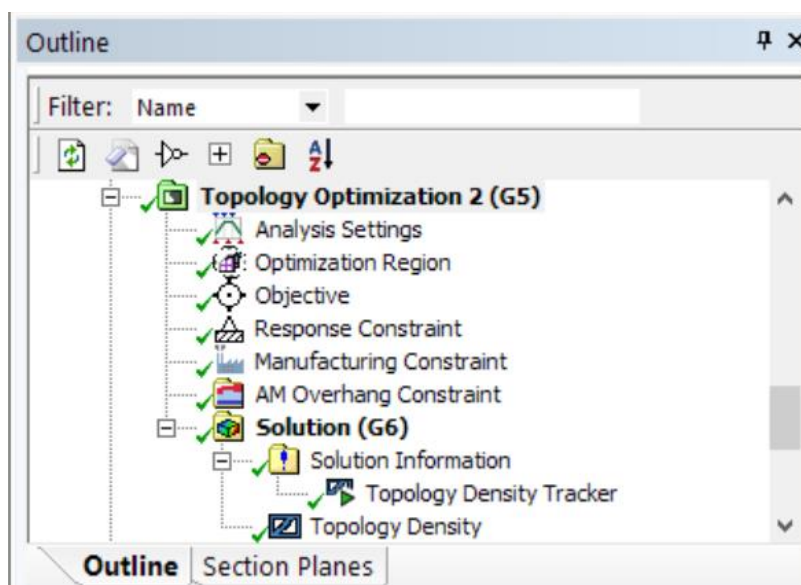


Figure 2.5.2.2: Ansys Workbench *Topology Optimization* general settings menu.

The most important submenus of the general settings menu (Figure 2.5.2.2) are now presented in detail.

In the image below it is possible to see the settings that can be done in the **Analysis Settings** submenu (Figure 2.5.2.3):

Details of "Analysis Settings"	
[-] Definition	
Maximum Number Of Iterations	500,
Minimum Normalized Density	1,e-003
Convergence Accuracy	0,1 %
Penalty Factor (Stiffness)	3,
Region of Manufacturing Constraint	Include Exclusions
Region of Min Member Size	Include Exclusions
[-] Solver Controls	
Solver Type	Program Controlled
[-] Output Controls	
Store Results At	All Iterations
[+] Analysis Data Management	

Figure 2.5.2.3: Analysis Settings submenu.

The *Definition* settings include:

- Maximum Number of Iterations: "This property specifies the maximum number of iterations performed for the topology optimization analysis. The solution process continues until the application achieves convergence accuracy or reaches the maximum number of iterations. The default value is 500" [17].
- Minimum Normalized Density: "This property requires a value greater than 0 and less than 1. The topology optimization analysis uses this value to extract the permissible range of retained threshold values. The default value is 0.001" [17].
- Convergence Accuracy: "This property specifies the convergence criteria of the topology optimization analysis. The solution process continues until the application achieves convergence accuracy or reaches the maximum number of iterations. This value must be less than or equal to 2. The default value is 0.1%" [17].
- Penalty Factor (Stiffness): "During the solution process, this property applies a penalty factor to the structural stiffness matrix in order to prevent the stiffness matrix from scaling linearly with the pseudo density. Therefore, the stiffness at each iteration, as needed, is modified using the expression:  $\text{Pseudo Density}^{\text{Penalty Factor (Stiffness)}}$ . The default value is 3" [17].
- Region of Manufacturing Constraint: "The options for this property are Include Exclusions (default) and Exclude Exclusions. When you specify Include Exclusions, the application also incorporates the Exclusion Region to satisfy the Pull Out Direction, Extrusion, Cyclic, and Symmetry manufacturing constraints" [17].
- Region of Min Member Size: "The options for this property are Include Exclusions and Exclude Exclusions (default). When you specify Include Exclusions, the application also incorporates the Exclusion Region to meet the minimum member size specified through the Member Size manufacturing constraint" [17].

The *Solver Controls* settings allow the user to select the solver that is wanted to be used. There are two solvers that can be chosen:

- Sequential Convex Programming (default if *Program Controlled* is selected): "The Sequential Convex Programming method is an extension of the method for moving asymptotes (MMA). The Sequential Convex Programming method requires the derivatives of all functions present in the topology optimization analysis" [17].
- Optimality Criteria: "The Optimality Criteria method can be used to solve topology optimization problems with a simple compliance objective that uses a volume or mass constraint" [17].

The *Output Controls* settings allow the user to set when to store the iteration's results.

The *Analysis Data Management* category includes other information and settings like for example the solver units that are wanted to be used.

In the image below it is possible to see the settings that can be done in the **Optimization Region** submenu (Figure 2.5.2.4):

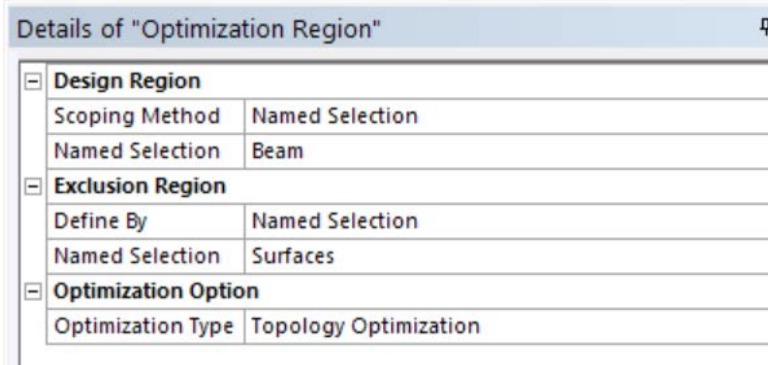


Figure 2.5.2.4: *Optimization Region* submenu.

The *Design Region* settings allow the user to choose the design space of the component. The design space is the part of the component that can be modified during the optimization.

The *Exclusion Region* settings allow the user to choose the non-design space of the component. The non-design space is the part of the component that is not allowed to be modified during the optimization.

The *Optimization Option* setting allow the user to choose between performing a topology optimization or performing a lattice optimization (Subchapter 2.7).

In the **Objective** submenu it is possible to set the objective of the topology optimization. It is possible to choose if minimizing the *Compliance* (maximizing the stiffness) of the component or if minimizing the *Mass* or the *Volume* of the component. It is also possible to select multiple objectives defining also a weight factor for every objective selected. If the topology optimization is linked to a modal analysis, instead of being linked to a static structural analysis, it is possible to choose also to maximize the *Frequency* response.

In the image below it is possible to see the settings that can be done in the **Response Constraint** submenu (Figure 2.5.2.5):

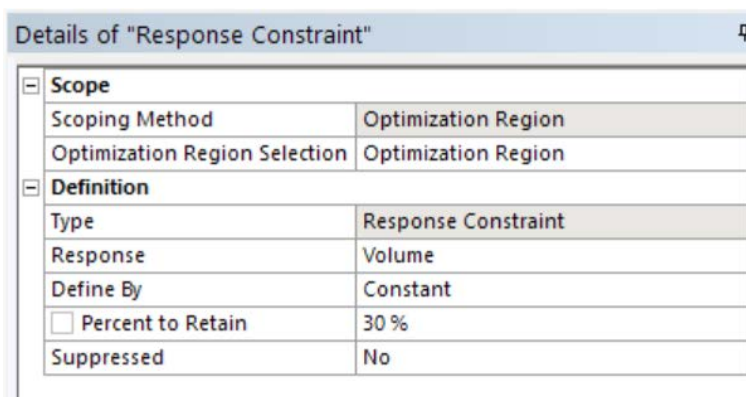


Figure 2.5.2.5: *Response Constraint* submenu.

The *Definition* settings allow the user to choose the desire response constraint. The response constraint is applied to the design space and it can be:

- To retain a constant percentage, or a percentage range, of the *Mass* or the *Volume* of the component.

- To specify a maximum tolerable value for the *Global Von-Mises stress* of the component (active in all the design space)
- To specify a maximum tolerable value for a *Local Von-Mises stress* (active in specific geometric entities that must be chosen).
- To specify a maximum tolerable value for a *Displacement* (X, Y and Z components) (active in specific geometric entities that must be chosen)
- To specify a maximum tolerable value for a *Reaction Force* (X, Y and Z components) (active in specific geometric entities that must be chosen)

If the topology optimization is linked to a modal analysis, instead of being linked to a static structural analysis, it is possible to choose a *Natural Frequency* constraint.

It is possible also to add multiple response constraints to the topology optimization.

It is possible to add several types of **Manufacturing Constraint** to the topology optimization:

- **Member Size**: “This subtype provides options to specify minimum thickness of the supporting structures and maximum thickness of connected parts in the final design” [20]
- **Pull Out Direction**: “This subtype is used for mold-based manufacturing processes. It enables you to specify the direction to remove the model from the mold in a manner that ensures the integrity of the model” [20].
- **Extrusion**: “Using this subtype, you can make sure that the resulting cross section of your final design is kept constant along the selected plane. For each element of the Optimization Region, the application requires at least two corner nodes to lie on the Axis specified for the Extrusion” [20].
- **Cyclic**: “Using this subtype, you control how the sectors are repeated, at the required times, along the specified axis and yields a design that is symmetric with respect to an axis of rotation” [20].
- **Symmetry**: “Using this subtype, you enforce a design that is symmetric with respect to a user-defined plane” [20].

In the image below it is possible to see the settings that can be done in the *Member Size Manufacturing Constraint* submenu, the manufacturing constraint that has been used in this thesis work (Figure 2.5.2.6):

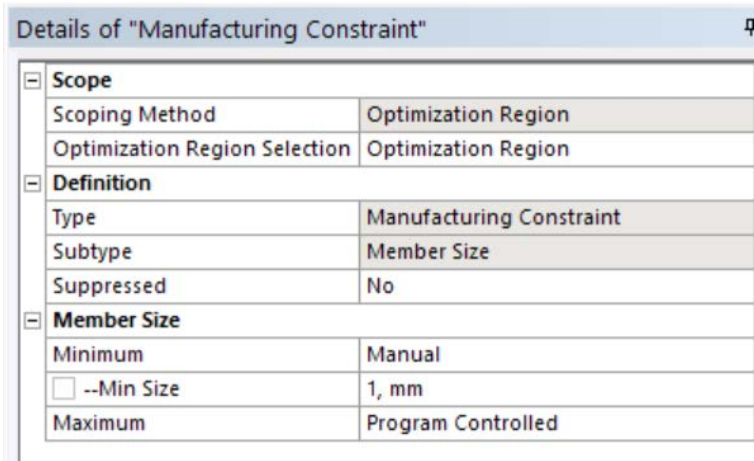


Figure 2.5.2.6: *Member Size Manufacturing Constraint* submenu.

The *Member Size* settings allow the user to choose the desire *Minimum* and/or *Maximum* member sizes:

- **Minimum**: “The options include Program Controlled (default) and Manual. Using the Program Controlled setting, the application automatically sets the minimum size at 2.5 times the mesh element size. Min Size: By default, this field is hidden. You display the property by setting the Minimum property to Manual. The application computes the default value using the mesh size of the generated mesh. This value can simplify the topology optimization solution run. The Program Controlled setting is applicable even when no Member Size is added to the Topology Optimization analysis” [20].

- **Maximum:** “The options include *Program Controlled* (default) and *Manual*. *Max Size*: By default, this field is hidden. You display the property by setting the *Maximum* property to *Manual*. The application does not specify a default value for this property. This is a required entry when you wish to specify a manufacturing process constraint such as casting, extrusion of parts, etc. This is a required entry when you wish to specify the maximum member size of connected parts in the final design” [20].

In the image below it is possible to see the settings that can be done in the **AM Overhang Constraint** submenu (Figure 2.5.2.7):

Details of "AM Overhang Constraint"	
<b>Scope</b>	
Scoping Method	Optimization Region
Optimization Region Selection	Optimization Region
<b>Definition</b>	
Type	AM Constraint
Subtype	Overhang Angle
Suppressed	No
<b>Location and Orientation</b>	
Coordinate System	Global Coordinate System
Build Direction	+Z Axis
Overhang Angle	45, °

Figure 2.5.2.7: *AM Overhang Constraint* submenu.

The *Location and Orientation* settings allow the user to select an axis that will be the *Build Direction* for a 3D printing process (it is also possible to choose axis of a different coordinate system than the default one) and to specify the *Overhang Angle*, characteristic of the 3D printing technology that will be used. The *Overhang Angle* is the minimum angle that the component's parts, like for example walls, can have to be printed successfully without supports. (N.B. the *Overhang Angle* is defined as the angle between the plane orthogonal to the *Build Direction* axis specified and the component's geometry).

Selecting ***Solution Information***, it is possible to see several things including the *Objective* and *Response Constraint* convergence. It is also possible, selecting ***Topology Density Tracker***, to observe graphically the changes of the component shape during the topology optimisation process, iteration by iteration.

In the image below it is possible to see the settings that can be done in the ***Topology Density*** submenu (Figure 2.5.2.8):

Details of "Topology Density"	
<b>Scope</b>	
Scoping Method	Optimization Region
Optimization Region	Optimization Region
<b>Definition</b>	
Type	Topology Density
By	Iteration
Iteration	Last
<input type="checkbox"/> Retained Threshold	0,5
Exclusions Participation	Yes
Calculate Time History	Yes
Suppressed	No
<b>Results</b>	
<b>Visibility</b>	
Show Optimized Region	Retained Region
<b>Information</b>	
Iteration Number	21

Figure 2.5.2.8: *Topology Density* submenu.

The *Iteration* setting allows the user to choose which iteration must be taken in account for showing the result in the *Graphic* space.

The *Retained Threshold* setting allows the user to set the minimum pseudo density value for retaining the component's material. The lower the threshold value, the more material is retained.

In the *Results* section it is possible to see some characteristics of the optimized component such as *Original Mass*, *Final Mass*, *Original Volume*, *Final Volume* and others.

The *Show Optimized Region* setting allows the user to choose if take in account and view in the *Graphic* space the *All Regions* of material, the *Retained Region* of material or the *Removed Region* of material.

The *Iteration Number* information specifies the number of iterations that have been performed during the topology optimisation.



### 2.5.3 Load Case 1: Inner support design with Topology Optimization

The goal of this second method that has been used is to develop a structural inner support for the hollow curved beam using the topology optimization tool. The topology optimization tells the designer where the material is needed and where the material is not needed: this is the best starting point for developing a structural inner support.

In the Subchapter 2.2.2 have been summarized all the steps that the designer should follow for a successful design of an inner support structure. That steps have been followed during this work:

1) To know the outer geometry of the beam.

The outer geometry of the curved beam that has been used is the one described in the Subchapter 2.2.1

2) To know the boundary conditions (Loads and Constraints).

The boundary conditions that have been used are the ones of the Load Case 1 described in the Subchapter 2.3.1.

3) To make a topology optimization of the beam full of material fixing the outer geometry as non-design space and to see the result of the placement of the retained material.

The topology optimization has been done with the main parameters showed in the table below (Table 2.5.3.1):

Material	Ansys default Structural Steel (Table 2.3.1)
Mesh Element Type	SOLID186
Mesh Element Order	Quadratic
Mesh Global Size	2 mm
Mesh Target Quality	0,6

Table 2.5.3.1: Main parameters of the topology optimization of the beam full of material with Load Case 1 applied.

The *design space* and the *non-design space* have been defined (Figure 2.5.3.1):

**B: Topology Optimization Surfaces**

Optimization Region  
Iteration Number: N/A

■ Design Region: Topology  
■ Exclusion Region

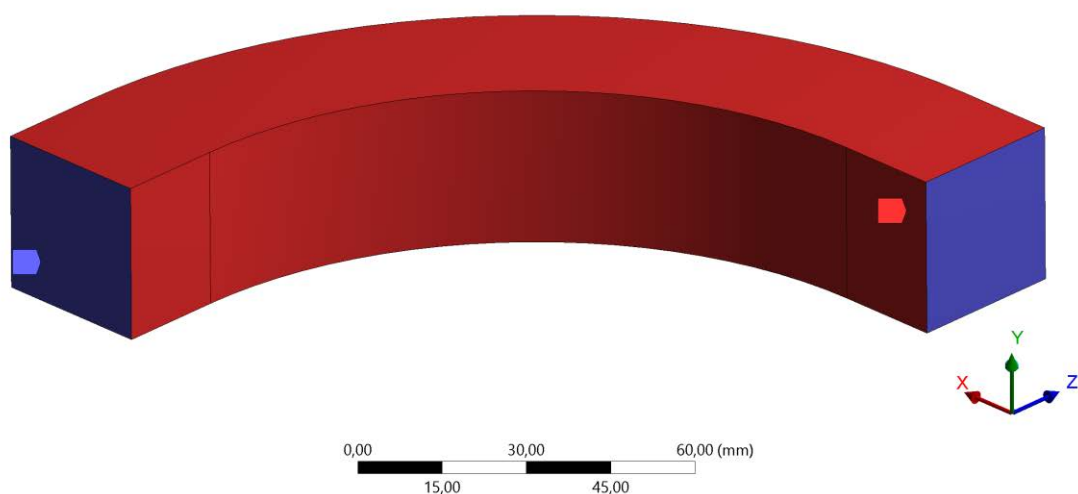


Figure 2.5.3.1: *Design space* and *non-design space*.

Has been taken the decision to define as *design space* all the full of material curved beam volume and to define as *non-design space* the outer surfaces of the curved beam, with the exclusion of the BCs surfaces that remain a design space. The decision about the *non-design space* has been taken because the purpose of this work is to build a structural inner support maintaining the integrity of the outer geometry of the beam.

To minimize *Compliance* (= maximize stiffness) has been chosen as the *Objective* of the topology optimization.

To retain a 30% of the *design space* volume has been set as the *Response Constraint*, to get as result a geometry that with the outer walls would weight about 50% less than the beam full of material.

One *Manufacturing Constraint* has been set specifying a minimum *Member Size* of 1 mm. This means that the topological solver cannot create a geometry member with a dimension less than 1 mm. 1 mm has been chosen because it is the minimum feature size that SLM process can build (Table 1.2.1).

The result of the *Retained Material* is shown in the image below (*Retained Threshold* = 0,5) (Figure 2.5.3.2):

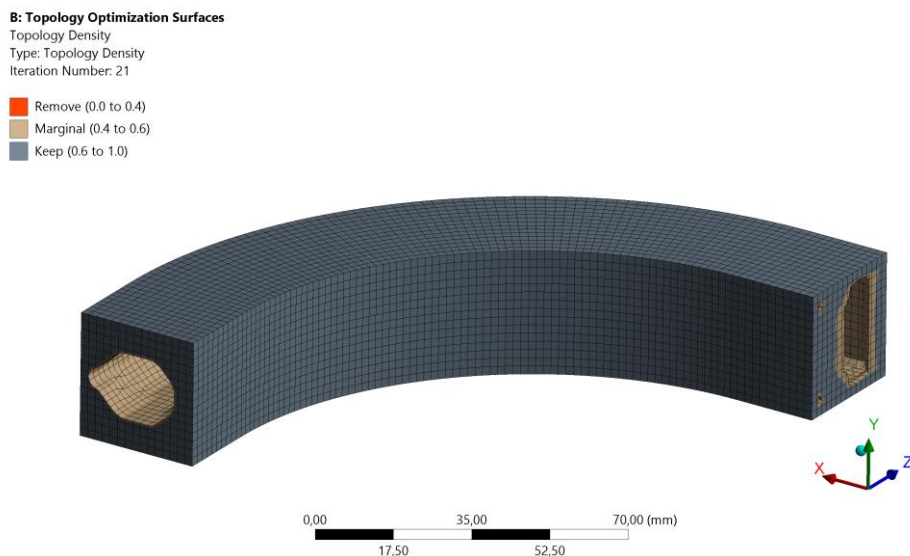


Figure 2.5.3.2: Topology optimization *Retained Material* result.

The result of the *Removed Material* is shown in the image below (*Retained Threshold* = 0,5) (figure 2.5.3.3):

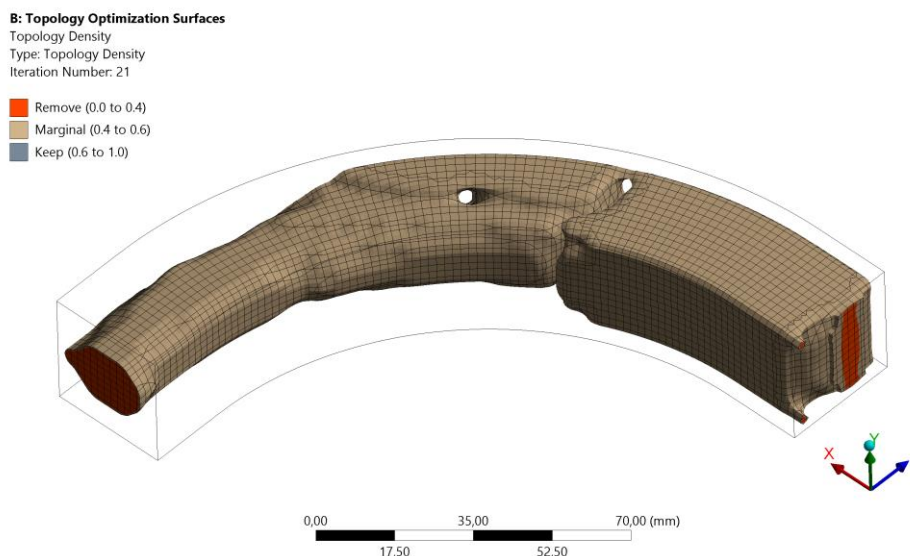


Figure 2.5.3.3: Topology optimization *Removed Material* result.



4) To take in account the isotropic/anisotropic nature of the print technology used.

The print technologies that have been used in this thesis work are the SLS and the SLM, both of them are almost isotropic technologies: the mechanical properties (at least in the elastic regime) of an object printed with one of these technologies do not vary with respect to the orientation of the object in the print volume. On the other hand, an example of an anisotropy technology is the FDM (Fused Deposition Material) one.

5) To place the beam into the print volume to be able to design the structural inner support adding material where the topology optimization placed the retained material.

Following the results of the topology optimization has been decided to not change the position of the beam in the print volume that remains the one of the iterative - intuitive optimization approach (Figure 2.4.1.4).

6) To design the self-supporting structural inner support taking in account the placement of the retained material of the topology optimization.

Has been designed a new structural inner support basic pattern (Figure 2.5.3.4) that is hollow in the centre zone of the beam and that is more modular, to be able to add material where needed in the exterior zones of the beam.

While designing the structural inner support basic pattern has also been payed attention to:

- Maximum overhang angle of  $40^\circ$  to be sure that the quality of the printing would be good (limit condition for SLM process is  $45^\circ$  (Table 1.2.1))
- The minimum size of the walls of 1 mm to be sure that the quality of the printing would be good (limit condition of SLS process for PA12 is 0,7 mm (Table 1.2.1))
- The maximum bridging length of 2 mm that SLM process can realize well without supports
- The minimum size of 3,5 mm of powder escape holes for SLS process (Table 1.2.1)

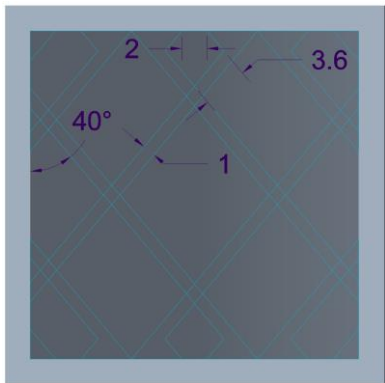


Figure 2.5.3.4: Structural inner support pattern sketch (mm).

Again, following the result of topology optimization has been divided the curved beam in three sectors (Figure 2.5.3.5), the fixed support is applied at the end of sector 1 and the load is applied at the end of sector 3.

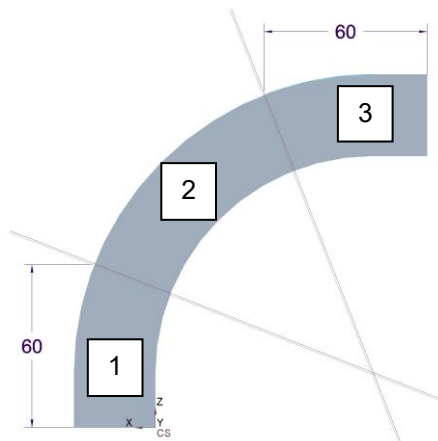


Figure 2.5.3.5: Representation of the three sectors division of the beam (mm).

The design goal was to replicate the position of the retained material of the topology optimization results filling of material in the right positions the basic pattern developed (Figure 2.5.3.4). Have been filled of material different zones of the basic pattern depending on the one of the three sectors considered. (Figure 2.5.3.5). Has been also payed attention to the uniformity of the walls: to print successfully with SLS process is important, as in the injection moulding process, that the walls are as uniform as possible to avoid deformations of the object.

In the sector 1 the basic pattern has been left open only in the centre zone of the beam (Figure 2.5.3.6):

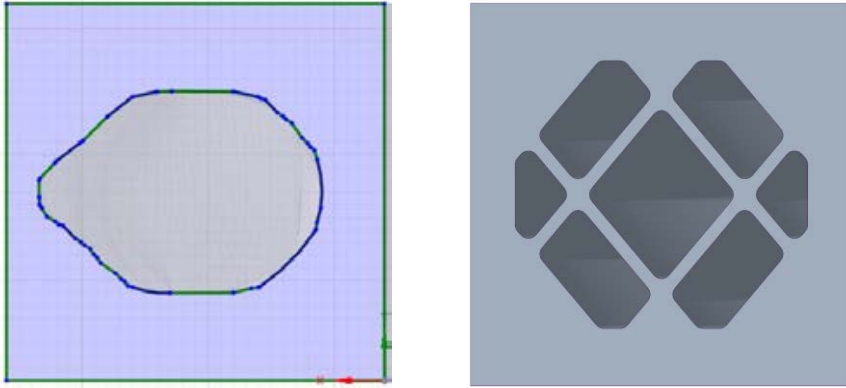


Figure 2.5.3.6: Sections of the sector 1: on the left of the topology optimized geometry and on the right of the support pattern developed.

In the sector 2 the basic pattern has been filled of material in the inner vertical wall zone and in the inner corners zone (Figure 2.5.3.7):

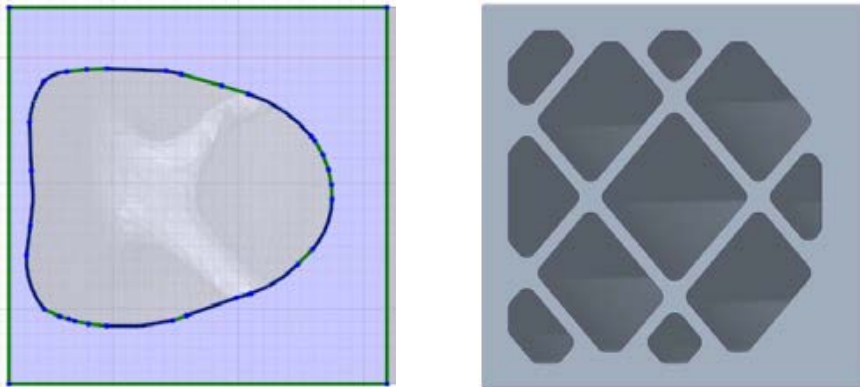


Figure 2.5.3.7: Sections of the sector 2: on the left of the topology optimized geometry and on the right of the support pattern developed.

In the sector 3 the basic pattern has not been filled of material; all the holes have been left open (Figure 2.5.3.8):

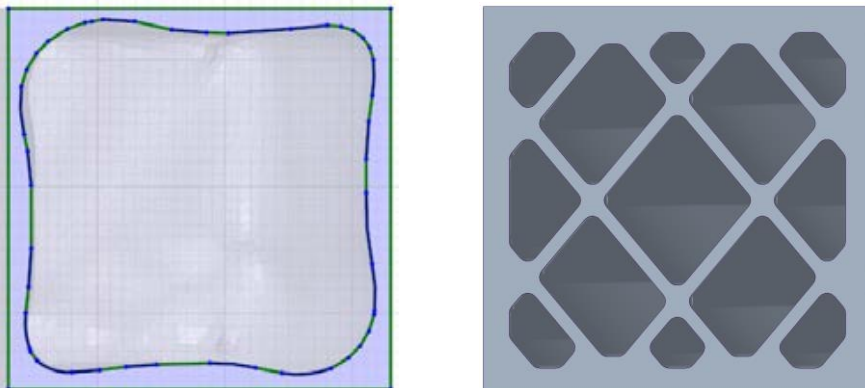


Figure 2.5.3.8: Sections of the sector 3: on the left of the topology optimized geometry and on the right of the support pattern developed.

Below are also shown the XZ-plane sections at near half of the height of the beam, as it comes from the topology optimization with Load Case 1 applied and of the beam with the structural inner support developed (Figure 2.5.3.9):

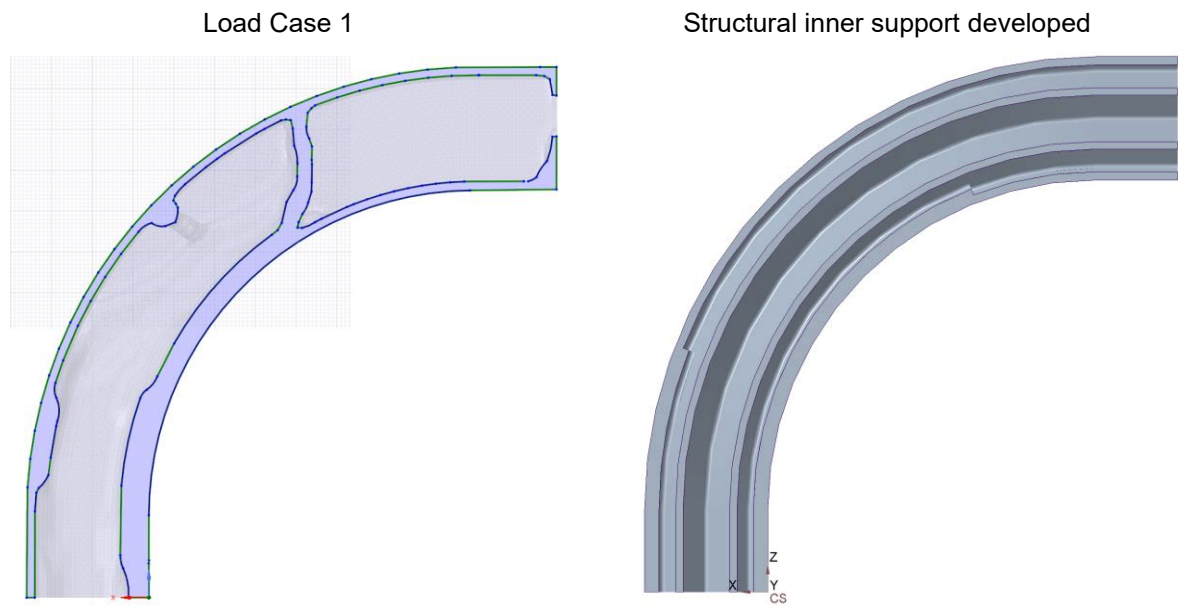


Figure 2.5.3.9: XZ-plane sections at near half of the height, on the left of the beam as it comes from the topology optimization with Load Case 1 applied and on the right of the beam with the structural inner support developed.

Below is shown an image of the curved beam with the structural inner support developed for the Load Case 1 (Figure 2.5.3.10):

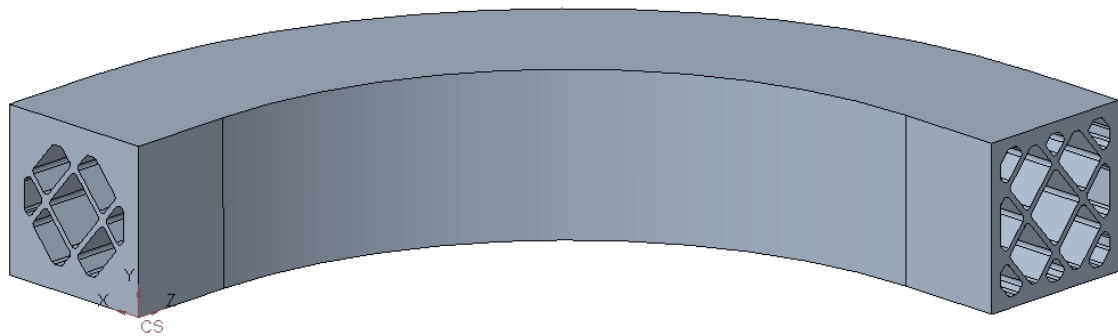


Figure 2.5.3.10: Curved beam with the structural inner support developed for the Load Case 1

### 2.5.4 Load Case 1: F.E.M. Analyses

The static structural F.E.M. analyses have been performed applying the Load Case 1 (Subchapter 2.3.1) and with the main parameters showed in the table below (Table 2.5.4.1):

Material	Ansys default Structural Steel (Table 2.3.1)
Mesh Element Type	SOLID187
Mesh Element Order	Quadratic
Mesh Global Size	1 mm
Mesh Target Quality	0,6

Table 2.5.4.1: Main parameters of the static structural F.E.M. analyses.

Two different F.E.M. analyses have been performed: the first one of the curved beam with the developed structural inner support, the second one of the curved beam as it comes from the topology optimization with Load Case 1 applied. The results of the Von Mises equivalent stress are showed in the images below (Figure 2.5.4.1, Figure 2.5.4.2):

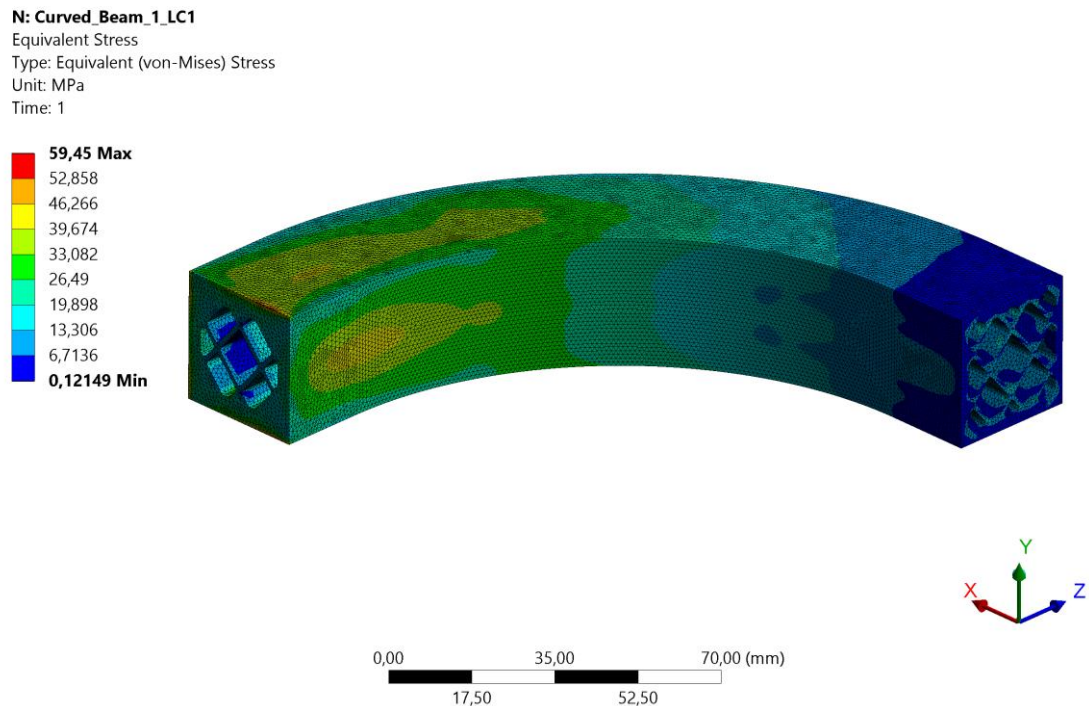


Figure 2.5.4.1: Von Mises equivalent stress of the curved beam with the developed structural inner support.

### C: Topology Validation

Equivalent Stress

Type: Equivalent (von-Mises) Stress

Unit: MPa

Time: 1

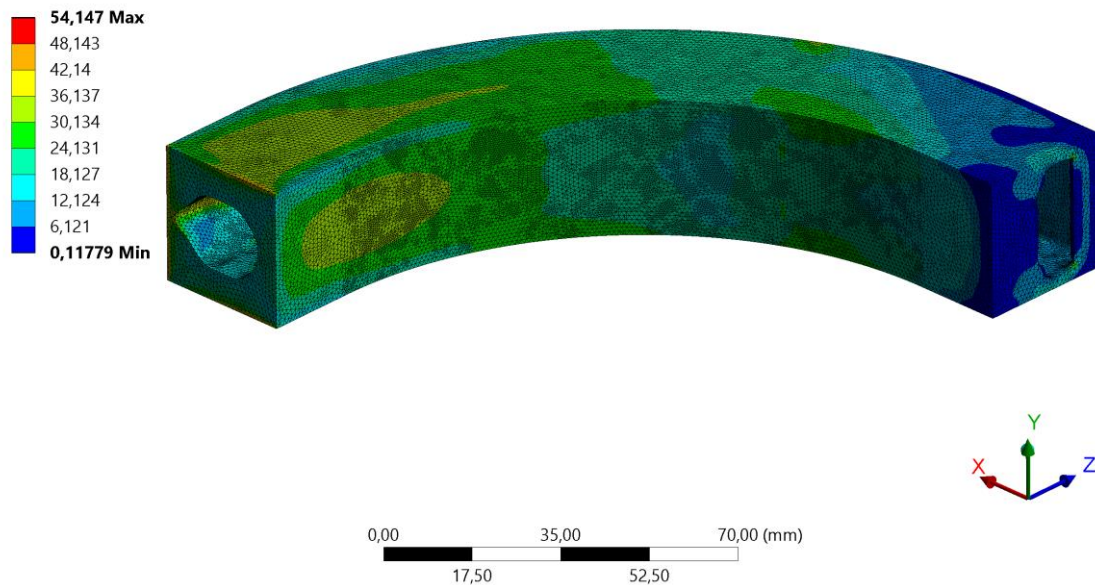


Figure 2.5.4.2: Von Mises equivalent stress of the curved beam as it comes from the topology optimization with Load Case 1 applied.

The results are summarized in the table below (Table 2.5.4.2):

	Full	Hollow	Pattern 3	Developed inner support	Topology Optimization
Weight [g]	1337	333	633	720	640
Y Displacement Max [mm]	0,142	0,562	0,242	0,188	0,184
Stiffness [N/mm]	5634	1424	3306	4255	4348
Stiffness/Weight (Maximum is better)	<b>4,21</b>	<b>4,28</b>	<b>5,22</b>	<b>5,91</b>	<b>6,79</b>

Table 2.5.4.2: Results comparison between the different curved beams.

The Stiffness/Weight ratio of the curved beam with the new structural inner support developed is 11,7 % higher than the curved beam with the previous Pattern 3 structural inner support. However, due to the support structure necessities, it is difficult to reach the Stiffness/Weight ratio of the topology optimized beam that has been optimized without caring about the impossibility of printing it with some additive manufacturing technologies, without adding to it some further supports.

The Stiffness/Weight ratio of the topology optimized curved beam is 13 % higher than the one of the curved beam with the new structural inner support developed and it is 23,1 % higher than the one of the curved beam with the previous Pattern 3 structural inner support.

### 2.5.5 Load Case 2: Topology Optimization

The topology optimization has been done with the main parameters showed in the table below (Table 2.5.5.1):

Material	Ansys default Structural Steel (Table 2.3.1)
Mesh Element Type	SOLID186
Mesh Element Order	Quadratic
Mesh Global Size	2 mm
Mesh Target Quality	0,6

Table 2.5.5.1: Main parameters of the topology optimization of the beam full of material with Load Case 2 applied.

The *design space* and the *non-design space* have been defined (Figure 2.5.5.1):

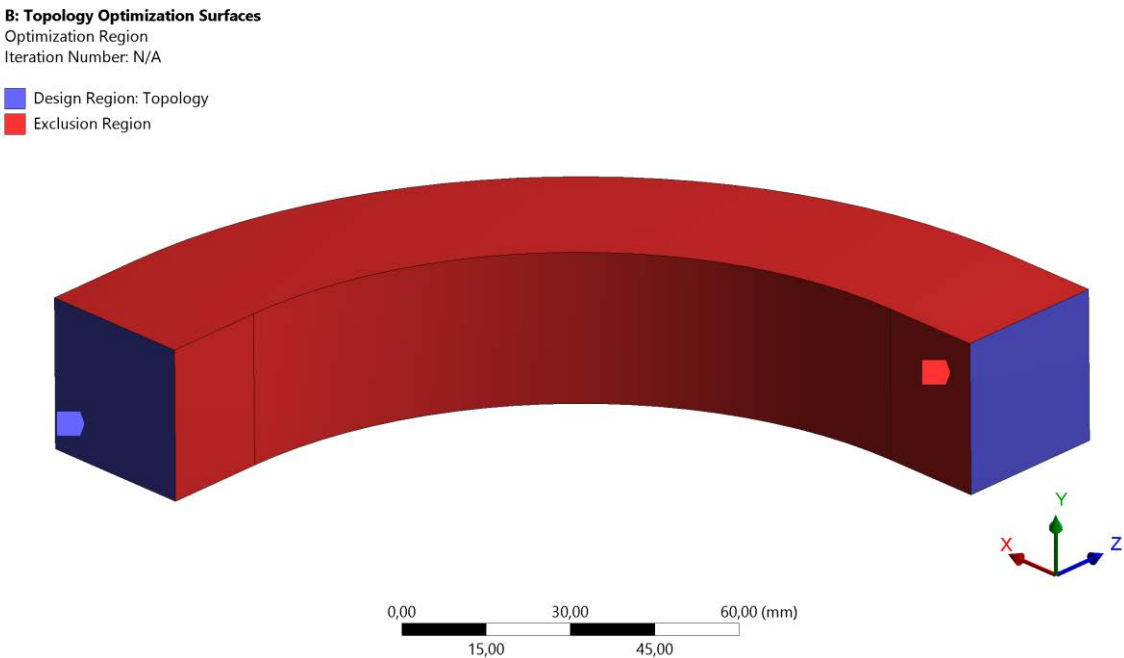


Figure 2.5.5.1: *Design space* and *non-design space*.

Has been taken the decision to define as *design space* all the full of material beam volume and to define as *non-design space* the outer surfaces of the beam, with the exclusion of the BCs surfaces that remain a design space. The decision about the *non-design space* has been taken because the purpose of this work is to build a structural inner support maintaining the integrity of the outer geometry of the beam.

To minimize *Compliance* (= maximize stiffness) has been chosen as the *Objective* of the topology optimization.

To retain a 30% of the *design space* volume has been set as the *Response Constraint*, to get as result a geometry that with the outer walls would weight about 50% less than the beam full of material.

One *Manufacturing Constraint* has been set specifying a minimum *Member Size* of 1 mm. This means that the topological solver cannot create a geometry member with a dimension less than 1 mm. 1 mm has been chosen because it is the minimum feature size that SLM process can build (Table 1.2.1).



The result of the *Retained Material* is shown in the image below (*Retained Threshold* = 0,5) (Figure 2.5.5.2):

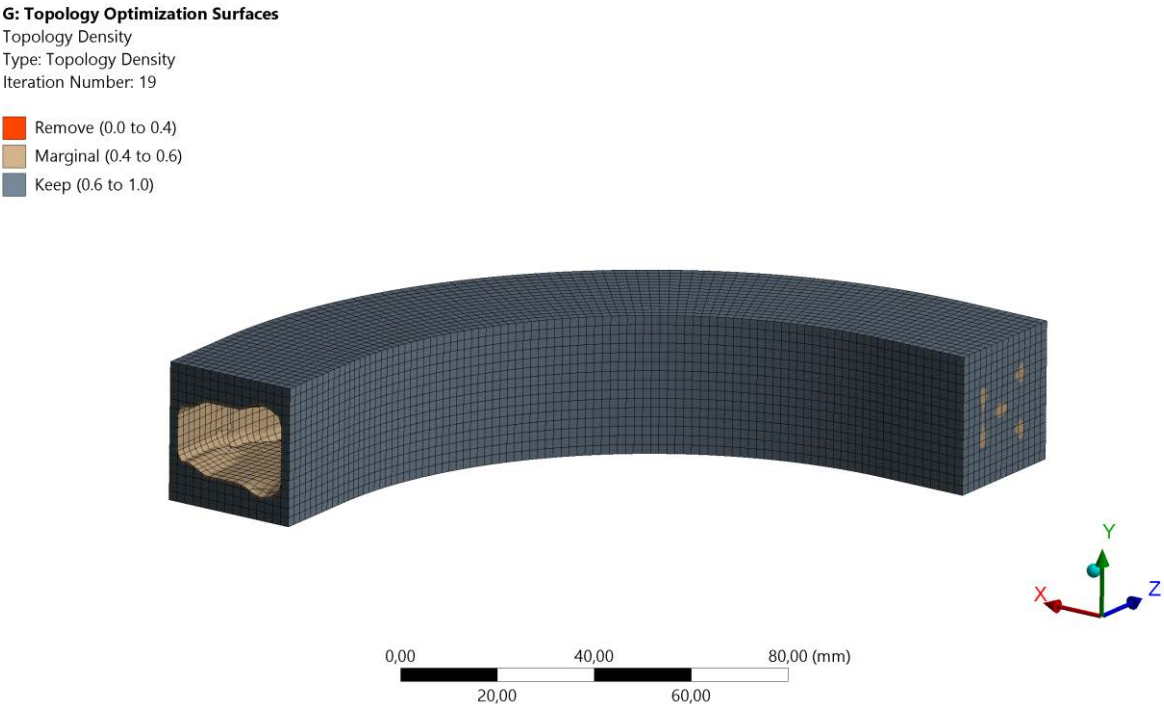


Figure 2.5.5.2: Topology optimization *Retained Material* result.

The result of the *Removed Material* is shown in the image below (*Retained Threshold* = 0,5) (Figure 2.5.5.3):

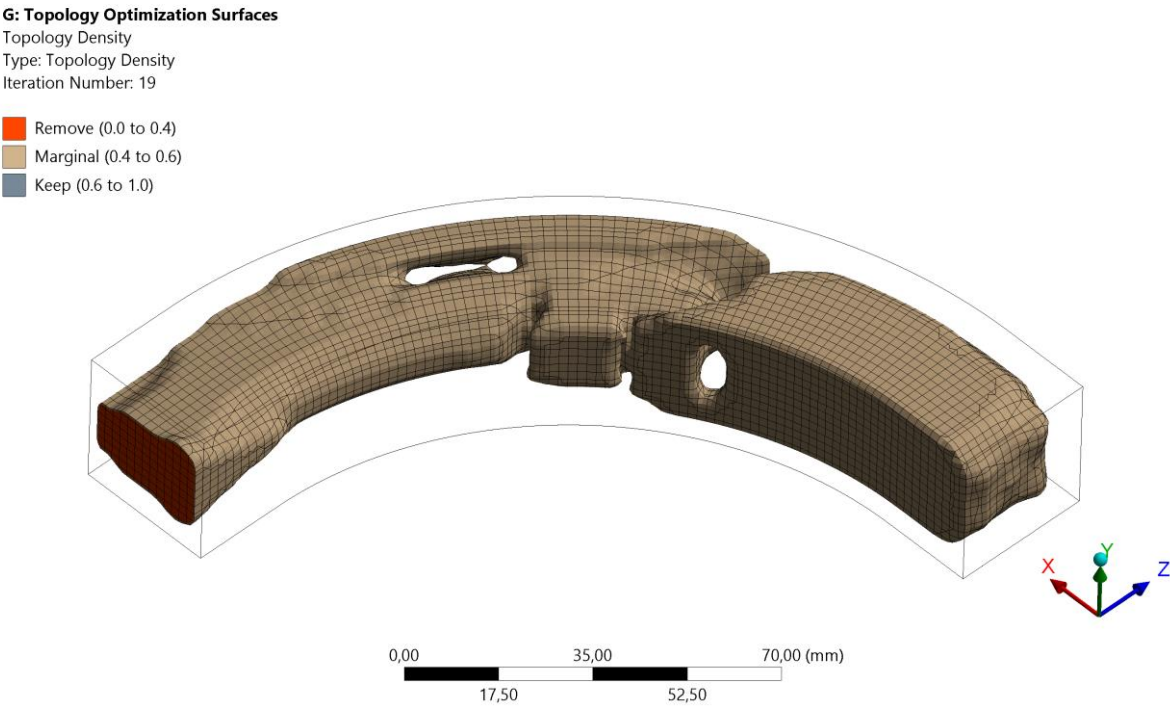


Figure 2.5.5.3: Topology optimization *Removed Material* result.

## 2.5.6 Load Case 3: Topology Optimization

The topology optimization has been done with the main parameters showed in the table below (Table 2.5.6.1):

Material	Ansys default Structural Steel (Table 2.3.1)
Mesh Element Type	SOLID186
Mesh Element Order	Quadratic
Mesh Global Size	2 mm
Mesh Target Quality	0,6

Table 2.5.6.1: Main parameters of the topology optimization of the beam full of material with Load Case 3 applied.

The *design space* and the *non-design space* have been defined (Figure 2.5.6.1):

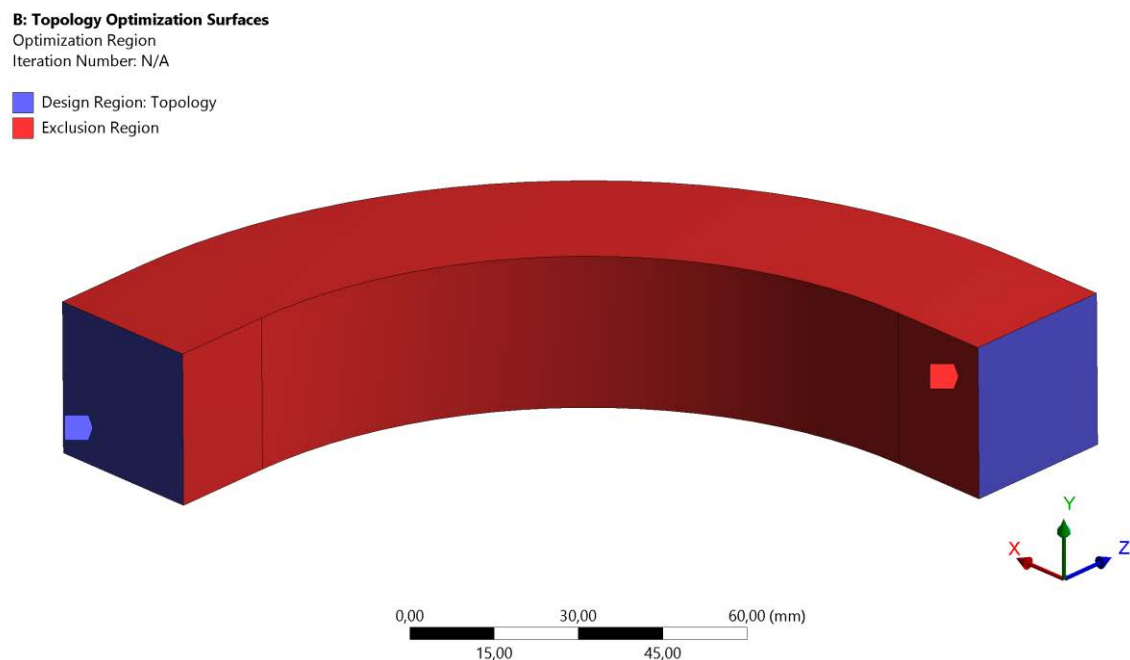


Figure 2.5.6.1: *Design space* and *non-design space*.

Has been taken the decision to define as *design space* all the full of material beam volume and to define as *non-design space* the outer surfaces of the beam, with the exclusion of the BCs surfaces that remain a design space. The decision about the *non-design space* has been taken because the purpose of this work is to build a structural inner support maintaining the integrity of the outer geometry of the beam.

To minimize *Compliance* (= maximize stiffness) has been chosen as the *Objective* of the topology optimization.

To retain a 30% of the *design space* volume has been set as the *Response Constraint*, to get as result a geometry that with the outer walls would weight about 50% less than the beam full of material.

One *Manufacturing Constraint* has been set specifying a minimum *Member Size* of 1 mm. This means that the topological solver cannot create a geometry member with a dimension less than 1 mm. 1 mm has been chosen because it is the minimum feature size that SLM process can build (Table 1.2.1).



The result of the *Retained Material* is shown in the image below (*Retained Threshold* = 0,5) (Figure 2.5.6.2):

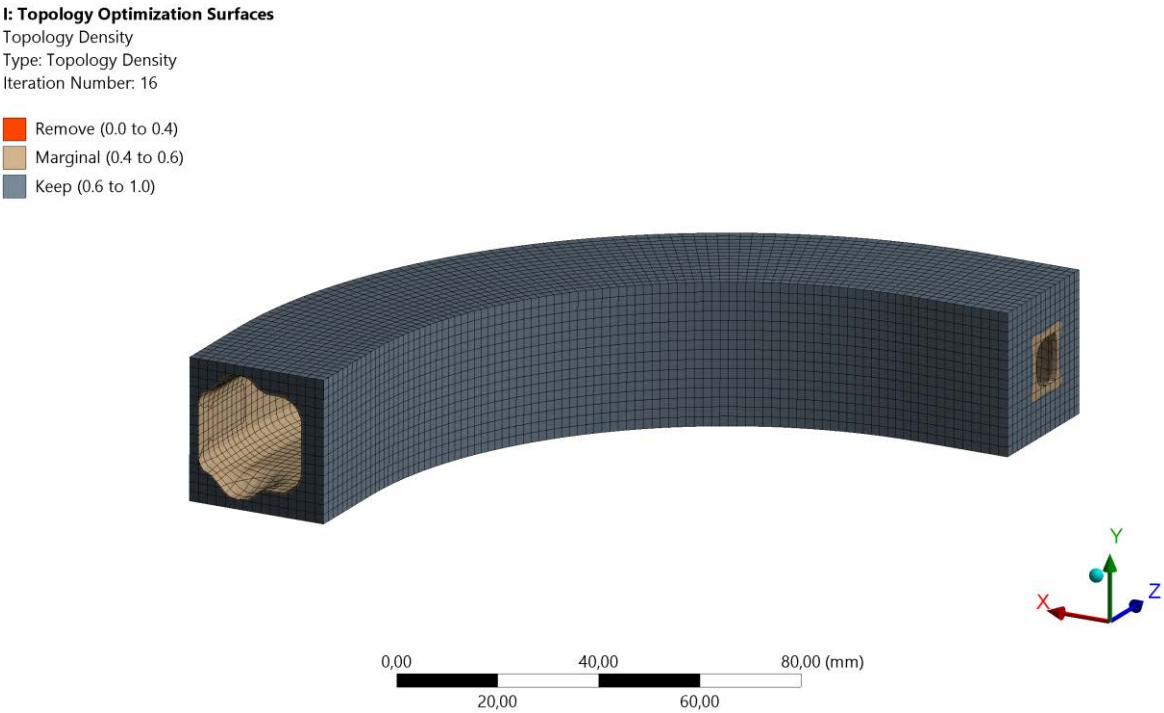


Figure 2.5.6.2: Topology optimization *Retained Material* result.

The result of the *Removed Material* is shown in the image below (*Retained Threshold* = 0,5) (Figure 2.5.6.3):

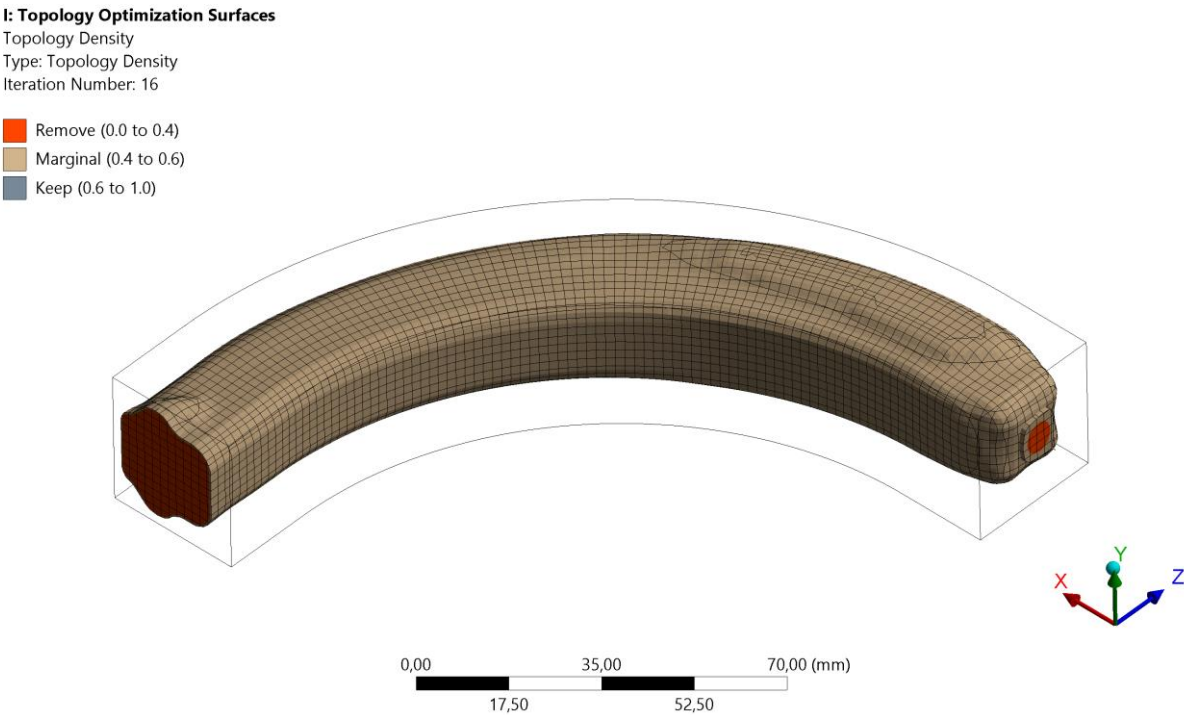


Figure 2.5.6.3: Topology optimization *Removed Material* result.

## 2.5.7 Load Cases 1+2+3: Inner support design upgrade

The aim of this subchapter is to develop a structural inner support that is suitable for carrying non only the Load Case 1 but also the Load Cases 2 and 3 and a sum of them. Has been decided to still use the pattern developed in Subchapter 2.5.3 and has been decided to upgrade the zones of the pattern filled of material taking in account also the results of the topology optimisations with Load Case 2 and with Load Case 3 applied. The beam still divided in three sectors (Figure 2.5.3.5).

Has been decided to leave the section of the sector 1 equal to the section developed before, for the curved beam with Load Case 1 applied, in Subchapter 2.5.3 (Figure 2.5.7.1):

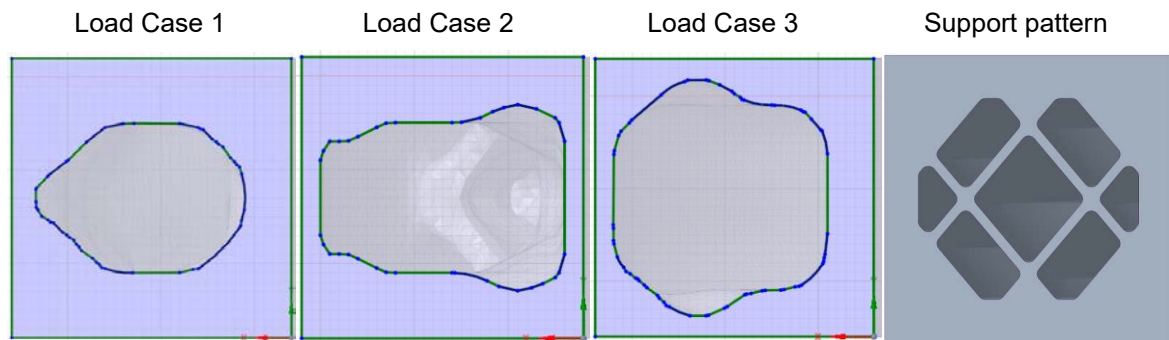


Figure 2.5.7.1: Sections of the sector 1: from the left to the right, of the topology optimized geometries and of the support pattern developed.

Has been decided to leave the section of the sector 2 equal to the section developed before, for the curved beam with Load Case 1 applied, in Subchapter 2.5.3 (Figure 2.5.7.2):

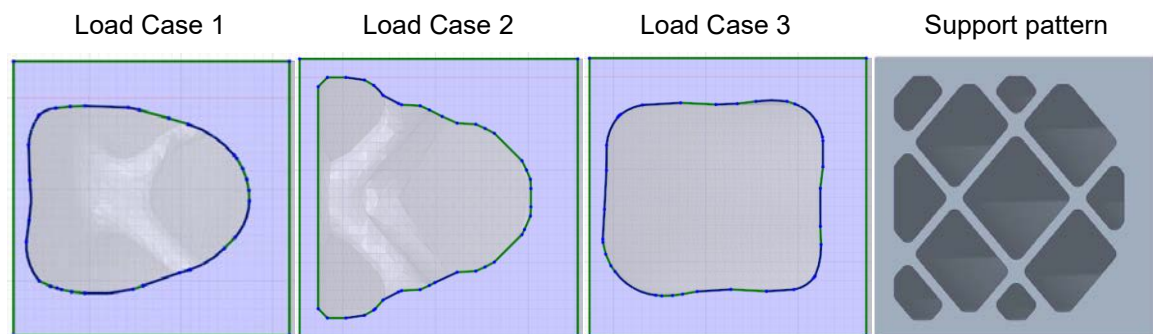


Figure 2.5.7.2: Sections of the sector 2: from the left to the right, of the topology optimized geometries and of the support pattern developed.

Has been decided to thicken the inner wall of the section of the sector 3 with respect to the section developed before, for the curved beam with Load Case 1 applied, in Subchapter 2.5.3 (Figure 2.5.7.3):

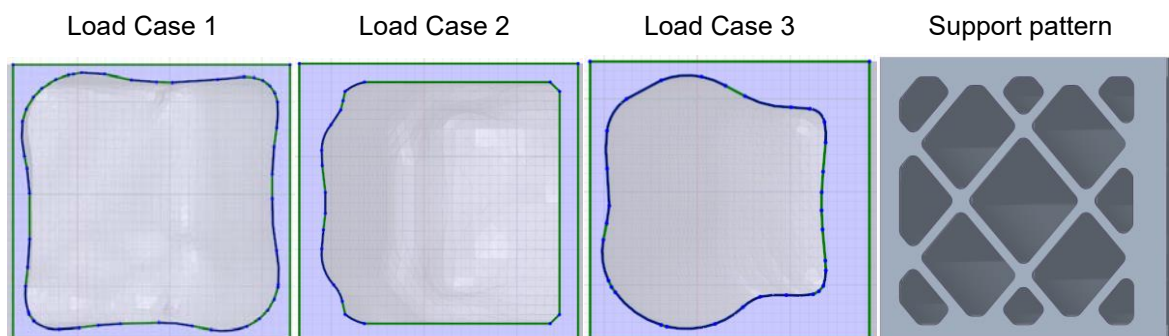


Figure 2.5.7.3: Sections of the sector 3: from the left to the right, of the topology optimized geometries and of the support pattern developed.

Below are shown the XZ-plane sections at near half of the height of the curved beam, as it comes from the topology optimizations with Load Case 1 and with Load Case 2 applied (Figure 2.5.7.4):

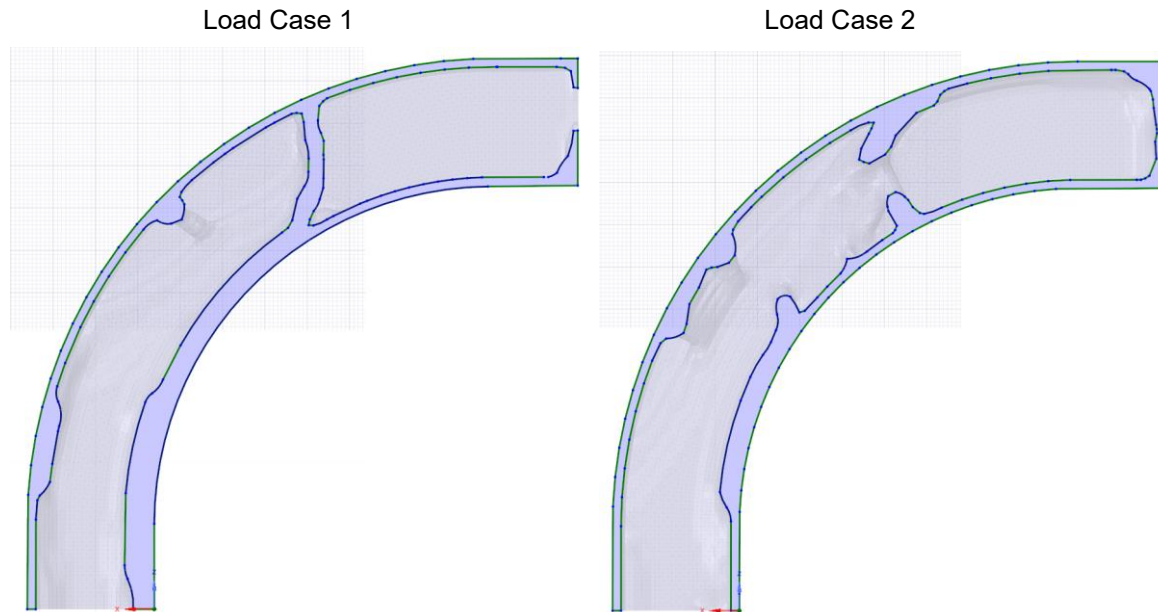


Figure 2.5.7.4: XZ-plane sections at near half of the height: on the left of the curved beam as it comes from the topology optimization with Load Case 1 applied and on the right of the curved beam as it comes from the topology optimization with Load Case 2 applied.

Below are shown the XZ-plane sections at near half of the height of the curved beam, as it comes from the topology optimization with Load Case 3 applied and of the curved beam with the structural inner support developed (Figure 2.5.7.5).

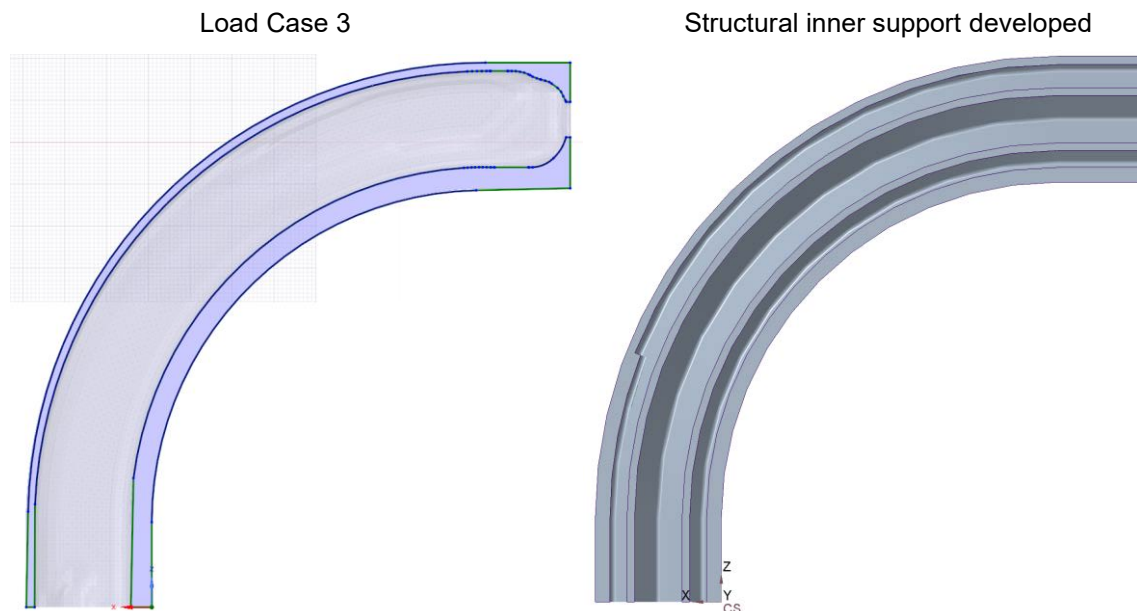


Figure 2.5.7.5: XZ-plane sections at near half of the height, on the left of the beam as it comes from the topology optimization with Load Case 3 applied and on the right of the beam with the structural inner support developed.

Below is shown an image of the complete curved beam with the structural inner support developed for the Load Cases 1+2+3 (Figure 2.5.7.6):

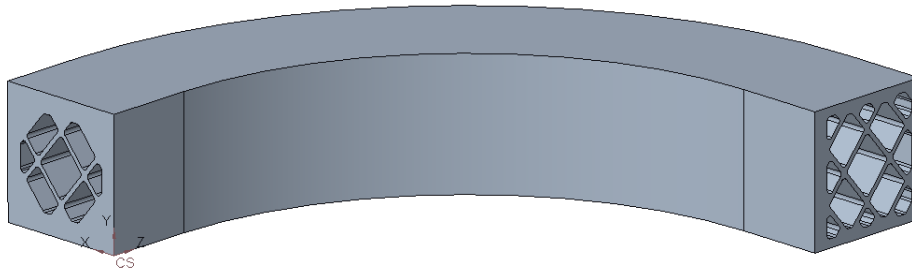


Figure 2.5.7.6: Curved beam with the structural inner support developed for the Load Cases 1+2+3

Has been also tried to increase the stiffness of the curved beam with the structural inner support just developed with two inner additional walls placed in the sector 2 as shown in the images below (Figure 2.5.7.7, Figure 2.5.7.8):

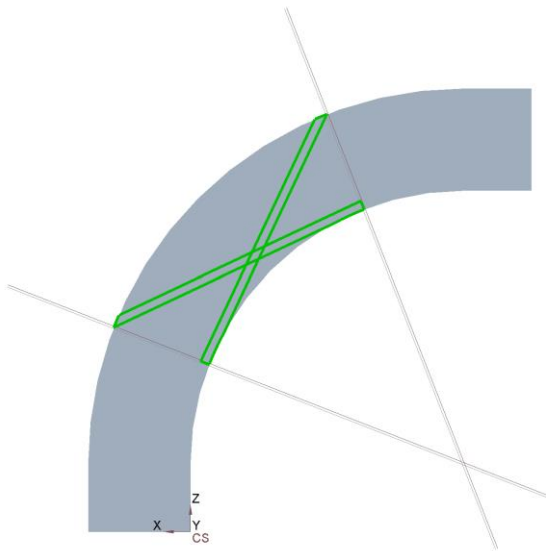


Figure 2.5.7.7: Additional inner walls position.

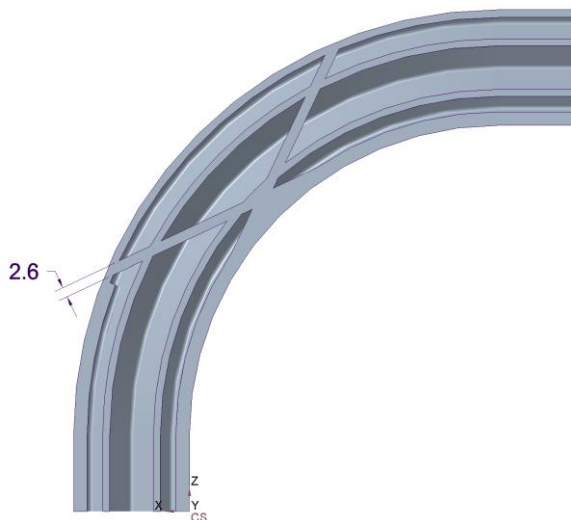


Figure 2.5.7.8: XZ-plane section at near half of the height of the curved beam, with the structural inner support just developed and with the two additional inner walls.

## 2.5.8 Load Cases 1+2+3: F.E.M. Analyses

The static structural F.E.M. analyses have been performed with the main parameters showed in the table below (Table 2.5.8.1):

Material	Anslys default Structural Steel (Table 2.3.1)
Mesh Element Type	SOLID187
Mesh Element Order	Quadratic
Mesh Global Size	1 mm
Mesh Target Quality	0,6

Table 2.5.8.1: Main parameters of the static structural F.E.M. analyses.

The static structural F.E.M. analysis of the curved beam full of material with Load Case 2 applied and with Load Case 3 applied have been already performed in Subchapter 2.3.2 and Subchapter 2.3.3 respectively.

Have been performed the static structural F.E.M. analyses of the hollow curved beam with Load Case 2 applied and with Load Case 3 applied. To not burden the discussion has been decided to show only the results of total displacement in the summarizing tables 2.5.8.2 and 2.5.8.3.

Have been performed the static structural F.E.M. analyses of the curved beam with the last developed structural inner support with Load Case 2 applied and with Load Case 3 applied. The Von Mises equivalent stress results are shown in the images below (Figure 2.5.8.1 for Load Case 2 and Figure 2.5.8.2 for Load Case 3):

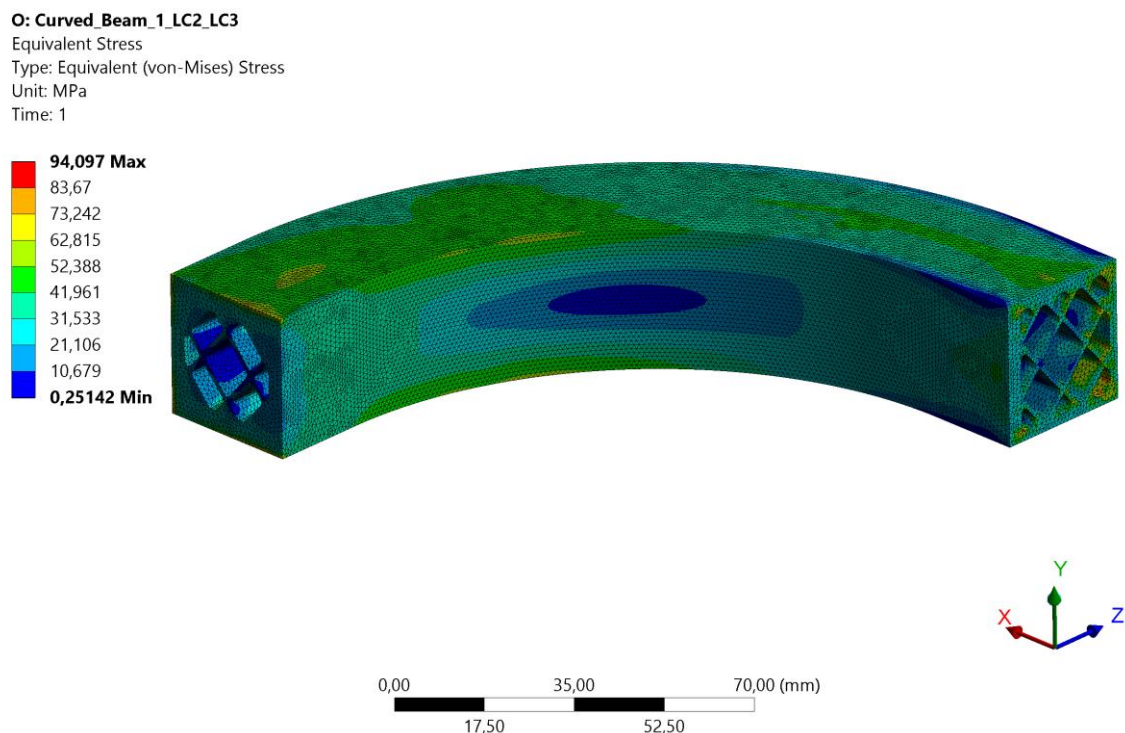


Figure 2.5.8.1: Von Mises equivalent stress of the curved beam with the last developed structural inner support and with Load Case 2 applied.



**O: Curved\_Beam\_1\_LC2\_LC3**  
 Equivalent Stress  
 Type: Equivalent (von-Mises) Stress  
 Unit: MPa  
 Time: 1

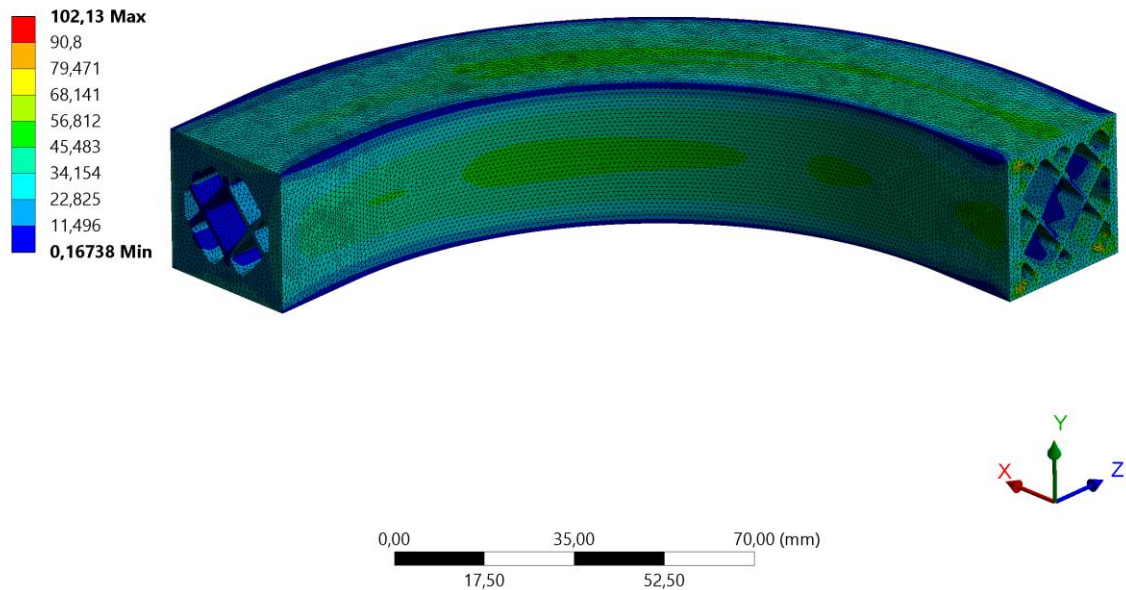


Figure 2.5.8.2: Von Mises equivalent stress of the curved beam with the last developed structural inner support and with Load Case 3 applied.

Have been performed the static structural F.E.M. analyses of the curved beam with the last developed structural inner support and with the two additional inner walls, with Load Case 2 applied and with Load Case 3 applied. The Von Mises equivalent stress results are shown in the images below (Figure 2.5.8.3 for Load Case 2 and Figure 2.5.8.4 for Load Case 3):

**R: Curved\_Beam\_1\_Walls\_LC2\_LC3**  
 Equivalent Stress  
 Type: Equivalent (von-Mises) Stress  
 Unit: MPa  
 Time: 1

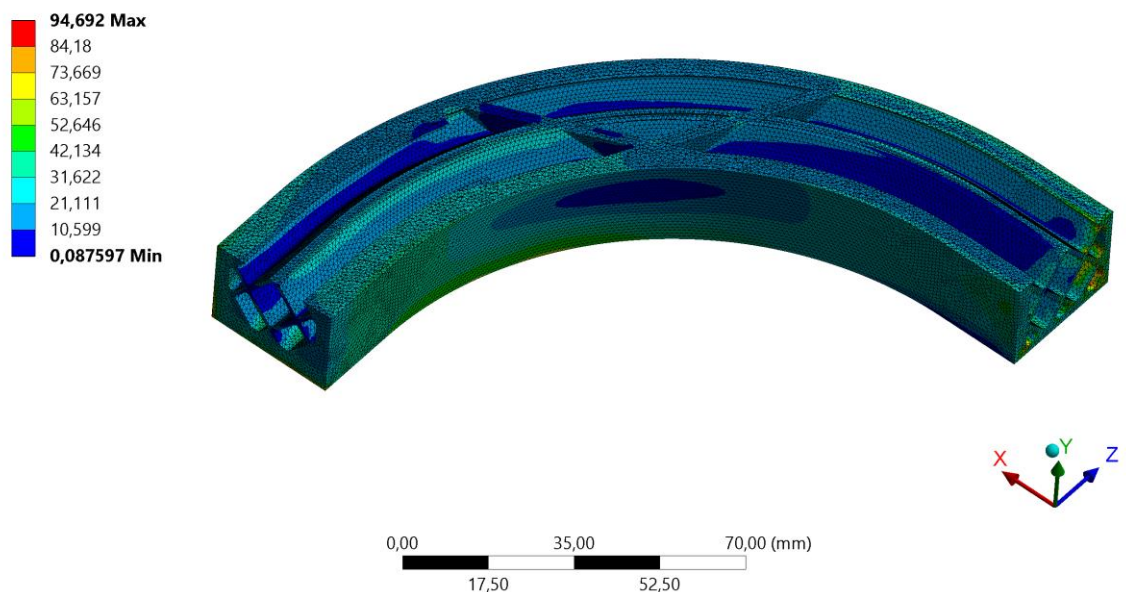


Figure 2.5.8.3: Von Mises equivalent stress of the curved beam with the last developed structural inner support and with the two inner additional walls, with Load Case 2 applied.

**R: Curved\_Beam\_1\_Walls\_LC2\_LC3**

Equivalent Stress

Type: Equivalent (von-Mises) Stress

Unit: MPa

Time: 1

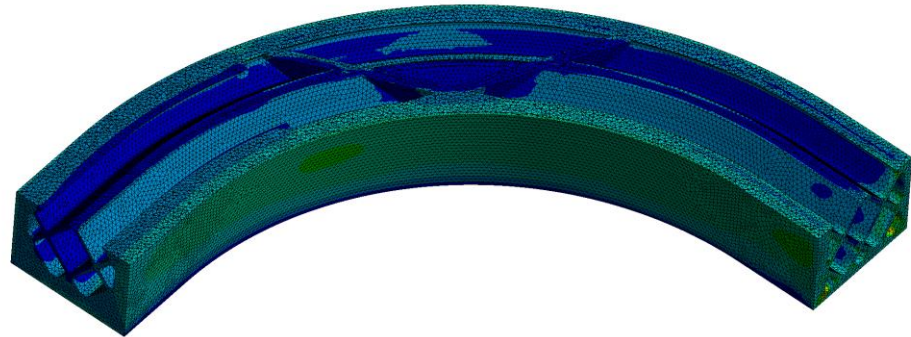
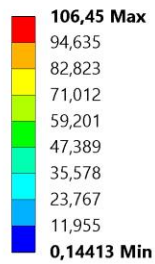


Figure 2.5.8.4: Von Mises equivalent stress of the curved beam with the last developed structural inner support and with the two inner additional walls, with Load Case 3 applied.

Have been performed the static structural F.E.M. analysis of the curved beam as it comes from the topology optimization with Load Case 2 applied. The Von Mises equivalent stresses is shown in the image below (Figure 2.5.8.5):

**F: Topology Validation**

Equivalent Stress

Type: Equivalent (von-Mises) Stress

Unit: MPa

Time: 1

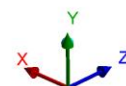
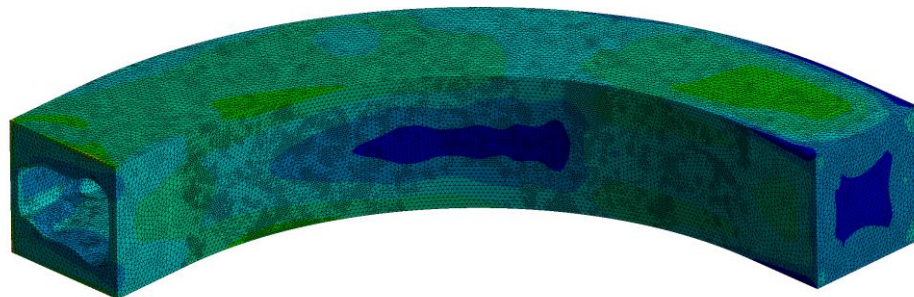
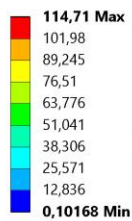


Figure 2.5.8.5: Von Mises equivalent stress of the curved beam as it comes from the topology optimization with Load Case 2 applied.

Have been performed the static structural F.E.M. analysis of the curved beam as it comes from the topology optimization with Load Case 3 applied. The Von Mises equivalent stresses is shown in the image below (Figure 2.5.8.6):

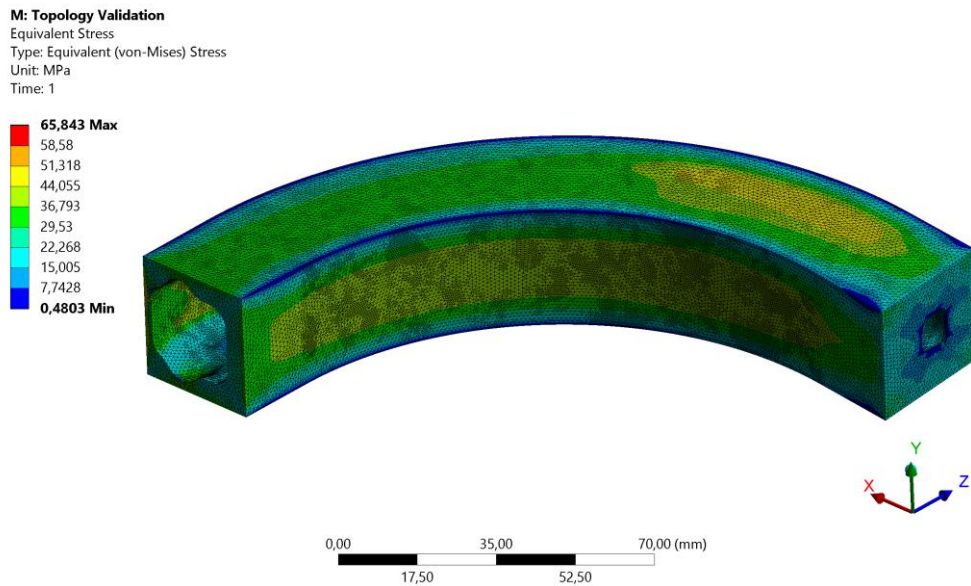


Figure 2.5.8.6: Von Mises equivalent stress of the curved beam as it comes from the topology optimization with Load Case 3 applied.

The results are summarized in the tables below (Table 2.5.8.2, Table 2.5.8.3):

Load Case 2	Full	Hollow	Developed inner support	Developed inner support with two walls	Topology Optimization
Weight [g]	1337	333	731	767	641
Total Displacement Max  [mm]	0,200	0,871	0,264	0,260	0,272
Weight * Displacement (Minimum is better)	<b>267</b>	<b>290</b>	<b>193</b>	<b>199</b>	<b>174</b>

Table 2.5.8.2: Results comparison between the different beams with Load Case 2 applied.

Load Case 3	Full	Hollow	Developed inner support	Developed inner support with two walls	Topology Optimization
Weight [g]	1337	333	731	767	641
Total Displacement Max  [mm]	0,122	0,338	0,171	0,168	0,172
Weight * Displacement (Minimum is better)	<b>163</b>	<b>113</b>	<b>125</b>	<b>129</b>	<b>110</b>

Table 2.5.8.3: Results comparison between the different beams with Load Case 3 applied.

The Weight \* Displacement indexes of the curved beam with the last structural inner support developed are 9.8 % and 12 % higher, for Load Case 2 and Load Case 3 respectively, with respect to the indexes of the curved beams as they come from the topology optimizations. It is a good result because due to the support structure necessities, it is difficult to reach the Weight \* Displacement indexes of the topology optimized beams, that have been optimized without caring about the impossibility of printing them with some additive manufacturing technologies without adding to them some further supports. The two inner additional walls configuration increases by 3 % the Weight \* Displacement indexes in both Load Case 2 scenario and Load Case 3 scenario, so it is not an efficient way of adding material to the last structural inner support developed.



Two buckling analyses have been performed: the first one of the curved beam with the last structural inner support developed and the second one of the curved beam with the last structural inner support developed and with the two additional inner walls, to see if the two additional inner walls can increase the minimum load of buckling to happen.

Has been taken in account the Load Case 2. To get as result of each of the two buckling analyses a single value of buckling force, a single force of -1 N has been applied in the same position where the single -800 N force, directed along the Y-axis, should be applied to generate also a +MX torsional moment of 80000 N\*mm (Figure 2.5.8.7).

**T: Curved\_Beam\_1\_Walls\_LC2\_1,5mm**

Static Structural

Time: 1, s

**A** Fixed Support

**B** Remote Force: 1, N

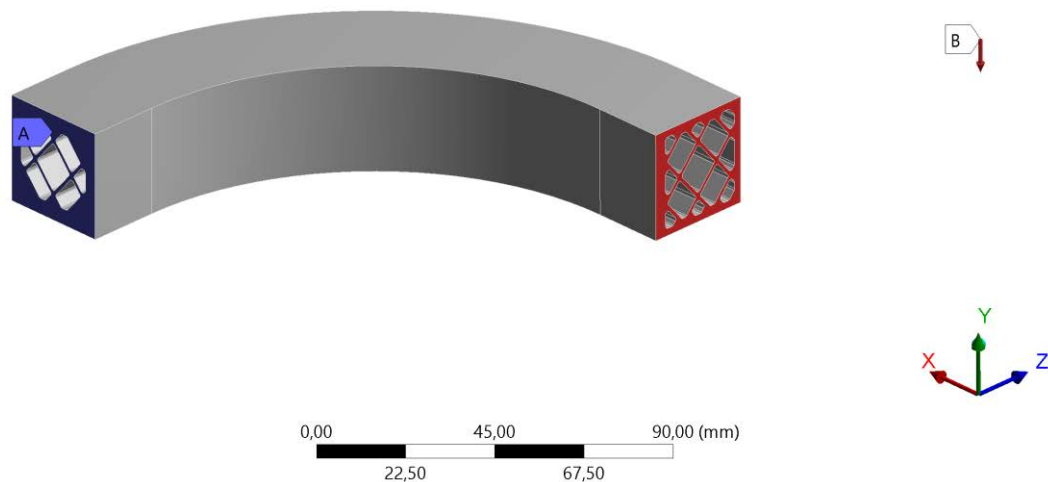


Figure 2.5.8.7: Boundary conditions for the buckling analyses.

For these buckling analyses, due to the 16gb of RAM of the computer used, a 1,5 mm mesh has been used instead of the 1mm mesh used for the static structural analyses that have been done before (Table 2.5.8.4).

Material	Ansys default Structural Steel (Table 2.3.1)
Mesh Element Type	SOLID187
Mesh Element Order	Quadratic
Mesh Global Size	1,5 mm
Mesh Target Quality	0,6

Table 2.5.8.4: Main parameters of the linear elastic buckling F.E.M. analyses.

The load multiplier of the mode number 4 for the curved beam without the two walls is the minimum ideal load that should be applied to the structure for buckling to happen.

The load multiplier of the mode number 3 for the curved beam with the two walls is the minimum ideal load that should be applied to the structure for buckling to happen.

In the image below (Figure 2.5.8.8) are highlighted the zones of the curved beam without the two walls where the buckling should happen:

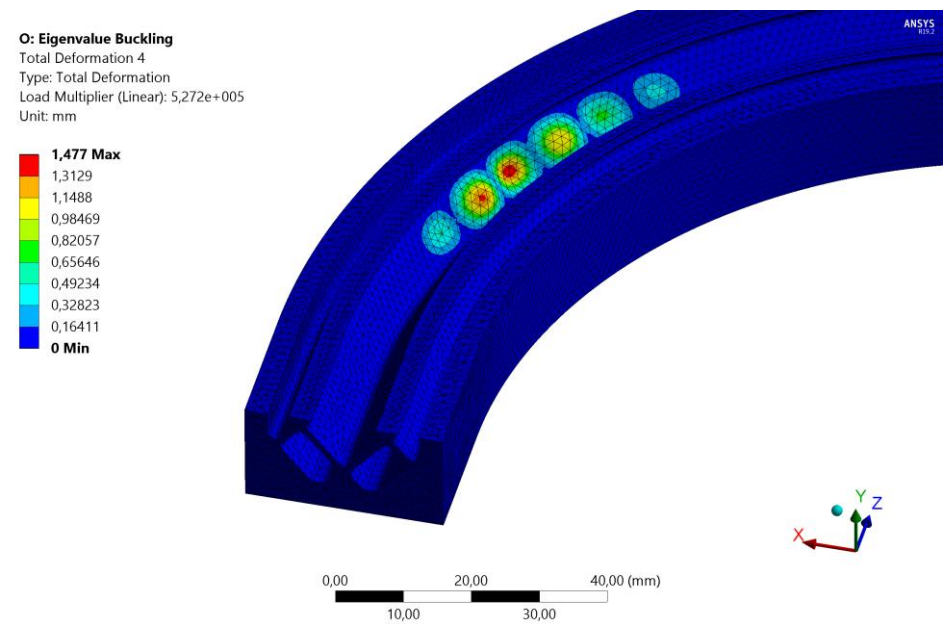


Figure 2.5.8.8: Displacement shape of the mode 4 that shows the zones of the curved beam without the two walls where the buckling should happen.

In the image below (Figure 2.5.8.9) are highlighted the zones of the curved beam with the two walls where the buckling should happen due to the load multiplier of mode number 4 that is not anymore, the minimum one.

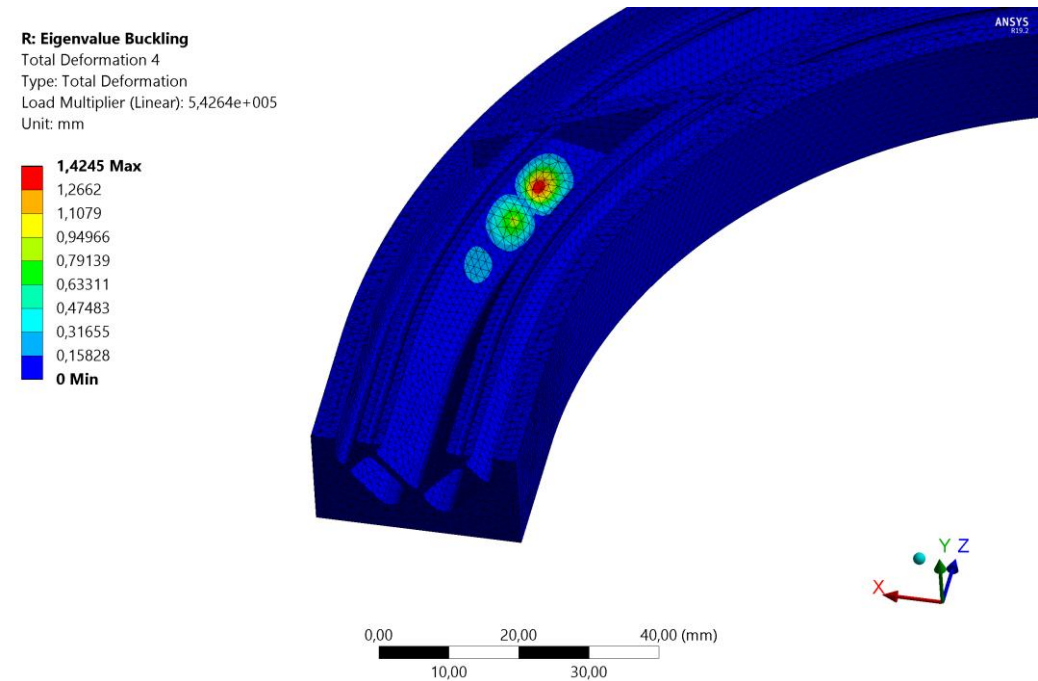


Figure 2.5.8.9: Displacement shape of the mode 4 that shows the zones of the curved beam with the two walls where the buckling should happen.

In the image below (Figure 2.5.8.10) are highlighted the zones of the curved beam with the two walls where the buckling should happen due to the load multiplier of mode number 3 that is the minimum one.

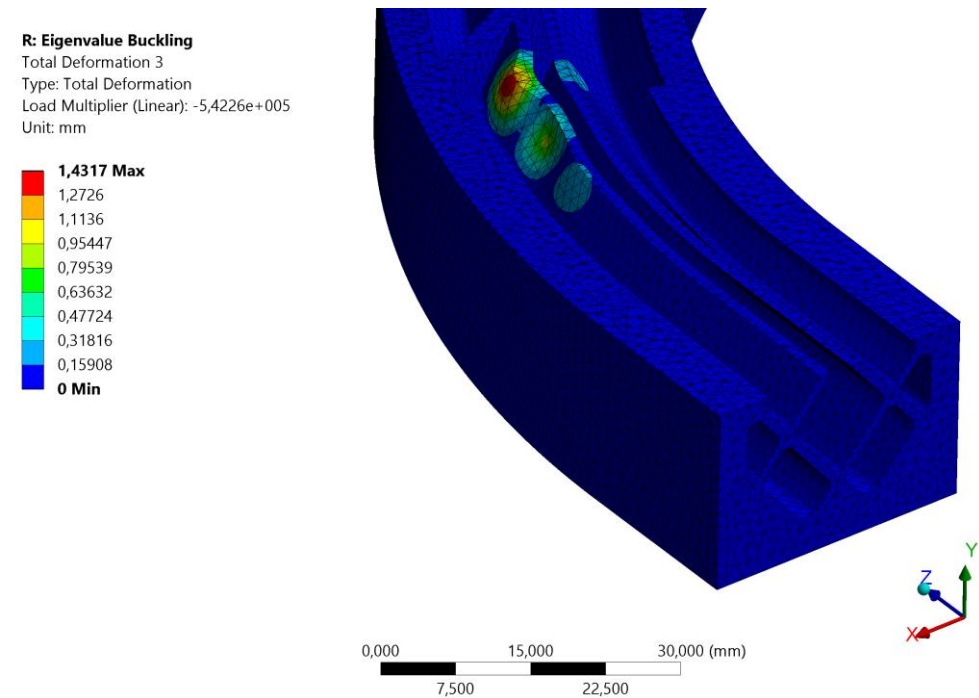


Figure 2.5.8.10: Displacement shape of the mode 3 that shows the zones of the curved beam with the two walls where the buckling should happen.

The results are summarized in the table below (Table 2.5.8.5):

	Load Multiplier (Minimum) [N]	Difference [%]
Curved beam without the two walls	527200	2,8
Curved beam with the two walls	542260	

Table 2.5.8.5: Results of the minimum load for buckling to happen for the curved beam without the two walls and for the curved beam with the two walls.

The increase of 2,8 % of the minimum load for buckling to happen for the curved beam with the two walls is too little to take in account this configuration as a good upgrade of the structural inner support developed without the two walls.

### 2.5.9 Load Case 4: Topology Optimization

The topology optimization has been done with the main parameters showed in the table below (Table 2.5.9.1):

Material	Ansys default Structural Steel (Table 2.3.1)
Mesh Element Type	SOLID186
Mesh Element Order	Quadratic
Mesh Global Size	2 mm
Mesh Target Quality	0,6

Table 2.5.9.1: Main parameters of the topology optimization of the beam full of material with Load Case 4 applied.

The *design space* and the *non-design space* have been defined (Figure 2.5.9.1):

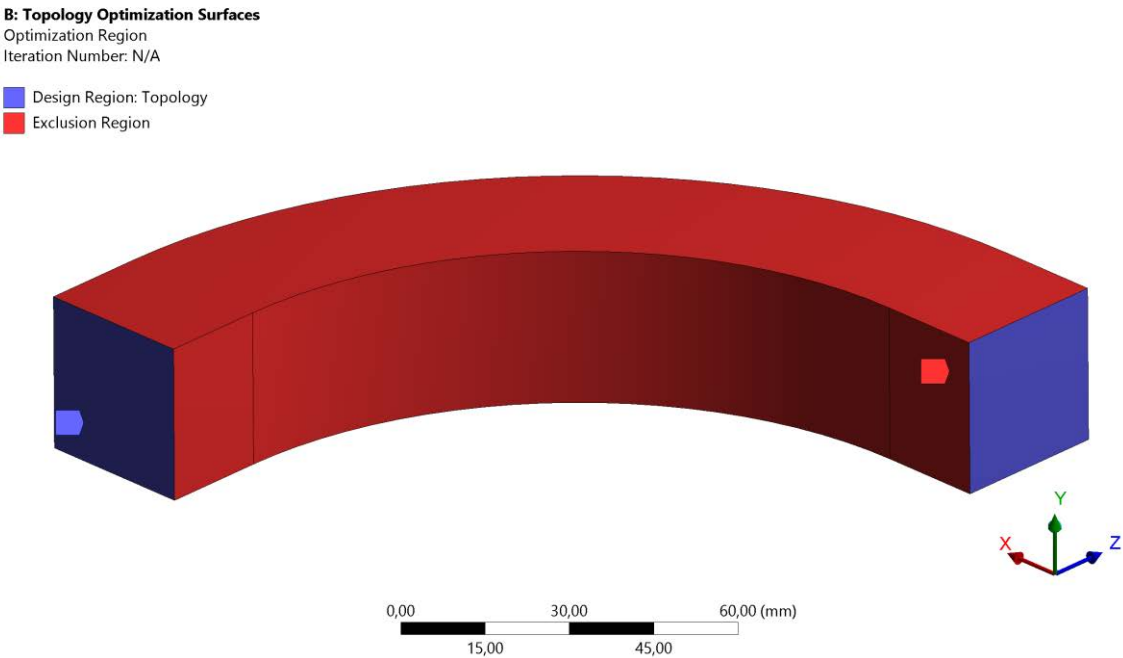


Figure 2.5.9.1: *Design space* and *non-design space*.

Has been taken the decision to define as *design space* all the full of material beam volume and to define as *non-design space* the outer surfaces of the beam, with the exclusion of the BCs surfaces that remain a design space. The decision about the *non-design space* has been taken because the purpose of this work is to build a structural inner support maintaining the integrity of the outer geometry of the beam.

To minimize *Compliance* (= maximize stiffness) has been chosen as the *Objective* of the topology optimization.

To retain a 30% of the *design space* volume has been set as the *Response Constraint*, to get as result a geometry that with the outer walls would weight about 50% less than the beam full of material.

One *Manufacturing Constraint* has been set specifying a minimum *Member Size* of 1 mm. This means that the topological solver cannot create a geometry member with a dimension less than 1 mm. 1 mm has been chosen because it is the minimum feature size that SLM process can build (Table 1.2.1).

The result of the *Retained Material* is shown in the images below (*Retained Threshold* = 0,5) (Figure 2.5.9.2, Figure 2.5.9.3):

**B: Topology Optimization**

Topology Density  
Type: Topology Density  
Iteration Number: 14

- Remove (0.0 to 0.4)
- Marginal (0.4 to 0.6)
- Keep (0.6 to 1.0)

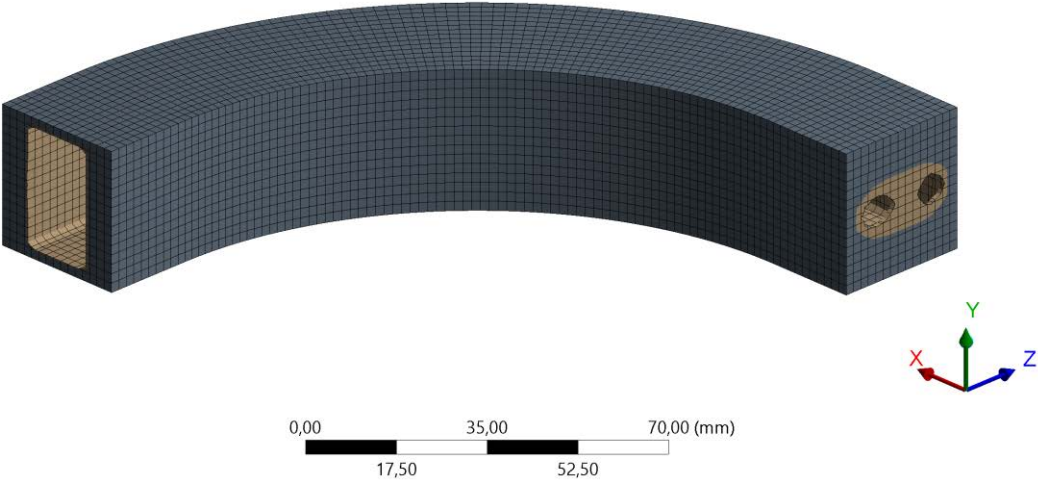


Figure 2.5.9.2: Topology optimization *Retained Material* result.

**B: Topology Optimization**

Topology Density  
Type: Topology Density  
Iteration Number: 14

- Remove (0.0 to 0.4)
- Marginal (0.4 to 0.6)
- Keep (0.6 to 1.0)

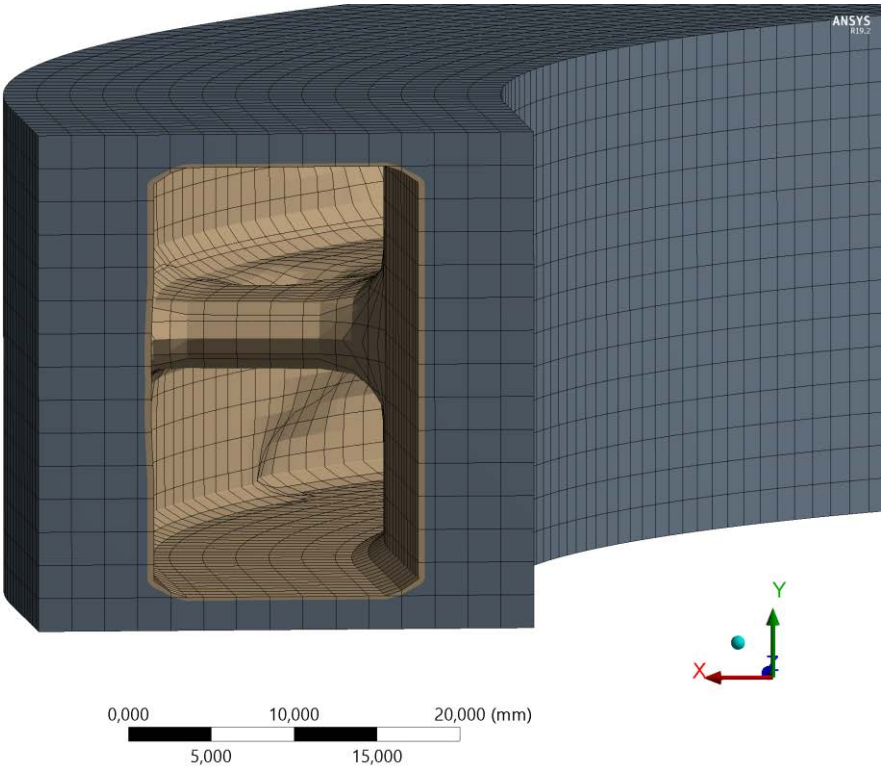


Figure 2.5.9.3: Topology optimization *Retained Material* zoom result.

The result of the *Removed Material* is shown in the image below (*Retained Threshold* = 0,5) (Figure 2.5.9.4):

**B: Topology Optimization**

Topology Density

Type: Topology Density

Iteration Number: 14

- Remove (0.0 to 0.4)
- Marginal (0.4 to 0.6)
- Keep (0.6 to 1.0)

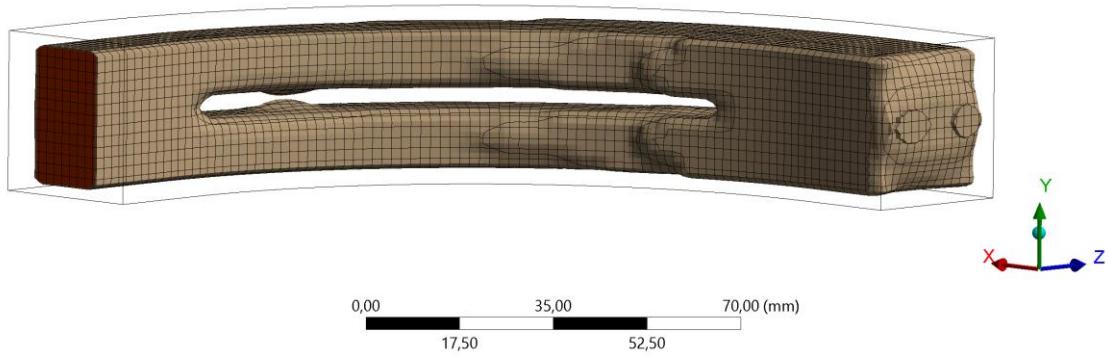


Figure 2.5.9.4: Topology optimization *Removed Material* result.

## 2.5.10 Load Case 5: Topology Optimization

The topology optimization has been done with the main parameters showed in the table below (Table 2.5.10.1):

Material	Ansys default Structural Steel (Table 2.3.1)
Mesh Element Type	SOLID186
Mesh Element Order	Quadratic
Mesh Global Size	2 mm
Mesh Target Quality	0,6

Table 2.5.10.1: Main parameters of the topology optimization of the beam full of material with Load Case 5 applied.

The *design space* and the *non-design space* have been defined (Figure 2.5.10.1):

### B: Topology Optimization Surfaces

Optimization Region  
Iteration Number: N/A

■ Design Region: Topology  
■ Exclusion Region

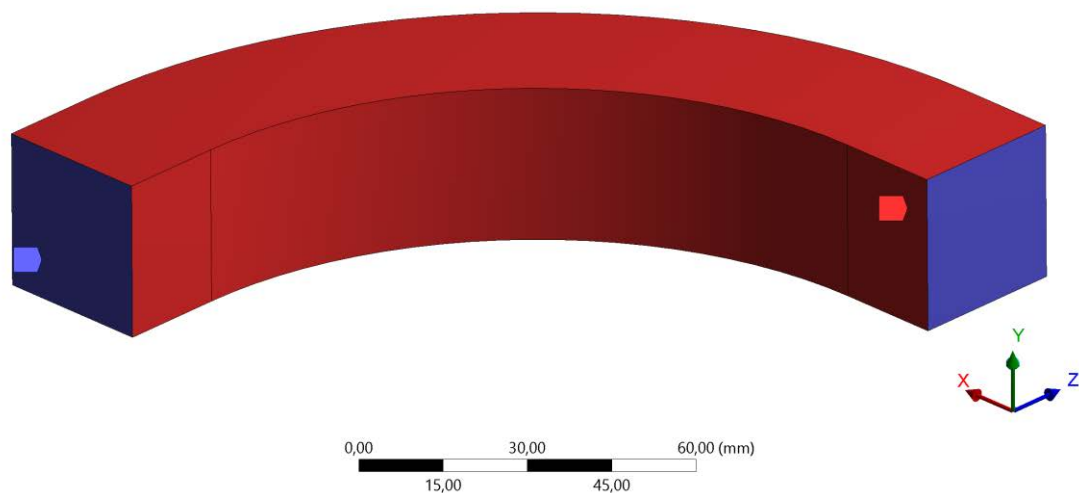


Figure 2.5.10.1: *Design space* and *non-design space*.

Has been taken the decision to define as *design space* all the full of material beam volume and to define as *non-design space* the outer surfaces of the beam, with the exclusion of the BCs surfaces that remain a design space. The decision about the *non-design space* has been taken because the purpose of this work is to build a structural inner support maintaining the integrity of the outer geometry of the beam.

To minimize *Compliance* (= maximize stiffness) has been chosen as the *Objective* of the topology optimization.

To retain a 30% of the *design space* volume has been set as the *Response Constraint*, to get as result a geometry that with the outer walls would weight about 50% less than the beam full of material.

One *Manufacturing Constraint* has been set specifying a minimum *Member Size* of 1 mm. This means that the topological solver cannot create a geometry member with a dimension less than 1 mm. 1 mm has been chosen because it is the minimum feature size that SLM process can build (Table 1.2.1).



The result of the *Retained Material* is shown in the image below (*Retained Threshold* = 0,5) (Figure 2.5.10.2, Figure 2.5.10.3):

**D: Topology Optimization**

Topology Density  
Type: Topology Density  
Iteration Number: 16

- Remove (0.0 to 0.4)
- Marginal (0.4 to 0.6)
- Keep (0.6 to 1.0)

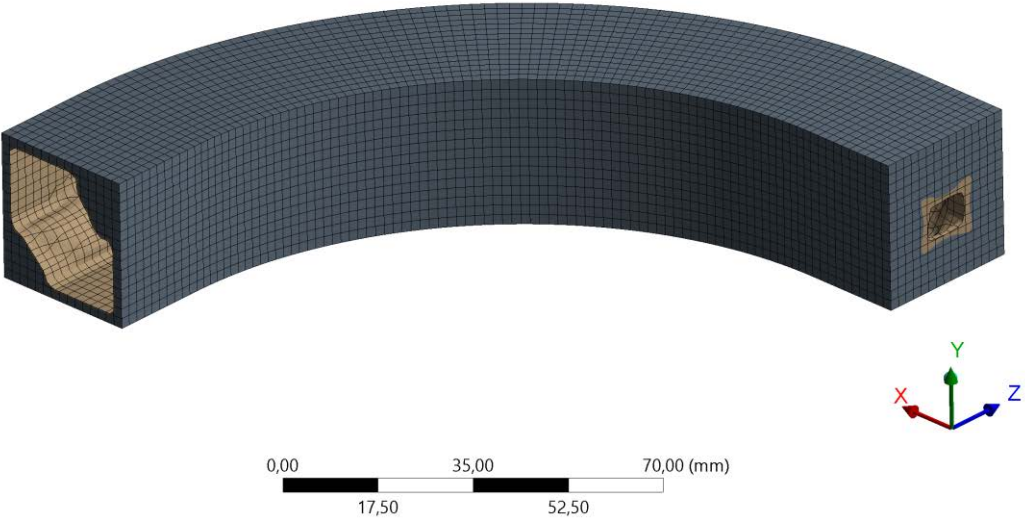


Figure 2.5.10.2: Topology optimization *Retained Material* result.

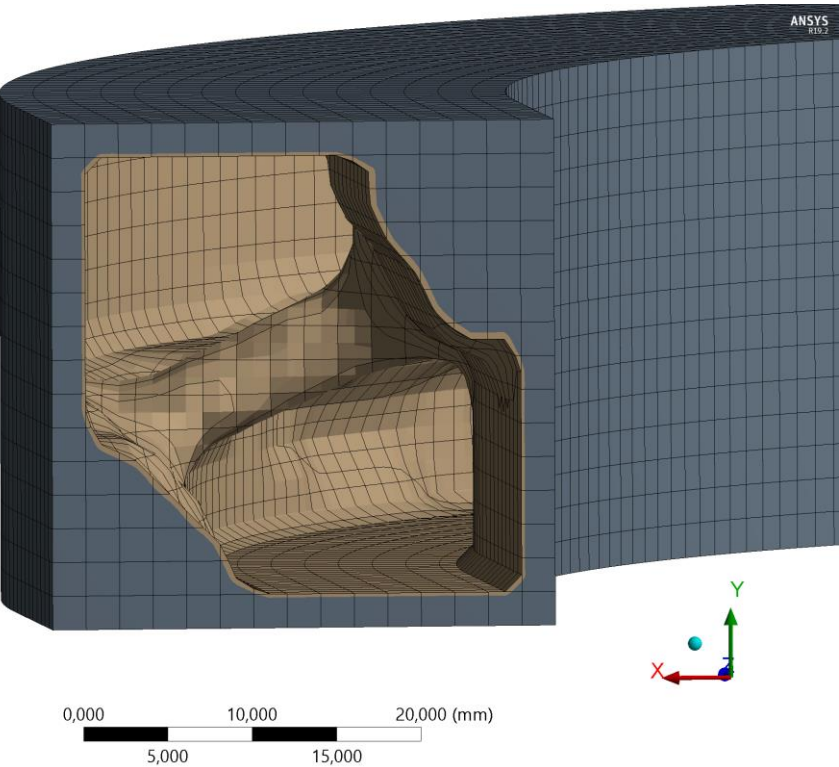


Figure 2.5.10.3: Topology optimization *Retained Material* zoom result.

The result of the *Removed Material* is shown in the image below (*Retained Threshold* = 0,5) (Figure 2.5.10.4):

**F: Topology Optimization**

Topology Density

Type: Topology Density

Iteration Number: 16

- Remove (0.0 to 0.4)
- Marginal (0.4 to 0.6)
- Keep (0.6 to 1.0)

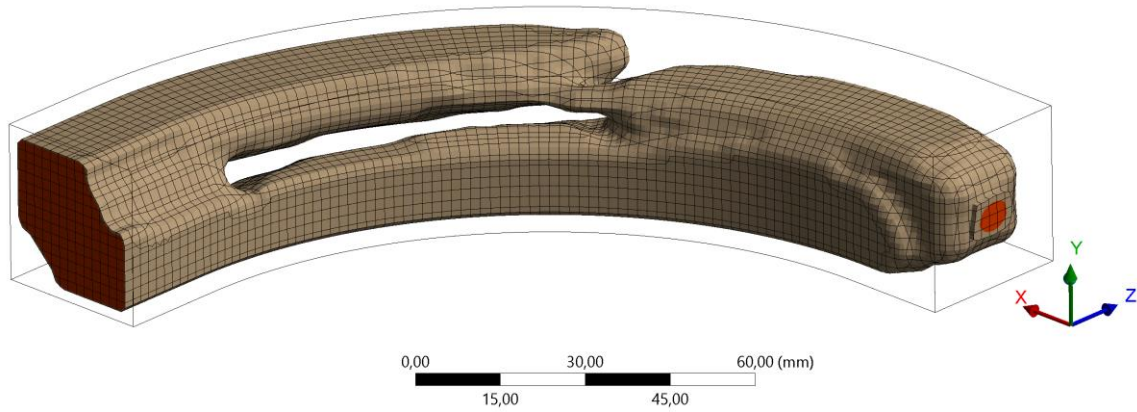


Figure 2.5.10.4: Topology optimization *Removed Material* result.

2.5.11 Load Case 6: Topology Optimization

The topology optimization has been done with the main parameters showed in the table below (Table 2.5.11.1):

Material	Ansys default Structural Steel (Table 2.3.1)
Mesh Element Type	SOLID186
Mesh Element Order	Quadratic
Mesh Global Size	2 mm
Mesh Target Quality	0,6

Table 2.5.11.1: Main parameters of the topology optimization of the beam full of material with Load Case 6 applied.

The *design space* and the *non-design space* have been defined (Figure 2.5.11.1):

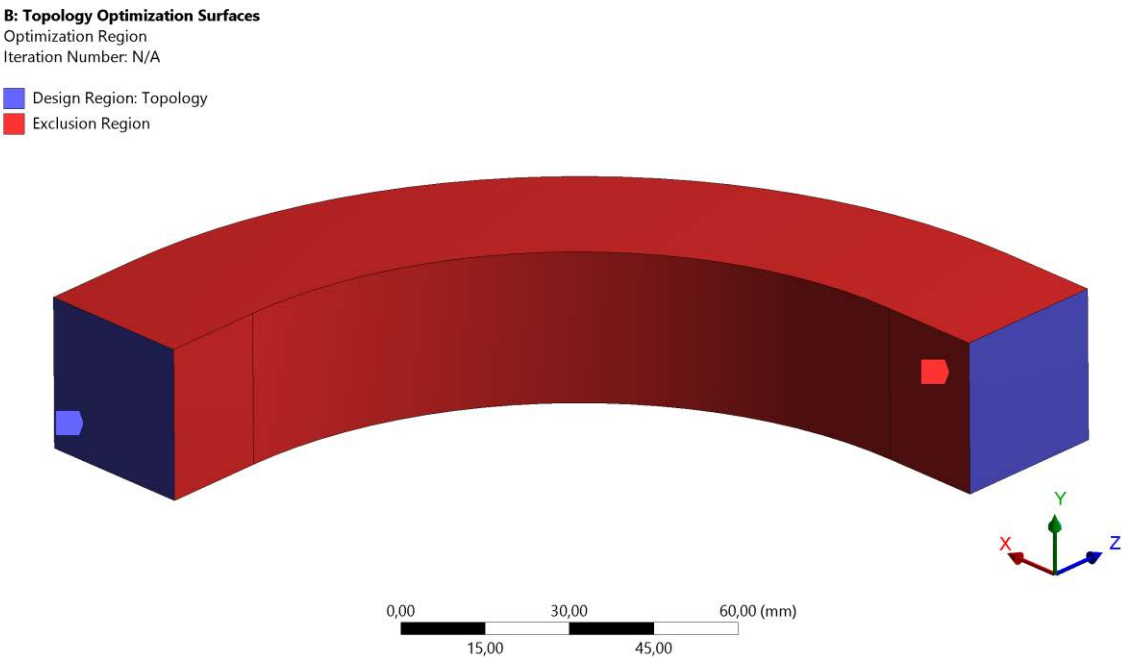


Figure 2.5.11.1: *Design space* and *non-design space*.

Has been taken the decision to define as *design space* all the full of material beam volume and to define as *non-design space* the outer surfaces of the beam, with the exclusion of the BCs surfaces that remain a design space. The decision about the *non-design space* has been taken because the purpose of this work is to build a structural inner support maintaining the integrity of the outer geometry of the beam.

To minimize *Compliance* (= maximize stiffness) has been chosen as the *Objective* of the topology optimization.

To retain a 30% of the *design space* volume has been set as the *Response Constraint*, to get as result a geometry that with the outer walls would weight about 50% less than the beam full of material.

One *Manufacturing Constraint* has been set specifying a minimum *Member Size* of 1 mm. This means that the topological solver cannot create a geometry member with a dimension less than 1 mm. 1 mm has been chosen because it is the minimum feature size that SLM process can build (Table 1.2.1).

The result of the *Retained Material* is shown in the image below (*Retained Threshold = 0,5*) (Figure 2.5.11.2, Figure 2.5.11.3):

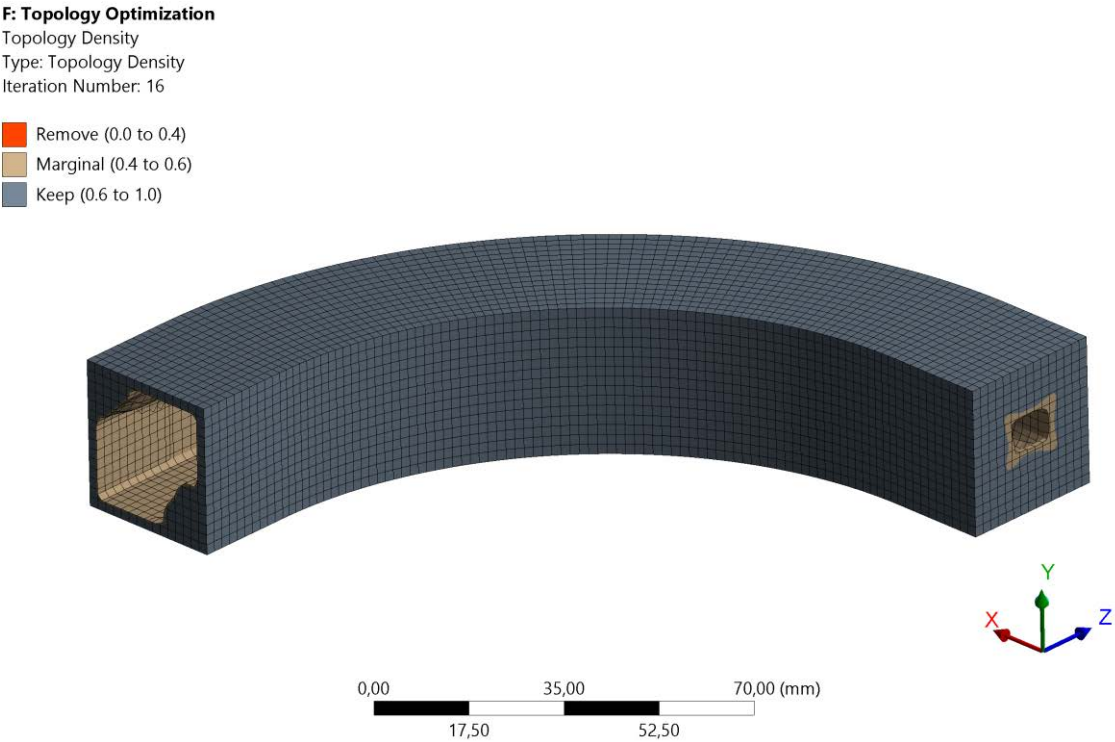


Figure 2.5.11.2: Topology optimization *Retained Material* result.

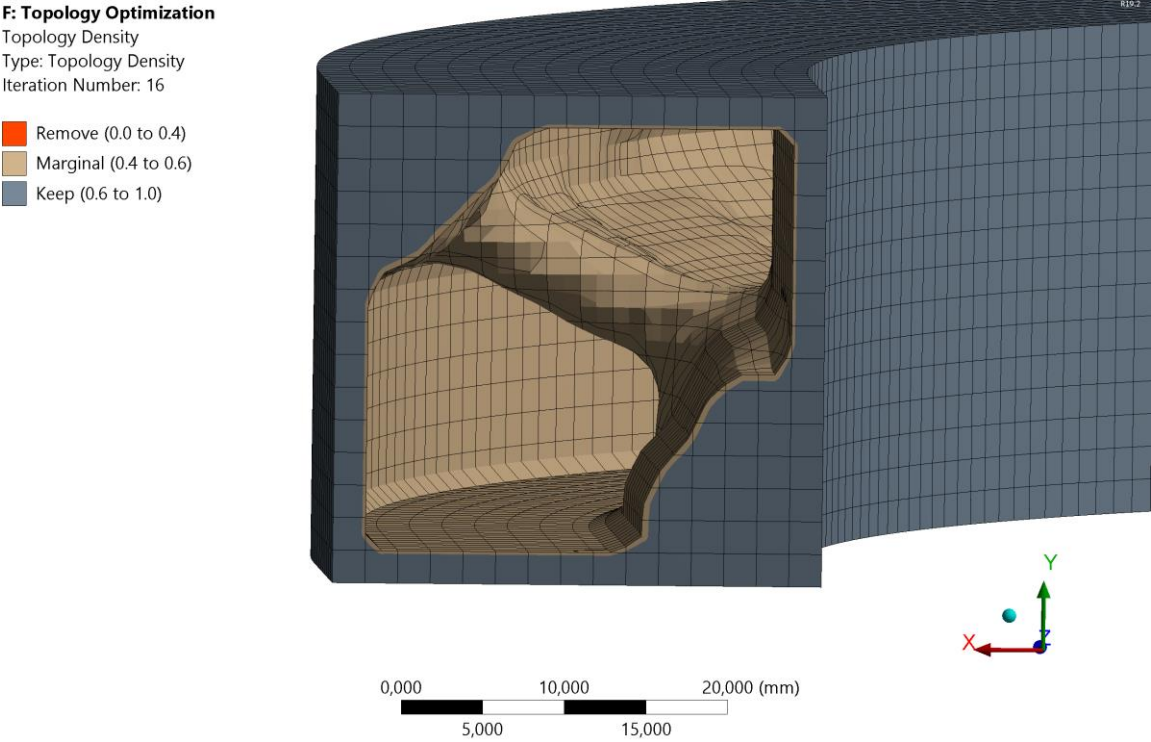


Figure 2.5.11.3: Topology optimization *Retained Material* zoom result.

The result of the *Removed Material* is shown in the image below (*Retained Threshold* = 0,5) (Figure 2.5.11.4):

**K: Topology Optimization**

Topology Density

Type: Topology Density

Iteration Number: 16

- Remove (0.0 to 0.4)
- Marginal (0.4 to 0.6)
- Keep (0.6 to 1.0)

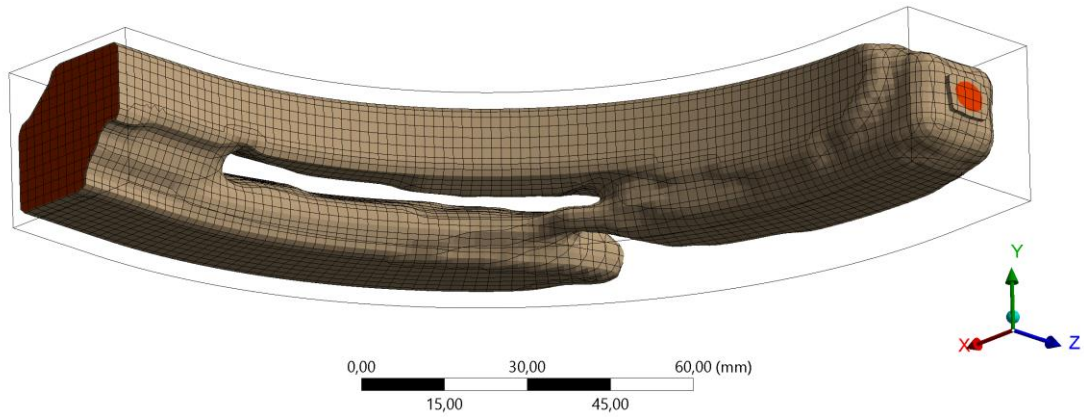


Figure 2.5.11.4: Topology optimization *Removed Material* result.

## 2.5.12 Load Cases 4+5+6: Inner support design upgrade

The aim of this subchapter is to develop a structural inner support that is suitable for carrying the Load Cases 4, 5 and 6 and a sum of them.

Following the results of the topology optimizations with Load Cases 4, 5 and 6 applied, has been decided to change the position of the curved beam in the print volume to be able of developing a more effective structural inner support (Figure 2.5.12.1).

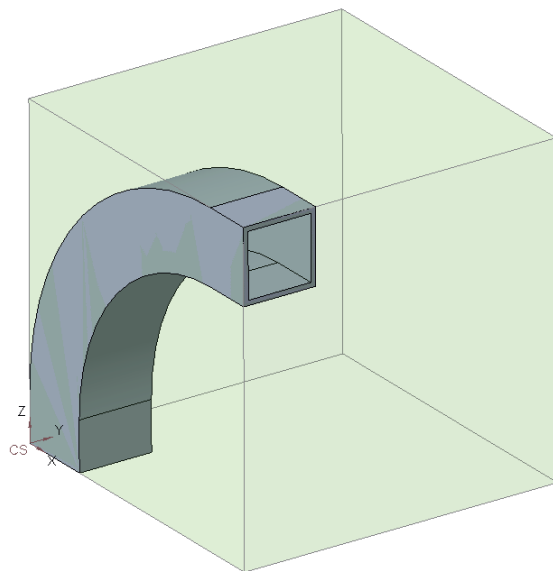


Figure 2.5.12.1: Hollow curved beam placement in the print volume (Z-axis is the print direction).

Has been decided to still use the pattern developed in Subchapter 2.5.3. Has been decided to rotate it by 90° with respect to the hollow curved beam outer geometry to orient the inner pattern's walls in a more suitable direction with respect to the new position of the beam in the print volume. The zones of the pattern have been filled of material taking in account the results of the Load Case 4, the Load Case 5 and the Load Case 6 topology optimizations. The beam still divided in three sectors (Figure 2.5.3.5).

Has been decided to fill of material the pattern in an equal way in all of the three sectors sections of the curved beam. This choice can be understood by looking at the following images (Figure 2.5.12.2, Figure 2.5.12.3, Figure 2.5.12.4): it is possible to notice that all the corners, in all the three sectors sections that result from the topology optimizations, are full of material and that the center of the beam, except for some reinforcement ribs, is void.

Sector 1 (Figure 2.5.12.2):





Figure 2.5.12.2: Sections of the sector 1: from the left to the right, of the topology optimized geometries and of the support pattern developed.

Sector 2 (Figure 2.5.12.3):

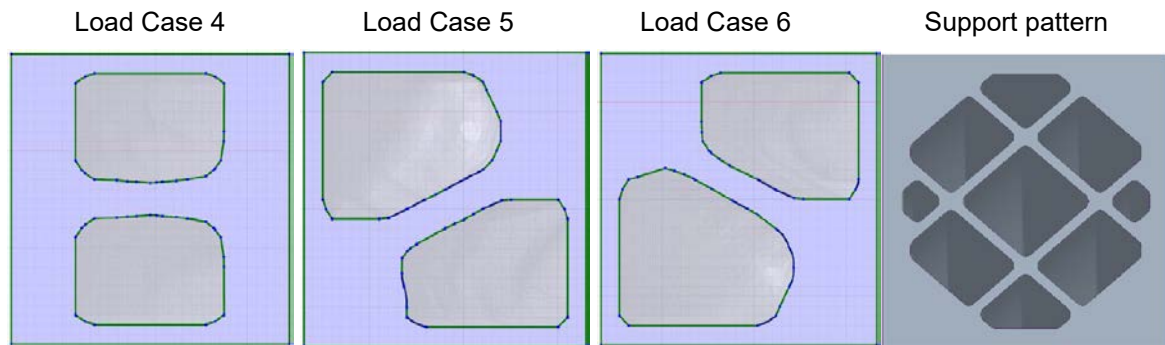


Figure 2.5.12.3: Sections of the sector 2: from the left to the right, of the topology optimized geometries and of the support pattern developed.

Sector 3 (Figure 2.5.12.4):

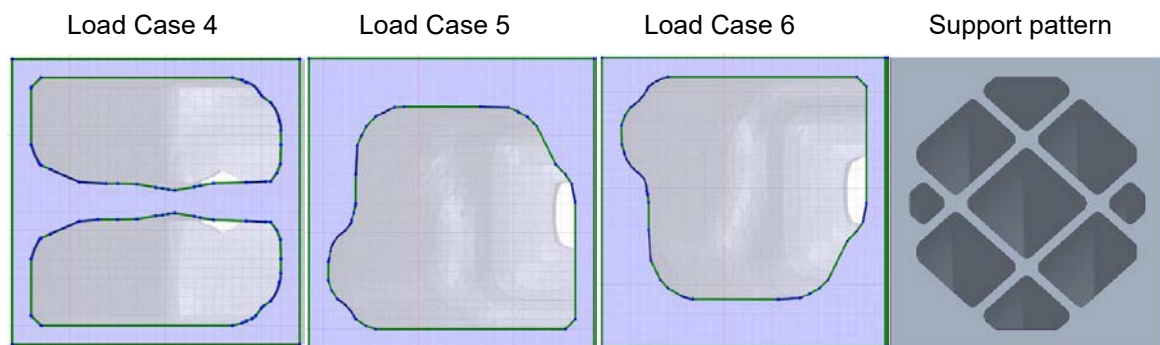


Figure 2.5.12.4: Sections of the sector 3: from the left to the right, of the topology optimized geometries and of the support pattern developed.

Below are shown the XZ-plane sections at near half of the height of the beam, as it comes from the topology optimizations with Load Case 4 and Load Case 5 applied (Figure 2.5.12.5).

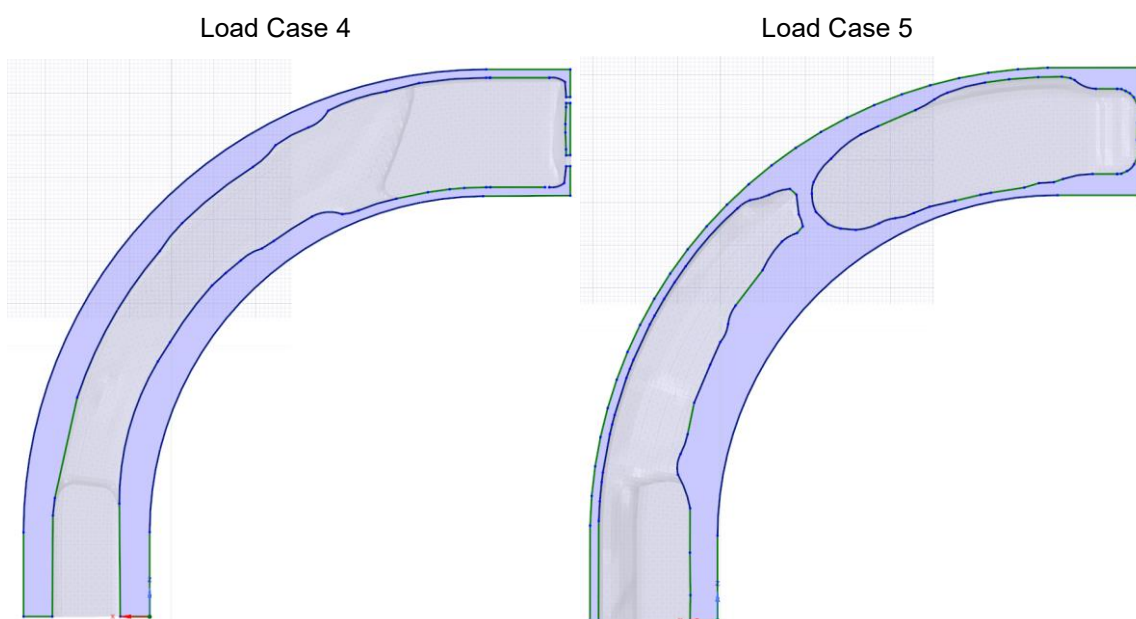




Figure 2.5.12.5: XZ-plane sections at near half of the height: on the left of the beam as it comes from the topology optimization with Load Case 4 applied and on the right of the beam as it comes from the topology optimization with Load Case 5 applied.

Below are shown the XZ-plane sections at near half of the height of the beam, as it comes from the topology optimization with Load Case 6 applied and of the beam with the structural inner support developed (Figure 2.5.12.6).

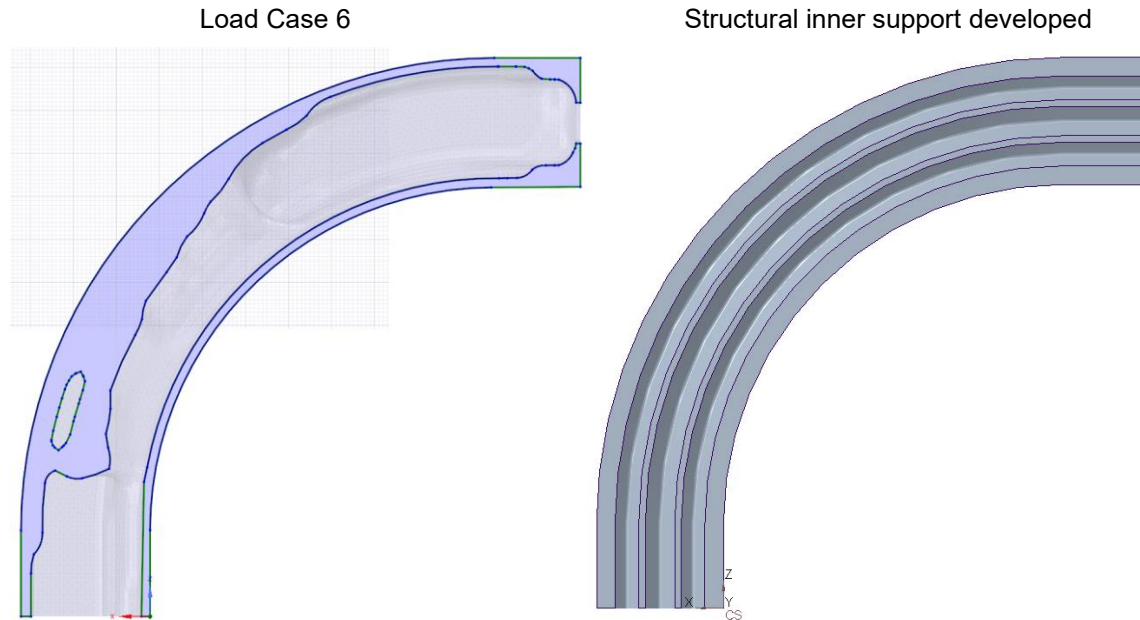


Figure 2.5.12.6: XZ-plane sections at near half of the height: on the left of the beam as it comes from the topology optimization with Load Case 6 applied and on the right of the beam with the structural inner support developed.

Below is shown an image of the curved beam with the structural inner support developed for the Load Cases 4+5+6 (Figure 2.5.12.7):

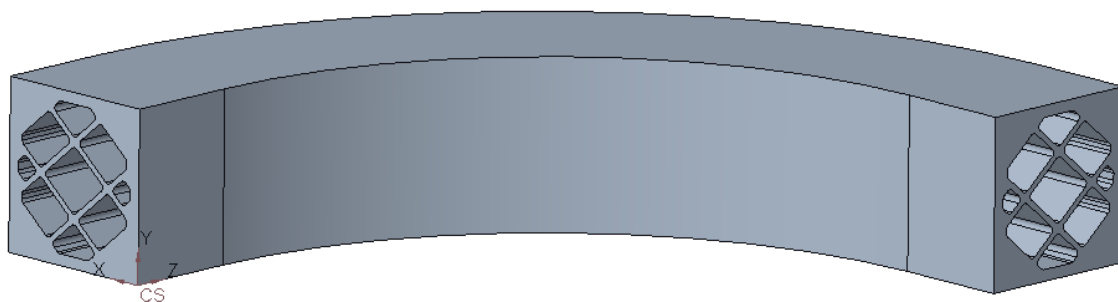


Figure 2.5.12.7: Curved beam with the structural inner support developed for the Load Cases 4+5+6.

### 2.5.13 Load Cases 4+5+6: F.E.M. Analyses

The static structural F.E.M. analyses have been performed with the main parameters showed in the table below (Table 2.5.13.1):

Material	Ansys default Structural Steel (Table 2.3.1)
Mesh Element Type	SOLID187
Mesh Element Order	Quadratic
Mesh Global Size	1 mm
Mesh Target Quality	0,6

Table 2.5.13.1: Main parameters of the static structural F.E.M. Analyses.

The static structural F.E.M. analysis of the curved beam full of material with Load Case 5 applied and with Load Case 6 applied have been already performed in Subchapter 2.3.5 and Subchapter 2.3.6 respectively.

Have been performed the static structural F.E.M. analyses of the hollow curved beam with Load Case 5 applied and with Load Case 6 applied. To not burden the discussion has been decided to show only the results of total displacement in the summarizing tables 2.5.13.2 and 2.5.13.3.

Have been performed the static structural F.E.M. analyses of the curved beam with the structural inner support developed with Load Case 5 applied and with Load Case 6 applied. The Von Mises equivalent stress results are shown in the images below (Figure 2.5.13.1 for Load Case 5 and Figure 2.5.13.2 for Load Case 6):

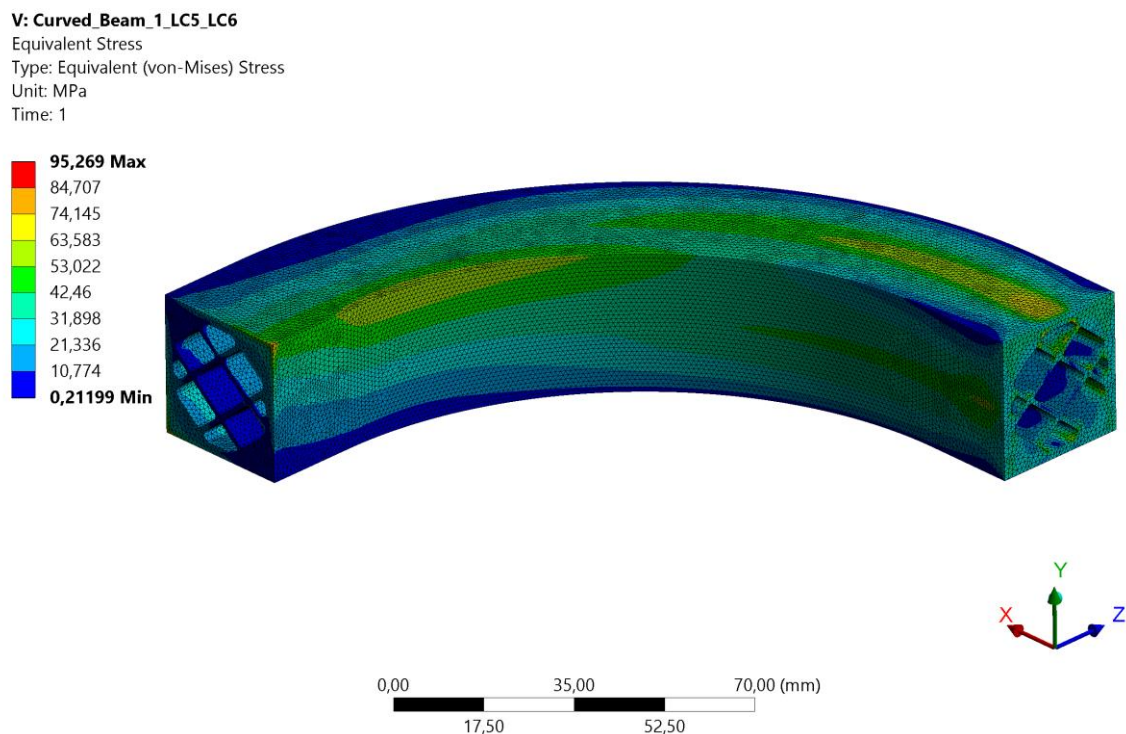


Figure 2.5.13.1: Von Mises equivalent stress of the curved beam with the structural inner support developed and with Load Case 5 applied.

**V: Curved\_Beam\_1\_LC5\_LC6**  
 Equivalent Stress  
 Type: Equivalent (von-Mises) Stress  
 Unit: MPa  
 Time: 1

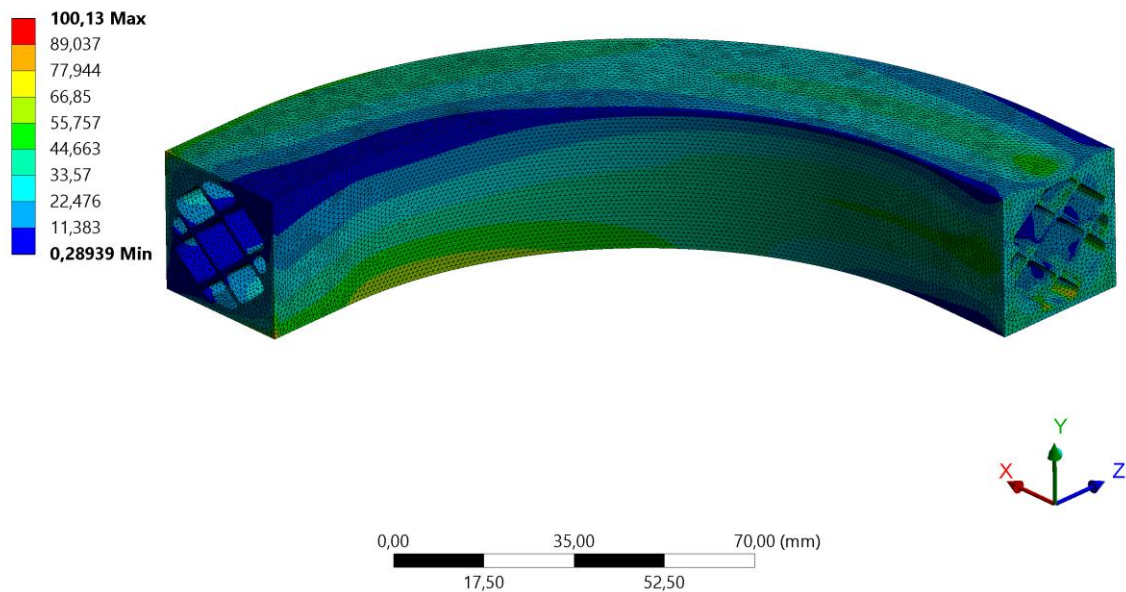


Figure 2.5.13.2: Von Mises equivalent stress of the curved beam with the structural inner support developed and with Load Case 6 applied.

Have been performed the static structural F.E.M. analysis of the curved beam as it comes from the topology optimization with Load Case 5 applied. The Von Mises equivalent stresses is shown in the image below (Figure 2.5.13.3):

**G: Topology Validation**  
 Equivalent Stress  
 Type: Equivalent (von-Mises) Stress  
 Unit: MPa  
 Time: 1

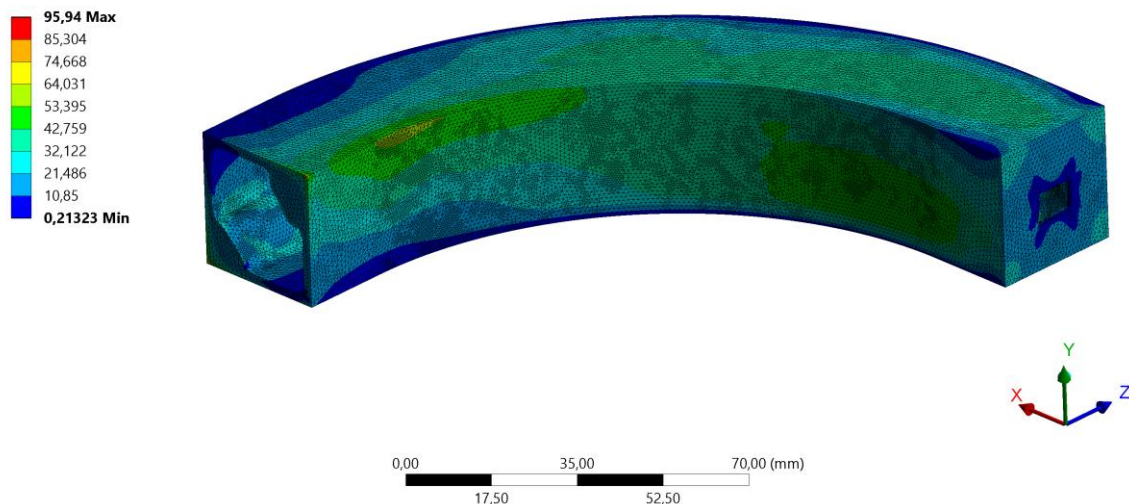


Figure 2.5.13.3: Von Mises equivalent stress of the curved beam as it comes from the topology optimization with Load Case 5 applied.

Have been performed the static structural F.E.M. analysis of the curved beam as it comes from the topology optimization with Load Case 6 applied. The Von Mises equivalent stresses is shown in the image below (Figure 2.5.13.4):

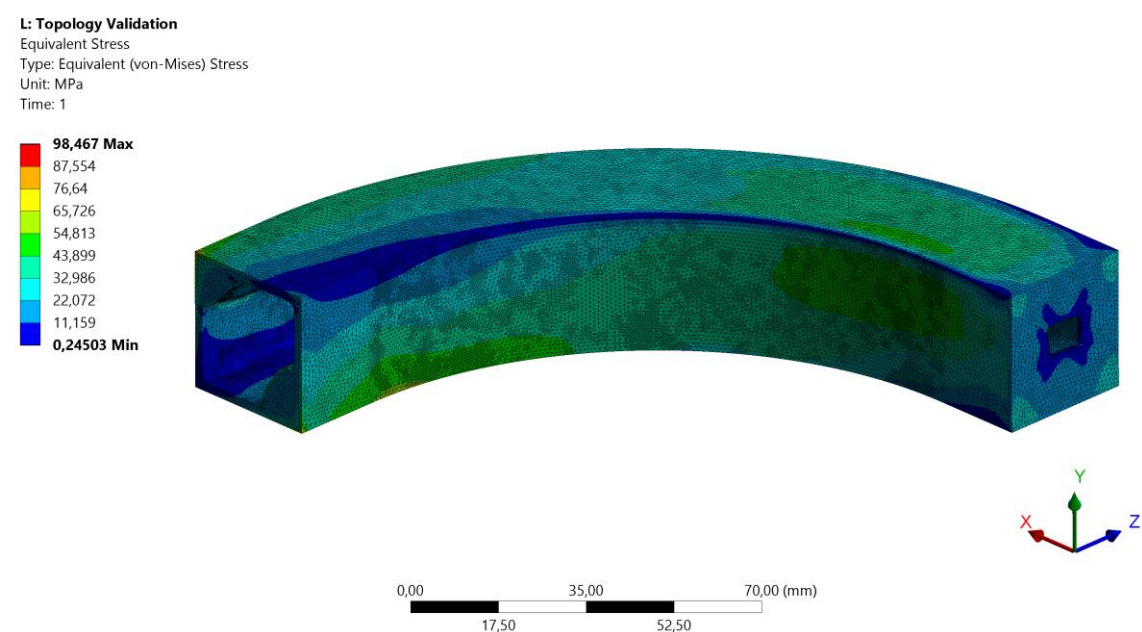


Figure 2.5.13.4: Von Mises equivalent stress of the curved beam as it comes from the topology optimization with Load Case 6 applied.

The results are summarized in the tables below (Table 2.5.13.2, Table 2.5.13.3):

Load Case 5	Full	Hollow	Developed inner support	Topology Optimization
Weight [g]	1337	333	720	642
Total Displacement Max  [mm]	0,132	0,475	0,192	0,166
Weight * Displacement (Minimum is better)	<b>177</b>	<b>158</b>	<b>138</b>	<b>107</b>

Table 2.5.13.2: Results comparison between the different beams with Load Case 5 applied.

Load Case 6	Full	Hollow	Developed inner support	Topology Optimization
Weight [g]	1337	333	720	642
Total Displacement Max  [mm]	0,132	0,474	0,192	0,166
Weight * Displacement (Minimum is better)	<b>177</b>	<b>158</b>	<b>138</b>	<b>107</b>

Table 2.5.13.3: Results comparison between the different beams with Load Case 6 applied.

The Weight \* Displacement indexes of the curved beam with the last structural inner support developed are 22,5 % higher, for both Load Case 5 and Load Case 6, with respect to the indexes of the curved beams as they come from the topology optimizations. It is a not bad result because due to the support structure necessities, it is difficult to reach the Weight \* Displacement indexes of the topology optimized beams, that have been optimized without caring about the impossibility of printing them with some additive manufacturing technologies without adding to them some further supports.

It would be possible to improve the performance of the structural inner support deciding to develop it by taking in account only the result of the topology optimisation with Load Case 5 applied or the result of the topology optimisation with Load Case 6 applied. In this case it would be possible to remove material from two opposite corners of the pattern’s section, that depend from the Load Case

that has been considered, along all the beam (Figure 2.5.13.5, Figure 2.5.13.6) with as result a more lightweight beam with better performances. This approach is a further optimization of the structural inner support and it is useful if are well known the specific loads that the curved beam would work with, however if the designer wants to have an optimized geometry that can work well with different loads applied it is natural that, except in rare cases, a compromise must be accepted.

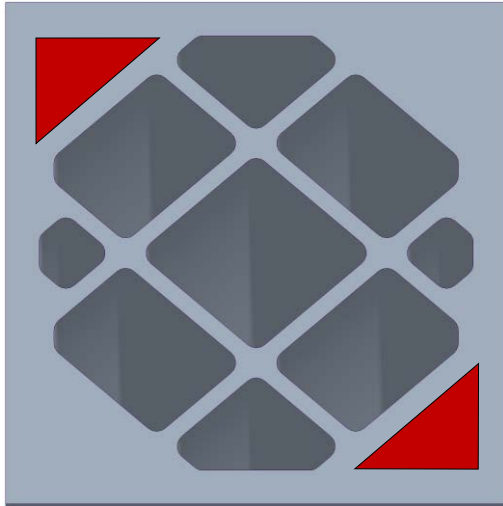


Figure 2.5.13.5: Pattern's section with highlighted in red the material to be removed for having a more optimized geometry only taking in account the result of the topology optimization with Load Case 5 applied.

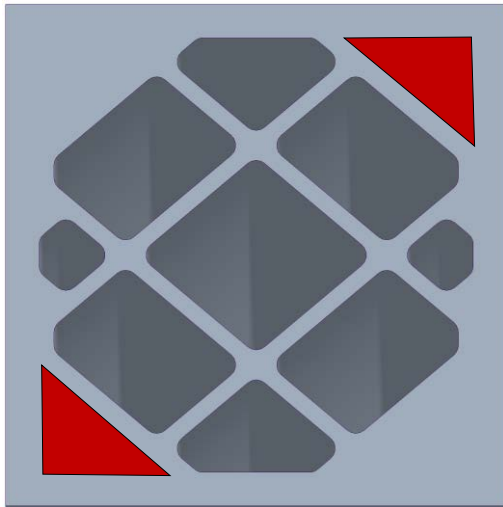


Figure 2.5.13.6: Pattern's section with highlighted in red the material to be removed for having a more optimized geometry only taking in account the result of the topology optimization with Load Case 6 applied.



2.6 Mathematical design optimization: Topology optimization with overhang constraint

2.6.1 Load Case 2: Inner support design with Topology Optimization

The goal of this third used method is to develop an inner support structure for the hollow curved beam using the topology optimization tool with the possibility of adding an overhang constraint to force the algorithm to optimize the component creating a self-supporting structure with respect to the selected print direction. After the optimization with the overhang constraint the component can be immediately printed without the needs of further geometric adjustments.

In the Subchapter 2.2.2 have been summarized all the steps that the designer should follow for a successful design of an inner support structure. That steps have been followed during this work:

1) To know the outer geometry of the beam.

The outer geometry of the beam that has been used is the one described in the Subchapter 2.2.1

2) To know the boundary conditions (Loads and Constraints).

The boundary conditions that have been used are the ones of the Load Case 2 described in the Subchapter 2.3.2.

3) To take in account the isotropic/anisotropic nature of the print technology used.

The print technologies that have been used in this thesis work are the SLS and the SLM, both of them are almost isotropic technologies: the mechanical properties (at least in the elastic regime) of an object printed with one of these technologies do not vary with respect to the orientation of the object in the print volume. On the other hand, an example of an anisotropy technology is the FDM (Fused Deposition Material) one.

4) To make a topology optimization of the beam full of material fixing the outer geometry as non-design space and specifying an overhang constraint related to the print direction.

The topology optimization has been done with the main parameters showed in the table below (Table 2.6.1.1):

Material	Ansys default Structural Steel (Table 2.3.1)
Mesh Element Type	SOLID186
Mesh Element Order	Quadratic
Mesh Global Size	2 mm
Mesh Target Quality	0,6

Table 2.6.1.1: Main parameters of the topology optimization of the beam full of material with Load Case 2 applied.

The *design space* and the *non-design space* have been defined (Figure 2.6.1.1):

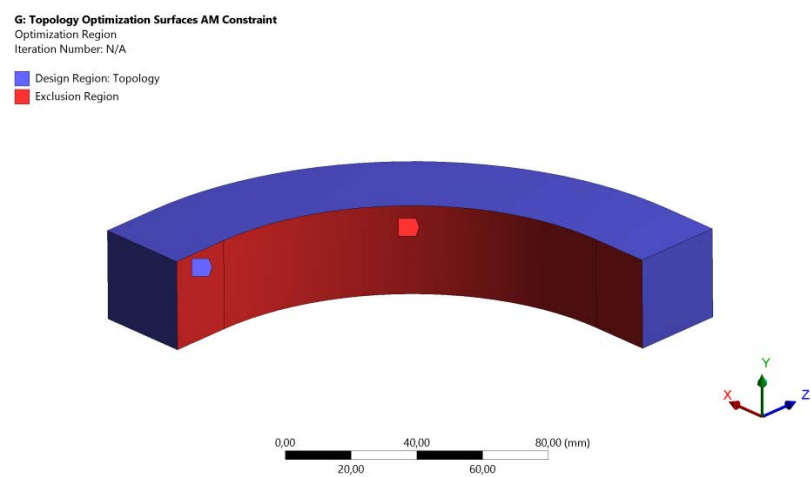


Figure 2.6.1.1: Design space and non-design space.

The software can follow the AM overhang constraint only in the design space region of the beam, for this reason the surfaces of the beam that must be supported must be set as design space to let the software build the inner support for them. Furthermore, if the surfaces to be supported are not stressed the optimization algorithm will remove material from them because they are set as design space for the reason above. So, to try to obtain a curved beam ready to print from a topology optimization with the outer surfaces to be supported retained, it is important that the surfaces of interest are almost all along stressed. In this case the surface that must be supported is the upper surface of the curved beam because has been chosen the position of the beam in the print volume as the one of the iterative - intuitive optimization approach (Figure 2.4.1.4). With the -FY force plus the +MX moment of Load Case 2 the upper surface of interest is almost all along stressed (Figure 2.3.2.2).

To minimize *Compliance* (= maximize stiffness) has been chosen as the *Objective* of the topology optimization.

To retain a 30% of the *design space* volume has been set as the *Response Constraint*, to get as result a geometry that with the outer walls would weight about 50% less than the beam full of material.

One *Manufacturing Constraint* has been set specifying a minimum *Member Size* of 1 mm. This means that the topological solver cannot create a geometry member with a dimension less than 1 mm. 1 mm has been chosen because it is the minimum feature size that SLM process can build (Table 1.2.1).

An *AM Overhang constraint* has been set specifying the print direction as the positive Y-axis and the *Overhang Angle* value of 50°. This means that the curved beam cannot have parts, like for example inner walls, inclined less than 50° with respect to the XZ-plane. (N.B. the *Overhang Angle* is defined as the angle between the plane orthogonal to the *Build Direction* axis specified, XZ-plane in this case, and the component's geometry)

The result of the *Retained Material* is shown below (*Retained Threshold* = 0,5) (Figure 2.6.1.2):

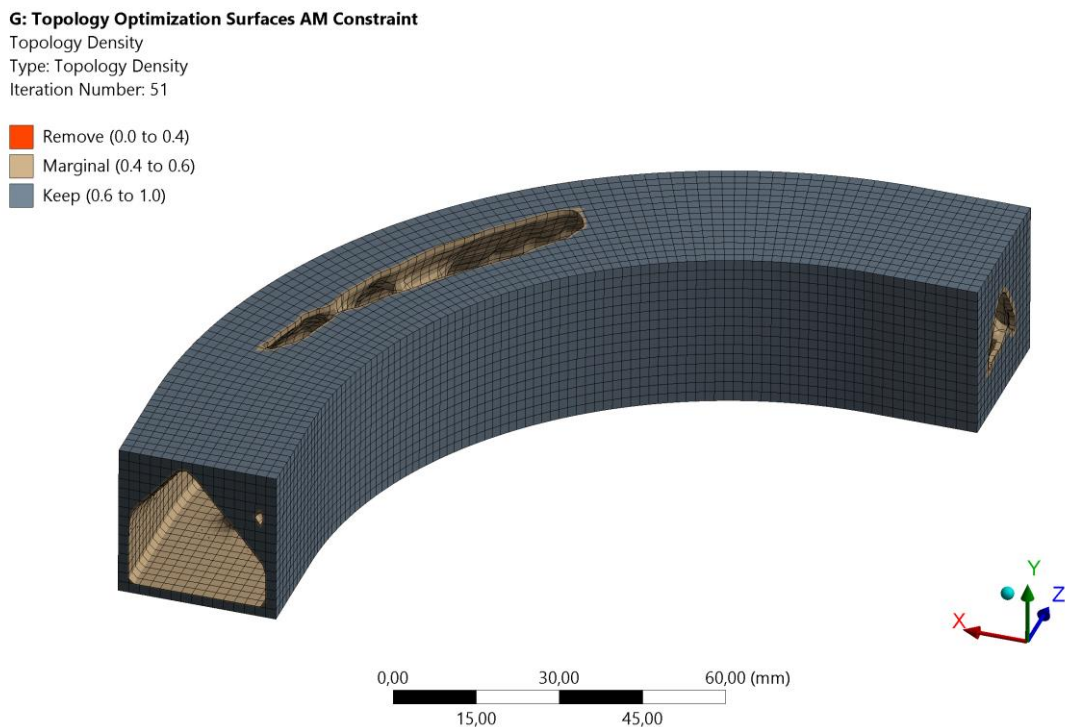


Figure 2.6.1.2: Topology optimization *Retained Material* result with 30% of retained volume constraint.

It is possible to see that the optimization algorithm has kept most of the upper surface but not all of it. Has been found that a minimum of 45% of the *design space* volume to retain must be set as the *response constraint* if the goal is to keep as retained material also all the upper surface.



The result is shown below (*Retained Threshold* = 0,5) (Figure 2.6.1.3):

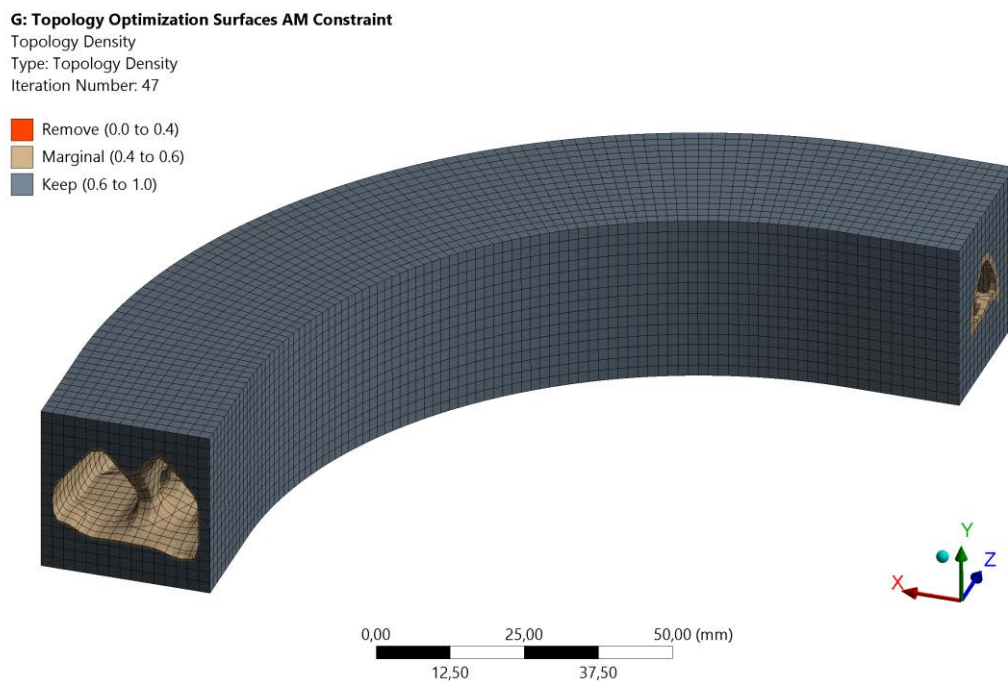


Figure 2.6.1.3: Topology optimization *Retained Material* result with 45% of retained volume constraint.

Below is shown an XZ-plane section at near half of the height of the optimized geometry (Figure 2.6.1.4):

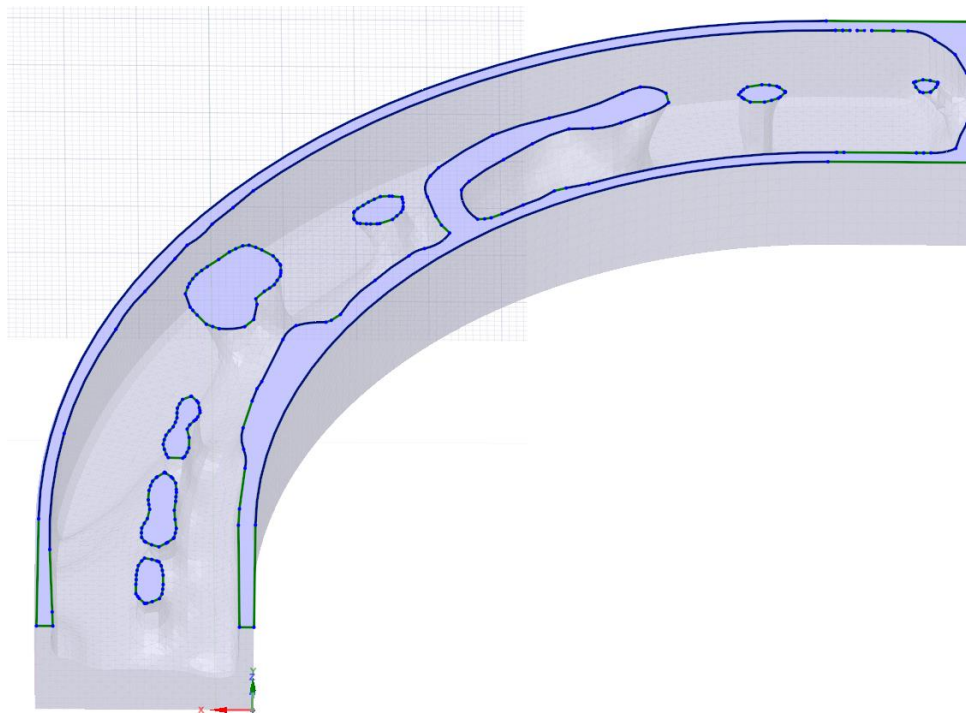


Figure 2.6.1.4: XZ-plane section at near half of the height of the optimized geometry.

## 2.6.2 Load Case 2: F.E.M. Analysis

The static structural F.E.M. analysis have been performed with the main parameters showed in the table below (Table 2.6.2.1):

Material	Ansys default Structural Steel (Table 2.3.1)
Mesh Element Type	SOLID187
Mesh Element Order	Quadratic
Mesh Global Size	1 mm
Mesh Target Quality	0,6

Table 2.6.2.1: Main parameters of the static structural F.E.M. analysis.

Has been performed the static structural F.E.M. analysis of the curved beam as it comes from the topology optimization with Load Case 2 applied and with the AM overhang constraint. The Von Mises equivalent stresses is shown in the image below (Figure 2.6.2.1):

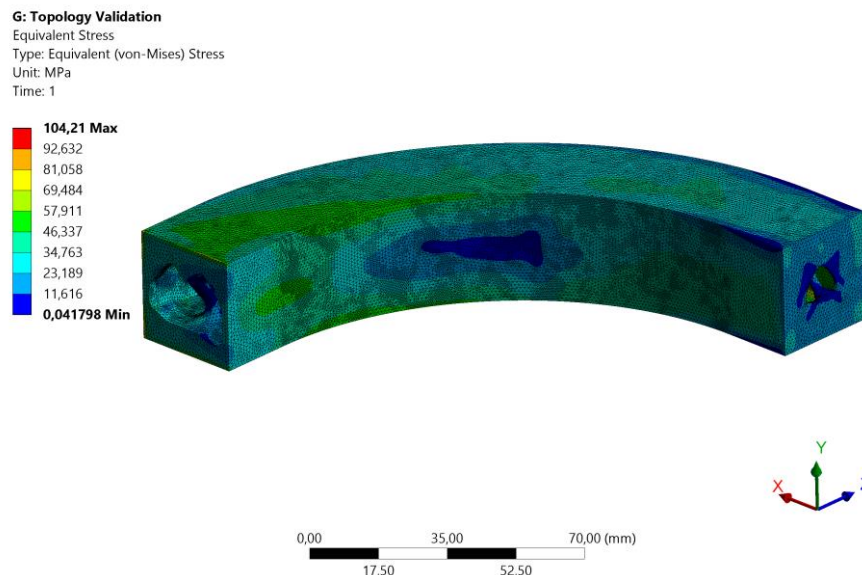


Figure 2.6.2.1: Von Mises equivalent stress of the curved beam as it comes from the topology optimization with Load Case 2 applied and with the AM overhang constraint.

The results are summarized in the table below (Table 2.6.2.1):

Load Case 2	Full	Hollow	Developed inner support	Topology Optimization	Topology Optimization AM constraint
Weight [g]	1337	333	731	641	754
Total Displacement Max  [mm]	0,200	0,871	0,264	0,272	0,265
Weight * Displacement (Minimum is better)	<b>267</b>	<b>290</b>	<b>193</b>	<b>174</b>	<b>200</b>

Table 2.6.2.1: Results comparison between the different beams with Load Case 2 applied.

The index of the topology optimized curved beam with the AM overhang constraint is 3,5 % higher than the index of the curved beam with the developed structural inner support (Subchapter 2.5.7). Maybe, the reason of this unexpected result may be found in the software handling of the AM overhang constraint.

### 2.6.3 Load Case 3: Inner support design with Topology Optimization

In the Subchapter 2.2.2 have been summarized all the steps that the designer should follow for a successful design of an inner support structure. That steps have been followed during this work:

1) To know the outer geometry of the beam.

The outer geometry of the beam that has been used in this example is the one described in the Subchapter 2.2.1

2) To know the boundary conditions (Loads and Constraints).

The boundary conditions that have been used in this example are the ones of the Load Case 3 described in the Subchapter 2.3.3.

3) To take in account the isotropic/anisotropic nature of the print technology used.

The print technologies that have been used in this thesis work are the SLS and the SLM, both of them are almost isotropic technologies: the mechanical properties (at least in the elastic regime) of an object printed with one of these technologies do not vary with respect to the orientation of the object in the print volume. On the other hand, an example of an anisotropy technology is the FDM (Fused Deposition Material) one.

4) To make a topology optimization of the beam full of material fixing the outer geometry as non-design space and specifying an overhang constraint related to the print direction.

The topology optimization has been done with the main parameters showed in the table below (Table 2.6.3.1):

Material	Ansys default Structural Steel (Table 2.3.1)
Mesh Element Type	SOLID186
Mesh Element Order	Quadratic
Mesh Global Size	2 mm
Mesh Target Quality	0,6

Table 2.6.3.1: Main parameters of the topology optimization of the beam full of material with Load Case 3 applied.

The *design space* and the *non-design space* have been defined (Figure 2.6.3.1):

G: Topology Optimization Surfaces AM Constraint  
Optimization Region  
Iteration Number: N/A  
■ Design Region: Topology  
■ Exclusion Region

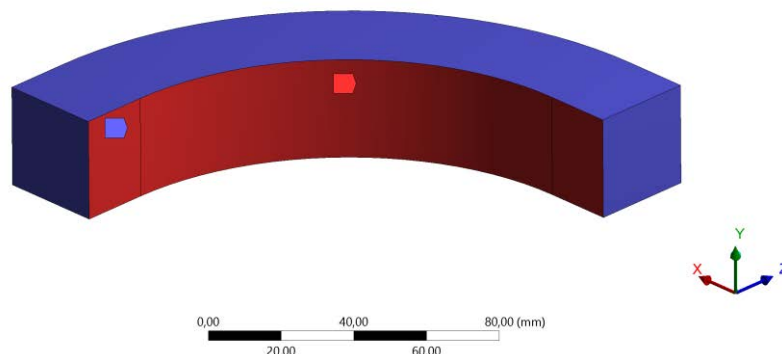


Figure 2.6.3.1: Design space and non-design space.

To minimize *Compliance* (= maximize stiffness) has been chosen as the *Objective* of the topology optimization.

To retain a 45% of the *design space* volume has been set as the *response constraint*, to get as result a geometry that would have a comparable weight with respect to the developed structural inner support (Subchapter 2.5.7) and with respect to the optimized geometry with AM overhang constraint for the Load Case 2 (Subchapter 2.6.1).

One *Manufacturing Constraint* has been set specifying a minimum *Member Size* of 1 mm. This means that the topological solver cannot create a geometry member with a dimension less than 1 mm. 1 mm has been chosen because it is the minimum feature size that SLM process can build (Table 1.2.1).

An *AM Overhang constraint* has been set specifying the print direction as the positive Y-axis and the *Overhang Angle* value of 50°. This means that the curved beam cannot have parts, like for example inner walls, inclined less than 50° with respect to the XZ-plane. (N.B. the *Overhang Angle* is defined as the angle between the plane orthogonal to the *Build Direction* axis specified, XZ-plane in this case, and the component's geometry)

The result of the *Retained Material* is shown below (*Retained Threshold* = 0,5) (Figure 2.6.3.2):

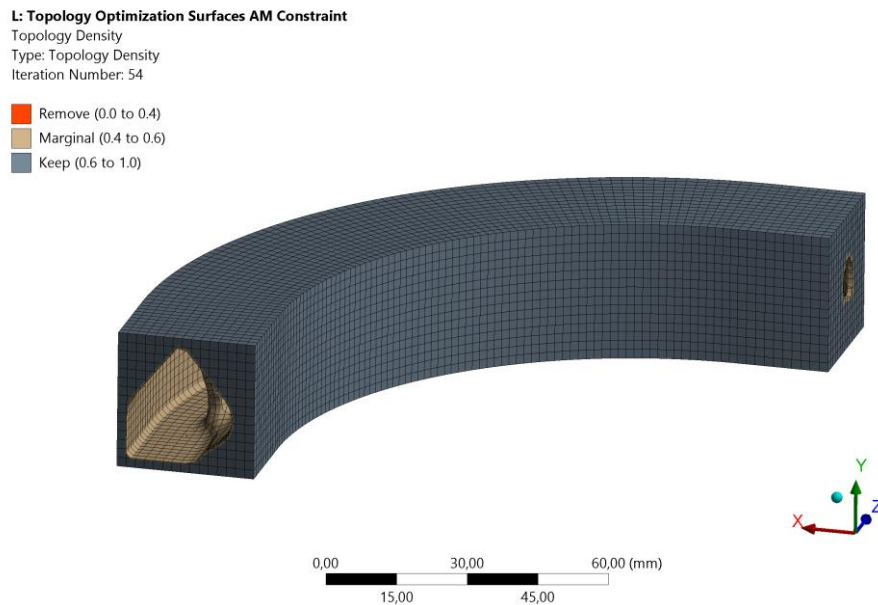


Figure 2.6.3.2: Topology optimization *Retained Material* result.

Below is shown an XZ-plane section at near half of the height of the optimized geometry (Figure 2.6.3.3):

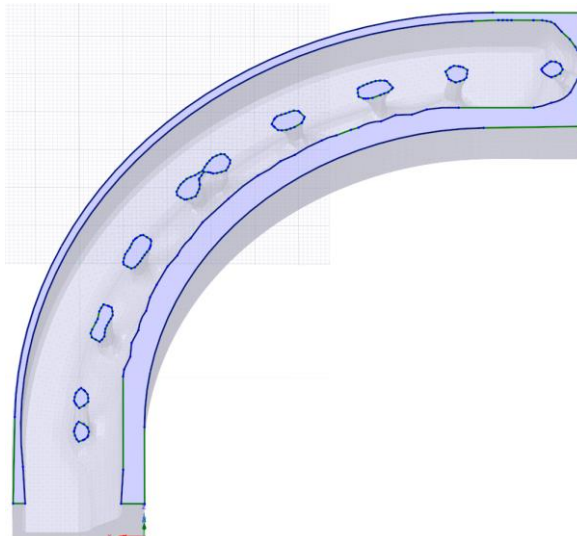


Figure 2.6.3.3: XZ-plane section at near half of the height of the optimized geometry.

## 2.6.4 Load Case 3: F.E.M. Analysis

The static structural F.E.M. analyses have been performed with the main parameters showed in the table below (Table 2.6.4.1):

Material	Ansys default Structural Steel (Table 2.3.1)
Mesh Element Type	SOLID187
Mesh Element Order	Quadratic
Mesh Global Size	1 mm
Mesh Target Quality	0,6

Table 2.6.4.1: Main parameters of the static structural F.E.M. analyses.

Has been performed the static structural F.E.M. analysis of the curved beam as it comes from the topology optimization with Load Case 3 applied and with the AM overhang constraint. The Von Mises equivalent stresses is shown in the image below (Figure 2.6.4.1):

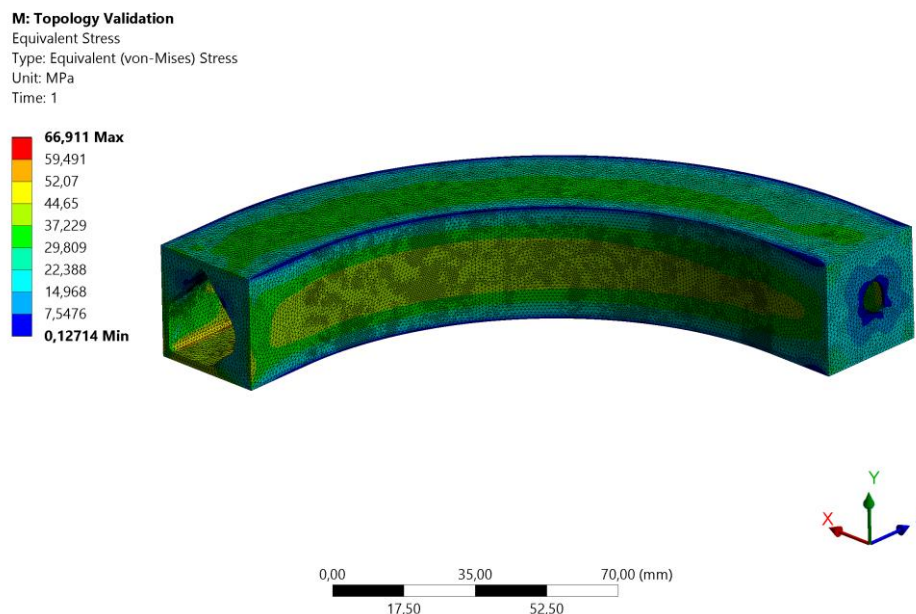


Figure 2.6.4.1: Von Mises equivalent stress of the curved beam as it comes from the topology optimization with Load Case 3 applied and with the AM overhang constraint.

The results are summarized in the table below (Table 2.6.4.1):

Load Case 3	Full	Hollow	Developed inner support	Topology Optimization	Topology Optimization AM constraint
Weight [g]	1337	333	731	641	747
Total Displacement Max  [mm]	0,122	0,338	0,171	0,172	0,183
Weight * Displacement (Minimum is better)	<b>163</b>	<b>113</b>	<b>125</b>	<b>110</b>	<b>137</b>

Table 2.6.4.1: Results comparison between the different beams with Load Case 3 applied.

The index of the topology optimized curved beam with the AM overhang constraint is 8,8 % higher than the index of the curved beam with the developed structural inner support (Subchapter 2.5.7). Maybe, the reason of this unexpected result may be found in the software handling of the AM overhang constraint.

Has been decided to make a F.E.M. analysis of the topology optimized curved beam with AM overhang constraint for the Load Case 2 also in the Load Case 3 condition and has been decided to make a F.E.M. simulation of the topology optimized curved beam with AM overhang constraint for the Load Case 3 also in the Load Case 2 condition.

The results are summarized in the tables below (Table 2.6.4.2, Table 2.6.4.3):

Load Case 3	Developed inner support	Topology Optimization	Topology Optimization AM constraint Load Case 3	Topology Optimization AM constraint Load Case 2
Weight [g]	731	641	747	754
Total Displacement Max  [mm]	0,171	0,172	0,183	0,193
Weight * Displacement (Minimum is better)	<b>125</b>	<b>110</b>	<b>137</b>	<b>146</b>

Table 2.6.4.2: Results comparison between the different beams with Load Case 3 applied.

Load Case 2	Developed inner support	Topology Optimization	Topology Optimization AM constraint Load Case 2	Topology Optimization AM constraint Load Case 3
Weight [g]	731	641	754	747
Total Displacement Max  [mm]	0,264	0,272	0,265	0,302
Weight * Displacement (Minimum is better)	<b>193</b>	<b>174</b>	<b>200</b>	<b>226</b>

Table 2.6.4.3: Results comparison between the different beams with Load Case 2 applied.

The topology optimized curved beam with AM overhang constraint for the Load Case 2 performs better in the Load Case 3 condition (increasing the Weight \* Displacement index by 6,2 % with respect to the index of the topology optimized curved beam for Load Case 3 itself) than the topology optimized curved beam with AM overhang constraint for the Load Case 3 performs in the Load Case 2 condition (increasing the Weight \* Displacement index by 11,5 % with respect to the index of the topology optimized curved beam for Load Case 2 itself).

However, until now, the best choice to develop a structural inner support for a hollow curved beam is to follow the approach of Subchapter 2.5: to make a topology optimization avoiding the use of the AM overhang constraint and to design a custom structural inner support “only” following the suggestions given by the topology optimisation.



## 2.7 Mathematical design optimization: Lattice Optimization

### 2.7.1 Variable density Lattice Optimization with Ansys Workbench

To perform a successful variable density lattice optimization with Ansys Workbench the step to follow are:

- 1) To perform a *Static Structural* F.E.M. simulation of the component that is wanted to be optimized.  
The geometry of the component should comprehend also the chosen design space, the design space is necessary to be present because during the lattice optimization process the software creates an optimized variable density lattice structure to substitute the design space full of material. The density of the lattice structure varies area by area according to the stresses that are present in the 3D finite elements of the full of material design space. The boundary conditions must be the ones that are wanted for the lattice optimization.
- 2) To link a new *Topology Optimization* to the *Static Structural* F.E.M. simulation performed before (Figure 2.7.1.1). (In Ansys Workbench at this initial stage there is not a proper distinction between a topology optimization and a lattice optimization)

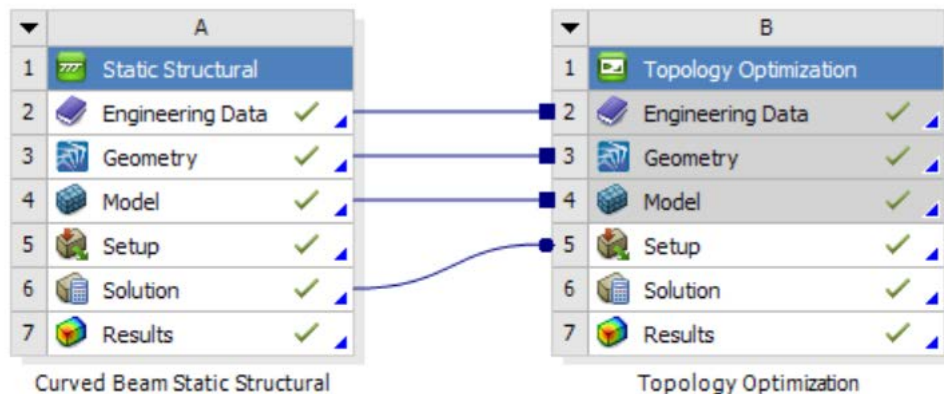


Figure 2.7.1.1: Topology Optimization linked to the Static Structural simulation in Ansys Workbench Project Schematic.

- 4) To set-up and to run the lattice optimization, the general settings menu is shown in the image below (Figure 2.7.1.2):

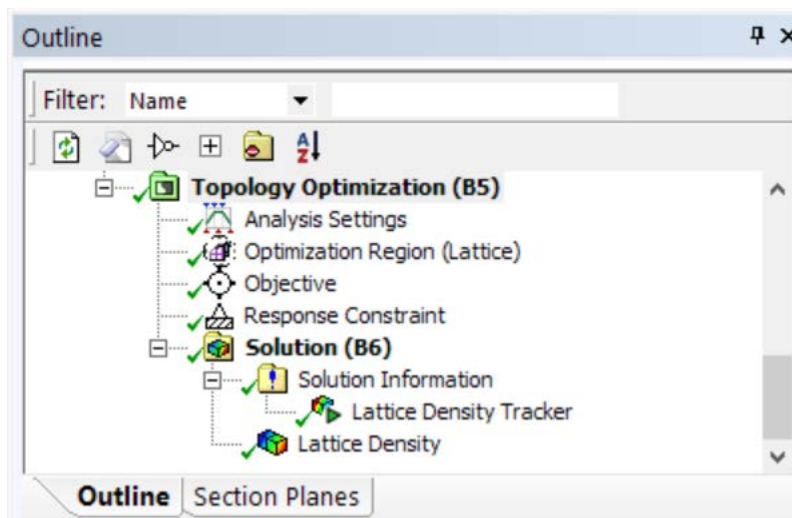


Figure 2.7.1.2: Ansys Workbench Lattice Optimization general settings menu.



The most important submenus of the general settings menu (Figure 2.7.1.2) are now presented in detail.

The **Analysis Settings** submenu is very similar to the Topology Optimization's one showed in Subchapter 2.5.2 (Figure 2.5.2.3). The only difference is that the settings *Penalty Factor (Stiffness)* and *Region of Min Member Size* are not present because not needed for a lattice optimisation.

In the image below it is possible to see the settings that can be done in the **Optimization Region (Lattice)** submenu (Figure 2.7.1.3):

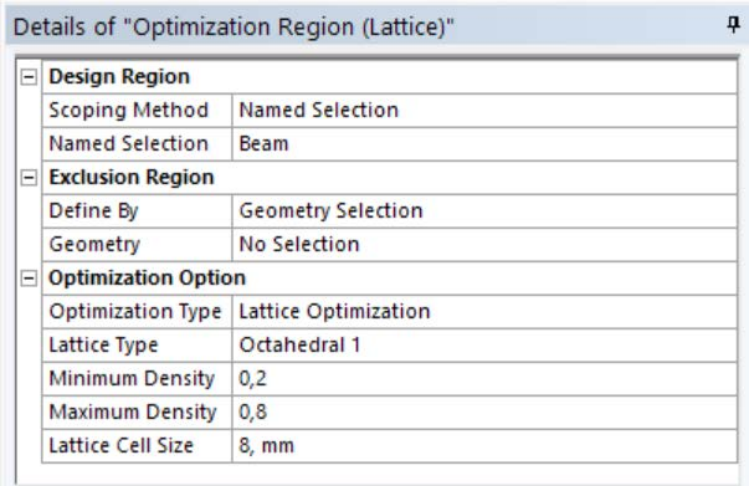


Figure 2.7.1.3: *Optimization Region (Lattice)* submenu.

The *Design Region* settings allow the user to choose the design space of the component. The design space is the part of the component that can be modified during the optimization.

The *Exclusion Region* settings allow the user to choose the non-design space of the component. The non-design space is the part of the component that is not allowed to be modified during the optimization.

The *Optimization Option* setting allow the user to choose between performing a *topology optimization* or performing a *lattice optimization*. Once the *lattice optimization* option has been chosen, new settings appears:

The *Lattice Type* setting allows the user to choose different types of lattice cell structure. It is possible to see them in the following image (Figure 2.7.1.4):

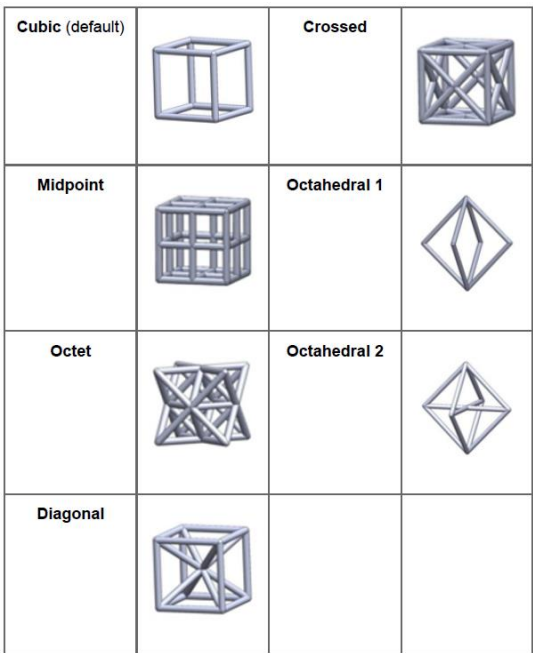


Figure 2.7.1.4: Different types of lattice cell structure [22].

The *Minimum Density* property “specifies a minimum density in order to avoid lattice structures that are too thin” [22].

The *Maximum Density* property “specifies a maximum density. The element will be considered as full for densities higher than the Maximum Density” [22].

The *Lattice Cell Size* property “specifies the lattice cell size to be used when rebuilding the lattice geometry for printing” [22].

In the **Objective** submenu it is possible to set the objective of the lattice optimization. It is possible to choose if minimizing the *Compliance* (maximizing the stiffness) of the component or if minimizing the *Mass* or the *Volume* of the component. It is also possible to select multiple objectives defining also a weight factor for every objective selected. If the topology optimization is linked to a modal analysis, instead of being linked to a static structural analysis, it is possible to choose also to maximize the *Frequency* response.

The **Response Constraint** submenu is very similar to the Topology Optimization’s one showed in Subchapter 2.5.2 (Figure 2.5.2.5). The only difference is that with a lattice optimisation it is not possible to set a *Local Von-Mises Stress* constraint or a *Reaction Force* constraint.

The **Manufacturing Constraint** submenu is very similar to the Topology Optimization’s one showed in Subchapter 2.5.2. The only difference is that with a lattice optimisation it is not possible to set a *Member Size*, a *Pull Out Direction* or an *Extrusion* manufacturing constraint. With a lattice optimisation it is not possible also to add an **AM Overhang Constraint**.

Selecting **Solution Information**, it is possible to see several things including the *Objective* and *Response Constraint* convergence. It is also possible, selecting **Lattice Density Tracker**, to observe graphically the changes of the lattice density values in the design space during the optimization process, iteration by iteration.

In the image below it is possible to see the settings that can be done in the **Lattice Density** submenu (Figure 2.7.1.5):

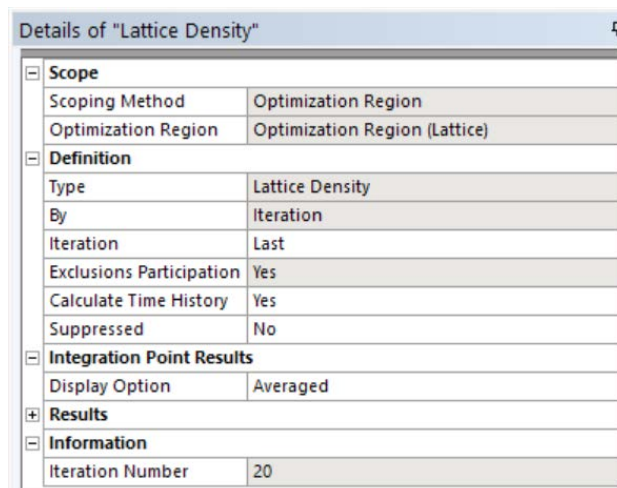


Figure 2.7.1.5: *Lattice Density* submenu.

The *Iteration* setting allows the user to choose which iteration must be taken in account for showing the lattice density result in the *Graphic* space.

In the *Results* section it is possible to see some characteristics of the optimized component such as *Original Mass*, *Final Mass*, *Original Volume*, *Final Volume* and others.

The *Iteration Number* information specifies the number of iterations that have been performed during the lattice optimisation.

## 2.7.2 Load Case 2: Inner support design with Lattice Optimization

The goal of this fourth used method is to develop a structural inner support for the hollow curved beam using the lattice optimization tool of Ansys Workbench. The aim is to obtain a curved beam with a lattice inner support to be immediately printed without the needs of further geometric adjustments.

In the Subchapter 2.2.2 have been summarized all the steps that the designer should follow for a successful design of an inner support structure. That steps have been followed during this work:

1) To know the outer geometry of the beam.

The outer geometry of the beam that has been used is the one described in the Subchapter 2.2.1

2) To know the boundary conditions (Loads and Constraints).

The boundary conditions that have been used are the ones of the Load Case 2 described in the Subchapter 2.3.2. The only difference is that a change of the global coordinate system has been performed: The Y-axis of the vertical force now become the Z-axis and the X-axis of the positive moment now become the Y-axis. This change has been done because of the fixed Z-axis build direction that has the Ansys Space Claim software for the lattice cells.

3) To take in account the isotropic/anisotropic nature of the print technology used.

The print technologies that have been used in this thesis work are the SLS and the SLM, both of them are almost isotropic technologies: the mechanical properties (at least in the elastic regime) of an object printed with one of these technologies do not vary with respect to the orientation of the object in the print volume. On the other hand, an example of an anisotropy technology is the FDM (Fused Deposition Material) one.

4) To make a variable density lattice optimization of the beam full of material, choosing a proper lattice type together with the orientation of the curved beam into the print volume, to being able of using the lattice structure as a structural inner support.

The variable density lattice optimizations have been done with the main parameters showed in the table below (Table 2.7.2.1):

Material	Ansys default Structural Steel (Table 2.3.1)
Mesh Element Type	SOLID186
Mesh Element Order	Quadratic
Mesh Global Size	2 mm
Mesh Target Quality	0,6

Table 2.7.2.1: Main parameters of the variable density lattice optimization of the beam full of material with Load Case 2 applied.

The *design space* and the *non-design space* have been defined (Figure 2.7.2.1):

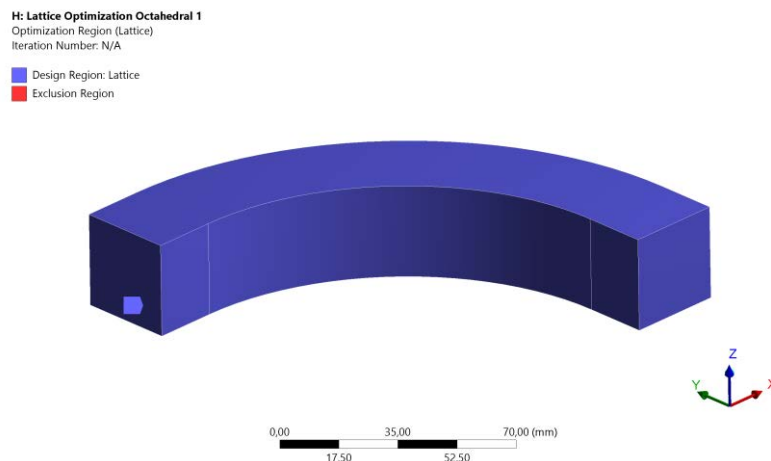


Figure 2.7.2.1: *Design space* and *non-design space*.

Has been chosen to set as *design space* the entire volume of the beam.

Has been chosen the position of the beam in the print volume as the one of the iterative - intuitive optimization approach (Figure 2.4.1.4), so in this case the Z-axis is the print direction and it is also the default build direction that has the Ansys Space Claim software for the lattice cells.

*Octahedral 1 Lattice Type* (Figure 2.7.1.4) has been chosen because it didn't have 90° overhang beams, but it had 45° beams: very useful for carrying the torsional stresses and borderline with respect to the limit overhang value of 45° for the SLM technology.

A *Minimum Density* of 0,2 has been chosen to avoid the creation of too thin lattice beams that can result in a bad quality printing and so in a bad structural integrity of the too thin lattice beams.

A *Maximum Density* of 0,8 has been chosen to avoid the creation of too thick lattice beams that can result in a not clean facets geometry with the consequence of meshing problems.

A *Lattice Cell Size* of 8 mm has been chosen to avoid a too heavy result geometry that would have been difficult to handle with the hardware available.

Minimize *Compliance* (= maximize stiffness) has been chosen as the *objective* of the lattice optimization.

To retain a 30% of the design space volume has been set as the *response constraint*.

The Variable Lattice Density result is shown in the images below (Figure 2.7.2.2, Figure 2.7.2.3):

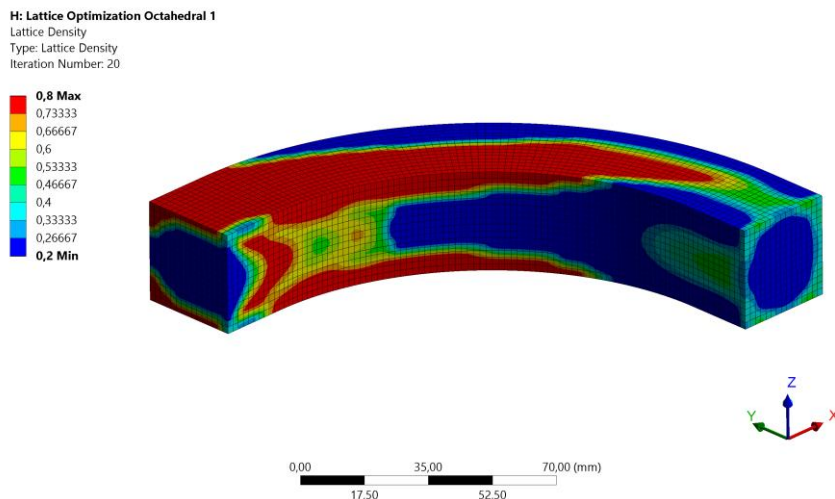


Figure 2.7.2.2: Octahedral 1 lattice optimization density result.

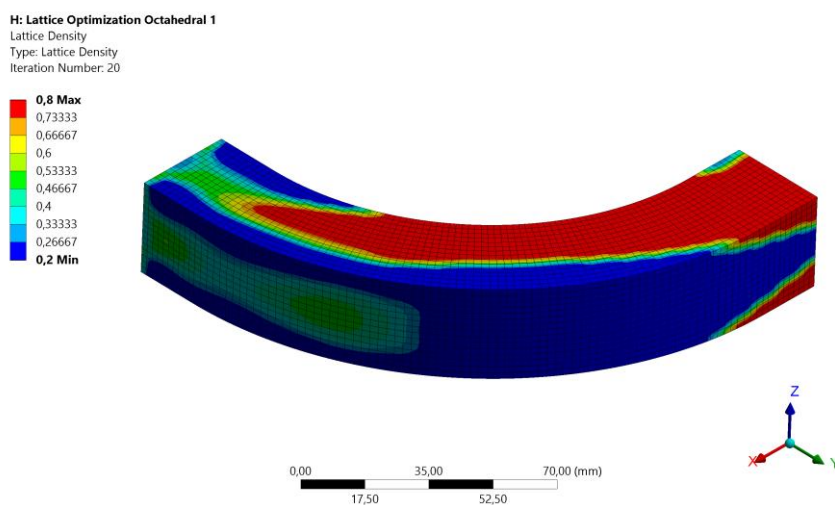


Figure 2.7.2.3: Octahedral 1 lattice optimization density result.

5) To build the optimized lattice structure inner support.

The optimized geometry has been built with the Space Claim Ansys software. In the images below (Figure 2.7.2.4, Figure 2.7.2.5 and Figure 2.7.2.6) it is possible to see the built beam with the inner variable density lattice support. The boundary walls of the beam are 2 mm thick.

Fix support zone (Figure 2.7.2.4):

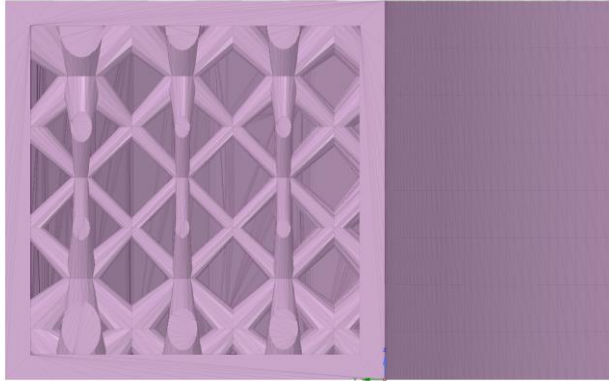


Figure 2.7.2.4: Fix support zone of the curved beam with the Octahedral 1 lattice inner support.

Load zone (Figure 2.7.2.5):

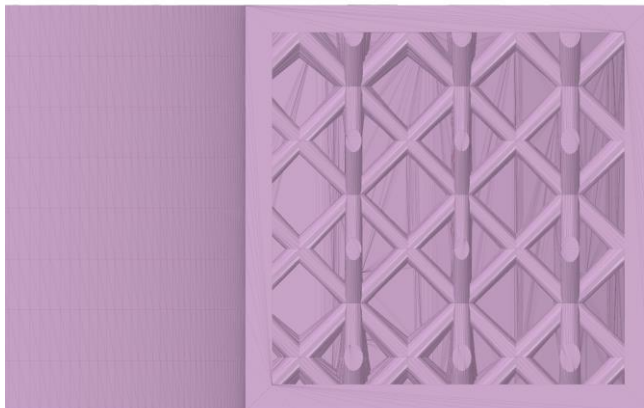


Figure 2.7.2.5: Load zone of the curved beam with the Octahedral 1 lattice inner support.

XY-plane section immediately below the upper wall (Figure 2.7.2.6):

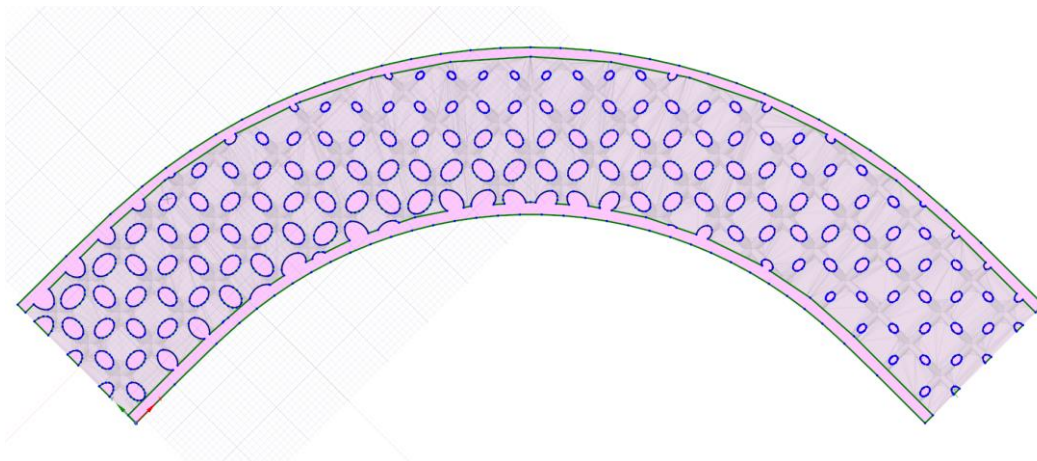


Figure 2.7.2.6: XY-plane section of the curved beam with Octahedral 1 inner support, immediately below the upper wall.



Has been decided to build the structural inner support also with another type of lattice structure to make a comparison with the previous one.

The same *design space* and the same *non-design space* of the Octahedral 1 lattice optimization have been chosen (Figure 2.7.2.1).

*Octet Lattice Type* (Figure 2.7.1.4) has been chosen.

A *Minimum Density* of 0,2 and a *Maximum Density* of 0,8 have been chosen for the same reasons explained in the *Octahedral 1* lattice optimization. These values have been chosen also for maintaining them constant excluding their influence in the *Octet* and *Octahedral 1* lattice inner supports comparison.

A *Lattice Cell Size* of 12 mm has been chosen, instead of the 8 mm chosen in the *Octahedral 1* lattice optimization, because of the bigger number of single beams that are present in the *Octet* lattice cell. An 8 mm *Lattice Cell Size* with the *Octet* lattice type would have result in a cell full of material in the zones with the *Maximum Density* of 0,8.

Minimize *Compliance* (= maximize stiffness) has been chosen as the *objective* of the lattice optimization.

To retain a 30% of the design space volume has been set as the *response constraint*.

The Variable Lattice Density result is shown in the images below (Figure 2.7.2.7, Figure 2.7.2.8):

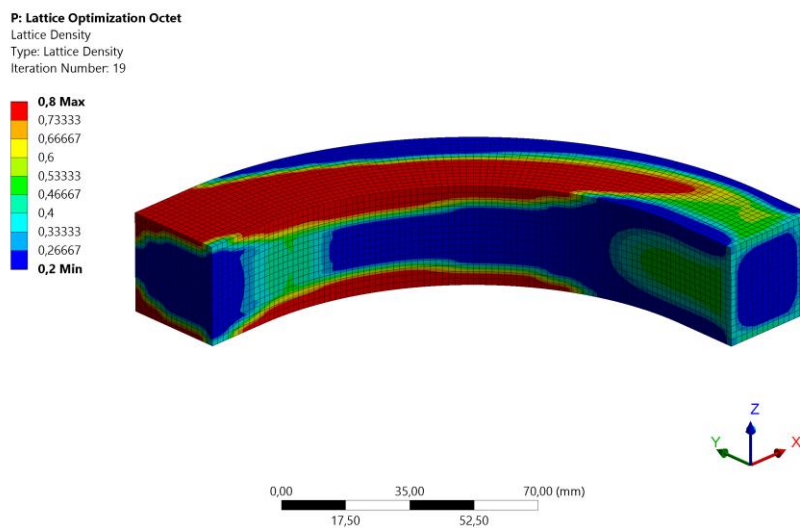


Figure 2.7.2.7: Octet lattice optimization density result.

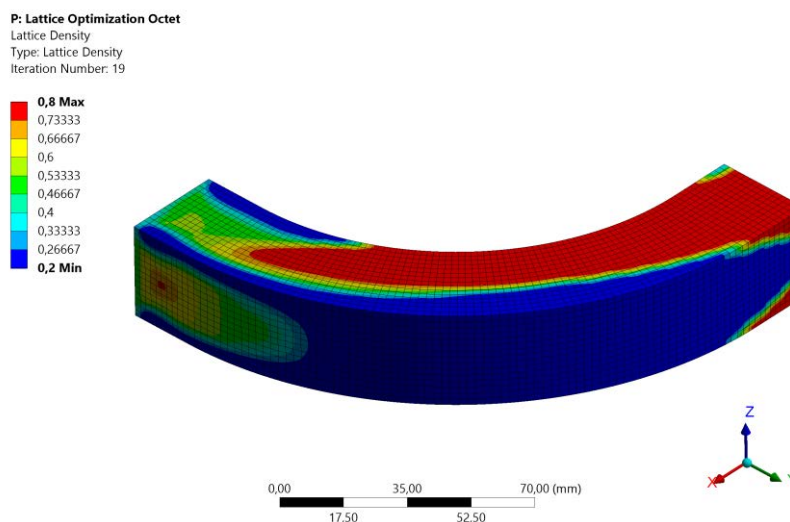


Figure 2.7.2.8: Octet lattice optimization density result.

The optimized geometry has been built with the Space Claim Ansys software. In the images below (Figure 2.7.2.9, Figure 2.7.2.10 and Figure 2.7.2.11) it is possible to see the built beam with the inner variable density lattice support. The boundary walls of the beam are 2 mm thick.

Fix support zone (Figure 2.7.2.9):

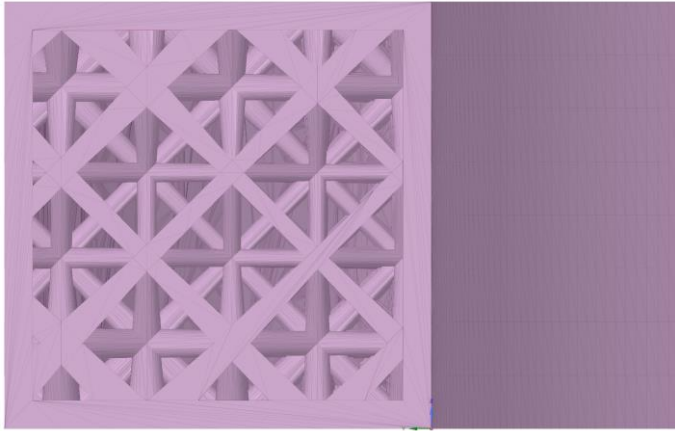


Figure 2.7.2.9: Fix support zone of the curved beam with the Octet lattice inner support.

Load zone (Figure 2.7.2.10):

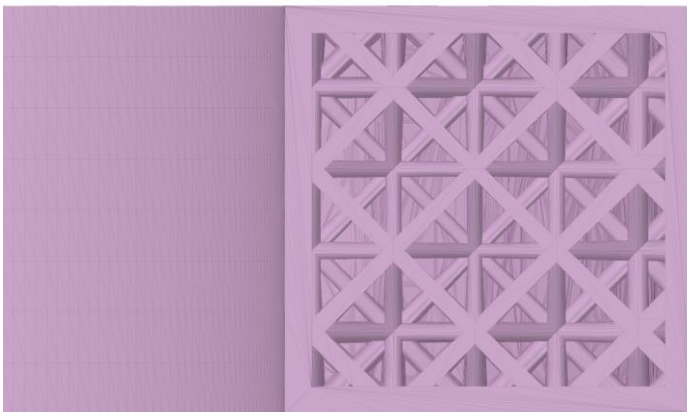


Figure 2.7.2.10: Load zone of the curved beam with the Octet lattice inner support.

XY-plane section immediately below the upper wall (Figure 2.7.2.11):

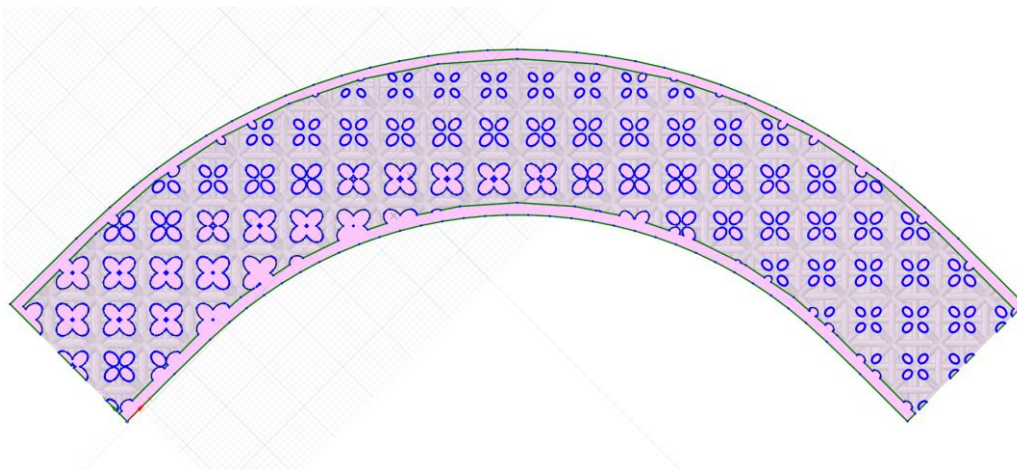


Figure 2.7.2.11: XY-plane section of the curved beam with Octet inner support, immediately below the upper wall.



### 2.7.3 Load Case 2: F.E.M. Analysis

The static structural F.E.M. analyses have been performed with the main parameters showed in the table below (Table 2.7.3.1):

Material	Ansys default Structural Steel (Table 2.3.1)
Mesh Element Type	SOLID187
Mesh Element Order	Quadratic
Mesh Global Size	0,8 mm
Mesh Target Quality	0,6

Table 2.7.3.1: Main parameters of the static structural F.E.M. analyses.

Has been performed the static structural F.E.M. analysis of the curved beam with the Octahedral 1 lattice inner support structure and with Load Case 2 applied.

To be able of meshing the geometry, has been necessary to use the *Virtual Topology* tool. It is a tool that allows the user to simply the geometry of the component directly in the *Mechanical* environment, with the aim of a consequential successful mesh. The options are a lot, a good description of all the possibilities of this tool is given in [23]. In the case of this thesis has been used a *Repair* method with a *Repair Slivers* behaviour. Has been set a *Max Sliver Width* of 1 mm and a *Min Sliver Width* of 0 mm. The working principle of the tool in this scenario is that all the slivers surfaces with dimensions in between the *Max Sliver Width* and the *Min Sliver Width* have been merged to create bigger slivers easier to be meshed. The *Max Sliver Width* and the *Min Sliver Width* values have been chosen in relation of the dimension of the mesh used and with the idea of not changing dramatically the geometry of the lattice's beams.

In the image below (Figure 2.7.3.1) it is possible to see the *Virtual Topology, Repair Slivers* result.

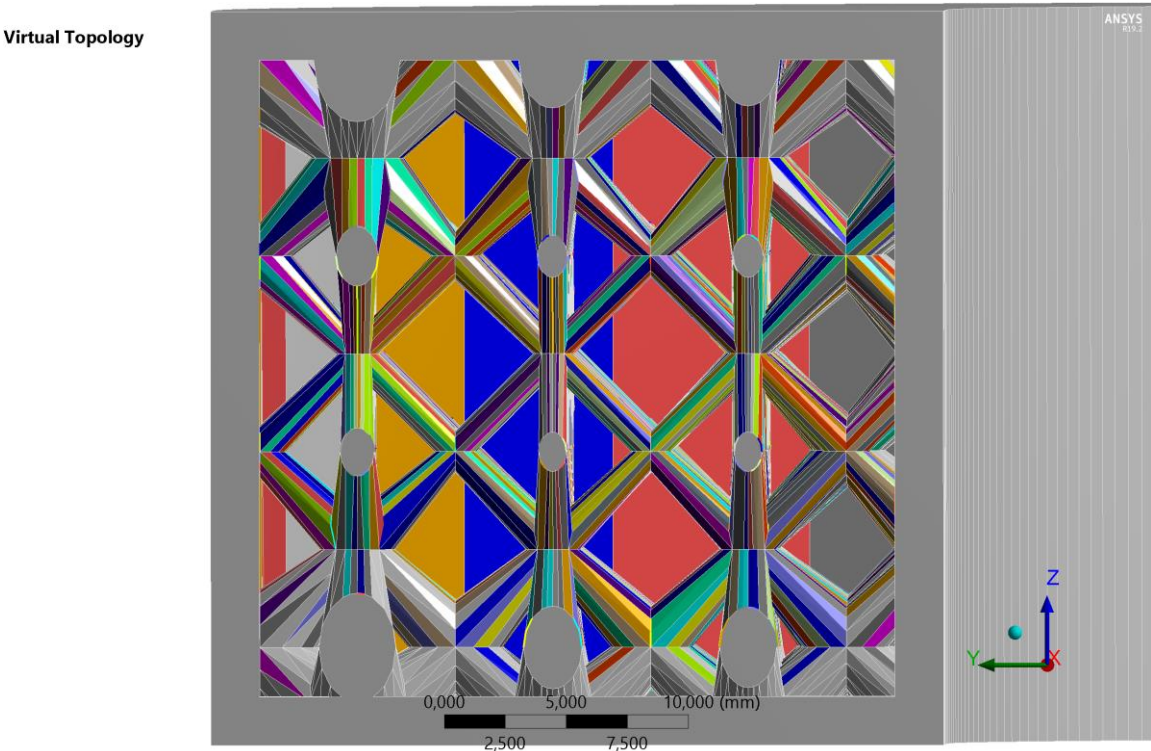


Figure 2.7.3.1: *Virtual Topology, Repair Slivers* result.

The Von Mises equivalent stress of the curved beam with the Octahedral 1 lattice inner support structure and Load Case 2 applied is shown in the image below (Figure 2.7.3.2):

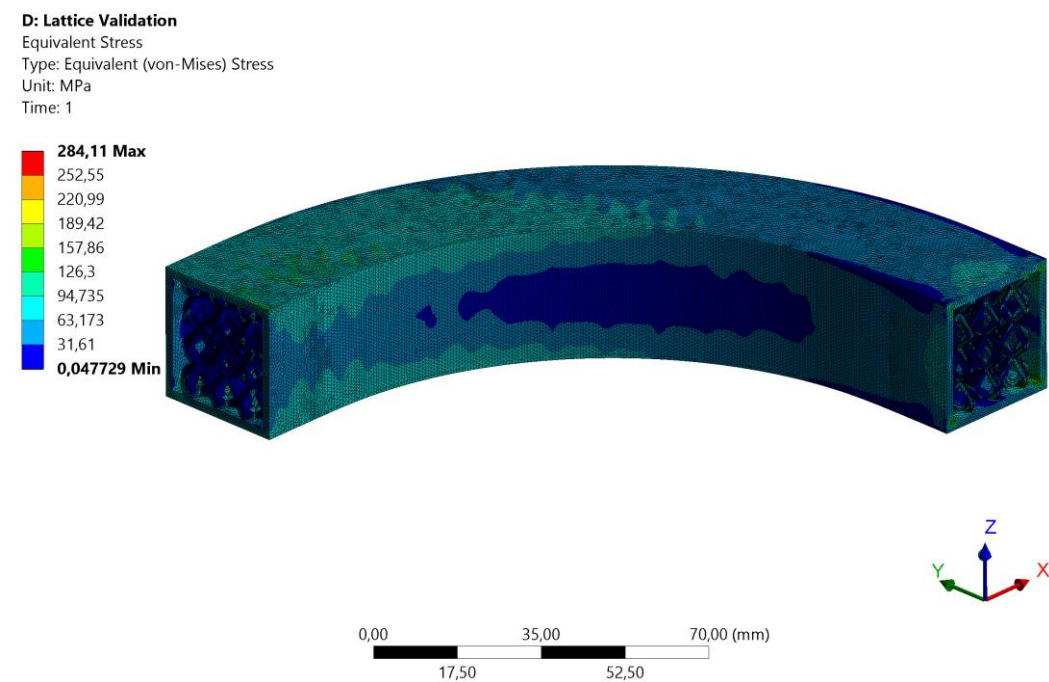


Figure 2.7.3.2: Von Mises equivalent stress of curved beam with the Octahedral 1 lattice inner support structure and with Load Case 2 applied.

Has been performed the static structural F.E.M. analysis of the curved beam with the Octet lattice inner support structure and with Load Case 2 applied. The same type of *Virtual Topology Repair* used for the Octahedral 1 lattice structural inner support has been used.

The Von Mises equivalent stress of the curved beam with the Octet lattice inner support structure and Load Case 2 applied is shown in the image below (Figure 2.7.3.3):

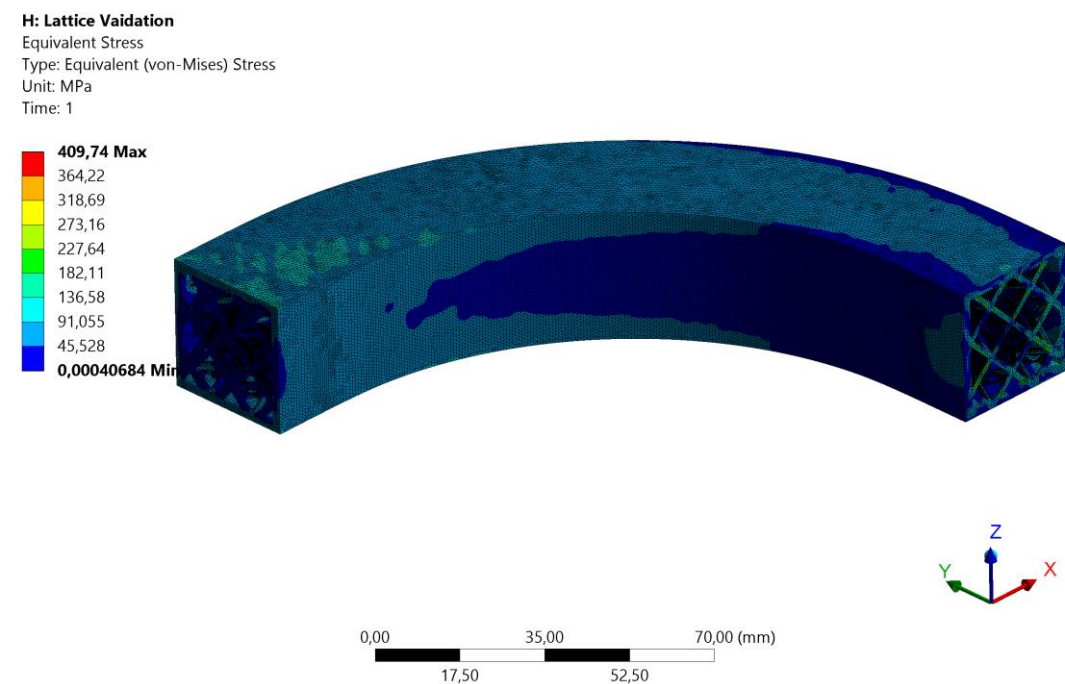


Figure 2.7.3.3: Von Mises equivalent stress of curved beam with the Octet lattice inner support structure and with Load Case 2 applied.

The results are summarized in the tables below (Table 2.7.3.2, Table 2.7.3.3):

Load Case 2	Full	Hollow	Developed inner support	Topology Optimization	Lattice Optimization Octahedral 1
Weight [g]	1337	333	731	641	475
Total Displacement Max  [mm]	0,200	0,871	0,264	0,272	0,450
Weight * Displacement (Minimum is better)	<b>267</b>	<b>290</b>	<b>193</b>	<b>174</b>	<b>214</b>

Table 2.7.3.2: Results comparison between the different beams with Load Case 2 applied.

Load Case 2	Full	Hollow	Developed inner support	Topology Optimization	Lattice Optimization Octet
Weight [g]	1337	333	731	641	484
Total Displacement Max  [mm]	0,200	0,871	0,264	0,272	0,450
Weight * Displacement (Minimum is better)	<b>267</b>	<b>290</b>	<b>193</b>	<b>174</b>	<b>218</b>

Table 2.7.3.3: Results comparison between the different beams with Load Case 2 applied.

It is possible to see that the index of the curved beam with the Octahedral 1 lattice structural inner support is 1,8 % lower than the one of the curved beam with the Octet lattice structural inner support. However, the index of the better performing curved beam with the Octahedral 1 inner support structure is 9,8 % higher than the one of the curved beam with the structural inner support developed in Subchapter 2.5.7. The very big advantage that the curved beams with the structural inner support made by lattice have is the very low weight. If the main goal for a certain design is to keep the weight as low as possible without having strict restrictions on the stiffness of the component, the lattice optimized inner support structure could be the best choice.

In conclusion, the best overall choice to develop a structural inner support for a hollow curved beam still be the approach of Subchapter 2.5: to make a topology optimization avoiding the use of the AM overhang constraint and to design a custom structural inner support “only” following the suggestions given by the topology optimisation.

It is important to point out that the considerations about the performances of the different inner support structures have been done in relation with the results obtained in this thesis work. For example, the lower performances of the lattice structural inner supports that have been found in this thesis work could not be true in other design scenarios or with other optimized lattice structures.

# CHAPTER 3: Laboratory tests of developed curved beams

## 3.1 Clamps design and realization

In this subchapter has been presented the development and the realization of the clamps needed for being able of testing the designed curved beams with the chosen Load Case 2 (Subchapter 2.3.2) boundary conditions (to be adapted for a real test set-up).

Has been decided to build the clamps in the Machine Design laboratory of Ljubljana's University where there is a band saw, a manual milling, a lathe, a drill press and welding possibilities. The material chosen was the S355 for the possibility to easy work with it and because some S355 blocks were already available in the University's laboratory.

The design of the clamps must have been as simple as possible because of the possible need of building some new parts and/or changing some parts of the clamps between the various experiments, due to the very high contact pressure that was expected between the Maraging steel specimens and the S355 clamps.

The system of clamps plus the specimen had to be mounted on the table of the MTS 25 kN test machine (Figure 3.1.1).

### Tabletop Load Frame Specifications

Model 370.02 tabletop load frames are available standard or extended heights with the actuator configured integral to load frame crosshead.

Load Frame Specifications <sub>1</sub>	Diagram Detail	Units	MODEL	
			370.02	370.02 100 Hz Elastomer
Force capacity (rated dynamic force)		kN (kip)	25 (5.5)	25 (5.5)
Available actuator ratings <sub>1</sub> (nominal)		kN (kip)	<b>15, 25</b> <b>(3.3, 5.5)</b>	<b>15, 25</b> <b>(3.3, 5.5)</b>
Actuator dynamic stroke <sub>1</sub>		mm (in)	<b>100, 150</b> <b>(4, 6)</b>	<b>100, 150</b> <b>(4, 6)</b>
Min vertical test space - standard height <sub>2</sub>	A	mm (in)	144 (5.7)	144 (5.7)
Max vertical test space - standard height <sub>3</sub>	A	mm (in)	827 (32.6)	827 (32.6)
Min vertical test space - extended height <sub>2</sub>	A	mm (in)	398 (15.7)	398 (15.7)
Max vertical test space - extended height <sub>3</sub>	A	mm (in)	1335 (52.6)	1335 (52.6)
Working height <sub>4</sub>	B	mm (in)	230 <sub>8</sub> (9.1)	230 <sub>8</sub> (9.1)
Column spacing	C	mm (in)	460 (18.1)	460 (18.1)
Column diameter (test space width)	D	mm (in)	76.2 (3.00)	76.2 (3.00)
Base width	E	mm (in)	622 (24.5)	622 (24.5)
Base depth	F	mm (in)	577 (22.7)	577 (22.7)
Diagonal clearance - standard height <sub>5</sub>	G	mm (in)	1750 <sub>8</sub> (68.9)	1750 <sub>8</sub> (68.9)
Diagonal clearance - extended height <sub>5</sub>	G	mm (in)	2250 <sub>8</sub> (88.6)	2250 <sub>8</sub> (88.6)
Overall height - standard height <sub>6</sub>	H	mm (in)	1989 <sub>8</sub> (78.3)	1989 <sub>8</sub> (78.3)
Overall height - extended height <sub>6</sub>	H	mm (in)	2624 <sub>8</sub> (103.3)	2624 <sub>8</sub> (103.3)
Stiffness <sub>7</sub>		N/m (lb/in)	345 x 10 <sup>6</sup> (1.95 x 10 <sup>6</sup> )	345 x 10 <sup>6</sup> (1.95 x 10 <sup>6</sup> )
Weight		kg (lb)	248 (547)	286 (630)

1. All load frame specifications listed in this chart are based upon the actuator ratings and dynamic stroke values indicated by bold text.
2. **Min Vertical Test Space:** Span between force transducer and piston rod face when fully retracted at beginning of the dynamic stroke; crosshead down, no alignment fixture.
3. **Max Vertical Test Space:** Span between force transducer and piston rod face when fully retracted at beginning of the dynamic stroke; crosshead up, no alignment fixture.
4. **Working Height:** Floor to top of work surface; includes standard FabCell isolation.
5. **Diagonal Clearance:** Hose height: tip of foot with FabCell; crosshead down.
6. **Overall Height:** From floor, including standard FabCell isolation, to top of the hoses or highest point on actuator; crosshead fully raised.
7. Measured at crosshead height of 600 mm (23.6 in).
8. For load frames with optional pneumatic/elastomeric vibration isolation mounts, add 37 mm (1.44 in) to dimensions B, G, and H.

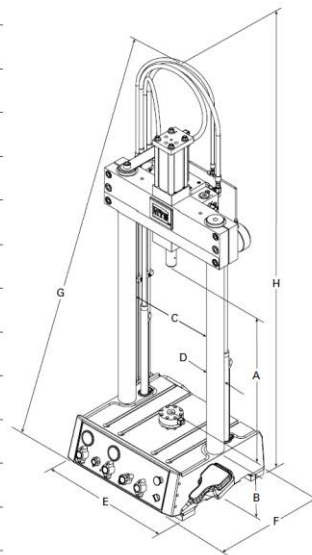


Figure 3.1.1: MTS 25 kN 370.02 characteristics [24].

The most useful dimensions of the slots of the MTS table and of the distances between the table slots and the default lower grip of the machine were not specified in the MTS technical brochure (Figure 3.1.1), so the measurements have been taken manually (Figure 3.1.2, Figure 3.1.3):

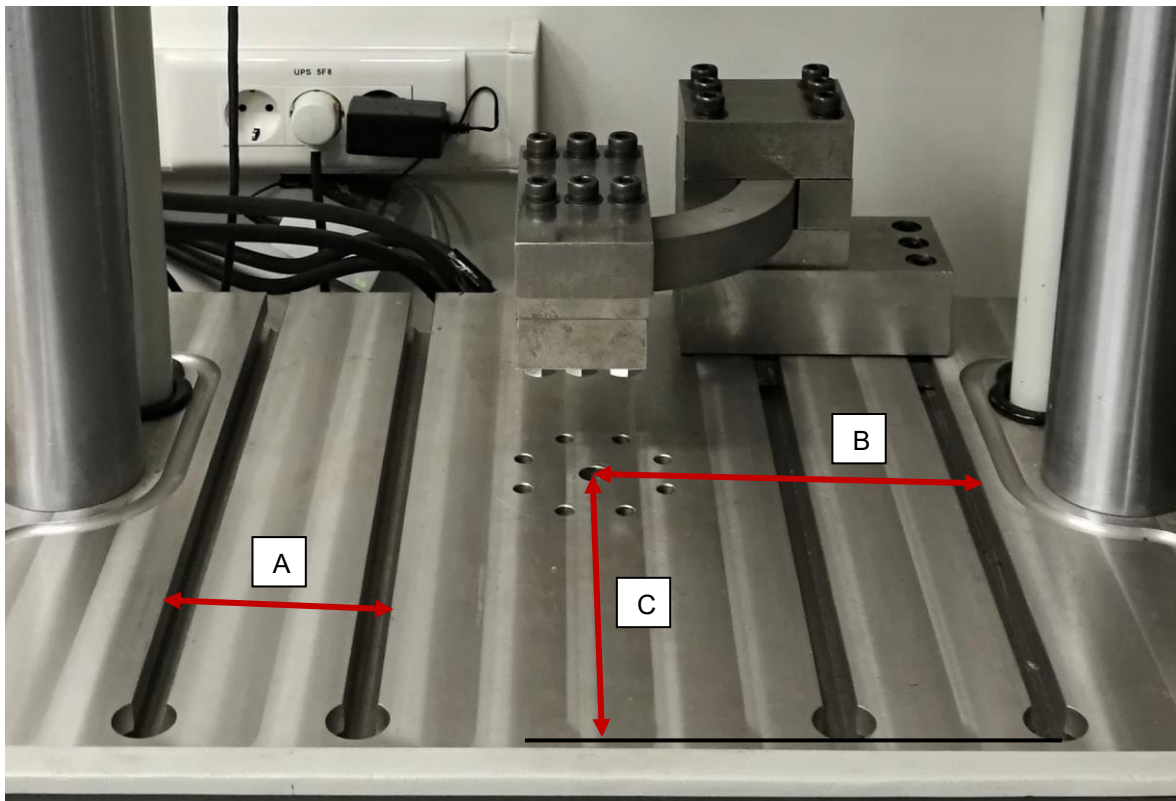


Figure 3.1.2: Useful distances of the MTS 25 kN table.

A = 102,5 mm is the distance between the two external edges of two near slots.

B = 197 mm is the distance between the external edge of an external slot and the very centre of the lower default grip.

C = 215 mm is the distance between the end of the slots in the front side of the machine and the very centre of the lower default grip.

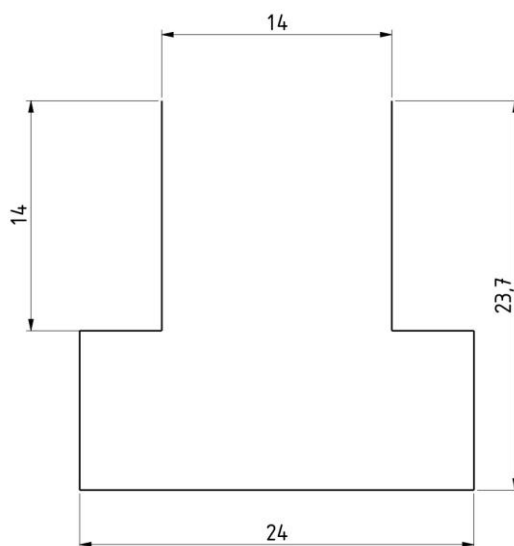


Figure 3.1.3: Dimensions of the section of the MTS 25 kN table slots (mm).



For safety purpose has been decided to clamp 40 mm of beam's both fix and load sides (Figure 3.1.3), instead of the 20 mm initially planned (Figure 2.2.1.2), to prevent the sliding out of the specimen from the clamping system. This decision has been taken because of the very high load that had to be applied to the Maraging steel version of the 3D printed curved beam to reach and exceed the yield stress.

About the bolts have been chosen to use M10 bolts grade 12.9 due to the dimension limitations of the MTS 25 kN table slots.

Has been calculated a bolts preload of 38976 N (following the UNI 10011), has been decided to apply a preload of 37500 N to each of the bolts, that preload value needs a tightening torque of 75 Nm.

After few design iterations, considering also the steel that was already available at University, in the following images (Figure 3.1.4, Figure 3.1.5, Figure 3.1.6, figure 3.1.7) has been presented the final design of the clamping system:

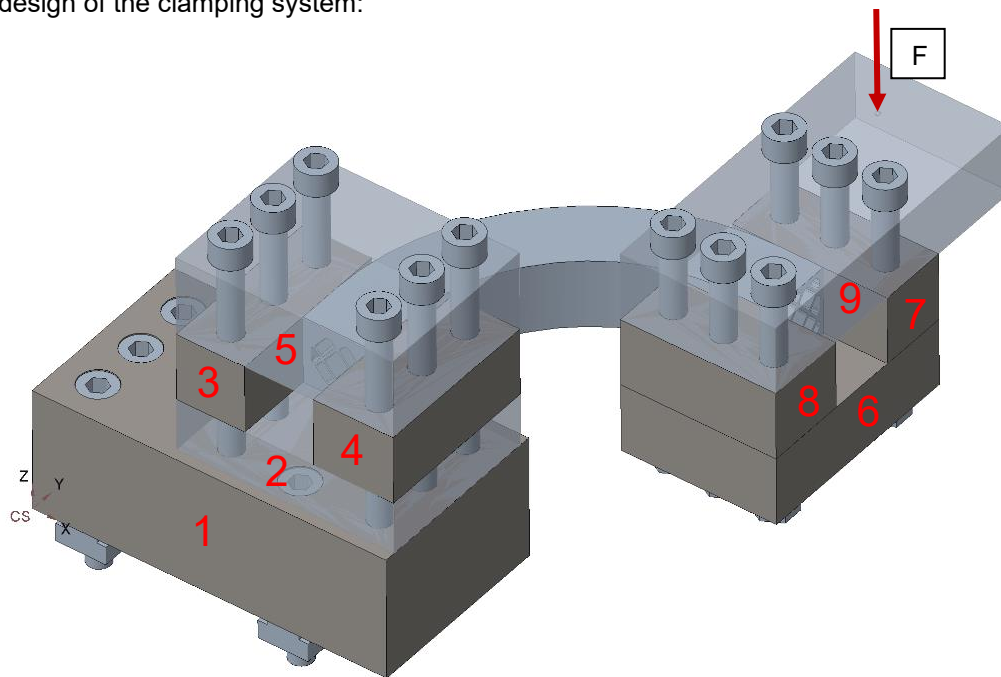


Figure 3.1.4: Overall view of the clamping system composed by the fix clamp assembly, the curved beam and the load clamp assembly.

The fix clamp assembly is composed by the following parts (Figure 3.1.4) (the 2D technical drawings of all the parts can be found in Annex C):

- 1) *Base*: base to be bolted to the MTS 25 kN table
- 2) *Fix 1*: base for the curved beam
- 3) *Fix 2*: lateral external guide for the curved beam
- 4) *Fix 3*: lateral internal guide for the curved beam
- 5) *Fix 4*: upper plate that, together with the base, applies the clamping pressure to the beam

The load clamp assembly is composed by the following parts (Figure 3.1.4):

- 6) *Load 1*: base for the curved beam
- 7) *Load 2*: lateral external guide for the curved beam
- 8) *Load 3*: lateral internal guide for the curved beam
- 9) *Load 4*: upper plate that, together with the base, applies the clamping pressure to the beam

It is possible to see in Figure 3.1.4 that the force  $F$  is applied in an eccentric way with respect to the load end of the curved beam. This has been done to replicate the boundary conditions of the Load Case 2 (Subchapter 2.3.2) in which the curved beam is loaded not only with a vertical force but also with a clockwise torsional moment.



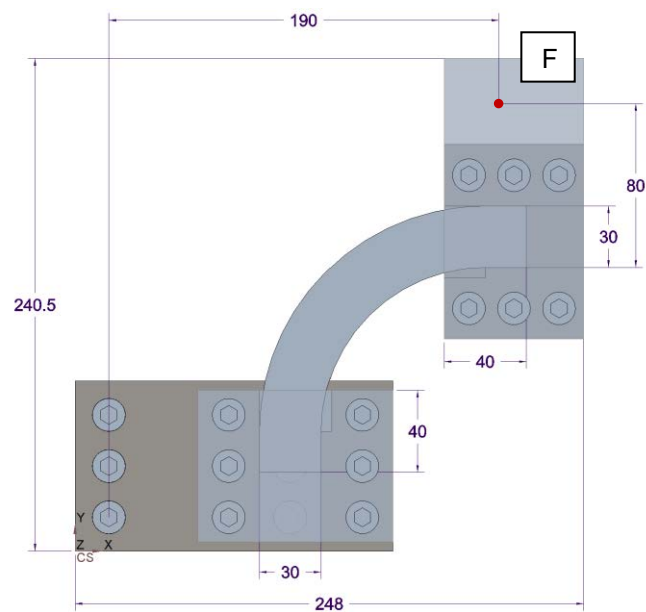


Figure 3.1.5: Top view of the clamping system with the main dimensions indicated (mm). It is possible to see also the force application point (in red).

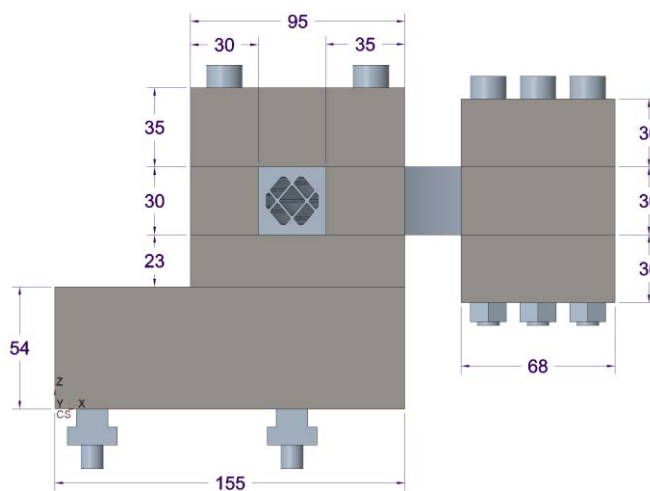


Figure 3.1.6: Front view of the clamping system with the main dimensions indicated (mm).

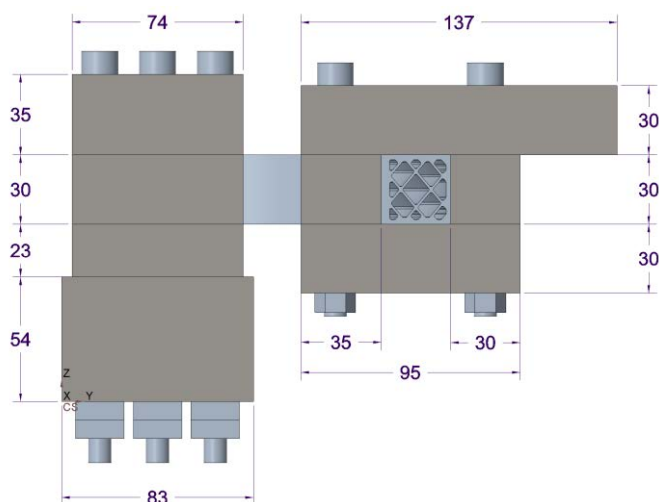


Figure 3.1.7: Side view of the clamping system with the main dimensions indicated (mm).

### 3.1.1 Clamping system F.E.M. analyses

Due to the computational capability available has been decided to split the F.E.M. analyses of the clamp system in two simulations: the first one is about the fix clamp assembly that has to fix the beam to the MTS table and the second one is about the load clamp assembly that is used to apply the load to the beam. The beam specimen is present in both the simulations.

Has been also modelled a small clearance of 0,5 mm between the lower surface of the *Fix 4* part and the upper surfaces of the *Fix 2* and *Fix 3* parts and between the lower surface of the *Load 4* part and the upper surfaces of the *Load 2* and *Load 3* parts. That clearance value has been used in the reality to be sure that the clamps would have clamped correctly the specimens.

Has been decided to use a force value of 24 kN: the maximum force that the MTS 25 kN test machine can apply, with a little safety factor.

The static structural F.E.M. analyses have been performed with the main parameters showed in the table below (Table 3.1.1.1):

Material for the curved beam	Maraging W400 (Table 3.1.1.2)
Material for the bolts	Bolts steel (Table 3.1.1.3)
Material for the clamp parts	S355 (Table 3.1.1.4)
Mesh Element Type	SOLID187
Mesh Element Order	Quadratic
Mesh Global Size for the curved beam	1,5 mm
Mesh Global Size for the bolts	2 mm
Mesh global Size for the clamp parts	3 mm
Mesh Target Quality	0,6

Table 3.1.1.1: Main parameters of the static structural F.E.M. analyses.

Density [kg/m <sup>3</sup> ]	8100
Young's Modulus [MPa]	198000
Poisson's Ratio [/]	0,3
Tensile Yield Strength [MPa]	950
Tensile Ultimate Strength [MPa]	1500

Table 3.1.1.2: Properties of the Maraging W400.

Density [kg/m <sup>3</sup> ]	7850
Young's Modulus [MPa]	206000
Poisson's Ratio [/]	0,3
Tensile Yield Strength [MPa]	1080
Tensile Ultimate Strength [MPa]	1200

Table 3.1.1.3: Properties of the Bolts steel (assuming the bolts grade to be 12.9).

Density [kg/m <sup>3</sup> ]	7850
Young's Modulus [MPa]	206000
Poisson's Ratio [/]	0,3
Tensile Yield Strength [MPa]	355
Tensile Ultimate Strength [MPa]	490

Table 3.1.1.4: Properties of the S355.

### Fix clamp assembly F.E.M. analysis

Have been applied the boundary conditions that are shown in the images below (Figure 3.1.1.1, Figure 3.1.1.2):

**B: Fix\_Clamp\_Assembly**  
Displacement Z  
Time: 1, s  
**A** Displacement Z  
**B** Remote Force: 24000 N

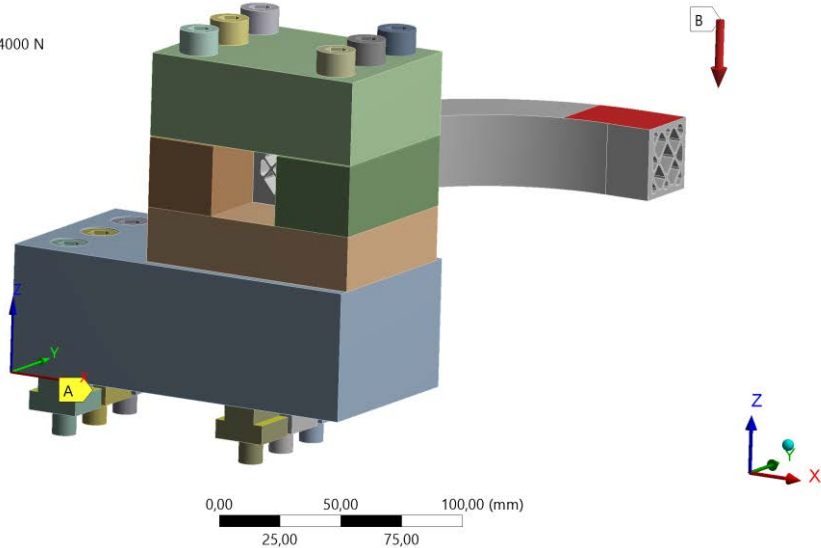


Figure 3.1.1.1: It is possible to see one of the two faces where the remote force has been applied on and it is possible to see that has been applied a displacement constraint, 0 mm in Z-axis, on the faces of the special bolts (Figure 3.1.2.8) that are in contact with the upper surfaces of the MTS 25 kN table slots.

**B: Fix\_Clamp\_Assembly**  
Displacement X , Y  
Time: 1, s  
**A** Displacement X , Y  
**B** Remote Force: 24000 N

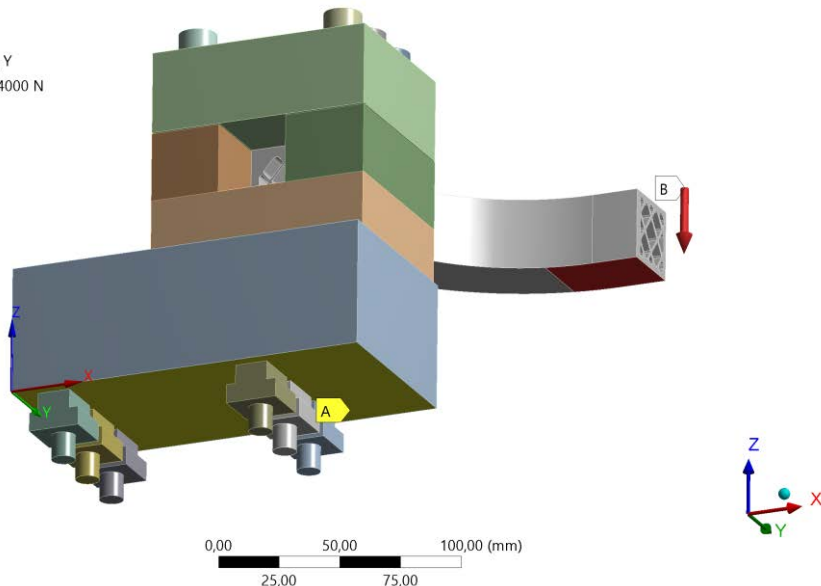


Figure 3.1.1.2: It is possible to see the second of the two faces where the remote force has been applied on and it is possible to see that has been applied a displacement constraint, 0 mm in X-axis and in Y-axis, on the lower face of the *Base* part. This has been done because of the idea that the X-axis and the Y-axis displacement constraints would be given by the friction force between the *Base* part lower surface and the MTS 25 kN table.

In the images below (Figure 3.1.1.3, Figure 3.1.1.4) it is possible to see all the contact types that have been set in this finite element model:

**Frictional - Beam To Fix 1 and Fix 4**

- A** Bonded - Fix 2 and Fix 3 To Fix 1
- B** Bonded - Fix 1 To Base
- C** Frictional - Fix 4 To Fix 2 and Fix 3
- D** Frictional - Beam To Fix 1 and Fix 4

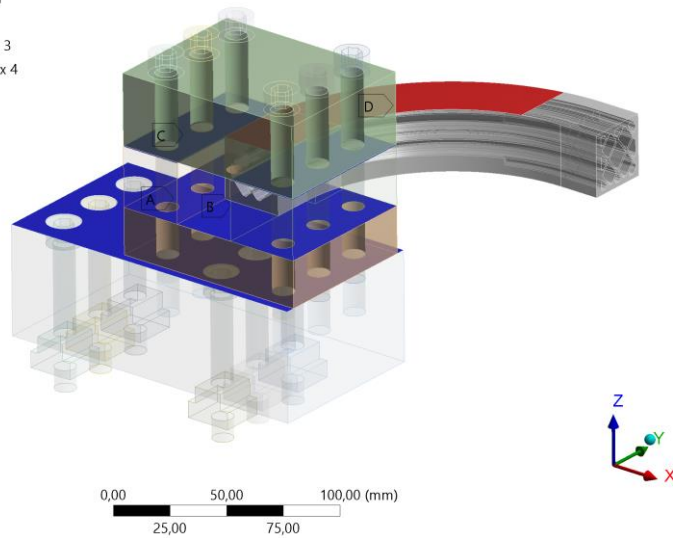


Figure 3.1.1.3: First group of contact types that have been set in the finite element model.

In the first group of contact types there are:

- A) A *Bonded* contact between the lower surfaces of the *Fix 2* and the *Fix 3* parts (*Contact Bodies*) and the upper surface of the *Fix 1* part (*Target Bodies*)
- B) A *Bonded* contact between the lower surface of the *Fix 1* part (*Contact Bodies*) and the upper surface of the *Base* part (*Target Bodies*)
- C) A *Frictional* contact between the lower surface of the *Fix 4* part (*Contact Bodies*) and the upper surfaces of the *Fix 2* and the *Fix 3* parts (*Target Bodies*). The static friction coefficient value has been set to 0,7, a common value for a steel to steel contact without lubricants.
- D) A *Frictional* contact between the lower and upper surfaces of the curved beam (*Contact Bodies*) and, respectively, the upper surface of the *Fix 1* part and the lower surface of the *Fix 4* part (*Target Bodies*). The static friction coefficient value has been set to 0,7, a common value for a steel to steel contact without lubricants.

**Bonded - Bolts To Fix 4**

- A** Bonded - Bolts To Fix 4
- B** Bonded - Upper Bolts To Base
- C** Bonded - Lower Bolts To Base

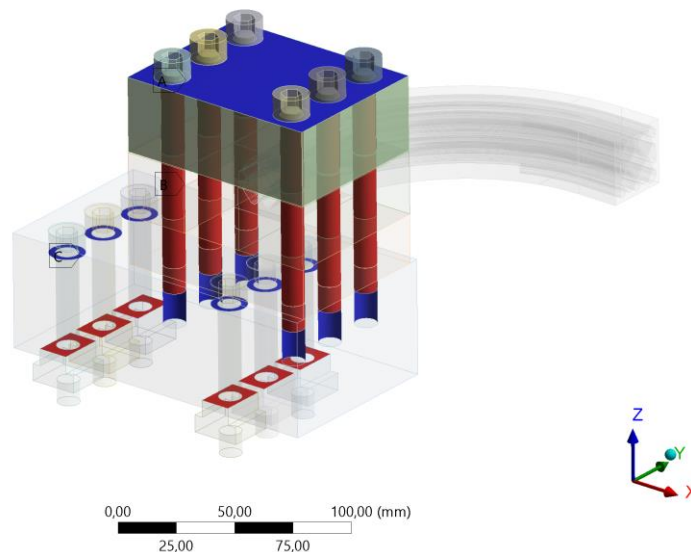


Figure 3.1.1.4: Second group of contact types that have been set in the finite element model.

In the second group of contact types there are:

- A) A *Bonded* contact between the lower surfaces of the six heads of the upper bolts (*Contact Bodies*) and the upper surface of the *Fix 4* part (*Target Bodies*)
- B) A *Bonded* contact between the lateral surfaces of the six stems of the upper bolts (*Contact Bodies*) and the lateral surfaces of the six holes in the *Base* part (*Target Bodies*)
- C) A *Bonded* contact between the lower surfaces of the six heads of the lower bolts and the upper surfaces of the six special nuts (*Contact Bodies*) and, respectively, the upper surfaces of the six holes in the *Base* part and the lower surface of the *Base* part (*Target Bodies*)

Have been applied a 37500 N preload to all the twelve bolts that are present in the fix clamp assembly with the Ansys *Bolt Pretension* tool (Figure 3.1.1.5):

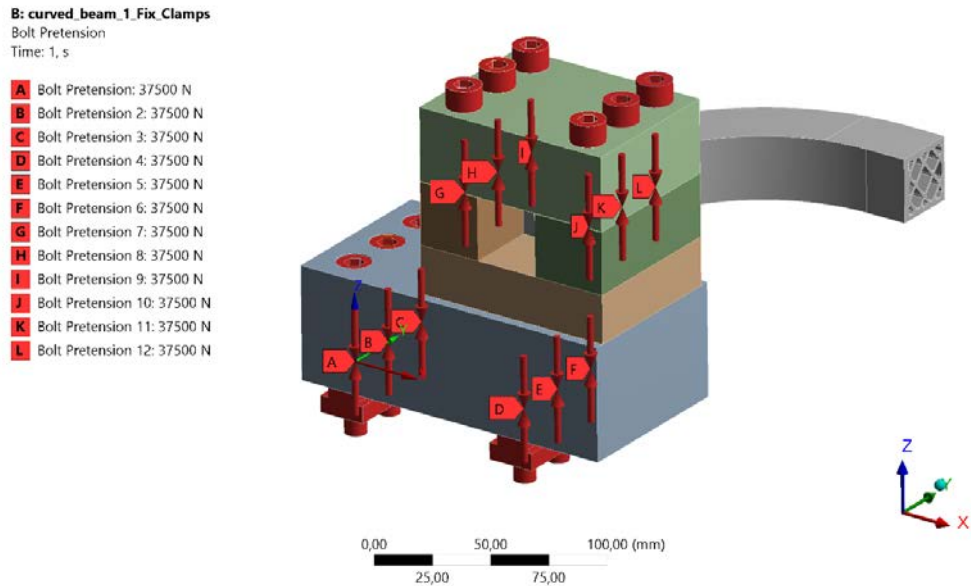


Figure 3.1.1.5: Preload applied to all the twelve bolts that are present in the fix clamp assembly.

In the images below (Figure 3.1.1.6, Figure 3.1.1.7, Figure 3.1.1.8, Figure 3.1.1.9) it is possible to see the Von Mises equivalent stress results:

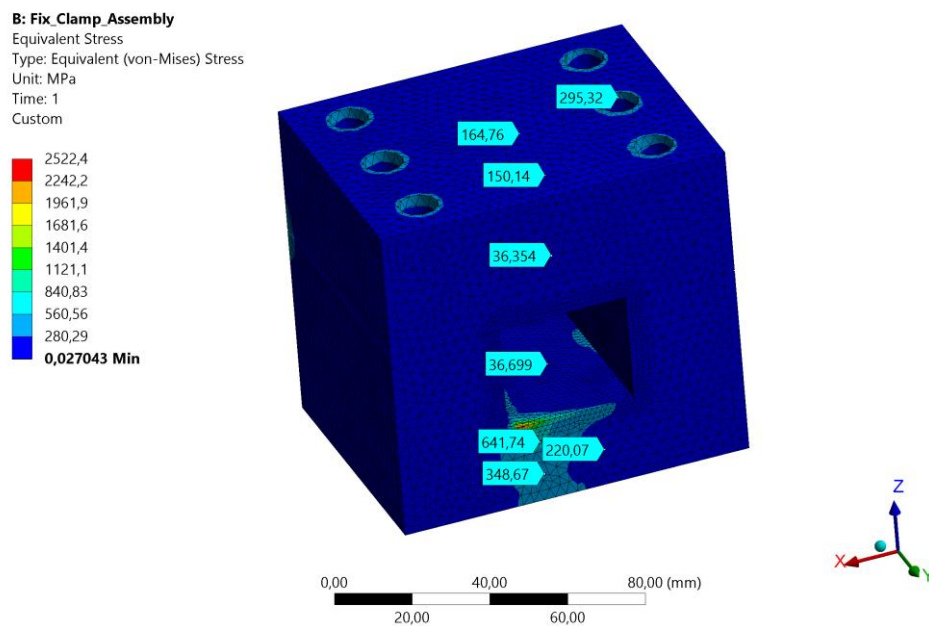


Figure 3.1.1.6: Von Mises equivalent stress of *Fix 1*, *Fix 2*, *Fix 3* and *Fix 4* parts.

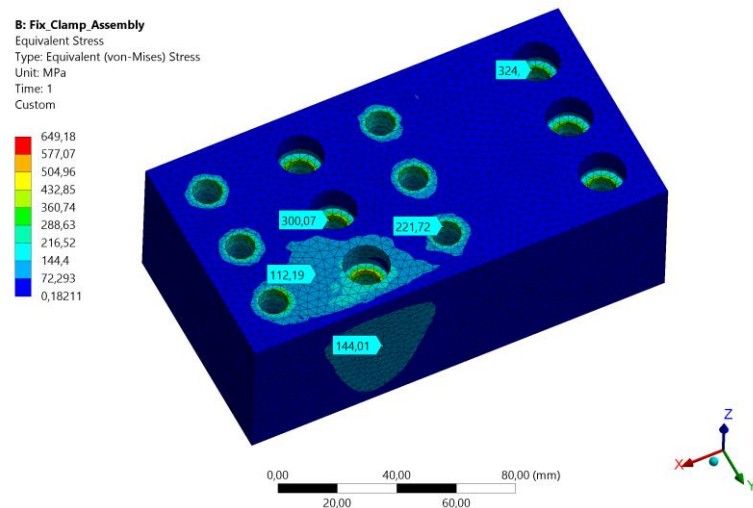


Figure 3.1.1.7: Von Mises equivalent stress of the *base* part.

It is possible to see that generally the stresses are below the yield strength of the S355 (355 MPa). However, there are some high stresses in some small slices of material: around the holes for the bolts and where the curved beam is in contact with the *Fix 1* and *Fix 4* parts. The slices of material with very high stresses are very small so has been thought that there would be no strength problems in realizing and using these clamps.

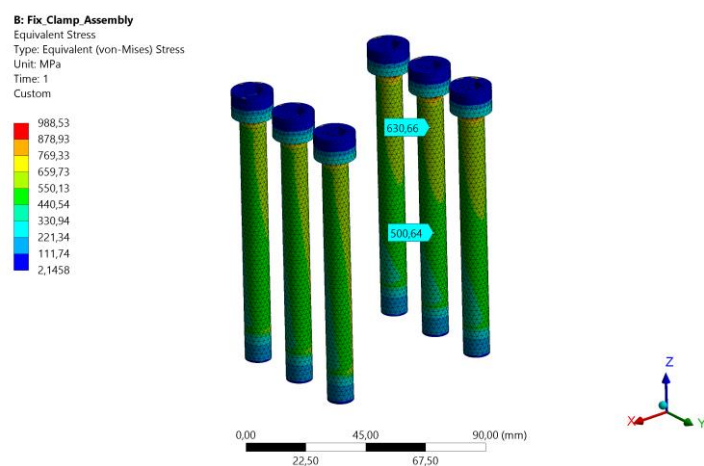


Figure 3.1.1.8: Von Mises equivalent stress of the upper bolts.

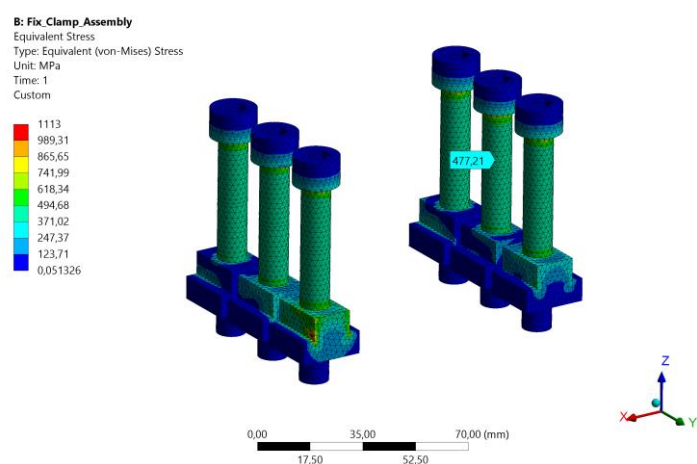


Figure 3.1.1.9: Von Mises equivalent stress of the lower bolts.



It is possible to see that generally, despite some high stresses of small parts of the bolts, especially in the edges, the stresses are below the yield strength value for a 12.9 bolt (1080 MPa).

### Load clamp assembly F.E.M. analysis

Have been applied the boundary conditions that are shown in the images below (Figure 3.1.1.10):

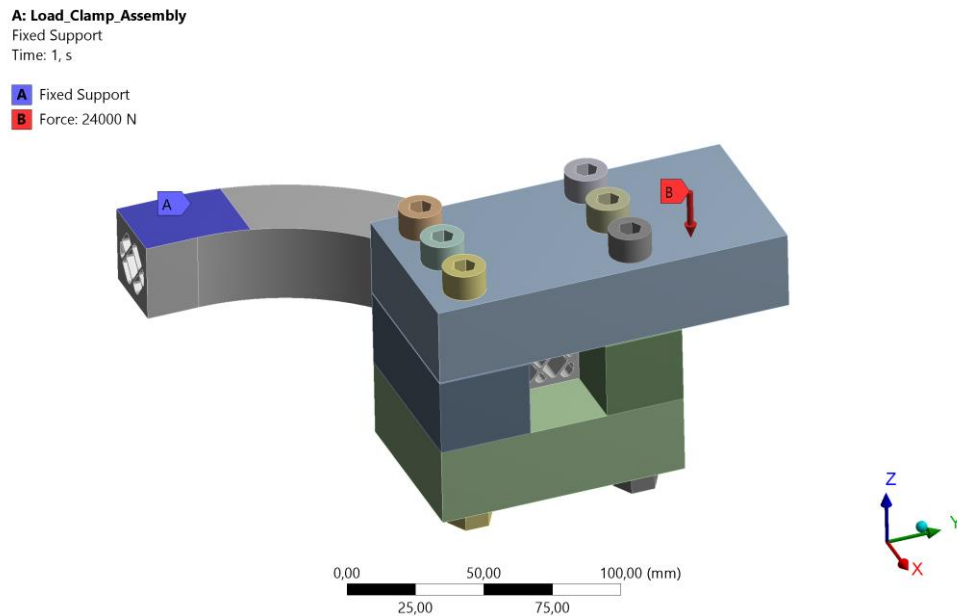


Figure 3.1.1.10: It is possible to see one of the two opposite faces of the beam where the fix constraint has been applied on and it is possible to see the vertical force that has been applied to the *Load 4* part of the load clamp assembly.

In the image below (Figure 3.1.1.11) it is possible to see all the contact types that have been set in this finite element model:

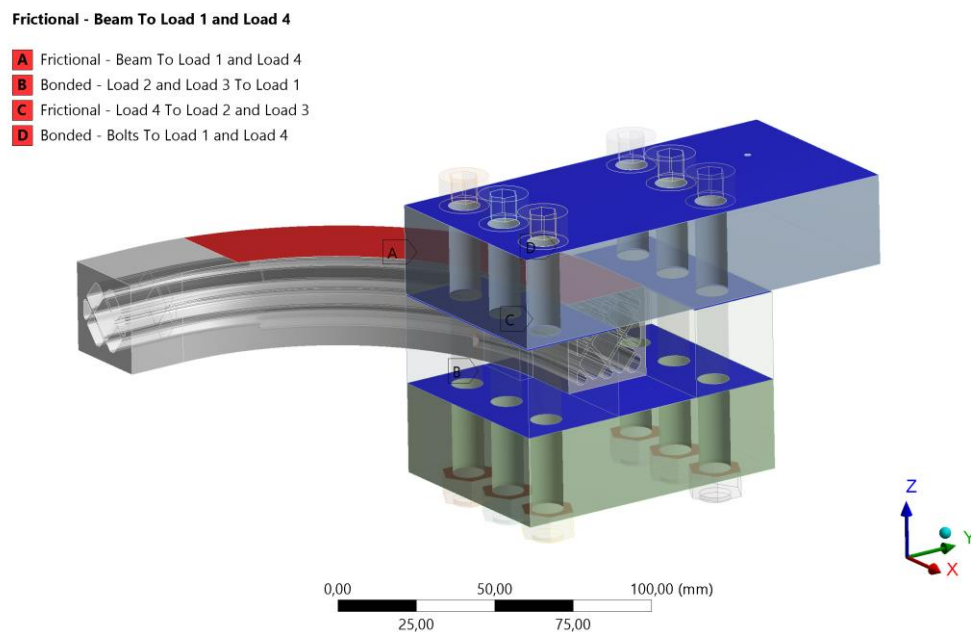


Figure 3.1.1.11: Contact types that have been set in the finite element model.

There are:

- A) A *Frictional* contact between the lower and upper surfaces of the curved beam (*Contact Bodies*) and, respectively, the upper surface of the *Load 1* part and the lower surface of the *Load 4* part (*Target Bodies*). The static friction coefficient value has been set to 0,7, a common value for a steel to steel contact without lubricants.
- B) A *Bonded* contact between the lower surfaces of the *Load 2* and the *Load 3* parts (*Contact Bodies*) and the upper surface of the *Load 1* part (*Target Bodies*)
- C) A *Frictional* contact between the lower surface of the *Load 4* part (*Contact Bodies*) and the upper surfaces of the *Load 2* and the *Load 3* parts (*Target Bodies*). The static friction coefficient value has been set to 0,7, a common value for a steel to steel contact without lubricants.
- D) A *Bonded* contact between the lower surfaces of the six heads of the bolts and the upper surfaces of the six nuts (*Contact Bodies*) and, respectively, the upper surface of the *Load 4* part and the lower surface of the *Load 1* part (*Target Bodies*)

Have been applied a 37500 N preload to all the six bolts that are present in the load clamp assembly with the Ansys *Bolt Pretension* tool (Figure 3.1.1.12):

**A: Load\_Clamp\_Assembly**

Bolt Pretension

Time: 1, s

- A** Bolt Pretension: 37500 N
- B** Bolt Pretension 2: 37500 N
- C** Bolt Pretension 3: 37500 N
- D** Bolt Pretension 4: 37500 N
- E** Bolt Pretension 5: 37500 N
- F** Bolt Pretension 6: 37500 N

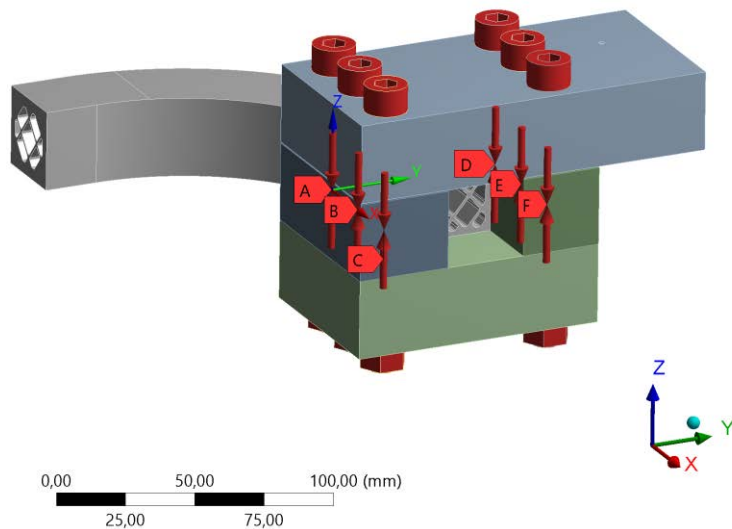


Figure 3.1.1.12: Preload applied to all the six bolts that are present in the load clamp assembly.

In the images below (Figure 3.1.1.13, Figure 3.1.1.14) it is possible to see the Von Mises equivalent stress results:

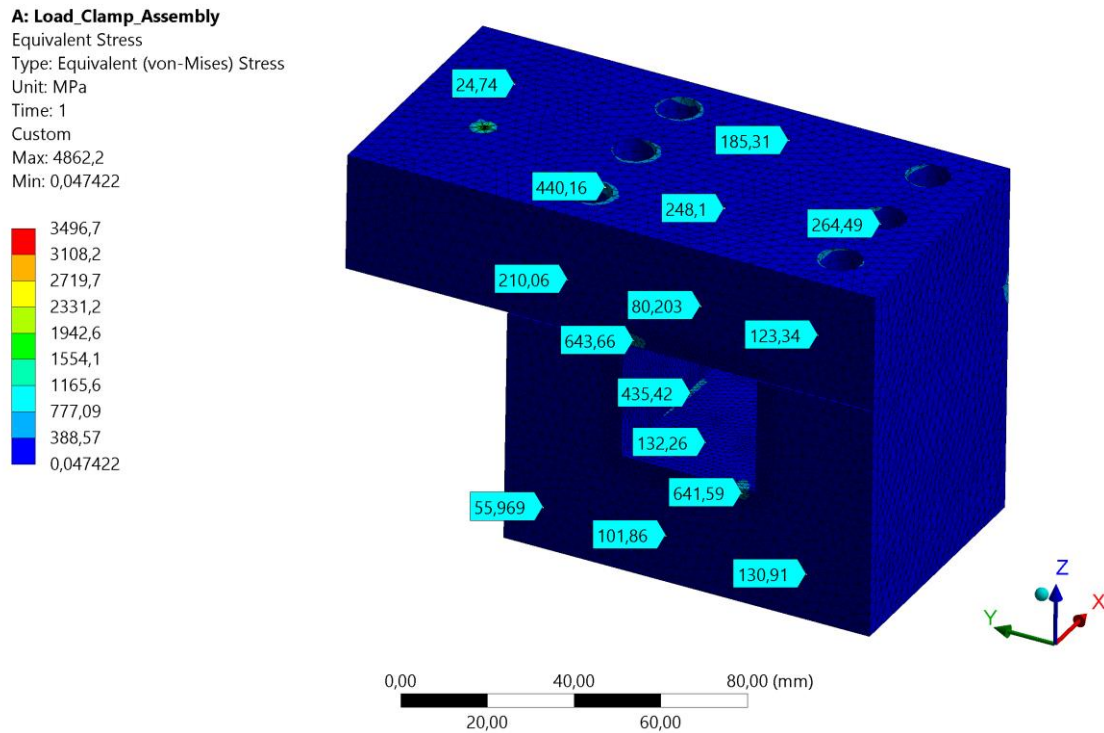


Figure 3.1.1.13: Von Mises equivalent stress of the load clamp assembly

It is possible to see that generally the stresses are below the yield strength of the S355 (355 MPa). However, there are some high stresses in some small slices of material: around the holes for the bolts, where the force has been applied and where the curved beam is in contact with the *Load 1* and *Load 4* parts. The slices of material with very high stresses are very small so has been thought that there would be no strength problems in realizing and using these clamps.

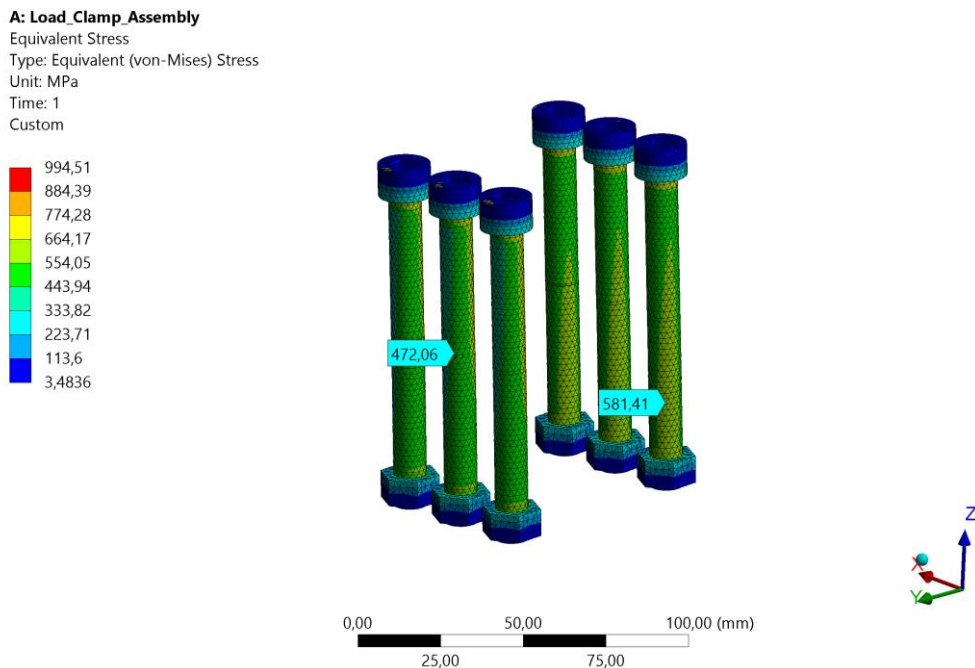


Figure 3.1.1.14: Von Mises equivalent stress of the bolts.

It is possible to see that despite some high stresses of small parts of the bolts, especially in the edges, generally the stresses are very below the yield strength for a 12.9 bolt (1080 MPa).

### 3.1.2 Clamping system realization

As mentioned before, the clamping system has been realized in the Machine Design laboratory of the Ljubljana's University. Has been used a three axis milling machine (Figure 3.1.2.1.) to mill the clamping parts from some rough blocks made of S355.



Figure 3.1.2.1: View of the central part of the three axis milling machine. It is possible to see also the *Base* part during the holes threading process.

In the image below (Figure 3.1.2.2) it is possible to see the fix clamp assembly after the complete realization:

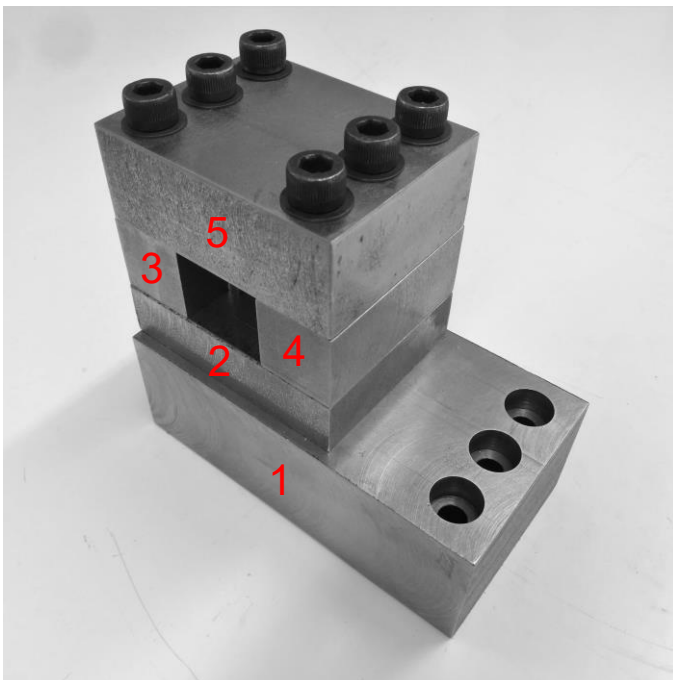


Figure 3.1.2.2: Fix clamp assembly.

In the images below (Figure 3.1.2.3, Figure 3.1.2.4, Figure 3.1.2.5, Figure 3.1.2.6, Figure 3.2.1.7) it is possible to see all the single milled parts that are present in the fix clamp assembly:



Figure 3.1.2.3: *Base* part.

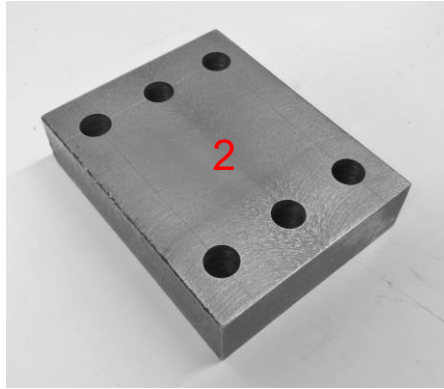


Figure 3.1.2.4: *Fix 1* part.



Figure 3.1.2.5: *Fix 2* part.



Figure 3.1.2.6: *Fix 3* part.



Figure 3.1.2.7: *Fix 4* part.

In the image below (Figure 3.1.2.8) it is possible to see the nut type that has been used to bolt the *Base* part to the MTS 25 kN table. It is a special nut designed for sliding in the slots of the milling machine table, slots that have been seen be equal to the ones of the MTS 25 kN machine.



Figure 3.1.2.8: Special nut for bolting the *Base* part to the MTS 25 kN table.

During the tests of the PA12 curved beams, after the very first test has been performed, has been decided to add another piece to the fix clamp assembly (Figure 3.1.2.9) to lift the beams due to their large deformation. In this way has been avoided the load clamp assembly to touch the MTS 25 kN table. With this PA12 set-up the six upper M10 bolts 12.9 of the fix clamp assembly have been substituted by six more longer M10 threaded rods 8.8, their strength was more than enough for the loads that have been used in the PA12 curved beam tests.

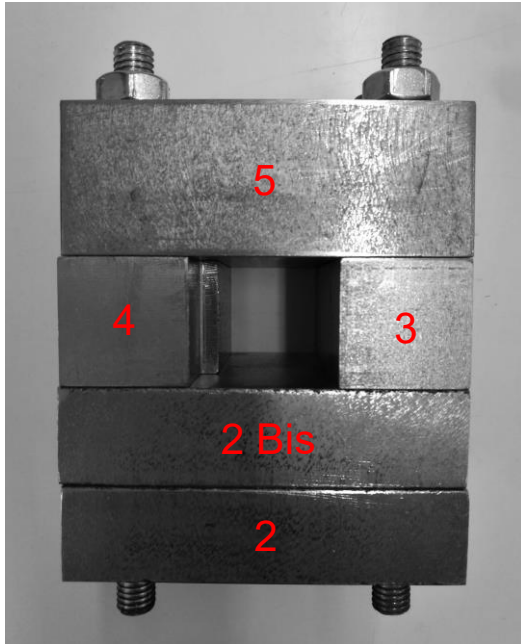


Figure 3.1.2.9: Fix clamp assembly with the added piece to lift the curved beams (image without the *Base* part).

In the image below (Figure 3.1.2.10) it is possible to see the load clamp assembly after the complete realization:

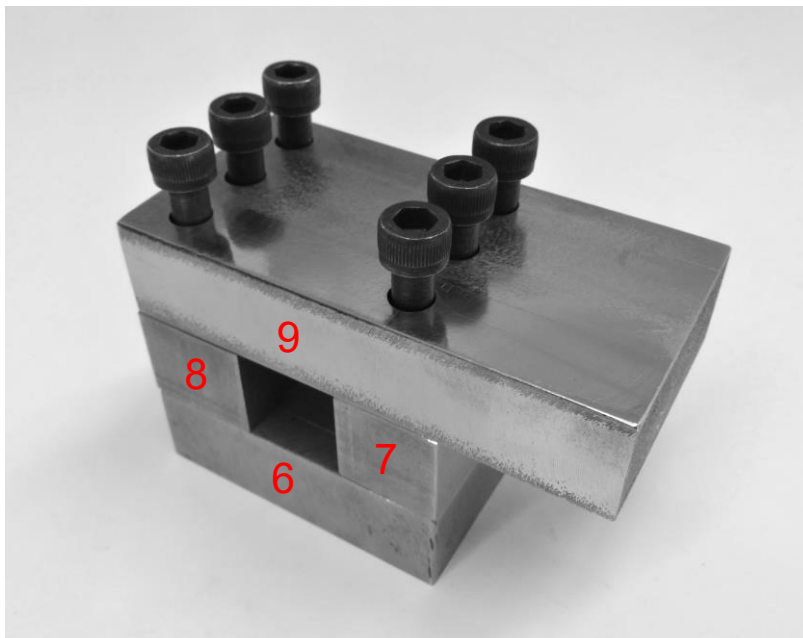


Figure 3.1.2.10: Load clamp assembly.



In the images below (Figure 3.1.2.11, Figure 3.1.2.12, Figure 3.1.2.13, Figure 3.1.2.14) it is possible to see all the single milled parts that are present in the load clamp assembly:

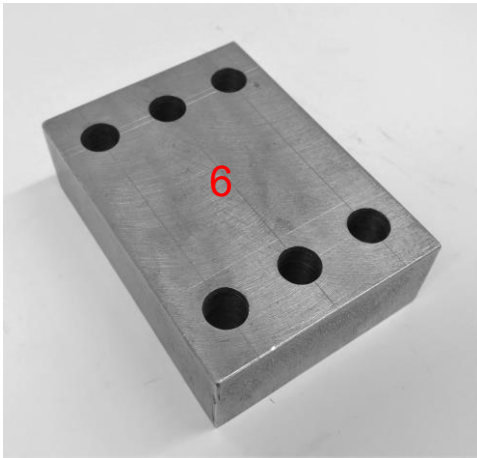


Figure 3.1.2.11: *Load 1* part.

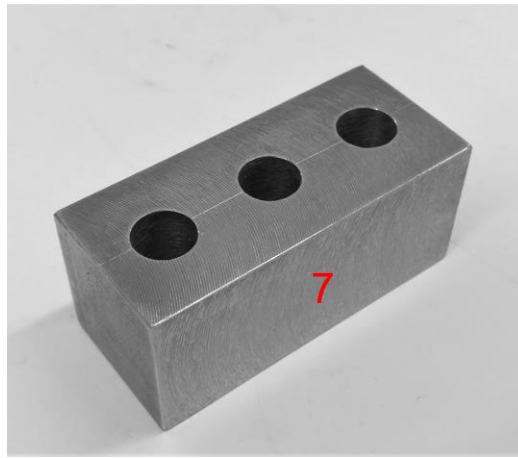


Figure 3.1.2.12: *Load 2* part.

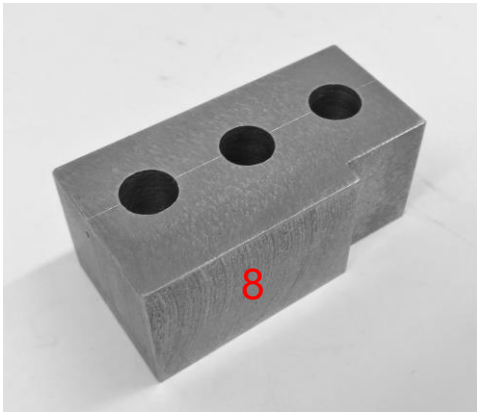


Figure 3.1.2.13: *Load 3* part.



Figure 3.1.2.14: *Load 4* part.

### 3.2 Static tests

The first goal of the static tests was to make a comparison between the forces needed to break a Maraging steel curved beam specimen and a PA12 curved beam specimen with the same structural inner support.

The second goal of the static tests was to compare the forces needed to break different PA12 curved beam specimens with some of the different structural inner supports developed in Chapter 2.

#### 3.2.1 Maraging steel specimens and PA12 specimens

##### Maraging steel specimens

The Maraging steel specimens have been printed thanks to an external company. Have been printed four curved beam specimens with the inner support developed in Subchapter 2.5.7.

The first idea was using only one of the four available curved beams for the static tests (Figure 3.2.1.1).

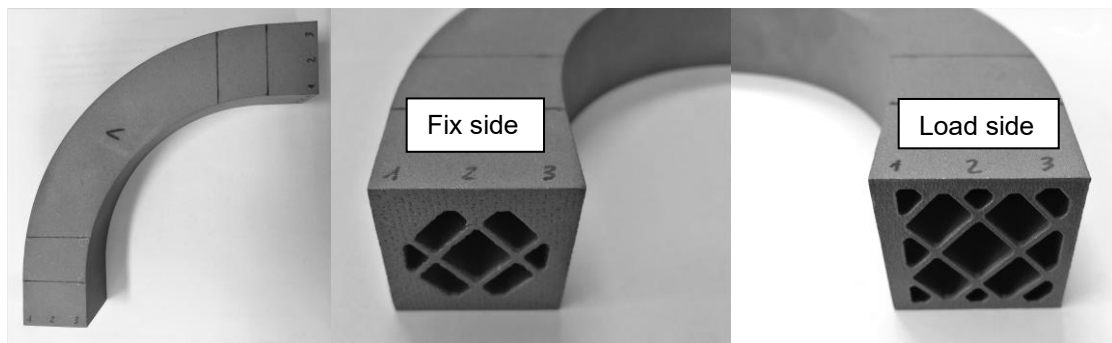


Figure 3.2.1.1: Different views of the number one 3D printed Maraging steel curved beam.

The first static test of the Maraging steel curved beam didn't perform as expected because with a load of 24 kN (the maximum load that the 25 kN MTS machine can apply, with a safety factor) the beam only yielded a little bit in the fix zone. Looking at the force - displacement chart has been possible to see also that the stiffness of the clamps wasn't enough (Figure 3.2.3.7).

Has been decided to modify a second Maraging steel curved beam with four notches made from the edges of the beam with the milling machine (Figure 3.1.2.1) to weaken the weakest section of the beam (Figure 3.2.1.2). The weakest section of the beam has been found thanks to the first static test of the PA12 version of the beam and as expected, it was the boundary section between the inner support structure of the sector 1 of the beam and the inner support structure of the sector 2 of the beam (Figure 3.2.3.2). For milling the four notches has been used a cutting disc 3 mm thick and with a diameter of 125 mm. (Accurate details of the curved beam geometry with the four notches can be found in Annex D)

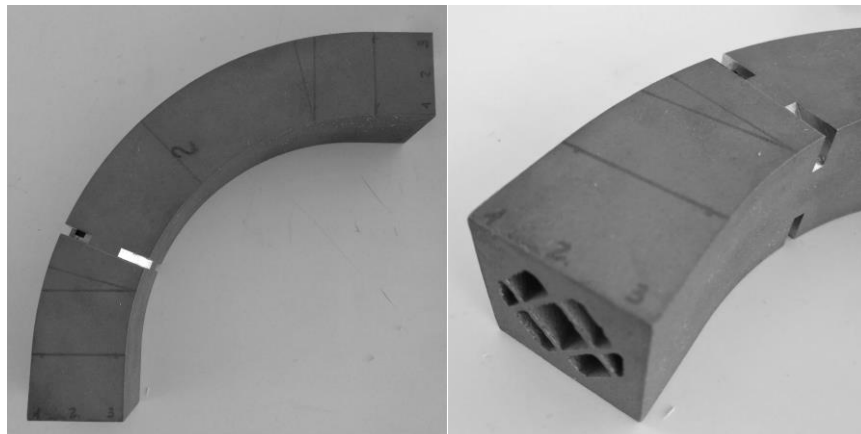


Figure 3.2.1.2: Different views of the number two 3D printed Maraging steel curved beam, after the milling from the edges of the four notches.

### PA12 Specimens

The PA12 specimens have been printed in the Machine Design laboratory of the Faculty of Mechanical Engineering of Ljubljana's University using a "Lisa" by "Sinterit" 3D printer (Figure 4.1.1). The number of specimens that could be printed was reasonably "unlimited".

The PA12 specimens have been printed reducing all the dimensions of the 3D models by 5% (Figure 3.2.1.3, Figure 3.2.1.4). This has been done because even if the print volume of the "Lisa" 3D printer by "Sinterit" for the maximum accuracy for PA materials is 90x130x130, It has seen with the experience that it is better to print objects that are enclosed in a volume of 90x120x130.



Figure 3.2.1.3: XY-plane view of the PA12 curved beam with the structural inner support developed in Subchapter 2.5.7 (mm).

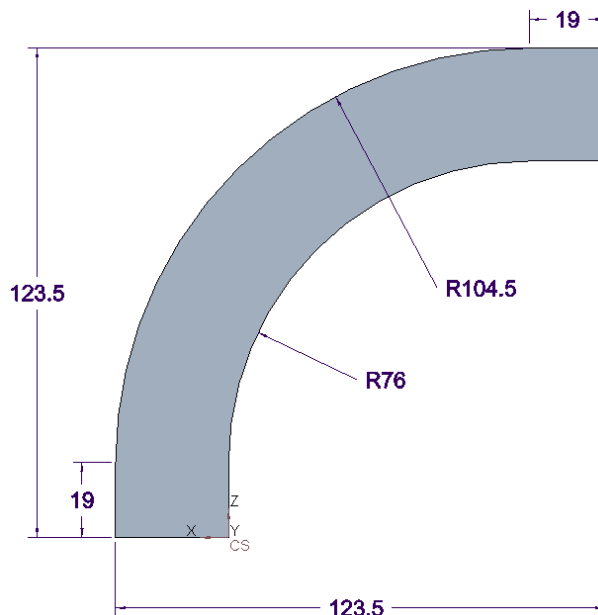


Figure 3.2.1.4: XZ-plane view of the PA12 curved beam with the structural inner support developed in Subchapter 2.5.7 (mm).

Four curved beam specimens with the structural inner support developed in Subchapter 2.5.7 have been printed. The first one (Figure 3.2.1.5), without the four notches have been used to make the very first test to check that everything was fine. The second one and the third one, without the four notches, have been used to make a comparison with the other PA12 curved beam specimens with different structural inner supports.

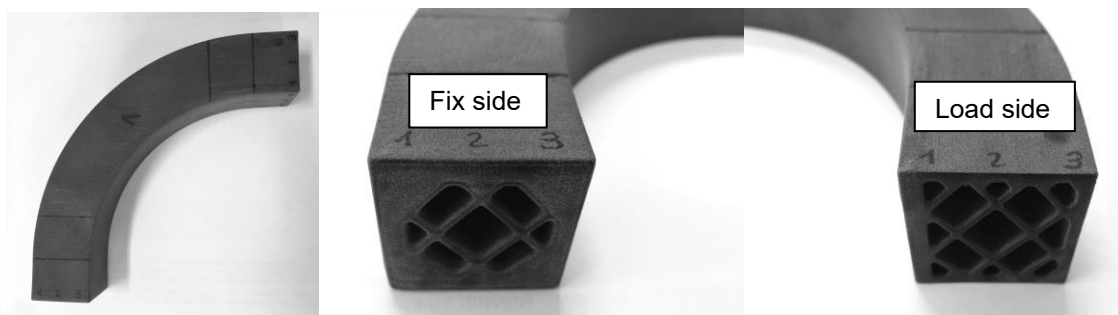


Figure 3.2.1.5: Different views of the number one 3D printed PA12 curved beam with the structural inner support developed in Subchapter 2.5.7.

The four notches have been done in the fourth PA12 specimen (figure 3.2.1.6) in the same positions of the Maraging steel's ones and with the same milling machine and cutting disc. (Accurate details of the PA12 curved beam geometry with the four notches can be found in Annex D)

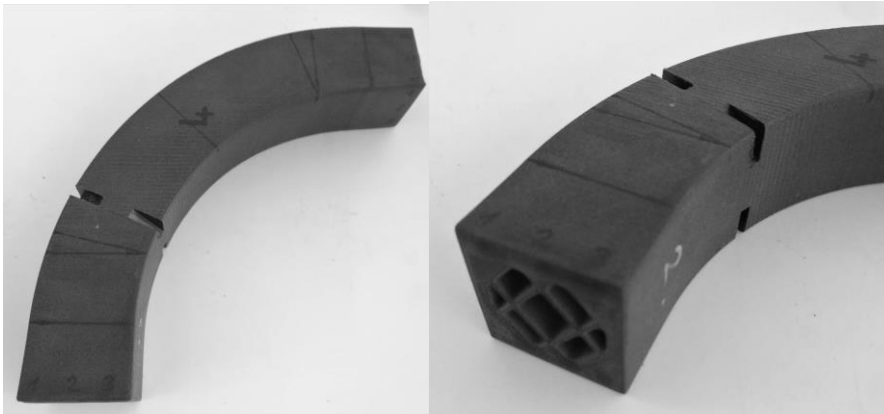


Figure 3.2.1.6: Different views of the number four 3D printed PA12 curved beam with the structural inner support developed in Subchapter 2.5.7, after the milling of the four notches.

Has been printed a curved beam specimen with the *Octahedral 1* variable lattice inner support developed in subchapter 2.7.2 (Figure 3.2.1.7).

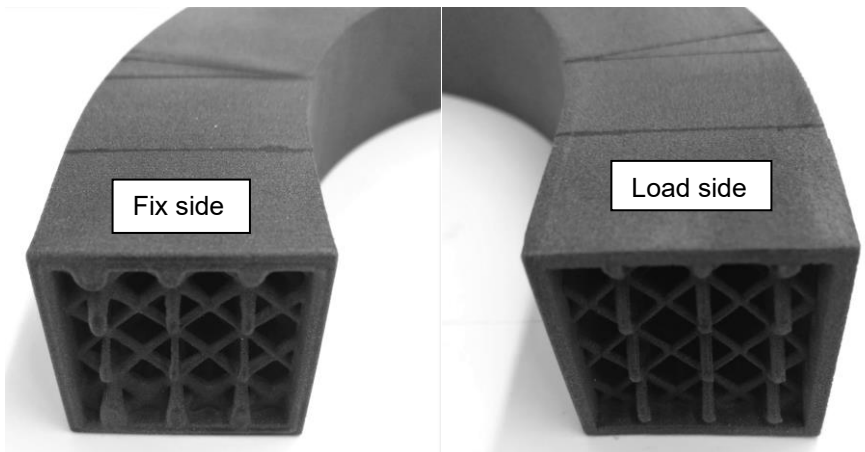


Figure 3.2.1.7: Different views of the number one 3D printed PA12 curved beam with the *Octahedral 1* variable lattice inner support.

Has been printed a curved beam specimen with the *Octet* variable lattice inner support developed in subchapter 2.7.2 (Figure 3.2.1.8).

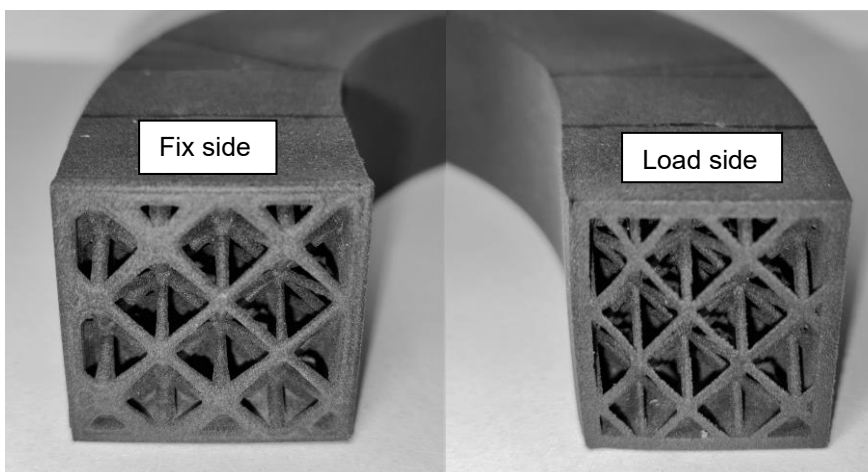


Figure 3.2.1.8: Different views of the number one 3D printed PA12 curved beam with the *Octet* variable lattice inner support.

### 3.2.2 Tests set-up description

The static tests have been done with an MTS 25 kN machine (model 370.02), the lower grip has been removed (Figure 3.2.2.1).



Figure 3.2.2.1: View of the 25 kN MTS test machine with the lower grip removed and with the Maraging steel clamps set - up.

The boundary conditions scheme was the one of the Load Case 2 (Subchapter 2.3.2) adapted to create the torsional moment with only one vertical eccentric force (Figure 3.1.4). The load clamp assembly and the fix clamp assembly were clamping the beam for the first 40 mm from respectively the load end of the beam and the fix end of the beam (Figure 3.1.5).

To be sure that the clamps were effectively clamping the beams and to use the designed and realized clamps also for the smaller PA12 beams, have been used some slats (Figure 3.2.2.2) with a thickness of 0,5 mm or 1,5 mm to be interposed between the upper surfaces of the beams and the clamps. Has been used one slat 0,5 mm thick to be interposed between the upper surfaces of the Maraging beams and the *Fix 4* part of the fix clamp assembly and the same for the *Load 4* part of the load clamp assembly. Has been used one slat 0,5 mm thick plus one slat 1,5 mm thick to be interposed between the upper surfaces of the PA12 beams and the *Fix 4* part of the fix clamp assembly and the same for the *Load 4* part of the load clamp assembly.



Figure 3.2.2.2: View of the two types of slat that have been used. On the left there is the 0,5 mm thick one and, on the right, there is the 1,5 mm thick one.

The load has been applied from the upper grip of the 25 kN MTS machine to the *Load 4* part of the load clamp assembly thanks to a custom made tool with a bearing ball (Figure 3.2.2.3). The bearing ball has been wet with oil to further reduce the friction between the applying load tool and the upper surface of the *Load 4* part of the load clamp assembly.



Figure 3.2.2.3: View of the custom made tool with the bearing ball.

An overview of the test's configuration is showed in the images below (Figure 3.2.2.4, Figure 3.2.2.5):

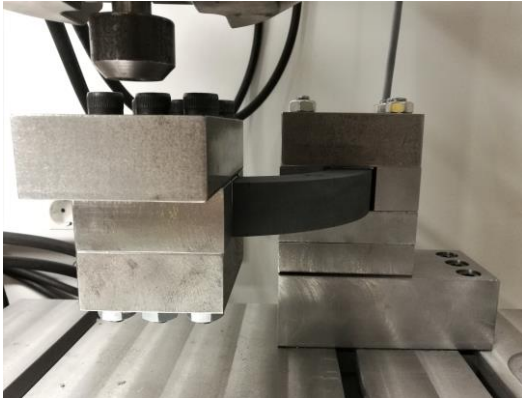


Figure 3.2.2.4: View of the PA12 clamps set - up with the number two PA12 curved beam with the structural inner support developed in Subchapter 2.5.7.

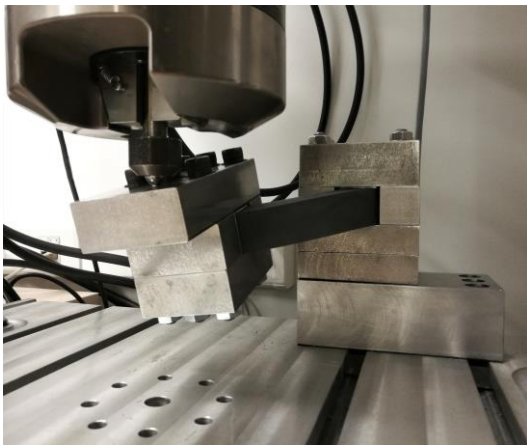


Figure 3.2.2.5: View of the PA12 clamps set - up while the actuator was applying the load to break the number two PA12 curved beam with the structural inner support developed in Subchapter 2.5.7.

In the table below are summarized some parameters common to all the tests performed (Table 3.2.2.1):

Room's temperature range [°C]	23 - 27
Upper grip pressure [MPa]	15
Actuator control	Displacement
Speed PA12 specimens [mm/min]	1,5
Speed Maraging steel specimens [mm/min]	0,5
Load cell values dispersion [N] at -0,5 kN (For PA12 specimens)	$\pm 4,8$
Load cell values dispersion [N] at -17,5 kN (For Maraging steel specimens)	$\pm 40$

Table 3.2.2.1: Static tests common parameters.



### 3.2.3 Test results

In all the static tests performed the force applied by the actuator to the *Load 4* part of the load clamp assembly started from almost 0 N and went down with negative values until the break of the specimens. Also, the displacement measured by the actuator started from almost 0 mm and went down with negative values until the break of the specimens.

However, for making the force - displacement charts more directly understandable the forces and the displacements have been represented in absolute value so, starting from 0 N or 0 mm and growing to positive values.

The forces that are shown in all the charts below are the forces recorded by the load cell of the actuator. That forces do not include the initial and constant contribute of the load clamp assembly weight: the load clamp assembly weights 4,87 kg so there is a constant force applied to the beam's load end of - 47,8 N. It is not possible to sum directly the 47,8 N force to the forces represented in the charts below because the centre of gravity of the load clamp assembly doesn't coincide with the force application point of the *Load 4* part of the load clamp assembly itself. However, it would be possible considering this force for example to validate a F.E.M. that replicates a test performed: in this case the idea is to apply to the beam not only the remote force applied in reality by the actuator of the MTS testing machine but to apply also the force due to the weight of the load clamp assembly in its centre of gravity position.

In the following image (Figure 3.2.3.1) it is possible to see the force - displacement chart of the tested PA12 curved beams.

"PA12 topology 2" and "PA12 topology 3" are the curved beams number 2 and number 3 with the structural inner support designed in Subchapter 2.5.7.

"PA12 Octahedral 1" and "PA12 Octet" are the curved beams with the variable density lattice inner support designed in subchapter 2.7.2.

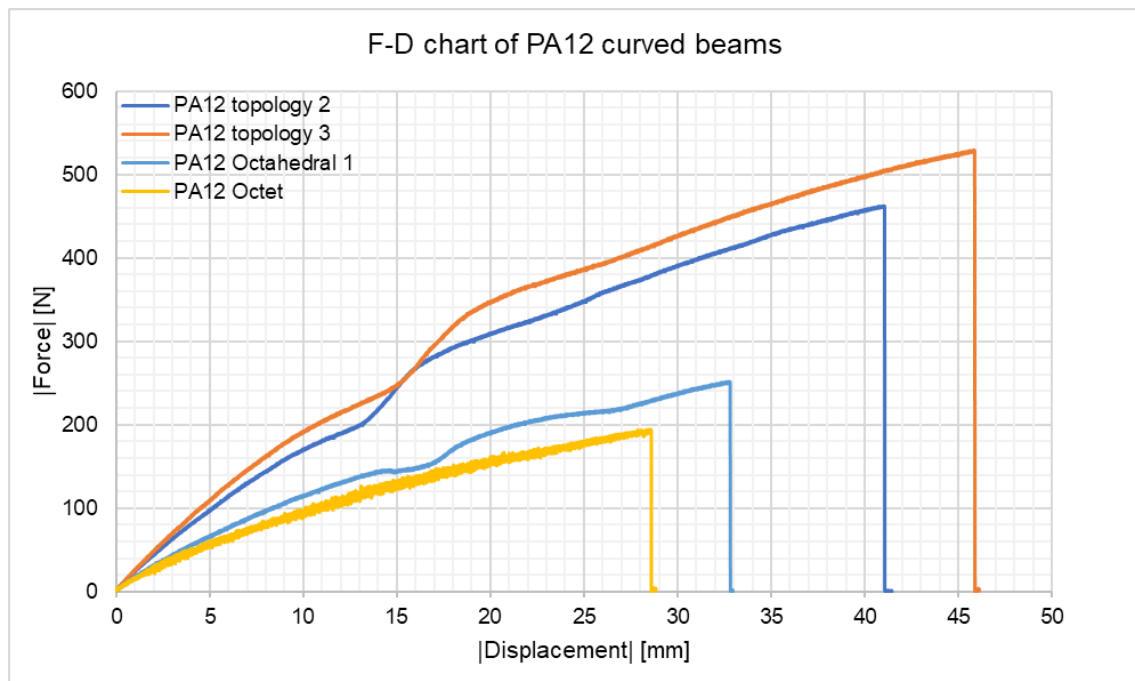


Figure 3.2.3.1: Force - displacement chart of the tested PA12 curved beams.

It is possible to see that the beams with the variable density lattice inner support are less stiff and the average required force to break them is 55 % lower than the average one required to break the beams with the structural inner support developed in Subchapter 2.5.7.

In the images below it is possible to see the broken PA12 curved beams (Figure 3.2.3.2, Figure 3.2.3.3, Figure 3.2.3.4) (the red lines indicate the end of the fix clamp):

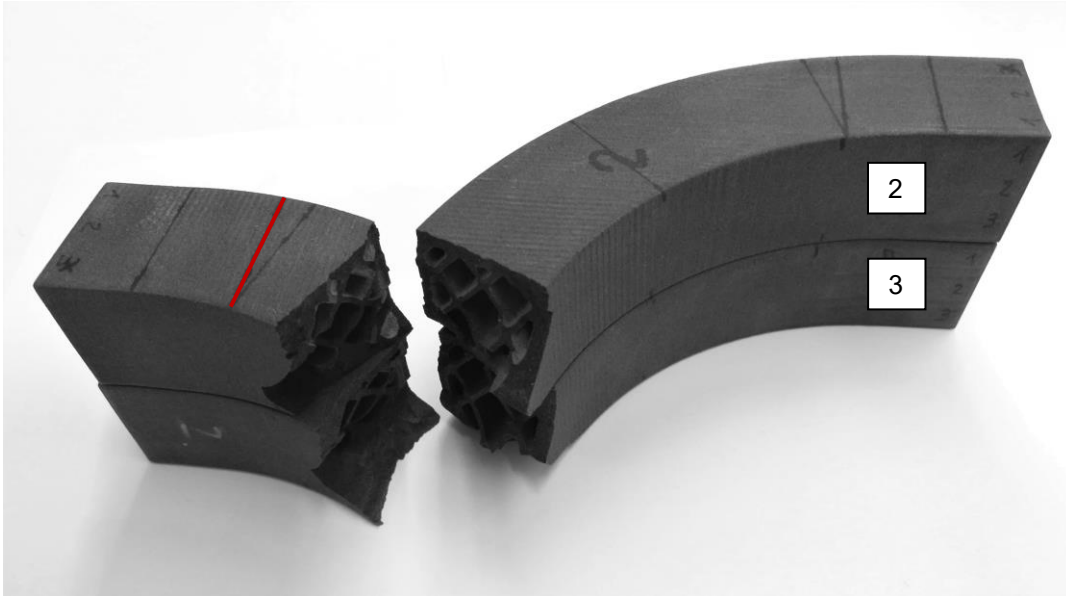


Figure 3.2.3.2: View of the broken number 2 and number 3 PA12 curved beams with the inner support structure developed in Subchapter 2.5.7. The beams broke not immediately after the fix clamp but in the boundary section between the inner support structure of the sector 1 of the beam and the inner support structure of the sector 2 of the beam (Subchapter 2.5.7).

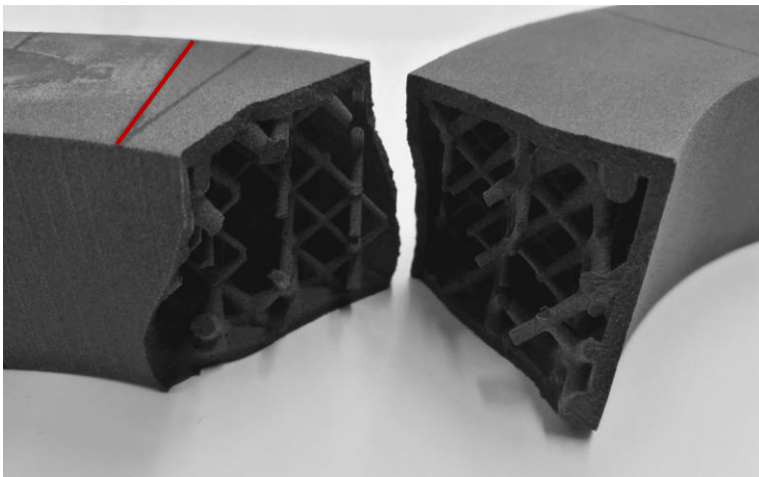


Figure 3.2.3.3: View of the broken PA12 curved beam with the *Octahedral 1* inner lattice support.

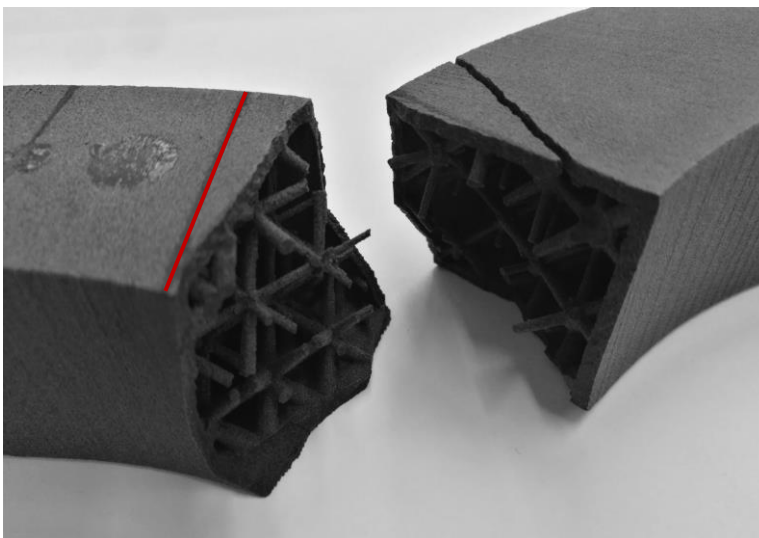


Figure 3.2.3.4: View of the broken PA12 curved beam with the *Octet* lattice inner support.

In the following image (Figure 3.2.3.5) it is possible to see the force - displacement chart of the PA12 curved beam number four with the structural inner support developed in Subchapter 2.5.7 and with the four notches.

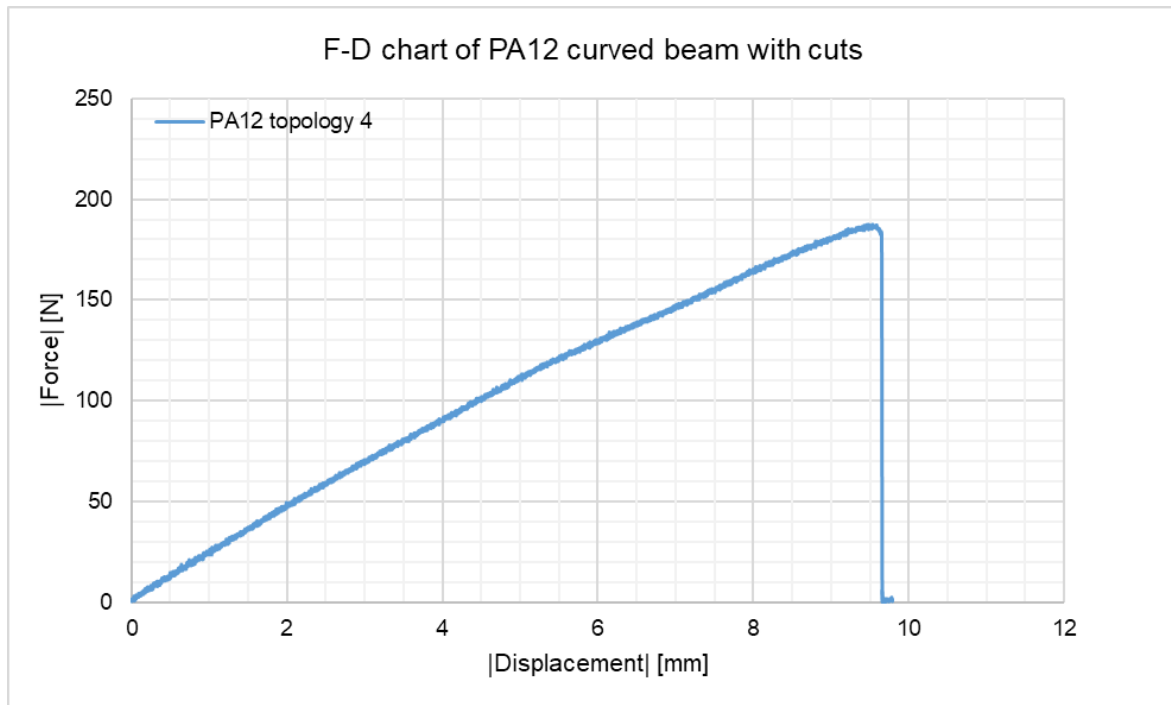


Figure 3.2.3.5: Force - displacement chart of the PA12 curved beam number four with the structural inner support developed in Subchapter 2.5.7 and with the four notches.

In the following image (Figure 3.2.3.6) it is possible to see the force - displacement chart of the Maraging steel curved beam number two with the structural inner support developed in Subchapter 2.5.7 and with the four notches.

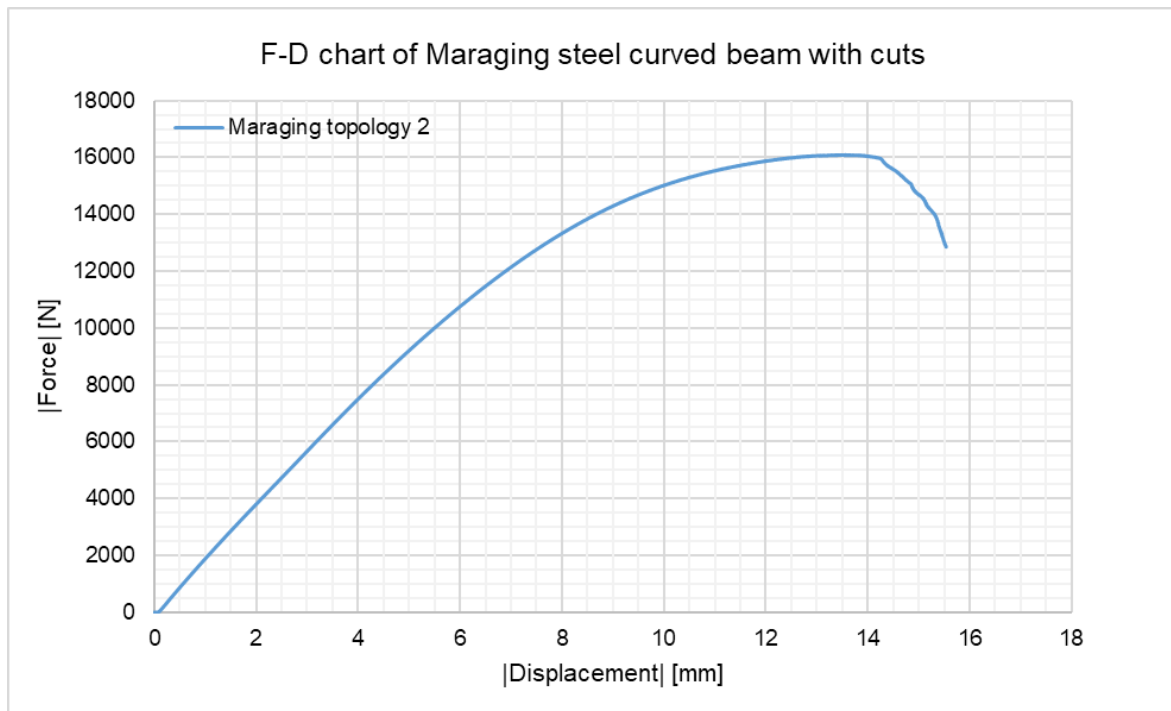


Figure 3.2.3.6: Force - displacement chart of the Maraging steel curved beam number two with the structural inner support developed in Subchapter 2.5.7 and with the four notches.

In the following image (Figure 3.2.3.7) it is possible to see the force - displacement chart of the Maraging steel curved beam number one with the structural inner support developed in Subchapter 2.5.7.

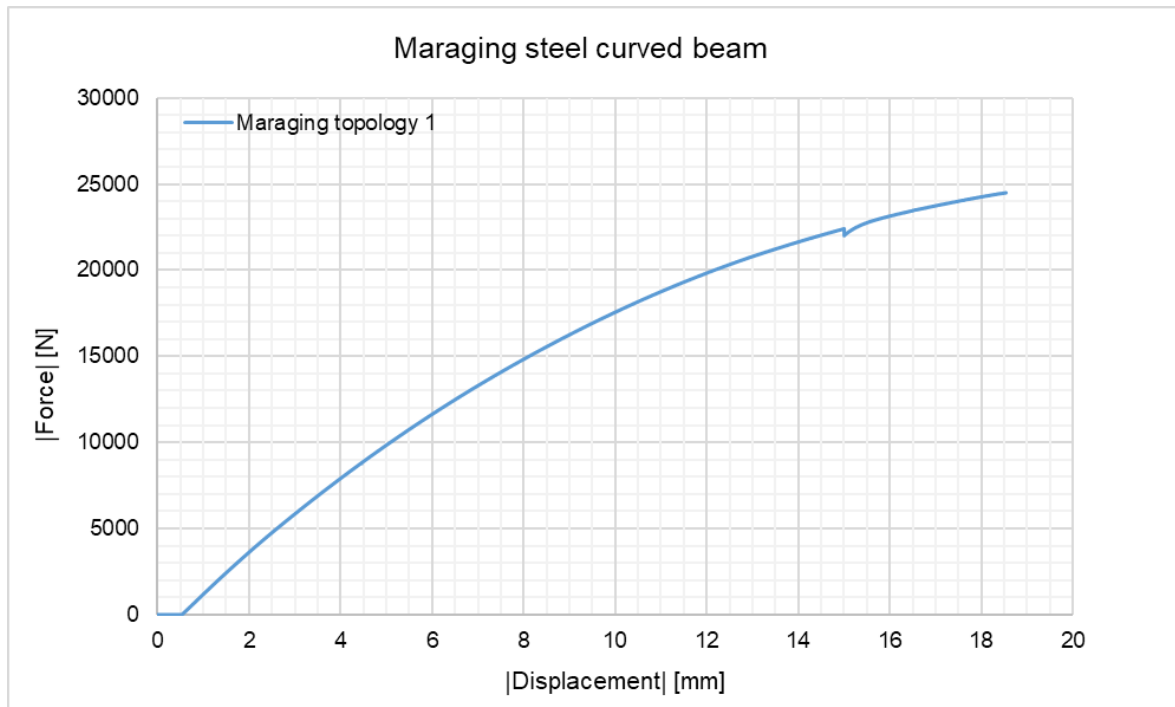


Figure 3.2.3.7: Force - displacement chart of the Maraging steel curved beam number one with the structural inner support developed in Subchapter 2.5.7.

The first static test of the Maraging steel curved beam (Figure 3.2.3.7) didn't perform as expected because with a load of 24 kN curved beam didn't break, it only yielded a little bit in the fix zone. It is also not possible to distinguish clearly an elastic regime in the chart; this has thought been because of the too low stiffness of the clamps with respect to the Maraging beam without the four notches. The second static test of the Maraging curved beam with the four notches (Figure 3.2.3.6) did perform better; the beam broke with a load of 16 kN and it is possible to recognize in the chart an elastic regime.

In the image below (Figure 3.2.3.8) it is possible to see the Maraging curved beams that have been used for the static tests. It is possible to see the notches milled from the edges also in the beam number one because after the first static test that didn't perform well, before testing a new specimen, has been try the notches configuration on the already tested beam number 1 to be sure that it would work.



Figure 3.2.3.8: Maraging steel curved beams, number 1 and number 2, broken after the static tests.

### 3.3 Fatigue tests

Have been done two fatigue tests of the Maraging steel curved beams and three fatigue tests of the PA12 curved beams for investigating their durability.

#### 3.3.1 Maraging steel specimens and PA12 specimens

##### Maraging steel specimens

Have been used the last two of the four Maraging steel curved beams with the structural inner support developed in Subchapter 2.5.7 available. Also, for the fatigue tests, due to the high loads, have been milled the four notches in the two beam specimens (Figure 3.2.1.2).

##### PA12 Specimens

Have been printed four PA12 curved beams with the structural inner support developed in Subchapter 2.5.7. Have been milled the four notches in the four beam specimens (Figure 3.2.1.6) with the aim of making a comparison between the fatigue behaviour of the PA12 beams and of the Maraging steel beams with the same geometry and the same load levels calculated as % of the break forces measured during the static tests.

Have been done three different tests with different load levels, the fourth beam has been printed because of an overshoot of the machine that happened during a test.

#### 3.3.2 Tests set-up description

The fatigue tests of the curved beams have been made with the same set-up of the static tests described in Subchapter 3.2.2. The only things that have been changed were of course the loads applied to the beams.

Has been decided to do the fatigue tests with a load ratio equal to 0,1 because with the set-up used the actuator of the 25 kN MTS machine could only press the load clamp assembly fixed to the beam. Has been decided to use a ratio equal to 0,1 and not a ratio equal to 0 because with a ratio equal to 0,1 the bearing ball would have been always in contact, during the tests, with both the actuator custom made tool and with the *Load 4* part of the load clamp assembly fixed to the beam.

Has been set the actuator of the machine in displacement control and for each test have been set a target maximum negative force, a target minimum negative force and a constant actuator moving speed. During a test the actuator started moving downwards until the load cell measured the maximum negative force, when the maximum negative force was reached the direction of the actuator changed and it started to moving upwards until the load cell measured the minimum negative force, when the minimum negative force was reached the actuator changed direction and started to moving downwards again. This repetition of actuator movements realized a triangle shape load wave that is possible to see in figure 3.3.2.1:

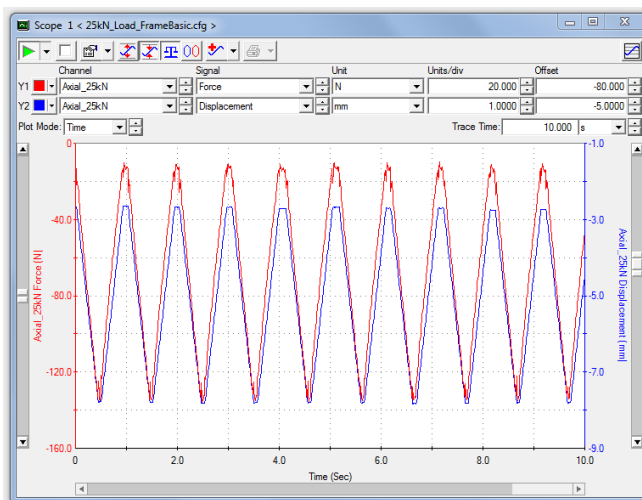


Figure 3.3.2.1: Triangle shape load wave (red) and the consequential triangle shape displacement wave (blue).

In the table below are summarized some parameters common to all the tests performed (Table 3.3.2.1):

Room's temperature range [°C]	23 - 27
Upper grip pressure [MPa]	15
Load cell values dispersion [N] at -0,5 kN (For PA12 specimens)	± 4,8
Load cell values dispersion [N] at -10 kN (For Maraging steel specimens)	± 31

Table 3.3.2.1: Fatigue tests common parameters.

### 3.3.3 Test results

The forces that have been applied during the fatigue cycles do not include the initial and constant contribute of the load clamp assembly weight: the load clamp assembly weights 4,87 kg so there is a constant force applied to the beam's load end of - 47,8 N. It is not possible to sum directly the 47,8 N force to the forces applied by the actuator because the centre of gravity of the load clamp assembly doesn't coincide with the force application point of the *Load 4* part of the load clamp assembly itself.

In the following tables (Table 3.3.3.1, Table 3.3.3.2, Table 3.3.3.3) are summarized the three tests of the three PA12 curved beams with the structural inner support developed in Subchapter 2.5.7 and with the four notches. Each test has been done with a different load level.

Specimen	PA12 topology 5
Maximum negative load [N] (50% of the break force equal to 190 N)	-95
Minimum negative load [N] (equal to 0,1*Maximum negative load)	-9,5
Force amplitude [N]	-42,8
Actuator speed [mm/s]	10
Number of cycles until break	195050

Table 3.3.3.1: Fatigue test of PA12 curved beam with 50% of break force applied.

Specimen	PA12 topology 8
Maximum negative load [N] (60% of the break force equal to 190 N)	-114
Minimum negative load [N] (equal to 0,1*Maximum negative load)	-11,4
Force amplitude [N]	-51,3
Actuator speed [mm/s]	10
Number of cycles until break	18958

Table 3.3.3.2: Fatigue test of PA12 curved beam with 60% of break force applied.

Specimen	PA12 topology 7
Maximum negative load [N] (70% of the break force equal to 190 N)	-133
Minimum negative load [N] (equal to 0,1*Maximum negative load)	-13,3
Force amplitude [N]	-59,9
Actuator speed [mm/s]	10
Number of cycles until break	804

Table 3.3.3.3: Fatigue test of PA12 curved beam with 70% of break force applied.



In the image below (Figure 3.3.3.1) it is possible to see a chart that shows the durability of the PA12 curved beams with the structural inner support developed in Subchapter 2.5.7 and with the four notches. In the vertical axis of the chart there are the force amplitudes that have been applied in the three different tests that have been performed. In the horizontal axis of the chart there are the number of cycles until the beams broke in the three tests that have been performed.

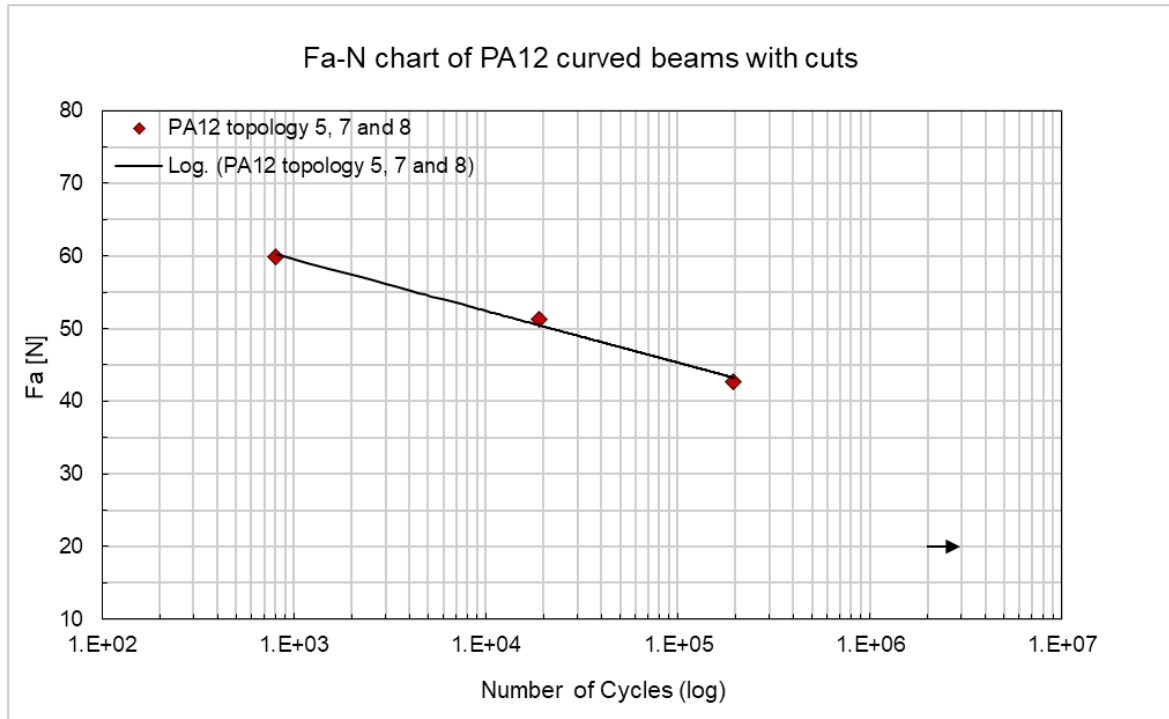


Figure 3.3.3.1: Fa-N chart of PA12 curved beams with the structural inner support developed in Subchapter 2.5.7 and with the four notches.

In the images below (Figure 3.3.3.2, Figure 3.3.3.3) it is possible to see the three PA12 broken curved beam specimens:

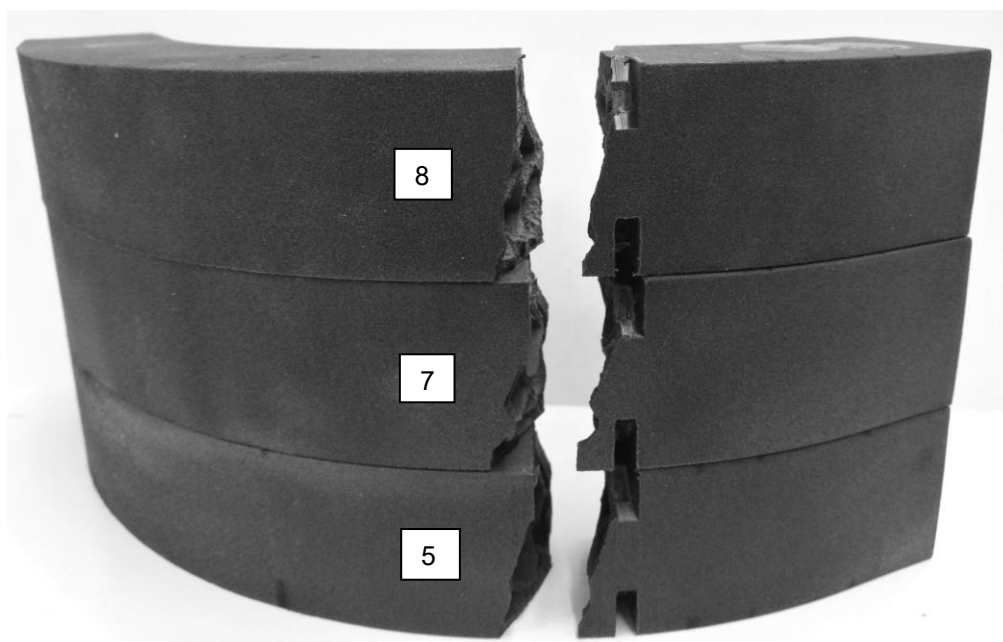


Figure 3.3.3.2: View of the PA12 broken curved beam specimens.

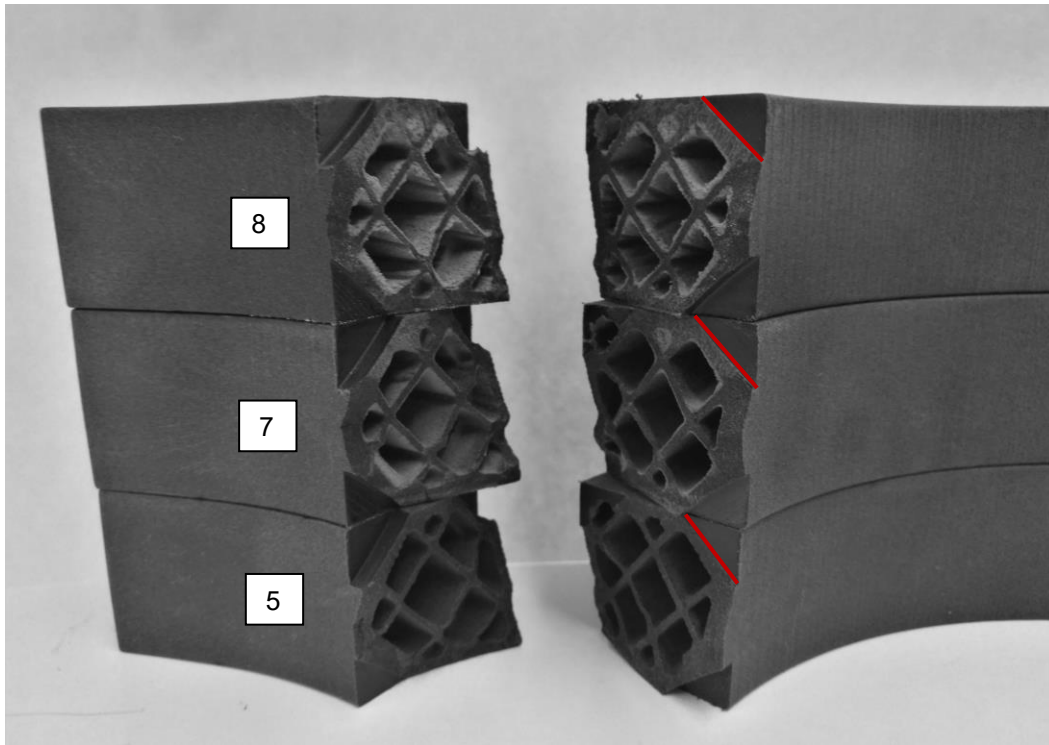


Figure 3.3.3.3: View of the PA12 broken curved beam specimens, with red lines are highlighted the edges of the notches from where the crack started forming and growing.

In the following tables (Table 3.3.3.4, Table 3.3.3.5) are summarized the two tests of the two Maraging steel curved beams with the structural inner support developed in Subchapter 2.5.7 and with the four notches. Each test has been done with a different load level.

Specimen	Maraging topology 3
Maximum negative load [N] (50% of the break force equal to 16000 N)	-8000
Minimum negative load [N] (equal to 0,1*Maximum negative load)	-800
Force amplitude [N]	-3600
Actuator speed [mm/s]	10
Number of cycles until break	3590

Table 3.3.3.4: Fatigue test of Maraging steel curved beam with 50% of break force applied.

Specimen	Maraging topology 4
Maximum negative load [N] (70% of the break force equal to 16000 N)	-11200
Minimum negative load [N] (equal to 0,1*Maximum negative load)	-1120
Force amplitude [N]	-5040
Actuator speed [mm/s]	10
Number of cycles until break	1593

Table 3.3.3.5: Fatigue test of Maraging steel curved beam with 70% of break force applied.

In the image below (Figure 3.3.3.4) it is possible to see a chart that shows the durability of the Maraging steel curved beams with the structural inner support developed in Subchapter 2.5.7 and with the four notches. In the vertical axis of the chart there are the force amplitudes that have been applied in the two different tests that have been performed. In the horizontal axis of the chart there are the number of cycles until the beams broke in the two tests that have been performed.

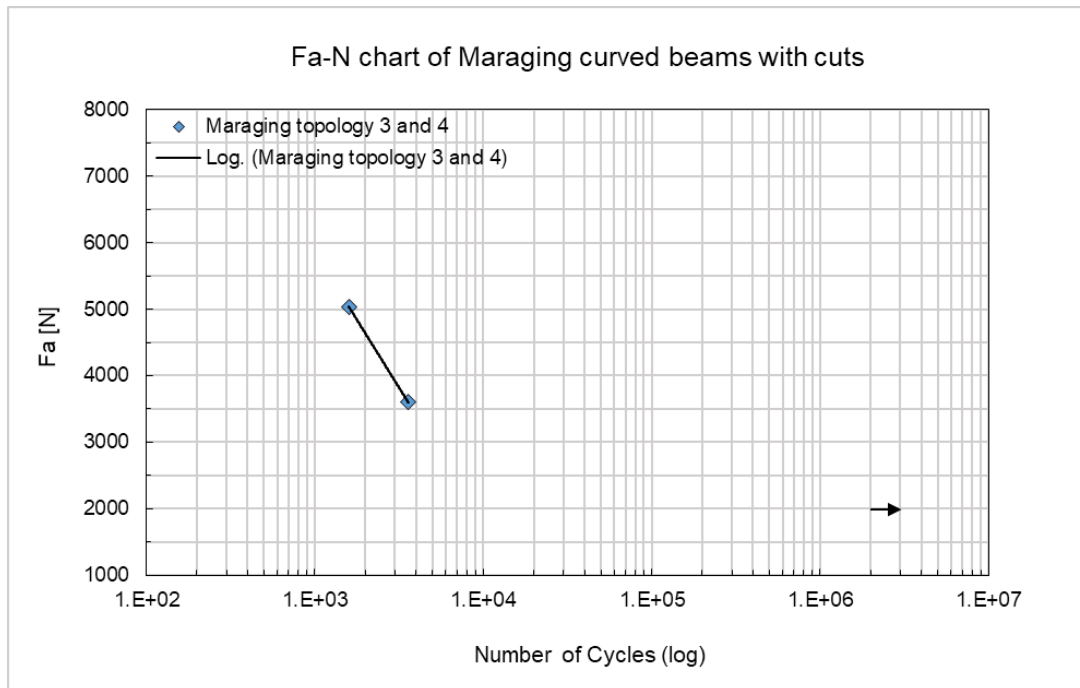


Figure 3.3.3.4: Fa-N chart of Maraging steel curved beams with the structural inner support developed in Subchapter 2.5.7 and with the four notches.

In the image below (Figure 3.3.3.5) it is possible to see all the Maraging steel curved beams that have been tested, also the number 3 and number 4 ones that have been used for the fatigue tests.

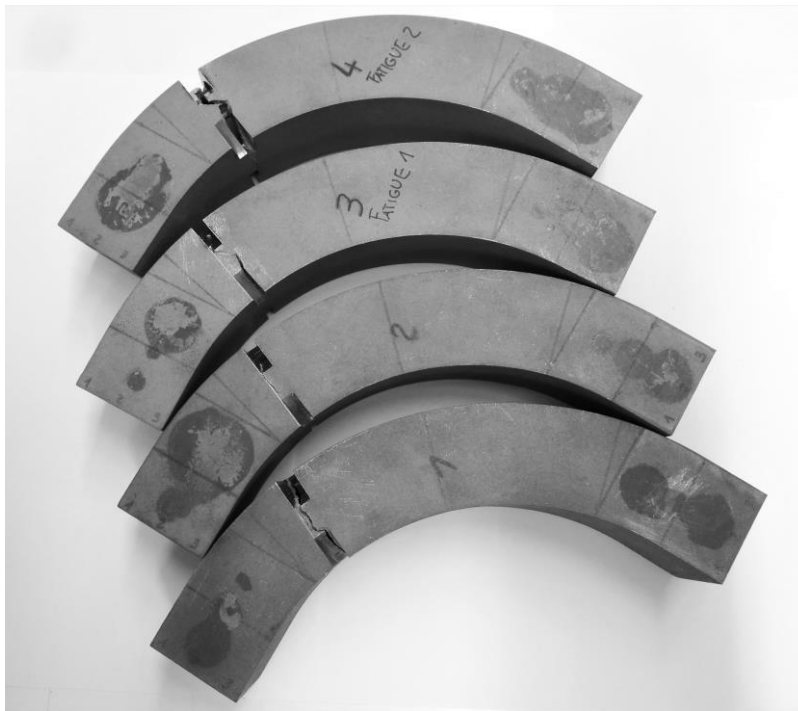


Figure 3.3.3.5: Broken Maraging steel curved beams with the structural inner support developed in Subchapter 2.5.7 and with the four notches.

# CHAPTER 4: Characterization of the PA12 material 3D printed with SLS technology

## 4.1 Specimens production

The PA12 specimens, used for characterizing the PA12 material, have been printed using a SLS “Lisa” by “Sinterit” 3D printer (Figure 4.1.1). The printer was in the Machine Design laboratory of the Faculty of Mechanical Engineering of Ljubljana’s University and it was the same one that has been used to print the PA12 curved beams tested in Chapter 3. The only difference between this printer and a standard SLS printer is that in the “Lisa” printer the laser head moves in X and Y directions (Z-axis is the layers building direction) instead of having a fix laser and a scanning mirrors mechanism, as showed in the standard SLS process description (Figure 1.2.1).



Figure 4.1.1: View of the SLS “Lisa” by “Sinterit” 3D printer.

From the little window highlighted with a red circle in Figure 4.1.1, it was possible to see the 3D printing process while the printer was working (Figure 4.1.2):



Figure 4.1.2: Partial view from the top of the printer of the XY-plane of the printing chamber while the printer was printing two PA12 curved beams with the Octahedral 1 lattice structural inner support (Subchapter 2.7.2). It is possible to distinguish the black powder of the sections of the beams cured by the laser and the surrounding not cured lighter powder. It is also possible to see three of the heater bulbs used for pre-heating the powders [25].

Has been used the “Sinterit Studio” software to prepare the G-code for printing the specimens. It is a very user-friendly and basic software that guides the user step by step in the printing process. The disadvantage of this software is that there are not so many changes that the user can do about the parameters of the print process.

In the image below (Figure 4.1.3) it is possible to see the first “Preset” section of the software. In this section it is possible to set [26]:

- The “Sinterit” *Printer Model*
- The used “Sinterit” *Powder Type*
- The desired *Layer Height [mm]*: The *Layer Height* can be increased or decreased with respect to a default suggested value set automatically by the software after the *Powder Type* has been selected. Increasing the *Layer Height*, it is possible to achieve greater print speed but with losing in accuracy. On the other hand, decreasing the *Layer height*, it is possible to achieve greater accuracy but with losing in print speed.
- The desired *Laser Power Ratio*: The laser power can be increased or decreased with respect to a default value set automatically by the software after the *Powder Type* has been selected. The default *Laser Power Ratio* is 1.0, by increasing it (for example setting it to 1.2) is possible to achieve greater durability of the printed objects but there is the possibility of losing in precision and in print speed. On the other hand, decreasing the *Laser Power Ratio* (for example setting it to 0.8) it is possible to achieve greater precision of the printed objects and higher print speed but there is the possibility of losing in durability.
- The desired *Print Surface Temperature Offset [°C]*: The print surface temperature can be slightly increased or decreased with respect to a default value set automatically by the software after the *Powder Type* has been selected.
- The *Shrink Ratio* in X, Y and Z axes: It is possible to slightly expand or contract the objects in a desired direction to make them have the right dimensions after the print has finished and the objects cooled down. The allowed *Shrink Ratio* range is from 0.9 to 1.1.

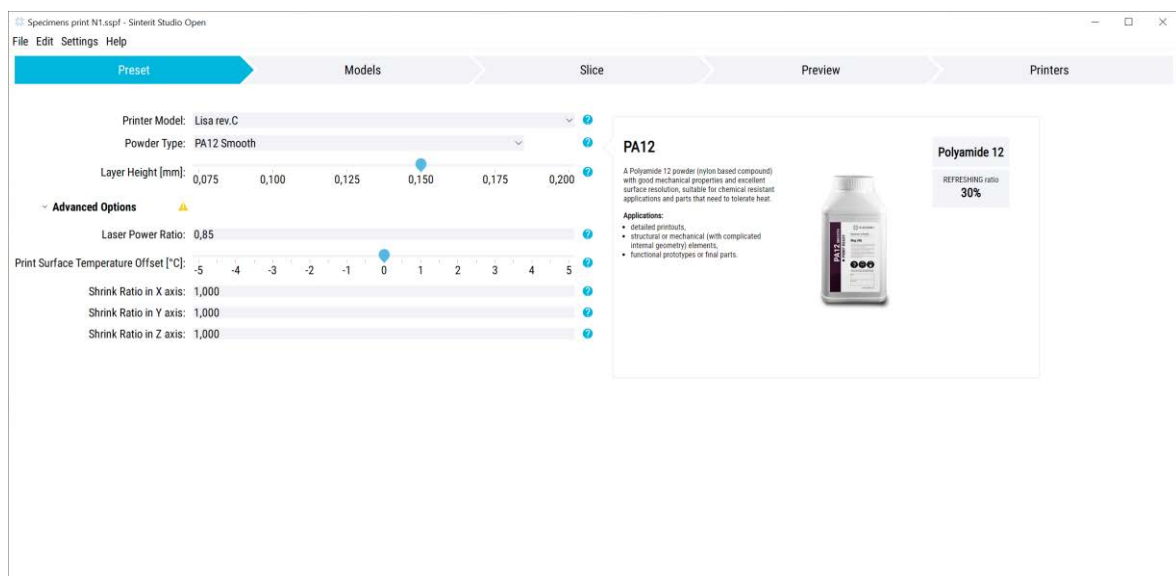


Figure 4.1.3: View of the first “Preset” section of the software with the settings that have been used to print the PA12 specimens used in this Chapter 4.

In the image below (Figure 4.1.4) it is possible to see the second “Models” section of the software. In this section it is possible to import the 3D CAD geometries of the object that are wanted to be printed and it is possible to arrange them in the print volume.

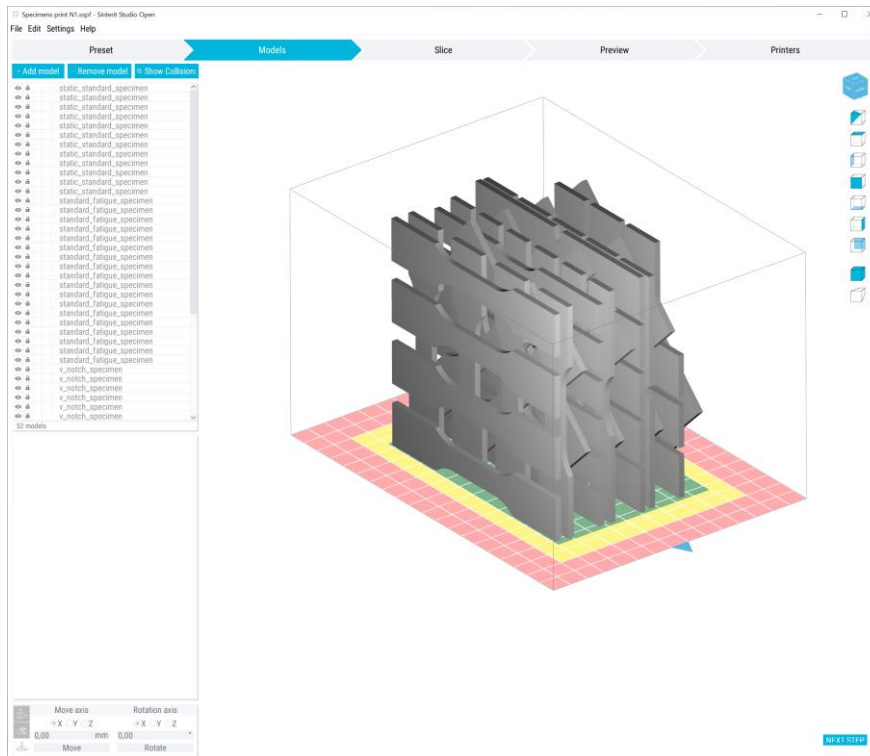


Figure 4.1.4: View of the second “Models” section of the software. It is possible to see the specimen 3D CAD models, used for the tensile and fatigue tests, arranged in the print volume with 0°, 45° and 90° directions. It is also possible to notice that the green surface of the print volume base represents the surface 90 x 130 mm of the maximum accuracy space for printing the PA12 material. The entire maximum accuracy volume is 90 x 130 x 130 mm [26].

In the third “Slice” section of the software it is possible to slice into layers the previously imported 3D objects and saving the file for printing [26].

In the fourth “Preview” section of the software it is possible to view the layers of the previously sliced 3D objects [26].

In the last “Printers” section of the software it is possible to see the state of the printers connected by Wi-Fi [26].

After the specimens have been removed from the print bed when the prints were finished and the print chamber cooled down, has been used a “Sinterit” sandblaster machine (Figure 4.1.5) to sandblast all the specimens for removing the unfused powder weakly attached to the specimen’s surfaces.



Figure 4.1.5: View of the “Sinterit” sandblaster.



## 4.2 Tensile tests of plain specimens

In this subchapter have been presented the tensile tests of the PA12 plain specimens that have been performed. The specimens have been printed with the SLS technology as explained in the previous Subchapter 4.1.

### 4.2.1 Specimens dimensions

The detailed dimensions of the specimens that have been used for tensile tests are shown in the image below (Figure 4.2.1.1). The specimen geometry is an adjustment of the *Type I* standard specimen of the ASTM D638-14. The main changes have been done in the lengths of the specimen's clamp zones because the overall specimen length was limited to 120 mm to be able of printing the specimens with the University's SLS printer: "Lisa" by "Sinterit".

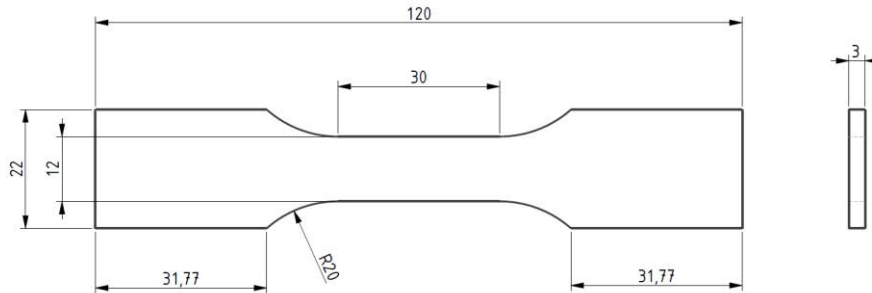


Figure 4.2.1.1: 2D technical drawing of the plain specimens that have been used for the tensile tests.

After the specimens have been printed, have been performed the measurements, with a calliper, of the width and thickness of the central part (30 mm long in Figure 4.2.1.1) of every specimen. Has been considered for the calculation of the stresses the minimum cross sectional area that have been found along the central part, for every individual specimen. The width and thickness and the relative minimum cross sectional area have been reported, for every specimen, in the table below (Table 4.2.1.1):

Specimen's name	Width [mm]	Thickness [mm]	Area [mm <sup>2</sup> ]
0TPA12_1	11,85	2,99	35,43
0TPA12_2	11,93	3,03	36,15
0TPA12_3	11,82	2,99	35,34
0TPA12_4	11,93	3,02	36,03
0TPA12_5	11,96	3,05	36,48
0TPA12_6	11,78	2,92	34,40
45TPA12_1	11,98	3,05	36,54
45TPA12_2	12,00	3,10	37,20
45TPA12_3	12,00	3,10	37,20
45TPA12_4	11,98	3,10	37,14
45TPA12_5	11,90	3,03	36,06
90TPA12_1	12,01	3,02	36,27
90TPA12_2	12,04	3,02	36,36
90TPA12_3	12,02	3,05	36,66
90TPA12_4	12,03	2,99	35,97
90TPA12_5	11,90	3,02	35,94
90TFPA12_1	11,95	3,14	37,52
90TFPA12_2	11,93	3,12	37,22
90TFPA12_3	12,03	3,14	37,77
90TFPA12_4	12,05	3,14	37,84

Table 4.2.1.1: Measures of all the PA12 specimens that have been used for the static tests.

## 4.2.2 Tests set-up description

Have been tested five specimens for each of the three printing orientations:  $0^\circ$ ,  $45^\circ$ ,  $90^\circ$  (Figure 4.2.2.1).

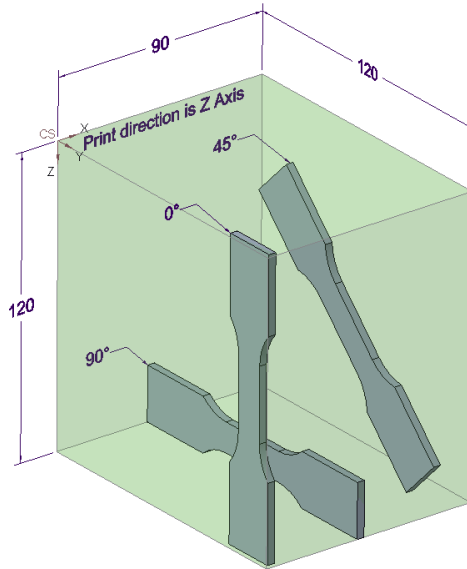


Figure 4.2.2.1: Specimens  $0^\circ$ ,  $45^\circ$ ,  $90^\circ$  print orientations with respect to the Z-axis print direction.

Has been used the MTS 25 kN machine (model 370.02, Figure 3.1.1) of the Machine Design laboratory of the Faculty of Mechanical Engineering of Ljubljana's University.

Has been used an MTS mechanical extensometer (Figure 4.2.2.2) to measure the longitudinal strain [%], has been also used a video extensometer (Figure 4.2.2.3) mounted on a tripod to measure the longitudinal strain [%] and the transversal strain [%] to be able to calculate also the Poisson's ratio of the PA12 material.



Figure 4.2.2.2: Mechanical extensometer fixed to the specimen.

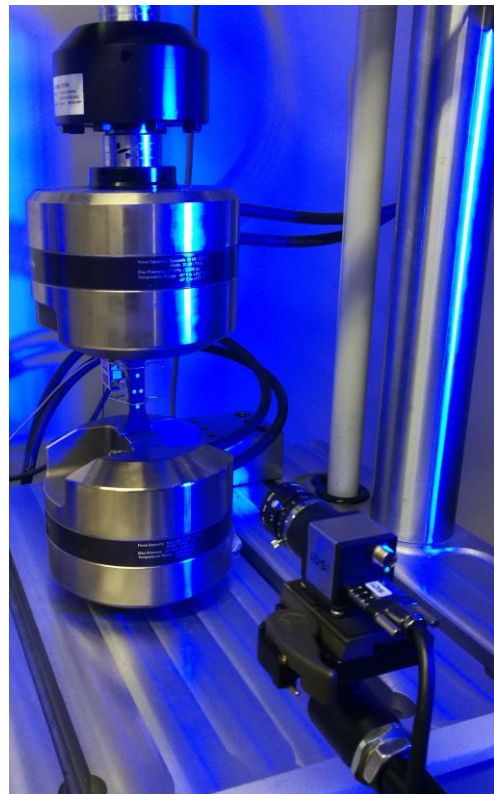


Figure 4.2.2.3: Video extensometer.

The video extensimeter has been connected to the computer via USB 2.0 and not via USB 3.0, this slow connection caused an initial delay and more noise in capturing strain data as it is possible to see in Annex E, where all the Stress-Strain charts for every single specimen tested have been presented. Despite the noise, it is possible to see that ideally deleting the initial delay and translating down the video extensometer curves, they match the mechanical extensometer ones. However, for the longitudinal strain results have been taken into account the mechanical extensometer data and for calculating the Poisson's ratios have been used the ratios between the transversal strains measured by the video extensometer and the longitudinal strains measured by the mechanical extensometer. A filter has also been applied to avoid in the Poisson's ratios average calculation values below 0,3 (It is not physically correct that the Poisson's ratio of a polyamide is equal or lower with respect to the Poisson's ratio of a steel) and values greater than 0,5 (It is not physically correct that the Poisson's ratio of a polyamide is equal or greater with respect to the Poisson's ratio of a rubber material).

In the table below have been summarized some parameters common for all the tensile tests performed (Table 4.2.2.1):

Room's temperature range [°C]	24 - 27
Grips pressure [MPa]	10
Speed [mm/min]	5
Load cell values dispersion average [N] from 0,5 kN to 1,5 kN	± 13,3

Table 4.2.2.1: Common parameters for all the tensile tests performed.

### 4.2.3 Tests results

In the table below (Table 4.2.3.1) have been summarized the results of the tensile tests performed. The names of the specimens are designed as follow:

- The first number specifies the print orientation: 0° or 45° or 90° (Figure 4.2.2.1).
- "T" specifies that it is a tensile test specimen.
- "PA12" specifies the material of the specimen.
- The last number after the underscore specifies the specimen's number.

About the 0° specimens' number 3, 4, 5 an unknown problem occurred: the MTS software didn't save the extensometer data. However, has been decided to use the break force registered by the actuator load cell and has been decided to perform another test (specimen number 6) to have at least three complete data set for the 0° specimens.

Specimen's name	Break Force [N]	Break Stress [MPa]	Break Strain [%]	$\sigma_{P0,2}$ [MPa]	Poisson's ratio [I]	Young's modulus [MPa]	Room temperature [°C]
0TPA12_1	915	26	2,72	19,5	0,39	1230	24,6
0TPA12_2	966	27	2,64	20,8	0,42	1280	24,6
0TPA12_3	989	28	NA	NA	NA	NA	24,6
0TPA12_4	927	26	NA	NA	NA	NA	24,6
0TPA12_5	948	26	NA	NA	NA	NA	24,6
0TPA12_6	823	24	2,45	20,0	0,43	1199	25,8
<b>Average</b>	<b>928</b>	<b>26</b>	<b>2,60</b>	<b>20</b>	<b>0,41</b>	<b>1236</b>	
<b>Standard Deviation</b>	57,90	1,33	0,14	0,66	0,02	40,87	
45TPA12_1	1156	32	4,87	20,3	0,42	1225	25,1
45TPA12_2	1197	32	5,14	20,1	0,42	1235	25,1
45TPA12_3	1125	30	4,15	20,5	0,33	1286	25,1
45TPA12_4	1206	32	5,32	19,9	0,49	1228	25,1

45TPA12_5	1093	30	4,28	20,6	0,42	1249	25,1
<b>Average</b>	<b>1155</b>	<b>31</b>	<b>4,75</b>	<b>20</b>	<b>0,42</b>	<b>1245</b>	
<b>Standard Deviation</b>	47,72	1,04	0,52	0,30	0,06	24,93	
90TPA12_1	1331	37	7,07	20,3	0,45	1176	26,8
90TPA12_2	1373	38	9,02	19,8	0,41	1100	26,8
90TPA12_3	1383	38	8,27	21,0	0,47	1202	26,8
90TPA12_4	1307	36	6,88	21,4	0,36	1225	26,8
90TPA12_5	1295	36	7,60	20,8	0,38	1096	26,8
<b>Average</b>	<b>1338</b>	<b>37</b>	<b>7.77</b>	<b>21</b>	<b>0,41</b>	<b>1160</b>	
<b>Standard Deviation</b>	39,08	0,79	0,88	0,62	0,05	59,04	
<b>TOT Average</b>	<b>1127</b>	<b>31</b>	<b>5,42</b>	<b>20</b>	<b>0,41</b>	<b>1210</b>	
<b>TOT Standard Dev.</b>	181,81	4,75	2,20	0,54	0,04	58,05	

Table 4.2.3.1: Tensile tests results of the PA12 specimens.

It is possible to see, from Table 4.2.3.1, that the average break stress of the 45° oriented specimens is 16% greater than the one of the 0° oriented specimens and that the average break stress of the 90° oriented specimens is 16.2% greater than the one of the 45° oriented specimens.

It is also possible to see that the average break strain of the 45° oriented specimens is 45.3% greater than the one of the 0° oriented specimens and that the average break strain of the 90° oriented specimens is 38.9% greater than the one of the 45° oriented specimens.

It is also possible to see that the average Young's Modulus of the 0° oriented specimens is almost equal to the one of the 45° oriented specimens and that the average Young's Modulus for the 90° oriented specimens is 6.8% lower than the one of the 45° oriented specimens.

In the following image (Figure 4.2.3.1) it is possible to see the Stress - Strain curves of the 0° PA12 specimens.

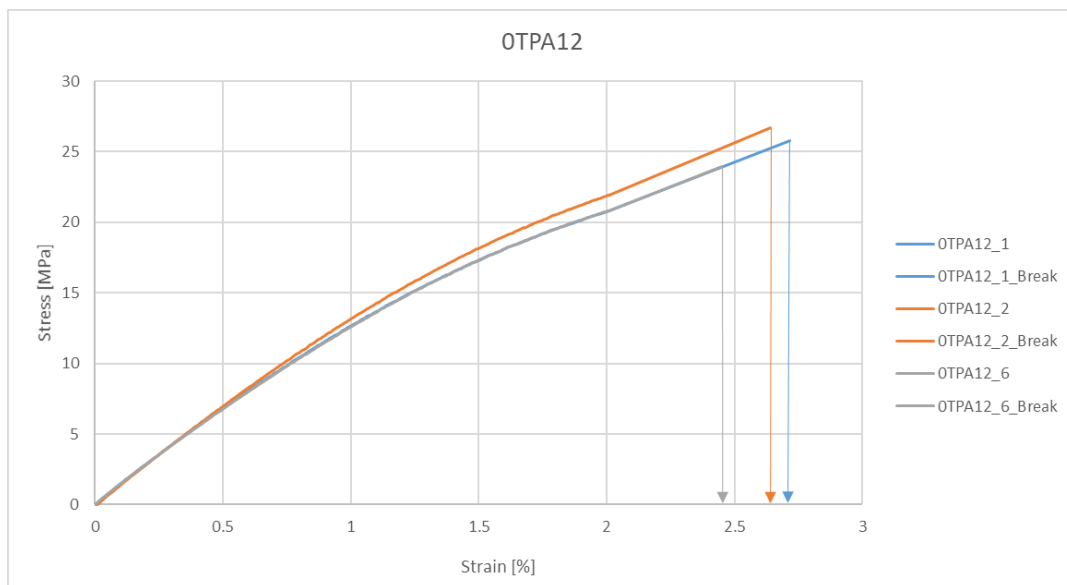


Figure 4.2.3.1: 0° PA12 specimens Stress - Strain curves.

To avoid possible mechanical extensometer damages has been decided to remove it when the specimens reached a strain value of 2%, before the specimens broke.

However, the break force has been registered by the actuator load cell so has been possible to continue the Stress - Strain curve with a straight line from the 2% strain to the calculated break strain. To calculate the straight line equation for each specimen, has been performed a linear regression of the stress and strain data from 1,5% to 2% of strain.

In the following image (Figure 4.2.3.2) it is possible to see the broken 0° PA12 specimens:

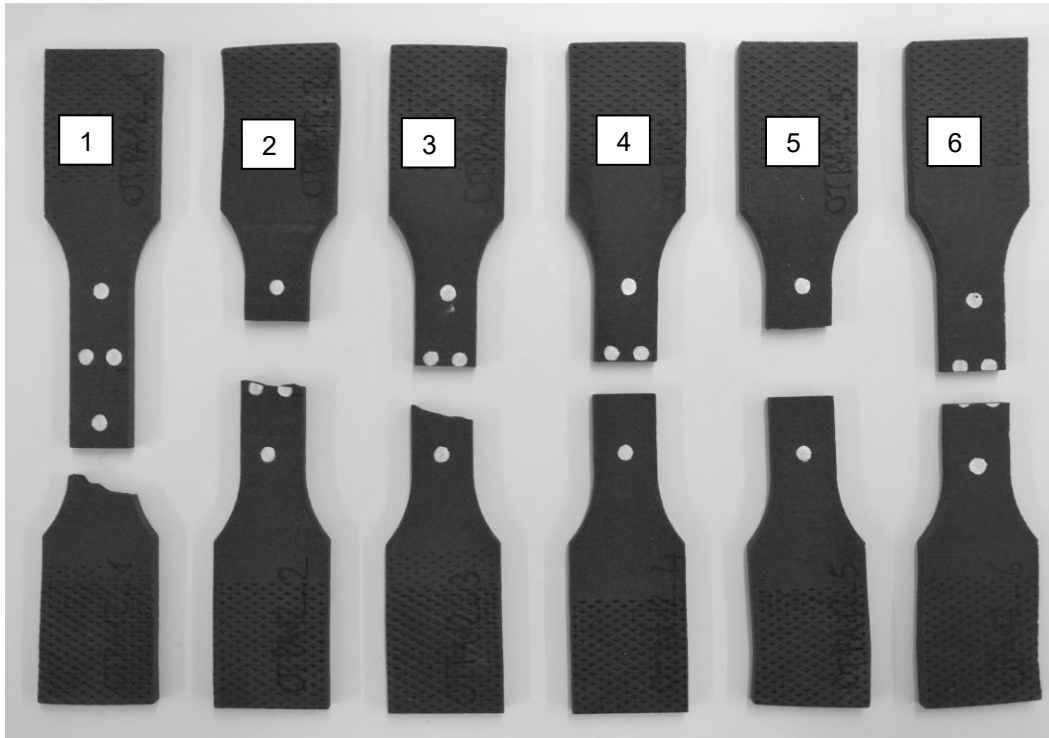


Figure 4.2.3.2: Broken 0° PA12 specimens.

In the following image (Figure 4.2.3.3) it is possible to see the Stress - Strain curves of the 45° PA12 specimens.

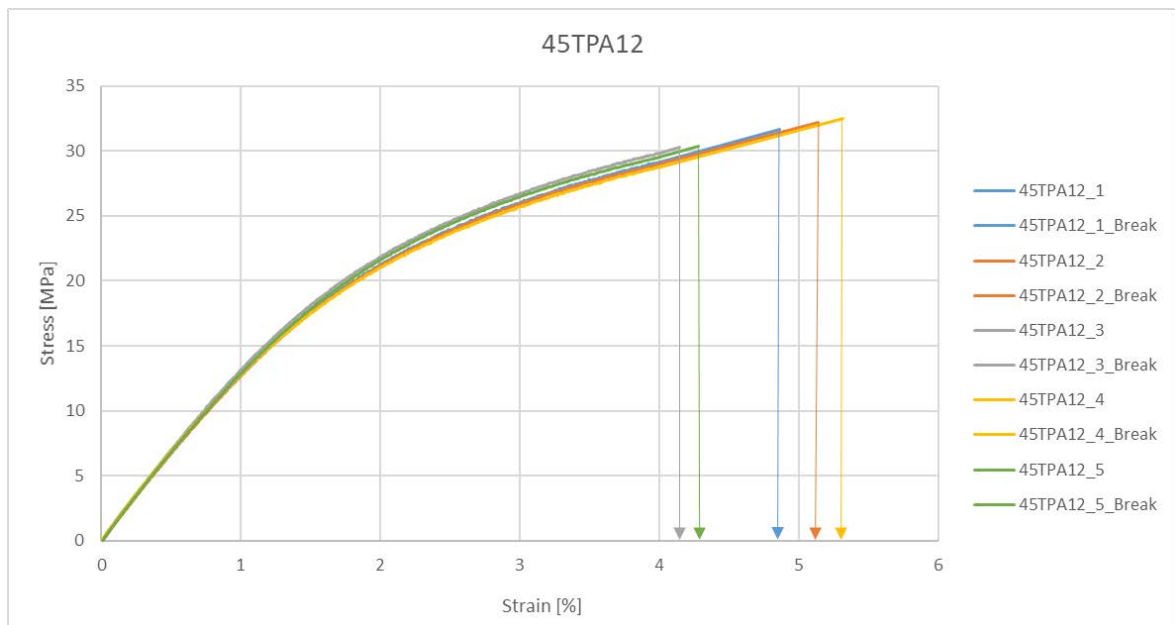


Figure 4.2.3.3: 45° PA12 specimens Stress - Strain curves.

To avoid possible mechanical extensometer damages has been decided to remove it when the specimens reached a strain value of 4%, before the specimens broke.

However, the break force has been registered by the actuator load cell so has been possible to continue the Stress - Strain curve with a straight line from the 4% strain to the calculated break strain. To calculate the straight line equation for each specimen, has been performed a linear regression of the stress and strain data from 3,5% to 4% of strain.

In the following image (Figure 4.2.3.4) it is possible to see the broken 45° PA12 specimens:

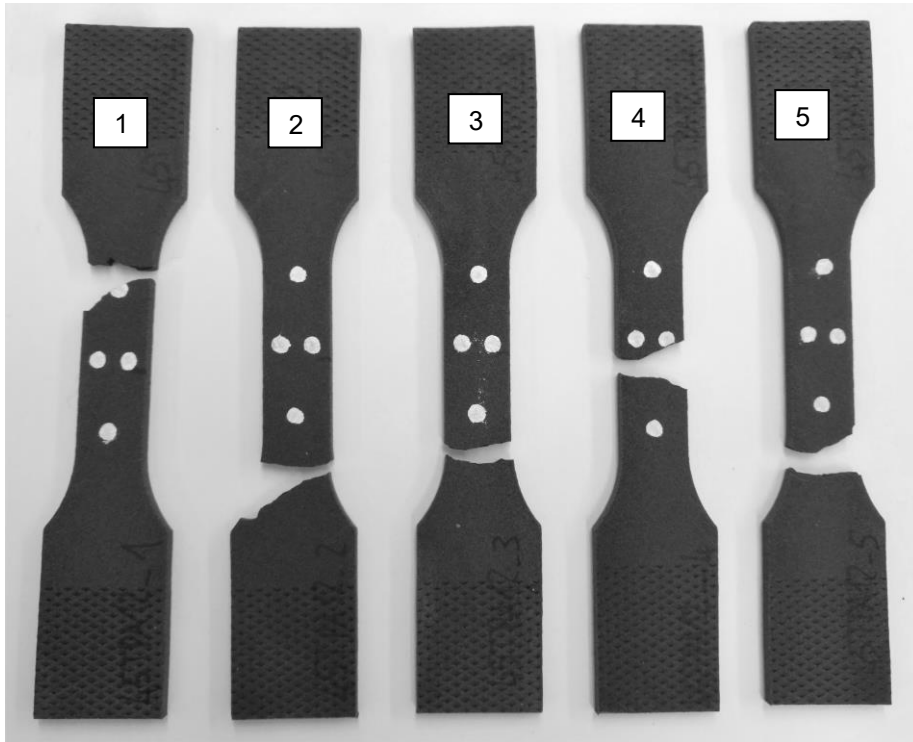


Figure 4.2.3.4: Broken 45° PA12 specimens.

In the following image (Figure 4.2.3.5) it is possible to see the Stress - Strain curves of the 90° PA12 specimens.

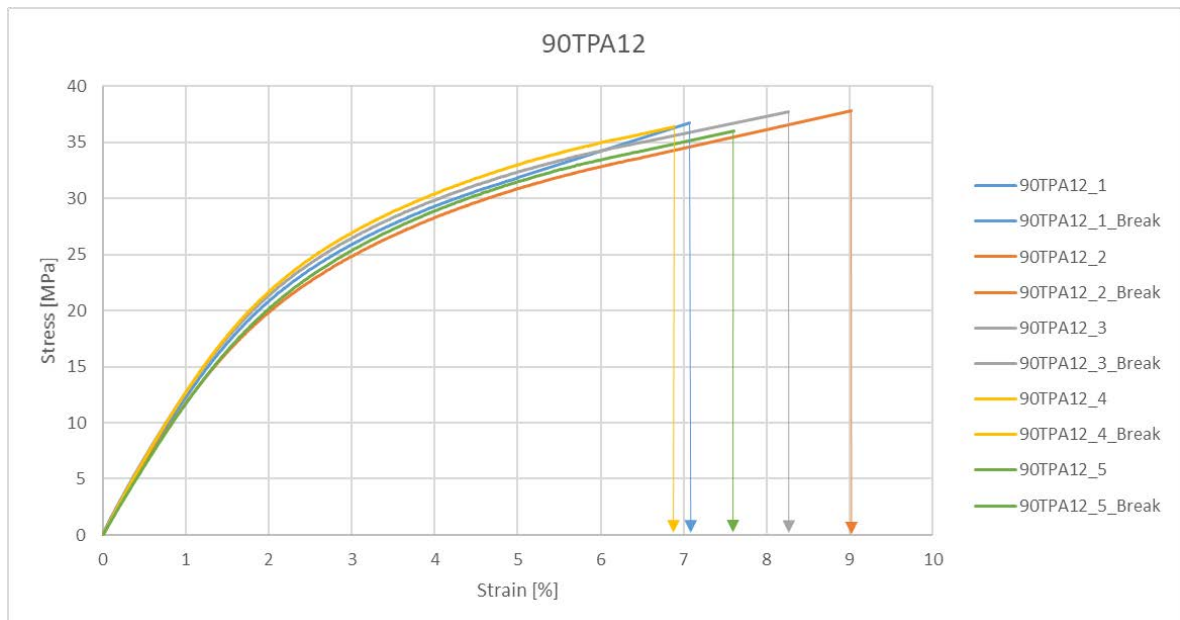


Figure 4.2.3.5: 90° PA12 specimens Stress - Strain curves.

To avoid possible mechanical extensometer damages has been decided to remove it when the specimens reached a strain value of 6,5%, before the specimens broke.

However, the break force has been registered by the actuator load cell so has been possible to continue the Stress - Strain curve with a straight line from the 6,5% strain to the calculated break strain. To calculate the straight line equation for each specimen, has been performed a linear regression of the stress and strain data from 6% to 6,5% of strain.



In the following image (Figure 4.2.3.6) it is possible to see the broken 90° PA12 specimens:

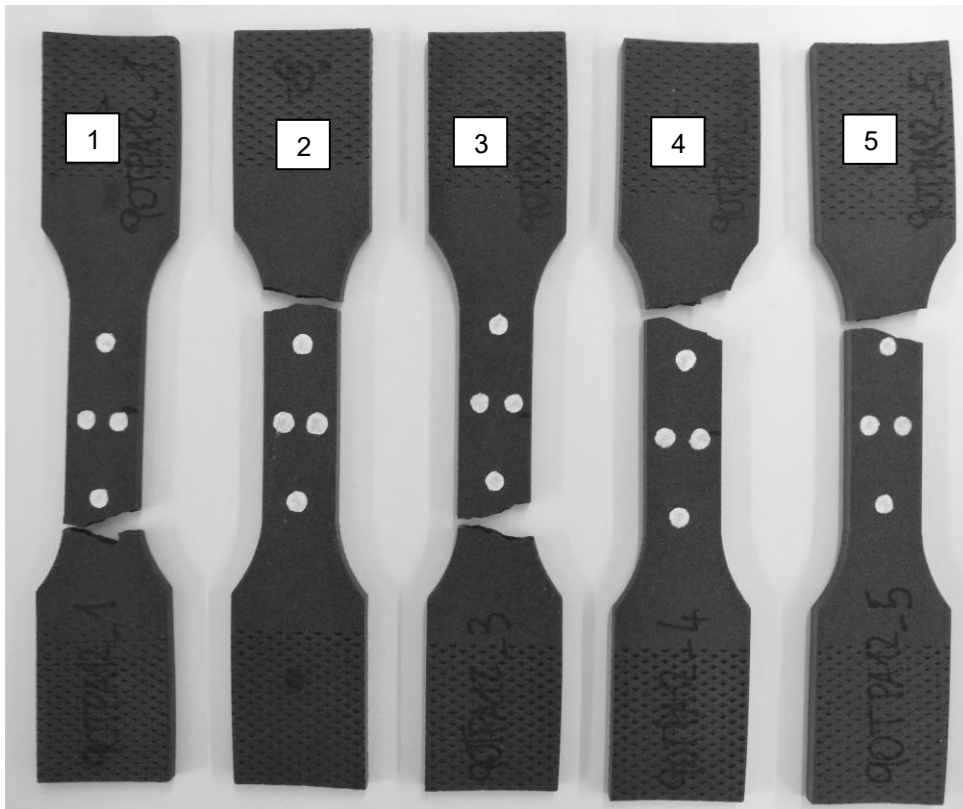


Figure 4.2.3.6: Broken 90° PA12 specimens.

In the image below (Figure 4.2.3.7) it is possible to see the Stress - Strain curves of the PA12 specimens all together to have a complete overview:

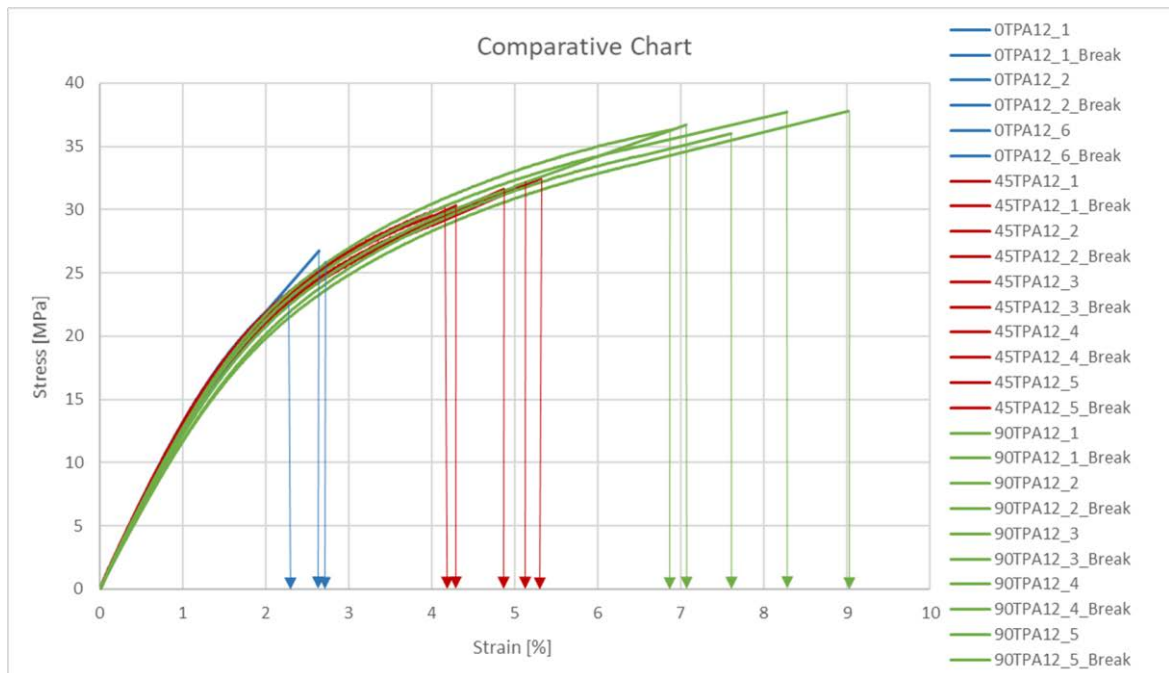


Figure 4.2.3.7: 0°, 45°, 90° PA12 specimens Stress - Strain curves.

It is interesting to see that the PA12 material is almost isotropic with respect to the print orientation in the elastic regime, but it is anisotropic with respect to the print orientation in the plastic regime: the break stress and the break strain change with respect to the print direction.

Has been decided to perform four more tensile tests of four more specimens printed with the 90° orientation but with the bigger surfaces of the specimen's geometry flat with respect to the building chamber XY-plane (Figure 4.2.3.8):

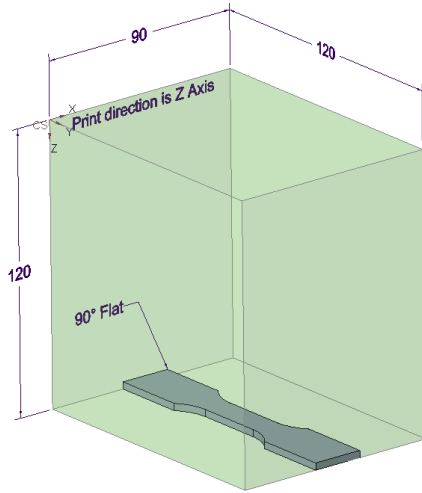


Figure 4.2.3.8: Specimen 90° Flat print orientation with respect to the Z-axis print direction.

In the table below (Table 4.2.3.2) have been summarized the results of the tensile tests performed:

Specimen's name	Break Force [N]	Break Stress [MPa]	Break Strain [%]	$\sigma_{P0,2}$ [MPa]	Poisson's ratio [/]	Young's modulus [MPa]	Room temperature [°C]
90FTPA12_1	1290	34	6,12	21,6	0,43	1502	23,2
90FTPA12_2	1247	34	5,78	20,8	0,40	1437	23,8
90FTPA12_3	1323	35	7,74	21,0	0,47	1272	23,8
90FTPA12_4	1336	35	7,41	20,9	0,41	1359	23,8
<b>Average</b>	<b>1299</b>	<b>35</b>	<b>6,76</b>	<b>21</b>	<b>0,43</b>	<b>1393</b>	
<b>Standard Deviation</b>	39,71	0,80	0,96	0,36	0,03	99,35	

Table 4.2.3.2: Tensile tests results of the PA12 specimens with the new 90° Flat orientation.

In the following image (Figure 4.2.3.9) it is possible to see the Stress - Strain curves of the 90° Flat PA12 specimens.

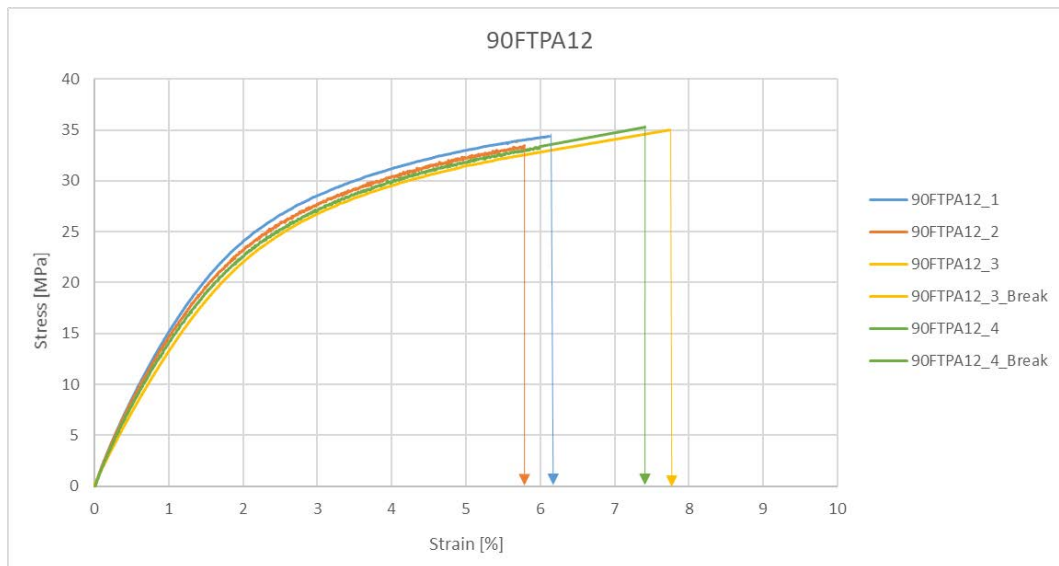


Figure 4.3.2.9: 90° Flat PA12 specimens Stress - Strain curves.

To avoid possible mechanical extensometer damages has been decided to remove it when the specimens reached a strain value of 6 %, before the specimens broke.

However, the break force has been registered by the actuator load cell so has been possible to continue the Stress - Strain curve with a straight line from the 6% strain to the calculated break strain. To calculate the straight line equation for each specimen, has been performed a linear regression of the stress and strain data from 5 % to 6 % of strain.

The specimen number 1 and the specimen number 2 broke before the mechanical extensometer could be removed.

In the following image (Figure 4.2.3.10) it is possible to see the broken 90° Flat PA12 specimens:

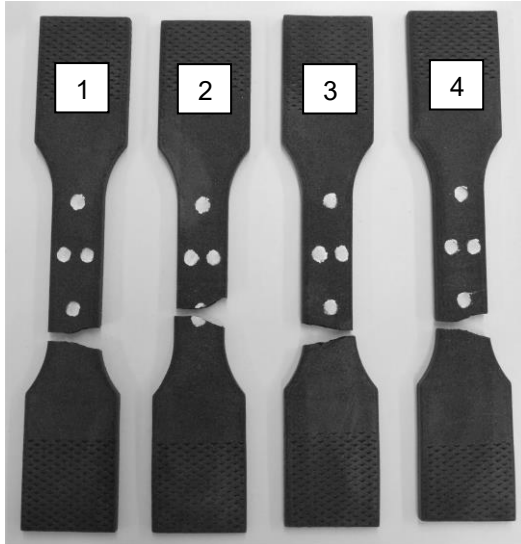


Figure 4.2.3.10: Broken 90° Flat PA12 specimens.

In the image below (Figure 4.2.3.11) it is possible to see the Stress - Strain curves of the PA12 specimens all together, with also the 90° Flat, to have a complete overview:

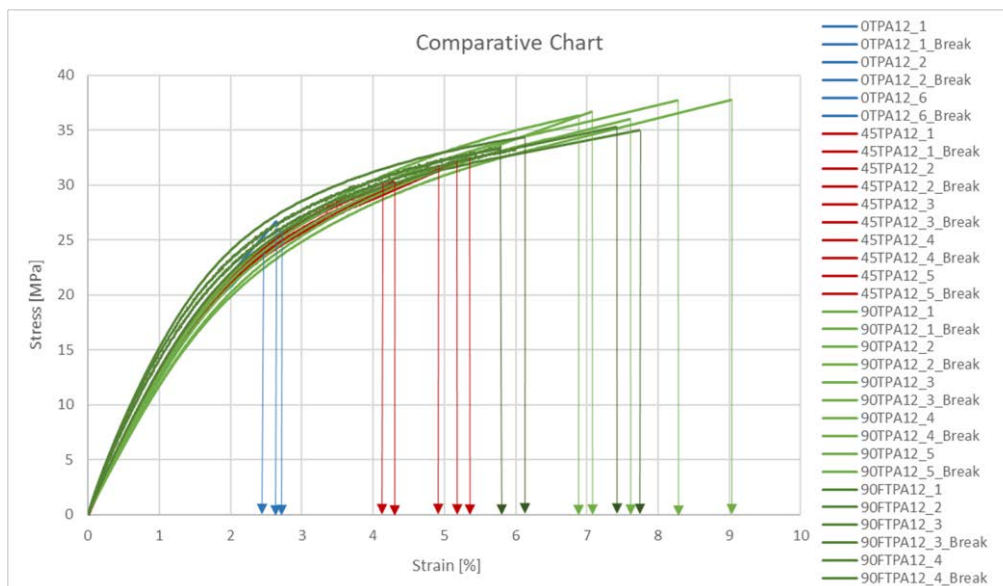


Figure 4.2.3.11: 0°, 45°, 90° and 90° Flat PA12 specimens Stress - Strain curves.

It is interesting to see that the PA12 material printed with the 90° Flat orientation has slightly different mechanical properties, also in the elastic regime, with respect to the other three orientations investigated before. In particular the average Young's Modulus of the 90° Flat oriented specimens is 13% greater than the average Young's Modulus of the 0°, 45° and 90° oriented specimens.

### 4.3 Fatigue tests of plain specimens

In this subchapter have been presented the fatigue tests of the PA12 plain specimens that have been performed. The specimens have been printed with the SLS technology as explained in the Subchapter 4.1.

#### 4.3.1 Specimens dimensions

The detailed dimensions of the plain specimens that have been used for fatigue tests are shown in the image below (Figure 4.3.1.1):

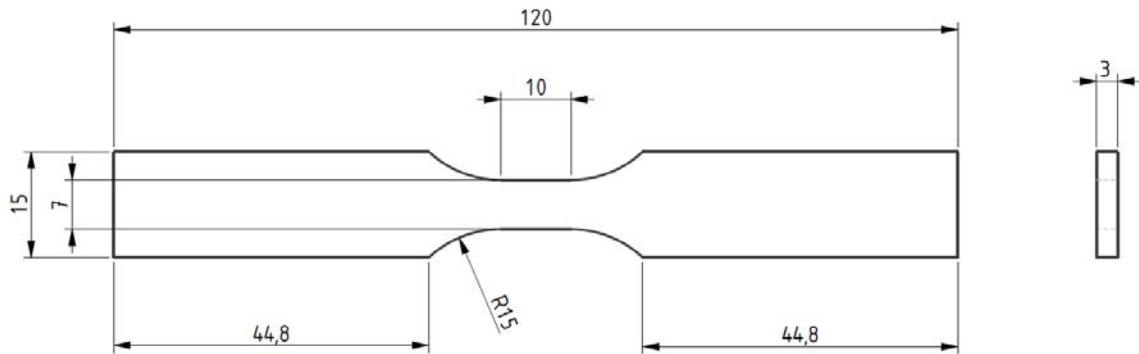


Figure 4.3.1.1: 2D technical drawing of the plain specimens that have been used for the fatigue tests.

After the specimens have been printed, have been performed the measurements, with a calliper, of the width and thickness of the central part (10 mm long in Figure 4.3.1.1) of every specimen. Has been considered for the calculation of the stresses the minimum cross sectional area that have been found along the central part, for every individual specimen. The width and thickness and the relative minimum cross sectional area have been reported, for every specimen, in the table below (Table 4.3.1.1):

Specimen's name	Width [mm]	Thickness [mm]	Area [mm <sup>2</sup> ]
0LPA12_-1_1	6.81	2.95	20.09
0LPA12_-1_2	6.86	3.02	20.72
0LPA12_-1_3	6.89	2.98	20.53
0LPA12_-1_4	6.80	2.92	19.86
0LPA12_-1_5	6.83	2.93	20.01
0LPA12_-1_6	6.83	2.93	20.01
0LPA12_-1_7	6.90	2.98	20.56
0LPA12_-1_8	6.85	3.00	20.55
0LPA12_-1_9	6.88	3.01	20.71
0LPA12_-1_10	6.96	3.00	20.88
0LPA12_-1_11	6.88	2.95	20.30
0LPA12_-1_12	6.83	2.93	20.01
45LPA12_-1_1	6.93	2.97	20.58
45LPA12_-1_2	7.04	3.03	21.33
45LPA12_-1_3	6.96	2.95	20.53
45LPA12_-1_4	6.97	2.97	20.70
45LPA12_-1_5	7.00	3.00	21.00
45LPA12_-1_6	6.94	2.96	20.54
45LPA12_-1_7	6.98	2.98	20.80
45LPA12_-1_8	6.90	2.95	20.36

45LPA12_-1_9	7.12	3.12	22.21
45LPA12_-1_10	7.02	3.08	21.62
45LPA12_-1_11	7.03	3.03	21.30
45LPA12_-1_12	7.01	3.01	21.10
90LPA12_-1_1	6.93	3.00	20.79
90LPA12_-1_2	7.08	3.00	21.24
90LPA12_-1_3	7.03	3.00	21.09
90LPA12_-1_4	7.05	2.98	21.01
90LPA12_-1_5	6.86	2.96	20.31
90LPA12_-1_6	7.04	2.97	20.91
90LPA12_-1_7	6.96	3.01	20.95
90LPA12_-1_8	7.08	3.01	21.31
90LPA12_-1_9	7.12	3.04	21.64
90LPA12_-1_10	7.12	3.05	21.72
90LPA12_-1_11	7.00	3.05	21.35
90LPA12_-1_12	6.94	3.03	21.03
90LPA12_-1_13	7.10	3.03	21.51
90LPA12_-1_14	7.10	3.02	21.44

Table 4.3.1.1: Measures of all the PA12 plain specimens that have been used for the fatigue tests.

#### 4.3.2 Tests set-up description

Have been tested twelve specimens for each of the three printing orientations: 0°, 45°, 90°. The printing orientations are the same ones described in the Subchapter 4.2.2 for the tensile tests (Figure 4.2.2.1).

Has been used the Schenck resonance machine of the Machine Design laboratory of the Faculty of Mechanical Engineering of Ljubljana's University (Figure 4.3.2.1). It is a very efficient machine that can be used for fatigue tests. The machine has been previously updated, by the Professor Jernej Klemenc and his PhD students, with a control system with a software written in LabVIEW and with a new 5 kN load cell.



Figure 4.3.2.1: Schenck resonance machine.

Has been prepared a set-up that could cool down the specimens with compressed air during the tests and that could measure the specimen's temperature during the tests (Figure 4.3.2.2). This has been done because of the needs of maintaining the specimen's temperature under the glass transition temperature, 55° for PA12, for avoiding changes in mechanical properties. The frequency of the fatigue load cycles could not be controlled due to the working principle of the Schenck



resonance machine that has been used: greater the amplitude of the load applied to the specimens, greater the frequency of the fatigue load cycles and vice versa.



Figure 4.3.2.2: View of the prepared set-up for the fatigue tests of the PA12 specimens. It is possible to see a plain specimens clamped, the FLIR thermal imaging camera that has been used to monitor the specimen's temperature, the nozzle, connected to the compressed air circuit of the laboratory, that has been used to blow fresh air to the specimens.

In the images below it is possible to see two examples of thermal imaging camera captures: one is about the regime temperature of 26 °C of the 90LPA12\_-1\_6 specimen (Figure 4.3.2.3) and the second one is an example about the temperature reached just before the break of the plain specimens with the highest stress levels applied that lasted very few cycles in the regime phase (Figure 4.3.2.4) (45LPA12\_-1\_1, 45LPA12\_-1\_2, 45LPA12\_-1\_3, 90LPA12\_-1\_1, 90LPA12\_-1\_2, 90LPA12\_-1\_3). These specimens didn't show a proper regime temperature value because they lasted too few cycles in the regime phase; the temperature slowly increased constantly from the transitory and when the specimens were near to break the temperature increased more rapidly until the final break temperature.

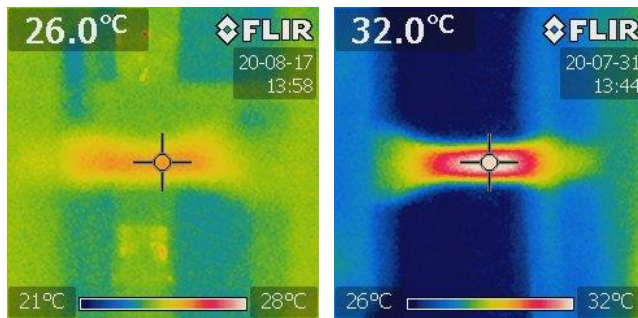


Figure 4.3.2.3: (on the left) Regime temperature value of the 90LPA12\_-1\_6 specimen.

Figure 4.3.2.4: (on the right) Temperature value example, just before the break, of the specimens that lasted very few cycles in the regime phase.

In the table below have been summarized some parameters common for all the fatigue tests of plain specimens performed (Table 4.3.2.1):

Room's temperature range [°C]	23 - 27
Specimens temperature range [°C]	23 - 27
Compressed air average pressure [bar]	2
Fatigue load cycles frequencies range [Hz]	16.9 – 18.3
Fatigue load cycles ratio [/]	-1
Load cell values dispersion average [N]	± 5

Table 4.3.2.1: Common parameters for all the fatigue tests of plain specimens performed.



### 4.3.3 Tests results

In the tables below (Table 4.3.3.1, Table 4.3.3.2, Table 4.3.3.3) have been summarized the results of the fatigue tests of the plain specimens that have been performed. The names of the specimens are designed as follow:

- The first number specifies the print orientation: 0° or 45° or 90° (Figure 4.2.2.1).
- “L” specifies that it is a plain specimen.
- “PA12” specifies the material of the specimen.
- “-1” specifies the load ratio of the fatigue cycles applied to the specimen.
- The last number specifies the specimen's number.

Due to the working principle of the Schenck resonance machine, the load cycles started always from 0 N amplitude and then the amplitude increased until the regime value was reached. To take in account these transient amplitude cycles has been decided to sum to the regime amplitude cycles half of the transient amplitude cycles.

The index “I” in the tables below can be 0 or 1: 0 means that the specimen broke and 1 means that the specimen did a runout, without breaking.

Specimen's name	R	F <sub>a</sub> [N]	σ <sub>a</sub> [MPa]	N. Cycles transient	N. Cycles total	I	F [Hz]	Temp. [°C]
0LPA12_-1_1	-1	366	<b>18.2</b>	11250	<b>8029</b>	0	17.7	27
0LPA12_-1_2	-1	377	<b>18.2</b>	7777	<b>8379</b>	0	17.8	27
0LPA12_-1_3	-1	374	<b>18.2</b>	3746	<b>5029</b>	0	17.8	27
0LPA12_-1_4	-1	258	<b>13.0</b>	5233	<b>203590</b>	0	17.0	26
0LPA12_-1_5	-1	260	<b>13.0</b>	5059	<b>112617</b>	0	17.0	26
0LPA12_-1_6	-1	260	<b>13.0</b>	10336	<b>203015</b>	0	17.0	25/26
0LPA12_-1_7	-1	329	<b>16.0</b>	4699	<b>11285</b>	0	17.5	26
0LPA12_-1_8	-1	319	<b>15.5</b>	4925	<b>19913</b>	0	17.5	24
0LPA12_-1_9	-1	321	<b>15.5</b>	4468	<b>51723</b>	0	17.5	23
0LPA12_-1_10	-1	251	<b>12.0</b>	5540	<b>335176</b>	0	16.9	25
0LPA12_-1_11	-1	223	<b>11.0</b>	4879	<b>2676901</b>	1	16.6	24
0LPA12_-1_12	-1	230	<b>11.5</b>	4825	<b>774619</b>	0	16.9	23

Table 4.3.3.1: Results of fatigue tests of plain specimens with 0° print orientation.

Specimen's name	R	F <sub>a</sub> [N]	σ <sub>a</sub> [MPa]	N. Cycles transient	N. Cycles total	I	F [Hz]	Temp. [°C]
45LPA12_-1_1	-1	447	<b>21.7</b>	2564	<b>1561</b>	0	17.9	24/32
45LPA12_-1_2	-1	463	<b>21.7</b>	3097	<b>2313</b>	0	18.0	24/30
45LPA12_-1_3	-1	446	<b>21.7</b>	2508	<b>1773</b>	0	17.9	24/29
45LPA12_-1_4	-1	321	<b>15.5</b>	8818	<b>131638</b>	0	17.5	26
45LPA12_-1_5	-1	326	<b>15.5</b>	4620	<b>186091</b>	0	17.5	25
45LPA12_-1_6	-1	318	<b>15.5</b>	13569	<b>133702</b>	0	17.5	26
45LPA12_-1_7	-1	385	<b>18.5</b>	3376	<b>21100</b>	0	17.9	23
45LPA12_-1_8	-1	377	<b>18.5</b>	4039	<b>31794</b>	0	17.8	NA
45LPA12_-1_9	-1	433	<b>19.5</b>	2983	<b>6682</b>	0	18.1	NA
45LPA12_-1_10	-1	314	<b>14.5</b>	5083	<b>253206</b>	0	17.5	25
45LPA12_-1_11	-1	292	<b>13.7</b>	4680	<b>605783</b>	0	17.4	23
45LPA12_-1_12	-1	268	<b>12.7</b>	4791	<b>669089</b>	0	17.1	23

Table 4.3.3.2: Results of fatigue tests of plain specimens with 45° print orientation.

Specimen's name	R	F <sub>a</sub> [N]	$\sigma_a$ [Mpa]	N. Cycles transient	N. Cycles total	I	F [Hz]	Temp. [°C]
90LPA12_-1_1	-1	524	<b>25.2</b>	2683	<b>1359</b>	0	18.2	24/33
90LPA12_-1_2	-1	535	<b>25.2</b>	2787	<b>1425</b>	0	18.2	24/28
90LPA12_-1_3	-1	531	<b>25.2</b>	2467	<b>1364</b>	0	18.2	24/32
90LPA12_-1_4	-1	378	<b>18.0</b>	7665	<b>233669</b>	0	17.8	26
90LPA12_-1_5	-1	366	<b>18.0</b>	4186	<b>255601</b>	0	17.8	25/26
90LPA12_-1_6	-1	376	<b>18.0</b>	7841	<b>515940</b>	0	17.8	25/26
90LPA12_-1_7	-1	409	<b>19.5</b>	3057	<b>86522</b>	0	17.9	24
90LPA12_-1_8	-1	448	<b>21.0</b>	3026	<b>4520</b>	0	18.1	23
90LPA12_-1_9	-1	422	<b>19.5</b>	3414	<b>6196</b>	0	17.9	24
90LPA12_-1_10	-1	358	<b>16.5</b>	4895	<b>933175</b>	0	17.9	24
90LPA12_-1_11	-1	363	<b>17.0</b>	4073	<b>705224</b>	0	17.9	24
90LPA12_-1_12	-1	326	<b>15.5</b>	5253	<b>646846</b>	0	17.6	23
90LPA12_-1_13	-1	452	<b>21.0</b>	3234	<b>24419</b>	0	18.3	28
90LPA12_-1_14	-1	418	<b>19.5</b>	3457	<b>36638</b>	0	18.2	26

Table 4.3.3.3: Results of fatigue tests of plain specimens with 90° print orientation. The specimens number 8 and 9, highlighted in red, have been considered outliers and so have not been considered in the further elaboration of the experimental data.

In the image below (Figure 4.3.3.1) it is possible to see the S-N chart of the plain specimens tested with the three different orientations 0°, 45°, 90°.

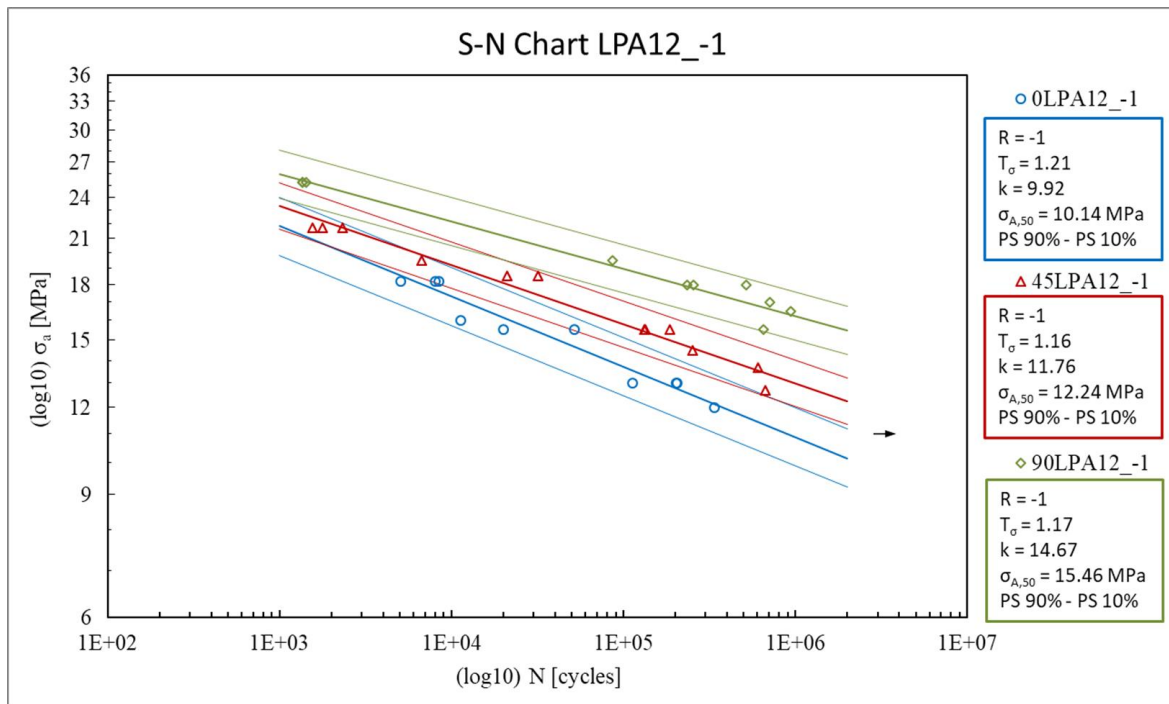


Figure 4.3.3.1: S-N chart of the plain specimens tested with the three different orientations of 0°, 45° and 90°.

It is possible to see in figure 4.3.3.1 that, considering for example a constant value of stress amplitude applied to the specimens, the 90° oriented plain specimens can survive more cycles than the 45° oriented plain specimens that, in turn, can survive more cycles than the 0° oriented plain specimens.

In the images below it is possible to see three examples of three broken plain specimens, one for each of the three orientations considered.

In the images below (Figure 4.3.3.2, Figure 4.3.3.3, Figure 4.3.3.4) it is possible to see the 0LPA12\_-1\_4 broken specimen as the example of the 0° plain broken specimens:

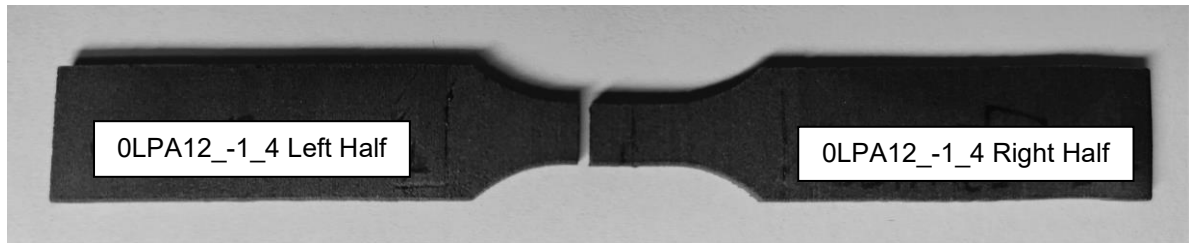


Figure 4.3.3.2: View of the 0LPA12\_-1\_4 broken specimen.

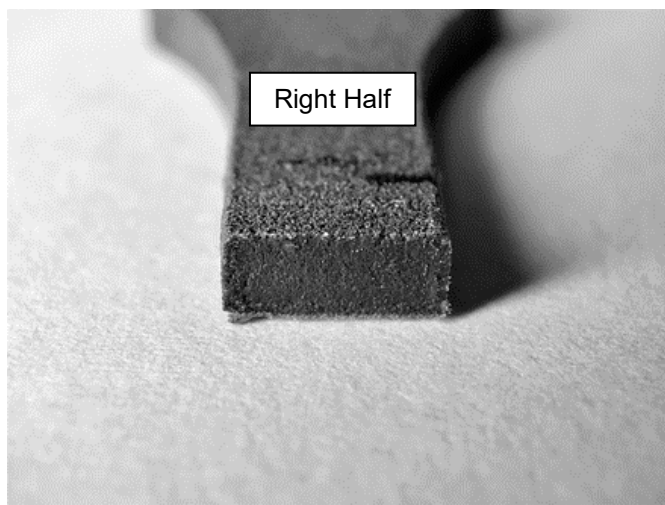


Figure 4.3.3.3: View of the right half (Figure 4.3.3.2) of the 0LPA12\_-1\_4 broken specimen.

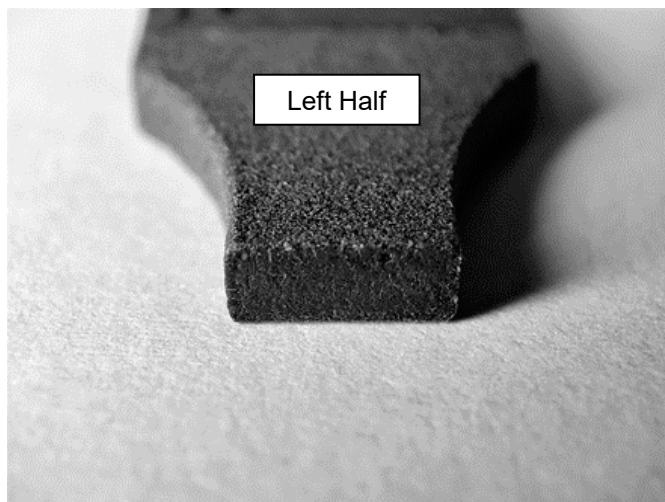


Figure 4.3.3.4: View of the left half (Figure 4.3.3.2) of the 0LPA12\_-1\_4 broken specimen.

The failure behaviour for all the plain 0° specimens is a brittle break, orthogonal to the longitudinal axis of the specimens. It is very difficult to distinguish between the initial brittle break when the crack starts and grows and the final brittle break, when the resistant cross section is no more enough to sustain the applied load.

In the images below (Figure 4.3.3.5, Figure 4.3.3.6, Figure 4.3.3.7) it is possible to see the 45LPA12\_-1\_5 broken specimen as the example of the 45° plain broken specimens:

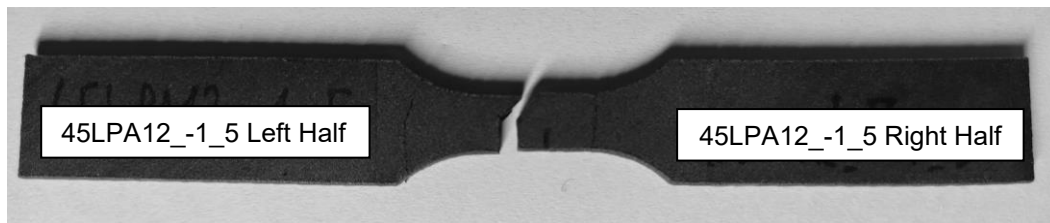


Figure 4.3.3.5: View of the 45LPA12\_-1\_5 broken specimen.

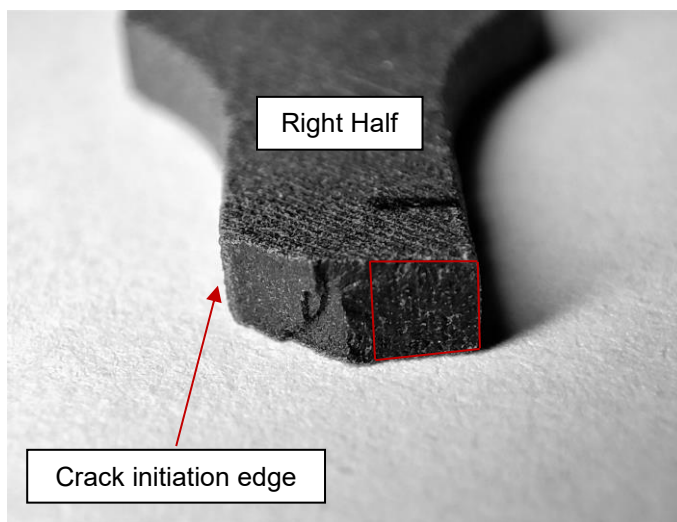


Figure 4.3.3.6: View of the right half (Figure 4.3.3.5) of the 45LPA12\_-1\_5 broken specimen. In red has been highlighted, approximately, the resistant cross section that should be no more able to sustain the load applied to the specimen, calculated dividing the amplitude force applied to the specimen of 326 N by the UTS of 31 MPa, result from the tensile tests performed in Subchapter 4.2.

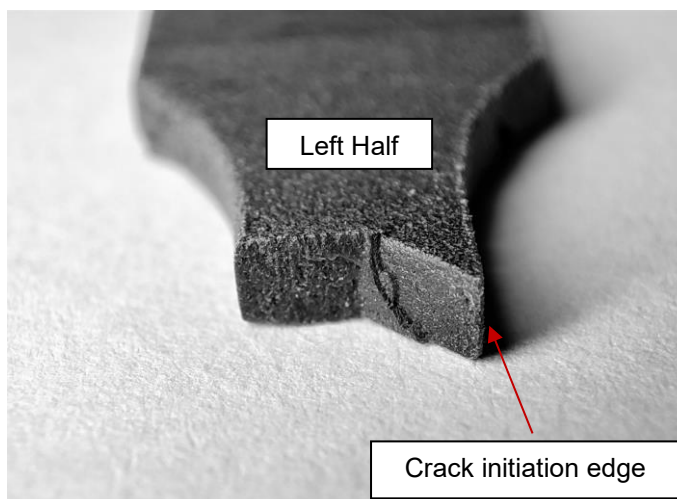


Figure 4.3.3.7: View of the left half (Figure 4.3.3.5) of the 45LPA12\_-1\_5 broken specimen.

The failure behaviour for all the plain 45° specimens is an initial brittle break, 45° oriented, where the crack starts and grows and then a ductile break, orthogonal to the longitudinal axis of the specimens, when the resistant cross section is no more enough to sustain the applied load.

In the images below (Figure 4.3.3.8, Figure 4.3.3.9, Figure 4.3.3.10) it is possible to see the 90LPA12\_-1\_1 broken specimen as the example of the 90° plain broken specimens:

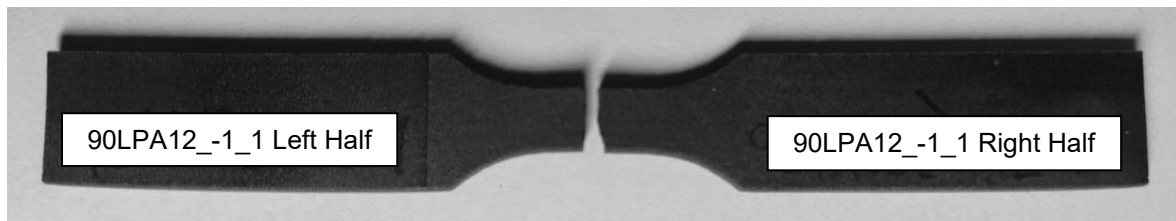


Figure 4.3.3.8: View of the 90LPA12\_-1\_1 broken specimen.

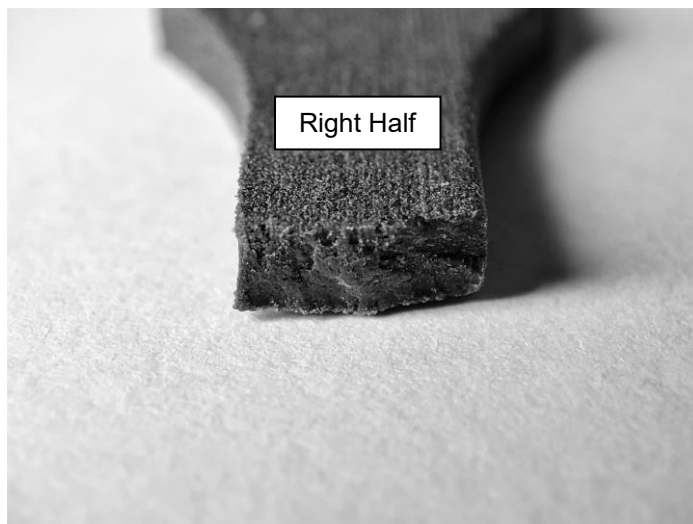


Figure 4.3.3.9: View of the right half (Figure 4.3.3.8) of the 90LPA12\_-1\_1 broken specimen.

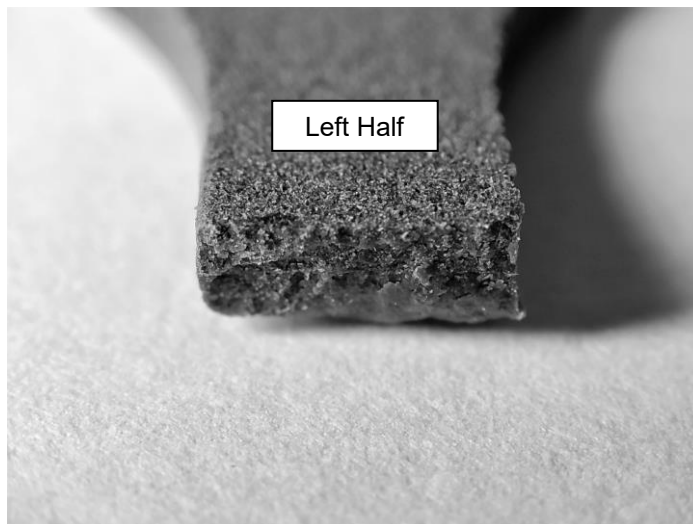


Figure 4.3.3.10: View of the left half (Figure 4.3.3.8) of the 90LPA12\_-1\_1 broken specimen.

In the 90° oriented plain specimens it is difficult to distinguish between the initial brittle break when the crack starts and grows and the final ductile break, when the resistant cross section is no more enough to sustain the applied load.

## 4.4 Fatigue tests of rounded V-notch specimens

In this subchapter have been presented the fatigue tests of the PA12 rounded V-notch specimens that have been performed. The specimens have been printed with the SLS technology as explained in the Subchapter 4.1.

### 4.4.1 Specimens dimensions and preparation

The detailed dimensions of the rounded V-notch specimens that have been used for fatigue tests are shown in the image below (Figure 4.4.1.1):

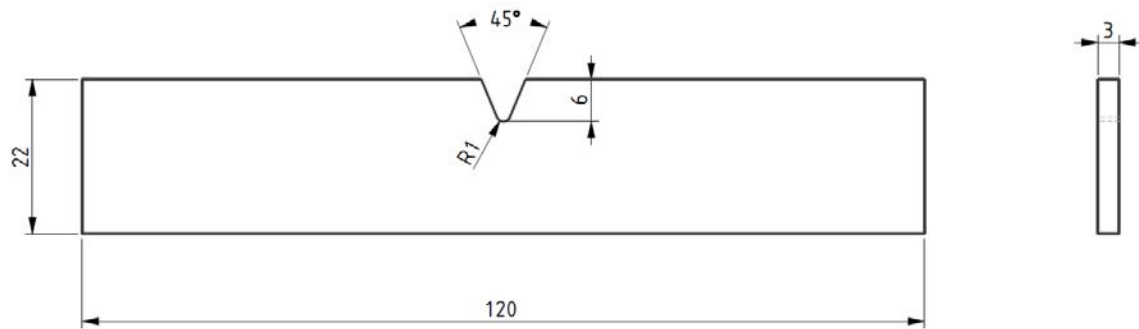


Figure 4.4.1.1: 2D technical drawing of the rounded V-notch specimens that have been used for the fatigue tests.

After the sandblast operation (Subchapter 4.1), common for all the SLS printed parts used in this thesis work, the rounded V-notches of all the specimens have been refined using the small “Proxxon PF 360” milling machine with a 2 mm diameter milling tool to be sure that the dimensions of the notches would be as equal as possible in all the specimens (Figure 4.4.1.2).

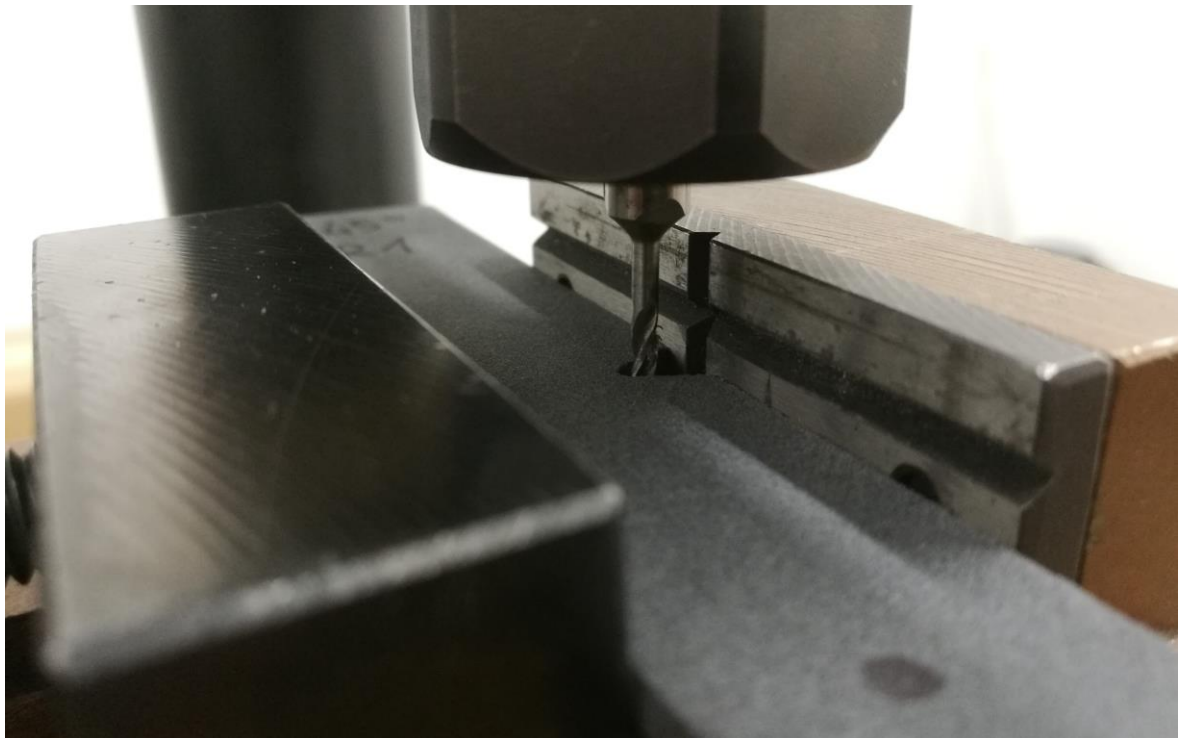


Figure 4.4.1.2: Rounded V-notch refinement with the small “Proxxon PF 360” milling machine.



After all the rounded V-notches have been refined, a picture of every specimen with a calliper nearby has been taken with a Canon reflex with the aim of measuring the notches dimensions thanks to an image elaboration post-process.

The pictures that have been taken for every rounded V-notch specimen are like the one below (Figure 4.4.1.3):

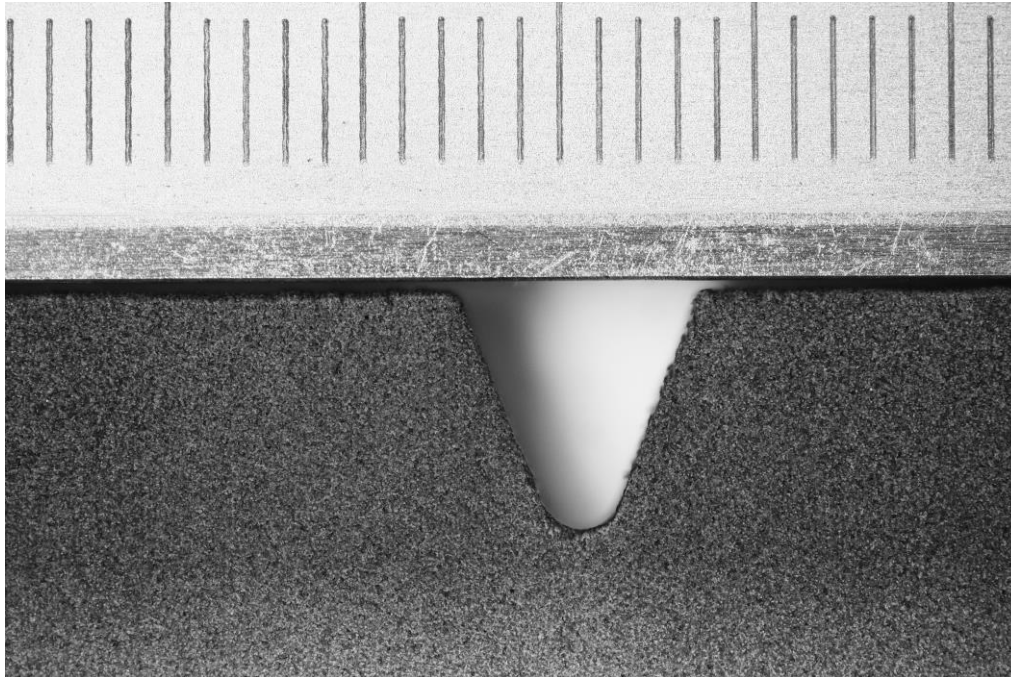


Figure 4.4.1.3: Image of a rounded V-notch specimen with a calliper nearby.

To post-process the pictures has been used the opensource software “ImageJ”:

The first step is to open the specimen’s image (Figure 4.4.1.4) and to draw a line between a known distance to set the scale (“Analyze”, “Set Scale”): how many pixels are equal to the known distance (Figure 4.4.1.5).



Figure 4.4.1.4: Specimen’s image opened.

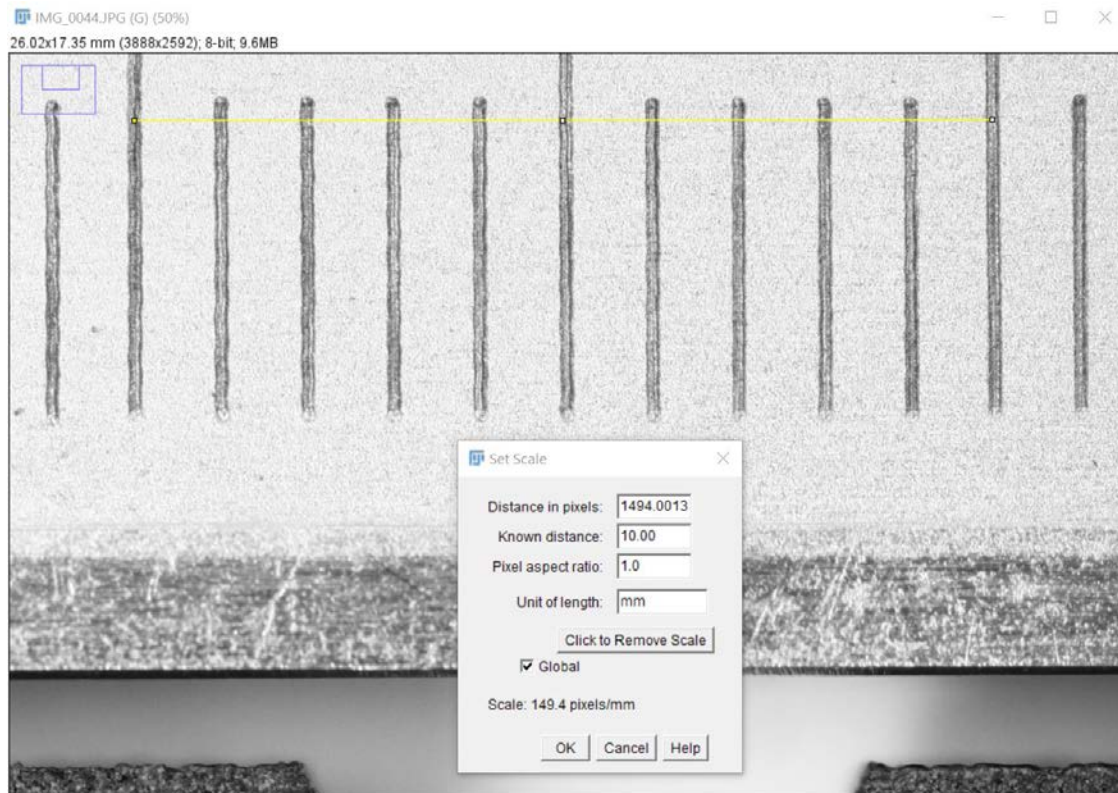


Figure 4.4.1.5: Draw of the line useful to set the scale for the further measurement.

The second step is to sharp two times a selected rectangular zone around the rounded V-notch to be able to identify more clearly the boundaries of the notch itself ("Process", "Sharpen") (Figure 4.4.1.6).

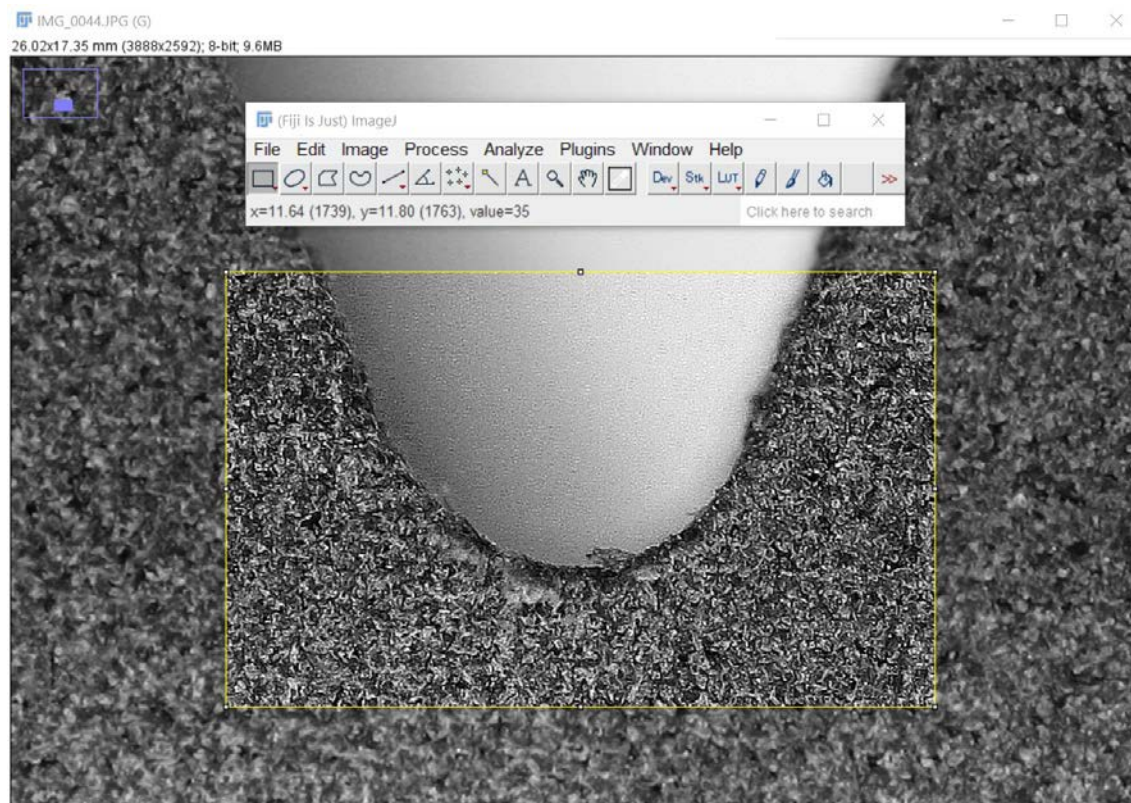


Figure 4.4.1.6: Two times sharpened area around the rounded V-notch.



The third and last step is to draw an “Elliptical selection” and to degenerate it into a perfect circle to be able to measure the diameter of the rounded V-notch (“Analyze”, “Measure”) (Figure 4.4.1.7).

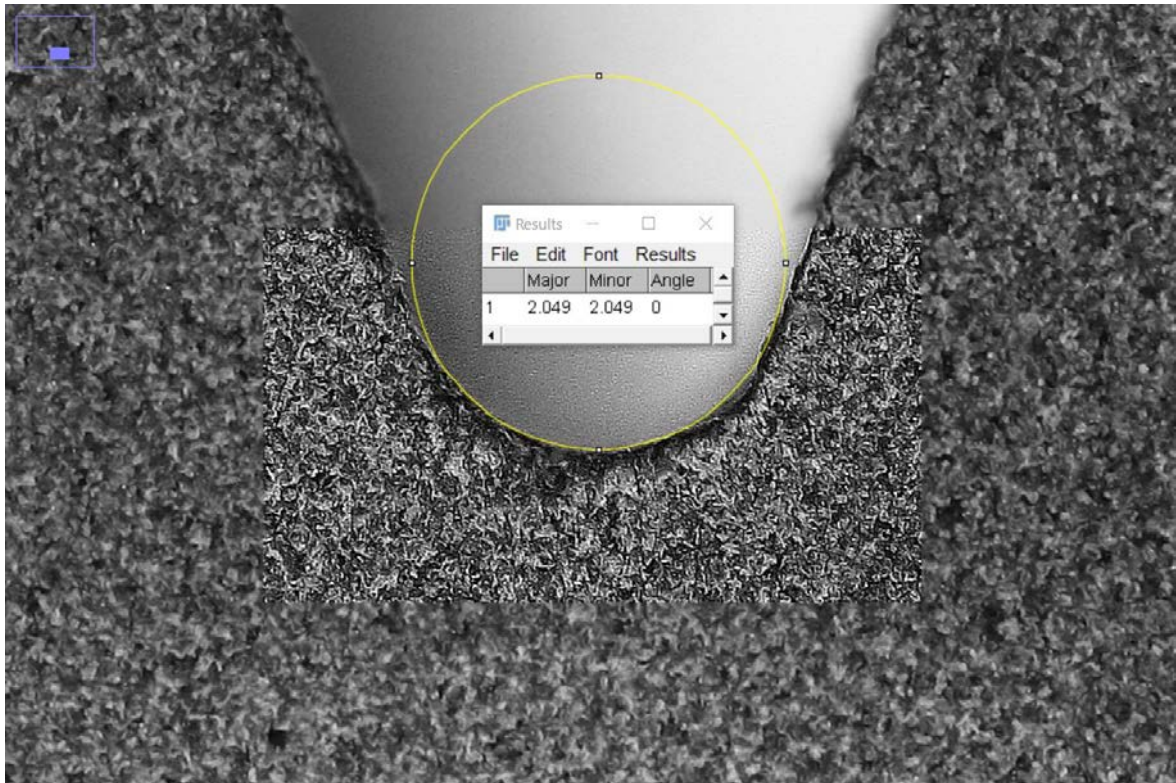


Figure 4.4.1.7: Measure of the diameter of the rounded V-notch.

The images of the measured diameters of the rounded V-notches for all the specimens have been presented in Annex F.

Only for the 90° orientation specimens, due to the warping occurred during the printing process, have been straightened the opposite sides to the rounded V-notches of all the specimens using the “Proxxon PF 360” milling machine (Figure 4.4.1.8).

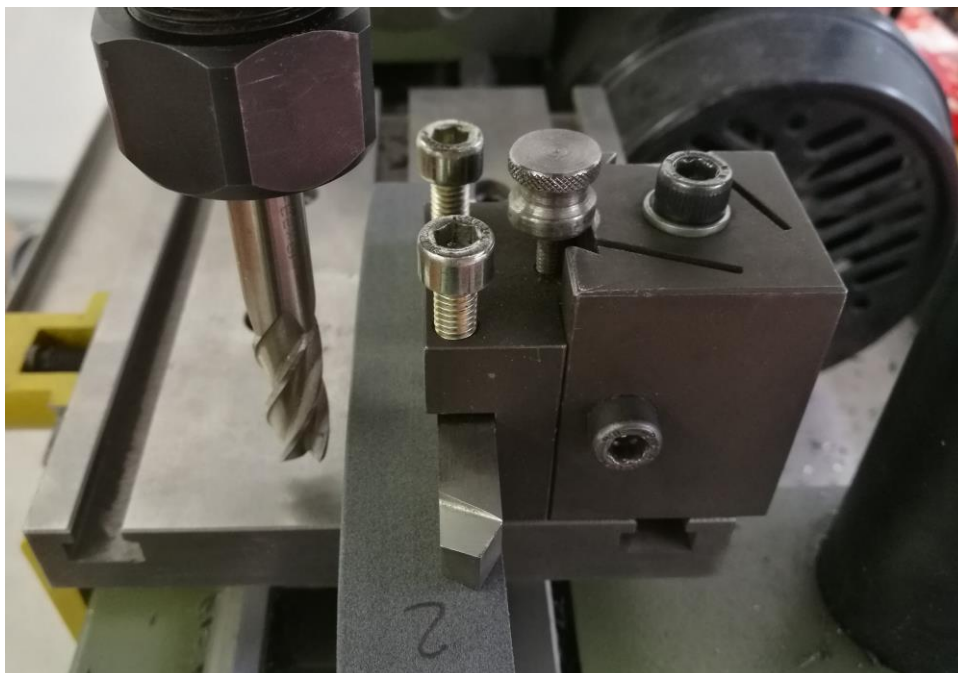


Figure 4.4.1.8: Straightening of the opposite side to the rounded V-notch of a specimen using the “Proxxon PF 360” milling machine.

In the image below (Figure 4.4.1.9) it is possible to see the 90VR1PA12\_-1\_8 specimen before the straightening procedure:



Figure 4.4.1.9: View of the 90VR1PA12\_-1\_8 specimen before the straightening procedure.

In the image below (Figure 4.4.1.10) it is possible to see the 90VR1PA12\_-1\_8 specimen after the straightening procedure:

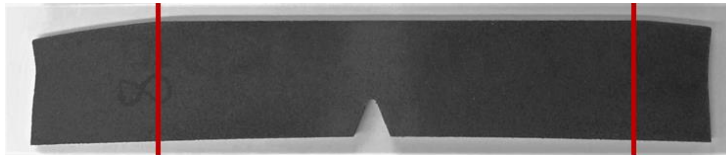


Figure 4.4.1.10: View of the 90VR1PA12\_-1\_8 specimen after the straightening procedure; the straightened central part of the specimen is included in between the two red lines that have been drawn. The test machine grips clamped the specimen until much further than where the straightened part begin.

In the table below (Table 4.4.1.1) have been summarized the width, the thickness and the relative cross sectional area in the centre of the specimen, immediately below the V-notch's apex, of all the specimens that have been tested. Has been summarized also the V-notch measured fillet diameter for all the specimens that have been tested. The measures of widths and thicknesses have been taken with a calliper, the measures of the V-notches fillet diameters have been taken with the image post-processing procedure explained above.

Specimen's name	Width [mm]	Thickness [mm]	Area [mm <sup>2</sup> ]	V-notch fillet diameter [mm]
0VR1PA12_-1_4	15.75	2.90	45.68	2.10
0VR1PA12_-1_6	15.88	3.08	48.91	2.12
0VR1PA12_-1_1	15.55	3.07	47.74	2.05
0VR1PA12_-1_1BIS	15.52	2.94	45.63	2.01
0VR1PA12_-1_5	15.65	3.00	46.95	2.02
0VR1PA12_-1_2	15.80	2.98	47.08	2.05
0VR1PA12_-1_3	15.90	3.03	48.18	2.10
0VR1PA12_-1_7	15.58	2.95	45.96	2.01
0VR1PA12_-1_9	15.70	2.96	46.47	2.01
0VR1PA12_-1_10	15.47	3.05	47.18	2.15
0VR1PA12_-1_8	15.15	2.84	43.03	1.98
0VR1PA12_-1_11	15.31	3.03	46.39	1.97
0VR1PA12_-1_12	15.47	3.03	46.87	1.99
45VR1PA12_-1_1	15.53	2.99	46.43	2.03
45VR1PA12_-1_4	15.61	3.00	46.83	2.07
45VR1PA12_-1_5	15.60	2.98	46.49	2.00
45VR1PA12_-1_2	15.70	3.04	47.73	1.96
45VR1PA12_-1_6	15.65	3.08	48.20	2.02
45VR1PA12_-1_7	15.66	3.10	48.55	2.04
45VR1PA12_-1_3	15.50	3.05	47.28	2.01
45VR1PA12_-1_8	15.82	3.07	48.57	2.02
45VR1PA12_-1_9	15.38	3.04	46.76	2.00
45VR1PA12_-1_10	15.56	3.06	47.61	2.02

45VR1PA12_-1_11	15.66	3.06	47.92	1.99
45VR1PA12_-1_12	15.64	3.09	48.33	1.98
90VR1PA12_-1_1	13.62	3.01	41.00	1.92
90VR1PA12_-1_2	13.62	3.02	41.13	1.95
90VR1PA12_-1_3	14.47	3.02	43.70	2.02
90VR1PA12_-1_4	14.64	3.10	45.38	2.08
90VR1PA12_-1_5	14.61	3.01	43.98	2.06
90VR1PA12_-1_6	14.53	3.05	44.32	1.98
90VR1PA12_-1_7	14.58	3.01	43.89	2.02
90VR1PA12_-1_8	13.85	2.97	41.13	1.98
90VR1PA12_-1_9	14.80	3.10	45.88	1.99
90VR1PA12_-1_10	13.02	3.05	39.71	1.98
90VR1PA12_-1_11	14.27	3.06	43.67	2.00
90VR1PA12_-1_12	15.07	3.12	47.02	2.03

Table 4.4.1.1: Measures of all the PA12 rounded V-notch specimens that have been used for the fatigue tests.

#### 4.4.2 Tests set-up description

Have been tested almost twelve specimens for each of the three printing orientations: 0°, 45°, 90°. The printing orientations are the same ones described in the Subchapter 4.2.2 for the tensile tests (Figure 4.2.2.1).

Has been used the very same Schenck resonance machine and the very same set-up described in Subchapter 4.3.2 for the fatigue tests of the plain specimens.

In the image below (Figure 4.4.2.1) it is possible to see an example of a thermo camera measurement of a 45° rounded V-notch specimen. It is interesting to see that the maximum temperature is in a hot spot immediately below the V-notch's apex, where the stresses are higher, and that the temperature profile follows the 45° orientation.

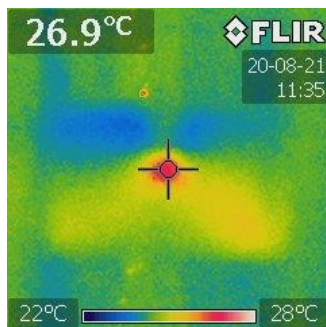


Figure 4.4.2.1: Thermo camera measurement of a 45° rounded V-notch specimen.

In the table below have been summarized some parameters common for all the fatigue tests of the rounded V-notch specimens performed (Table 4.4.2.1):

Room's temperature range [°C]	23 - 27
Specimens temperature range [°C]	22 - 28
Compressed air average pressure [bar]	1.1
Fatigue load cycles frequencies range [Hz]	14.3 – 19.7
Fatigue load cycles ratio [/]	-1
Load cell values dispersion average [N]	± 5

Table 4.4.2.1: Common parameters for all the fatigue tests of the rounded V-notch specimens performed.

#### 4.4.3 Tests results

In the tables below (Table 4.4.3.1, Table 4.4.3.2, Table 4.4.3.3) have been summarized the results of the fatigue tests of the rounded V-notch specimens that have been performed. The names of the specimens are designed as follow:

- The first number specifies the print orientation: 0° or 45° or 90° (Figure 4.2.2.1).
- “VR1” specifies that it is a V-notch specimen with a 1 mm fillet radius.
- “PA12” specifies the material of the specimen.
- “-1” specifies the load ratio of the fatigue cycles applied to the specimen.
- The last number specifies the specimen's number.

Due to the working principle of the Schenck resonance machine, the load cycles started always from 0N amplitude and then the amplitude increased until the regime value was reached. To take in account these transient amplitude cycles has been decided to sum to the regime amplitude cycles half of the transient amplitude cycles.

The index “I” in the tables below can be 0 or 1: 0 means that the specimen broke and 1 means that the specimen did a runout, without breaking.

Specimen's name	R	F <sub>a</sub> [N]	σ <sub>a</sub> [MPa]	N. Cycles transient	N. Cycles total	I	F [Hz]	Temp. [°C]
0VR1PA12_-1_4	-1	594	<b>13.0</b>	3259	<b>1630</b>	0	NA	24
0VR1PA12_-1_6	-1	509	<b>10.4</b>	4966	<b>9034</b>	0	19.4	24/25
0VR1PA12_-1_1	-1	496	<b>10.4</b>	4347	<b>4407</b>	0	19.2	25
0VR1PA12_-1_1BIS	-1	475	<b>10.4</b>	4282	<b>2141</b>	0	NA	25/26
0VR1PA12_-1_5	-1	376	<b>8.0</b>	4684	<b>88471</b>	0	18.4	23
0VR1PA12_-1_2	-1	377	<b>8.0</b>	4602	<b>16078</b>	0	18.4	26
0VR1PA12_-1_3	-1	385	<b>8.0</b>	3987	<b>12978</b>	0	18.4	25/26
0VR1PA12_-1_7	-1	276	<b>6.0</b>	4690	<b>297085</b>	0	17.3	26
0VR1PA12_-1_9	-1	279	<b>6.0</b>	4935	<b>251064</b>	0	17.3	23
0VR1PA12_-1_10	-1	330	<b>7.0</b>	4302	<b>118640</b>	0	18.0	23
0VR1PA12_-1_8	-1	129	<b>3.0</b>	8810	<b>2000003</b>	1	14.3	23/26
0VR1PA12_-1_11	-1	232	<b>5.0</b>	5063	<b>2997480</b>	1	16.3	NA
0VR1PA12_-1_12	-1	248	<b>5.3</b>	4667	<b>222823</b>	0	16.9	23

Table 4.4.3.1: Results of fatigue tests of rounded V-notch specimens with 0° print orientation.

Specimen's name	R	F <sub>a</sub> [N]	σ <sub>a</sub> [MPa]	N. Cycles transient	N. Cycles total	I	F [Hz]	Temp. [°C]
45VR1PA12_-1_1	-1	557	<b>12.0</b>	4444	<b>4110</b>	0	19.5	24/26
45VR1PA12_-1_4	-1	562	<b>12.0</b>	4359	<b>7736</b>	0	19.5	22/23
45VR1PA12_-1_5	-1	558	<b>12.0</b>	4879	<b>4314</b>	0	19.6	26/27
45VR1PA12_-1_2	-1	430	<b>9.0</b>	4482	<b>56467</b>	0	18.9	23/24
45VR1PA12_-1_6	-1	434	<b>9.0</b>	4480	<b>35502</b>	0	18.9	26
45VR1PA12_-1_7	-1	437	<b>9.0</b>	4282	<b>26326</b>	0	18.9	26/27
45VR1PA12_-1_3	-1	331	<b>7.0</b>	4376	<b>497449</b>	0	17.9	25/26
45VR1PA12_-1_8	-1	389	<b>8.0</b>	4196	<b>112359</b>	0	18.6	23
45VR1PA12_-1_9	-1	351	<b>7.5</b>	4329	<b>186919</b>	0	18.2	23
45VR1PA12_-1_10	-1	286	<b>6.0</b>	4918	<b>2640130</b>	1	17.5	NA
45VR1PA12_-1_11	-1	311	<b>6.5</b>	4665	<b>1345705</b>	0	17.8	23
45VR1PA12_-1_12	-1	314	<b>6.5</b>	4153	<b>1531642</b>	0	17.8	NA

Table 4.4.3.2: Results of fatigue tests of rounded V-notch specimens with 45° print orientation.



Specimen's name	R	F <sub>a</sub> [N]	σ <sub>a</sub> [MPa]	N. Cycles transient	N. Cycles total	I	F [Hz]	Temp. [°C]
90VR1PA12_-1_1	-1	574	<b>14.0</b>	4095	<b>10552</b>	0	19.4	27/28
90VR1PA12_-1_2	-1	576	<b>14.0</b>	4222	<b>4761</b>	0	19.4	27/28
90VR1PA12_-1_3	-1	612	<b>14.0</b>	4064	<b>7078</b>	0	19.7	27/28
90VR1PA12_-1_4	-1	499	<b>11.0</b>	4283	<b>88255</b>	0	19.2	25
90VR1PA12_-1_5	-1	484	<b>11.0</b>	4271	<b>33820</b>	0	19.1	27
90VR1PA12_-1_6	-1	487	<b>11.0</b>	4557	<b>39885</b>	0	19.2	24/25
90VR1PA12_-1_7	-1	395	<b>9.0</b>	8773	<b>325765</b>	0	18.7	22
90VR1PA12_-1_8	-1	395	<b>9.6</b>	4091	<b>87809</b>	0	18.6	22
90VR1PA12_-1_9	-1	413	<b>9.0</b>	3997	<b>151644</b>	0	18.8	22
90VR1PA12_-1_10	-1	258	<b>6.5</b>	4539	<b>414807</b>	0	17.0	22
90VR1PA12_-1_11	-1	284	<b>6.5</b>	9644	<b>2961830</b>	0	17.4	23
90VR1PA12_-1_12	-1	306	<b>6.5</b>	4439	<b>3476950</b>	1	17.7	24

Table 4.4.3.3: Results of fatigue tests of rounded V-notch specimens with 90° print orientation. The specimen number 10, highlighted in red, has been considered an outlier and so has not been considered in the further elaboration of the experimental data.

In the image below (Figure 4.4.3.1) it is possible to see the S-N chart of the rounded V-notch specimens tested with the three different orientations 0°, 45°, 90°.

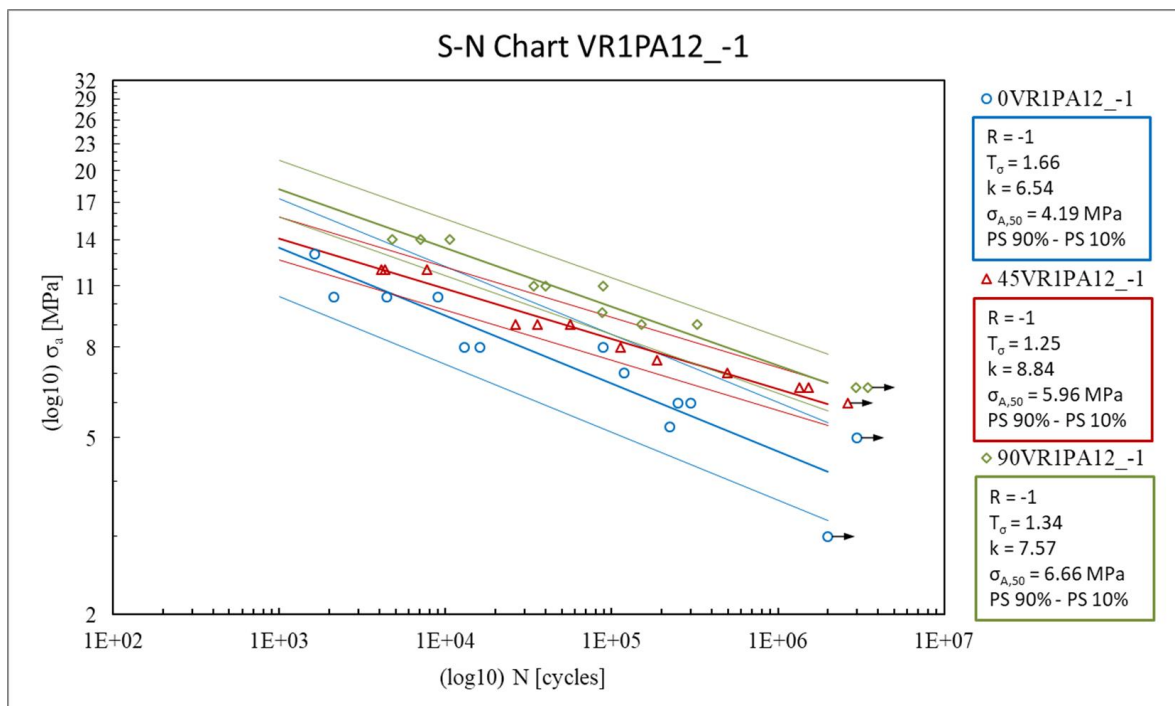


Figure 4.4.3.1: S-N chart of the rounded V-notch specimens tested with the three different orientations of 0°, 45° and 90°. The plotted amplitude stresses are the net stresses, referred to the central cross sections of the specimens under the V-notches apices.

It is possible to see in figure 4.4.3.1 that, considering for example a constant value of stress amplitude applied to the specimens, the 90° oriented rounded V-notch specimens can survive more cycles than the 45° oriented rounded V-notch specimens that, in turn, can survive more cycles than the 0° oriented rounded V-notch specimens.

In the images below it is possible to see three examples of three broken rounded V-notch specimens, one for each of the three orientations considered.

In the images below (Figure 4.4.3.2, Figure 4.4.3.3, Figure 4.4.3.4) it is possible to see the 0VR1PA12\_-1\_6 broken specimen as the example of the 0° rounded V-notch broken specimens:

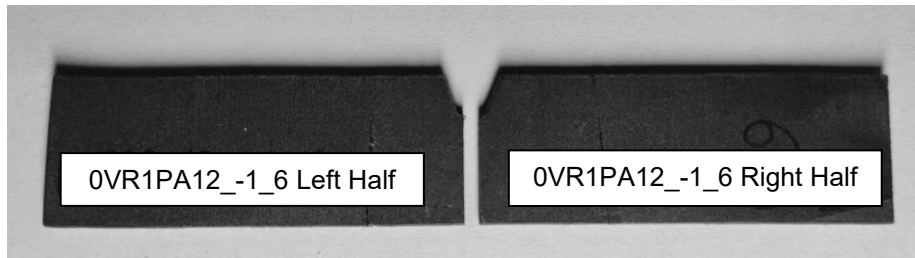


Figure 4.4.3.2: View of the 0VR1PA12\_-1\_6 broken specimen.

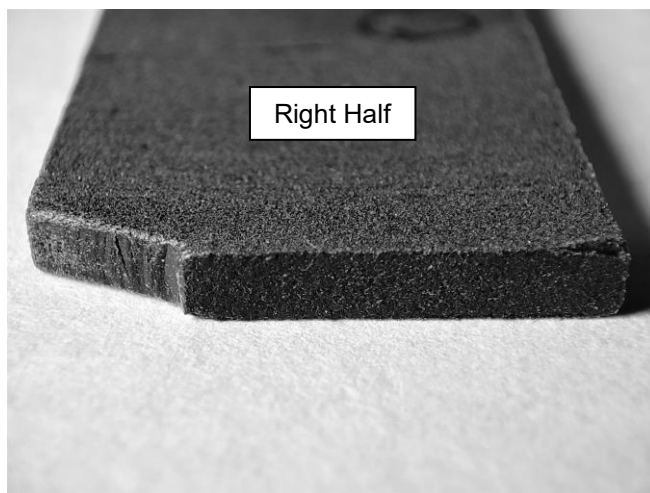


Figure 4.4.3.3: View of the right half (Figure 4.4.3.2) of the 0VR1PA12\_-1\_6 broken specimen.

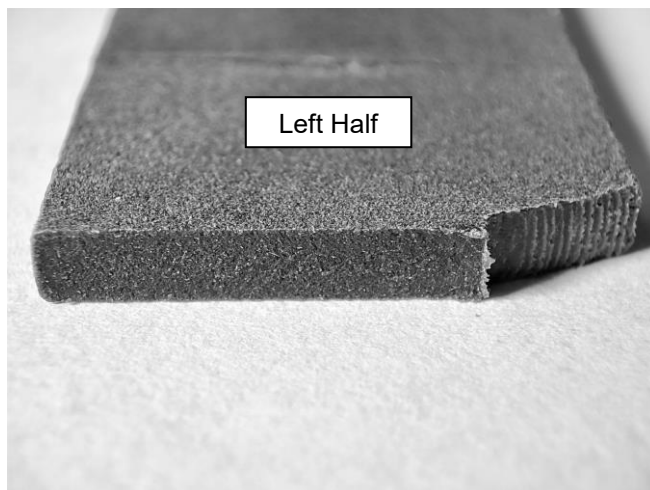


Figure 4.4.3.4: View of the left half (Figure 4.4.3.2) of the 0VR1PA12\_-1\_6 broken specimen.

The failure behaviour for all the rounded V-notch 0° specimens is a brittle break orthogonal to the longitudinal axis of the specimens. It is very difficult to distinguish between the initial brittle break when the crack starts and grows and the final brittle break, when the resistant cross section is no more enough to sustain the applied load.

In the images below (Figure 4.4.3.5, Figure 4.4.3.6, Figure 4.4.3.7) it is possible to see the 45VR1PA12\_-1\_6 broken specimen as the example of the 45° rounded V-notch broken specimens:

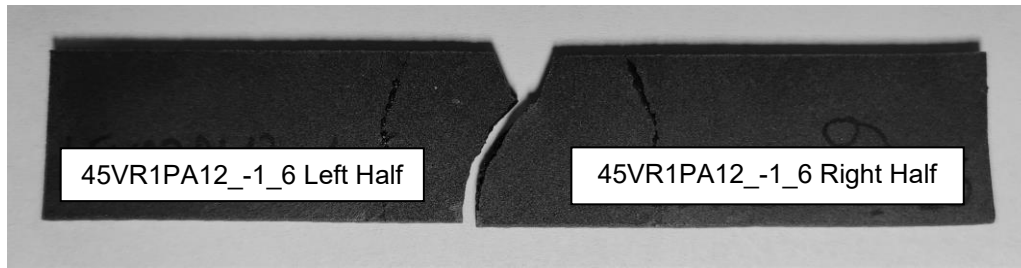


Figure 4.4.3.5: View of the 45VR1PA12\_-1\_6 broken specimen.

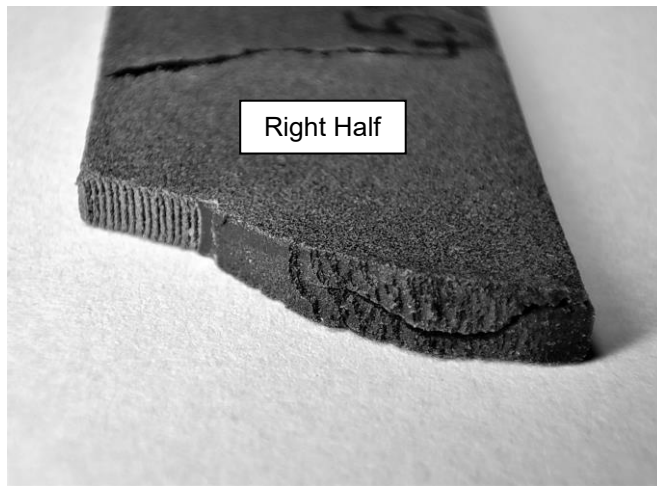


Figure 4.4.3.6: View of the right half (Figure 4.4.3.5) of the 45VR1PA12\_-1\_6 broken specimen.

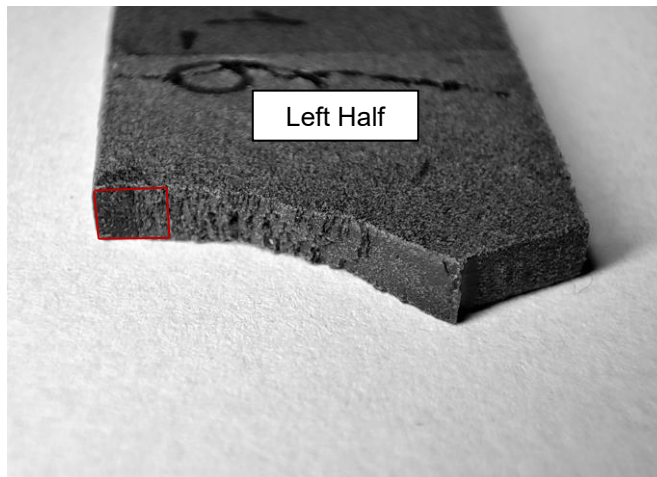


Figure 4.4.3.7: View of the left half (Figure 4.4.3.5) of the 45VR1PA12\_-1\_6 broken specimen. In red has been highlighted, approximately, the resistant cross section that should be no more able to sustain the load applied to the specimen, calculated dividing the amplitude force applied to the specimen of 434 N by the UTS of 31 MPa, result from the tensile tests performed in Subchapter 4.2.

The failure behaviour for all the rounded V-notch 45° specimens is an initial brittle break, 45° oriented, where the crack starts and grows and then a ductile break, orthogonal to the longitudinal axis of the specimens, when the resistant cross section is no more enough to sustain the applied load.

In the images below (Figure 4.4.3.8, Figure 4.4.3.9, Figure 4.4.3.10) it is possible to see the 90VR1PA12\_-1\_6 broken specimen as the example of the 90° rounded V-notch broken specimens:

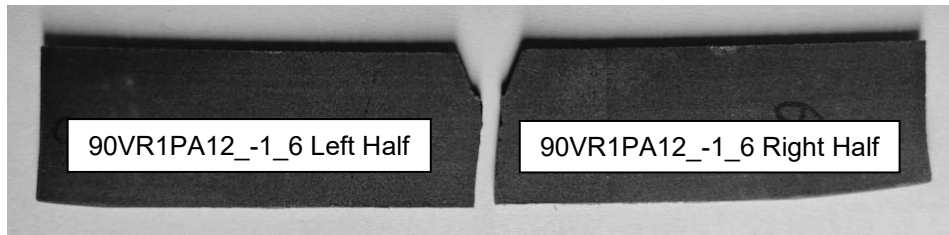


Figure 4.4.3.8: View of the 90VR1PA12\_-1\_6 broken specimen.

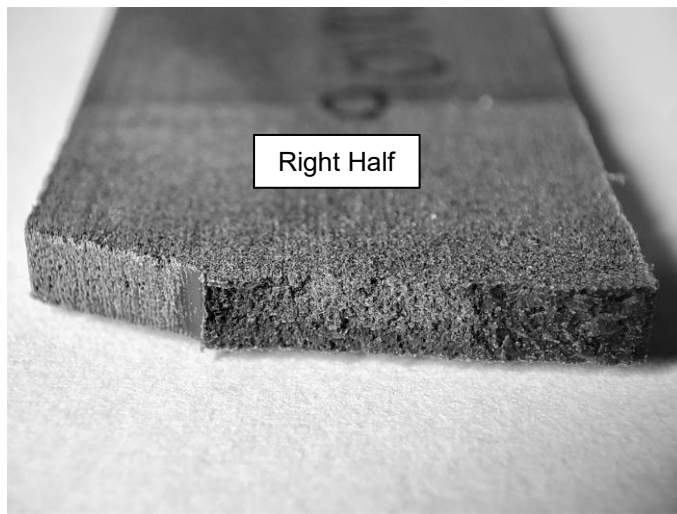


Figure 4.4.3.9: View of the right half (Figure 4.4.3.8) of the 90VR1PA12\_-1\_6 broken specimen.

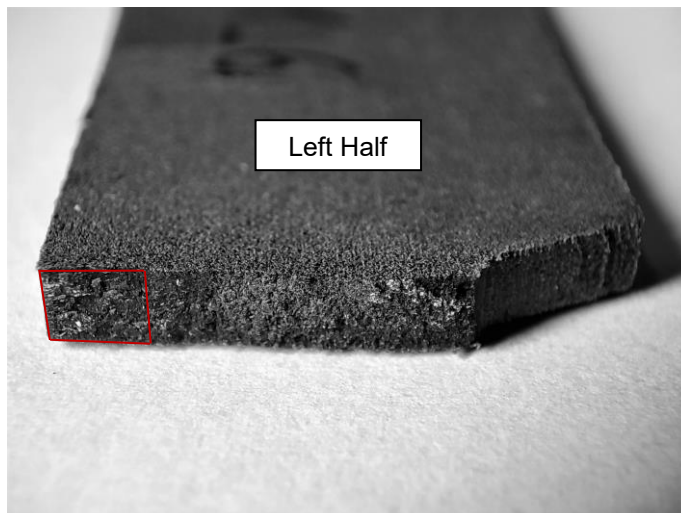


Figure 4.4.3.10: View of the left half (Figure 4.4.3.8) of the 90VR1PA12\_-1\_6 broken specimen. In red has been highlighted, approximately, the resistant cross section that should be no more able to sustain the load applied to the specimen, calculated dividing the amplitude force applied to the specimen of 487 N by the UTS of 37 MPa, result from the tensile tests performed in Subchapter 4.2.

In the 90° oriented rounded V-notch specimens it is difficult to distinguish between the initial brittle break when the crack starts and grows and the final ductile break, when the resistant cross section is no more enough to sustain the applied load.

### 4.5 Fatigue tests of sharp V-notch specimens

In this subchapter have been presented the fatigue tests of the PA12 sharp V-notch specimens that have been performed. The specimens have been printed with the SLS technology as explained in the Subchapter 4.1.

#### 4.5.1 Specimens dimensions and preparation

The detailed dimensions of the sharp V-notch specimens that have been used for fatigue tests are shown in the image below (Figure 4.5.1.1):

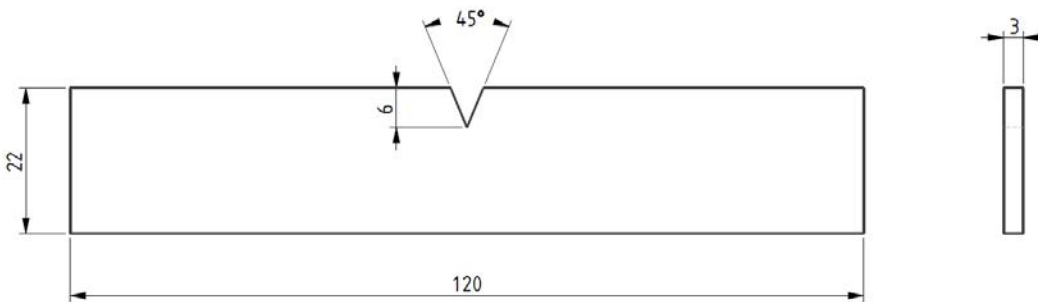


Figure 4.5.1.1: 2D technical drawing of the sharp V-notch specimens that have been used for fatigue tests.

After the sandblast operation (Subchapter 4.1), common for all the SLS printed parts used in this thesis work, only for the 90° orientation specimens, due to the warping occurred during the printing process, have been straightened the opposite sides to the sharp V-notches of all the specimens using the “Proxxon PF 360” milling machine (Figure 4.4.1.8, Subchapter 4.4.1).

After all the 90° specimens have been straightened, a picture of every specimen with a calliper nearby has been taken with a Canon reflex with the aim of measuring the width under the V-notch’s apex thanks to an image elaboration post-process. Measuring the specimen’s widths under the sharp V-notches with a calliper would have led to inaccurate measurements. To post-process the pictures has been used the opensource software “ImageJ” with a used procedure very similar to the one explained in Subchapter 4.4.1 for the measurement of the fillet radii of the rounded V-notches.

In the image below (Figure 4.5.1.2) it is possible to see an example of measurement that have been performed. The images of all the measured specimens have been reported in Annex G.

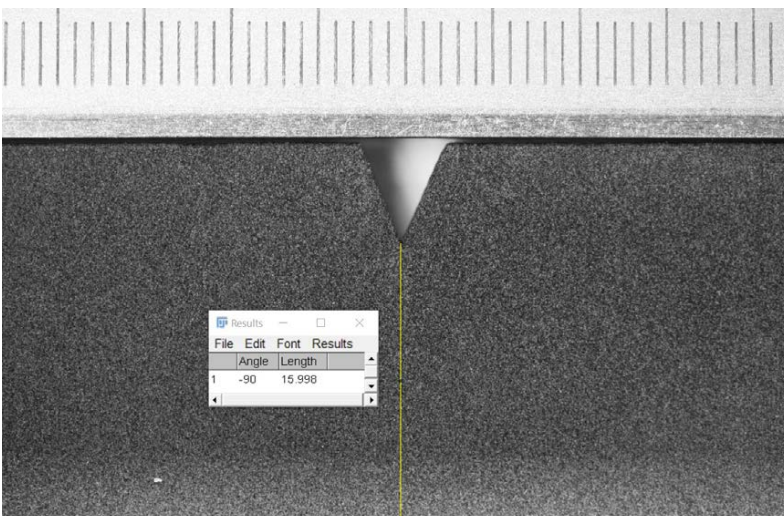


Figure 4.5.1.2: Measurement of the 0VR0PA12\_-1\_1 specimen’s width under the sharp V-notch.

In the table below (Table 4.5.1.1) have been summarized the width, the thickness and the relative cross sectional area in the centre of the specimen, immediately below the V-notch’s apex, of all the specimens that have been tested. The measures of thicknesses have been taken with a calliper, the



measures of the widths under the V-notches apexes have been taken with the image post-processing procedure mentioned above.

Specimen's name	Width [mm]	Thickness [mm]	Area [mm <sup>2</sup> ]
0VR0PA12_-1_1	16.00	2.95	47.20
0VR0PA12_-1_5	16.20	3.06	49.57
0VR0PA12_-1_2	16.00	2.90	46.40
0VR0PA12_-1_4	16.17	2.95	47.70
0VR0PA12_-1_6	16.16	2.95	47.67
0VR0PA12_-1_7	16.03	2.90	46.49
0VR0PA12_-1_8	16.04	2.95	47.32
0VR0PA12_-1_3	16.15	3.02	48.77
45VR0PA12_-1_1	15.61	2.82	44.02
45VR0PA12_-1_4	15.68	2.85	44.69
45VR0PA12_-1_2	15.79	2.88	45.48
45VR0PA12_-1_3	15.82	2.93	46.35
45VR0PA12_-1_5	15.86	2.87	45.52
45VR0PA12_-1_6	15.72	2.84	44.64
45VR0PA12_-1_7	15.82	2.92	46.19
45VR0PA12_-1_8	15.79	2.86	45.16
90VR0PA12_-1_1	12.70	2.94	37.34
90VR0PA12_-1_4	13.99	2.99	41.83
90VR0PA12_1_1BIS	14.21	3.03	43.06
90VR0PA12_-1_2	13.60	2.98	40.53
90VR0PA12_-1_3	14.46	3.04	43.96
90VR0PA12_-1_5	14.99	3.05	45.72
90VR0PA12_-1_6	14.86	3.03	45.03
90VR0PA12_-1_7	14.23	3.00	42.69
90VR0PA12_-1_8	15.18	3.03	46.00

Table 4.5.1.1: Measures of all the PA12 sharp V-notch specimens that have been used for the fatigue tests.

## 4.5.2 Tests set-up description

Have been tested almost eight specimens for each of the three printing orientations: 0°, 45°, 90°. The printing orientations are the same ones described in the Subchapter 4.2.2 for the tensile tests (Figure 4.2.2.1).

Has been used the very same Schenck resonance machine and the very same set-up described in Subchapter 4.3.2 for the fatigue tests of the plain specimens.

In the table below have been summarized some parameters common for all the fatigue tests of the sharp V-notch specimens performed (Table 4.5.2.1):

Room's temperature range [°C]	23 - 27
Specimens temperature range [°C]	21 - 27
Compressed air average pressure [bar]	1.1
Fatigue load cycles frequencies range [Hz]	14.7 – 18.9
Fatigue load cycles ratio [I]	-1
Load cell values dispersion average [N]	± 5

Table 4.5.2.1: Common parameters for all the fatigue tests of the sharp V-notch specimens performed.



### 4.5.3 Tests results

In the tables below (Table 4.5.3.1, Table 4.5.3.2, Table 4.5.3.3) have been summarized the results of the fatigue tests of the sharp V-notch specimens that have been performed. The names of the specimens are designed as follow:

- The first number specifies the print orientation: 0° or 45° or 90° (Figure 4.2.2.1).
- “VR0” specifies that it is a V-notch specimen with a 0 mm fillet radius.
- “PA12” specifies the material of the specimen.
- “-1” specifies the load ratio of the fatigue cycles applied to the specimen.
- The last number specifies the specimen's number.

Due to the working principle of the Schenck resonance machine, the load cycles started always from 0N amplitude and then the amplitude increased until the regime value was reached. To take in account these transient amplitude cycles has been decided to sum to the regime amplitude cycles half of the transient amplitude cycles.

The index “I” in the tables below can be 0 or 1: 0 means that the specimen broke and 1 means that the specimen did a runout, without breaking.

Specimen's name	R	F <sub>a</sub> [N]	σ <sub>a</sub> [MPa]	N. Cycles transient	N. Cycles total	I	F [Hz]	Temp. [°C]
0VR0PA12_-1_1	-1	368	<b>7.8</b>	4465	<b>3475</b>	0	18.3	23/24
0VR0PA12_-1_5	-1	397	<b>8.0</b>	4366	<b>2652</b>	0	18.4	25
0VR0PA12_-1_2	-1	278	<b>6.0</b>	4166	<b>16623</b>	0	17.3	24
0VR0PA12_-1_4	-1	286	<b>6.0</b>	4901	<b>12911</b>	0	17.5	24/25
0VR0PA12_-1_6	-1	215	<b>4.5</b>	5378	<b>240292</b>	0	16.4	23
0VR0PA12_-1_7	-1	209	<b>4.5</b>	5231	<b>165232</b>	0	16.2	23
0VR0PA12_-1_8	-1	166	<b>3.5</b>	4745	<b>2992754</b>	1	15.2	21
0VR0PA12_-1_3	-1	146	<b>3.0</b>	4441	<b>1997793</b>	1	14.7	23/25

Table 4.5.3.1: Results of fatigue tests of sharp V-notch specimens with 0° print orientation.

Specimen's name	R	F <sub>a</sub> [N]	σ <sub>a</sub> [MPa]	N. Cycles transient	N. Cycles total	I	F [Hz]	Temp. [°C]
45VR0PA12_-1_1	-1	396	<b>9.0</b>	4135	<b>13115</b>	0	18.5	23
45VR0PA12_-1_4	-1	402	<b>9.0</b>	4341	<b>17988</b>	0	18.6	25/26
45VR0PA12_-1_2	-1	318	<b>7.0</b>	4457	<b>122831</b>	0	17.8	22/24
45VR0PA12_-1_3	-1	324	<b>7.0</b>	4769	<b>123988</b>	0	17.8	26/27
45VR0PA12_-1_5	-1	273	<b>6.0</b>	4866	<b>142200</b>	0	17.3	25/26
45VR0PA12_-1_6	-1	268	<b>6.0</b>	4526	<b>90891</b>	0	17.2	24/25
45VR0PA12_-1_7	-1	185	<b>4.0</b>	14753	<b>7480531</b>	1	15.8	22
45VR0PA12_-1_8	-1	217	<b>4.8</b>	10574	<b>1286687</b>	0	16.4	23

Table 4.5.3.2: Results of fatigue tests of sharp V-notch specimens with 45° print orientation.

Specimen's name	R	F <sub>a</sub> [N]	σ <sub>a</sub> [MPa]	N. Cycles transient	N. Cycles total	I	F [Hz]	Temp. [°C]
90VR0PA12_-1_1	-1	411	<b>11.0</b>	4206	<b>20965</b>	0	18.5	24/25
90VR0PA12_-1_4	-1	460	<b>11.0</b>	4663	<b>8440</b>	0	18.9	26/27
90VR0PA12_-1_1BIS	-1	344	<b>8.0</b>	4316	<b>86568</b>	0	18.0	24/26
90VR0PA12_-1_2	-1	324	<b>8.0</b>	4353	<b>76945</b>	0	17.8	26/27
90VR0PA12_-1_3	-1	264	<b>6.0</b>	4698	<b>614569</b>	0	17.1	26/27
90VR0PA12_-1_5	-1	320	<b>7.0</b>	4405	<b>187445</b>	0	17.8	27
90VR0PA12_-1_6	-1	248	<b>5.5</b>	4815	<b>494755</b>	0	16.9	ND
90VR0PA12_-1_7	-1	213	<b>5.0</b>	5062	<b>2495966</b>	0	16.3	22.5
90VR0PA12_-1_8	-1	225	<b>4.9</b>	4587	<b>4997710</b>	1	16.6	24

Table 4.5.3.3: Results of fatigue tests of sharp V-notch specimens with 90° print orientation.

In the image below (Figure 4.5.3.1) it is possible to see the S-N chart of the sharp V-notch specimens tested with the three different orientations 0°, 45°, 90°.

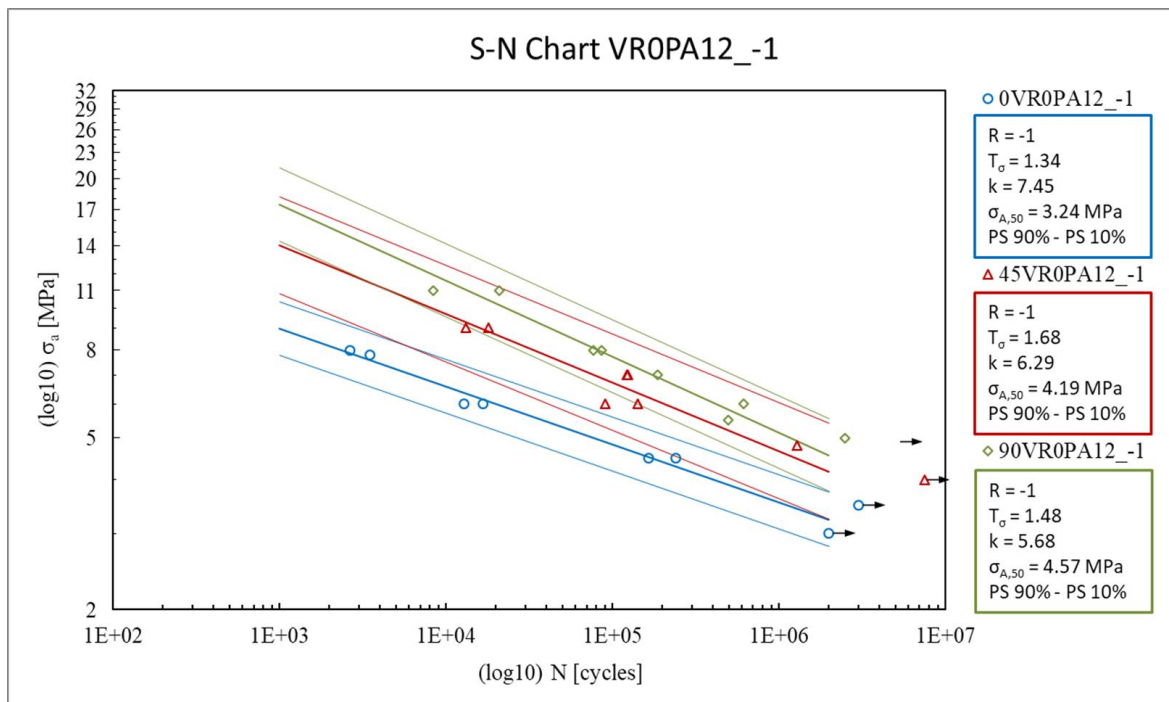


Figure 4.5.3.1: S-N chart of the sharp V-notch specimens tested with the three different orientations of 0°, 45° and 90°. The plotted amplitude stresses are the net stresses, referred to the central cross sections of the specimens under the V-notches apexes.

It is possible to see in figure 4.5.3.1 that, considering for example a constant value of stress amplitude applied to the specimens, the 90° oriented sharp V-notch specimens can survive more cycles than the 45° oriented sharp V-notch specimens that, in turn, can survive more cycles than the 0° oriented sharp V-notch specimens.

In the images below it is possible to see three examples of three broken sharp V-notch specimens, one for each of the three orientations considered.

In the images below (Figure 4.5.3.2, Figure 4.5.3.3, Figure 4.5.3.4) it is possible to see the 0VR0PA12\_-1\_2 broken specimen as the example of the 0° sharp V-notch broken specimens:

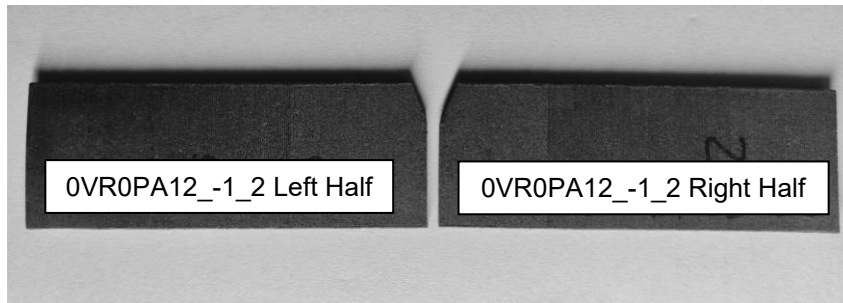


Figure 4.5.3.2: View of the 0VR0PA12\_-1\_2 broken specimen.

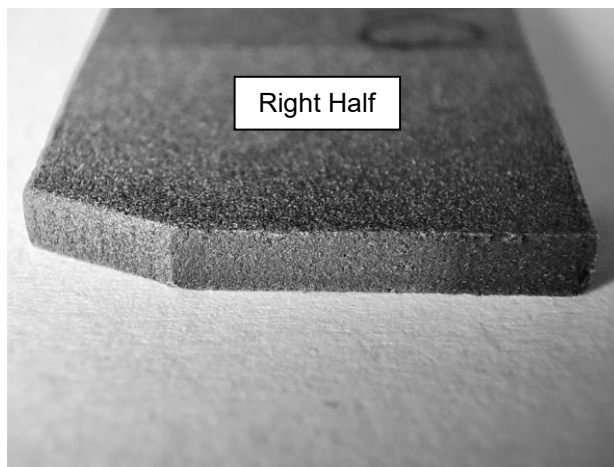


Figure 4.5.3.3: View of the right half (Figure 4.5.3.2) of the 0VR0PA12\_-1\_2 broken specimen.



Figure 4.5.3.4: View of the left half (Figure 4.5.3.2) of the 0VR0PA12\_-1\_2 broken specimen.

The failure behaviour for all the sharp V-notch 0° specimens is a brittle break orthogonal to the longitudinal axis of the specimens. It is very difficult to distinguish between the initial brittle break when the crack starts and grows and the final brittle break, when the resistant cross section is no more enough to sustain the applied load.

In the images below (Figure 4.5.3.5, Figure 4.5.3.06, Figure 4.5.3.7) it is possible to see the 45VR0PA12\_-1\_5 broken specimen as the example of the 45° sharp V-notch broken specimens:

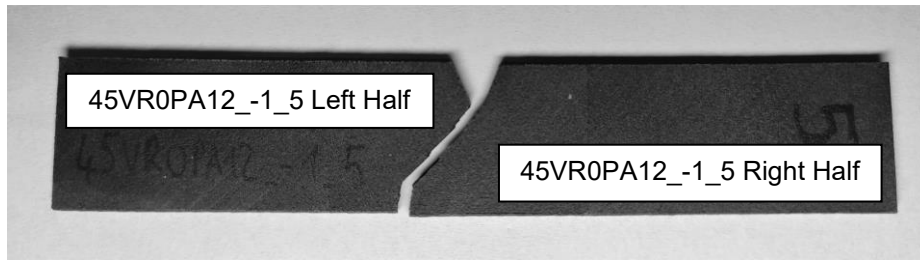


Figure 4.5.3.5: View of the 45VR0PA12\_-1\_5 broken specimen.

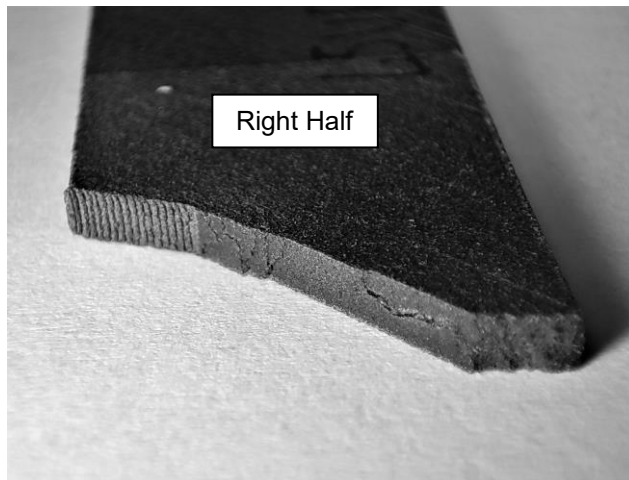


Figure 4.5.3.6: View of the right half (Figure 4.5.3.5) of the 45VR0PA12\_-1\_5 broken specimen.

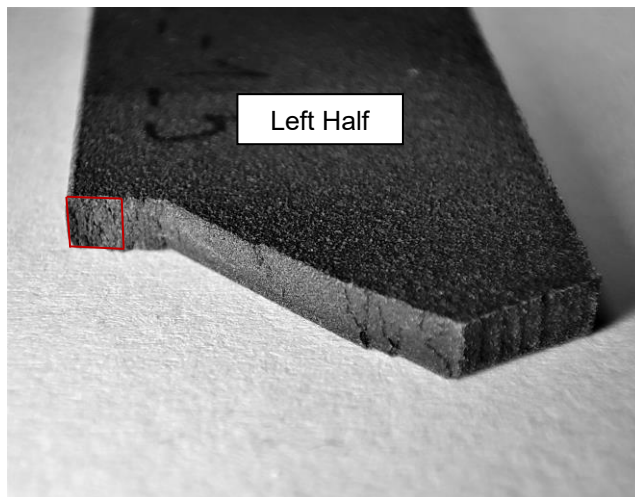


Figure 4.5.3.7: View of the left half (Figure 4.5.3.5) of the 45VR0PA12\_-1\_5 broken specimen. In red has been highlighted, approximately, the resistant cross section that should be no more able to sustain the load applied to the specimen, calculated dividing the amplitude force applied to the specimen of 273 N by the UTS of 31 MPa, result from the tensile tests performed in Subchapter 4.2.

The failure behaviour for all the sharp V-notch 45° specimens is an initial brittle break, 45° oriented, where the crack starts and grows and then a ductile break, orthogonal to the longitudinal axis of the specimens, when the resistant cross section is no more enough to sustain the applied load.

In the images below (Figure 4.5.3.8, Figure 4.5.3.9, Figure 4.5.3.10) it is possible to see the 90VR0PA12\_-1\_2 broken specimen as the example of the 90° sharp V-notch broken specimens:

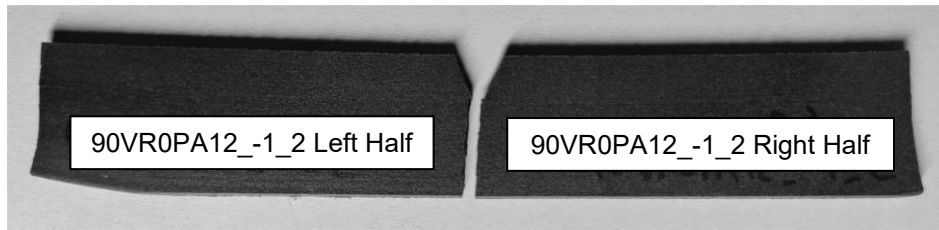


Figure 4.5.3.8: View of the 90VR0PA12\_-1\_2 broken specimen.

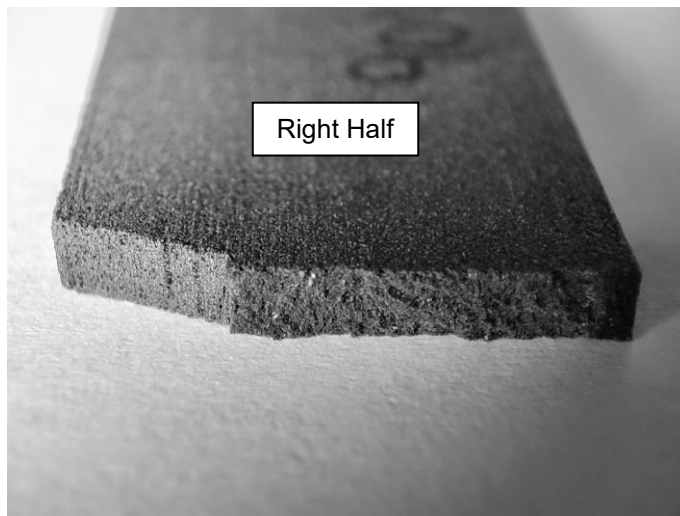


Figure 4.5.3.9: View of the right half (Figure 4.5.3.8) of the 90VR0PA12\_-1\_2 broken specimen.

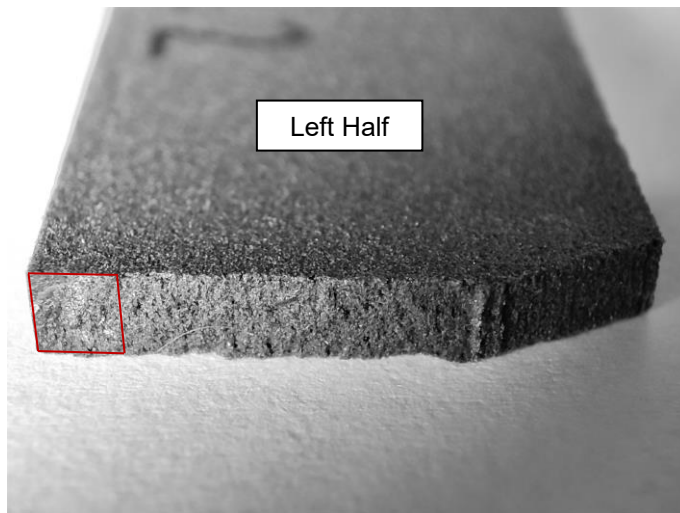


Figure 4.5.3.10: View of the left half (Figure 4.5.3.8) of the 90VR0PA12\_-1\_2 broken specimen. In red has been highlighted, approximately, the resistant cross section that should be no more able to sustain the load applied to the specimen, calculated dividing the amplitude force applied to the specimen of 324 N by the UTS of 37 MPa, result from the tensile tests performed in Subchapter 4.2.

In the 90° oriented rounded V-notch specimens it is difficult to distinguish between the initial brittle break when the crack starts and growths and the final ductile break, when the resistant cross section is no more enough to sustain the applied load.

## 4.6 S-N charts of all the tested specimens grouped by orientations: 0°, 45°, 90°

In this subchapter have been presented three charts that summarize the results of the fatigue tests of the plain specimens ("LPA12") (Subchapter 4.3), of the rounded V-notch specimens ("VR1PA12") (Subchapter 4.4) and of the sharp V-notch specimens ("VR0PA12") (Subchapter 4.5) that have been performed. The idea of these charts is to group the results no more following the specimen's geometries but following the print orientations angles.

A reminder of the three different orientations that have been considered is given in the image below (Figure 4.6.1):

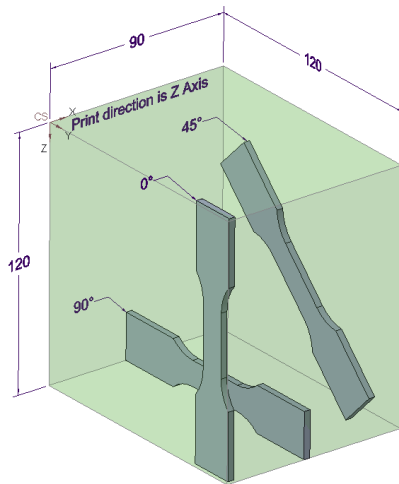


Figure 4.6.1: Specimens 0°, 45°, 90° print orientations with respect to the Z-axis print direction.

In Figure 4.6.2 it is possible to see the S-N chart of the plain specimens, rounded V-notch specimens and sharp V-notch specimens that have been printed with the 0° orientation.

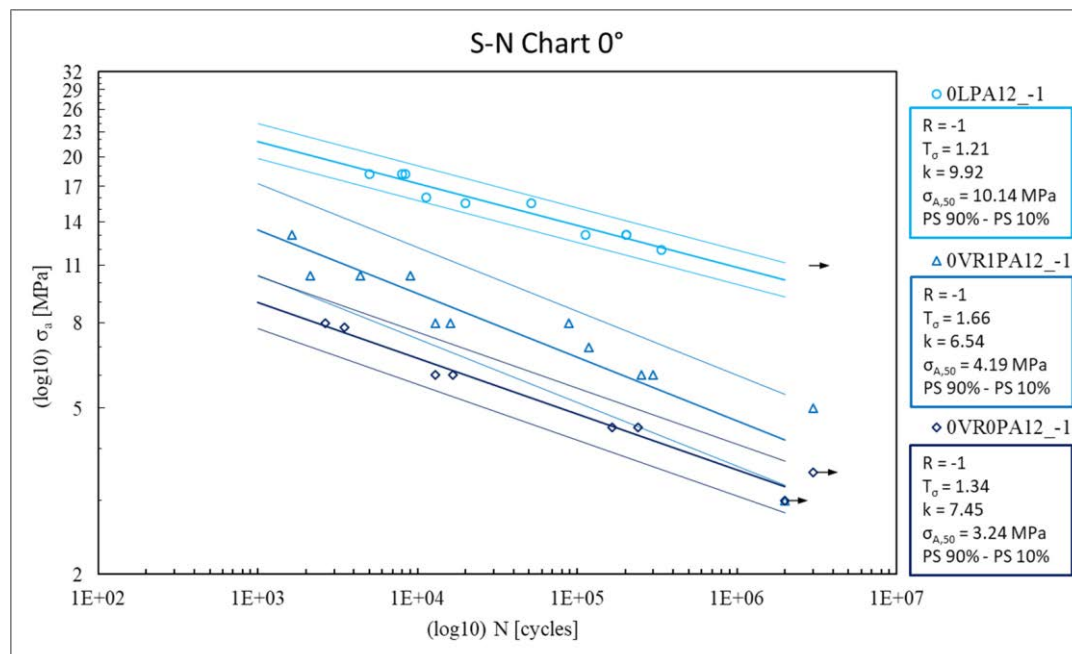


Figure 4.6.2: S-N chart of the plain specimens, rounded V-notch specimens and sharp V-notch specimens that have been printed with the 0° orientation. The plotted amplitude stresses are the net stresses, referred to the central cross sections of the specimens under the V-notches apices.

It is possible to see in figure 4.6.2 that, considering for example a constant value of stress amplitude applied to the specimens, as expected, the 0LPA12\_-1 specimens can survive more cycles than the 0VR1PA12\_-1 specimens that, in turn, can survive more cycles than the 0VR0PA12\_-1 specimens.



In Figure 4.6.3 it is possible to see the S-N chart of the plain specimens, rounded V-notch specimens and sharp V-notch specimens that have been printed with the 45° orientation.

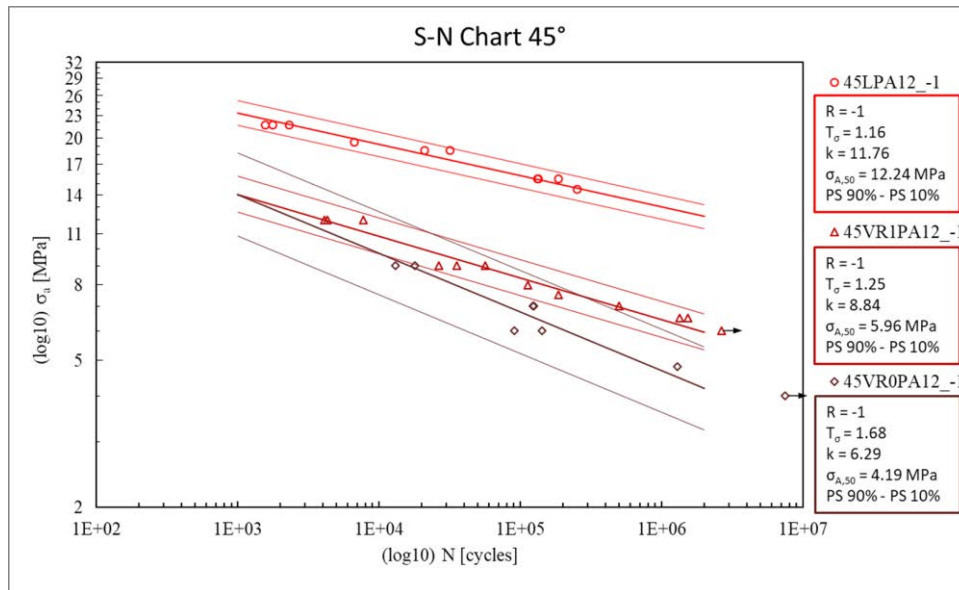


Figure 4.6.3: S-N chart of the plain specimens, rounded V-notch specimens and sharp V-notch specimens that have been printed with the 45° orientation. The plotted amplitude stresses are the net stresses, referred to the central cross sections of the specimens under the V-notches apices.

It is possible to see in figure 4.6.3 that, considering for example a constant value of stress amplitude applied to the specimens, as expected, the 45LPA12\_-1 specimens can survive more cycles than the 45VR1PA12\_-1 specimens that, in turn, can survive more cycles than the 45VR0PA12\_-1 specimens.

In Figure 4.6.4 it is possible to see the S-N chart of the plain specimens, rounded V-notch specimens and sharp V-notch specimens that have been printed with the 90° orientation.

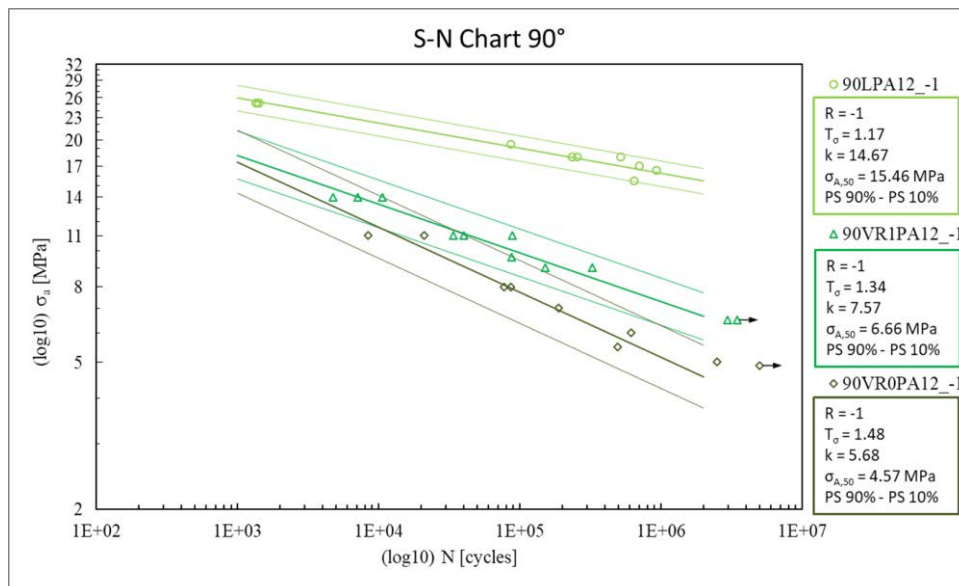


Figure 4.6.4: S-N chart of the plain specimens, rounded V-notch specimens and sharp V-notch specimens that have been printed with the 90° orientation. The plotted amplitude stresses are the net stresses, referred to the central cross sections of the specimens under the V-notches apices.

It is possible to see in figure 4.6.4 that, considering for example a constant value of stress amplitude applied to the specimens, as expected, the 90LPA12\_-1 specimens can survive more cycles than the 90VR1PA12\_-1 specimens that, in turn, can survive more cycles than the 90VR0PA12\_-1 specimens.

## 4.7 Calibration of the control radius Rc for the PA12 material

In this subchapter have been used the results of the fatigue tests of the plain (subchapter 4.3) and of the sharp V-notch (subchapter 4.5) PA12 specimens to calibrate the control radius ( $R_c$ ) of the PA12 material. The control radius is a property of the specific material considered and it is a key parameter to know to apply the SED (Strain Energy Density) local approach. The SED local approach has been developed by P. Lazzarin and R. Zambardi (Department of Management and Engineering, University of Padova) [29] and it is useful to predict the static and fatigue behaviour of sharp V-notched components. The approach considers the strain energy density, averaged in a structural volume with radius equal to  $R_c$ , as the entity that controls the failure. The approach is based on the Neuber's idea of the structural elementary volume: the materials are sensitive about the stresses averaged in a structural volume; the dimensions of the structural volume is a property of the material [27].

### 4.7.1 Calculation of the NSIF $K_1$ for the PA12 sharp V-notch specimen's geometry

The calculation of the  $K_1$  is the first step to be done for estimating the control radius ( $R_c$ ) of a specific material.  $K_1$  is the linear elastic notch stress intensity factor (NSIF) for a V-notch with a certain opening angle ( $2\alpha$ ) and subjected to a Mode I load application (Figure 4.7.1.1).

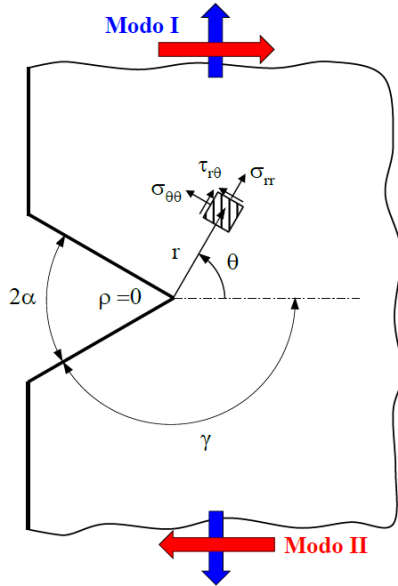


Figure 4.7.1.1: General sharp V-notch geometry with Mode I (blue) and Mode II (red) load application types [27].

Under the following working hypothesis [27]:

- Planar load application types: Mode I and Mode II.
- Small material's plastic zone: to be able to work with the linear elastic equations.
- Sharp notch:  $0 \leq \rho \leq 4 \cdot a_0$ , where  $a_0$  is the critical defect dimension, property of the material: if the defect is smaller than  $a_0$ , the fatigue life of the component is not affected by the defect.

The  $K_1$  definition given by Gross and Mendelson (1972) is:

$$K_1 = \sqrt{2 \cdot \pi} \cdot \lim_{r \rightarrow 0^+} (r^{1-\lambda_1} \cdot \sigma_{\theta\theta}) \text{ with } \theta = 0 \quad (\text{Eq. 4.7.1.1}) [27]$$

The opening angle ( $2\alpha$ ) enters in the  $K_1$  definition with the  $\lambda_1$  parameter:  $(1 - \lambda_1)$  is the singularity degree of the V-notch local stress field generated by a Mode I load application,  $(1 - \lambda_1)$  is a function of  $2\alpha$  (Williams, 1952) (Figure 4.7.1.2).

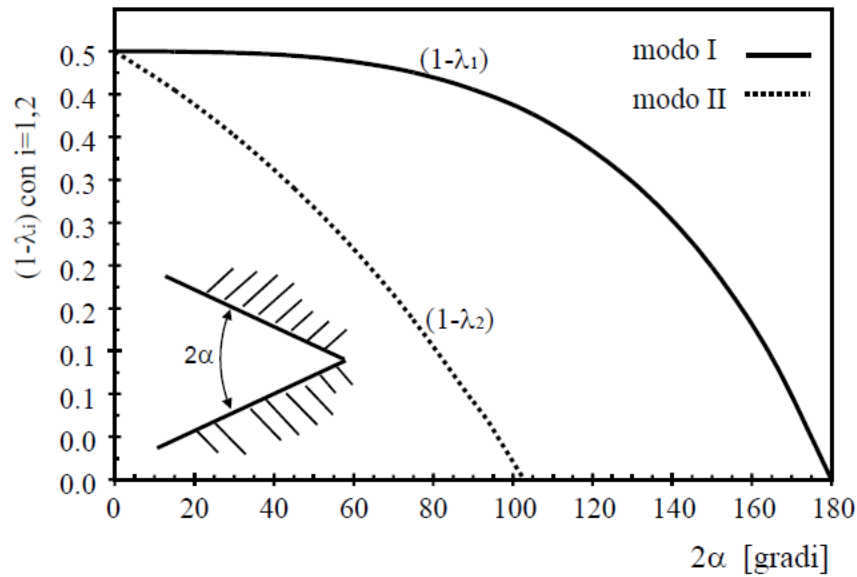


Figure 4.7.1.2:  $(1 - \lambda_i) - 2\alpha$  chart with  $i = 1$  for Mode I and  $i = 2$  for Mode II [27].

Has been decided to calculate the  $K_I$  for an averaged sharp V-notch geometry that it is possible to see in Figure 4.7.1.3. Has been calculated the average of the specimen's net widths under the notch's apexes (15,32 mm, Figure 4.7.1.3) and has been calculated the average of the specimen's thicknesses (2,95 mm, Figure 4.7.1.3) following the measurements of all the specimens that have been done and that have been summarized in Table 4.5.1.1. To determine the gross width of the averaged specimen has been add 6 mm to the calculated average net width. 6 mm is the V-notch depth, constant in all the printed specimens. Has been left the length of the averaged specimen equal to the nominal one: 120 mm. In the end, it is important to mention that in Figure 4.7.1.3 it is possible to see the  $45^\circ$  V-notch opening angle ( $2\alpha$  of Figure 4.7.1.1).

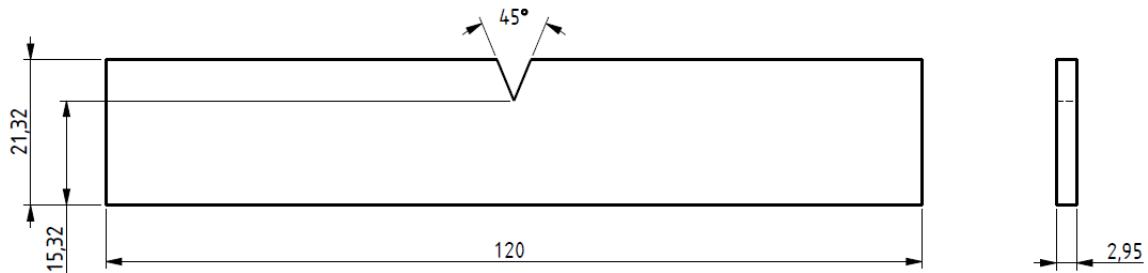


Figure 4.7.1.3: Averaged geometry of the sharp V-notch specimens.

Have been used two different approaches to calculate the  $K_I$  with the finite element tool: the standard approach, that calculates the  $K_I$  applying its definition (Eq. 4.7.1) and so that implies the use of a very fine mesh, and the *Peak Stress Method (PSM)* [27], an innovative approach developed by Giovanni Meneghetti (Machine Design Professor of Padova's University) that implies the use of a coarse mesh with respect to the mesh that must be used with the standard approach. The *Peak Stress Method* has been developed with the idea in mind that it should have been a fast and accurate method useful for the companies.

### Standard approach

For the F.E.M. analysis that have been performed to calculate the  $K_1$  with the standard approach, has been used the *Ansys Mechanical APDL* software and have been used the parameters summarized in the table below (Table 4.7.1.1):

Element Type	PLANE182
Element Technology (K1)	Simple Enhanced Strain
Element Behaviour (K3)	Plane Stress
Minimum element size [mm]	10 <sup>-4</sup>
Young's modulus (PA12, Table 4.2.3.1) [MPa]	1210
Poisson's ratio (PA12, Table 4.2.3.1) [/]	0.41

Table 4.7.1.1: Parameters that have been used in the F.E.M. analysis for calculating  $K_1$  with the standard approach.

The symmetry of the geometry with respect to the V-notch has been considered and used to lower the computational time of the analysis. Have been applied the boundary conditions that it is possible to see in Figure 4.7.1.4. In particular:

- Has been applied a gross tensile pressure of 0.7186 MPa on the left edge of the specimen (line between KPs 4 and 6) to have 1 MPa of net pressure in the specimen's section under the V-notch's apex (line between KPs 2 and 3).
- Has been applied a symmetry boundary constraint on the right edge of the specimen, under the V-notch's apex (line between KPs 2 and 3).
- Has been applied a vertical (Y-axis) displacement constraint in the KP 6 to eliminate the lability of the structure.

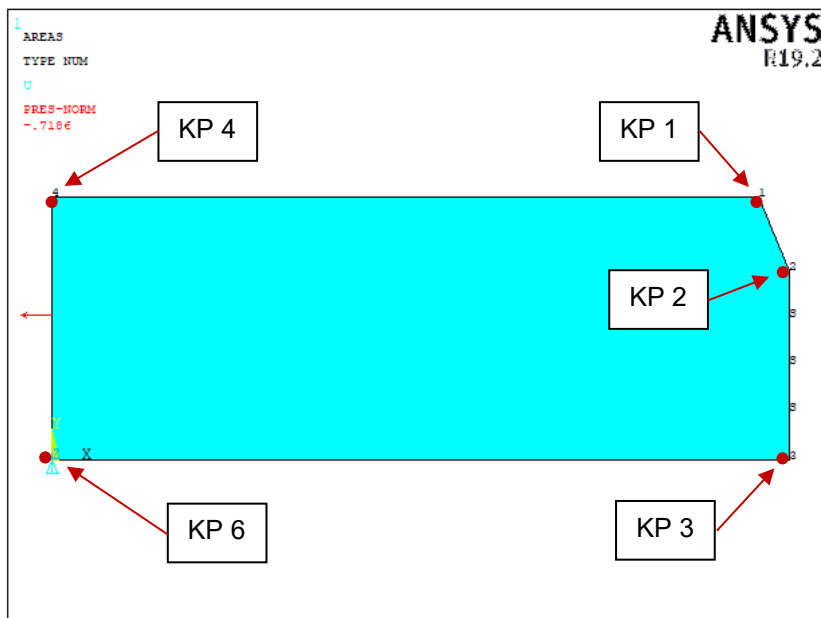


Figure 4.7.1.4: Boundary conditions of the F.E.M. analysis for calculating the  $K_1$  with the standard method.

In the images below (Figure 4.7.1.5, Figure 4.7.1.6) it is possible to see the mesh that have been created and used in the F.E.M. analysis. The mesh has been created with the *Ansys free-mesh generation* algorithm specifying only the desired element dimensions in the five key points represented in Figure 4.7.1.4:

- KP 2 specified element size:  $10^{-4}$  mm
- KPs 1 and 3 specified element size:  $10^{-2}$  mm
- KPs 4 and 6 specified element size:  $10^{-1}$  mm

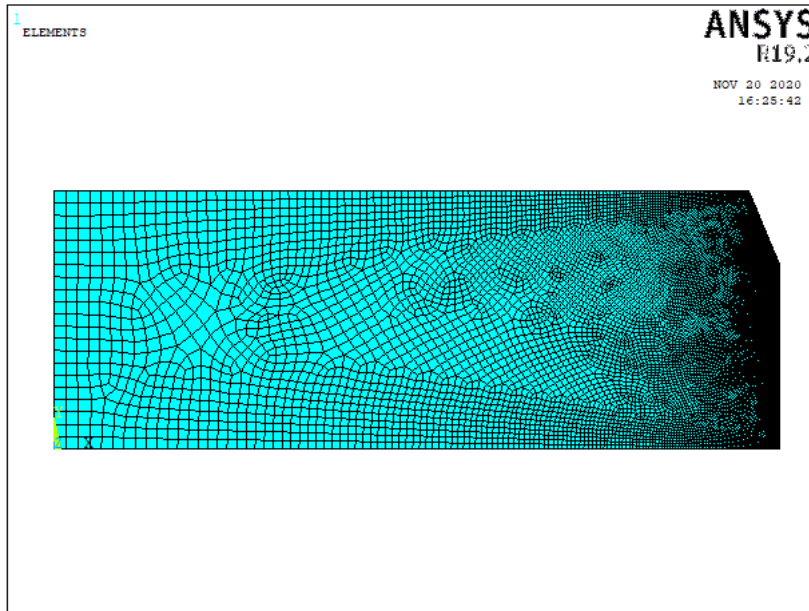


Figure 4.7.1.5: View of the mesh used in the F.E.M. analysis for calculating the  $K_1$  with the standard method.

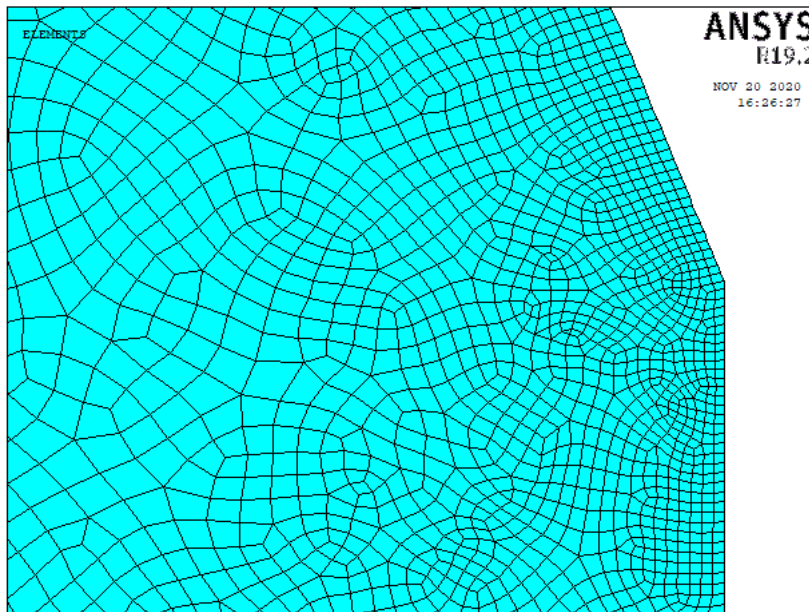


Figure 4.7.1.6: Zoom view of the mesh used in the F.E.M. analysis for calculating the  $K_1$  with the standard method. The zoom has been done in the proximity of the V-notch's apex and the smaller elements that it is possible to see are the  $10^{-4}$  minimum size elements of the mesh.

After the solution has been done, have been created a local coordinate system with the origin in the KP 2 (V-notch's apex) and with the X-axis directed from KP 2 to KP 3, so along the right side line of the specimen, under the V-notch's apex. Have been then listed all the coordinates of the nodes of the right side line of the specimen, under the V-notch's apex (line between KPs 2 and 3), with respect to the new local coordinate system created: The node in the KP 2 (V-notch's apex) had X-coordinate equal to zero and the node in the KP 3 had the X-coordinate equal to 15.32.

Have been then listed the X components of stress, this time with respect to the global coordinate system, of the very same nodes attached to the line that goes from KP 2 to KP 3.

Has been then calculated the  $K_1$  with the definition given before (Eq. 4.7.1) using  $\lambda_1 = 0.5050$ ; the  $\lambda_1$  value for  $2\alpha = 45^\circ$  that can be found in *Table 2* of [27].

In the image below (Figure 4.7.1.7) it is possible to see the chart that represents the analysis results:

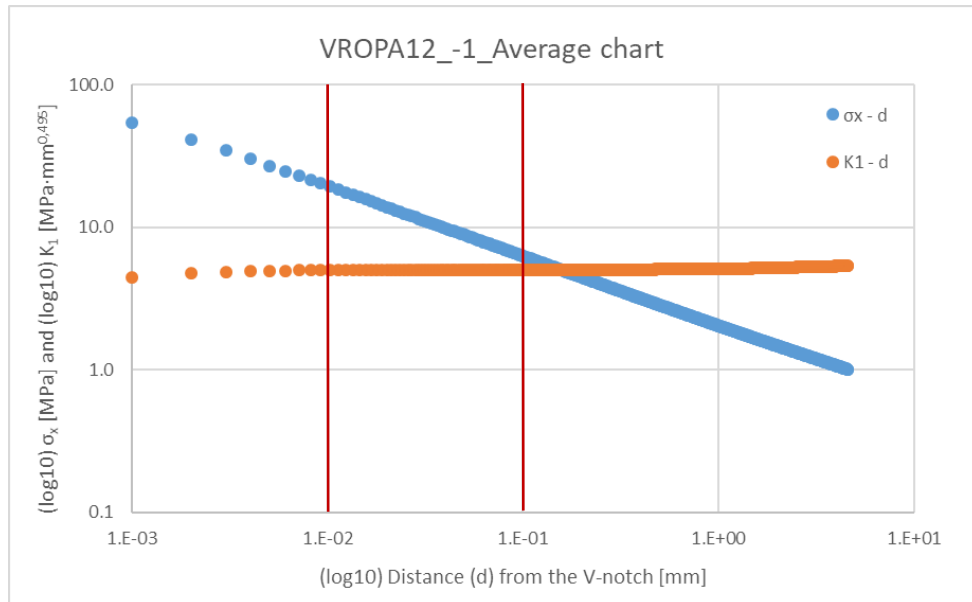


Figure 4.7.1.7: Chart with the distance from the KP 2 (V-notch's apex) in abscissa axis and with node's X component of stress and node's calculated  $K_1$  in the ordinate axis.

Has been decided to take the  $K_1$  value that comes from the average of the  $K_1$  values of the nodes with a distance, from the KP 2, between 0.01 mm and 0.1 mm (red lines in Figure 4.7.1.7).

The value is:  $K_1 = 5.040 \text{ MPa} \cdot \text{mm}^{0.495}$

#### Peak Stress Method approach

For the F.E.M. analysis that have been performed to calculate the  $K_1$  with the *Peak Stress Method*, have been used the *Ansys Mechanical APDL* software and have been used the parameters summarized in the table below (Table 4.7.1.2):

Element Type	PLANE182
Element Technology (K1)	Simple Enhanced Strain
Element Behaviour (K3)	Plane Stress
Global element size [mm]	1.8
Young's modulus (PA12, Table 4.2.3.1) [MPa]	1210
Poisson's ratio (PA12, Table 4.2.3.1) [/]	0.41

Table 4.7.1.2: Parameters that have been used in the F.E.M. analysis for calculating  $K_1$  with the *Peak Stress Method*.

The symmetry of the geometry with respect to the V-notch has been considered and used to lower the computational time of the analysis. Have been applied the very same boundary conditions, that it is possible to see in Figure 4.7.1.4, that have been used for calculating the  $K_1$  with the standard method.



In the image below (Figure 4.7.1.8) it is possible to see the mesh that have been created and used in the F.E.M. analysis. The mesh has been created with the *Ansys free-mesh generation* algorithm specifying only the *global element size* of 1.8 mm.

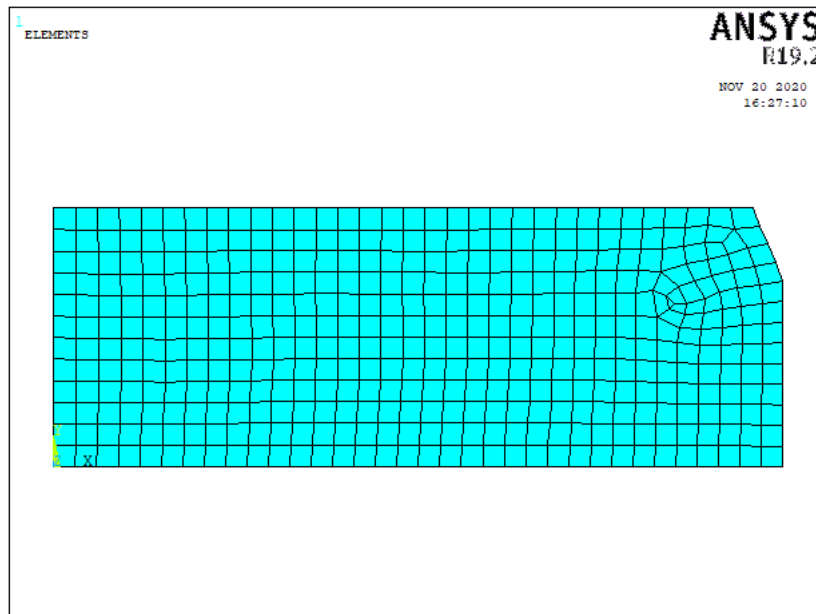


Figure 4.7.1.8: View of the mesh used in the F.E.M. analysis for calculating the  $K_1$  with the *Peak Stress Method*.

After the solution has been done, has been plotted the nodal solution of 1<sup>st</sup> Principal Stress (Figure 4.7.1.9):

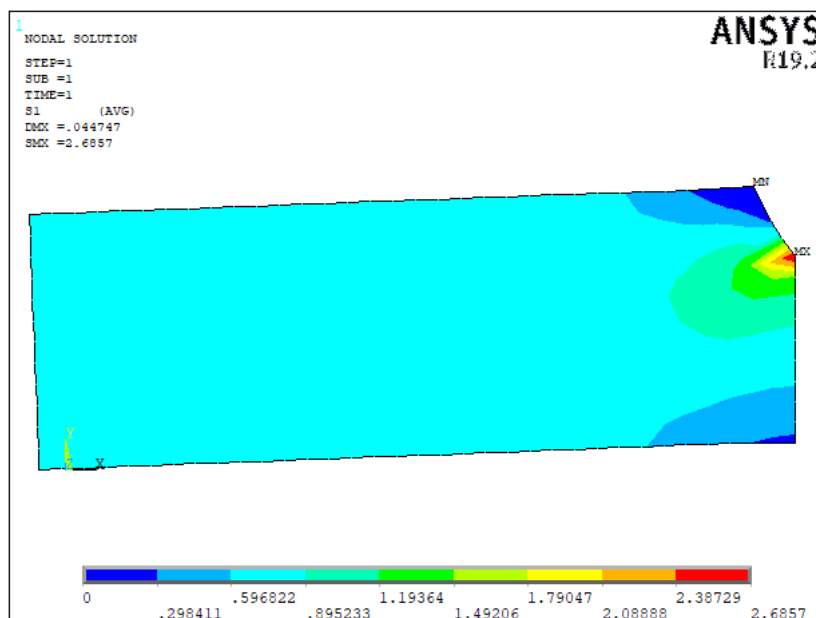


Figure 4.7.1.9: 1<sup>st</sup> Principal Stress result of the F.E.M. analysis.

As it is possible to see, the maximum 1<sup>st</sup> Principal Stress is in the KP 2; the KP of interest of the V-notch's apex. The stress value is 2.6857 MPa.

Has been then used the following formula to calculate the  $K_1$ :

$$K_1 = K_{FE}^* \cdot \sigma_{peak} \cdot d^{(1-\lambda_1)} \quad (\text{Eq. 4.7.1.2}) [27]$$

Where:

- $K_{FE}^*$  is a constant, function of the software used, of the element type used, of the mesh shape used. For the *Ansys* software, for the *PLANE182* element type with *Element Technology (K1)* set as *Simple Enhanced Strain*, for the mesh automatically generated with the *Ansys free-mesh generation* algorithm specifying only the *global element size*, it is possible to use:  $K_{FE}^* = 1.38$  [27].
- $\sigma_{peak} = 2.6857$  MPa is the 1<sup>st</sup> Principal Stress in the V-notch's apex (KP 2 in this analysis), result of the F.E.M. analysis.
- $d = 1.8$  mm is the *global element size* specified in the F.E.M. analysis.
- $(1 - \lambda_1)$  is the singularity degree of the V-notch local stress field generated by a Mode I load application. Has been used  $\lambda_1 = 0.5050$ ; the  $\lambda_1$  value for  $2\alpha = 45^\circ$  that can be found in *Table 2* of [27].

#### N.B.

There is a criteria to choose properly the *global element size*,  $d$ , parameter. The criteria is that the ratio  $a/d$  must be greater than 3 to obtain  $K_{FE}^* = 1.38 \pm 5\%$ , where  $a$  is the reference dimension of the notched component considered [27]. In this work has been considered the V-notch depth of 6 mm as the reference dimension of the notched component.

In the table below (Table 4.7.1.3) are summarized the result of the  $K_1$  calculated with both the standard method and the PSM method:

	d [mm]	a/d [/]	$K_{FE}^*$	$\lambda_1$ ( $2\alpha=45^\circ$ )	$\sigma_{a,net}$ [MPa]	$\sigma_{a,gross}$ [MPa]	$\sigma_{peak}$ [MPa]	$K_1$ [MPa·mm <sup>0.495</sup> ]	Difference [%]
PSM	1.8	3.3	1.38	0.5050	1	0.7186	2.6857	<b>4.958</b>	1.63
Standard	10 <sup>-4</sup>	/	/	0.5050	1	0.7186	/	<b>5.040</b>	

Table 4.7.1.3: Results of the  $K_1$  calculated with both the standard method and the PSM method.

It is possible to see that the PSM is a very valid approach to use because, if everything has been set properly, the error with respect to the standard method is minimum. The PSM is much faster than the standard method, not only because of the bigger element size and so the less time for the computer to solve the F.E.M. analysis, but also for the post-processing of the analysis's results: to read the 1<sup>st</sup> Principal Stress in the apex of the notch is much faster than to build the chart of Figure 4.7.1.7.

#### 4.7.2 Calculation of the control radius Rc for the PA12 material

It is possible to calculate the control radius Rc for a specific material by imposing equality between the values of the strain energy density of the plain material and of the strain energy density of the notched material. The values have to be calculated at a chosen reference number of cycles [27].

The range of the strain energy density for a notched material, with a pure Mode I of load application type, can be calculated with the following formula:

$$\Delta W_{notched} = C_W \cdot \frac{e_1}{E} \cdot \frac{\Delta K_1^2}{R_c^{2 \cdot (1-\lambda_1)}} \quad (\text{Eq. 4.7.2.1}) [27]$$

The range of the strain energy density for a plain material can be calculated with the following formula:

$$\Delta W_{plain} = C_W \cdot \frac{\Delta \sigma^2}{2 \cdot E} \quad (\text{Eq. 4.7.2.2}) [27]$$

The first term of both the above presented equations is the coefficient  $C_W$ . It is a coefficient that must be used when a range of energy is calculated and it is function of the load ratio of the fatigue cycles,  $R$ , that has been considered. The formula for  $C_W$  is given below:

$$C_W = \frac{1+R^2}{(1-R)^2} \quad (\text{Eq. 4.7.2.3}) [28]$$

It is possible to calculate that  $C_W = 1$  if  $R = 0$  and that  $C_W = 0.5$  if  $R = -1$ . This last case ( $C_W = 0.5$  for  $R = -1$ ) is the case that has been considered in the developing of this thesis work.

By imposing the equality:

$$\Delta W_{notched} = \Delta W_{plain} \quad (\text{Eq. 4.7.2.4})$$

It is possible to develop the final formula for the calculus of Rc:

$$R_c = \left( \sqrt{2 \cdot e_1} \cdot \left( \frac{\Delta K_{1D}}{\Delta \sigma_{D,plain}} \right) \right)^{\frac{1}{1-\lambda_1}} \quad (\text{Eq. 4.7.2.5}) [27]$$

It is possible to notice that  $C_W$  disappears in the equation (4.7.2.5) because it is present in both the equations (4.7.2.1) and (4.7.2.2).

The formula for evaluating the  $e_1$  term of the equation (4.7.2.5) is given below:

$$e_1 = \frac{I_1}{4 \cdot \lambda_1 \cdot \gamma} \quad (\text{Eq. 4.7.2.6}) [29]$$

Where:

- The value of the integral  $I_1$  can be found in *Table 1* of [29]. For the developing of this thesis work has been considered  $I_1 = 0.9918$  that is the  $I_1$  value for  $2\alpha=45^\circ$ , for the Plane Stress condition and for  $\nu = 0.3$ .
- $\gamma = (7/8)\pi$  rad (*Table 1* of [29] or from Figure 4.7.1.1 knowing  $2\alpha=45^\circ$ ).
- $\lambda_1 = 0.5050$  for  $2\alpha=45^\circ$  (*Table 1* of [29] or *Table 2* of [27]).

The  $\Delta K_{1D}$  term of the equation (4.7.2.5) is the range of the NSIF of the notched material for Mode I load application type, calculated at a chosen reference number of cycles  $D$ .

The  $\Delta \sigma_D$  term of the equation (4.7.2.5) is the stress range of the plain material calculated at a chosen reference number of cycles  $D$ .

For the developing of this thesis work has been chosen a reference number of cycles  $D = 1000000$  cycles.

To calculate the  $\Delta K_{1D}$  for the sharp V-notch specimens with 0°, 45°, 90° orientations has been:

- Calculated the  $\sigma_D$  at the reference number of cycles from the S-N chart, result of the fatigue tests, that can be found in Subchapter 4.5.3 (Figure 4.5.3.1):  

$$\sigma_{A,50}^k \cdot N_A = \sigma_D^k \cdot N_D \quad (\text{Eq. 4.7.2.7})$$
- Calculated the stress range  $\Delta\sigma_D$  by doubling the previous calculated  $\sigma_D$  since the fatigue tests have been performed with a load ratio  $R = -1$ .
- Calculated the range  $\Delta K_{1D}$  by multiplying the  $\Delta\sigma_D$  by the  $K_1$  value that has been found with the F.E.M. analysis of the previous Subchapter 4.7.1.

In the table below (Table 4.7.2.1) have been summarized the results of the calculation of the  $\Delta K_{1D}$  for the sharp V-notch specimens with 0°, 45°, 90° orientations:

	$\sigma_{A,50}$ [MPa]	k	Reference number of cycles (D)	$\sigma_D$ [MPa]	$\Delta\sigma_D$ [MPa]	$K_1$ [MPa·mm <sup>0.495</sup> ]	$\Delta K_{1D}$ [MPa·mm <sup>0.495</sup> ]
0°	3.24	7.45	1000000	3.56	7.11	5.040	<b>35.844</b>
45°	4.19	6.29	1000000	4.68	9.36	5.040	<b>47.156</b>
90°	4.57	5.68	1000000	5.16	10.33	5.040	<b>52.045</b>

Table 4.7.2.1: Results of the calculation of the  $\Delta K_{1D}$  for the sharp V-notch specimens with 0°, 45°, 90° orientations.

To calculate the  $\Delta\sigma_D$  for the plain specimens with 0°, 45°, 90° orientations has been:

- Calculated the  $\sigma_D$  at the reference number of cycles from the S-N chart, result of the fatigue tests, that can be found in Subchapter 4.3.3 (Figure 4.3.3.1) (Eq. 4.7.2.7).
- Calculated the stress range  $\Delta\sigma_D$  by doubling the previous calculated  $\sigma_D$  since the fatigue tests have been performed with a load ratio  $R = -1$ .

In the table below (Table 4.7.2.2) have been summarized the results of the calculation of the  $\Delta\sigma_D$  for the plain specimens with 0°, 45°, 90° orientations:

	$\sigma_{A,50}$ [MPa]	k	Reference number of cycles (D)	$\sigma_D$ [MPa]	$\Delta\sigma_D$ [MPa]
0°	10.14	9.92	1000000	10.87	<b>21.75</b>
45°	12.24	11.76	1000000	12.98	<b>25.97</b>
90°	15.46	14.67	1000000	16.21	<b>32.42</b>

Table 4.7.2.2: Results of the calculation of the  $\Delta\sigma_D$  for the plain specimens with 0°, 45°, 90° orientations.

To calculate the  $R_c$  for the PA12 material with 0°, 45°, 90° print orientations have been used the equation (4.7.2.5). In the table below (Table 4.7.2.3) have been summarized the calculations results:

Plane Stress	Reference number of cycles (D)	$\Delta\sigma_{D, \text{plain}}$ [MPa]	$\Delta K_{1D}$ [MPa·mm <sup>0.495</sup> ]	$\lambda_1$ (2α=45°)	$\gamma$ (2α=45°) [RAD]	$I_1$ (γ) with ν=0,3	$e_1$ (2α=45°)	$R_c$ [mm]
0°	1000000	21.75	35.844	0.5050	2.7489	0.9918	0.1786	<b>0.97</b>
45°	1000000	25.97	47.156	0.5050	2.7489	0.9918	0.1786	<b>1.18</b>
90°	1000000	32.42	52.045	0.5050	2.7489	0.9918	0.1786	<b>0.92</b>

Table 4.7.2.3: Results of the calculation of the  $R_c$  for the PA12 material with 0°, 45°, 90° print orientations.

## 4.8 SED approach for fatigue design of components made by PA12 material

In this subchapter have been built the  $\Delta W$ -N charts for the PA12 material, with the three different print orientations  $0^\circ$ ,  $45^\circ$  and  $90^\circ$ , using the fatigue test's results of the plain specimens and of the sharp V-notch specimens. Have been then applied the SED approach to the rounded V-notch specimens to validate the  $\Delta W$ -N charts developed, thanks to the data of the fatigue tests of the rounded V-notch specimens that have been performed. In both the sharp V-notch specimens and the rounded V-notch specimens the V-notch opening angle  $2\alpha$  is equal to  $45^\circ$ . However, a very big advantage of the SED approach is that it would be possible to compare the behaviour of components with different V-notch opening angles because the quantities to compare are energies with the very same unit of measure. On the other hand, with a more traditional NSIF approach it is not possible to compare the behaviour of components with different V-notch opening angles because the unit of measure of the NSIF is dependent from the opening angle  $2\alpha$  of the V-notch (Subchapter 4.7.1).

### 4.8.1 Creation of the $\Delta W$ -N charts for the PA12 material

In this subchapter have been built the  $\Delta W$ -N charts for the PA12 material with the three different print orientations  $0^\circ$ ,  $45^\circ$  and  $90^\circ$ . The charts can be used to predict the fatigue life of a notched PA12 component with the SED local approach.

To build the  $\Delta W$ -N charts have been elaborated together the results of the fatigue tests of plain specimens and the results of the fatigue tests of the sharp V-notch specimens.

To calculate the range of the strain energy density,  $\Delta W$ , for the sharp V-notch specimens has been used the equation (4.7.2.1).

To calculate the range of the strain energy density,  $\Delta W$ , for the plain specimens has been used the equation (4.7.2.2).

In the table below (Table 4.8.1.1) have been summarized all the parameter's values that have been used in the equations (4.7.2.1) and (4.7.2.2):

Print orientation	Young's modulus (PA12) [MPa]	Cw (R = -1)	$\lambda_1$ ( $2\alpha=45^\circ$ )	$e_1$ ( $2\alpha=45^\circ$ )	Rc [mm]
$0^\circ$	1210	0.5	0.5050	0.179	0.97
$45^\circ$	1210	0.5	0.5050	0.179	1.18
$90^\circ$	1210	0.5	0.5050	0.179	0.92

Table 4.8.1.1: Parameter's values that have been used in the equations (4.7.2.1) and (4.7.2.2).

In the table below (Table 4.8.1.2) have been summarized the calculations that have been done for estimating  $\Delta W$  for the plain specimens with  $0^\circ$  print orientation:

Specimen's name	$\sigma_a$ [MPa] (Table 4.3.3.1)	$\Delta\sigma$ [MPa]	$\Delta W$ [Nmm/mm <sup>3</sup> ]	Cycles to failure (Table 4.3.3.1)
0LPA12_-1_1	18.2	36.4	<b>0.27</b>	<b>8029</b>
0LPA12_-1_2	18.2	36.4	<b>0.27</b>	<b>8379</b>
0LPA12_-1_3	18.2	36.4	<b>0.27</b>	<b>5029</b>
0LPA12_-1_4	13.0	26.0	<b>0.14</b>	<b>203590</b>
0LPA12_-1_5	13.0	26.0	<b>0.14</b>	<b>112617</b>
0LPA12_-1_6	13.0	26.0	<b>0.14</b>	<b>203015</b>
0LPA12_-1_7	16.0	32.0	<b>0.21</b>	<b>11285</b>
0LPA12_-1_8	15.5	31.0	<b>0.20</b>	<b>19913</b>
0LPA12_-1_9	15.5	31.0	<b>0.20</b>	<b>51723</b>
0LPA12_-1_10	12.0	24.0	<b>0.12</b>	<b>335176</b>
0LPA12_-1_11	11.0	22.0	<b>0.10</b>	<b>2676901</b>
0LPA12_-1_12	11.5	23.0	<b>0.11</b>	<b>774619</b>

Table 4.8.1.2:  $\Delta W$  calculations for the  $0^\circ$  plain specimens.

In the table below (Table 4.8.1.3) have been summarized the calculations that have been done for estimating  $\Delta W$  for the sharp V-notch specimens with  $0^\circ$  print orientation:

Specimen's name	$\sigma_a$ [MPa] (Table 4.5.3.1)	$\Delta\sigma$ [MPa]	$\Delta K_I$ [MPa $\cdot$ mm <sup>0.495</sup> ]	$\Delta W$ [Nmm/mm <sup>3</sup> ]	Cycles to failure (Table 4.5.3.1)
0VR0PA12_-1_1	7.8	15.6	78.62	<b>0.4712</b>	<b>3475</b>
0VR0PA12_-1_5	8.0	16.0	80.64	<b>0.4957</b>	<b>2652</b>
0VR0PA12_-1_2	6.0	12.0	60.48	<b>0.2788</b>	<b>16623</b>
0VR0PA12_-1_4	6.0	12.0	60.48	<b>0.2788</b>	<b>12911</b>
0VR0PA12_-1_6	4.5	9.0	45.36	<b>0.1568</b>	<b>240292</b>
0VR0PA12_-1_7	4.5	9.0	45.36	<b>0.1568</b>	<b>165232</b>
0VR0PA12_-1_8	3.5	7.0	35.28	<b>0.0949</b>	<b>2992754</b>
0VR0PA12_-1_3	3.0	6.0	30.24	<b>0.0697</b>	<b>1997793</b>

Table 4.8.1.3:  $\Delta W$  calculations for the  $0^\circ$  sharp V-notch specimens.

In the image below (Figure 4.8.1.1) it is possible to see the  $\Delta W$ -N chart of the plain specimens plus the sharp V-notch specimens with the  $0^\circ$  print orientation.

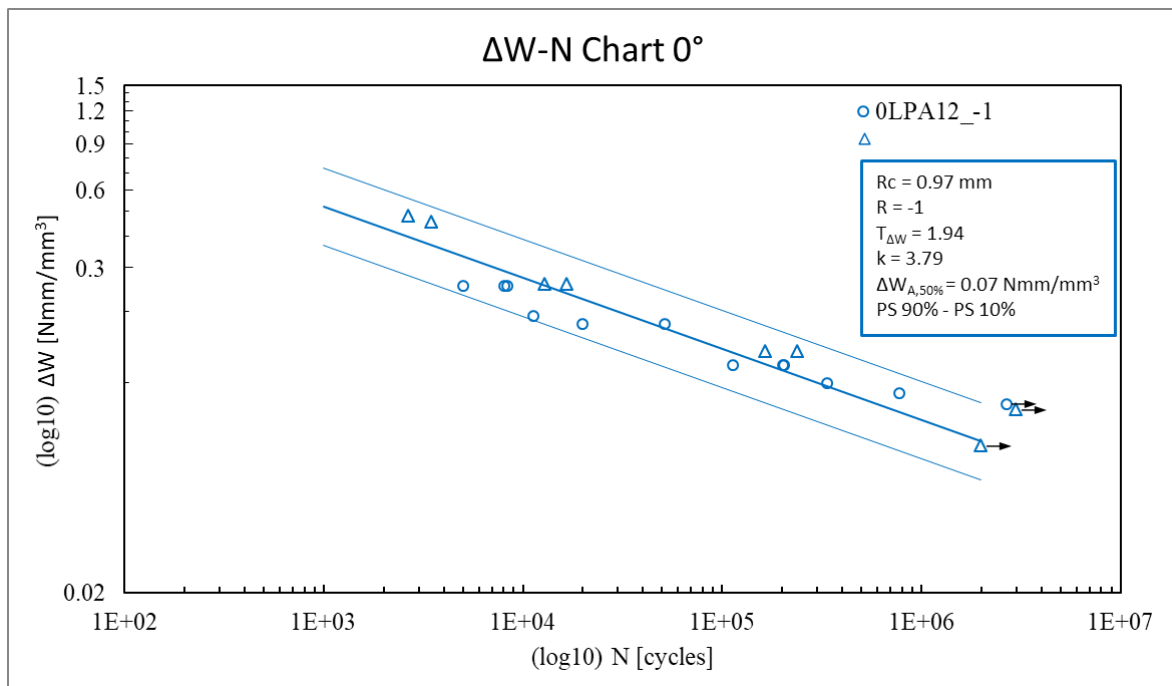


Figure 4.8.1.1:  $\Delta W$ -N chart of the plain specimens plus the sharp V-notch specimens with the  $0^\circ$  print orientation.



In the table below (Table 4.8.1.4) have been summarized the calculations that have been done for estimating  $\Delta W$  for the plain specimens with 45° print orientation:

Specimen's name	$\sigma_a$ [MPa] (Table 4.3.3.2)	$\Delta\sigma$ [MPa]	$\Delta W$ [Nmm/mm <sup>3</sup> ]	Cycles to failure (Table 4.3.3.2)
45LPA12_-1_1	21.7	43.4	<b>0.39</b>	<b>1561</b>
45LPA12_-1_2	21.7	43.4	<b>0.39</b>	<b>2313</b>
45LPA12_-1_3	21.7	43.4	<b>0.39</b>	<b>1773</b>
45LPA12_-1_4	15.5	31.0	<b>0.20</b>	<b>131638</b>
45LPA12_-1_5	15.5	31.0	<b>0.20</b>	<b>186091</b>
45LPA12_-1_6	15.5	31.0	<b>0.20</b>	<b>133702</b>
45LPA12_-1_7	18.5	37.0	<b>0.28</b>	<b>21100</b>
45LPA12_-1_8	18.5	37.0	<b>0.28</b>	<b>31794</b>
45LPA12_-1_9	19.5	39.0	<b>0.31</b>	<b>6682</b>
45LPA12_-1_10	14.5	29.0	<b>0.17</b>	<b>253206</b>
45LPA12_-1_11	13.7	27.4	<b>0.16</b>	<b>605783</b>
45LPA12_-1_12	12.7	25.4	<b>0.13</b>	<b>669089</b>

Table 4.8.1.4:  $\Delta W$  calculations for the 45° plain specimens.

In the table below (Table 4.8.1.5) have been summarized the calculations that have been done for estimating  $\Delta W$  for the sharp V-notch specimens with 45° print orientation:

Specimen's name	$\sigma_a$ [MPa] (Table 4.5.3.2)	$\Delta\sigma$ [MPa]	$\Delta K_I$ [MPa·mm <sup>0.495</sup> ]	$\Delta W$ [Nmm/mm <sup>3</sup> ]	Cycles to failure (Table 4.5.3.2)
45VR0PA12_-1_1	9.0	18.0	90.72	<b>0.5168</b>	<b>13115</b>
45VR0PA12_-1_4	9.0	18.0	90.72	<b>0.5168</b>	<b>17988</b>
45VR0PA12_-1_2	7.0	14.0	70.56	<b>0.3126</b>	<b>122831</b>
45VR0PA12_-1_3	7.0	14.0	70.56	<b>0.3126</b>	<b>123988</b>
45VR0PA12_-1_5	6.0	12.0	60.48	<b>0.2297</b>	<b>142200</b>
45VR0PA12_-1_6	6.0	12.0	60.48	<b>0.2297</b>	<b>90891</b>
45VR0PA12_-1_7	4.0	8.0	40.32	<b>0.1021</b>	<b>7480531</b>
45VR0PA12_-1_8	4.8	9.6	48.38	<b>0.1470</b>	<b>1286687</b>

Table 4.8.1.5:  $\Delta W$  calculations for the 45° sharp V-notch specimens.

In the image below (Figure 4.8.1.2) it is possible to see the  $\Delta W$ -N chart of the plain specimens plus the sharp V-notch specimens with the 45° print orientation.

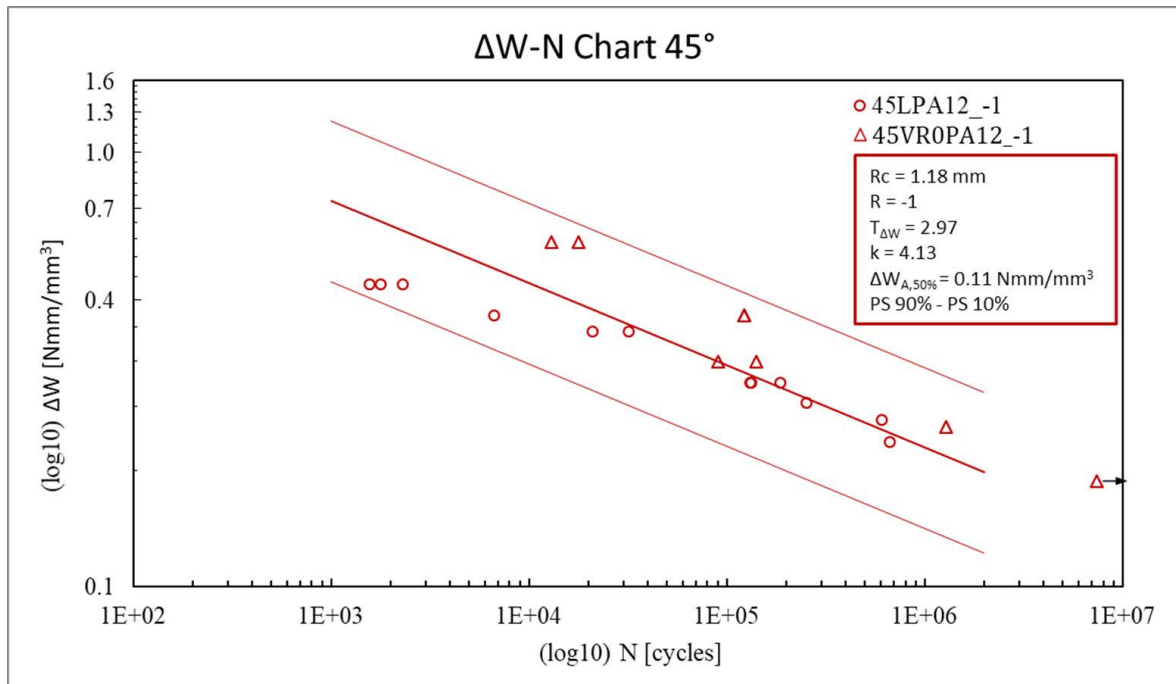


Figure 4.8.1.2:  $\Delta W$ -N chart of the plain specimens plus the sharp V-notch specimens with the 45° print orientation.

In the table below (Table 4.8.1.6) have been summarized the calculations that have been done for estimating  $\Delta W$  for the plain specimens with 90° print orientation:

Specimen's name	$\sigma_a$ [MPa] (Table 4.3.3.3)	$\Delta\sigma$ [MPa]	$\Delta W$ [Nmm/mm <sup>3</sup> ]	Cycles to failure (Table 4.3.3.3)
90LPA12_-1_1	25.2	50.4	<b>0.52</b>	<b>1359</b>
90LPA12_-1_2	25.2	50.4	<b>0.52</b>	<b>1425</b>
90LPA12_-1_3	25.2	50.4	<b>0.52</b>	<b>1364</b>
90LPA12_-1_4	18.0	36.0	<b>0.27</b>	<b>233669</b>
90LPA12_-1_5	18.0	36.0	<b>0.27</b>	<b>255601</b>
90LPA12_-1_6	18.0	36.0	<b>0.27</b>	<b>515940</b>
90LPA12_-1_7	19.5	39.0	<b>0.31</b>	<b>86522</b>
90LPA12_-1_10	16.5	33.0	<b>0.23</b>	<b>933175</b>
90LPA12_-1_11	17.0	34.0	<b>0.24</b>	<b>705224</b>
90LPA12_-1_12	15.5	31.0	<b>0.20</b>	<b>646846</b>
90LPA12_-1_13	21.0	42.0	<b>0.36</b>	<b>24419</b>
90LPA12_-1_14	19.5	39.0	<b>0.31</b>	<b>36638</b>

Table 4.8.1.6:  $\Delta W$  calculations for the 90° plain specimens.

In the table below (Table 4.8.1.7) have been summarized the calculations that have been done for estimating  $\Delta W$  for the sharp V-notch specimens with 90° print orientation:

Specimen's name	$\sigma_a$ [MPa] (Table 4.5.3.3)	$\Delta\sigma$ [MPa]	$\Delta K_1$ [MPa·mm <sup>0.495</sup> ]	$\Delta W$ [Nmm/mm <sup>3</sup> ]	Cycles to failure (Table 4.5.3.3)
90VR0PA12_-1_1	11.0	22.0	110.88	<b>0.9876</b>	<b>20965</b>
90VR0PA12_-1_4	11.0	22.0	110.88	<b>0.9876</b>	<b>8440</b>
90VR0PA12_1_1BIS	8.0	16.0	80.64	<b>0.5224</b>	<b>86568</b>
90VR0PA12_-1_2	8.0	16.0	80.64	<b>0.5224</b>	<b>76945</b>
90VR0PA12_-1_3	6.0	12.0	60.48	<b>0.2938</b>	<b>614569</b>
90VR0PA12_-1_5	7.0	14.0	70.56	<b>0.3999</b>	<b>187445</b>
90VR0PA12_-1_6	5.5	11.0	55.44	<b>0.2469</b>	<b>494755</b>
90VR0PA12_-1_7	5.0	10.0	50.40	<b>0.2041</b>	<b>2495966</b>
90VR0PA12_-1_8	4.9	9.8	49.39	<b>0.1960</b>	<b>4997710</b>

Table 4.8.1.7:  $\Delta W$  calculations for the 90° sharp V-notch specimens.

In the image below (Figure 4.8.1.3) it is possible to see the  $\Delta W$ -N chart of the plain specimens plus the sharp V-notch specimens with the 90° print orientation.

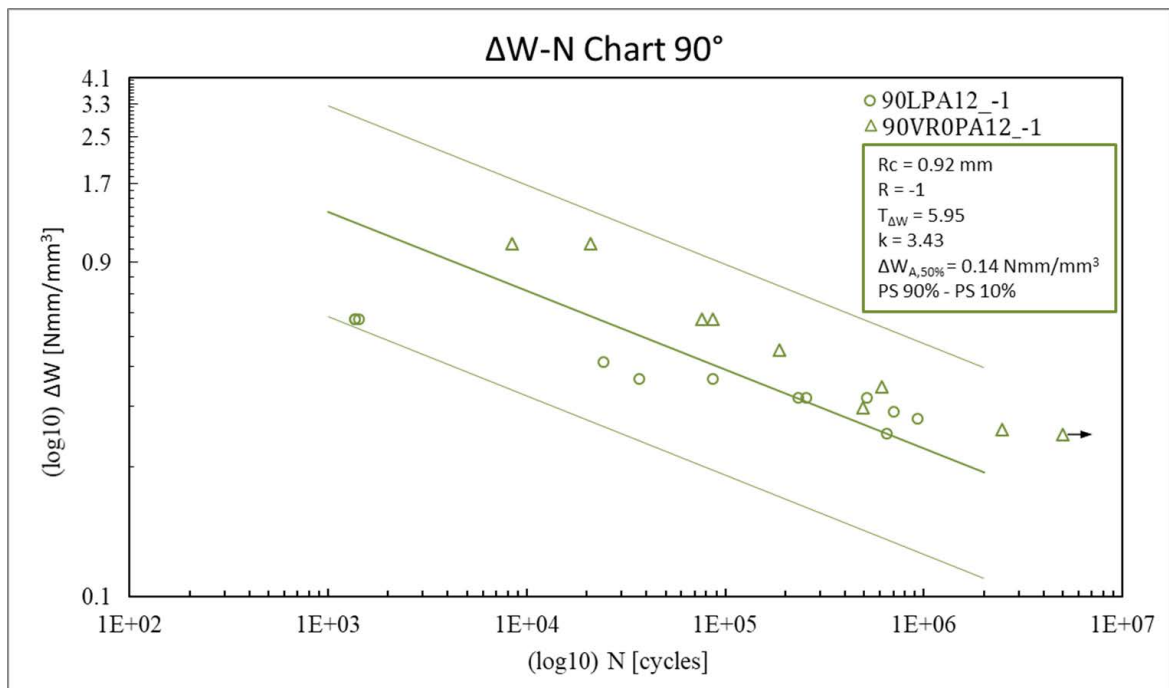


Figure 4.8.1.3:  $\Delta W$ -N chart of the plain specimens plus the sharp V-notch specimens with the 90° print orientation.

## 4.8.2 Application of the SED approach to the rounded V-notch specimens

Have been then applied the SED approach to the rounded V-notch specimens to validate the  $\Delta W-N$  charts developed (Subchapter 4.8.1), thanks to the data of the fatigue tests of the rounded V-notch specimens that have been performed.

The tests of the rounded V-notch specimens have been done with a fatigue load ratio  $R = -1$  and with a Mode I load application type (Subchapter 4.4).

Has been decided to consider an averaged rounded V-notch geometry that it is possible to see in Figure 4.8.2.1. Has been calculated the average of the specimen's net widths under the notch's apexes (15,23 mm, Figure 4.8.2.1) and has been calculated the average of the specimen's thicknesses (3,02 mm, Figure 4.8.2.1) following the measurements of all the specimens that have been done and that have been summarized in Table 4.4.1.1. To determine the gross width of the averaged specimen has been add 6 mm to the calculated average net width. 6 mm is the V-notch depth, almost constant in all the printed specimens. Has been left the length of the averaged specimen equal to the nominal one: 120 mm. In the end, it is important to mention that in Figure 4.8.2.1 it is possible to see the  $45^\circ$  V-notch opening angle ( $2\alpha$  of Figure 4.7.1.1).

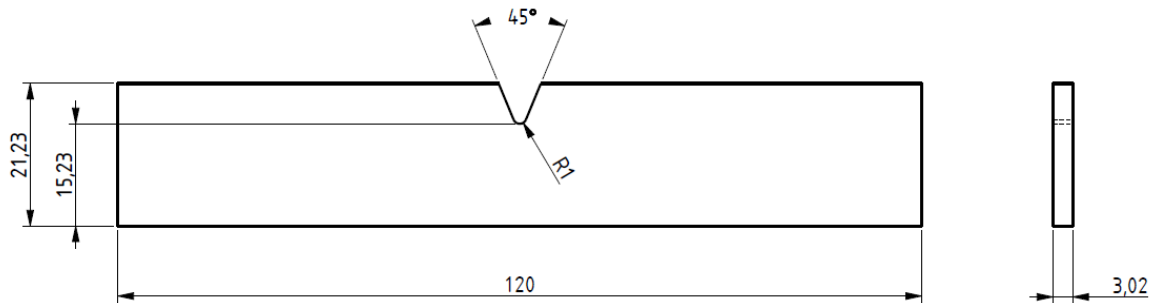


Figure 4.8.2.1: Averaged geometry of the rounded V-notch specimens.

The SED value is the strain energy density averaged in a control volume with a radius  $R_c$ . For a sharp V-notch with  $2\alpha$  opening angle and subjected to Mode I load application type, in a 2D view, the control volume becomes a circular sector with a radius  $R_c$  and with the centre in the V-notch apex point (Figure 4.8.2.2).

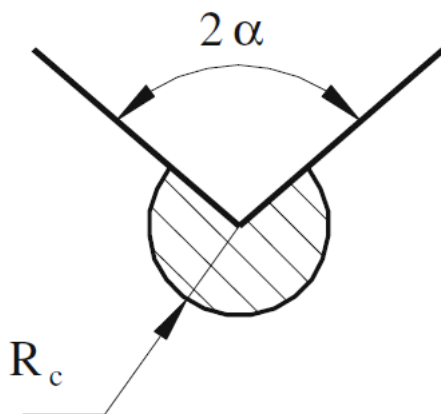


Figure 4.8.2.2: Control volume's area for a sharp V-notch with  $2\alpha$  opening angle and subjected to Mode I load application type (Fig. 2 of [30]).

However, for a rounded V-notch with  $2\alpha$  opening angle, with a fillet radius equal to  $\rho$  and subjected to Mode I load application type, the control volume's area becomes a circular sector with radius equal to  $R_c + r_0$  and centred in a point that is set back by  $r_0$  with respect to the V-notch's apex (Figure 4.8.2.3).

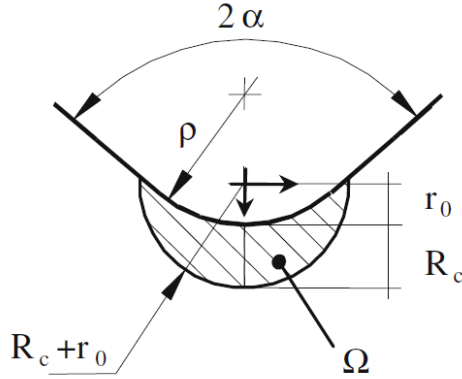


Figure 4.8.2.3: Control volume's area for a rounded V-notch with  $2\alpha$  opening angle, with a fillet radius equal to  $\rho$  and subjected to Mode I load application type (Fig. 2 of [30]).

The formulas to calculate  $r_0$  are:

$$r_0 = \frac{q-1}{q} \cdot \rho \quad (\text{Eq. 4.8.2.1}) [30]$$

Where:

$$q = \frac{2\pi-2\alpha}{\pi} \quad (\text{Eq. 4.8.2.2}) [30]$$

It is possible to see, in Figure 4.8.2.4, the control volume's area designed for the rounded V-notch geometry that has been used in this thesis.

- The V-notch opening angle is:  $2\alpha = 45^\circ$
- The fillet radius of the V-notch is:  $\rho = 1\text{ mm}$
- The control radius  $R_c = 1.02\text{ mm}$  that has been used is an average value calculated from the control radii that can be found in Table 4.7.2.3 for the three different print orientations:  $R_c = 0.97\text{ mm}$  for  $0^\circ$  orientation,  $R_c = 1.18\text{ mm}$  for  $45^\circ$  orientation,  $R_c = 0.92\text{ mm}$  for  $90^\circ$  orientation.
- $q = 1.75$  and so  $r_0 = 0.43\text{ mm}$  have been calculated with, respectively, the equations (4.8.2.2) and (4.8.2.1).
- The circular sector radius is so:  $(R_c + r_0) = 1.45\text{ mm}$

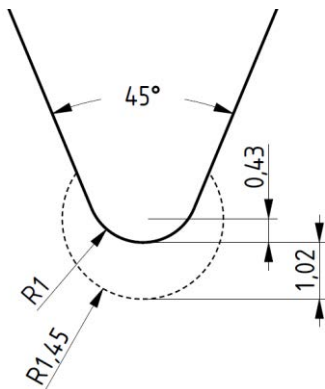


Figure 4.8.2.4: Control volume's area designed for the rounded V-notch geometry that has been used in this thesis.

For the F.E.M. analysis that have been performed to calculate the SED, has been used the *Ansys Mechanical APDL* software and have been used the parameters summarized in the table below (Table 4.8.2.1):

Element Type	PLANE183
Element Shape (K1)	Quadrilateral
Element Behaviour (K3)	Plane Stress
<i>Global element size</i> for the control volume's area [mm]	0.2
Young's modulus (PA12, Table 4.2.3.1) [MPa]	1210
Poisson's ratio (PA12, Table 4.2.3.1) [/]	0.41

Table 4.8.2.1: Parameters that have been used in the F.E.M. analysis to calculate the SED.

Have been applied the boundary conditions that it is possible to see in Figure 4.8.2.5. In particular:

- Has been applied a gross tensile pressure of 0.7174 MPa on the left edge of the specimen (line between KPs 1 and 2) to have 1 MPa of net pressure in the specimen's section under the V-notch's apex.
- Has been applied a horizontal (X-axis) displacement constraint on the right edge of the specimen (line between KPs 6 and 7).
- Has been applied a vertical (Y-axis) displacement constraint in the KPs 2 and 6 to eliminate the lability of the structure.

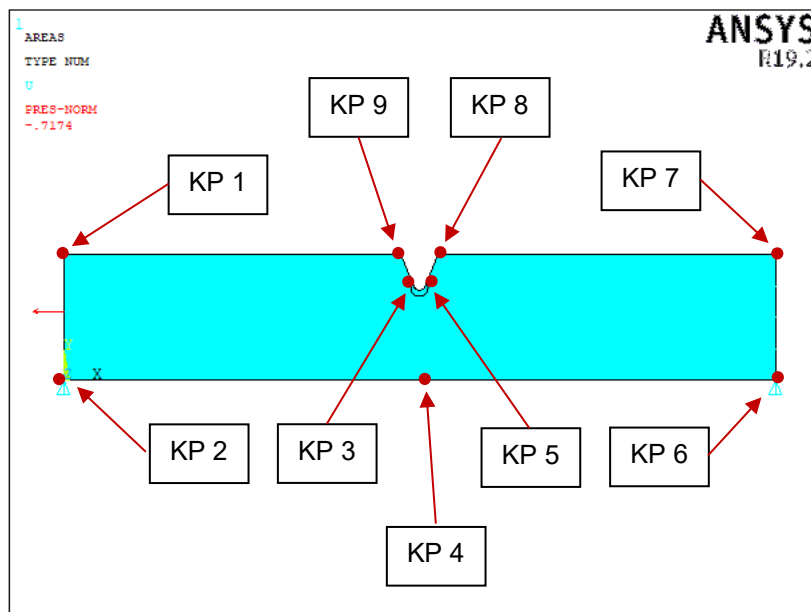


Figure 4.8.2.5: Boundary conditions of the F.E.M. analysis for calculating the SED.

In the images below (Figure 4.8.2.6, Figure 4.8.2.7, Figure 4.8.2.8) it is possible to see the mesh that have been created and used in the F.E.M. analysis. The mesh has been created with the *Ansys free-mesh generation* algorithm specifying the *global element size* of 0.2 mm for the control volume's area and specifying the desired element dimensions in the nine key points represented in Figure 4.8.2.5:

- KPs 3 and 5 specified element size: 0.2 mm
- KPs 4, 8 and 9 specified element size: 0.8 mm
- KPs 1, 2, 6 and 7 specified element size: 3 mm



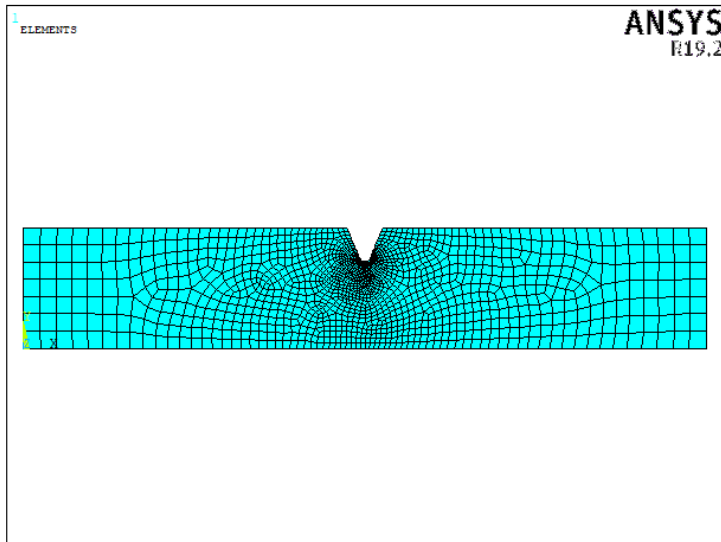


Figure 4.8.2.6: View of the mesh used in the F.E.M. analysis to calculate the SED.

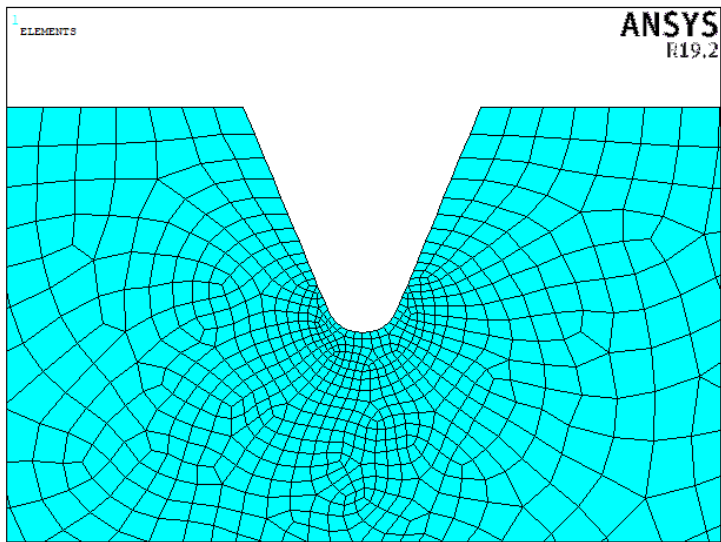


Figure 4.8.2.7: Zoom view of the mesh used in the F.E.M. analysis to calculate the SED.

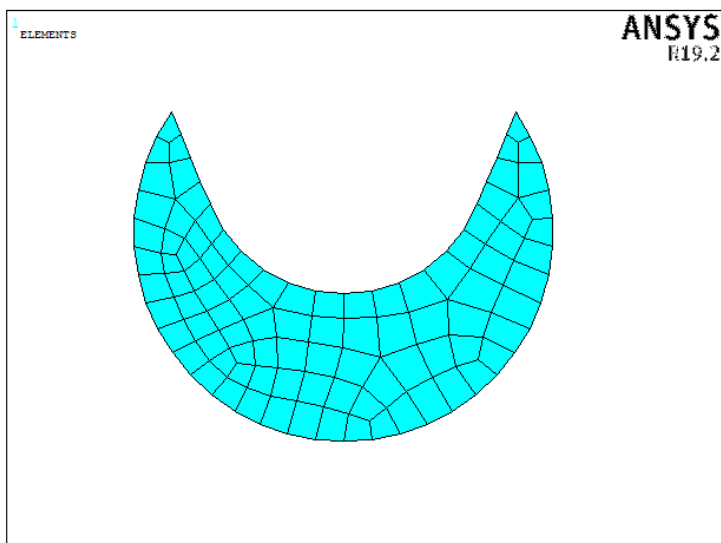


Figure 4.8.2.8: View of the control volume's area mesh used in the F.E.M. analysis to calculate the SED.

After the solution has been done, have been selected only the finite elements attached to the control volume's area and have been taken the sum of the strain energy of every finite element and the sum of the volume of every finite element. To calculate the SED has been performed the ratio between the sum of the strain energy of every finite element attached to the control volume's area and the sum of the volume of every finite element attached to the control volume's area.

The result is:  $SED = 0.0027847 \text{ Nmm/mm}^3$ .

In the image below (Figure 4.8.2.9) it is possible to see a plot of the SED of every single element of the control volume's area, calculated by performing the ratio between the strain energy of the single finite element and the volume of the very same single finite element.

It is possible to see that the two elements that have the maximum value of SED are the ones centred in the notch's apex.

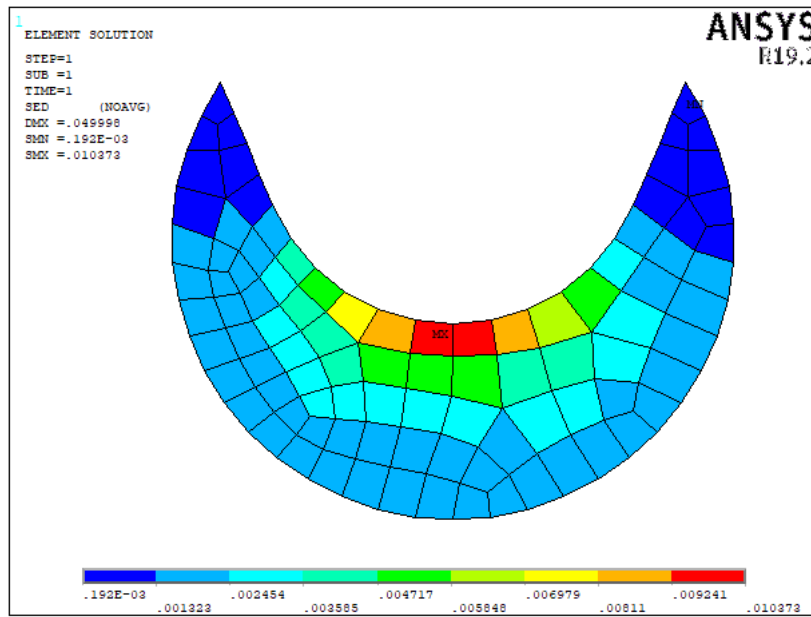


Figure 4.8.2.9: Plot of the SED value for every single finite element in the control volume's area.

Now that has been calculated the SED value with a net stress of 1 MPa, in the section under the V-notch's apex, have been calculated the SED values for all the net stress values that have been applied to the rounded V-notch specimens during the fatigue tests, described in Subchapter 4.4.

It is important to remember that the SED is not linearly proportional with the stress, the SED is proportional to the stress square:

$$SED_{\sigma \text{ MPa}} = SED_{1 \text{ MPa}} \cdot \left(\frac{\sigma}{1}\right)^2 \quad (\text{Eq. 4.8.2.3})$$

After the all SED values have been calculated, have been performed the calculation of the corresponding energy range  $\Delta W$  multiplying by two the SED values, since the fatigue tests have been performed with a load ratio equal to -1.

Now that all the energy ranges  $\Delta W$  have been calculated, it is possible to plot the obtained results in the  $\Delta W$ -N charts for the PA12 material with the three different print orientations  $0^\circ$ ,  $45^\circ$  and  $90^\circ$  developed in Subchapter 4.8.1 to validate them.

In the table below (4.8.2.2) it is possible to see the calculation of the SED and then of the  $\Delta W$  for the rounded V-notch specimens with  $0^\circ$  print orientation:

Specimen's name	R	$\sigma_a$ [MPa]	SED <sub>1 MPa</sub> [Nmm/mm <sup>3</sup> ]	SED <sub><math>\sigma_a</math></sub> [Nmm/mm <sup>3</sup> ]	$\Delta W$ [Nmm/mm <sup>3</sup> ]	N. Cycles total
0VR1PA12_-1_4	-1	13.0	0.0027847	0.4706131	<b>0.9412263</b>	<b>1630</b>
0VR1PA12_-1_6	-1	10.4	0.0027847	0.3011924	<b>0.6023848</b>	<b>9034</b>
0VR1PA12_-1_1	-1	10.4	0.0027847	0.3011924	<b>0.6023848</b>	<b>4407</b>
0VR1PA12_-1_1BIS	-1	10.4	0.0027847	0.3011924	<b>0.6023848</b>	<b>2141</b>
0VR1PA12_-1_5	-1	8.0	0.0027847	0.1782204	<b>0.3564407</b>	<b>88471</b>
0VR1PA12_-1_2	-1	8.0	0.0027847	0.1782204	<b>0.3564407</b>	<b>16078</b>
0VR1PA12_-1_3	-1	8.0	0.0027847	0.1782204	<b>0.3564407</b>	<b>12978</b>
0VR1PA12_-1_7	-1	6.0	0.0027847	0.1002490	<b>0.2004979</b>	<b>297085</b>
0VR1PA12_-1_9	-1	6.0	0.0027847	0.1002490	<b>0.2004979</b>	<b>251064</b>
0VR1PA12_-1_10	-1	7.0	0.0027847	0.1364500	<b>0.2728999</b>	<b>118640</b>
0VR1PA12_-1_8	-1	3.0	0.0027847	0.0250622	<b>0.0501245</b>	<b>2000003</b>
0VR1PA12_-1_11	-1	5.0	0.0027847	0.0696173	<b>0.1392347</b>	<b>2997480</b>
0VR1PA12_-1_12	-1	5.3	0.0027847	0.0782220	<b>0.1564441</b>	<b>222823</b>

Table 4.8.2.2: Calculation of the SED and then of the  $\Delta W$  for the rounded V-notch specimens with  $0^\circ$  print orientation.

In the image below (Figure 4.8.2.10) it is possible to see the  $\Delta W$ -N data of Table 4.8.2.2 plotted in the  $\Delta W$ -N chart for the PA12 material with  $0^\circ$  print orientation developed in Subchapter 4.8.1.

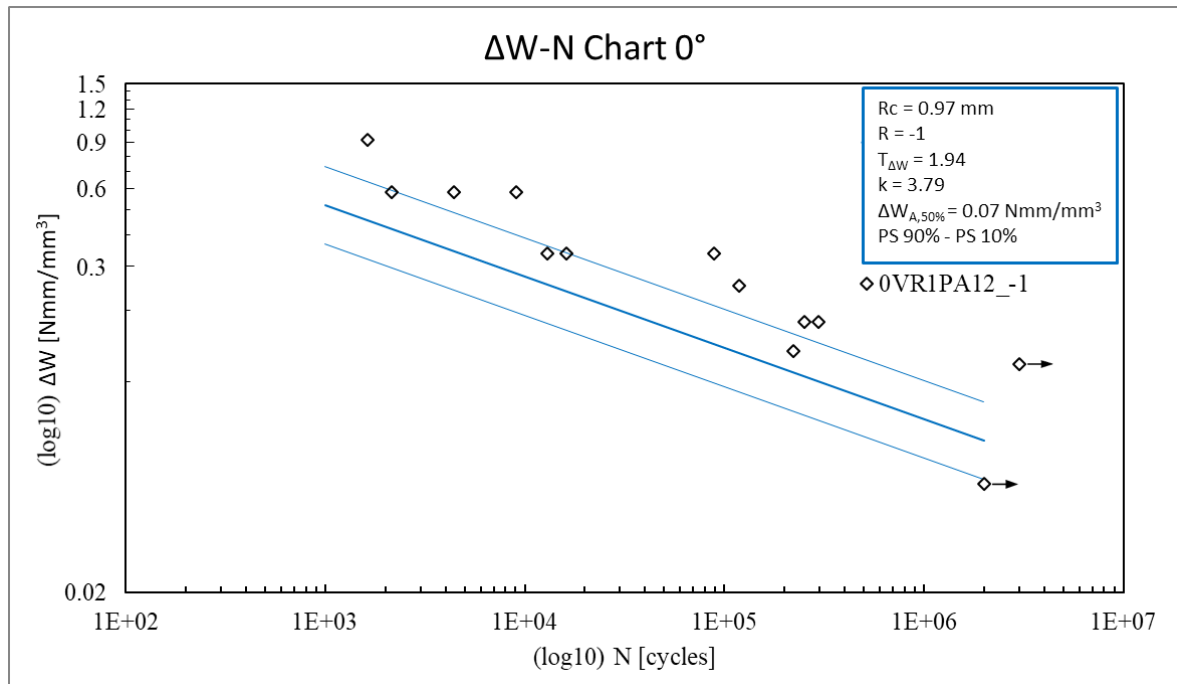


Figure 4.8.2.10:  $\Delta W$ -N data of Table 4.8.2.2 plotted in the  $\Delta W$ -N chart for the PA12 material with  $0^\circ$  print orientation developed in Subchapter 4.8.1.

It is possible to see in Figure 4.8.2.10 that not all the  $0^\circ$  rounded V-notch specimen's points are in the energy range band for the PA12 material with  $0^\circ$  orientation. It seems that the energy range band for the PA12 material with  $0^\circ$  orientation is in safety advantage.

In the table below (4.8.2.3) it is possible to see the calculation of the SED and then of the  $\Delta W$  for the rounded V-notch specimens with 45° print orientation:

Specimen's name	R	$\sigma_a$ [MPa]	SED <sub>1 MPa</sub> [Nmm/mm <sup>3</sup> ]	SED <sub><math>\sigma_a</math></sub> [Nmm/mm <sup>3</sup> ]	$\Delta W$ [Nmm/mm <sup>3</sup> ]	N. Cycles total
45VR1PA12_-1_1	-1	12.0	0.0027847	0.4009958	0.8019916	<b>4110</b>
45VR1PA12_-1_4	-1	12.0	0.0027847	0.4009958	0.8019916	<b>7736</b>
45VR1PA12_-1_5	-1	12.0	0.0027847	0.4009958	0.8019916	<b>4314</b>
45VR1PA12_-1_2	-1	9.0	0.0027847	0.2255601	0.4511203	<b>56467</b>
45VR1PA12_-1_6	-1	9.0	0.0027847	0.2255601	0.4511203	<b>35502</b>
45VR1PA12_-1_7	-1	9.0	0.0027847	0.2255601	0.4511203	<b>26326</b>
45VR1PA12_-1_3	-1	7.0	0.0027847	0.1364500	0.2728999	<b>497449</b>
45VR1PA12_-1_8	-1	8.0	0.0027847	0.1782204	0.3564407	<b>112359</b>
45VR1PA12_-1_9	-1	7.5	0.0027847	0.1566390	0.3132780	<b>186919</b>
45VR1PA12_-1_10	-1	6.0	0.0027847	0.1002490	0.2004979	<b>2640130</b>
45VR1PA12_-1_11	-1	6.5	0.0027847	0.1176533	0.2353066	<b>1345705</b>
45VR1PA12_-1_12	-1	6.5	0.0027847	0.1176533	0.2353066	<b>1531642</b>

Table 4.8.2.3: Calculation of the SED and then of the  $\Delta W$  for the rounded V-notch specimens with 45° print orientation.

In the image below (Figure 4.8.2.11) it is possible to see the  $\Delta W$ -N data of Table 4.8.2.3 plotted in the  $\Delta W$ -N chart for the PA12 material with 45° print orientation developed in Subchapter 4.8.1.

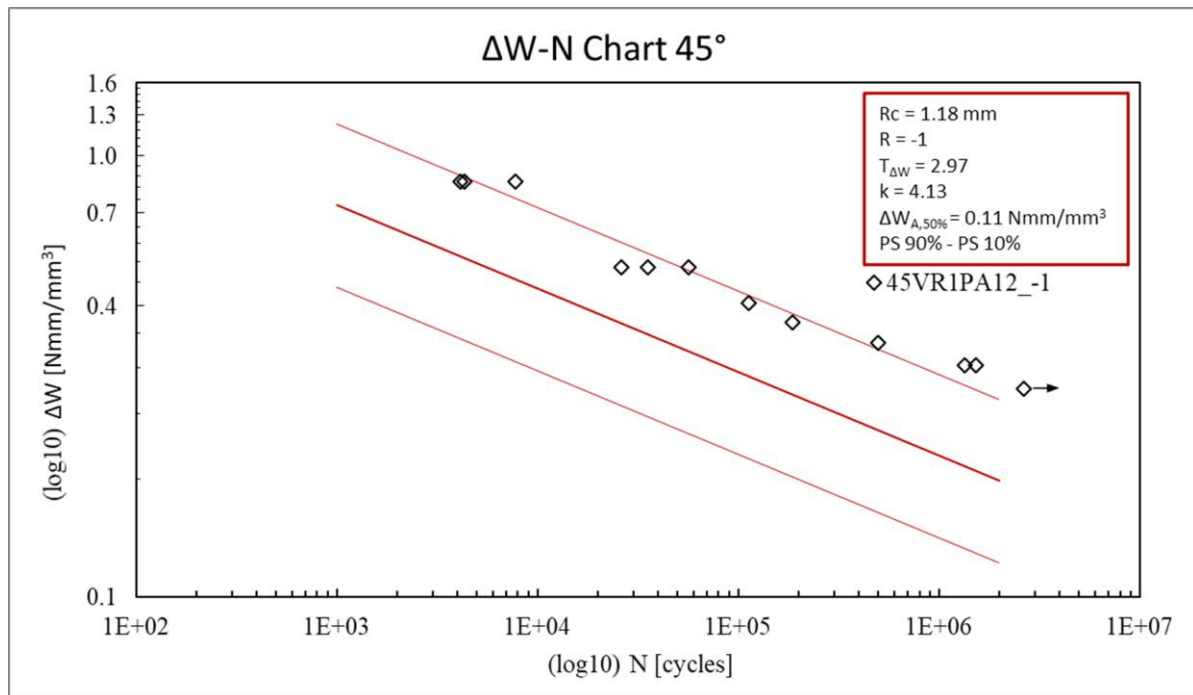


Figure 4.8.2.11:  $\Delta W$ -N data of Table 4.8.2.3 plotted in the  $\Delta W$ -N chart for the PA12 material with 45° print orientation developed in Subchapter 4.8.1.

It is possible to see in Figure 4.8.2.11 that not all the 45° rounded V-notch specimen's points are in the energy range band for the PA12 material with 45° orientation. It seems that the energy range band for the PA12 material with 45° orientation is in safety advantage.

In the table below (4.8.2.4) it is possible to see the calculation of the SED and then of the  $\Delta W$  for the rounded V-notch specimens with 90° print orientation:

Specimen's name	R	$\sigma_a$ [MPa]	SED <sub>1 MPa</sub> [Nmm/mm <sup>3</sup> ]	SED <sub><math>\sigma_a</math></sub> [Nmm/mm <sup>3</sup> ]	$\Delta W$ [Nmm/mm <sup>3</sup> ]	N. Cycles total
90VR1PA12_-1_1	-1	14.0	0.0027847	0.5457999	1.0915997	<b>10552</b>
90VR1PA12_-1_2	-1	14.0	0.0027847	0.5457999	1.0915997	<b>4761</b>
90VR1PA12_-1_3	-1	14.0	0.0027847	0.5457999	1.0915997	<b>7078</b>
90VR1PA12_-1_4	-1	11.0	0.0027847	0.3369479	0.6738957	<b>88255</b>
90VR1PA12_-1_5	-1	11.0	0.0027847	0.3369479	0.6738957	<b>33820</b>
90VR1PA12_-1_6	-1	11.0	0.0027847	0.3369479	0.6738957	<b>39885</b>
90VR1PA12_-1_7	-1	9.0	0.0027847	0.2255601	0.4511203	<b>325765</b>
90VR1PA12_-1_8	-1	9.6	0.0027847	0.2566373	0.5132746	<b>87809</b>
90VR1PA12_-1_9	-1	9.0	0.0027847	0.2255601	0.4511203	<b>151644</b>
90VR1PA12_-1_11	-1	6.5	0.0027847	0.1176533	0.2353066	<b>2961830</b>
90VR1PA12_-1_12	-1	6.5	0.0027847	0.1176533	0.2353066	<b>3476950</b>

Table 4.8.2.4: Calculation of the SED and then of the  $\Delta W$  for the rounded V-notch specimens with 90° print orientation.

In the image below (Figure 4.8.2.12) it is possible to see the  $\Delta W$ -N data of Table 4.8.2.4 plotted in the  $\Delta W$ -N chart for the PA12 material with 90° print orientation developed in Subchapter 4.8.1.

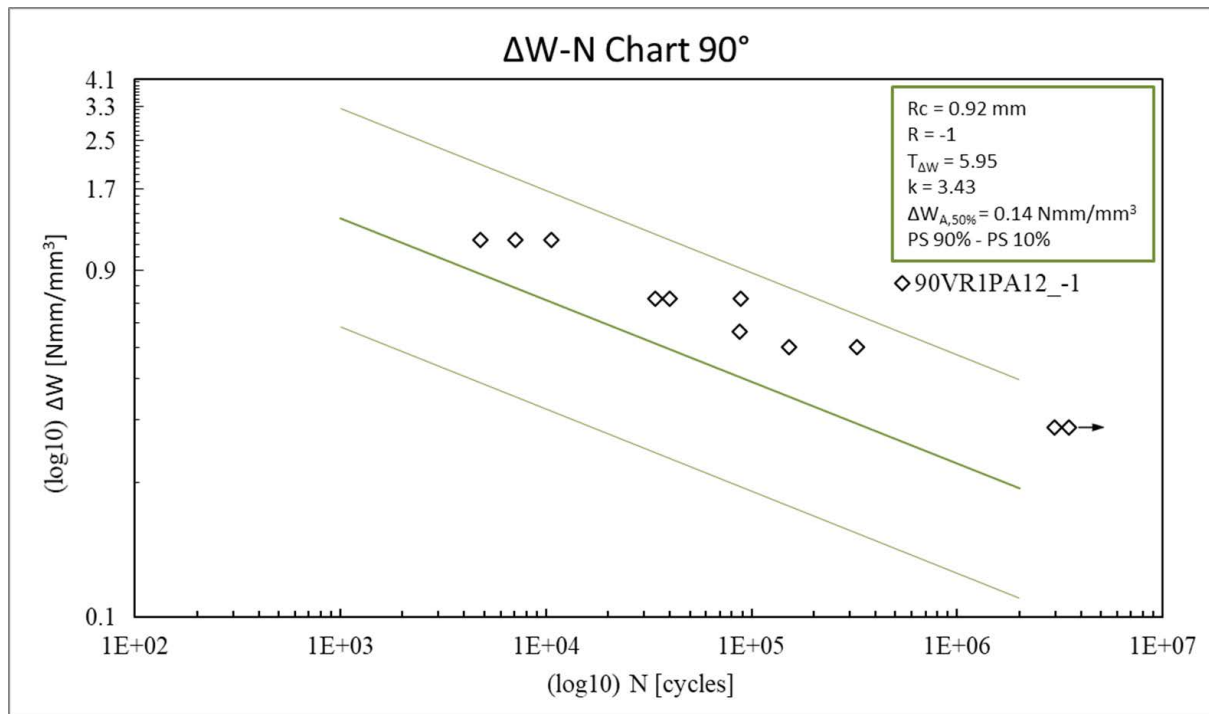


Figure 4.8.2.12:  $\Delta W$ -N data of Table 4.8.2.4 plotted in the  $\Delta W$ -N chart for the PA12 material with 90° print orientation developed in Subchapter 4.8.1.

It is possible to see in Figure 4.8.2.12 that all the 90° rounded V-notch specimen's points are in the upper part of the energy range band for the PA12 material with 90° orientation and the energy range band for the PA12 material with 90° orientation is still in safety advantage.

#### 4.9 Upgrade of the results of Subchapter 4.7 and Subchapter 4.8 with a more realistic specimen's F.E.M. analyses constraints

During the review of the Subchapters 4.7 and 4.8 has been noticed that the boundary conditions of the F.E.M. analyses performed didn't match perfectly with the real boundary conditions that have been applied by the Schenck machine during the fatigue tests that have been performed. In Figure 4.7.1.4 it is possible to see that, in the F.E.M. analysis performed to calculate  $K_1$ , has been constrained the Y-axis displacement only of the KP number 6 to prevent the lability of the system. This is not true because the specimens have been clamped by the fatigue machine's grips with an average length of 42.5 mm per side. If the specimen's geometry would have been a symmetric one, with respect to the longitudinal axis, the unprecise constraints of the F.E.M. analysis would not have affected the results. But, since the V-notch specimen's geometry are not symmetric with respect to the longitudinal axis the unprecise F.E.M. boundary conditions affects the analysis results.

So, has been decided to upgrade schematically all the results obtained in Subchapter 4.7 and Subchapter 4.8, asking the reader to refer at the above mentioned subchapters for the complete work's explanation.

##### Upgraded results of 4.7.1 Calculation of the NSIF $K_1$ for the PA12 sharp V-notch specimen's geometry

The symmetry of the geometry with respect to the V-notch has still been considered and used to lower the computational time of the analysis.

In the image below (Figure 4.9.1) it is possible to see the upgraded boundary conditions of the F.E.M. analysis that has been performed to calculate the  $K_1$  NSIF with the *Peak Stress Method* approach:

- Has been applied a gross tensile pressure of 0.7186 MPa on the left edge of the specimen (line between KPs 4 and 6) to have 1 MPa of net pressure in the specimen's section under the V-notch's apex (line between KPs 2 and 3).
- Has been applied a symmetry boundary constraint on the right edge of the specimen, under the V-notch's apex (line between KPs 2 and 3).
- Has been applied a vertical (Y-axis) displacement constraint in the line between the KPs 5 and 6 to simulate the 42.5 mm machine's grips average length per side.

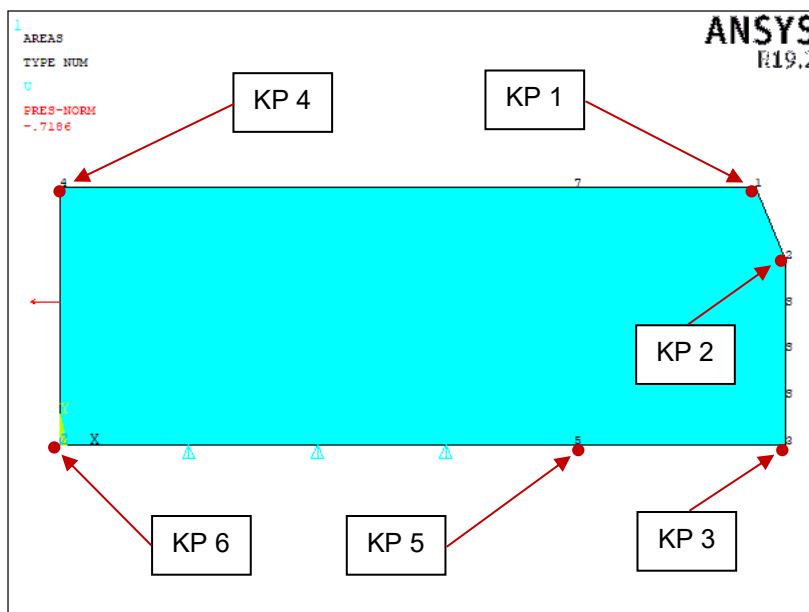


Figure 4.9.1: Upgraded boundary condition of the F.E.M. analysis that has been performed to calculate the  $K_1$  NSIF with the *Peak Stress Method* approach.



In the image below (Figure 4.9.2) it is possible to see the upgraded result of the 1<sup>st</sup> Principal Stress of the F.E.M. analysis that has been performed to calculate the  $K_1$  NSIF with the *Peak Stress Method* approach.

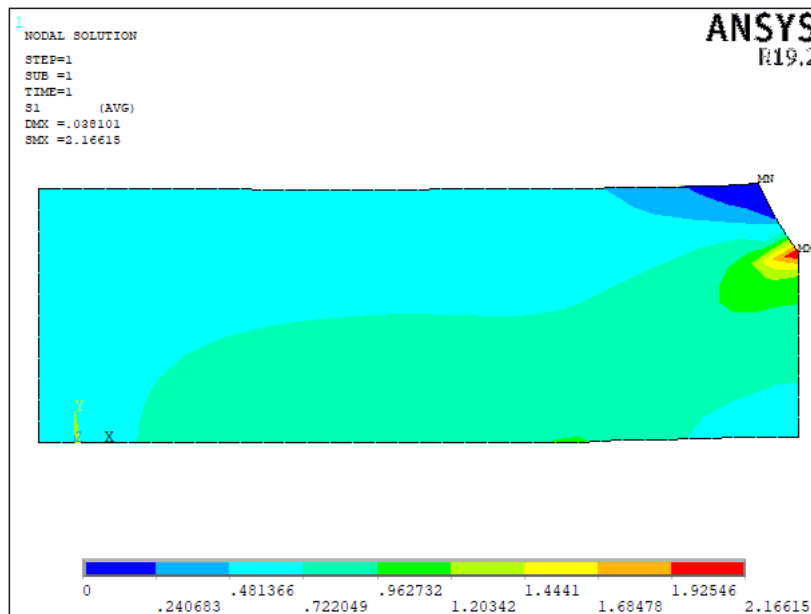


Figure 4.9.2: Upgraded result of the 1<sup>st</sup> Principal Stress of the F.E.M. analysis that has been performed to calculate the  $K_1$  NSIF with the *Peak Stress Method* approach.

In the table below (Table 4.9.1) is summarized the upgraded result of the  $K_1$  calculated the PSM method:

	d [mm]	a/d [/]	$K_{FE}^*$	$\lambda_1$ ( $2\alpha=45^\circ$ )	$\sigma_{a,net}$ [MPa]	$\sigma_{a,gross}$ [MPa]	$\sigma_{peak}$ [MPa]	$K_1$ [MPa·mm <sup>0.495</sup> ]
PSM	1.8	3.3	1.38	0.5050	1	0.7186	2.1662	<b>3.999</b>

Table 4.9.1: Upgraded result of the  $K_1$  calculated with the PSM method.

The  $K_1$  is now 19.3% lower than the one presented in Subchapter 4.7.1, so it is not a negligible change.

#### Upgraded results of 4.7.2 Calculation of the control radius Rc for the PA12 material

In the table below (Table 4.9.2) have been summarized the upgraded results of the calculation of the  $\Delta K_{1D}$  for the sharp V-notch specimens with 0°, 45°, 90° orientations:

	$\sigma_{A,50}$ [MPa]	k	Reference number of cycles (D)	$\sigma_D$ [MPa]	$\Delta\sigma_D$ [MPa]	$K_1$ [MPa·mm <sup>0.495</sup> ]	$\Delta K_{1D}$ [MPa·mm <sup>0.495</sup> ]
0°	3.24	7.45	1000000	3.56	7.11	3.999	<b>28.440</b>
45°	4.19	6.29	1000000	4.68	9.36	3.999	<b>37.416</b>
90°	4.57	5.68	1000000	5.16	10.33	3.999	<b>41.295</b>

Table 4.9.2: Upgraded results of the calculation of the  $\Delta K_{1D}$  for the sharp V-notch specimens with 0°, 45°, 90° orientations.

In the table below (Table 4.9.3) have been reported for completeness the results of the calculation of the  $\Delta\sigma_D$  for the plain specimens with 0°, 45°, 90° orientations, that did not change with respect to the results of Subchapter 4.7.2:

	$\sigma_{A,50}$ [MPa]	k	Reference number of cycles (D)	$\sigma_D$ [MPa]	$\Delta\sigma_D$ [MPa]
0°	10.14	9.92	1000000	10.87	<b>21.75</b>
45°	12.24	11.76	1000000	12.98	<b>25.97</b>
90°	15.46	14.67	1000000	16.21	<b>32.42</b>

Table 4.9.3: Results of the calculation of the  $\Delta\sigma_D$  for the plain specimens with 0°, 45°, 90° orientations.

To calculate the Rc for the PA12 material with 0°, 45°, 90° print orientations have been still used the equation (4.7.2.5) of Subchapter 4.7.2. In the table below (Table 4.9.4) have been summarized the calculations updated results:

Plane Stress	Reference number of cycles (D)	$\Delta\sigma_{D,plain}$ [MPa]	$\Delta K_{1D}$ [MPa·mm <sup>0.495</sup> ]	$\lambda_1$ (2α=45°)	$\gamma$ (2α=45°) [RAD]	$I_1$ (γ) with ν=0,3	$e_1$ (2α=45°)	Rc [mm]
0°	1000000	21.75	28.440	0.5050	2.7489	0.9918	0.1786	<b>0.61</b>
45°	1000000	25.97	37.416	0.5050	2.7489	0.9918	0.1786	<b>0.74</b>
90°	1000000	32.42	41.295	0.5050	2.7489	0.9918	0.1786	<b>0.58</b>

Table 4.9.4: Updated results of the calculation of the Rc for the PA12 material with 0°, 45°, 90° print orientations.

#### Upgraded results of 4.8.1 Creation of the $\Delta W$ -N charts for the PA12 material

In the table below (Table 4.9.5) have been summarized all the upgraded parameter's values that have been used in the equations (4.7.2.1) and (4.7.2.2), only the  $R_c$  values have changed in this table:

Print orientation	Young's modulus (PA12) [MPa]	$C_w$ ( $R = -1$ )	$\lambda_1$ ( $2\alpha=45^\circ$ )	$e_1$ ( $2\alpha=45^\circ$ )	$R_c$ [mm]
0°	1210	0.5	0.5050	0.179	0.61
45°	1210	0.5	0.5050	0.179	0.74
90°	1210	0.5	0.5050	0.179	0.58

Table 4.9.5: Upgraded parameter's values that have been used in the equations (4.7.2.1) and (4.7.2.2).

In the table below (Table 4.9.6) have been reported for completeness the results of the calculation that have been done for estimating  $\Delta W$  for the plain specimens with 0° print orientation (Eq. 4.7.2.2), that did not change with respect to the results of Subchapter 4.8.1:

Specimen's name	$\sigma_a$ [MPa] (Table 4.3.3.1)	$\Delta\sigma$ [MPa]	$\Delta W$ [Nmm/mm <sup>3</sup> ]	Cycles to failure (Table 4.3.3.1)
0LPA12_-1_1	18.2	36.4	<b>0.27</b>	<b>8029</b>
0LPA12_-1_2	18.2	36.4	<b>0.27</b>	<b>8379</b>
0LPA12_-1_3	18.2	36.4	<b>0.27</b>	<b>5029</b>
0LPA12_-1_4	13.0	26.0	<b>0.14</b>	<b>203590</b>
0LPA12_-1_5	13.0	26.0	<b>0.14</b>	<b>112617</b>
0LPA12_-1_6	13.0	26.0	<b>0.14</b>	<b>203015</b>
0LPA12_-1_7	16.0	32.0	<b>0.21</b>	<b>11285</b>
0LPA12_-1_8	15.5	31.0	<b>0.20</b>	<b>19913</b>
0LPA12_-1_9	15.5	31.0	<b>0.20</b>	<b>51723</b>
0LPA12_-1_10	12.0	24.0	<b>0.12</b>	<b>335176</b>
0LPA12_-1_11	11.0	22.0	<b>0.10</b>	<b>2676901</b>
0LPA12_-1_12	11.5	23.0	<b>0.11</b>	<b>774619</b>

Table 4.9.6:  $\Delta W$  calculations for the 0° plain specimens.

In the table below (Table 4.9.7) have been summarized the upgraded calculations that have been done for estimating  $\Delta W$  for the sharp V-notch specimens with 0° print orientation (Eq. 4.7.2.1):

Specimen's name	$\sigma_a$ [MPa] (Table 4.5.3.1)	$\Delta\sigma$ [MPa]	$\Delta K_1$ [MPa·mm <sup>0.495</sup> ]	$\Delta W$ [Nmm/mm <sup>3</sup> ]	Cycles to failure (Table 4.5.3.1)
0VR0PA12_-1_1	7.8	15.6	62.384	<b>0.4696</b>	<b>3475</b>
0VR0PA12_-1_5	8.0	16.0	63.984	<b>0.4940</b>	<b>2652</b>
0VR0PA12_-1_2	6.0	12.0	47.988	<b>0.2779</b>	<b>16623</b>
0VR0PA12_-1_4	6.0	12.0	47.988	<b>0.2779</b>	<b>12911</b>
0VR0PA12_-1_6	4.5	9.0	35.991	<b>0.1563</b>	<b>240292</b>
0VR0PA12_-1_7	4.5	9.0	35.991	<b>0.1563</b>	<b>165232</b>
0VR0PA12_-1_8	3.5	7.0	27.993	<b>0.0945</b>	<b>2992754</b>
0VR0PA12_-1_3	3.0	6.0	23.994	<b>0.0695</b>	<b>1997793</b>

Table 4.9.7: Upgraded  $\Delta W$  calculations for the 0° sharp V-notch specimens.

It is possible to notice that, despite the  $R_c$  and the  $\Delta K_1$  have been changed of about 20% with respect to the values, respectively, of Subchapter 4.7.2 and Subchapter 4.8.1, the  $\Delta W$  values have been changed of a negligible 0.35% with respect to the values of Subchapter 4.8.1.

However, in the image below (Figure 4.9.3) has been reported the upgraded  $\Delta W$ -N chart of the plain specimens plus the sharp V-notch specimens with the  $0^\circ$  print orientation.

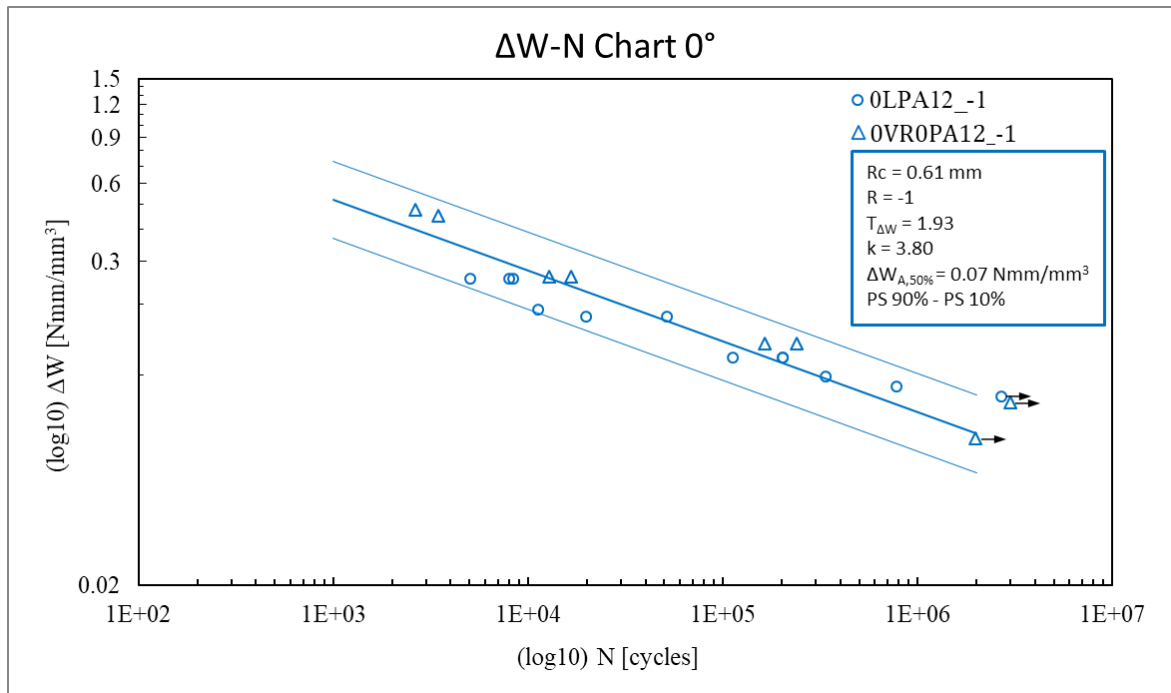


Figure 4.9.3: Upgraded  $\Delta W$ -N chart of the plain specimens plus the sharp V-notch specimens with the  $0^\circ$  print orientation.

In the table below (Table 4.9.8) have been summarized the upgraded calculations that have been done for estimating  $\Delta W$  for the plain specimens with  $45^\circ$  print orientation (Eq. 4.7.2.2), that did not change with respect to the results of Subchapter 4.8.1:

Specimen's name	$\sigma_a$ [MPa] (Table 4.3.3.2)	$\Delta\sigma$ [MPa]	$\Delta W$ [Nmm/mm³]	Cycles to failure (Table 4.3.3.2)
45LPA12_-1_1	21.7	43.4	<b>0.39</b>	<b>1561</b>
45LPA12_-1_2	21.7	43.4	<b>0.39</b>	<b>2313</b>
45LPA12_-1_3	21.7	43.4	<b>0.39</b>	<b>1773</b>
45LPA12_-1_4	15.5	31.0	<b>0.20</b>	<b>131638</b>
45LPA12_-1_5	15.5	31.0	<b>0.20</b>	<b>186091</b>
45LPA12_-1_6	15.5	31.0	<b>0.20</b>	<b>133702</b>
45LPA12_-1_7	18.5	37.0	<b>0.28</b>	<b>21100</b>
45LPA12_-1_8	18.5	37.0	<b>0.28</b>	<b>31794</b>
45LPA12_-1_9	19.5	39.0	<b>0.31</b>	<b>6682</b>
45LPA12_-1_10	14.5	29.0	<b>0.17</b>	<b>253206</b>
45LPA12_-1_11	13.7	27.4	<b>0.16</b>	<b>605783</b>
45LPA12_-1_12	12.7	25.4	<b>0.13</b>	<b>669089</b>

Table 4.9.8:  $\Delta W$  calculations for the  $45^\circ$  plain specimens.

In the table below (Table 4.9.9) have been summarized the upgraded calculations that have been done for estimating  $\Delta W$  for the sharp V-notch specimens with  $45^\circ$  print orientation (Eq. 4.7.2.1):

Specimen's name	$\sigma_a$ [MPa] (Table 4.5.3.2)	$\Delta\sigma$ [MPa]	$\Delta K_I$ [MPa $\cdot$ mm <sup>0.495</sup> ]	$\Delta W$ [Nmm/mm <sup>3</sup> ]	Cycles to failure (Table 4.5.3.2)
45VR0PA12_-1_1	9.0	18.0	71.982	<b>0.5164</b>	<b>13115</b>
45VR0PA12_-1_4	9.0	18.0	71.982	<b>0.5164</b>	<b>17988</b>
45VR0PA12_-1_2	7.0	14.0	55.986	<b>0.3124</b>	<b>122831</b>
45VR0PA12_-1_3	7.0	14.0	55.986	<b>0.3124</b>	<b>123988</b>
45VR0PA12_-1_5	6.0	12.0	47.988	<b>0.2295</b>	<b>142200</b>
45VR0PA12_-1_6	6.0	12.0	47.988	<b>0.2295</b>	<b>90891</b>
45VR0PA12_-1_7	4.0	8.0	31.992	<b>0.1020</b>	<b>7480531</b>
45VR0PA12_-1_8	4.8	9.6	38.390	<b>0.1469</b>	<b>1286687</b>

Table 4.9.9: Upgraded  $\Delta W$  calculations for the  $45^\circ$  sharp V-notch specimens.

It is possible to notice that, despite the  $R_c$  and the  $\Delta K_I$  have been changed of about 20% with respect to the values, respectively, of Subchapter 4.7.2 and Subchapter 4.8.1, the  $\Delta W$  values have been changed of a negligible 0.08% with respect to the values of Subchapter 4.8.1.

However, in the image below (Figure 4.9.4) has been reported the upgraded  $\Delta W$ -N chart of the plain specimens plus the sharp V-notch specimens with the  $45^\circ$  print orientation.

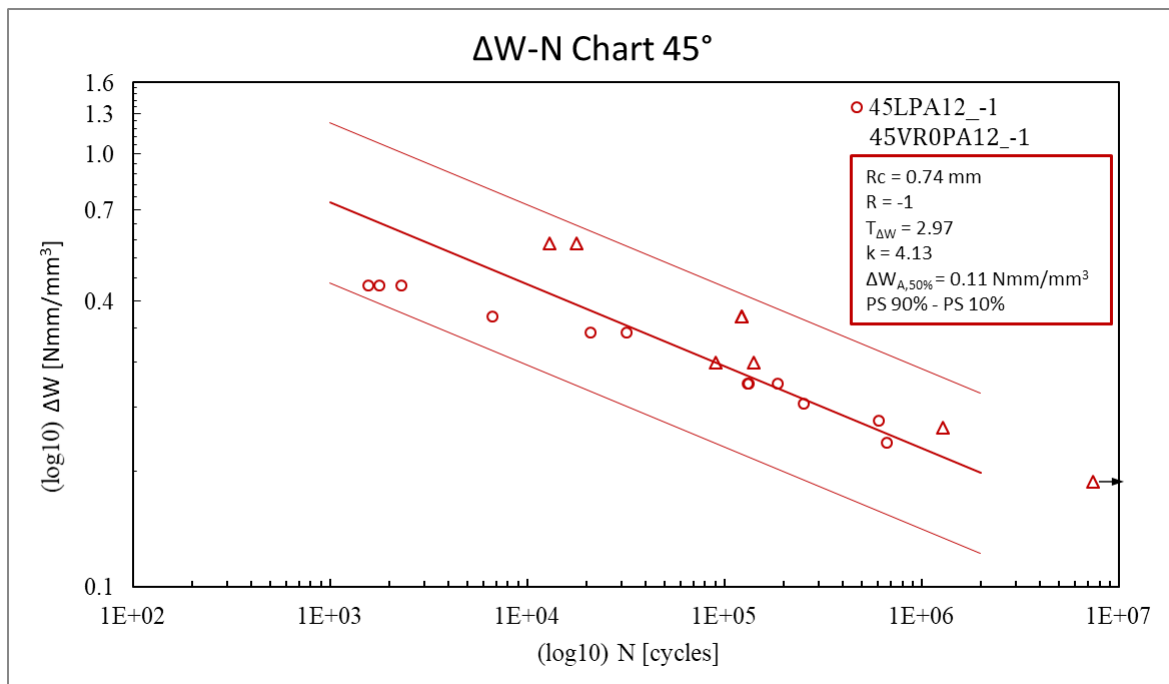


Figure 4.9.4: Upgraded  $\Delta W$ -N chart of the plain specimens plus the sharp V-notch specimens with the  $45^\circ$  print orientation.

In the table below (Table 4.9.10) have been reported for completeness the upgraded calculations that have been done for estimating  $\Delta W$  for the plain specimens with 90° print orientation (Eq. 4.7.2.2), that did not change with respect to the results of Subchapter 4.8.1:

Specimen's name	$\sigma_a$ [MPa] (Table 4.3.3.3)	$\Delta\sigma$ [MPa]	$\Delta W$ [Nmm/mm <sup>3</sup> ]	Cycles to failure (Table 4.3.3.3)
90LPA12_-1_1	25.2	50.4	<b>0.52</b>	<b>1359</b>
90LPA12_-1_2	25.2	50.4	<b>0.52</b>	<b>1425</b>
90LPA12_-1_3	25.2	50.4	<b>0.52</b>	<b>1364</b>
90LPA12_-1_4	18.0	36.0	<b>0.27</b>	<b>233669</b>
90LPA12_-1_5	18.0	36.0	<b>0.27</b>	<b>255601</b>
90LPA12_-1_6	18.0	36.0	<b>0.27</b>	<b>515940</b>
90LPA12_-1_7	19.5	39.0	<b>0.31</b>	<b>86522</b>
90LPA12_-1_10	16.5	33.0	<b>0.23</b>	<b>933175</b>
90LPA12_-1_11	17.0	34.0	<b>0.24</b>	<b>705224</b>
90LPA12_-1_12	15.5	31.0	<b>0.20</b>	<b>646846</b>
90LPA12_-1_13	21.0	42.0	<b>0.36</b>	<b>24419</b>
90LPA12_-1_14	19.5	39.0	<b>0.31</b>	<b>36638</b>

Table 4.9.10:  $\Delta W$  calculations for the 90° plain specimens.

In the table below (Table 4.9.11) have been summarized the upgraded calculations that have been done for estimating  $\Delta W$  for the sharp V-notch specimens with 90° print orientation (Eq. 4.7.2.1):

Specimen's name	$\sigma_a$ [MPa] (Table 4.5.3.3)	$\Delta\sigma$ [MPa]	$\Delta K_1$ [MPa·mm <sup>0.495</sup> ]	$\Delta W$ [Nmm/mm <sup>3</sup> ]	Cycles to failure (Table 4.5.3.3)
90VR0PA12_-1_1	11.0	22.0	87.978	<b>0.9817</b>	<b>20965</b>
90VR0PA12_-1_4	11.0	22.0	87.978	<b>0.9817</b>	<b>8440</b>
90VR0PA12_1_1BIS	8.0	16.0	63.984	<b>0.5193</b>	<b>86568</b>
90VR0PA12_-1_2	8.0	16.0	63.984	<b>0.5193</b>	<b>76945</b>
90VR0PA12_-1_3	6.0	12.0	47.988	<b>0.2921</b>	<b>614569</b>
90VR0PA12_-1_5	7.0	14.0	55.986	<b>0.3976</b>	<b>187445</b>
90VR0PA12_-1_6	5.5	11.0	43.989	<b>0.2454</b>	<b>494755</b>
90VR0PA12_-1_7	5.0	10.0	39.990	<b>0.2028</b>	<b>2495966</b>
90VR0PA12_-1_8	4.9	9.8	39.190	<b>0.1948</b>	<b>4997710</b>

Table 4.9.11: Upgraded  $\Delta W$  calculations for the 90° sharp V-notch specimens.

It is possible to notice that, despite the  $R_c$  and the  $\Delta K_1$  have been changed of about 20% with respect to the values, respectively, of Subchapter 4.7.2 and Subchapter 4.8.1, the  $\Delta W$  values have been changed of a negligible 0.6% with respect to the values of Subchapter 4.8.1.



However, in the image below (Figure 4.9.5) has been reported the upgraded  $\Delta W$ -N chart of the plain specimens plus the sharp V-notch specimens with the 90° print orientation.

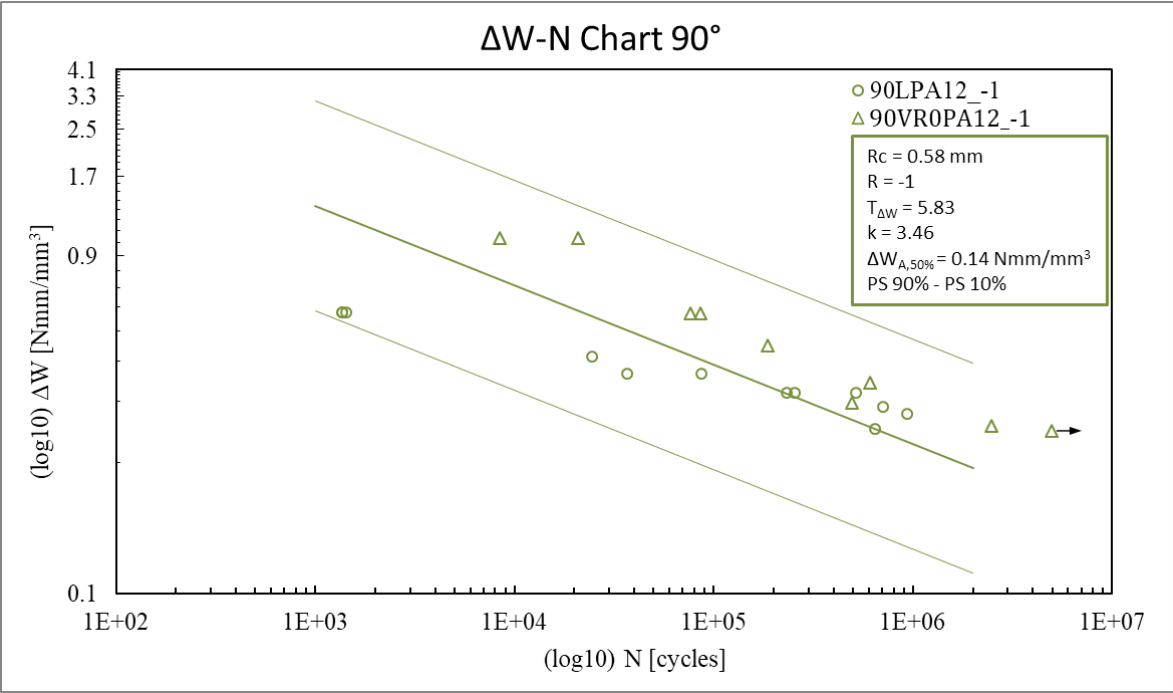


Figure 4.9.5: Upgraded  $\Delta W$ -N chart of the plain specimens plus the sharp V-notch specimens with the 90° print orientation.

#### Upgraded results of 4.8.2 Application of the SED approach to the rounded V-notch specimens

It is possible to see, in Figure 4.9.6, the upgraded control volume's area designed for the rounded V-notch geometry that has been used in this thesis.

- The V-notch opening angle is:  $2\alpha = 45^\circ$
- The fillet radius of the V-notch is:  $\rho = 1\text{ mm}$
- The control radius  $R_c = 0.64\text{ mm}$  that has been used is an average value calculated from the control radii that can be found in Table 4.9.5 for the three different print orientations:  $R_c = 0.61\text{ mm}$  for  $0^\circ$  orientation,  $R_c = 0.74\text{ mm}$  for  $45^\circ$  orientation,  $R_c = 0.58\text{ mm}$  for  $90^\circ$  orientation.
- $q = 1.75$  and so  $r_0 = 0.43\text{ mm}$  have been calculated with, respectively, the equations (4.8.2.2) and (4.8.2.1).
- The circular sector radius is so:  $(R_c + r_0) = 1.07\text{ mm}$

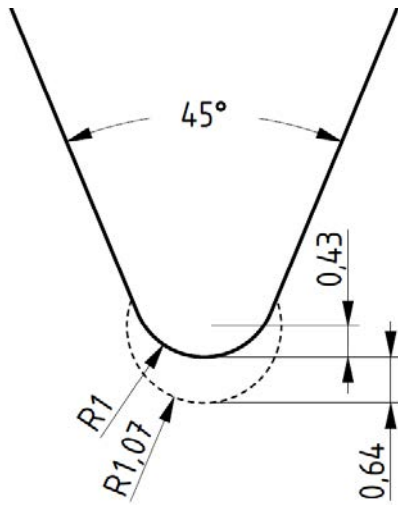


Figure 4.9.6: Upgraded control volume's area designed for the rounded V-notch geometry that has been used in this thesis.

For the F.E.M. analysis that have been performed to calculate the SED, has been used the *Ansys Mechanical APDL* software and have been used the upgraded parameters summarized in the table below (Table 4.9.12):

Element Type	PLANE183
Element Shape (K1)	Quadrilateral
Element Behaviour (K3)	Plane Stress
Global element size for the control volume's area [mm]	0.08
Young's modulus (PA12, Table 4.2.3.1) [MPa]	1210
Poisson's ratio (PA12, Table 4.2.3.1) [/]	0.41

Table 4.9.12: Upgraded parameters that have been used in the F.E.M. analysis to calculate the SED.

Have been applied the upgraded boundary conditions that it is possible to see in Figure 4.9.7. In particular:

- Has been applied a gross tensile pressure of 0.7174 MPa on the left edge of the specimen (line between KPs 1 and 2) to have 1 MPa of net pressure in the specimen's section under the V-notch's apex.
- Has been applied a horizontal (X-axis) displacement constraint on the right edge of the specimen (line between KPs 6 and 7).

- Has been applied a vertical (Y-axis) displacement constraint in the line between KPs 2 and 3 and in the line between KPs 5 and 6 to simulate the 42.5 mm machine's grips average length per side.

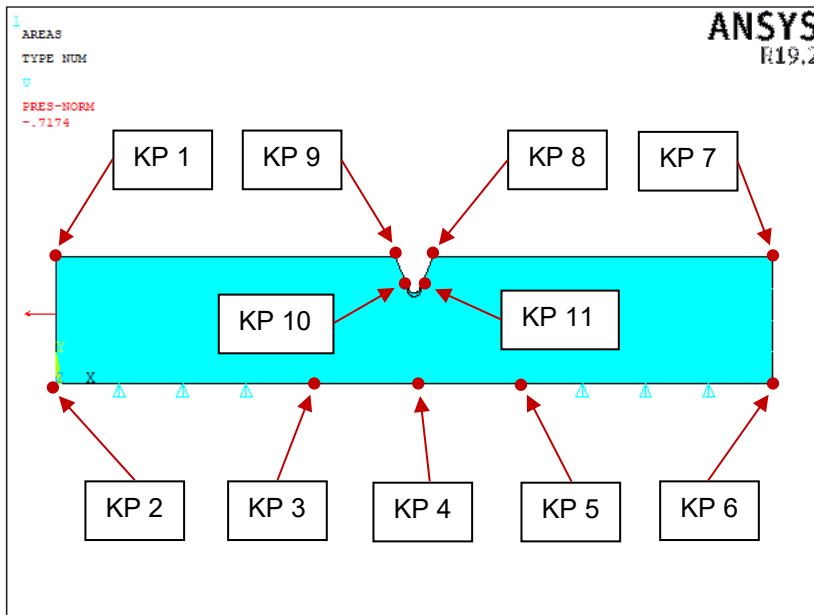


Figure 4.9.7: Upgraded boundary conditions of the F.E.M. analysis for calculating the SED.

In the images below (Figure 4.9.8, Figure 4.9.9, Figure 4.9.10) it is possible to see the upgraded mesh that have been created and used in the F.E.M. analysis. The mesh has been created with the *Ansys free-mesh generation* algorithm specifying the *global element size* of 0.08 mm for the control volume's area and specifying the desired element dimensions in the eleven key points represented in Figure 4.9.7:

- KPs 1, 2, 6 and 7 specified element size: 3 mm
- KPs 3 and 5 specified element size: 0.8 mm
- KPs 4, 8 and 9 specified element size: 0.5 mm
- KPs 10 and 11 specified element size: 0.08 mm

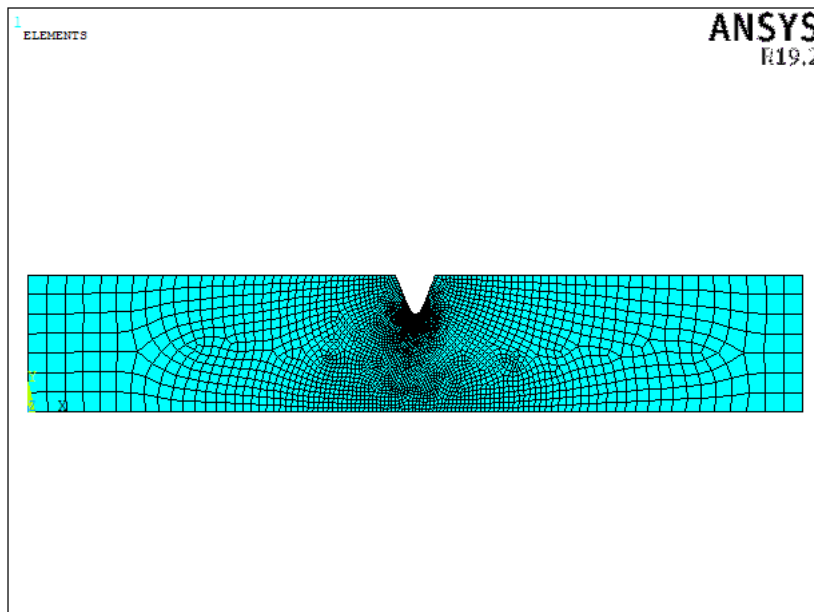


Figure 4.9.8: View of the upgraded mesh used in the F.E.M. analysis to calculate the SED.

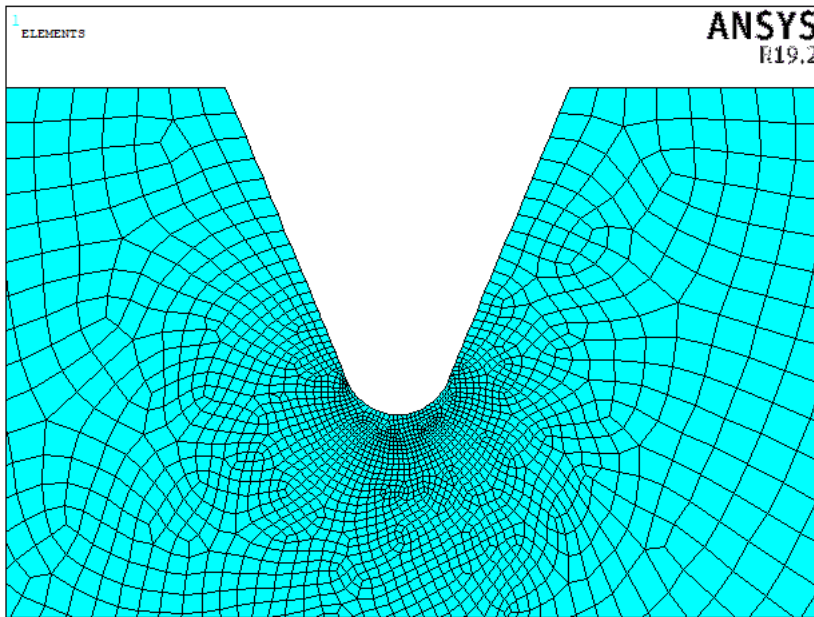


Figure 4.9.9: Zoom view of the upgraded mesh used in the F.E.M. analysis to calculate the SED.

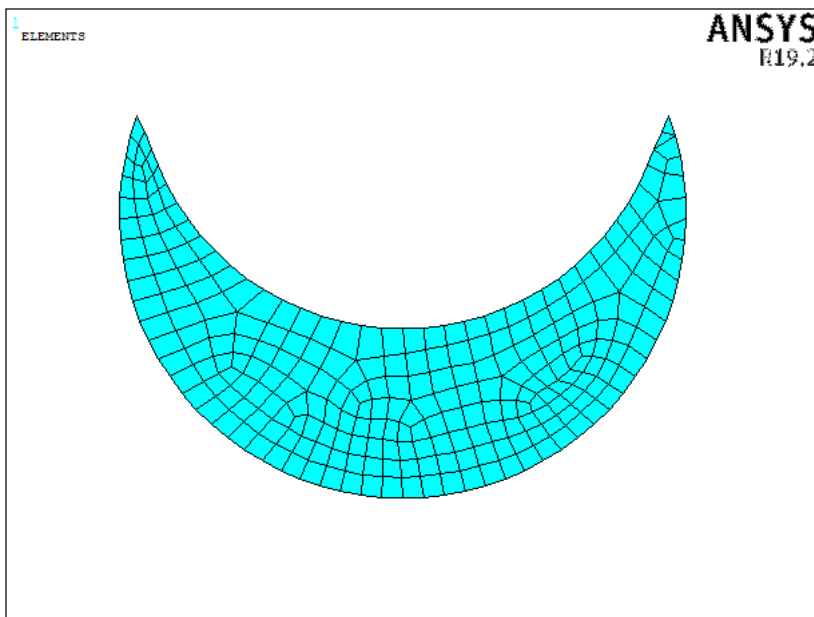


Figure 4.9.10: View of the control volume's area upgraded mesh used in the F.E.M. analysis to calculate the SED.

After the solution has been done, have been selected only the finite elements attached to the control volume's area and have been taken the sum of the strain energy of every finite element and the sum of the volume of every finite element. To calculate the SED has been performed the ratio between the sum of the strain energy of every finite element attached to the control volume's area and the sum of the volume of every finite element attached to the control volume's area.

The upgraded result is:  $\text{SED} = 0.0033241 \text{ Nmm/mm}^3$ , 16% greater than the value of Subchapter 4.8.2.

In the image below (Figure 4.9.11) it is possible to see a plot of the SED of every single element of the control volume's area, calculated by performing the ratio between the strain energy of the single finite element and the volume of the very same single finite element.

It is possible to see that the elements that have the maximum value of SED are the ones centred in the notch's apex.

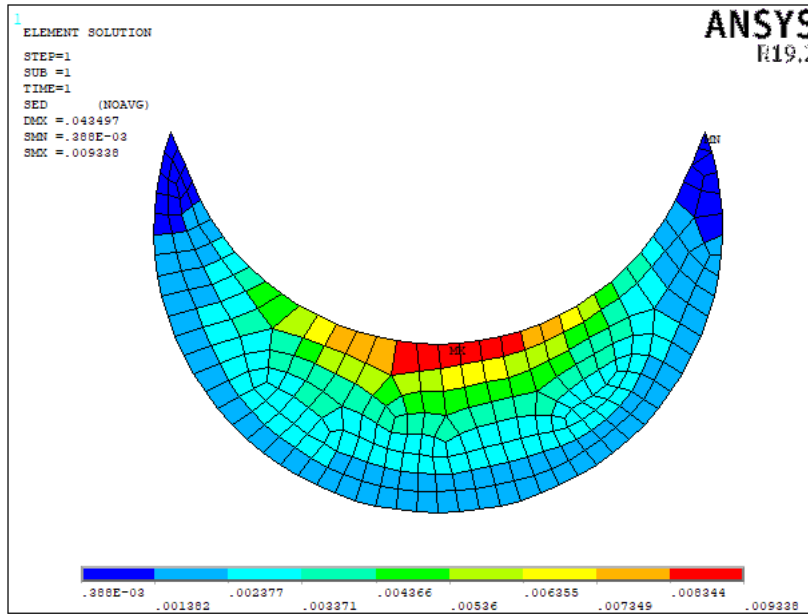


Figure 4.9.11: Plot of the upgraded SED value for every single finite element in the control volume's area.

Now that has been calculated the upgraded SED value with a net stress of 1 MPa, in the section under the V-notch's apex, have been calculated the upgraded SED values for all the net stress values that have been applied to the rounded V-notch specimens during the fatigue tests, described in Subchapter 4.4.

It is important to remember that the SED is not linearly proportional with the stress, the SED is proportional to the stress square:

$$SED_{\sigma \text{ MPa}} = SED_{1 \text{ MPa}} \cdot \left(\frac{\sigma}{1}\right)^2 \quad (\text{Eq. 4.9.1})$$

After the all upgraded SED values have been calculated, have been performed the calculation of the corresponding upgraded energy range  $\Delta W$  multiplying by two the SED values, since the fatigue tests have been performed with a load ratio equal to -1.

Now that all the upgraded energy ranges  $\Delta W$  have been calculated, it is possible to plot the obtained upgraded results in the upgraded  $\Delta W$ -N charts for the PA12 material with the three different print orientations  $0^\circ$ ,  $45^\circ$  and  $90^\circ$ , updated in Subchapter 4.9, to validate them.

In the table below (4.9.13) it is possible to see the upgraded calculation of the SED and then of the  $\Delta W$  for the rounded V-notch specimens with  $0^\circ$  print orientation:

Specimen's name	R	$\sigma_a$ [MPa]	SED <sub>1 MPa</sub> [Nmm/mm <sup>3</sup> ]	SED <sub><math>\sigma_a</math></sub> [Nmm/mm <sup>3</sup> ]	$\Delta W$ [Nmm/mm <sup>3</sup> ]	N. Cycles total
0VR1PA12_-1_4	-1	13.0	0.0033241	0.5617746	<b>1.1235491</b>	<b>1630</b>
0VR1PA12_-1_6	-1	10.4	0.0033241	0.3595357	<b>0.7190714</b>	<b>9034</b>
0VR1PA12_-1_1	-1	10.4	0.0033241	0.3595357	<b>0.7190714</b>	<b>4407</b>
0VR1PA12_-1_1BIS	-1	10.4	0.0033241	0.3595357	<b>0.7190714</b>	<b>2141</b>
0VR1PA12_-1_5	-1	8.0	0.0033241	0.2127430	<b>0.4254861</b>	<b>88471</b>
0VR1PA12_-1_2	-1	8.0	0.0033241	0.2127430	<b>0.4254861</b>	<b>16078</b>
0VR1PA12_-1_3	-1	8.0	0.0033241	0.2127430	<b>0.4254861</b>	<b>12978</b>
0VR1PA12_-1_7	-1	6.0	0.0033241	0.1196680	<b>0.2393359</b>	<b>297085</b>
0VR1PA12_-1_9	-1	6.0	0.0033241	0.1196680	<b>0.2393359</b>	<b>251064</b>
0VR1PA12_-1_10	-1	7.0	0.0033241	0.1628814	<b>0.3257628</b>	<b>118640</b>
0VR1PA12_-1_8	-1	3.0	0.0033241	0.0299170	<b>0.0598340</b>	<b>2000003</b>
0VR1PA12_-1_11	-1	5.0	0.0033241	0.0831027	<b>0.1662055</b>	<b>2997480</b>
0VR1PA12_-1_12	-1	5.3	0.0033241	0.0933742	<b>0.1867485</b>	<b>222823</b>

Table 4.9.13: Upgraded calculation of the SED and then of the  $\Delta W$  for the rounded V-notch specimens with  $0^\circ$  print orientation.

In the image below (Figure 4.9.12) it is possible to see the upgraded  $\Delta W$ -N data of Table 4.9.13 plotted in the upgraded  $\Delta W$ -N chart for the PA12 material with  $0^\circ$  print orientation:

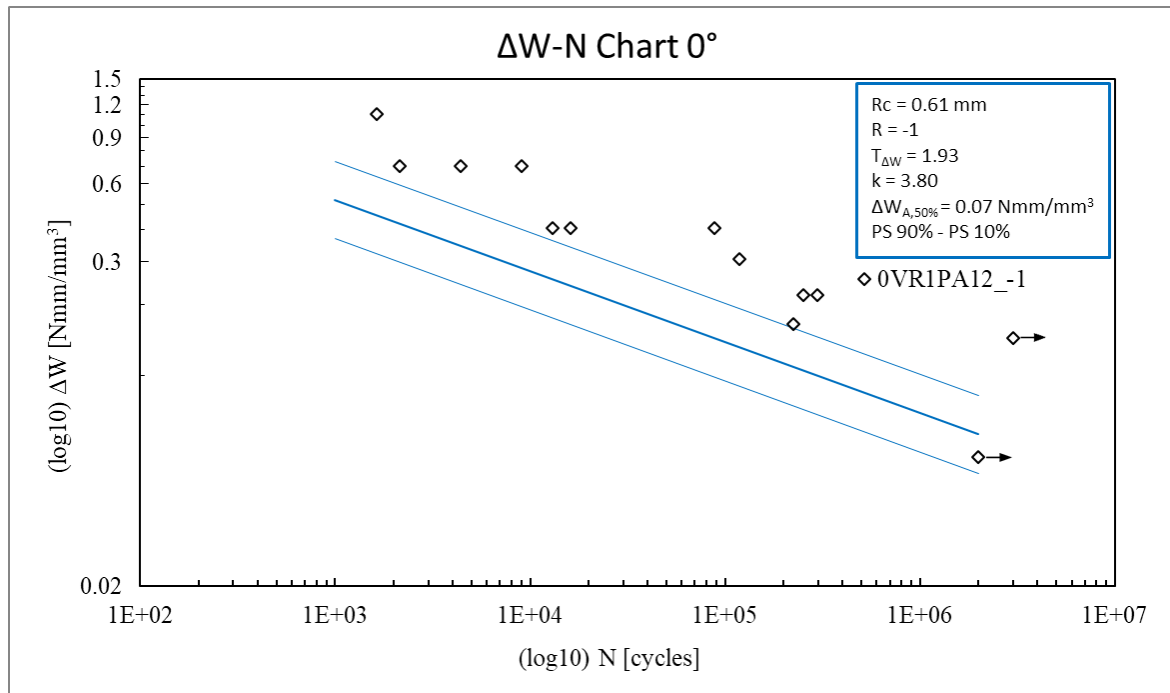


Figure 4.9.12: Upgraded  $\Delta W$ -N data of Table 4.9.13 plotted in the upgraded  $\Delta W$ -N chart for the PA12 material with  $0^\circ$  print orientation.

It is possible to see in Figure 4.9.12 that the upgraded  $0^\circ$  rounded V-notch specimen's points are not in the upgraded energy range band for the PA12 material with  $0^\circ$  orientation. It seems that the upgraded energy range band for the PA12 material with  $0^\circ$  orientation is still in safety advantage.



In the table below (4.9.14) it is possible to see the upgraded calculation of the SED and then of the  $\Delta W$  for the rounded V-notch specimens with 45° print orientation:

Specimen's name	R	$\sigma_a$ [MPa]	SED <sub>1 MPa</sub> [Nmm/mm <sup>3</sup> ]	SED <sub><math>\sigma_a</math></sub> [Nmm/mm <sup>3</sup> ]	$\Delta W$ [Nmm/mm <sup>3</sup> ]	N. Cycles total
45VR1PA12_-1_1	-1	12.0	0.0033241	0.4786718	<b>0.9573436</b>	<b>4110</b>
45VR1PA12_-1_4	-1	12.0	0.0033241	0.4786718	<b>0.9573436</b>	<b>7736</b>
45VR1PA12_-1_5	-1	12.0	0.0033241	0.4786718	<b>0.9573436</b>	<b>4314</b>
45VR1PA12_-1_2	-1	9.0	0.0033241	0.2692529	<b>0.5385058</b>	<b>56467</b>
45VR1PA12_-1_6	-1	9.0	0.0033241	0.2692529	<b>0.5385058</b>	<b>35502</b>
45VR1PA12_-1_7	-1	9.0	0.0033241	0.2692529	<b>0.5385058</b>	<b>26326</b>
45VR1PA12_-1_3	-1	7.0	0.0033241	0.1628814	<b>0.3257628</b>	<b>497449</b>
45VR1PA12_-1_8	-1	8.0	0.0033241	0.2127430	<b>0.4254861</b>	<b>112359</b>
45VR1PA12_-1_9	-1	7.5	0.0033241	0.1869812	<b>0.3739623</b>	<b>186919</b>
45VR1PA12_-1_10	-1	6.0	0.0033241	0.1196680	<b>0.2393359</b>	<b>2640130</b>
45VR1PA12_-1_11	-1	6.5	0.0033241	0.1404436	<b>0.2808873</b>	<b>1345705</b>
45VR1PA12_-1_12	-1	6.5	0.0033241	0.1404436	<b>0.2808873</b>	<b>1531642</b>

Table 4.9.14: Upgraded calculation of the SED and then of the  $\Delta W$  for the rounded V-notch specimens with 45° print orientation.

In the image below (Figure 4.9.13) it is possible to see the upgraded  $\Delta W$ -N data of Table 4.9.14 plotted in the upgraded  $\Delta W$ -N chart for the PA12 material with 45° print orientation.

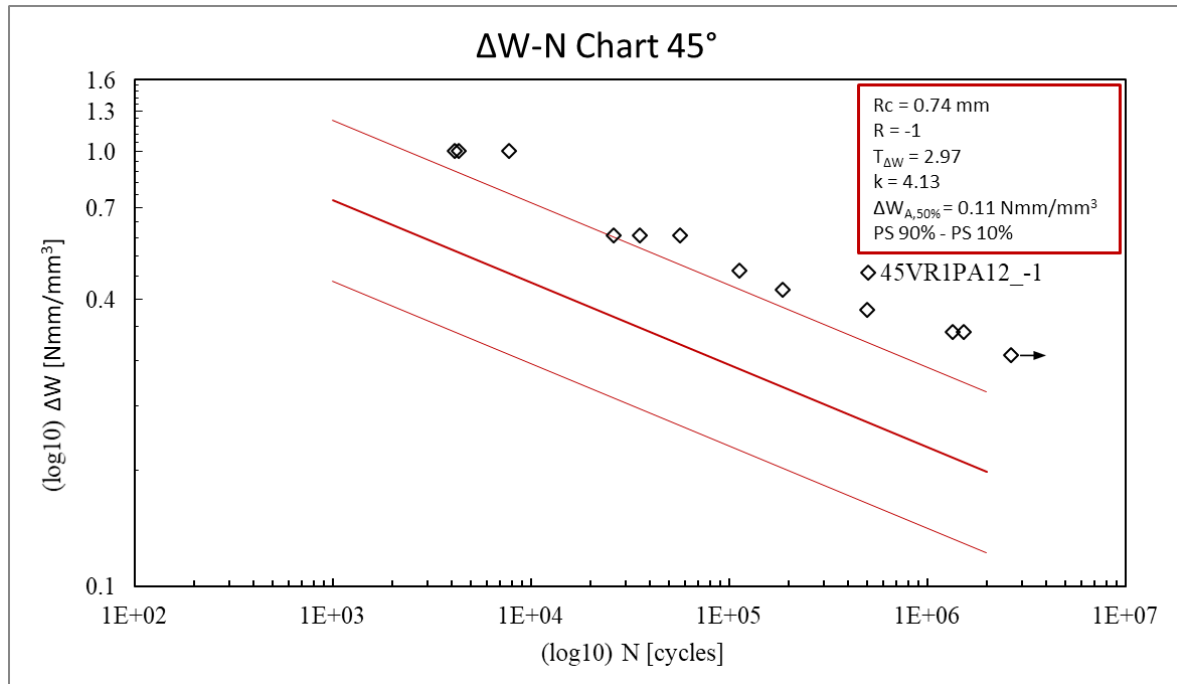


Figure 4.9.13: Upgraded  $\Delta W$ -N data of Table 4.9.14 plotted in the upgraded  $\Delta W$ -N chart for the PA12 material with 45° print orientation.

It is possible to see in Figure 4.9.13 that the upgraded 45° rounded V-notch specimen's points are not in the upgraded energy range band for the PA12 material with 45° orientation. It seems that the upgraded energy range band for the PA12 material with 45° orientation is still in safety advantage.

In the table below (4.9.15) it is possible to see the upgraded calculation of the SED and then of the  $\Delta W$  for the rounded V-notch specimens with 90° print orientation:

Specimen's name	R	$\sigma_a$ [MPa]	SED <sub>1 MPa</sub> [Nmm/mm <sup>3</sup> ]	SED <sub><math>\sigma_a</math></sub> [Nmm/mm <sup>3</sup> ]	$\Delta W$ [Nmm/mm <sup>3</sup> ]	N. Cycles total
90VR1PA12_-1_1	-1	14.0	0.0033241	0.6515255	<b>1.3030510</b>	<b>10552</b>
90VR1PA12_-1_2	-1	14.0	0.0033241	0.6515255	<b>1.3030510</b>	<b>4761</b>
90VR1PA12_-1_3	-1	14.0	0.0033241	0.6515255	<b>1.3030510</b>	<b>7078</b>
90VR1PA12_-1_4	-1	11.0	0.0033241	0.4022173	<b>0.8044346</b>	<b>88255</b>
90VR1PA12_-1_5	-1	11.0	0.0033241	0.4022173	<b>0.8044346</b>	<b>33820</b>
90VR1PA12_-1_6	-1	11.0	0.0033241	0.4022173	<b>0.8044346</b>	<b>39885</b>
90VR1PA12_-1_7	-1	9.0	0.0033241	0.2692529	<b>0.5385058</b>	<b>325765</b>
90VR1PA12_-1_8	-1	9.6	0.0033241	0.3063500	<b>0.6126999</b>	<b>87809</b>
90VR1PA12_-1_9	-1	9.0	0.0033241	0.2692529	<b>0.5385058</b>	<b>151644</b>
90VR1PA12_-1_11	-1	6.5	0.0033241	0.1404436	<b>0.2808873</b>	<b>2961830</b>
90VR1PA12_-1_12	-1	6.5	0.0033241	0.1404436	<b>0.2808873</b>	<b>3476950</b>

Table 4.9.15: Upgraded calculation of the SED and then of the  $\Delta W$  for the rounded V-notch specimens with 90° print orientation.

In the image below (Figure 4.9.14) it is possible to see the upgraded  $\Delta W$ -N data of Table 4.9.15 plotted in the upgraded  $\Delta W$ -N chart for the PA12 material with 90° print orientation.

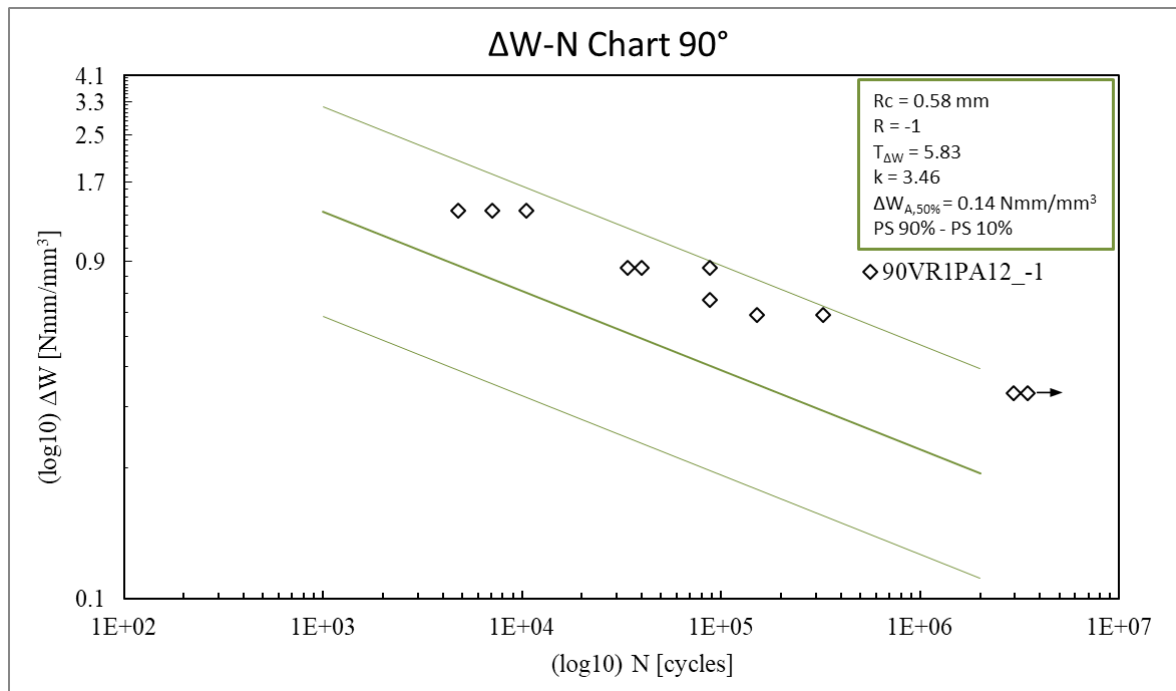


Figure 4.9.14: Upgraded  $\Delta W$ -N data of Table 4.9.15 plotted in the upgraded  $\Delta W$ -N chart for the PA12 material with 90° print orientation.

It is possible to see in Figure 4.9.14 that the upgraded 90° rounded V-notch specimen's points are in the upper part of the upgraded energy range band for the PA12 material with 90° orientation. It seems that the upgraded energy range band for the PA12 material with 90° orientation is still in safety advantage.

## Conclusion

The development of an optimized inner support structure for a hollow curved beam made by additive manufacturing technology, main objective of this Master Thesis, has been achieved.

Taking in account the results of **CHAPTER 2**, it is possible to say that the best approach, among the ones explored and used in this thesis, to apply to design an inner support structure, for the hollow curved beam geometry that has been taken in account, is to do a Topology Optimization of the beam full of material and then to design a custom inner support structure, placing the material, as better as possible, as indicated by the Topology Optimization's retained material. This approach was the one that led to the best component's performance in terms of (weight \* displacement) index.

It is possible to see that for the Load Case 2 the (weight \* displacement) index of the curved beam with the inner structural support developed with the approach mentioned above was 193 g\*mm (Subchapter 2.5.8), 3.5 % lower, and so 3.5 % better, than the one of the curved beam with the inner support structure developed with the Topology Optimization with AM Overhang Constraint approach, that was 200 g\*mm (Subchapter 2.6.2).

The Lattice Optimization approach led to a curved beam with an inner structural support that was less stiff and less strong than the ones developed with the other approaches. This fact has been confirmed also by the laboratory static tests that have been performed in **CHAPTER 3**; the average break force of the curved beams with the two lattice inner support structures developed was 55 % lower than the average one of the two curved beam with the structural inner support developed with the best approach mentioned above (Subchapter 3.2.3). The (weight \* displacement) index for the curved beam with the Octahedral 1 inner lattice support was 214 g\*mm and for the curved beam with the Octet inner lattice support it was 218 g\*mm (Subchapter 2.7.3), respectively 9.8 % and 11.5 % higher with respect to the 193 g\*mm value of the curved beam with the inner support structure developed with the best approach mentioned above.

However, the curved beams with the lattice optimized inner support structures were the lightest one, 35 % average lighter than the curved beams with the inner support structure developed with the best method mentioned above. So, if the main design goal for a component is the lightness, to be achieved also sacrificing the stiffness, the best solution is for sure the inner structural support made of lattice cells.

The second objective of this Master Thesis has been achieved. In particular, as it is possible to see in **CHAPTER 4**, has been completely characterized the PA12 material, succeeding also in the post-processing of the fatigue tests data to calibrate the control radius  $R_c$  for the PA12 material and to build the  $\Delta W-N$  charts for the PA12 material to be used to estimate the fatigue life of PA12 notched components with the *Strain Density Energy* approach.

The PA12 tensile tests results (Subchapter 4.2.3) show that the PA12 material is almost isotropic with respect to the print orientation in the elastic regime, but it is anisotropic with respect to the print orientation in the plastic regime: the break stress and the break strain change with respect to the print direction. It is possible to see, from Table 4.2.3.1, that the average break stress of the 45° oriented specimens is 16% greater than the one of the 0° oriented specimens and that the average break stress of the 90° oriented specimens is 16.2% greater than the one of the 45° oriented specimens. It is also possible to see that the average break strain of the 45° oriented specimens is 45.3% greater than the one of the 0° oriented specimens and that the average break strain of the 90° oriented specimens is 38.9% greater than the one of the 45° oriented specimens. It is also possible to see that the average Young's Modulus of the 0° oriented specimens is almost equal to the one of the 45° oriented specimens and that the average Young's Modulus for the 90° oriented specimens is 6.8% lower than the one of the 45° oriented specimens.

In the end, it is interesting to see that the PA12 material printed with the 90° Flat orientation has slightly different mechanical properties, also in the elastic regime, with respect to the other three orientations investigated before. In particular the average Young's Modulus of the 90° Flat oriented specimens is 13% greater than the average Young's Modulus of the 0°, 45° and 90° oriented specimens.

The PA12 fatigue tests results show, in Subchapter 4.3.3, that, considering for example a constant value of stress amplitude applied to the specimens, the 90° oriented plain specimens can survive more cycles than the 45° oriented plain specimens that, in turn, can survive more cycles than the 0° oriented plain specimens. In Subchapter 4.4.3 it is possible to see also that, considering for example a constant value of stress amplitude applied to the specimens, the 90° oriented rounded V-notch specimens can survive more cycles than the 45° oriented rounded V-notch specimens that, in turn, can survive more cycles than the 0° oriented rounded V-notch specimens. In Subchapter 4.5.3 It is possible to see also that, considering for example a constant value of stress amplitude applied to the specimens, the 90° oriented sharp V-notch specimens can survive more cycles than the 45° oriented sharp V-notch specimens that, in turn, can survive more cycles than the 0° oriented sharp V-notch specimens.

In Subchapter 4.6 It is possible to see that, considering for example a constant value of stress amplitude applied to the specimens, as expected, the 0LPA12\_-1 specimens can survive more cycles than the 0VR1PA12\_-1 specimens that, in turn, can survive more cycles than the 0VR0PA12\_-1 specimens. It is also possible to see that, considering for example a constant value of stress amplitude applied to the specimens, as expected, the 45LPA12\_-1 specimens can survive more cycles than the 45VR1PA12\_-1 specimens that, in turn, can survive more cycles than the 45VR0PA12\_-1 specimens. It is also possible to see that, considering for example a constant value of stress amplitude applied to the specimens, as expected, the 90LPA12\_-1 specimens can survive more cycles than the 90VR1PA12\_-1 specimens that, in turn, can survive more cycles than the 90VR0PA12\_-1 specimens.

In Subchapter 4.9 it is possible to see that the control radius for the PA12 material has been calibrated for the three different print orientations considered and that the  $\Delta W$ -N charts for the PA12 material have been built for the three different print orientations considered. However, it is possible to see, in Figure 4.9.12, that the 0° rounded V-notch specimen's points are not in the energy range band for the PA12 material with 0° orientation. It seems that the energy range band for the PA12 material with 0° orientation is in safety advantage. It is also possible to see, in Figure 4.9.13, that the 45° rounded V-notch specimen's points are not in the energy range band for the PA12 material with 45° orientation. It seems that also the energy range band for the PA12 material with 45° orientation is in safety advantage. It is also possible to see, in Figure 4.9.14, that the 90° rounded V-notch specimen's points are in the upper part of the energy range band for the PA12 material with 90° orientation. This is a better result and it seems that also the energy range band for the PA12 material with 90° orientation is in safety advantage.

The most immediate **future development** of this Master Thesis will be to apply the SED method to the PA12 curved beam with the structural inner support developed in Subchapter 2.5.7 and with the four milled notches, to estimate its fatigue life with the  $\Delta W$ -N charts developed. Then fatigue tests of the curved beam with a load cycle ratio equal to -1 will be performed to make a comparison between the tests results and the SED fatigue life estimation, to validate the  $\Delta W$ -N charts with a more complex notched PA12 component.

## References

- [1] Ben Redwood, Filemon Schöffner, Brian Garret, “*The 3D Printing Handbook. Technologies, design and applications*”, 3D Hubs B.V., Amsterdam, The Netherlands, 2017.
- [2] <https://www.3dhubs.com/knowledge-base/3d-printing-vs-cnc-machining/>
- [3] <https://www.3dhubs.com/knowledge-base/additive-manufacturing-technologies-overview/>
- [4] <https://www.additively.com/en/learn-about/laser-sintering>
- [5] <https://www.additively.com/en/learn-about/laser-melting>
- [6] <https://www.sinterit.com/selective-laser-sintering-in-details/>
- [7] Ian Gibson, David Rosen, Brent Stucker, “*Additive Manufacturing Technologies. 3D Printing, Rapid Prototyping, and Direct Digital Manufacturing, Second Edition*”, Springer.
- [8] <https://www.3dhubs.com/knowledge-base/how-design-parts-sls-3d-printing/>
- [9] <https://www.3dhubs.com/knowledge-base/how-design-parts-metal-3d-printing/>
- [10] <https://www.3dhubs.com/knowledge-base/introduction-sls-3d-printing/>
- [11] <https://www.3dhubs.com/knowledge-base/introduction-metal-3d-printing/>
- [12] M. Cloots, A.B. Spierings, K. Wegener, “Assessing new support minimizing strategies for the additive manufacturing technology SLM”, ResearchGate, 2013.
- [13] <http://www.media.fcaemea.com/uk-en/alfa-romeo/gallery/1672>
- [14] David Santos González, Almudena González Álvarez (Fundación Prodimtec), “*AM Manufacturing Feasibility Study & Technology Demonstration, EDA AM State of the Art & Strategic Report*”, 2018.
- [15] Peter W. Christensen, Anders Klarbring, “*An Introduction to Structural Optimization*”, Springer.
- [16] Ansys Mechanical User's Guide, “*Topology Optimization Analysis*”.
- [17] Ansys Mechanical User's Guide, “*Preparing the Topology Optimization Analysis*”.
- [18] Ansys Mechanical User's Guide, “*Objective*”.
- [19] Ansys Mechanical User's Guide, “*Response Constraint*”.
- [20] Ansys Mechanical User's Guide, “*Manufacturing Constraint*”.
- [21] Ansys Mechanical User's Guide, “*AM Overhang Constraint*”.
- [22] Ansys Mechanical User's Guide, “*Lattice Optimization Analysis*”.
- [23] Ansys Mechanical User's Guide, “*Creating and Managing Virtual Cells*”.
- [24] MTS Landmark® Testing Solutions technical brochure.
- [25] Sinterit Lisa, User Manual (Version 1.5). [www.sinterit.com](http://www.sinterit.com)
- [26] Sinterit Studio 2019, User Manual. [www.sinterit.com](http://www.sinterit.com)
- [27] Meneghetti G. and Campagnolo A. “*Progettazione a fatica di componenti meccanici indeboliti da intagli a V a spigolo vivo – applicazione ai giunti saldati*”. Padova's University, Industrial Engineering Department, Master's degree course in Mechanical Engineering, Course of Machine Design 2, (October 2017).
- [28] Lazzarin P., Sonsino C.M. and Zambardi R. “*A notch stress intensity approach to assess the multiaxial fatigue strength of welded tube-to-flange joints subjected to combined loadings*”. Fatigue and Fracture of Engineering Materials and Structures 27, 127–140, (2004).
- [29] Lazzarin P. and Zambardi R. “*A finite-volume-energy based approach to predict the static and fatigue behaviour of components with sharp V-shaped notches*”. International Journal of Fracture 112:275–298, (2001).
- [30] F. J. Gómez, M. Ellices, F. Berto, P. Lazzarin “*Local strain energy to assess the static failure of U-notches in plates under mixed mode loading*”. International Journal of Fracture 145:29–45, (2007).
- [31] Lazzarin P. and Berto F. “*Some expressions for the strain energy in a finite volume surrounding the root of blunt V-notches*”. International Journal of Fracture 135:161–185, (2005).

## Annex A: Ansys finite elements SOLID186 and SOLID187 comparison

In most of the F.E.M. analyses of this master thesis a 3D body had to be meshed.

Have been chosen two finite elements that have a quadratic shape function and that have a cubic shape (Ansys SOLID186) or a tetrahedron shape (Ansys SOLID187). The choice of which to use depended on the complexity of the geometry to mesh.

It was thought that would be useful to make a comparison between the results of a F.E.M. analysis of a simple cantilever beam using these two different elements to be sure that it was possible to make comparisons about stresses and displacements among different models that could need different mesh elements.

### Geometry:

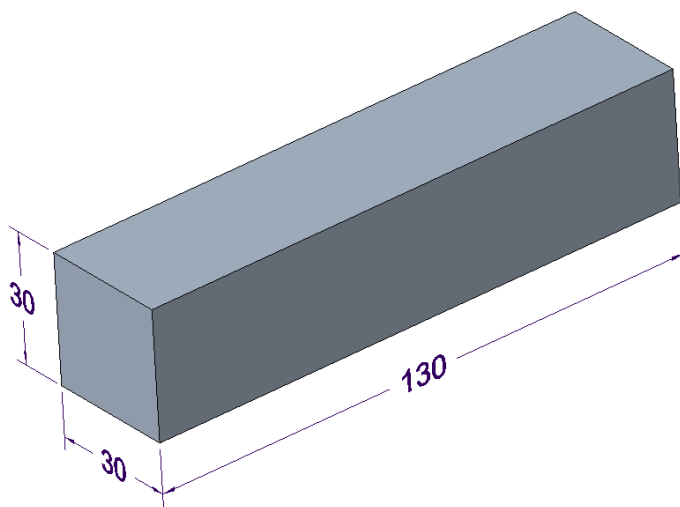


Figure A.1: Geometry of the beam (mm).

### Boundary Conditions:

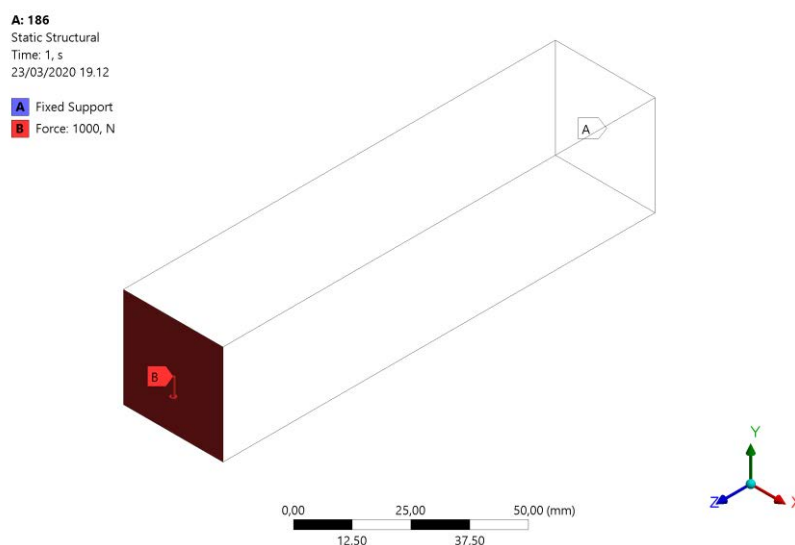


Figure A.2: Boundary conditions of the beam. Has been applied a fix support in one of the two opposite smaller faces of the beam and has been applied a vertical force, directed along the Y-axis, on the other of the two opposite smaller faces of the beam.



SOLID 186 analysis:

Material	Ansys default Structural Steel
Mesh Element Type	SOLID186
Mesh Element Order	Quadratic
Mesh Global Size	2 mm
Mesh Target Quality	0,6

Table A.1: Main parameters of the static structural F.E.M. analysis.

In the images below (Figure A.3, Figure A.4) it is possible to see the results of the F.E.M. analysis with the SOLID186 element type:

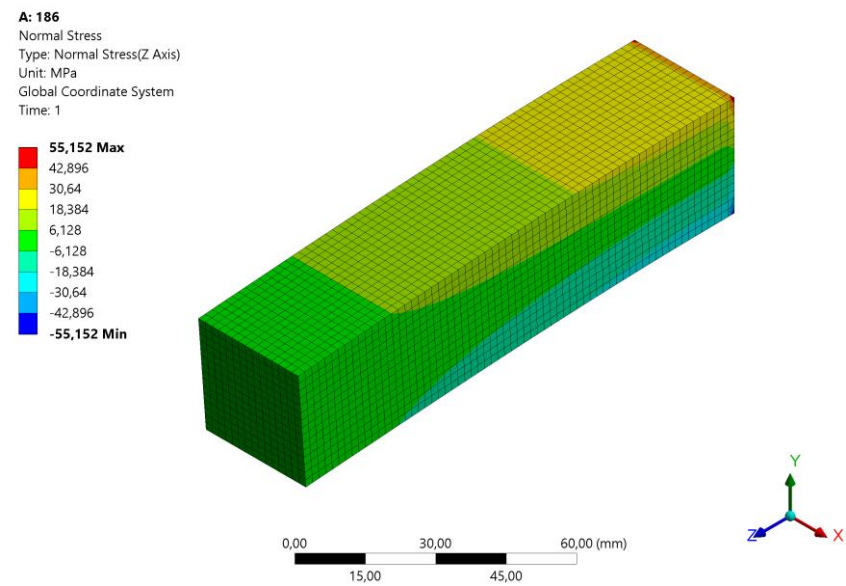


Figure A.3: Von Mises equivalent stress result of the F.E.M. analysis with the SOLID186 element type.

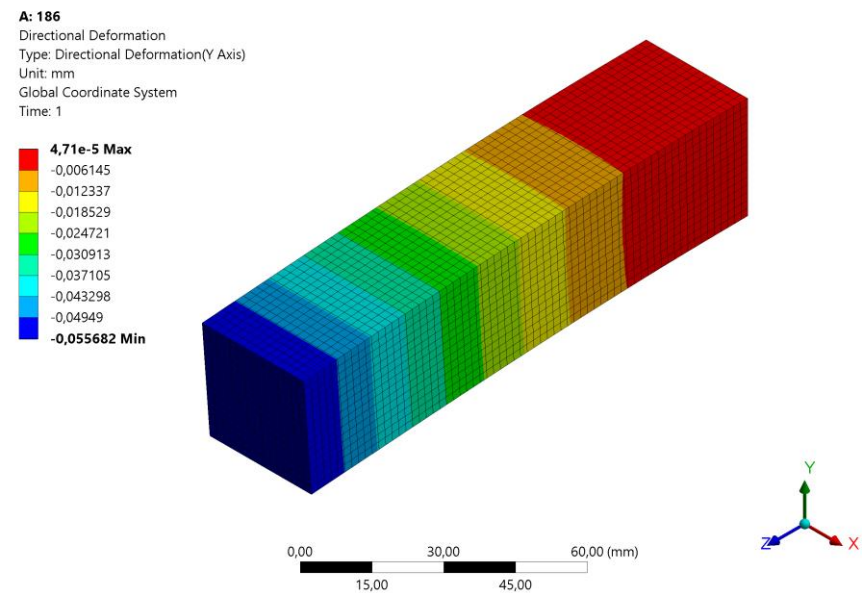


Figure A.4: Displacement along the Y-axis result of the F.E.M. analysis with the SOLID186 element type.

SOLID 187 analysis:

Material	Ansys default Structural Steel
Mesh Element Type	SOLID187
Mesh Element Order	Quadratic
Mesh Global Size	2 mm
Mesh Target Quality	0,6

Table A.2: Main parameters of the static structural F.E.M. analysis.

In the images below (Figure A.5, Figure A.6) it is possible to see the results of the F.E.M. analysis with the SOLID186 element type:

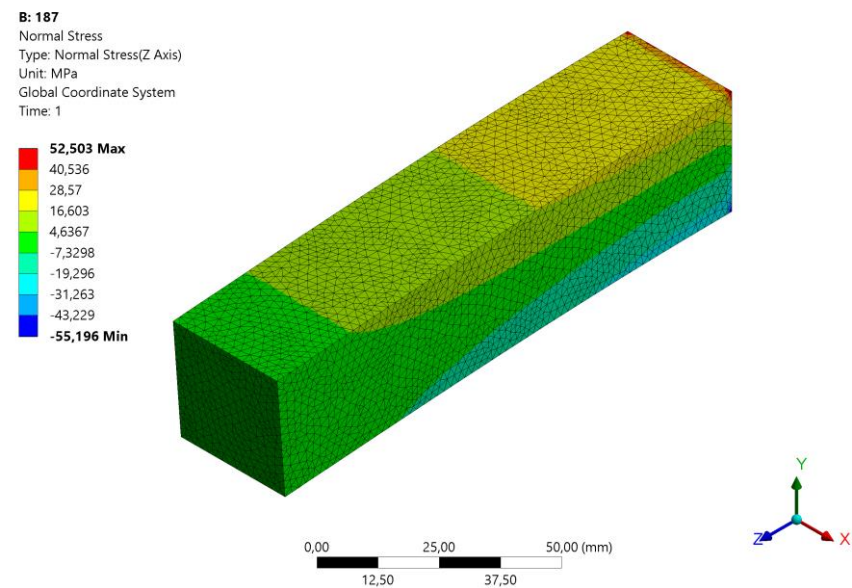


Figure A.5: Von Mises equivalent stress result of the F.E.M. analysis with the SOLID187 element type.

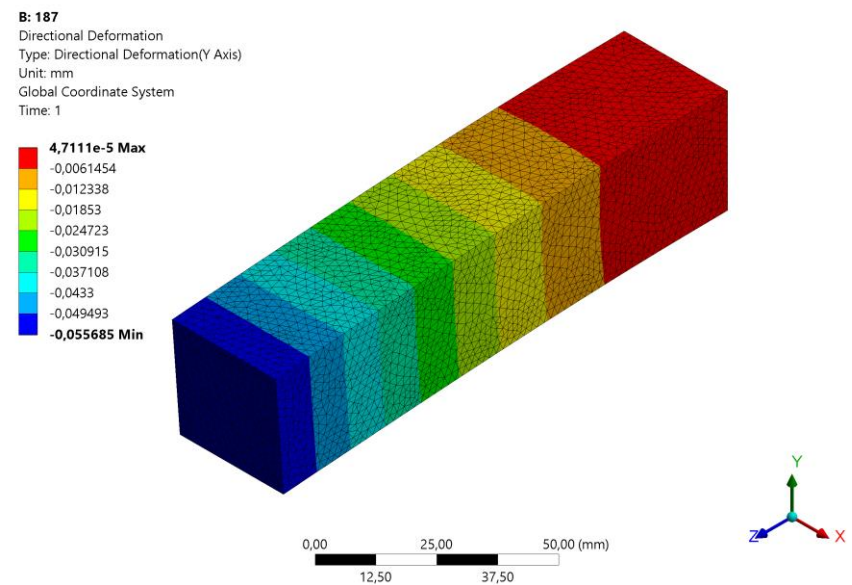


Figure A.6: Displacement along the Y-axis result of the F.E.M. analysis with the SOLID187 element type.

In the table below (Table A.3) are summarized the result of the two F.E.M. analyses that have been performed:

	SOLID186	SOLID187	Difference [%]
Maximum Stress [MPa]	55,152	52,503	4,8
Minimum Displacement [mm]	-0,0557	-0,0557	0

Table A.3: Results of the two F.E.M. analyses performed.

The difference between the two maximum stresses is not negligible.

There is no difference between the two minimum displacements; this is perfect for the aim of the Chapter 2 of this thesis work. In the Chapter 2 have been indeed taken in account the weights and the displacements values of the curved beams with the different structural inner supports developed to make comparisons between them.

# Annex B: Linear elastic buckling F.E.M. analysis of a slender column and comparison with the Euler’s theory

The main settings that have been used for the linear buckling analysis are shown in the table below (Table B.1):

Material	Ansys default Structural Steel (Table 2.3.1)
Mesh Element Type	SOLID187
Mesh Element Order	Quadratic
Mesh Global Size	1,5 mm
Mesh Target Quality	0,6

Table B.1: Main parameters of the linear elastic buckling F.E.M. analysis.

The dimensions of the square section of the slender column and its length are shown in the image below (Figure B.1):

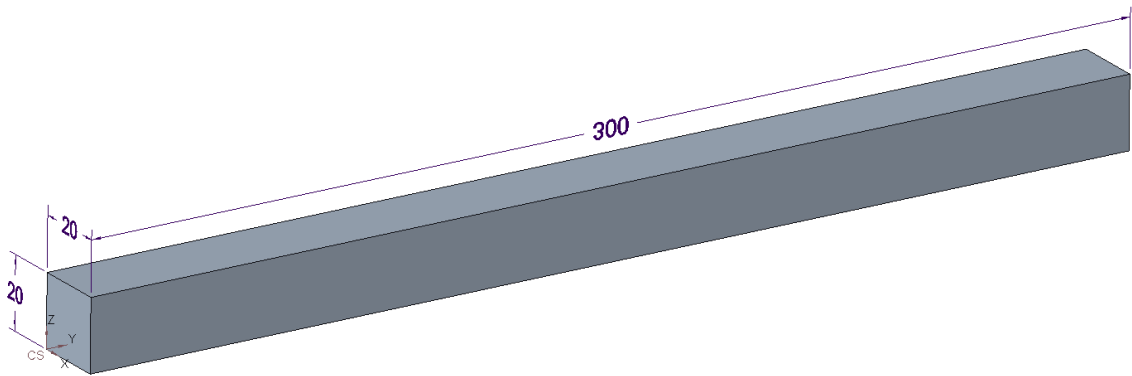


Figure B.1: Dimensions (mm) of the slender column.

The boundary conditions that have been used are shown in the image below (Figure B.2). Has been completely fixed one of the two smallest faces of the slender column and has been applied a force of 1 N on the opposite smallest face with the direction oriented along the Y-axis, the very vertical direction for the slender column.

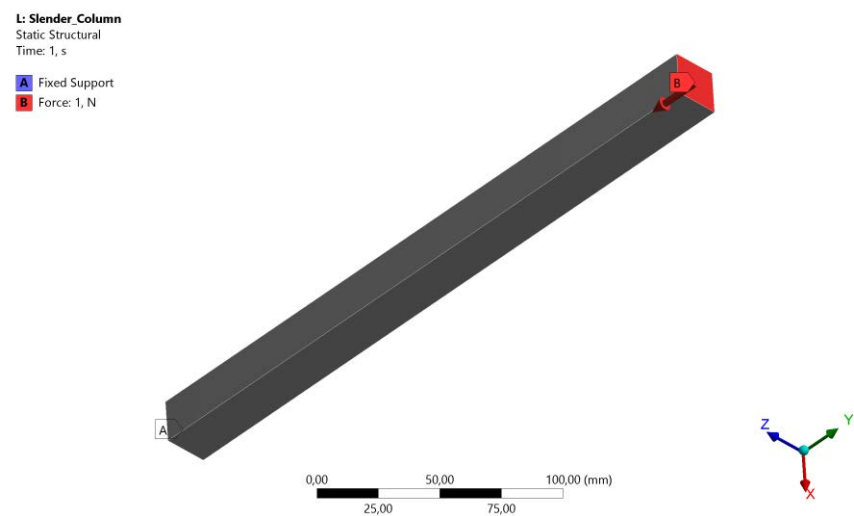


Figure B.2: Boundary conditions of the linear elastic buckling analysis.

A load of 1 N has been applied to get as a result of the simulation the load multiplier that is exactly the load that must be applied to the structure for buckling to happen.

In the image below (Figure B.3) are shown the first six modes of the eigenvalue problem, the most dangerous one is the minimum one taken in absolute value, the number 1.

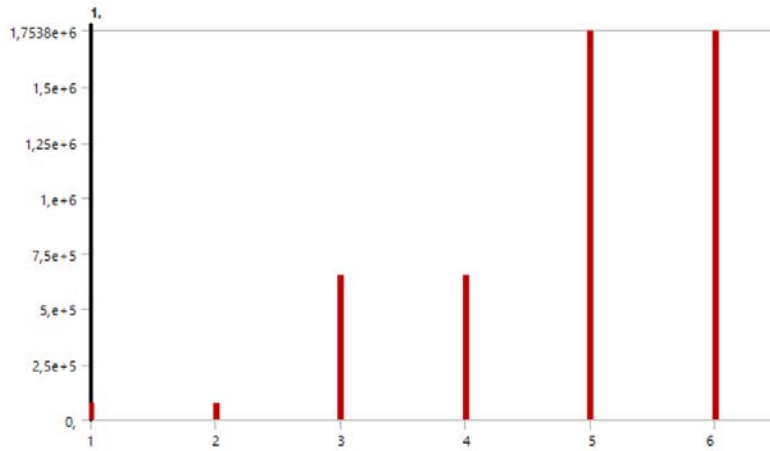


Figure B.3: First six modes resulting from the solution of the buckling eigenvalue problem.

The mode number 1 shows that the minimum ideal load that should be applied to the slender column for buckling to happen is 73199 N

The displacement shape of the slender column that happens when the first critical load is applied is shown in the image below (Figure B.4):

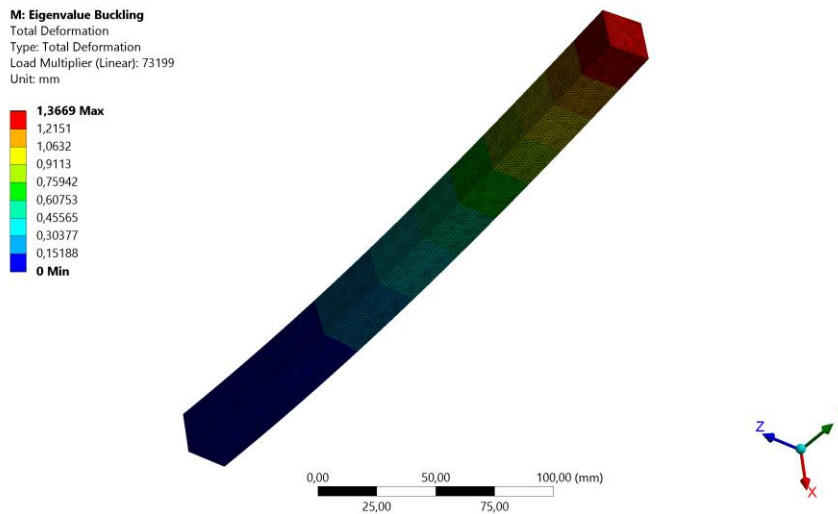


Figure B.4: Displacement shape of the slender column when the first critical load is applied.

Using the proper Euler's formula for the boundary conditions that have been applied in the F.E.M. analysis, it is possible to obtain:

$$L_{cr1} = \frac{\pi^2 \cdot E \cdot J}{(2 \cdot l)^2} = 73108 \text{ N} \quad (\text{Eq. B.1})$$

Where:

$E = 200000 \text{ MPa}$  = Young's modulus of the default Ansys Structural Steel material.

$J = 13333,33 \text{ mm}^4$  = moment of inertia of the square section of the slender beam.

$l = 300 \text{ mm}$  = length of the slender beam.

In the table below (Table B.2) are summarized the results of the F.E.M. analysis and of the calculus made with the Euler's formula:

	F.E.M. analysis	Euler's formula	Difference [%]
Minimum critical load [N]	73199	73108	0,1

Table B.2: Results summarized.

The error between the F.E.M. analysis result and the Euler's formula result is negligible.



# Annex C: Technical 2D drawings of the curved beam clamp system components

In this annex it is possible to find the 2D technical drawings of all the single parts that are present in the fix clamp assembly and in the load clamp assembly.

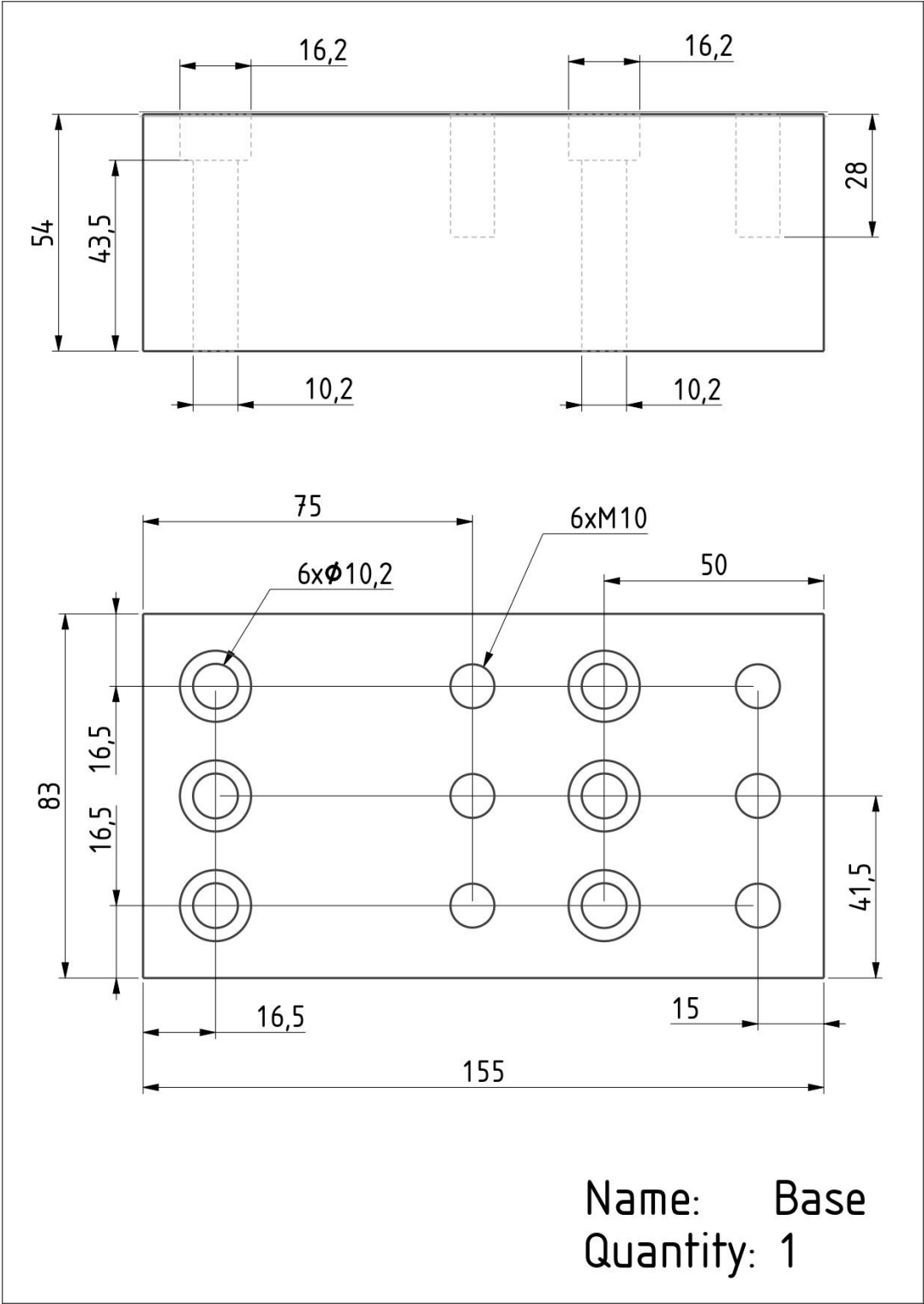
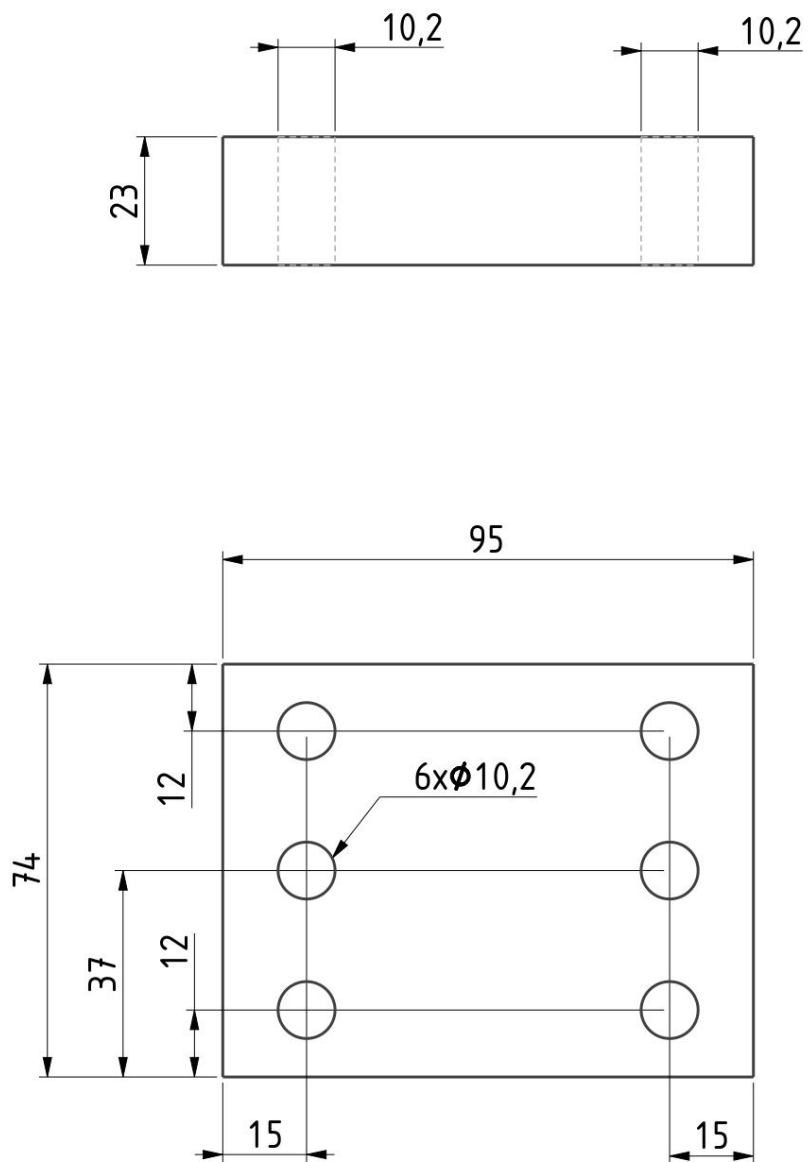
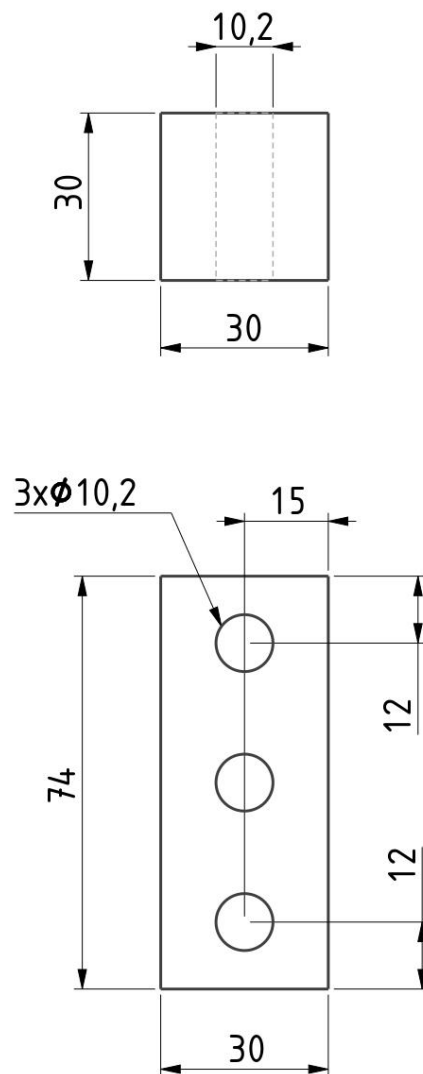


Figure C.1: 2D technical drawing of the *Base* part of the fix clamp assembly (mm).



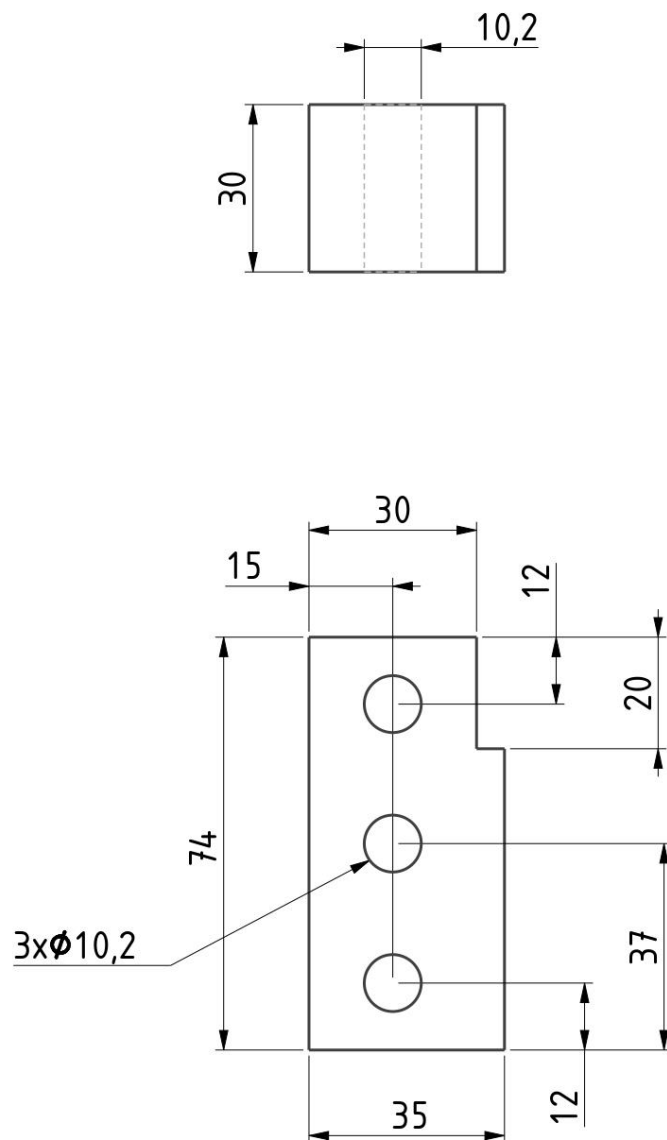
Name: Fix 1  
Quantity: 2

Figure C.2: 2D technical drawing of the *Fix 1* part of the fix clamp assembly (mm).



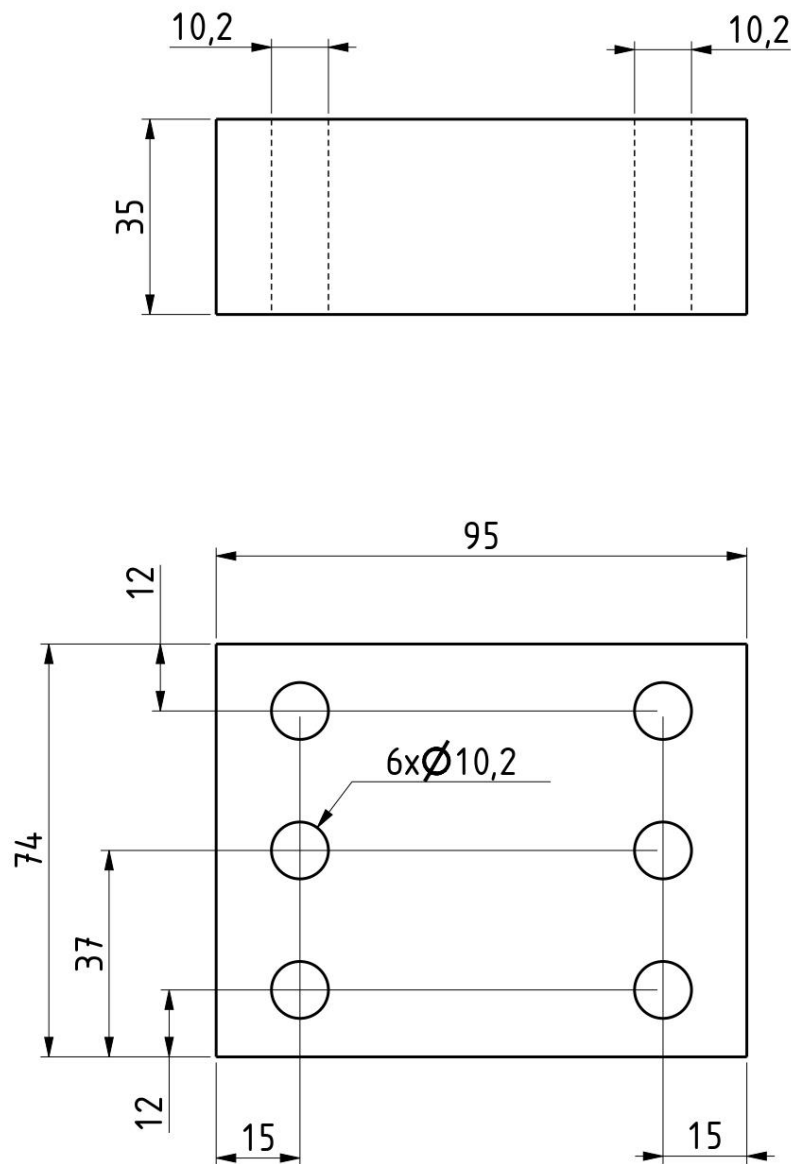
Name: Fix 2  
Quantity: 1

Figure C.3: 2D technical drawing of the *Fix 2* part of the fix clamp assembly (mm).



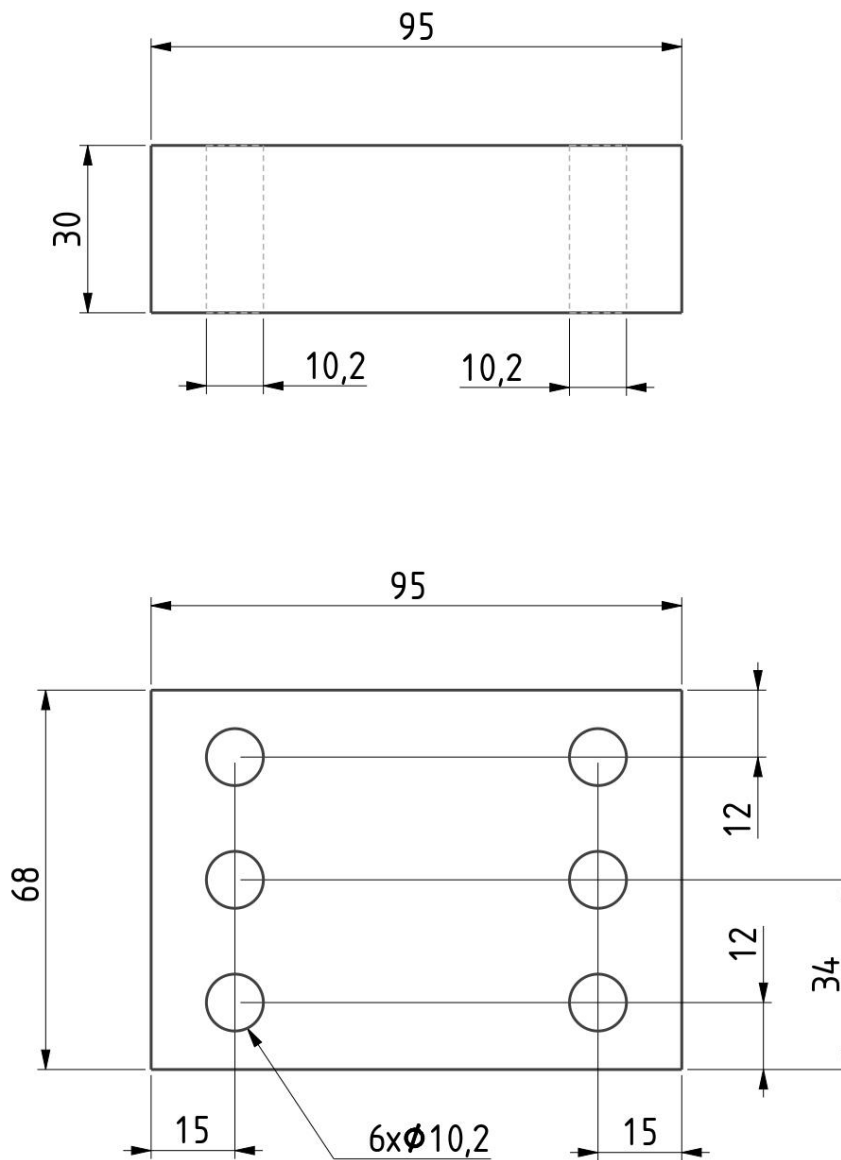
Name: Fix 3  
Quantity: 1

Figure C.4: 2D technical drawing of the *Fix 3* part of the fix clamp assembly (mm).



Name: Fix 4  
Quantity: 1

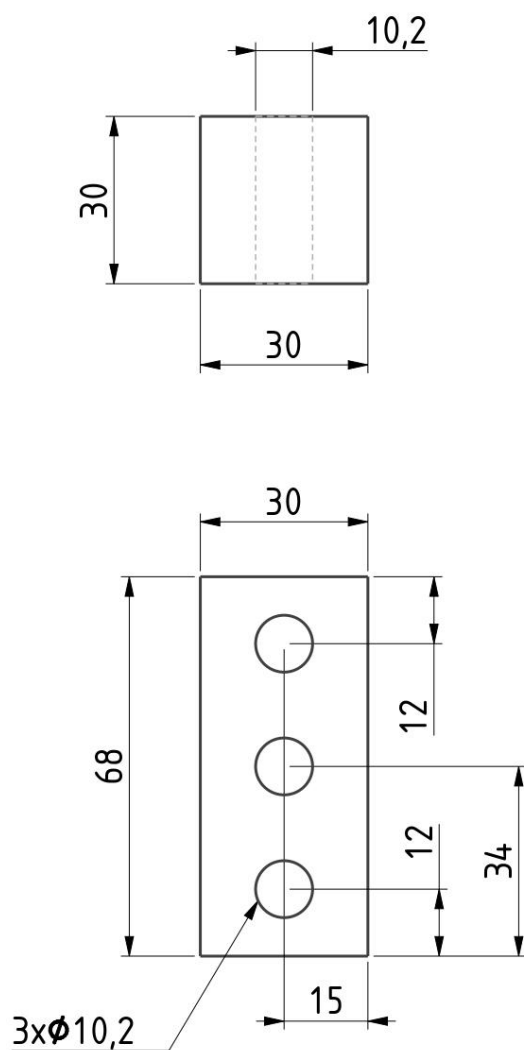
Figure C.5: 2D technical drawing of the *Fix 4* part of the fix clamp assembly (mm).



Name: Load 1  
Quantity: 1

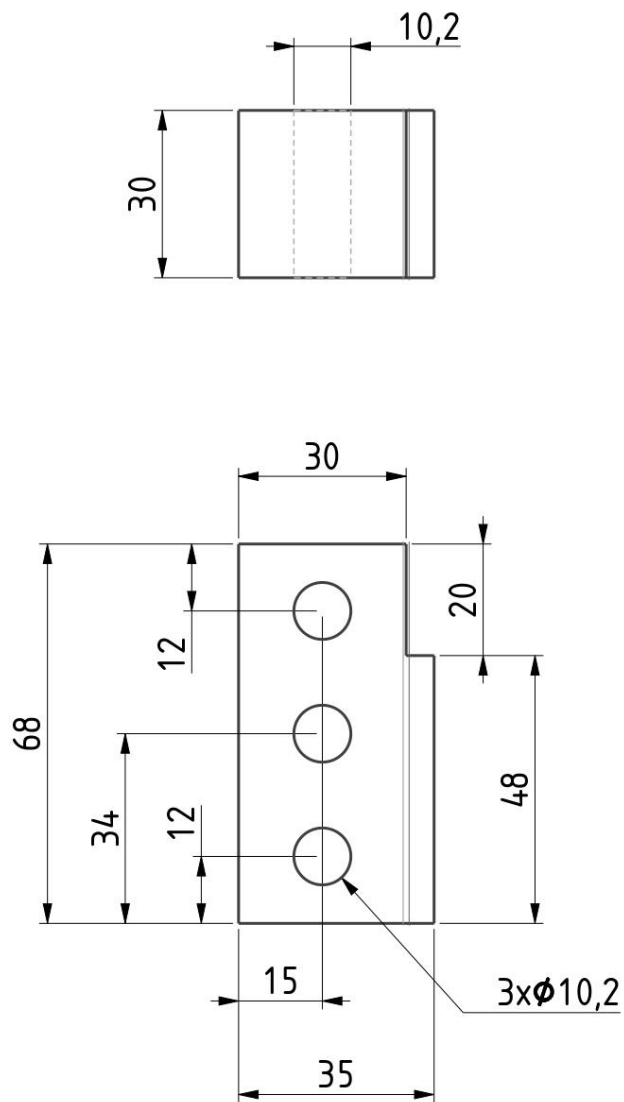
Figure C.6: 2D technical drawing of the *Load 1* part of the load clamp assembly (mm).





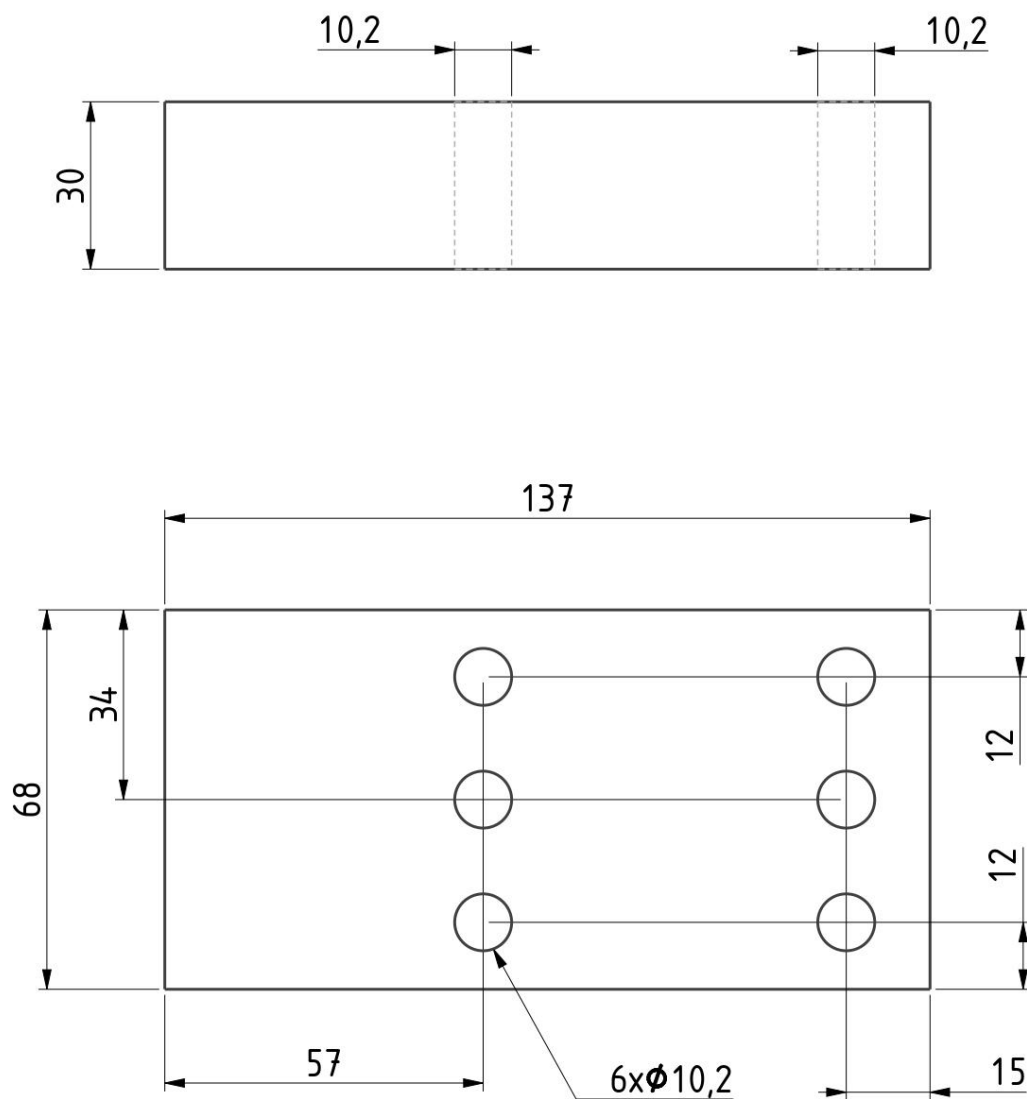
Name: Load 2  
Quantity: 1

Figure C.7: 2D technical drawing of the *Load 2* part of the load clamp assembly (mm).



Name: Load 3  
Quantity: 1

Figure C.8: 2D technical drawing of the *Load 3* part of the load clamp assembly (mm).



Name: Load 4  
Quantity: 1

Figure C.9: 2D technical drawing of the *Load 4* part of the load clamp assembly (mm).

## Annex D: Geometry of the PA12 and Maraging steel curved beams with the notches

In this annex it is possible to find more detailed dimensions (mm) of the Maraging steel curved beam with the four milled notches (Figure D.1, Figure D.2, Figure D.3, Figure D.4) and of the PA12 curved beam with the four milled notches (Figure D.5, Figure D.6, Figure D.7, Figure D.8).

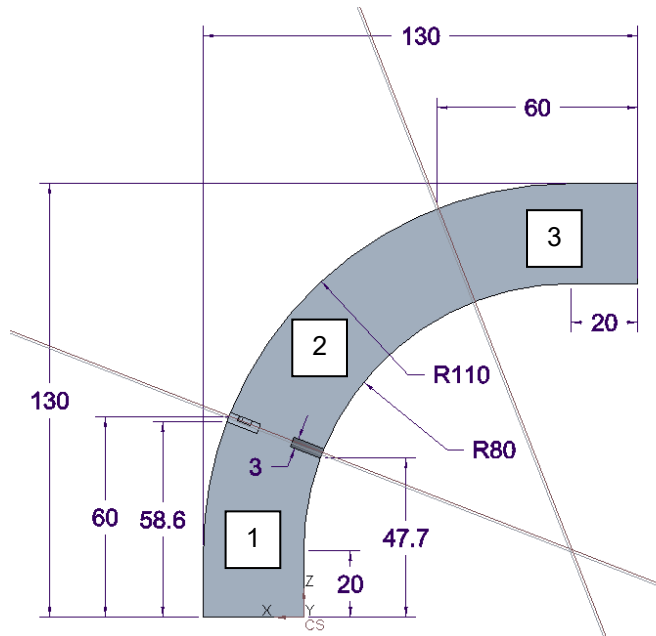


Figure D.1: XZ-plane view of the Maraging steel curved beam with the milled notches. The three sectors of the curved beam with the two dividing planes are indicated. (mm)

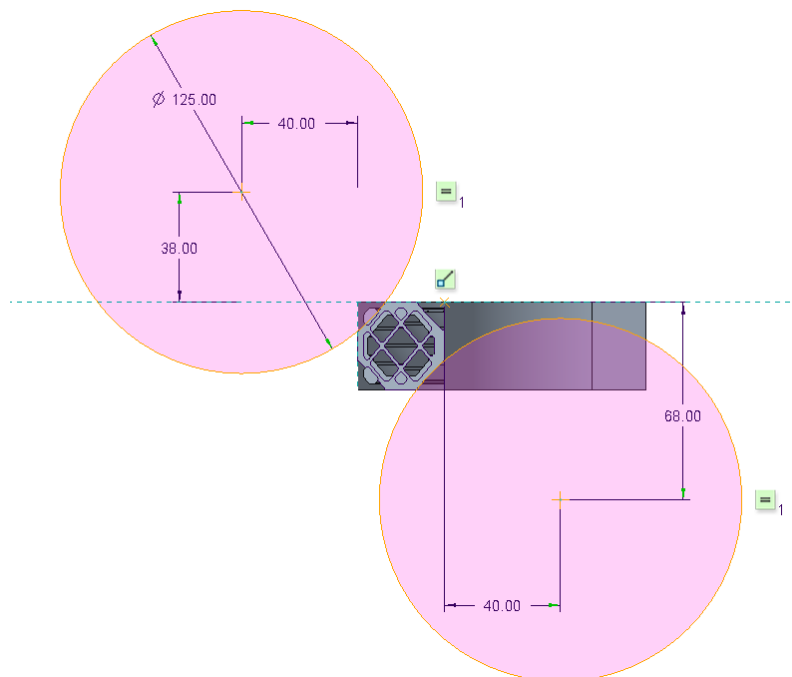


Figure D.2: View of the section of the Maraging steel curved beam made with the plane that is placed in the middle of the notches (Figure D.1). The pink circles represent the cutting disc 3 mm thick and with a diameter of 125 mm that has been used to mill the notches with the milling machine. (mm)

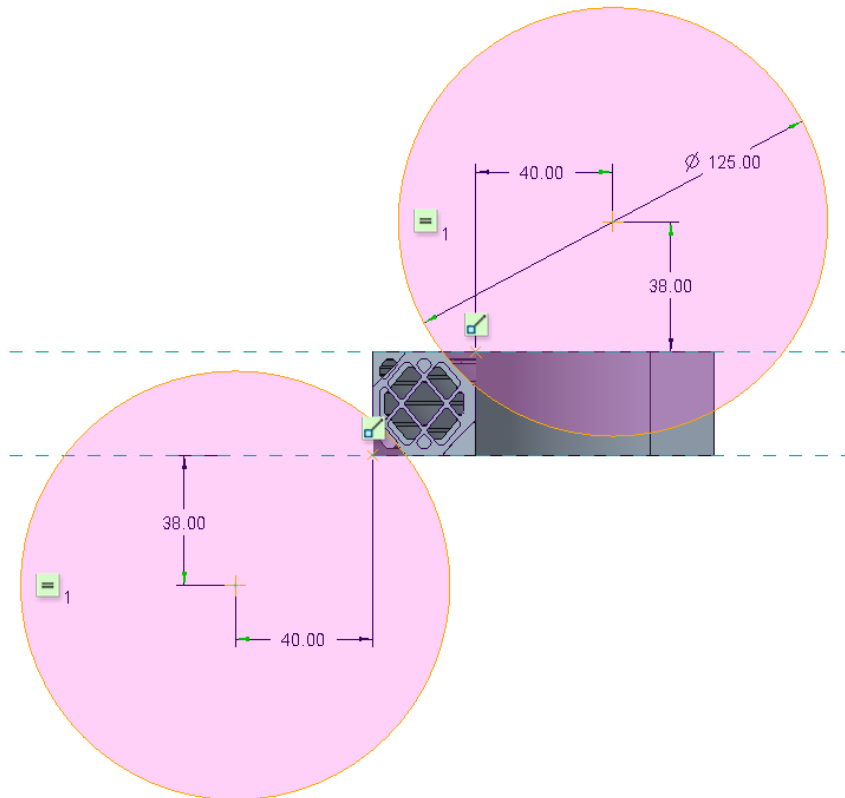


Figure D.3: View of the section of the Maraging steel curved beam made with the plane that is placed in the middle of the notches (Figure D.1). The pink circles represent the cutting disc 3 mm thick and with a diameter of 125 mm that has been used to mill the notches with the milling machine. (mm)

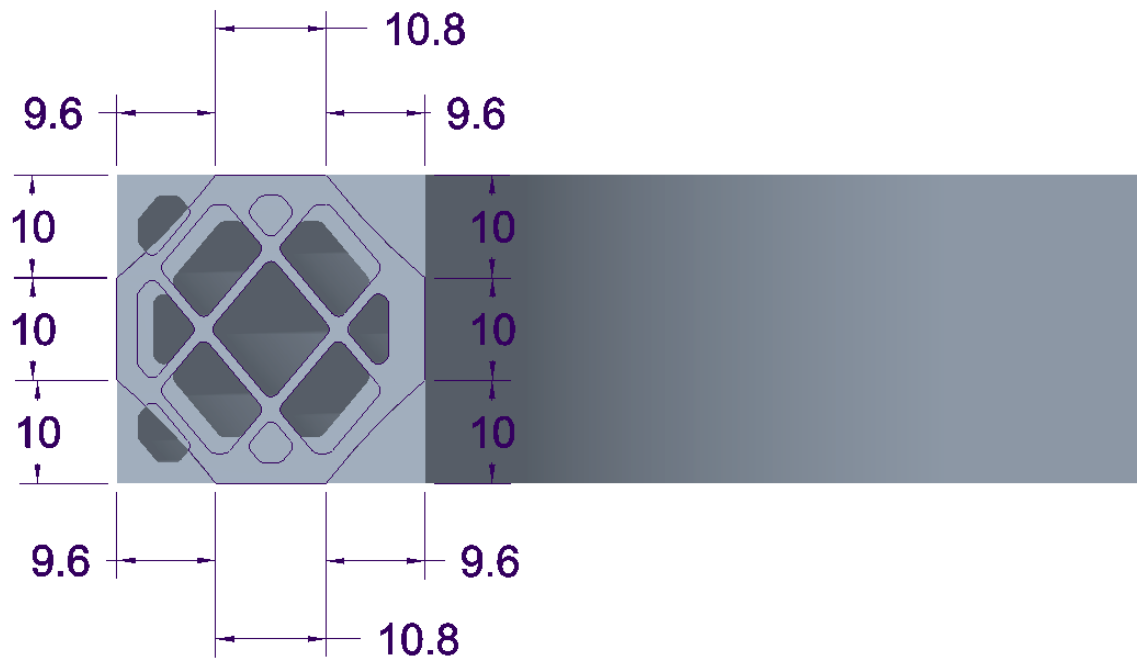


Figure D.4: View of the section of the Maraging steel curved beam made with the plane that is placed in the middle of the notches (Figure D.1). (mm)

It is important to remember that the PA12 curved beam has been reduced in dimensions by 5 %, however the cutting disc 3 mm thick and with a diameter of 125 mm that has been used to mill the notches with the milling machine still the same. So, has been tried to reduce the depths of the notches by almost 5 % but the thickness of the notches had to remain 3 mm.

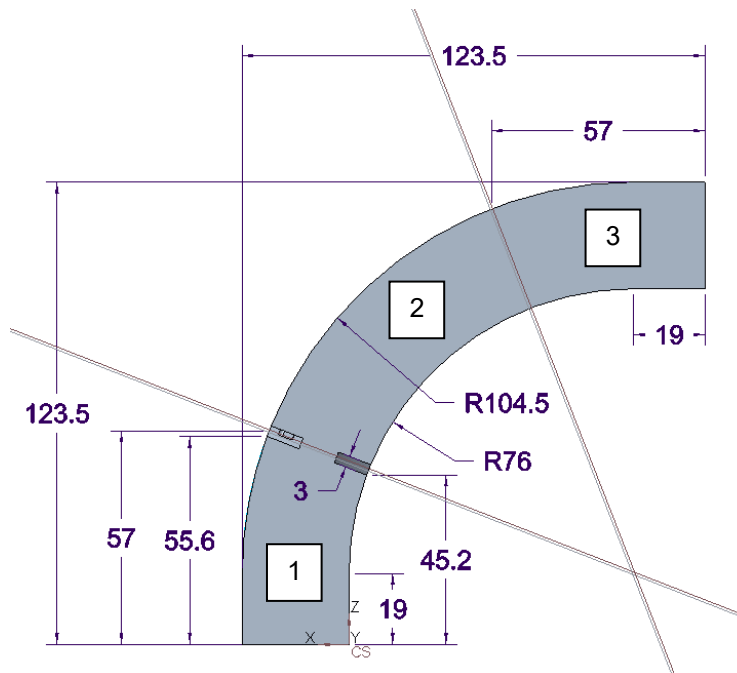


Figure D.5: XZ-plane view of the PA12 curved beam with the milled notches. The three sectors of the curved beam with the two dividing planes are indicated. (mm)

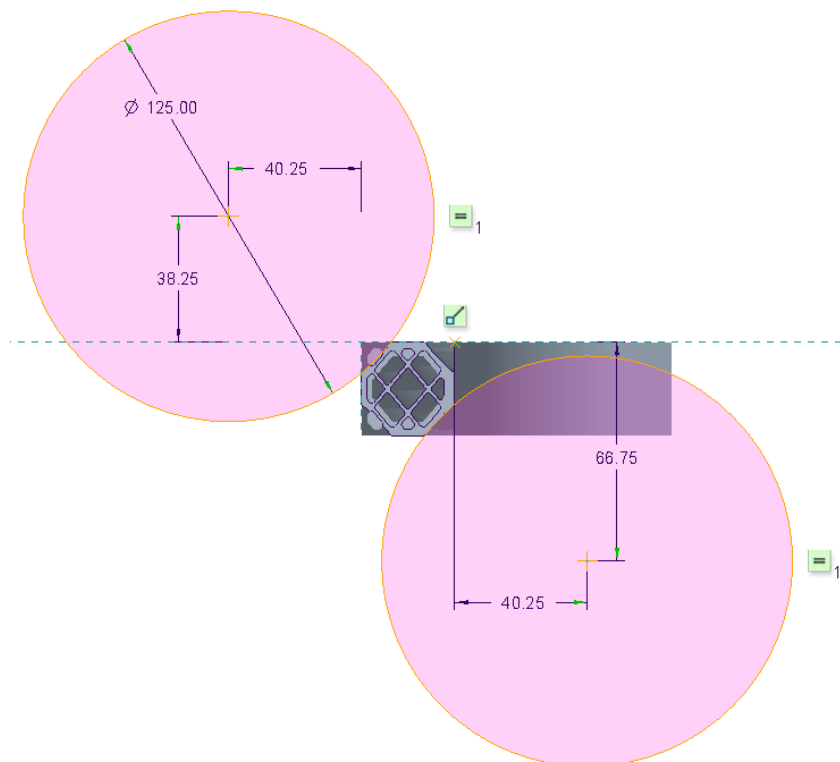


Figure D.6: View of the section of the PA12 curved beam made with the plane that is placed in the middle of the notches (Figure D.5). The pink circles represent the cutting disc 3 mm thick and with a diameter of 125 mm that has been used to mill the notches with the milling machine. (mm)



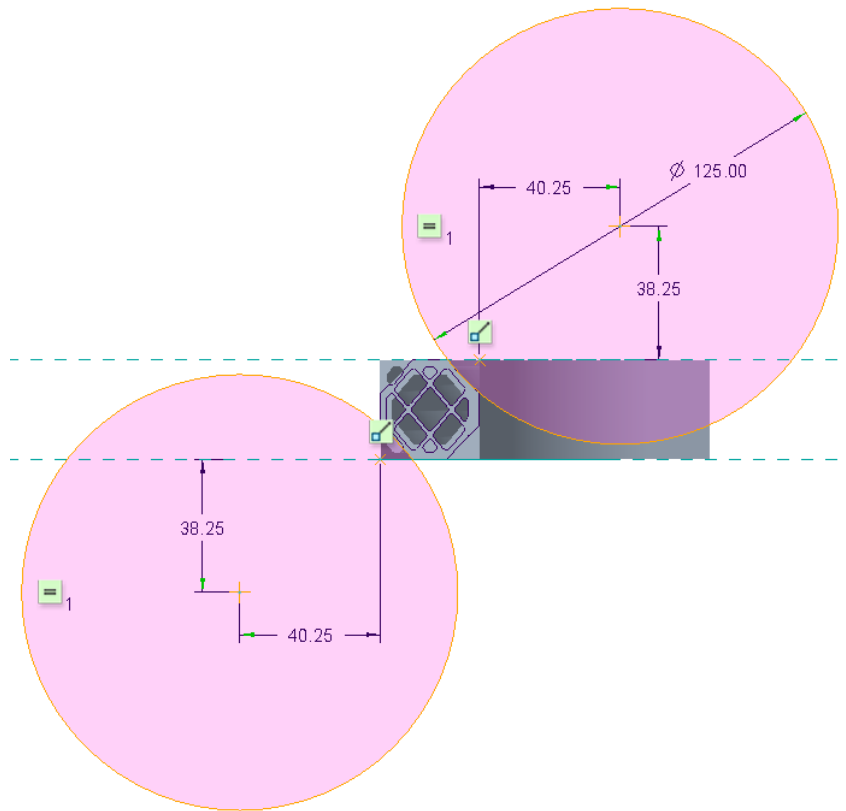


Figure D.7: View of the section of the PA12 curved beam made with the plane that is placed in the middle of the notches (Figure D.5). The pink circles represent the cutting disc 3 mm thick and with a diameter of 125 mm that has been used to mill the notches with the milling machine. (mm)

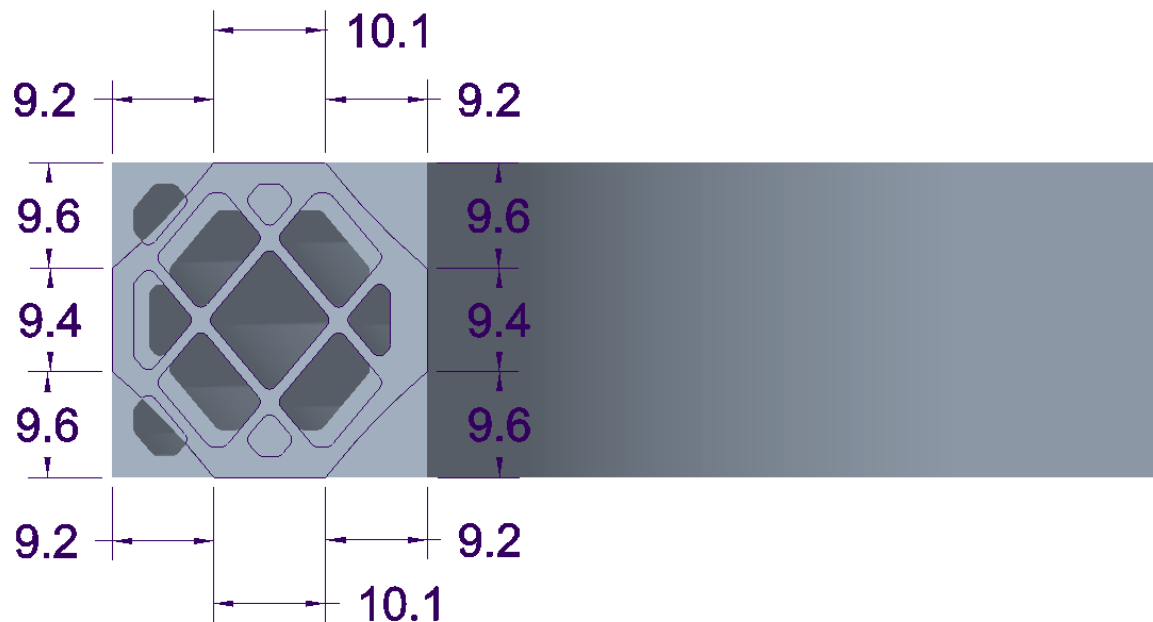


Figure D.8: View of the section of the PA12 curved beam made with the plane that is placed in the middle of the notches (Figure D.5). (mm)

## Annex E: Tensile tests Stress - Strain charts of the PA12 plain specimens

In this Annex it is possible to see the Stress - Strain charts of all the tensile tests of the PA12 specimens that have been performed.

In all the charts the Young's Modulus has been calculated by a linear regression of the Stress - Strain data from 0 MPa to 15 MPa, assuming a Yield stress value of 15 MPa for the PA12 material.

It is possible to see also that in all the charts the  $\sigma_{P,0.2}$  is almost 20 MPa.

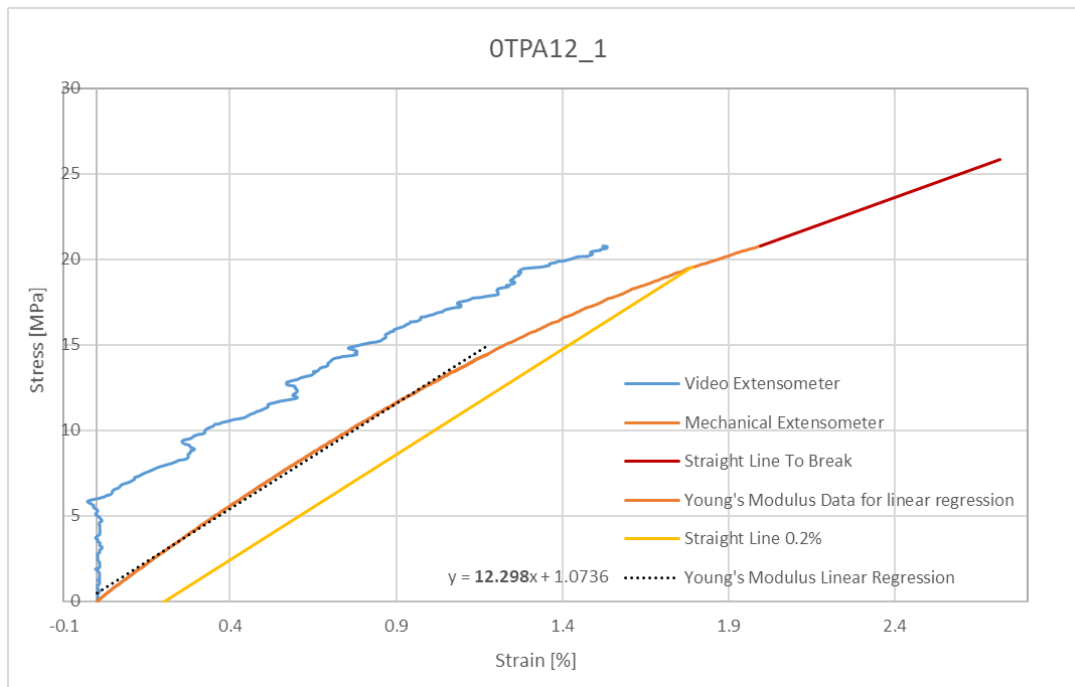


Figure E.1: Stress - Strain chart of the 0TPA12\_1 specimen.

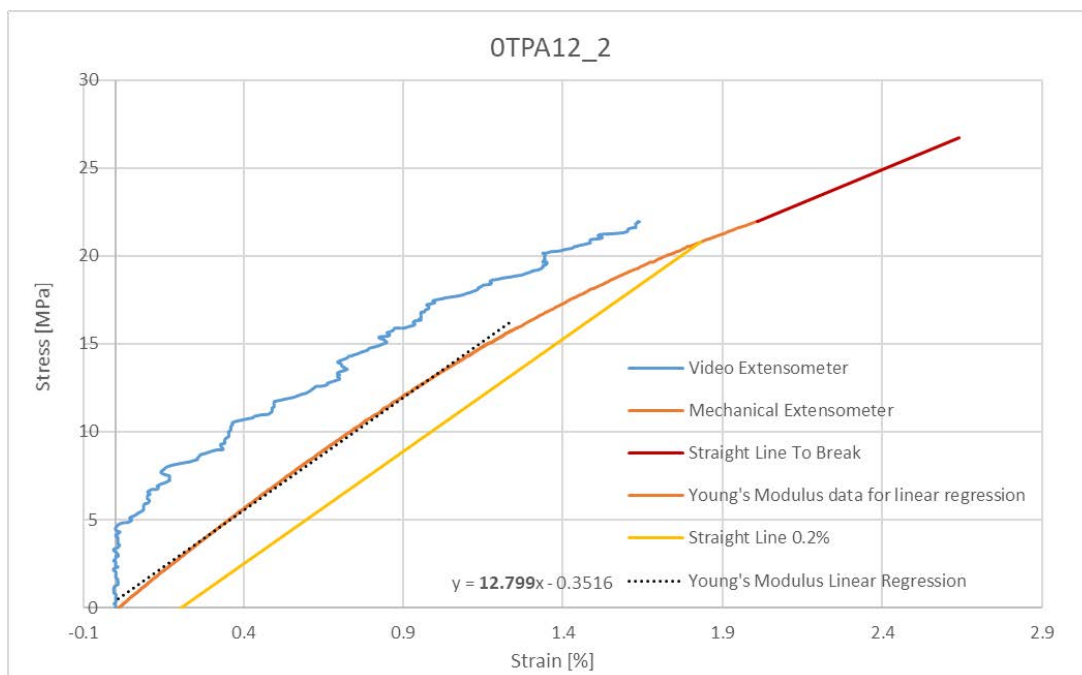


Figure E.2: Stress - Strain chart of the 0TPA12\_2 specimen.

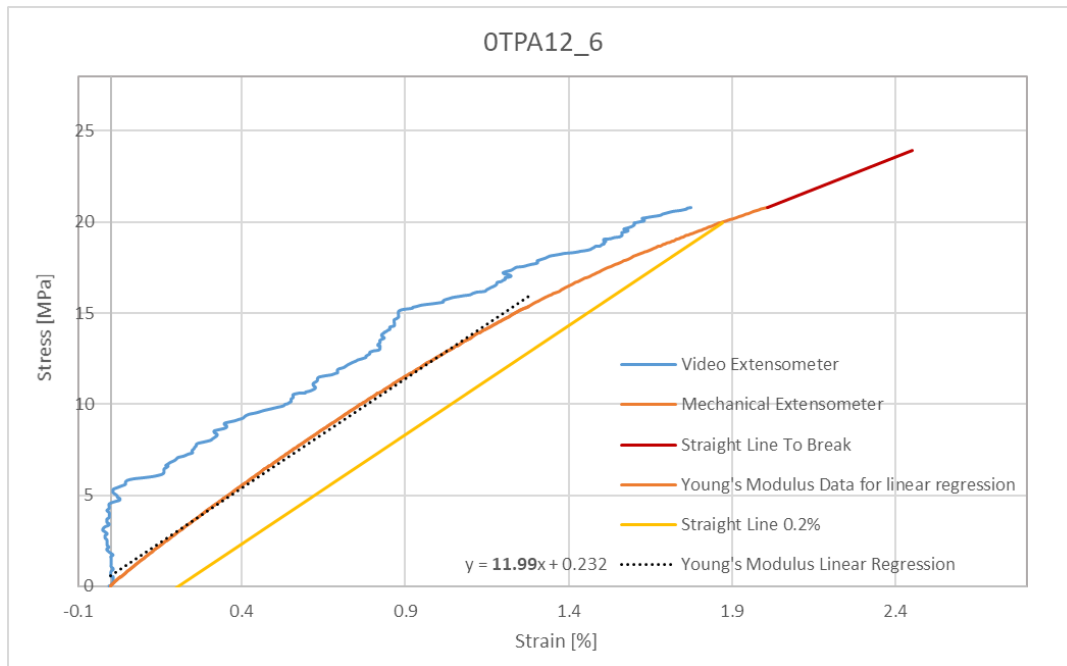


Figure E.3: Stress - Strain chart of the 0TPA12\_6 specimen.

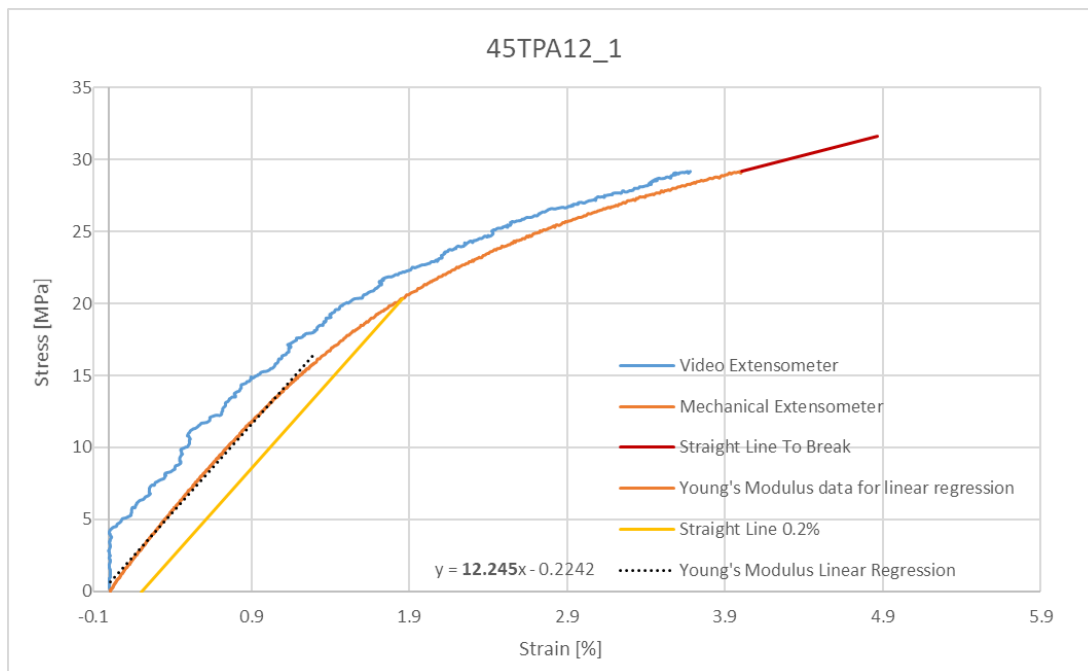


Figure E.4: Stress - Strain chart of the 45TPA12\_1 specimen.

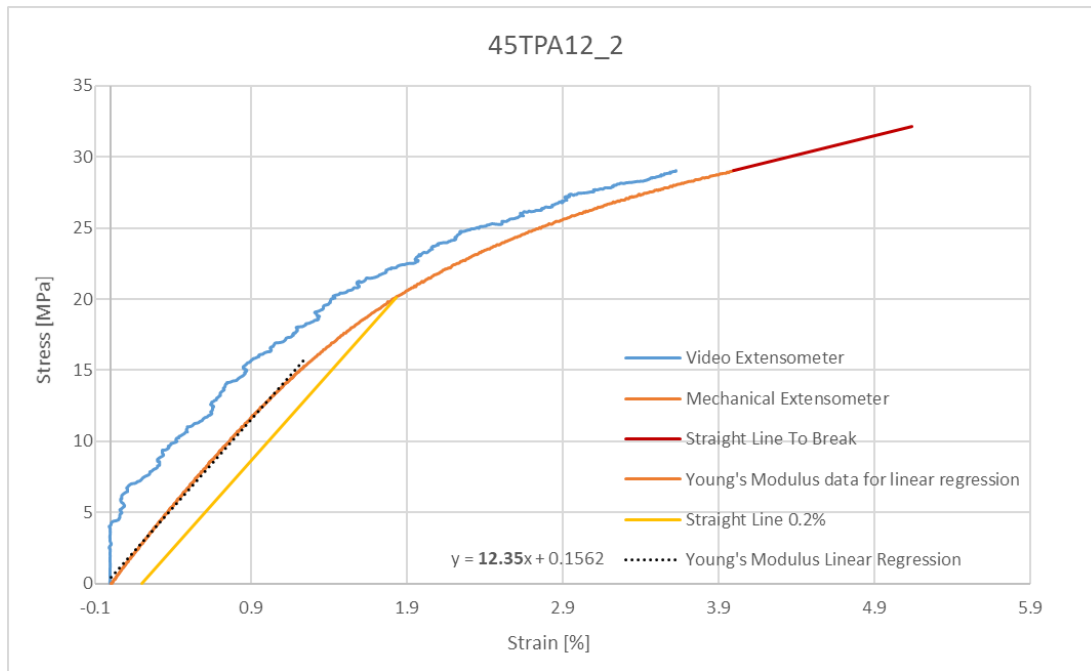


Figure E.5: Stress - Strain chart of the 45TPA12\_2 specimen.

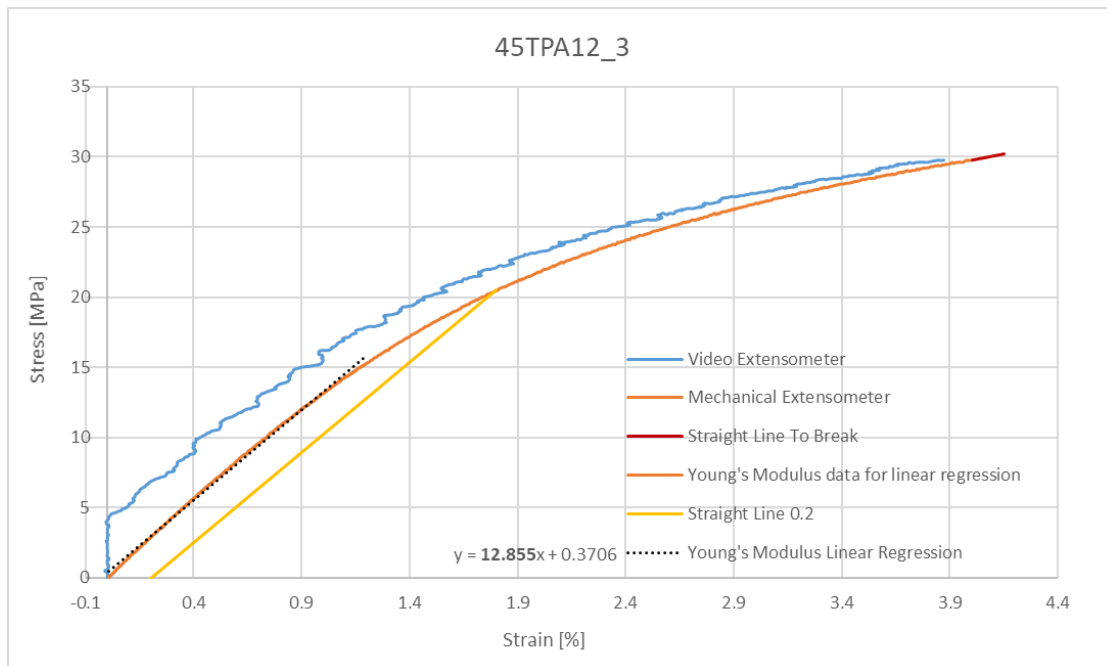


Figure E.6: Stress - Strain chart of the 45TPA12\_3 specimen.

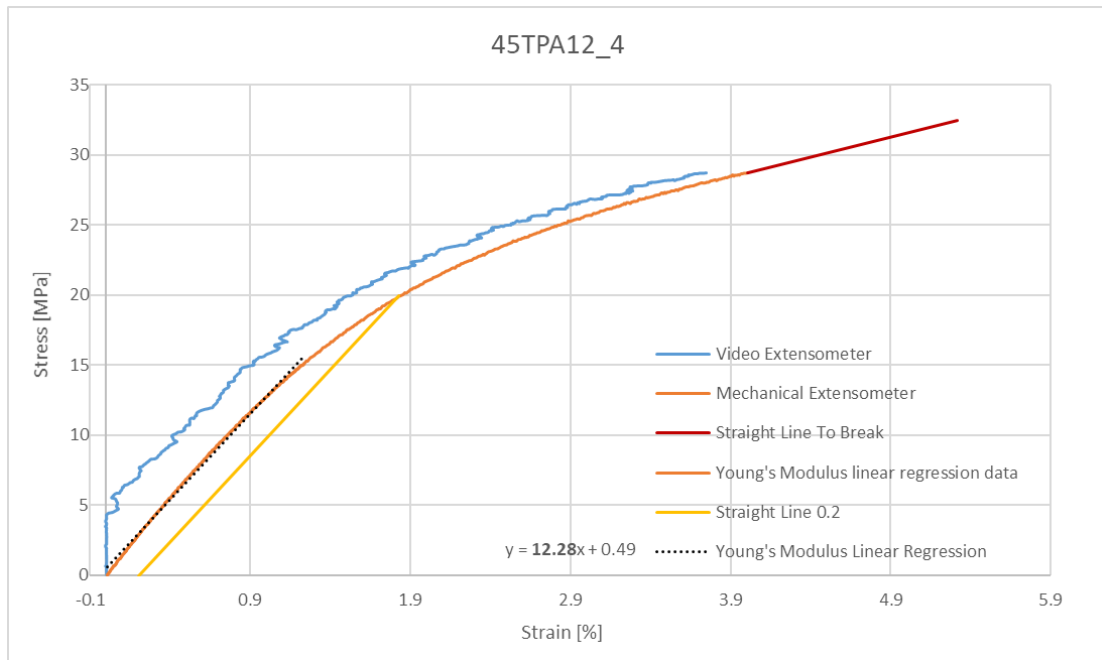


Figure E.7: Stress - Strain chart of the 45TPA12\_4 specimen.

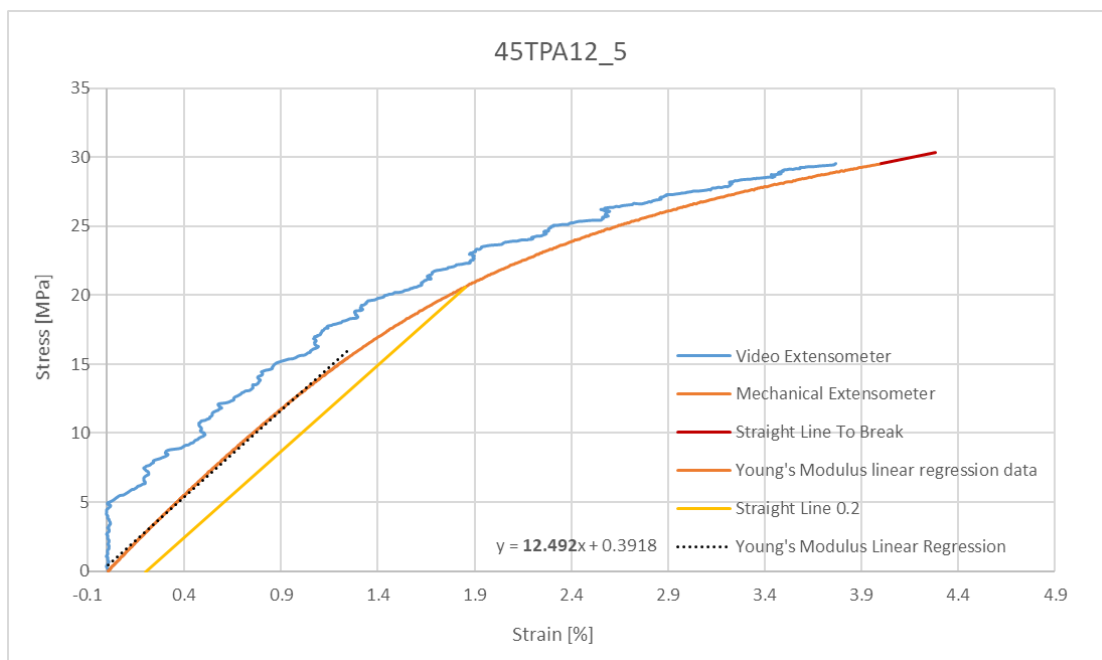


Figure E.8: Stress - Strain chart of the 45TPA12\_5 specimen.

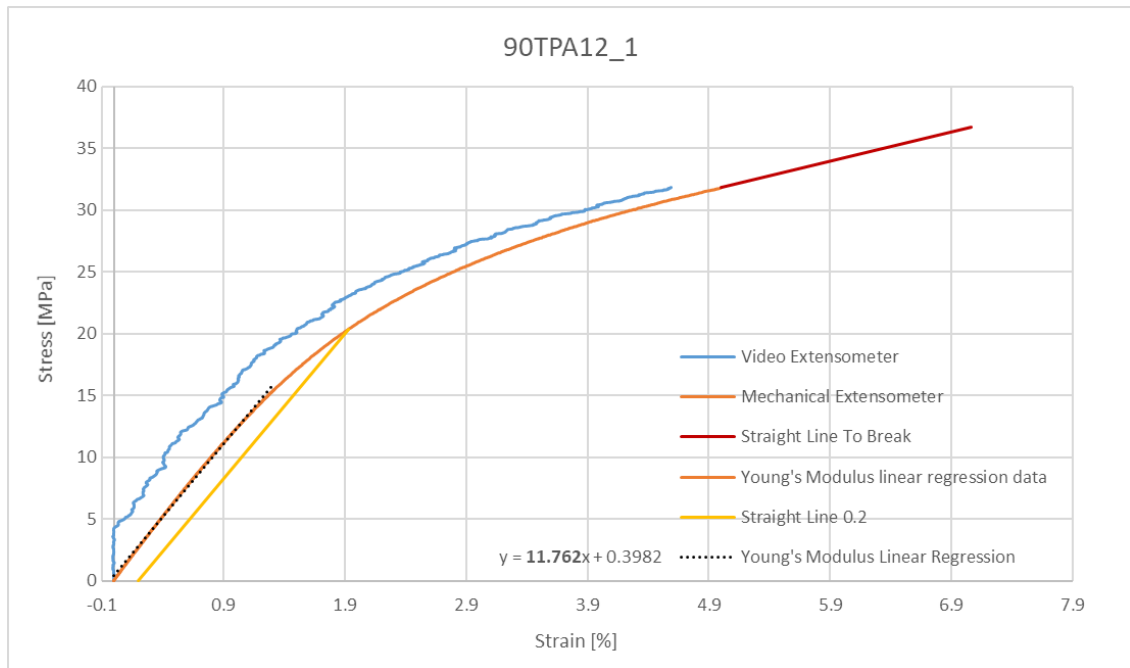


Figure E.9: Stress - Strain chart of the 90TPA12\_1 specimen.

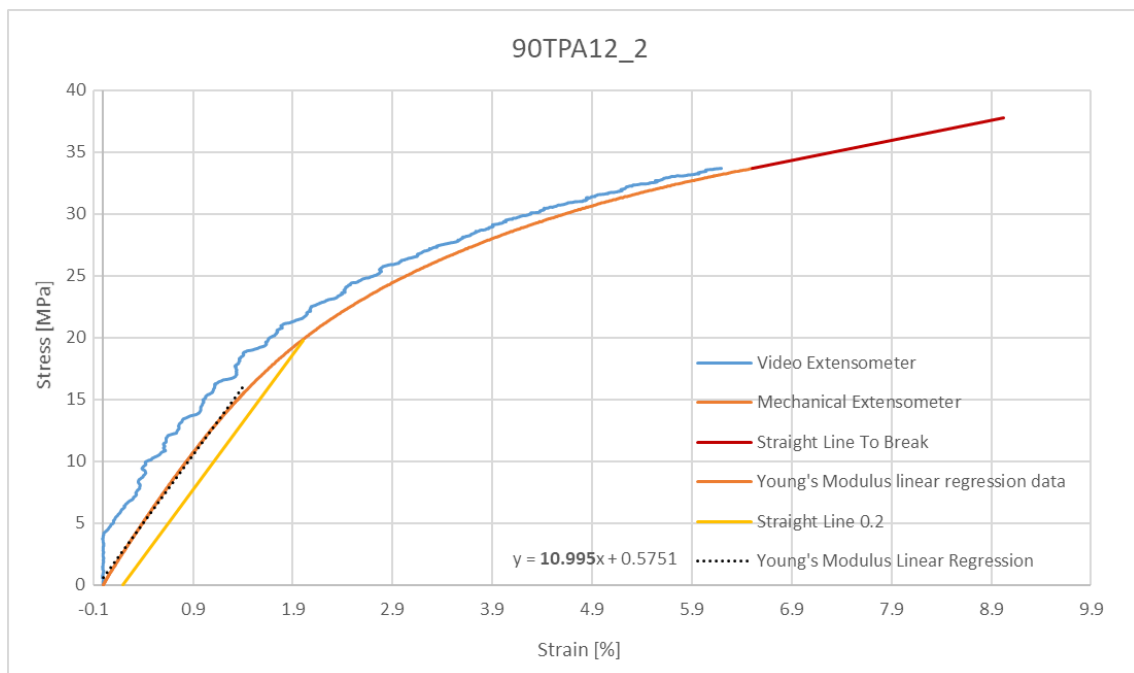


Figure E.10: Stress - Strain chart of the 90TPA12\_2 specimen.

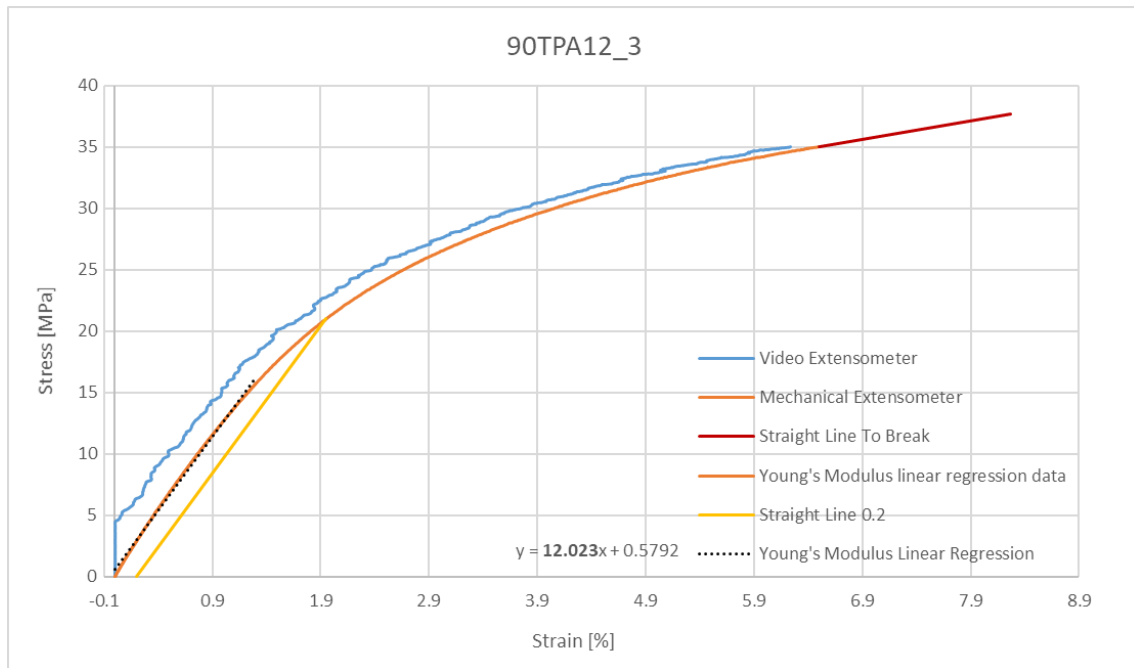


Figure E.11: Stress - Strain chart of the 90TPA12\_3 specimen.

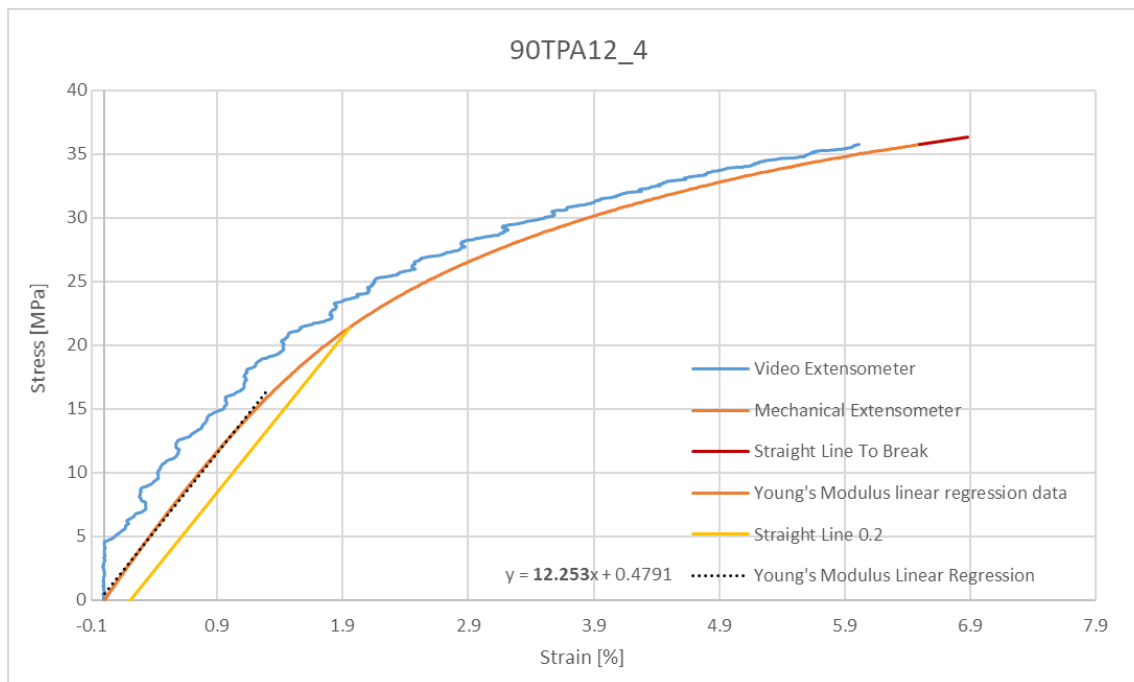


Figure E.12: Stress - Strain chart of the 90TPA12\_4 specimen.



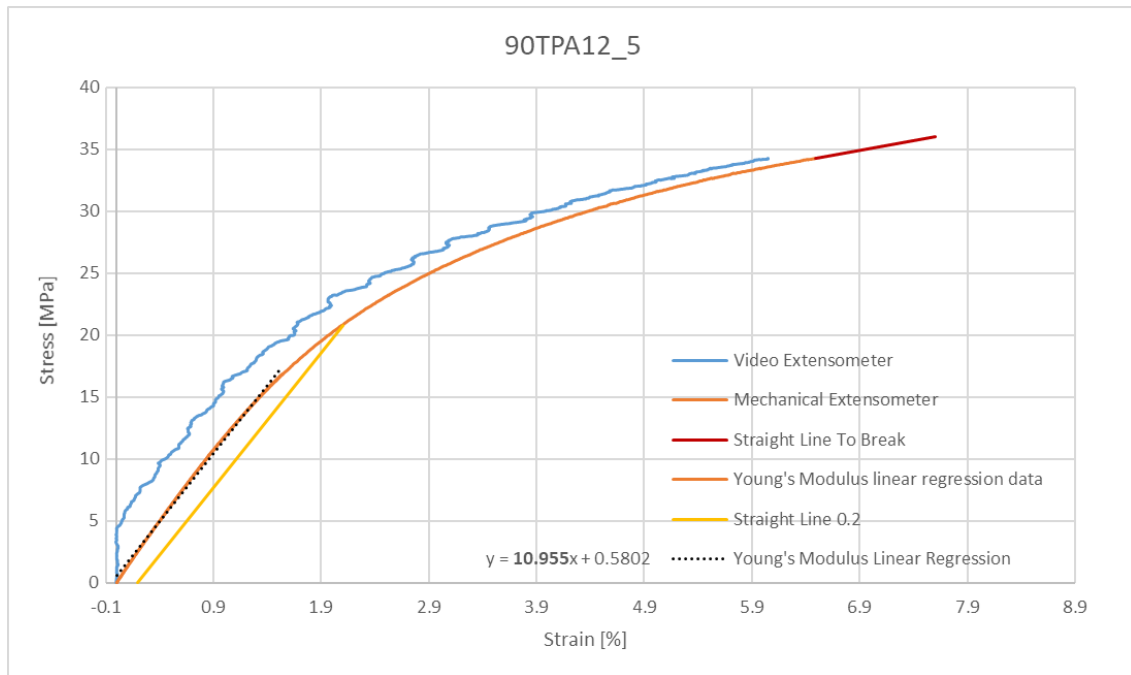


Figure E.13: Stress - Strain chart of the 90TPA12\_5 specimen.

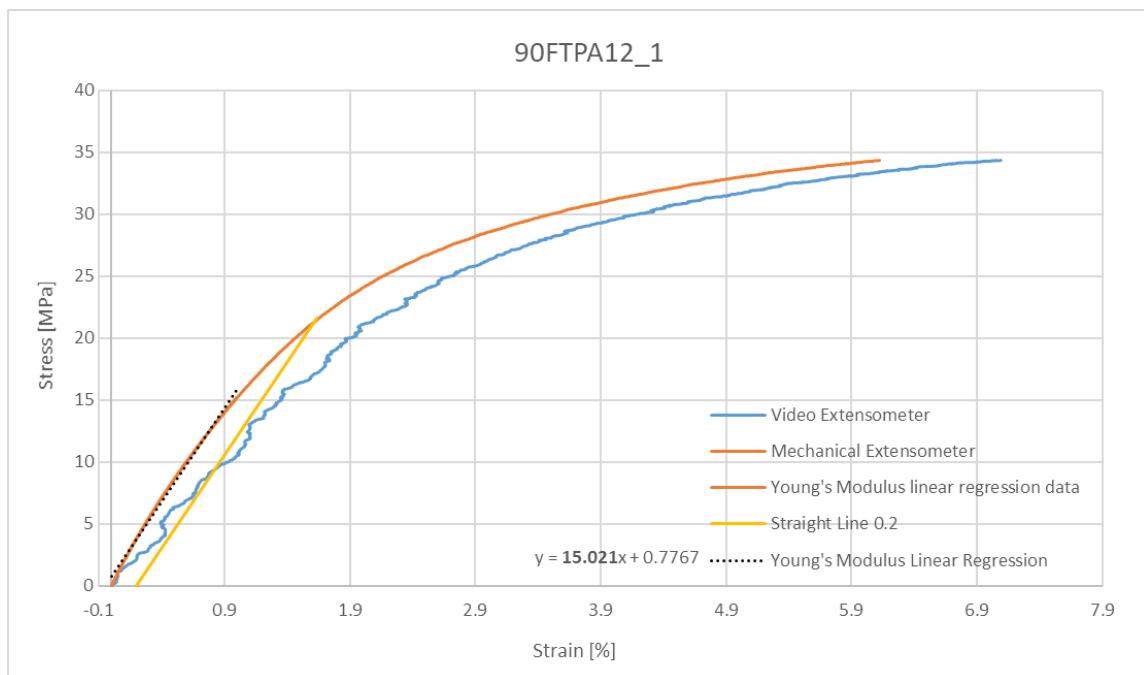


Figure E.14: Stress - Strain chart of the 90FTPA12\_1 specimen.

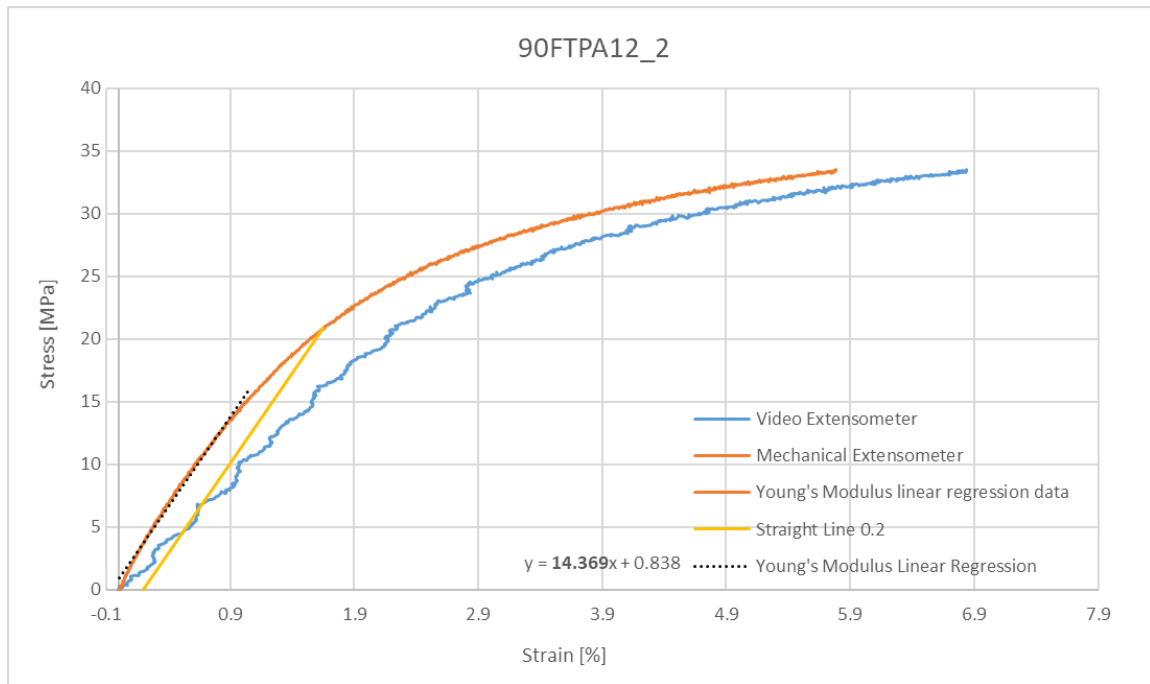


Figure E.15: Stress - Strain chart of the 90FPA12\_2 specimen.

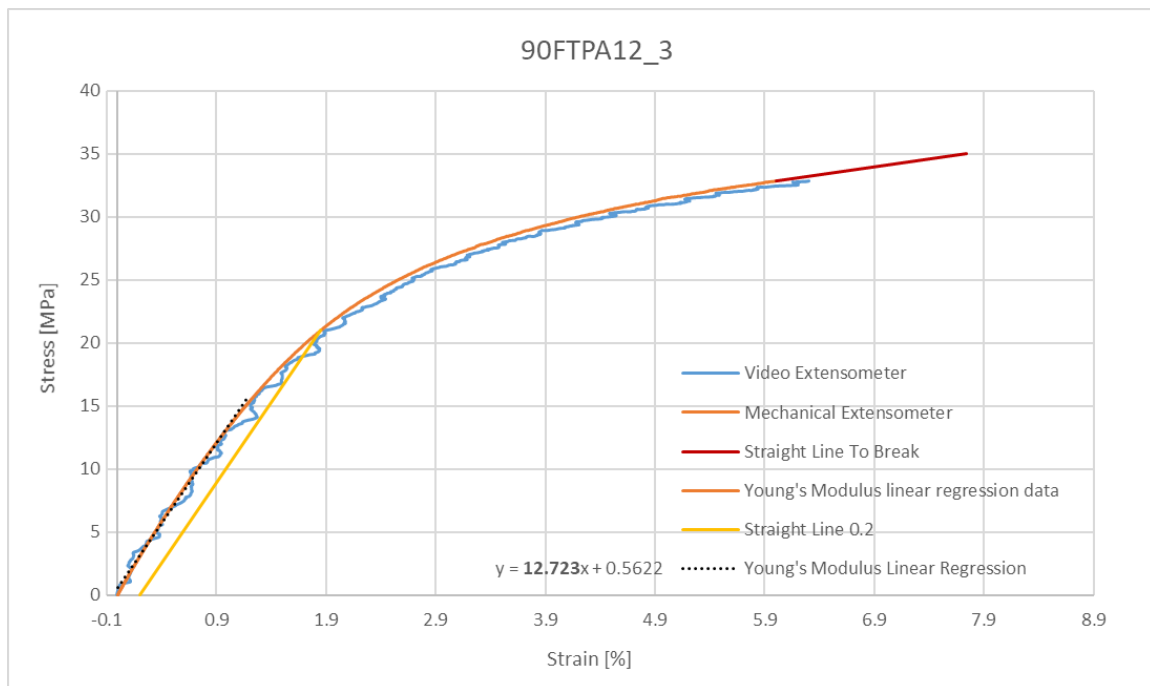


Figure E.16: Stress - Strain chart of the 90FPA12\_3 specimen.

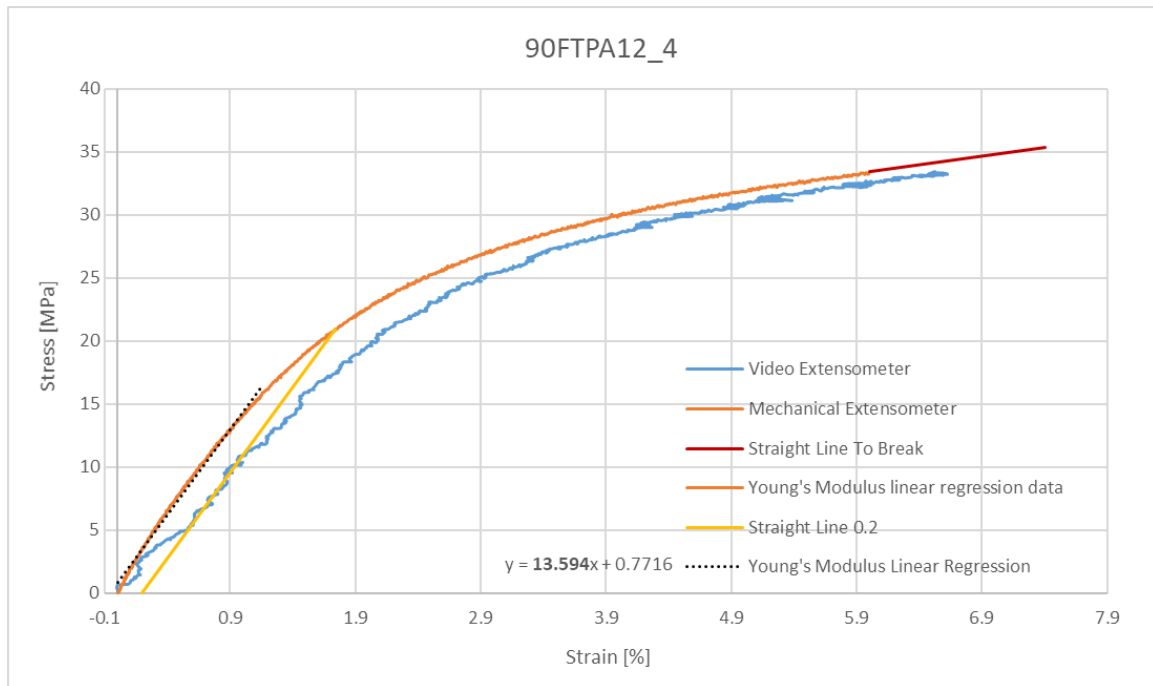


Figure E.17: Stress - Strain chart of the 90FPA12\_4 specimen.

# Annex F: Measurements of the fillet radii of the rounded V-notch specimens

In this annex have been reported all the images of all the measurements of the fillet radii of the rounded V-notch specimens. In the images it is possible to see the measured diameters of the V-notches apexes, to get the radii measurements it is possible to just divide by two the measured diameters.

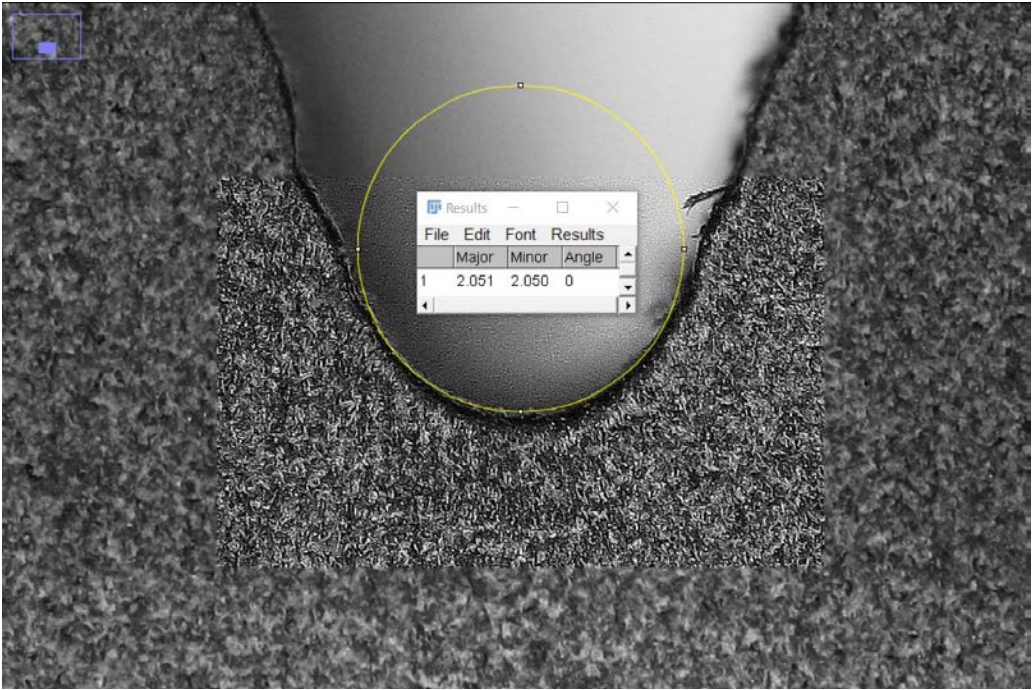


Figure F.1: Measure of the V-notch apex diameter of the 0VR1PA12\_-1\_1 specimen.

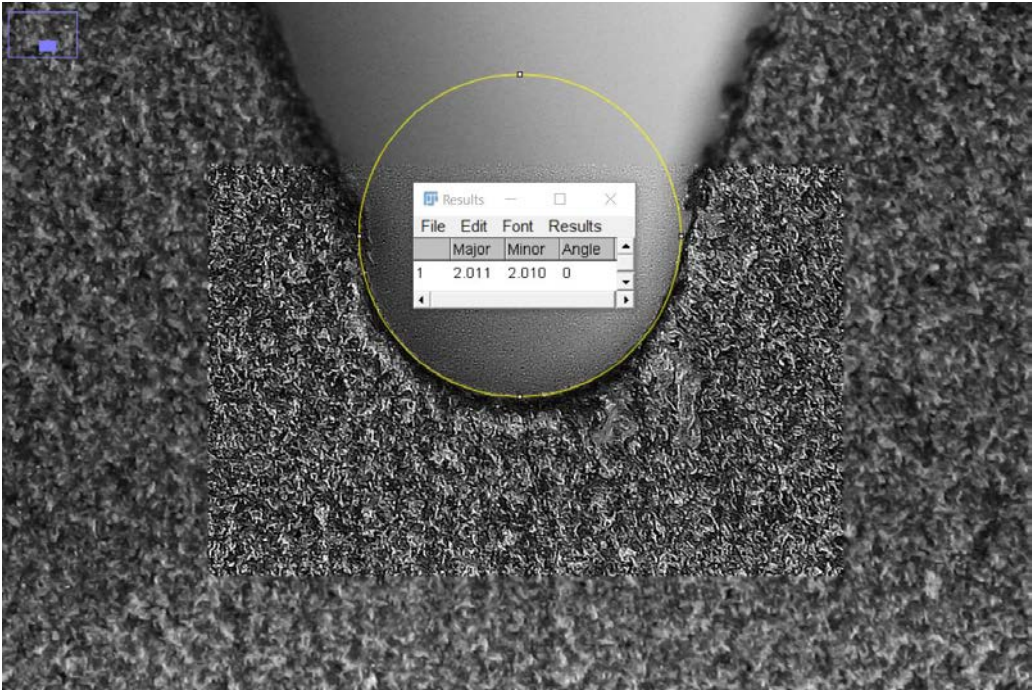


Figure F.2: Measure of the V-notch apex diameter of the 0VR1PA12\_-1\_1BIS specimen.



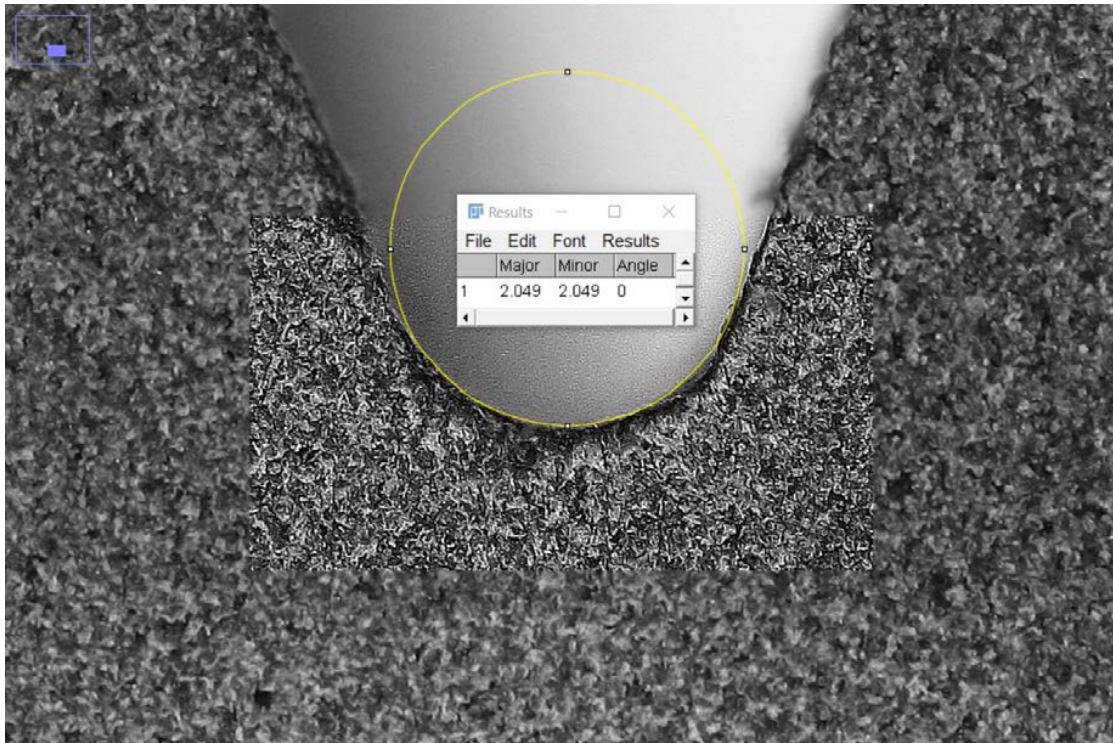


Figure F.3: Measure of the V-notch apex diameter of the 0VR1PA12\_-1\_2 specimen.

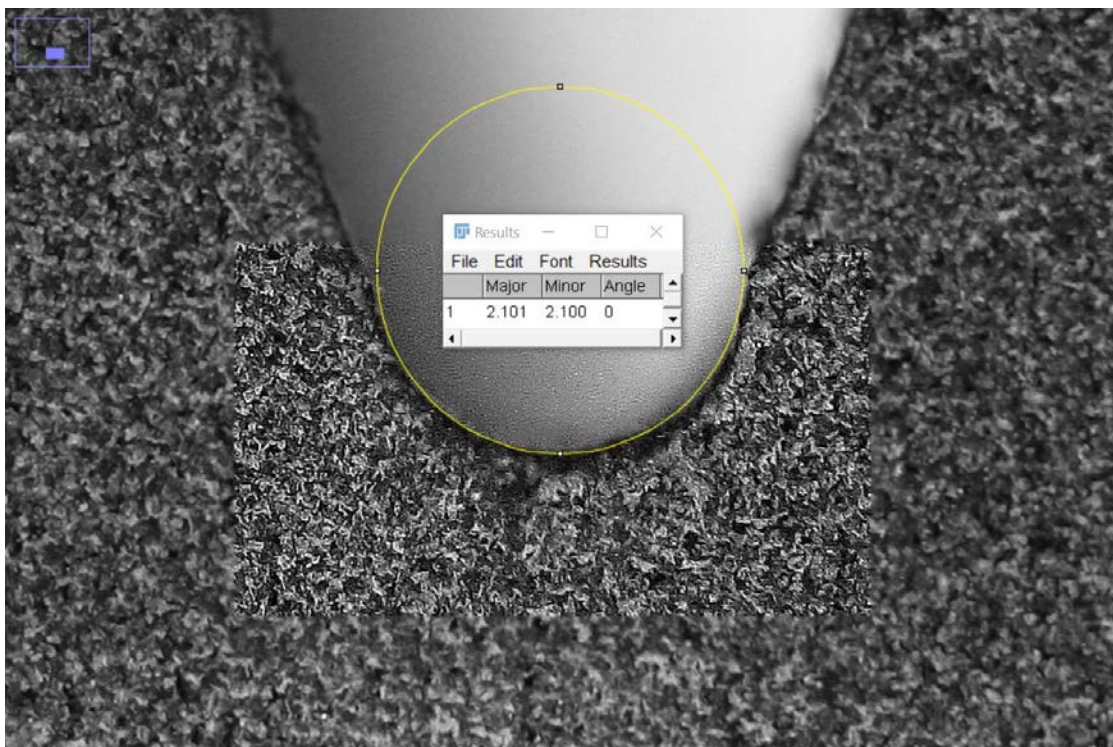


Figure F.4: Measure of the V-notch apex diameter of the 0VR1PA12\_-1\_3 specimen.



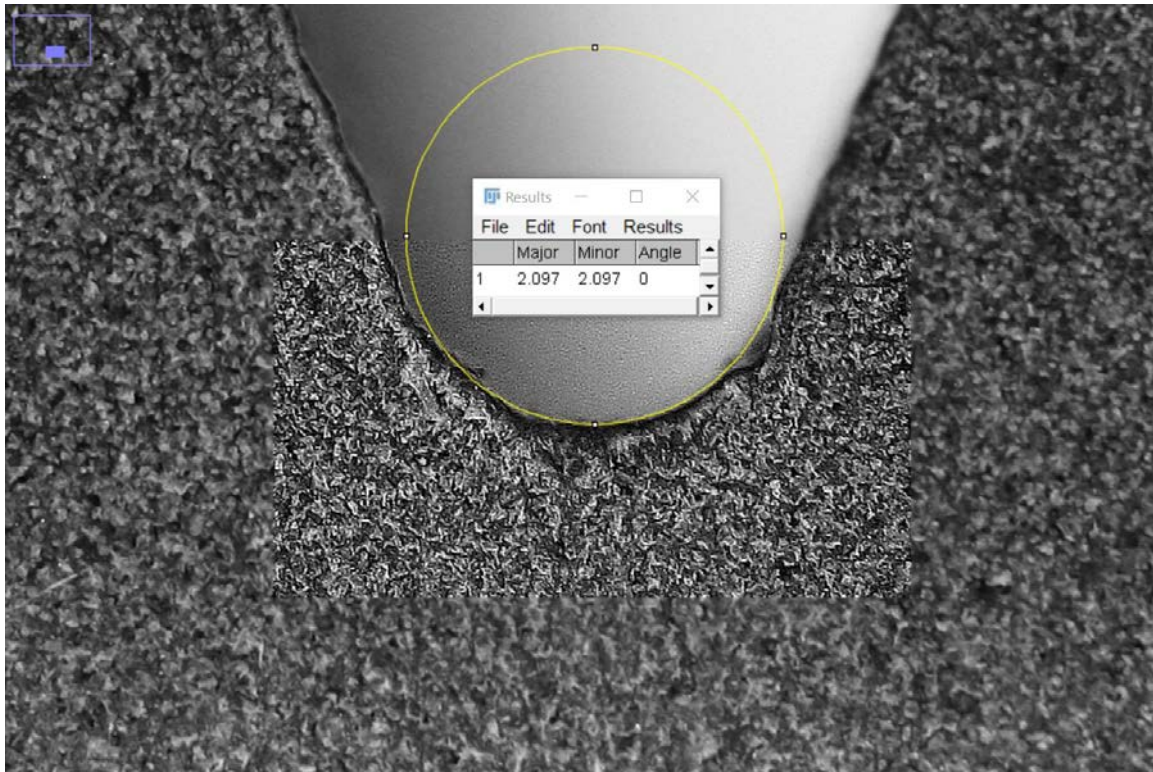


Figure F.5: Measure of the V-notch apex diameter of the 0VR1PA12\_-1\_4 specimen.

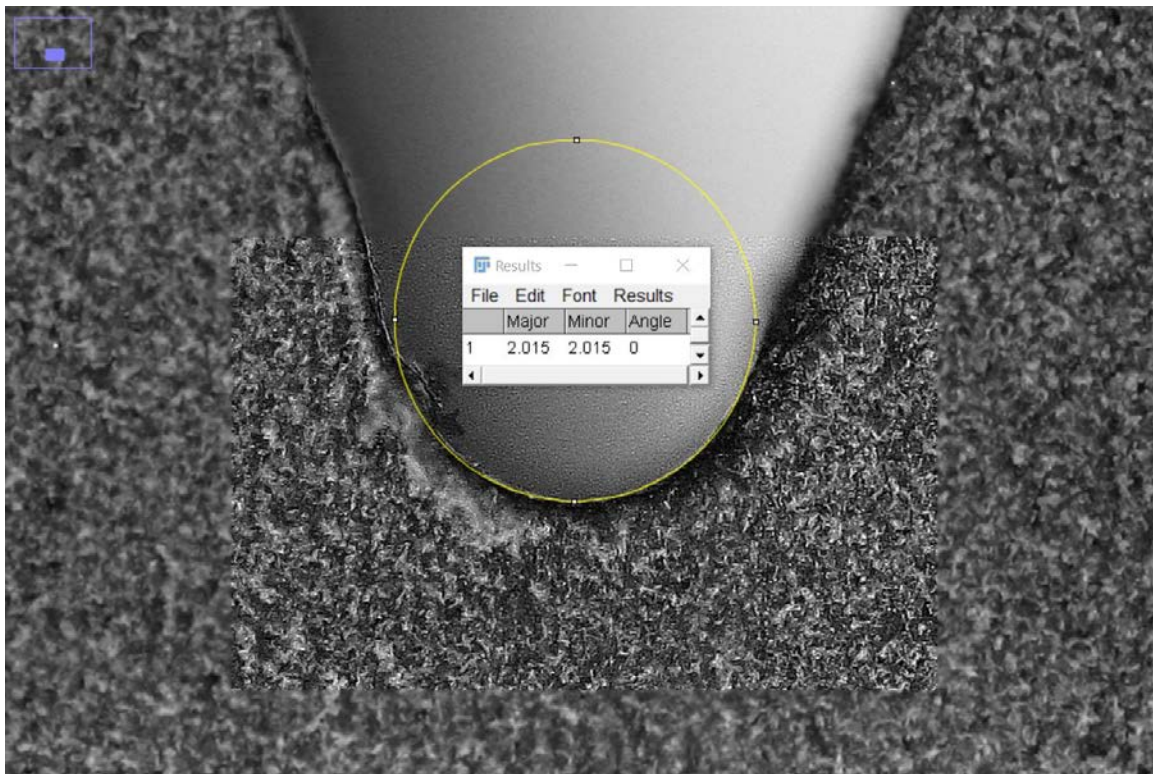


Figure F.6: Measure of the V-notch apex diameter of the 0VR1PA12\_-1\_5 specimen.



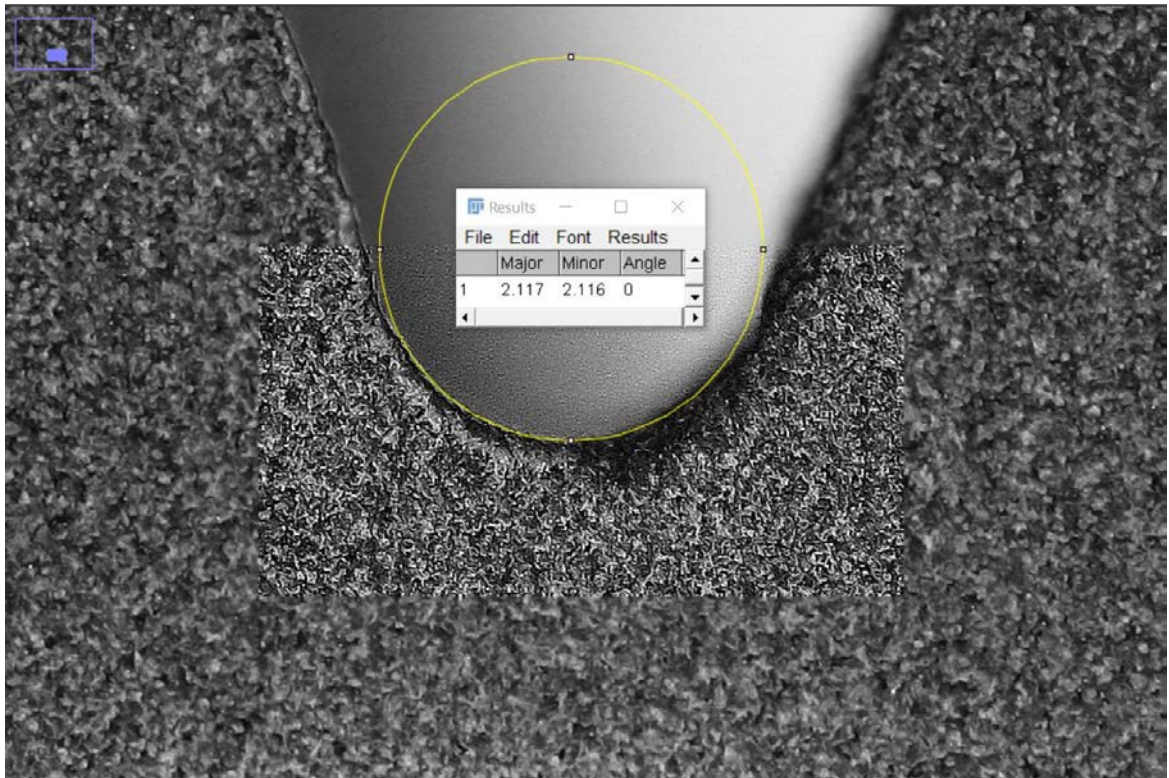


Figure F.7: Measure of the V-notch apex diameter of the 0VR1PA12\_-1\_6 specimen.

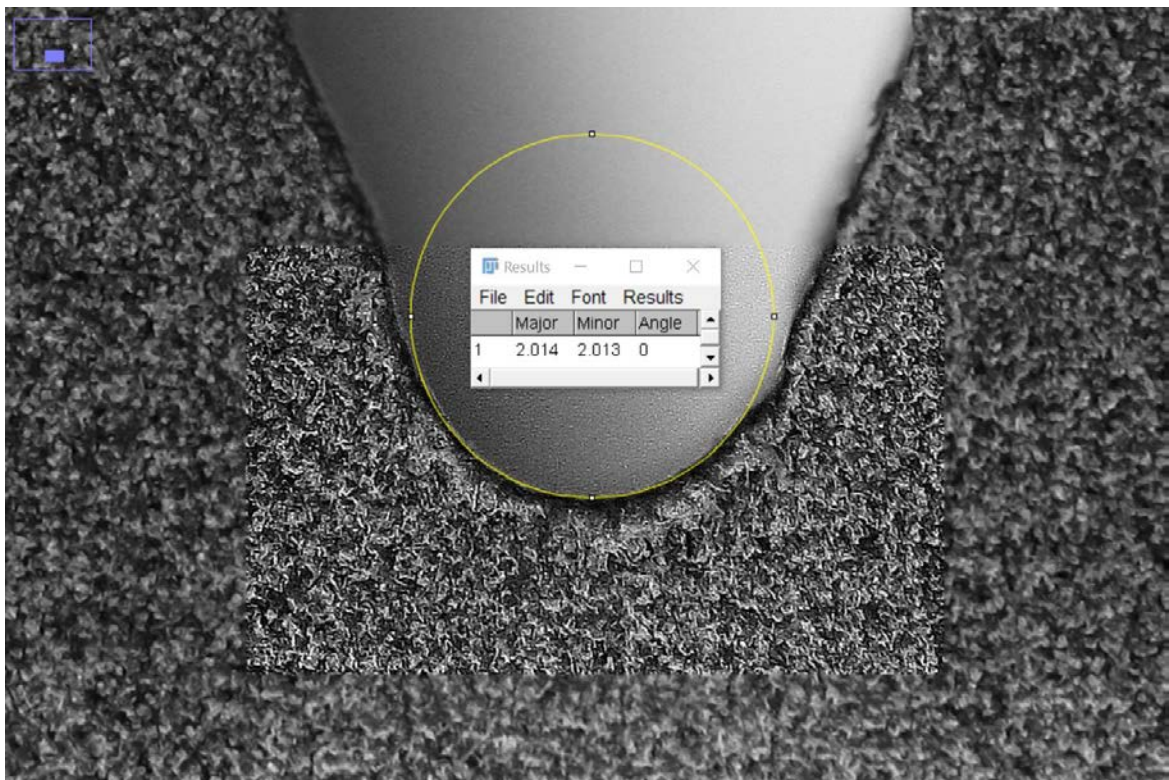


Figure F.8: Measure of the V-notch apex diameter of the 0VR1PA12\_-1\_7 specimen.



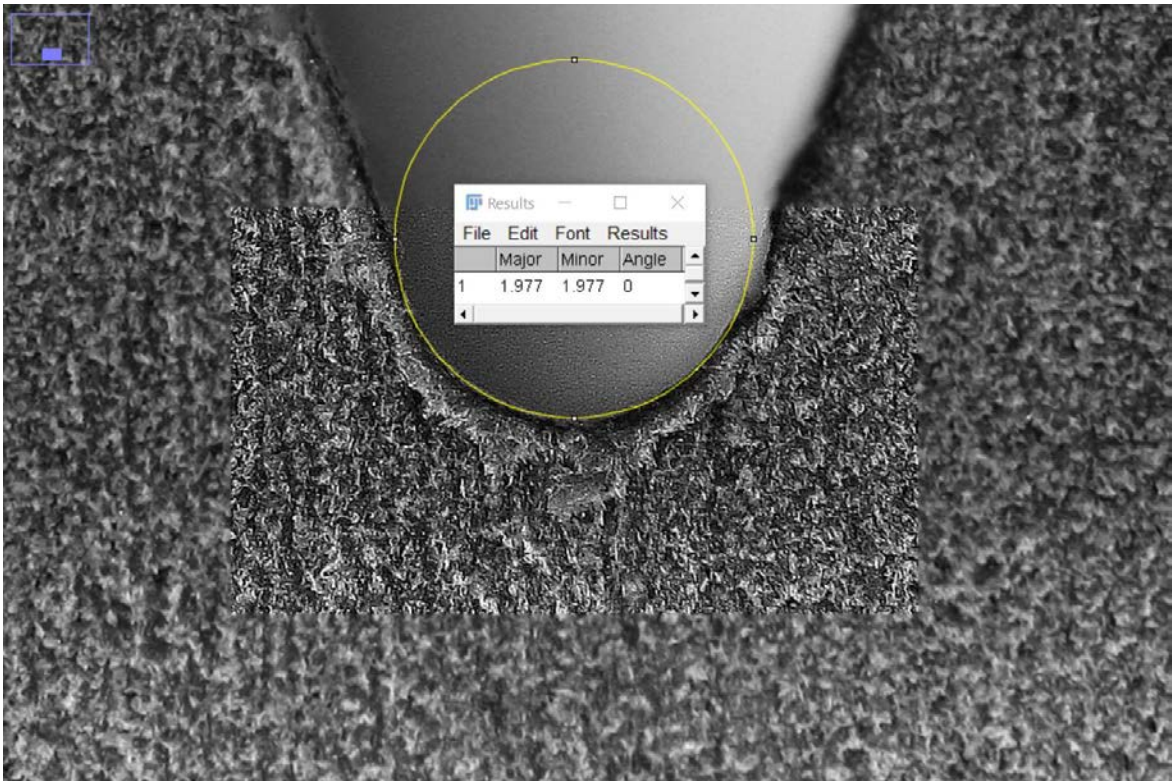


Figure F.9: Measure of the V-notch apex diameter of the 0VR1PA12\_-1\_8 specimen.

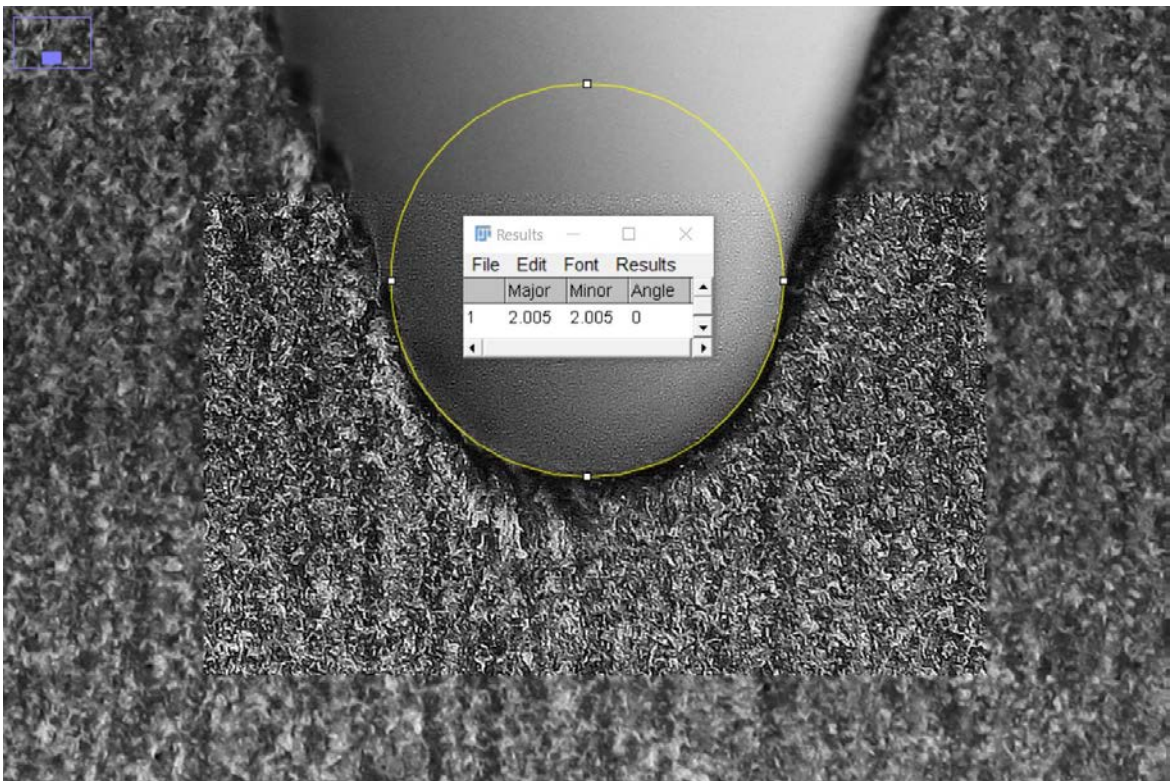


Figure F.10: Measure of the V-notch apex diameter of the 0VR1PA12\_-1\_9 specimen.



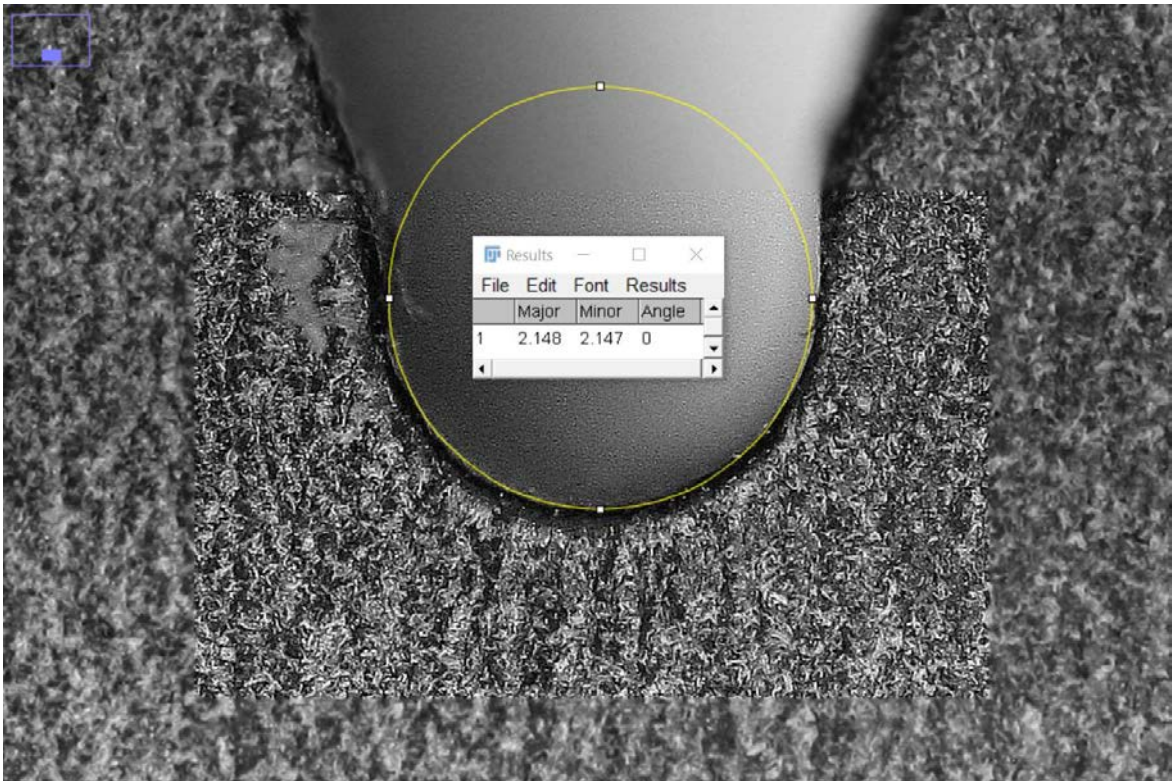


Figure F.11: Measure of the V-notch apex diameter of the 0VR1PA12\_-1\_10 specimen.

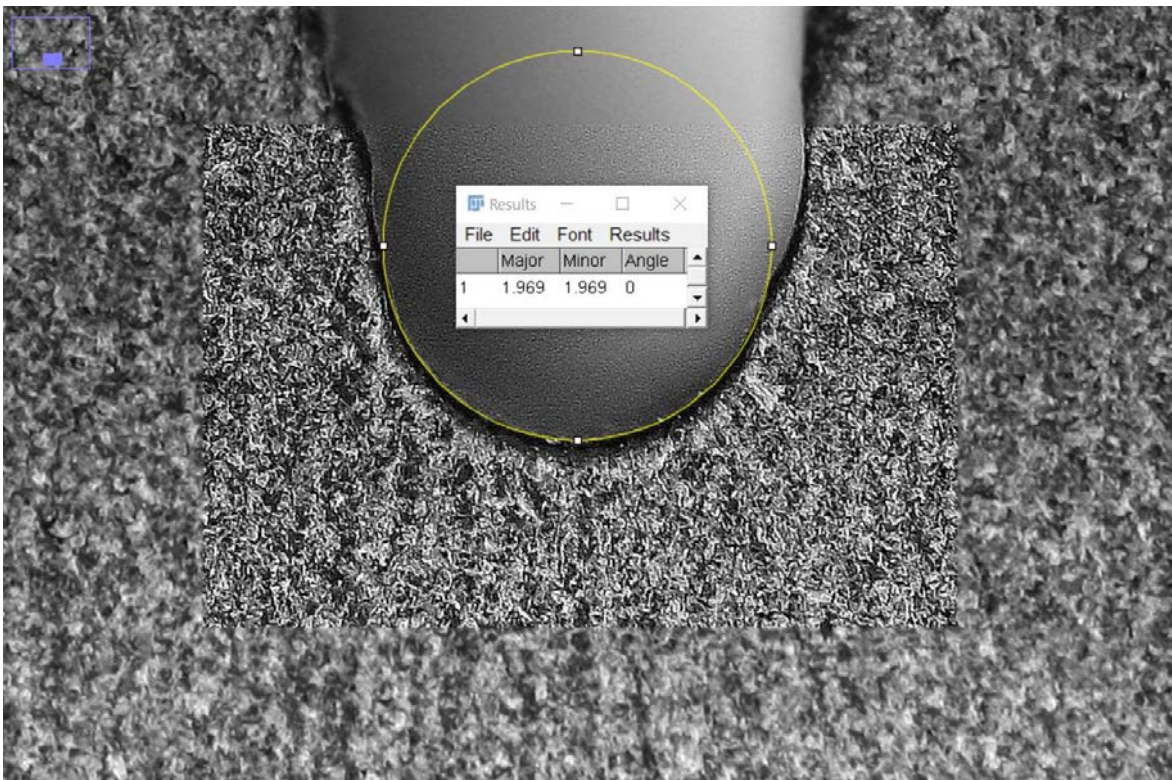


Figure F.12: Measure of the V-notch apex diameter of the 0VR1PA12\_-1\_11 specimen.



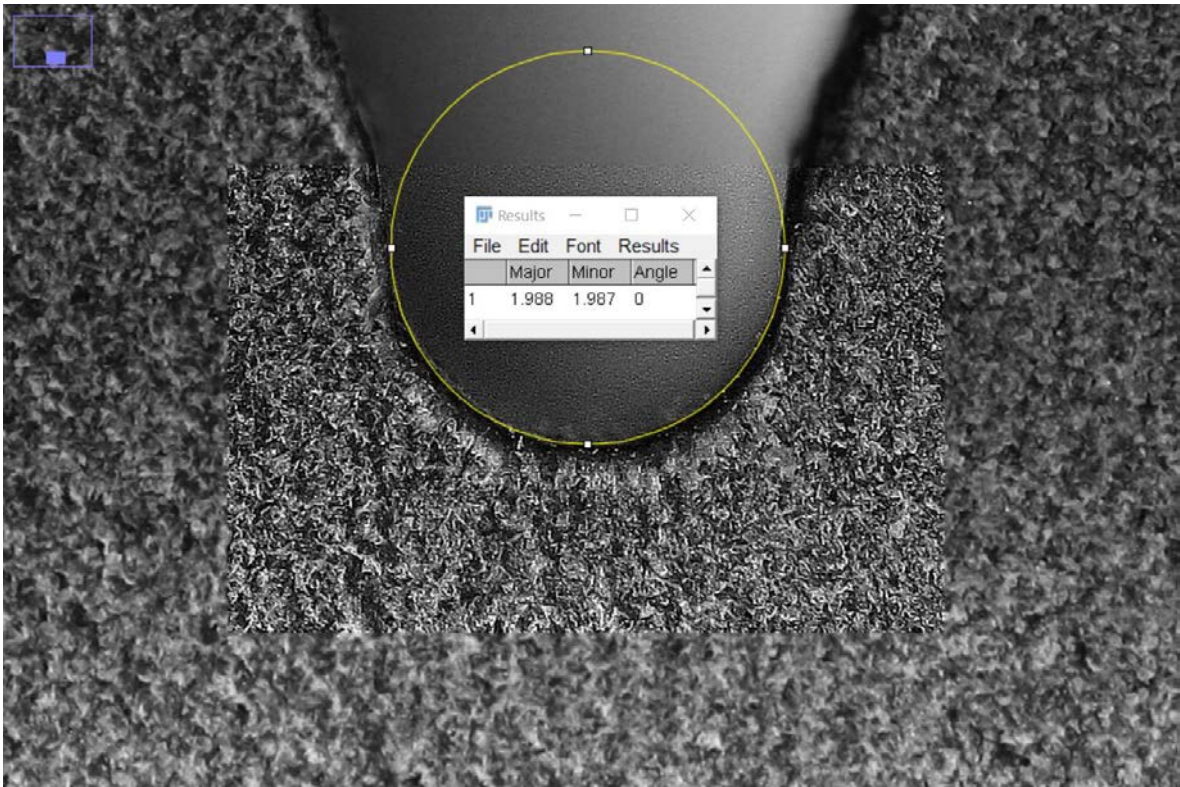


Figure F.13: Measure of the V-notch apex diameter of the 0VR1PA12\_-1\_12 specimen.

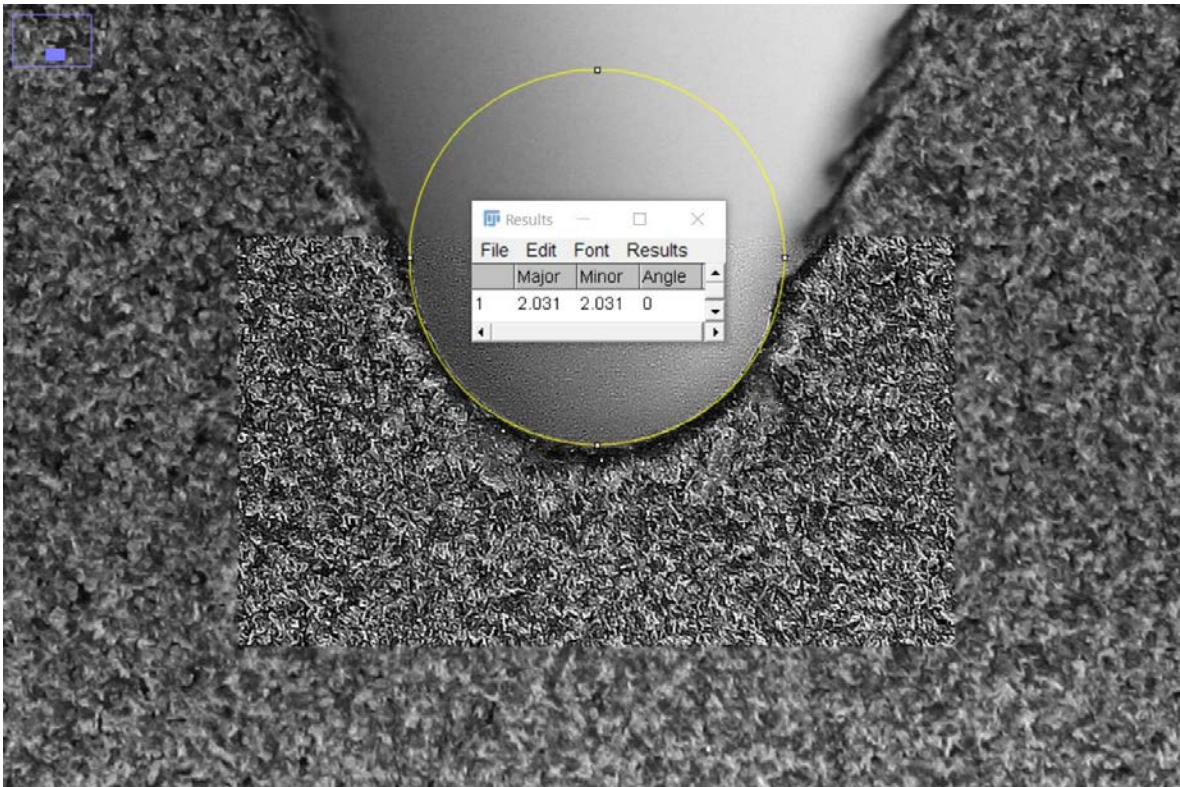


Figure F.14: Measure of the V-notch apex diameter of the 45VR1PA12\_-1\_1 specimen.



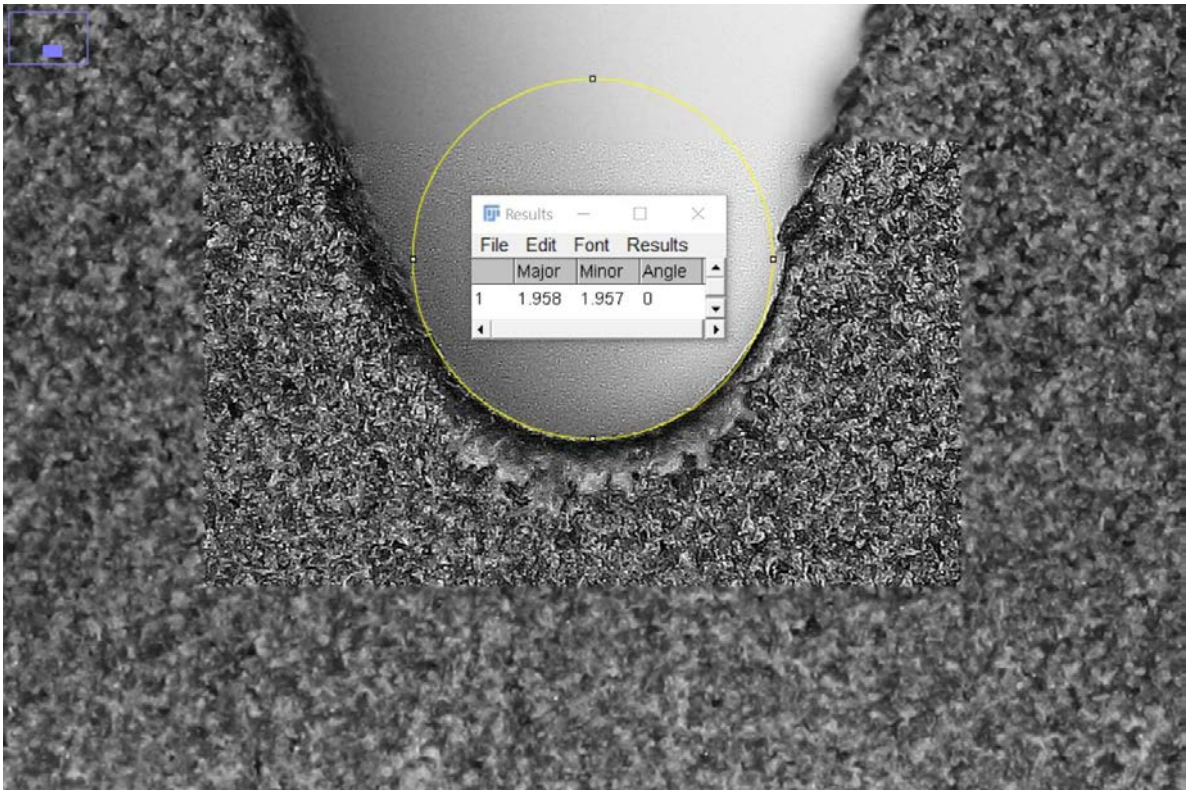


Figure F.15: Measure of the V-notch apex diameter of the 45VR1PA12\_-1\_2 specimen.

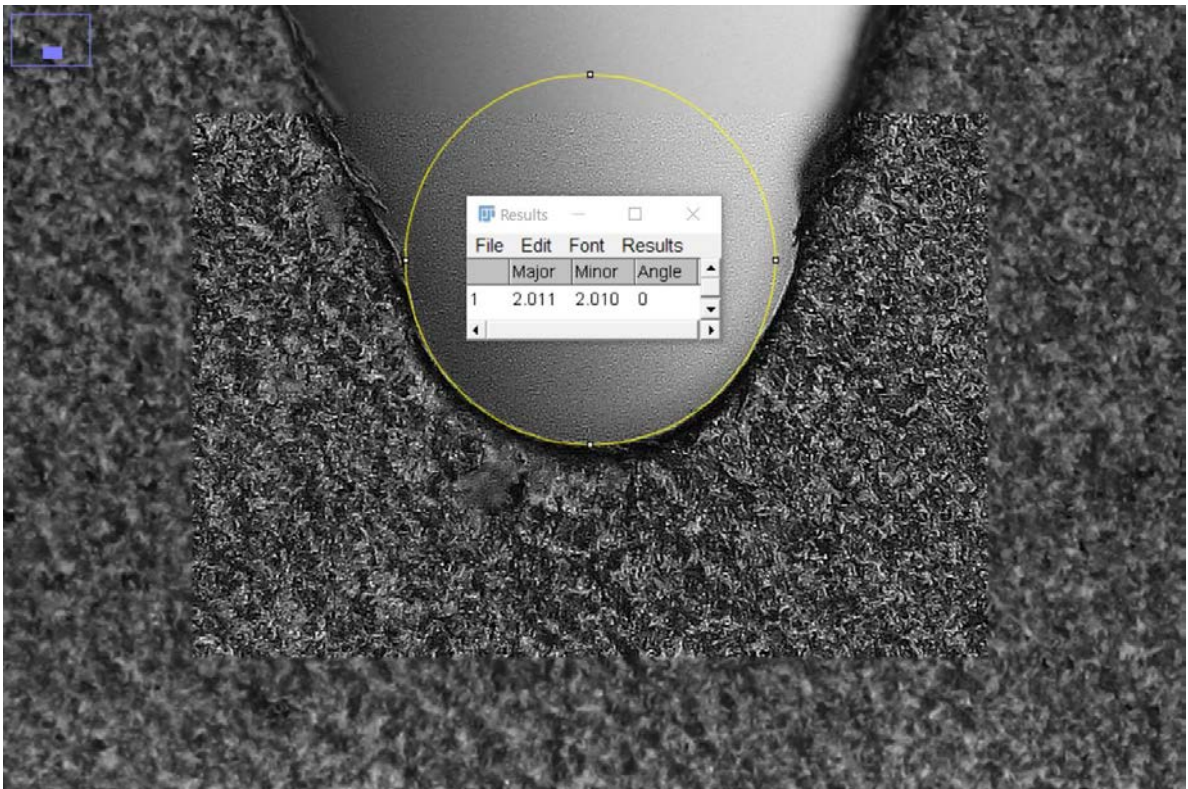


Figure F.16: Measure of the V-notch apex diameter of the 45VR1PA12\_-1\_3 specimen.



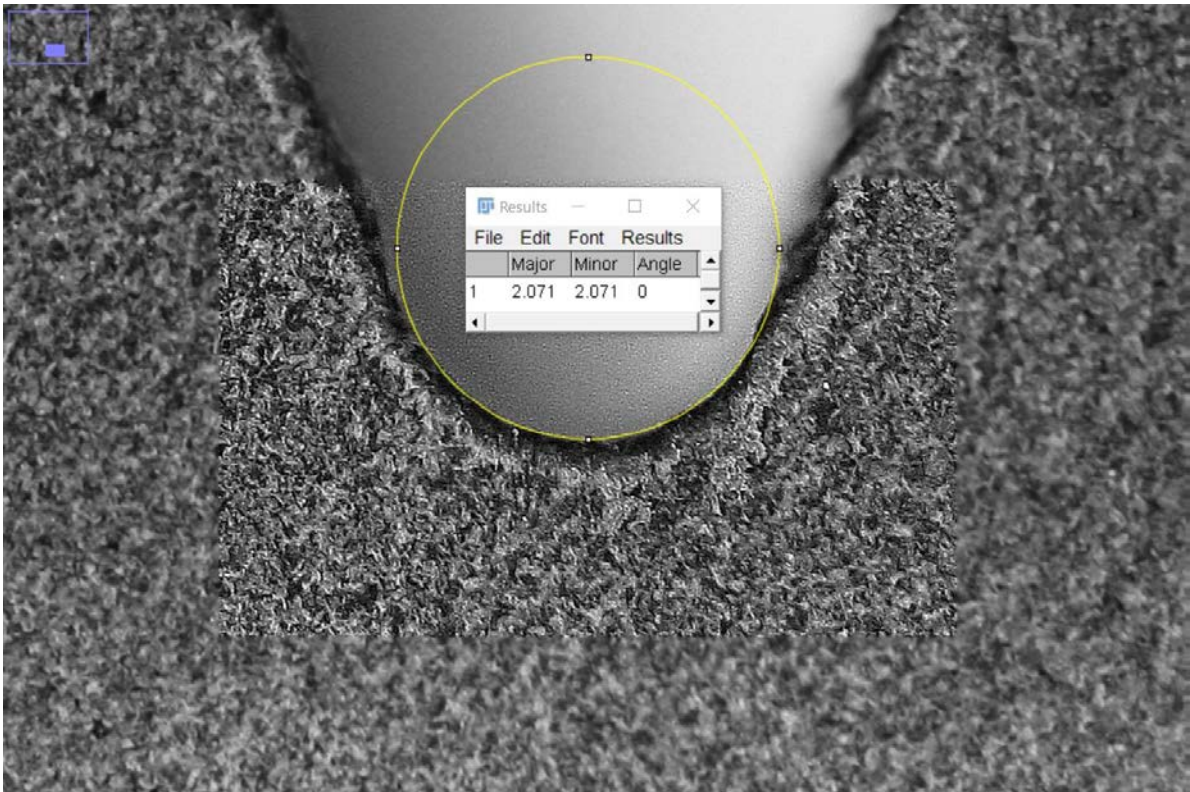


Figure F.17: Measure of the V-notch apex diameter of the 45VR1PA12\_-1\_4 specimen.

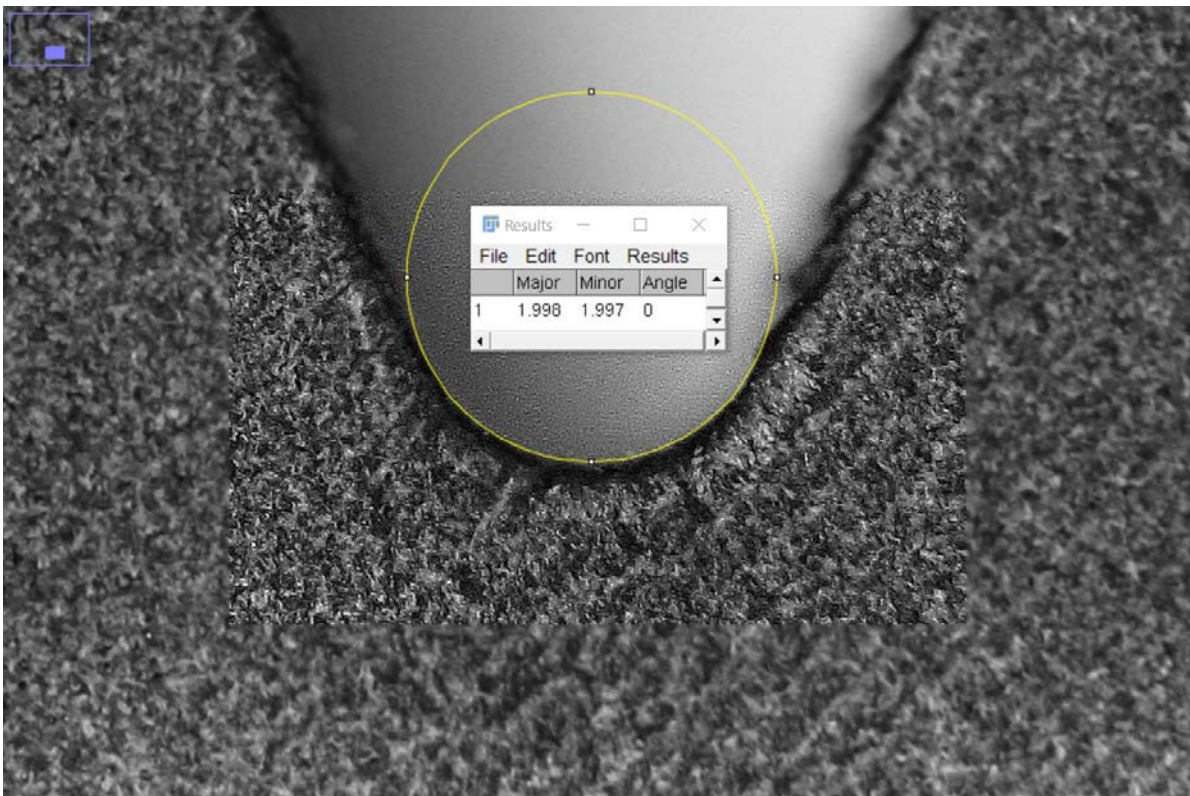


Figure F.18: Measure of the V-notch apex diameter of the 45VR1PA12\_-1\_5 specimen.



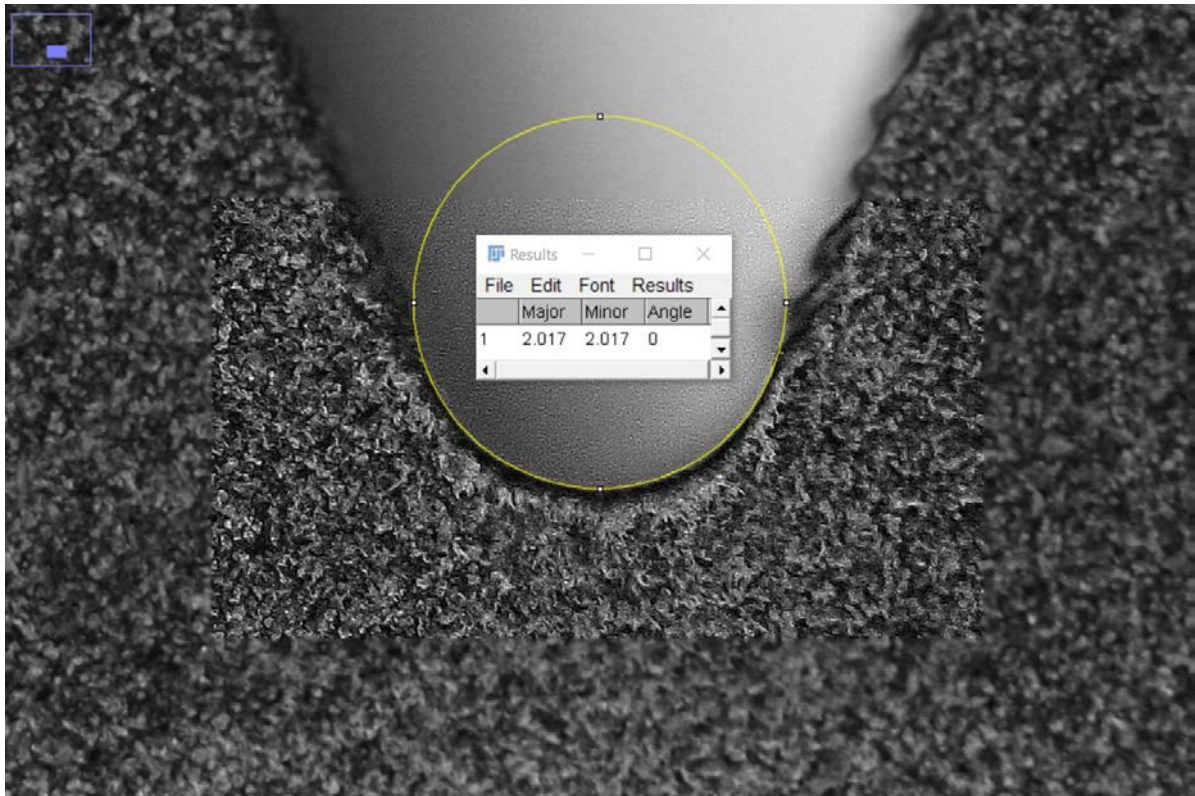


Figure F.19: Measure of the V-notch apex diameter of the 45VR1PA12\_-1\_6 specimen.



Figure F.20: Measure of the V-notch apex diameter of the 45VR1PA12\_-1\_7 specimen.



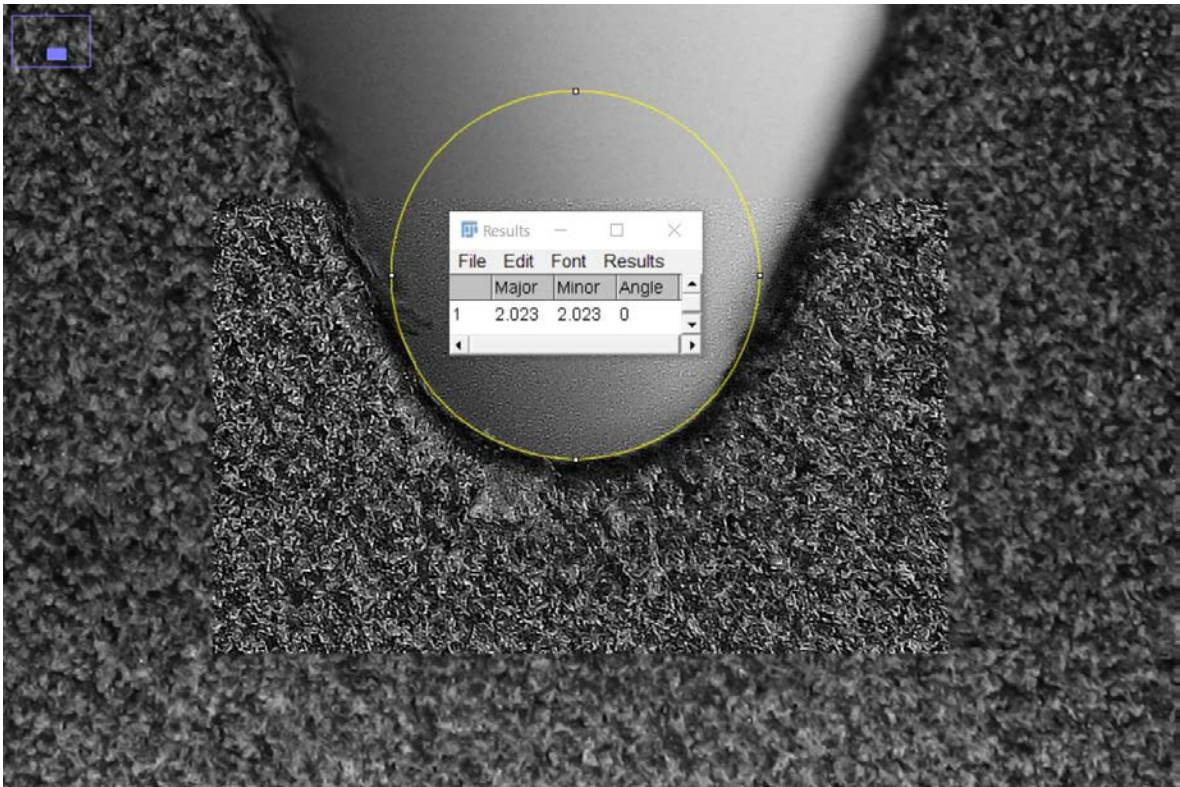


Figure F.21: Measure of the V-notch apex diameter of the 45VR1PA12\_-1\_8 specimen.

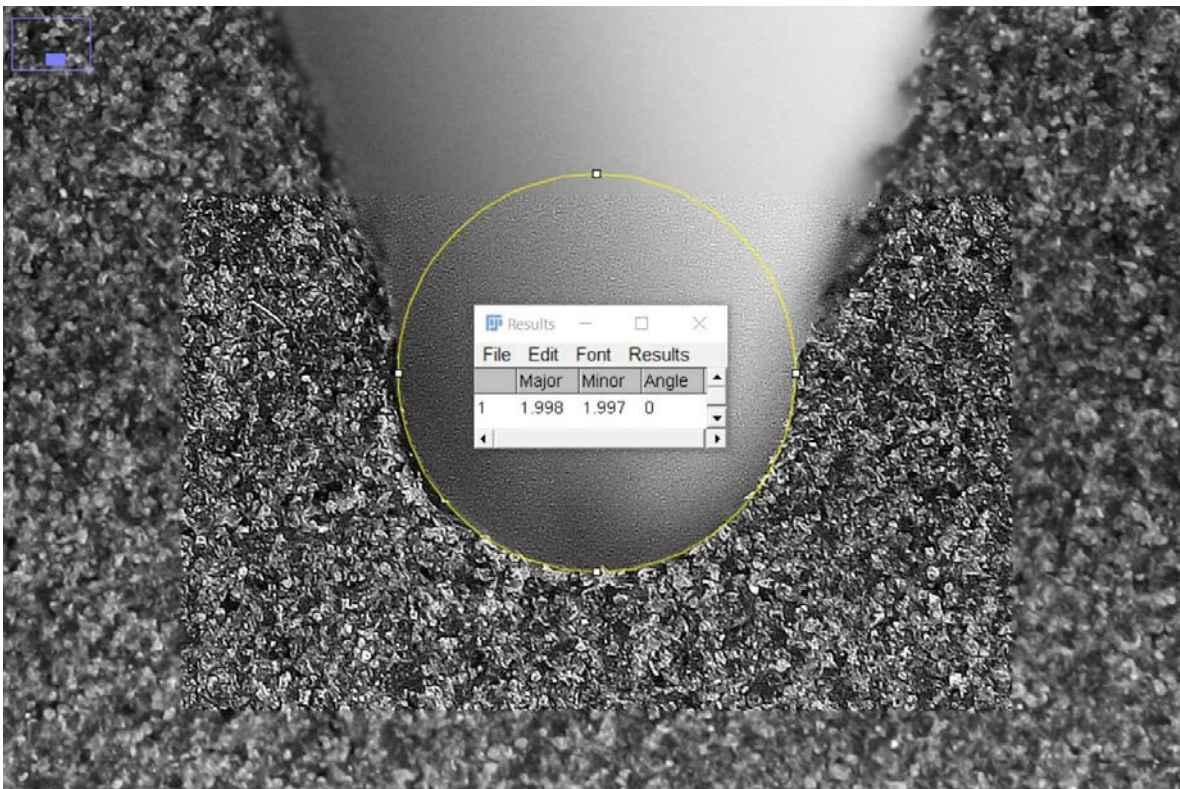


Figure F.22: Measure of the V-notch apex diameter of the 45VR1PA12\_-1\_9 specimen.



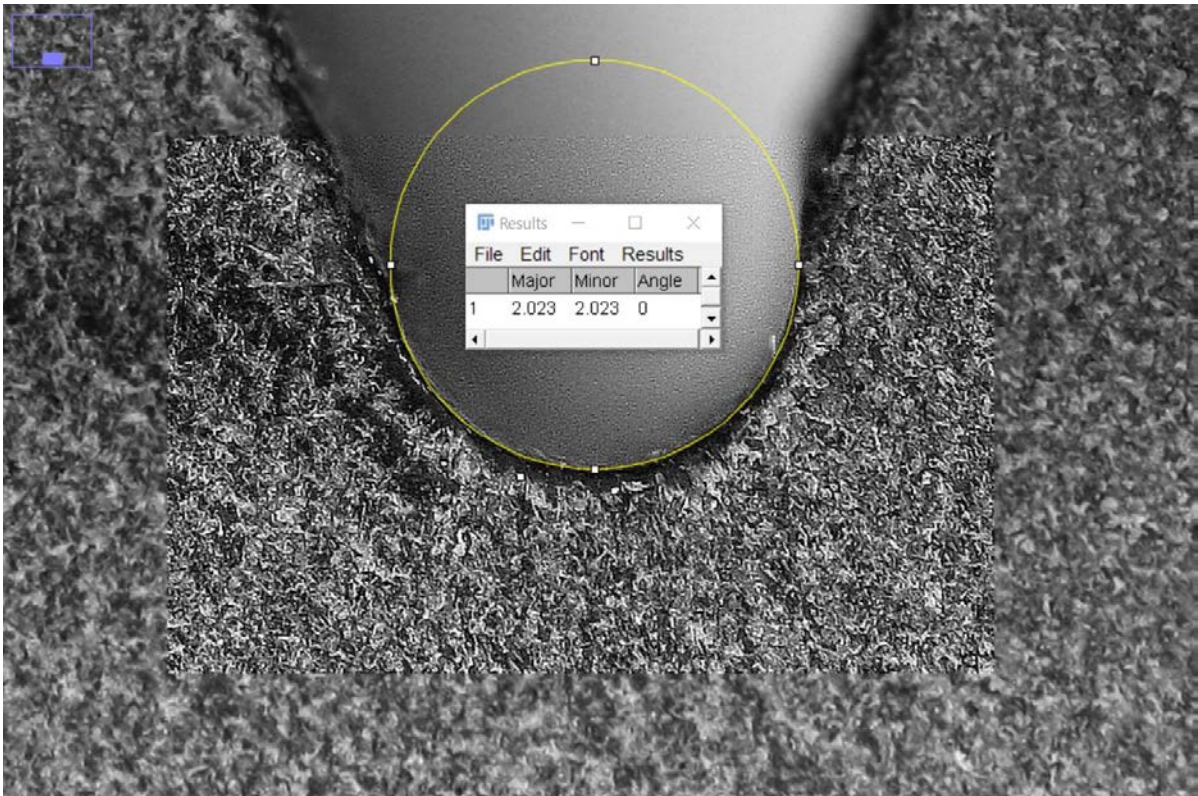


Figure F.23: Measure of the V-notch apex diameter of the 45VR1PA12\_-1\_10 specimen.

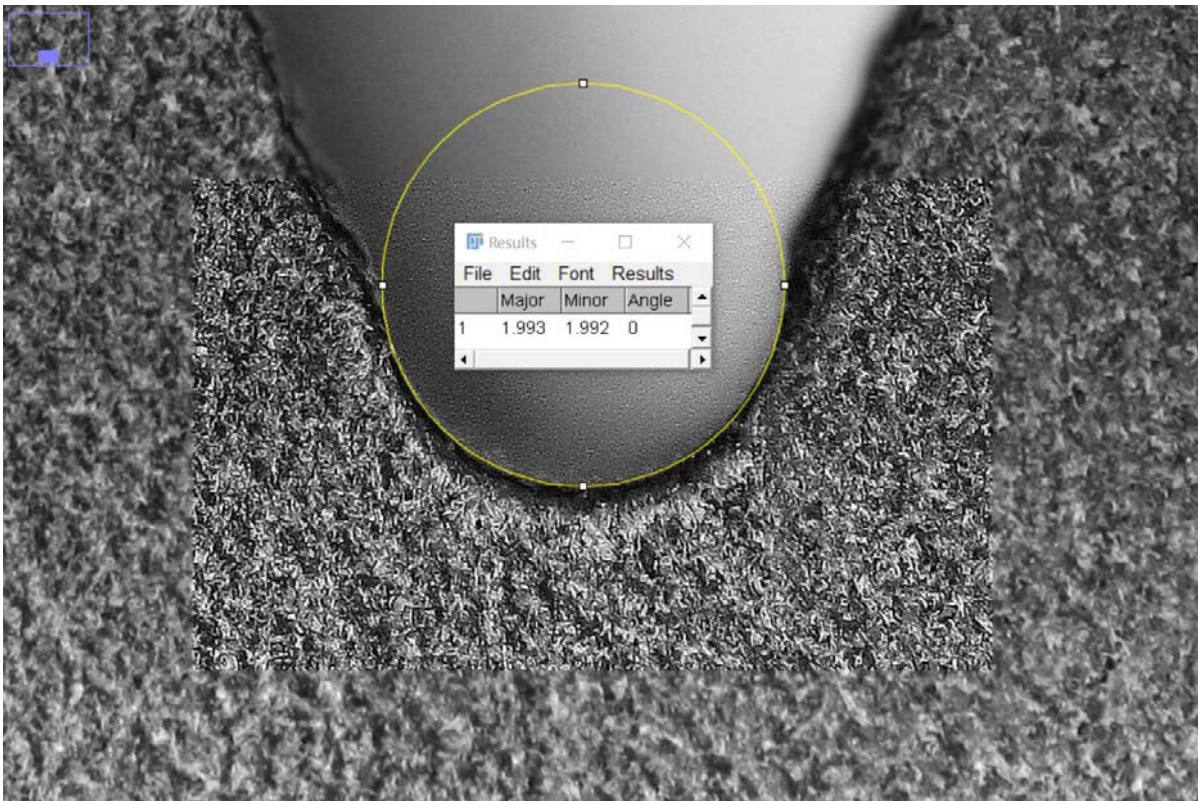


Figure F.24: Measure of the V-notch apex diameter of the 45VR1PA12\_-1\_11 specimen.



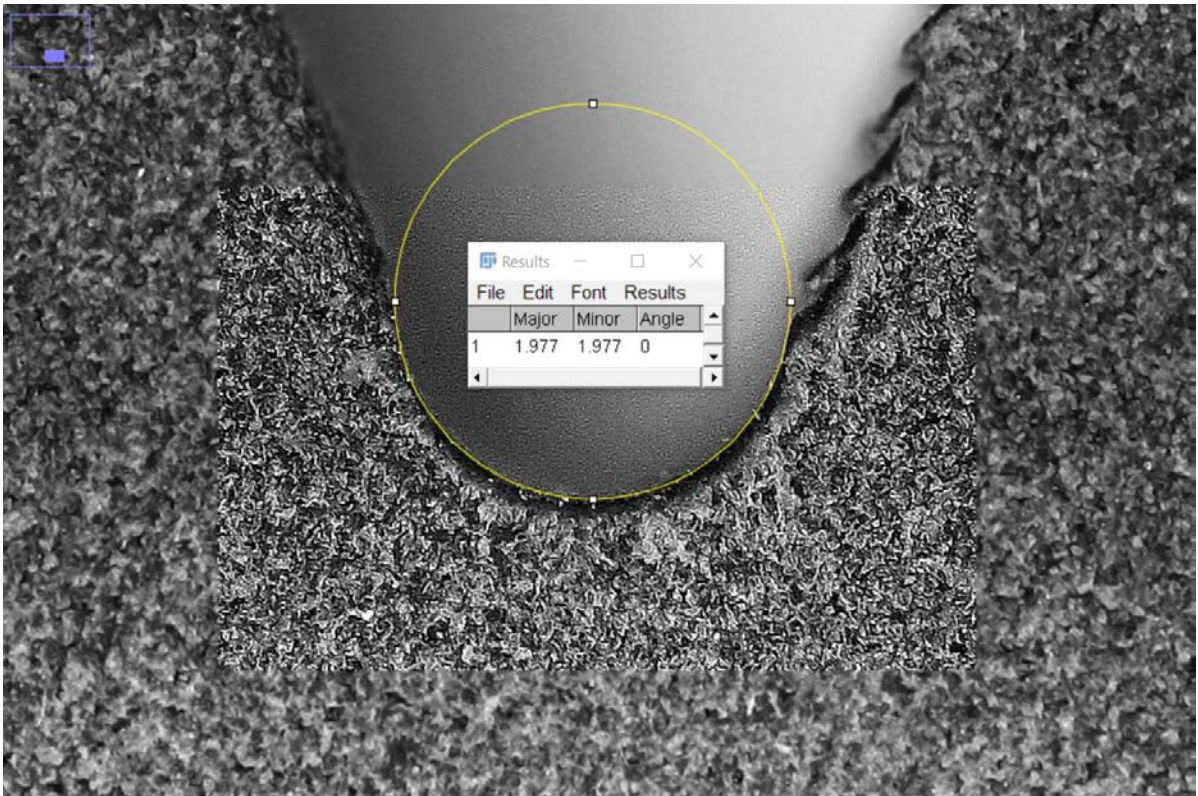


Figure F.25: Measure of the V-notch apex diameter of the 45VR1PA12\_-1\_12 specimen.

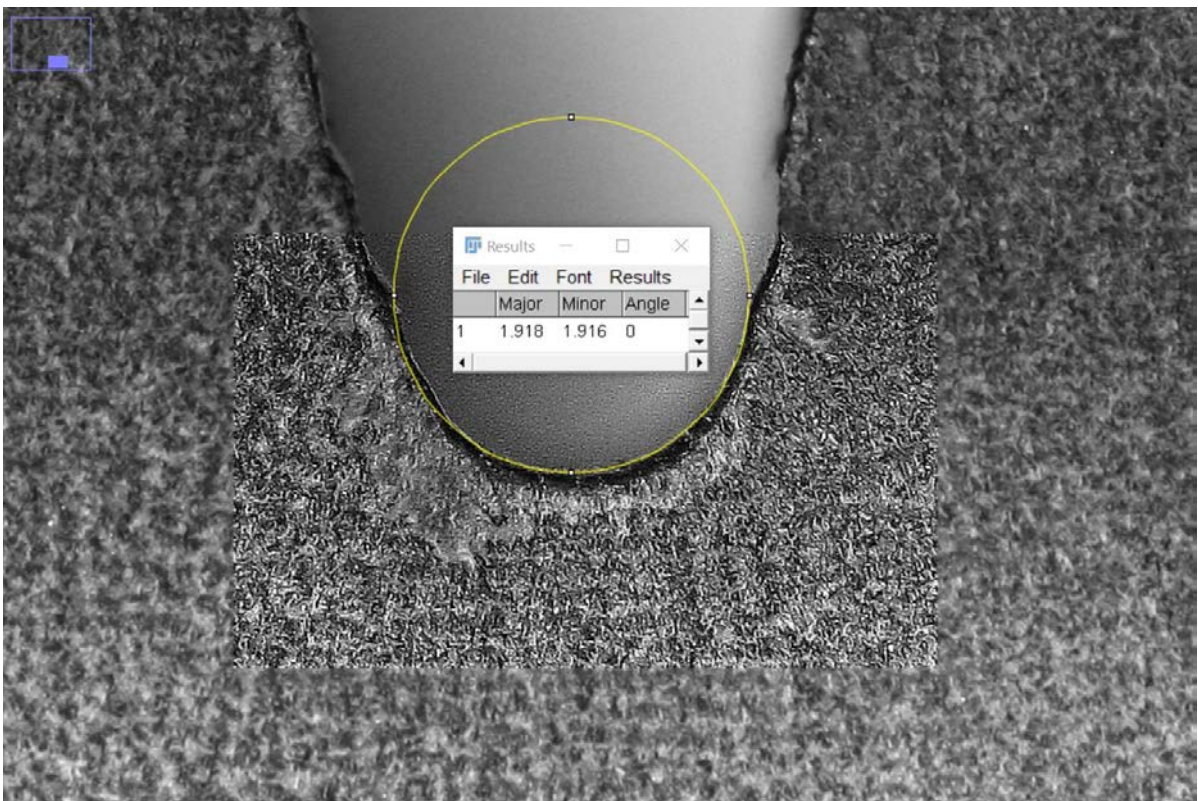


Figure F.26: Measure of the V-notch apex diameter of the 90VR1PA12\_-1\_1 specimen.



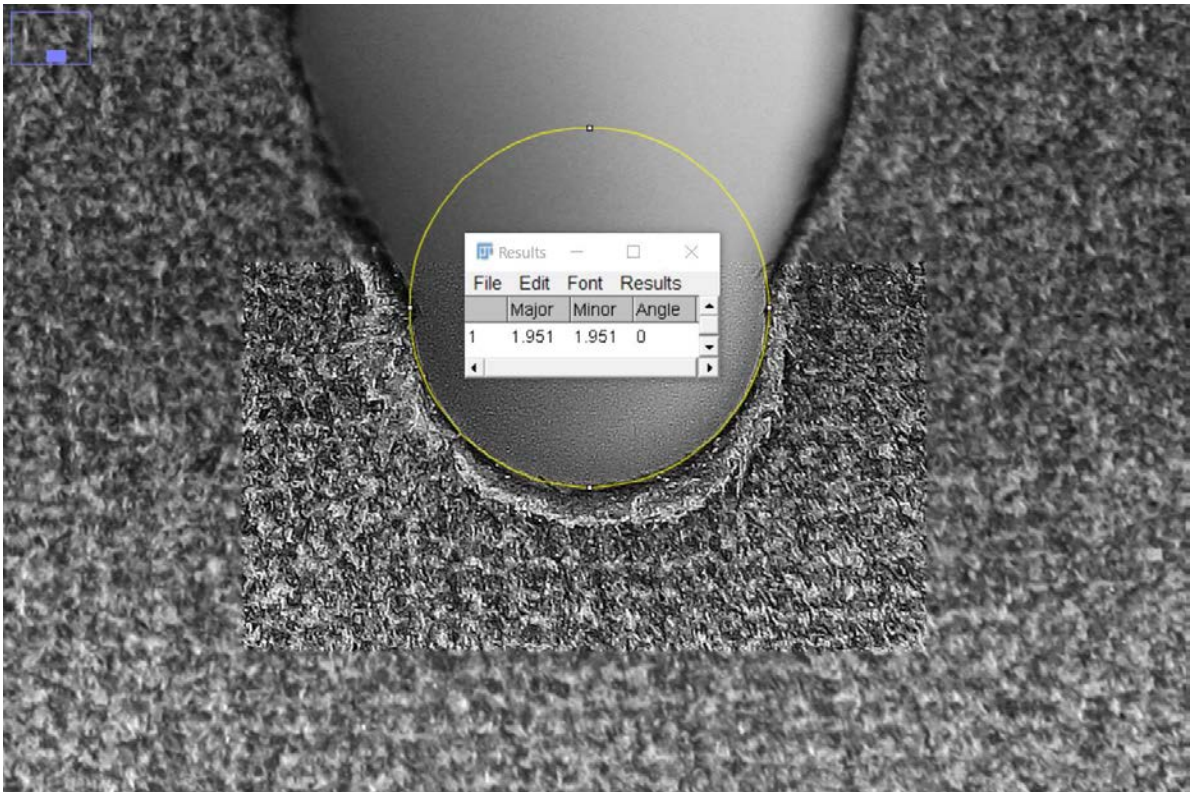


Figure F.27: Measure of the V-notch apex diameter of the 90VR1PA12\_-1\_2 specimen.



Figure F.28: Measure of the V-notch apex diameter of the 90VR1PA12\_-1\_3 specimen.



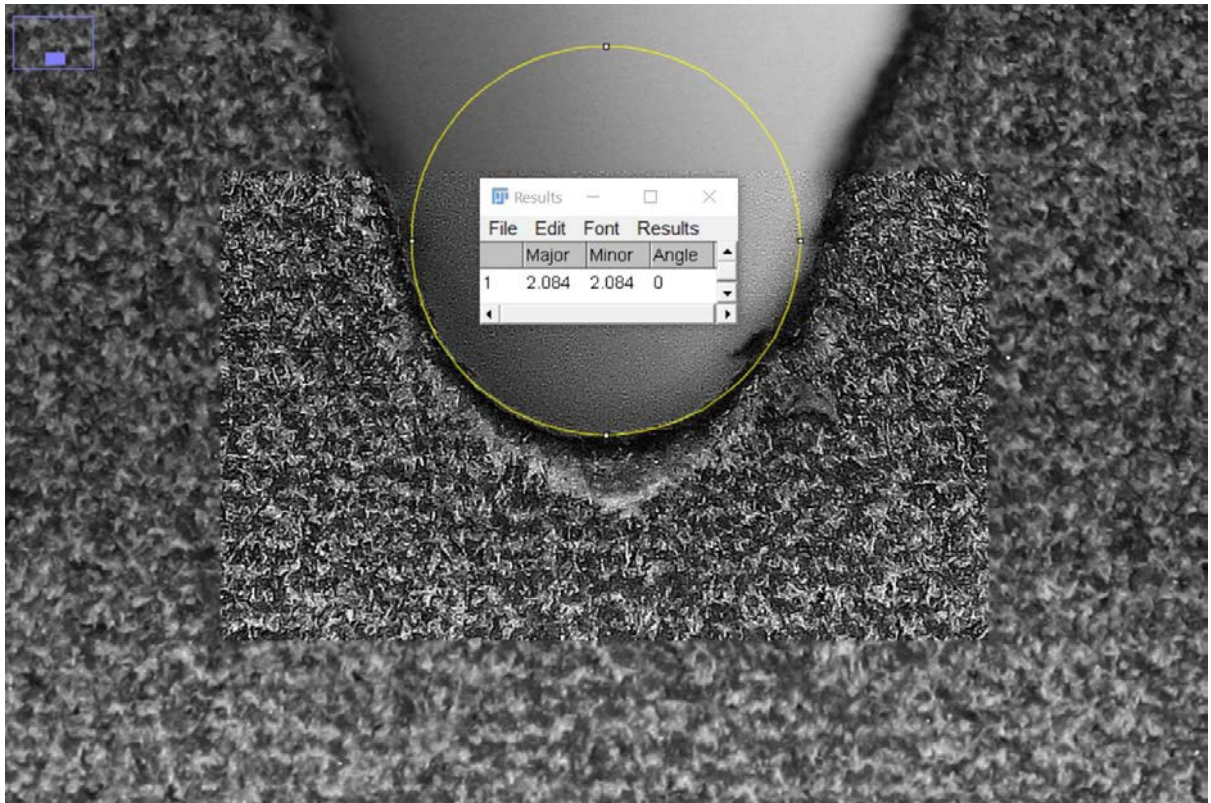


Figure F.29: Measure of the V-notch apex diameter of the 90VR1PA12\_-1\_4 specimen.

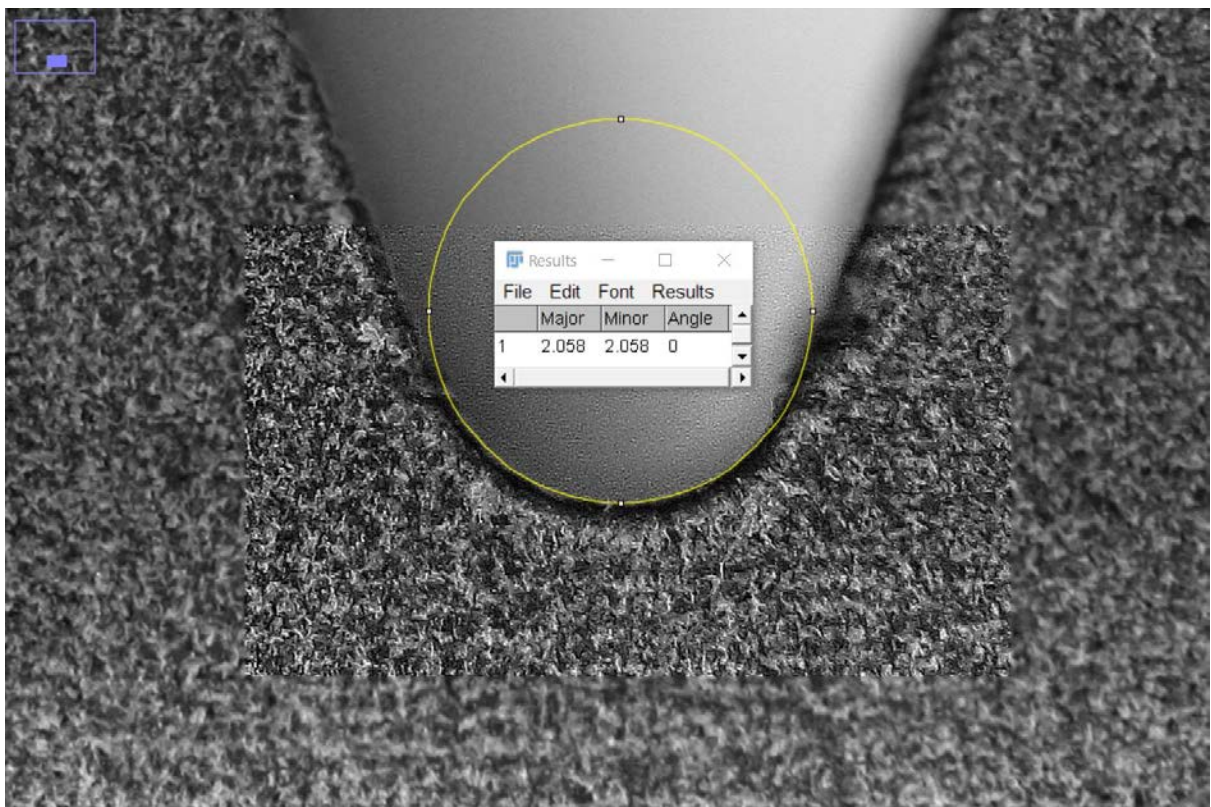


Figure F.30: Measure of the V-notch apex diameter of the 90VR1PA12\_-1\_5 specimen.





Figure F.31: Measure of the V-notch apex diameter of the 90VR1PA12\_-1\_6 specimen.

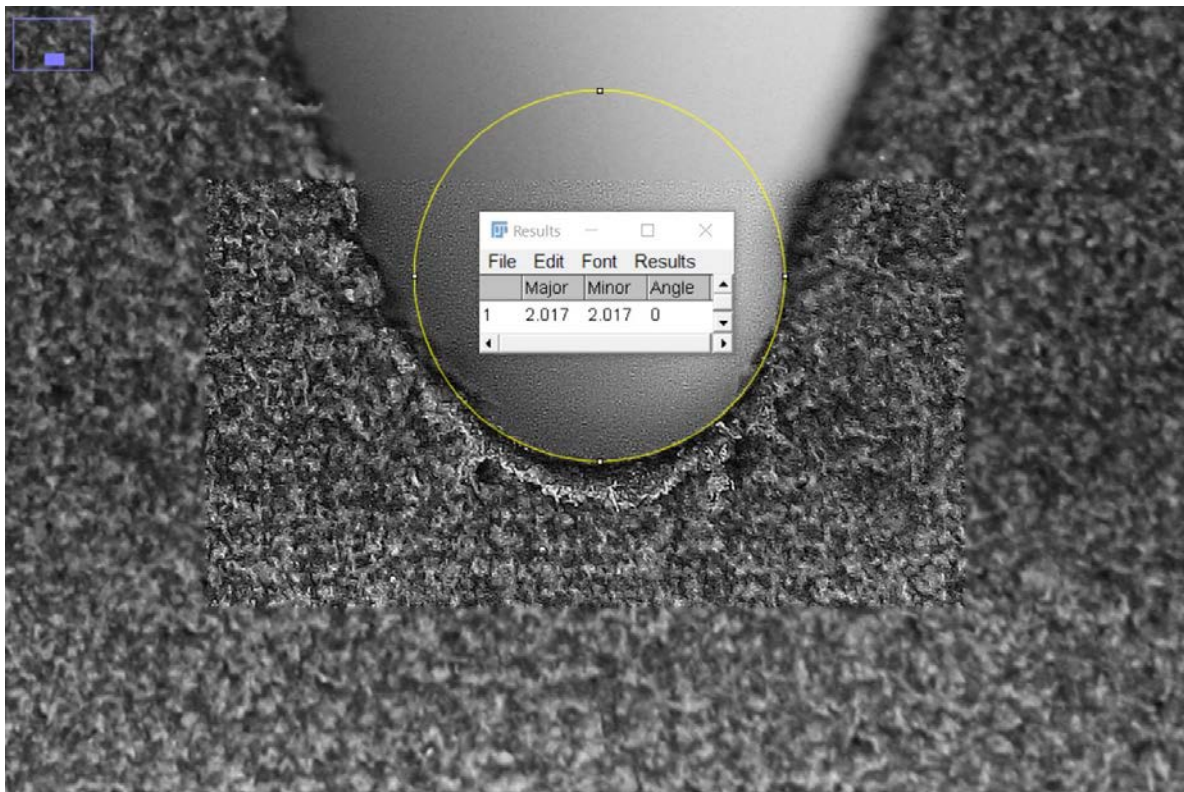


Figure F.32: Measure of the V-notch apex diameter of the 90VR1PA12\_-1\_7 specimen.



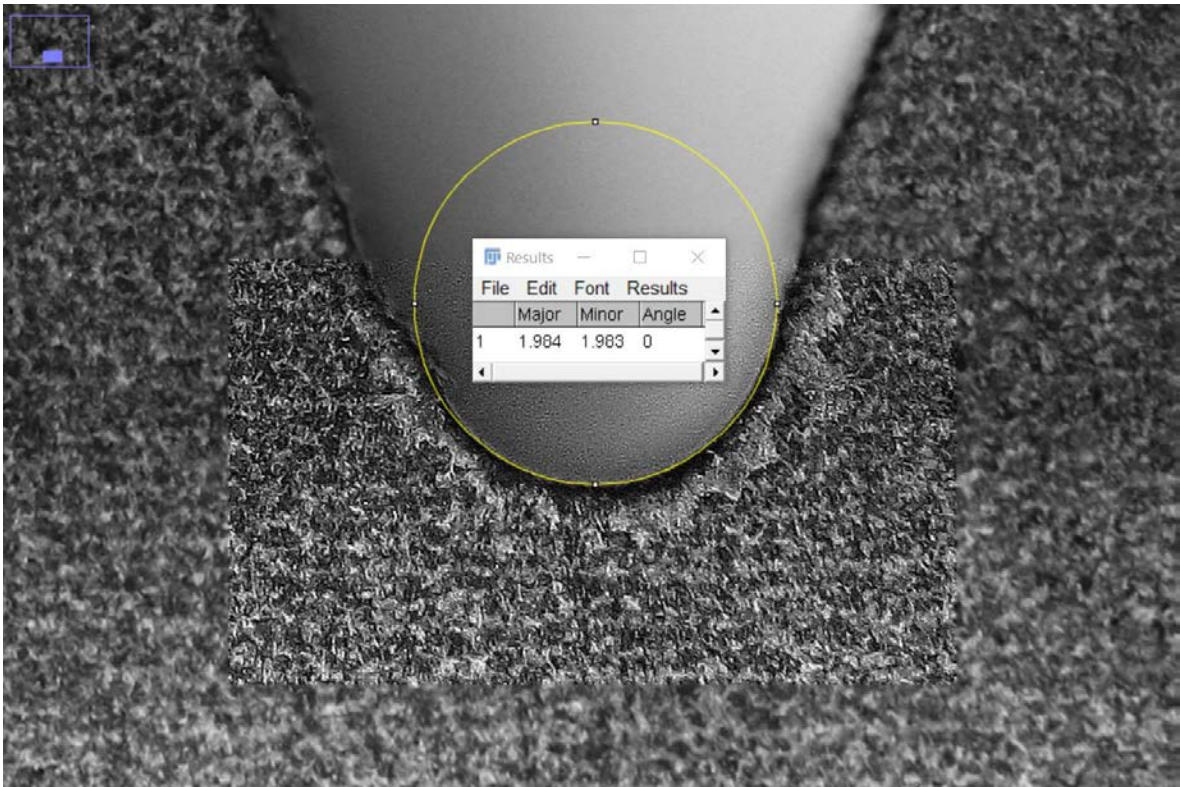


Figure F.33: Measure of the V-notch apex diameter of the 90VR1PA12\_-1\_8 specimen.

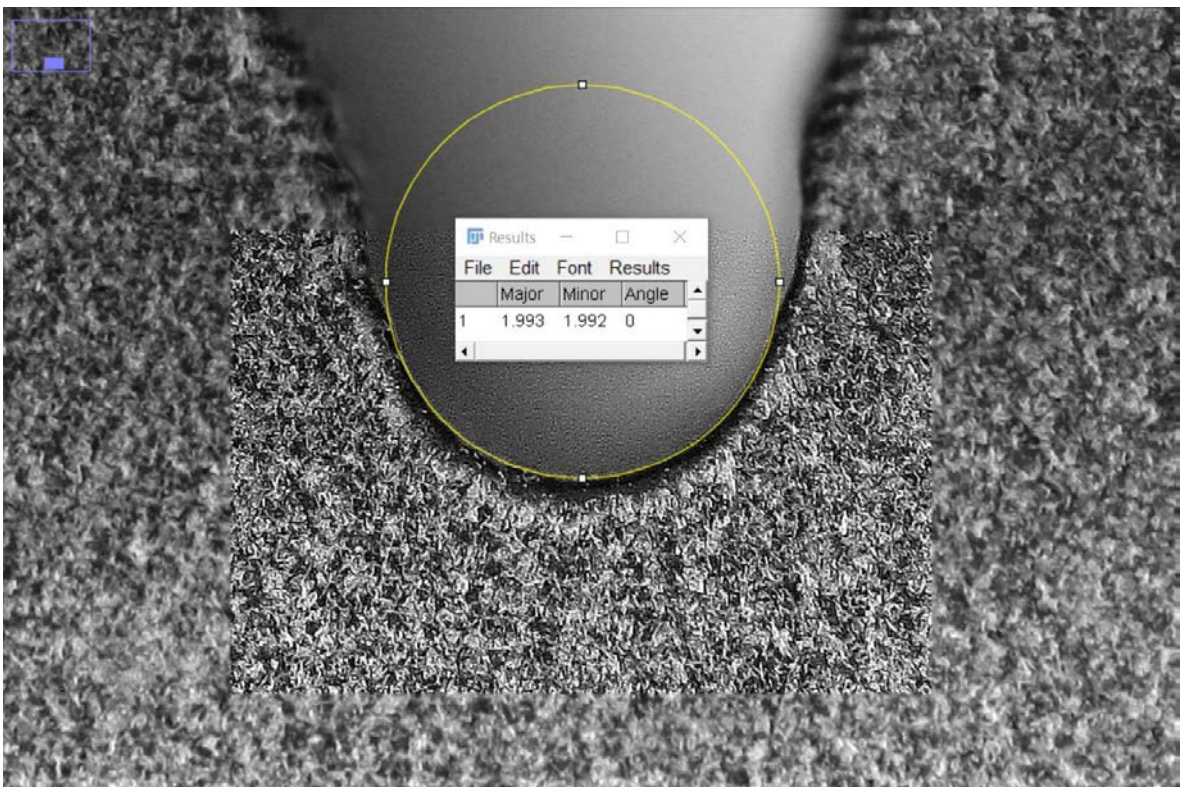


Figure F.34: Measure of the V-notch apex diameter of the 90VR1PA12\_-1\_9 specimen.



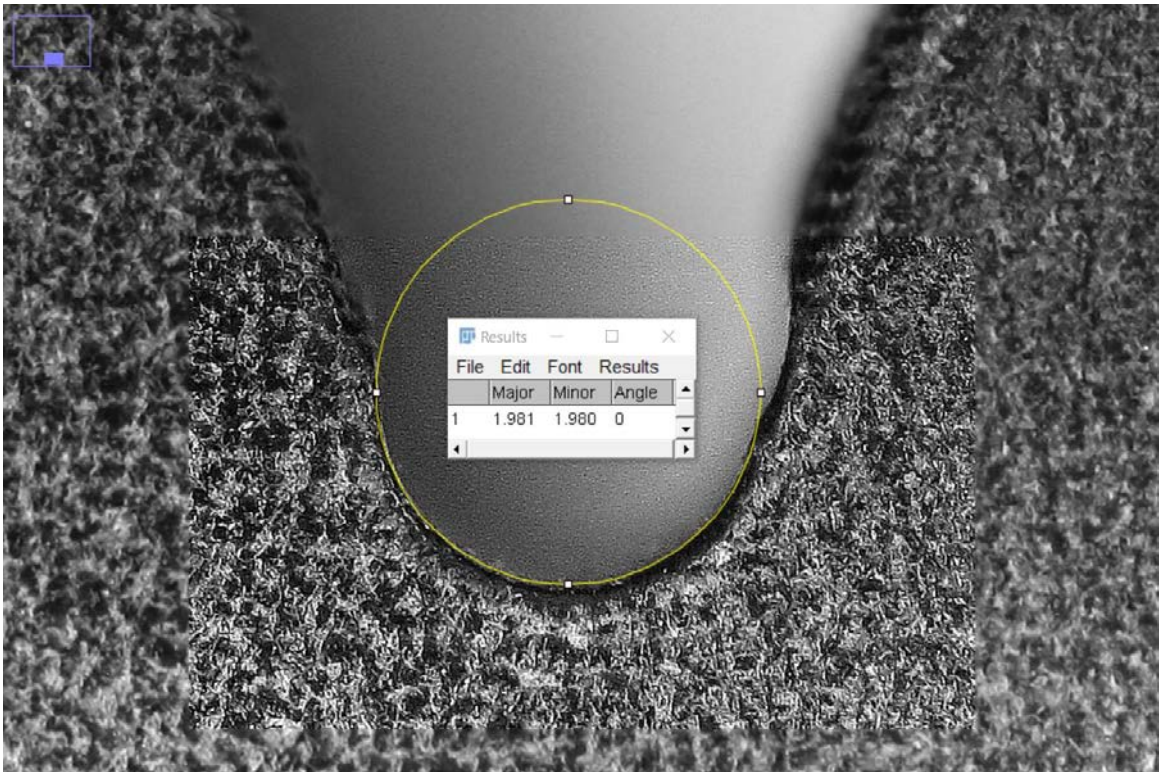


Figure F.35: Measure of the V-notch apex diameter of the 90VR1PA12\_-1\_10 specimen.



Figure F.36: Measure of the V-notch apex diameter of the 90VR1PA12\_-1\_11 specimen.



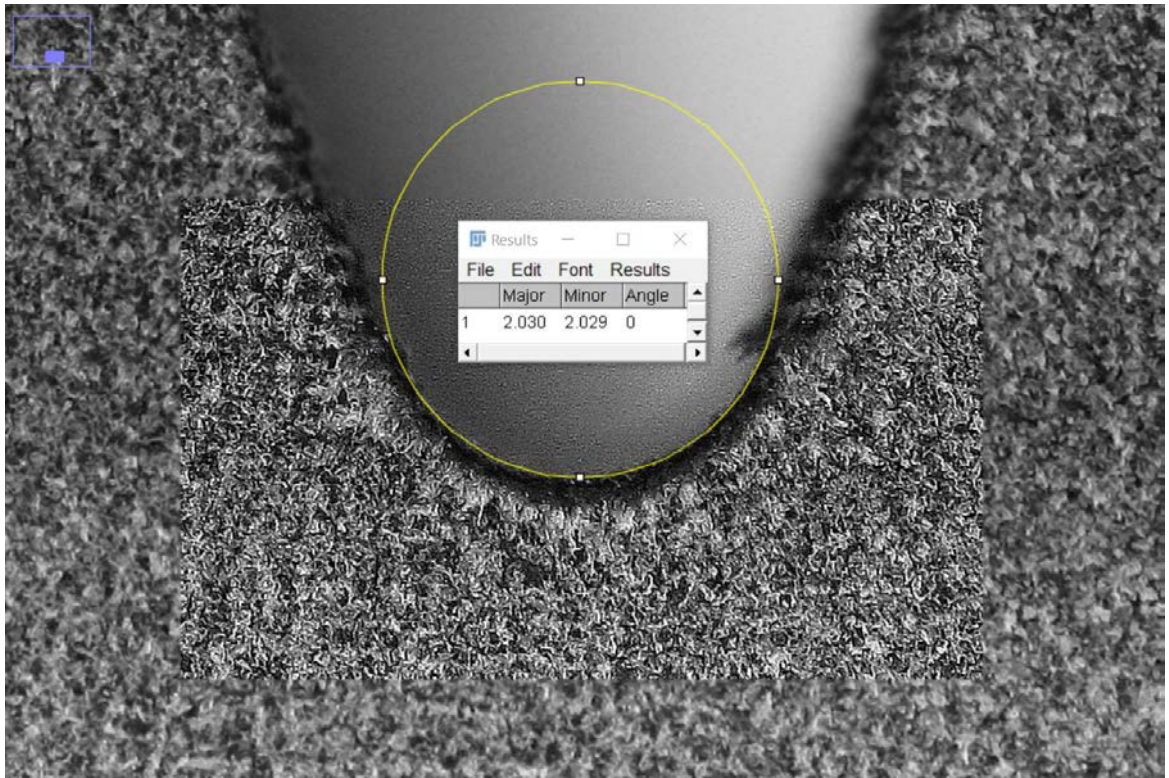


Figure F.37: Measure of the V-notch apex diameter of the 90VR1PA12\_-1\_12 specimen.

# Annex G: Measurements of net widths of the sharp V-notch specimens

In this annex have been reported all the images of all the measurements of the net widths of the sharp V-notch specimens.

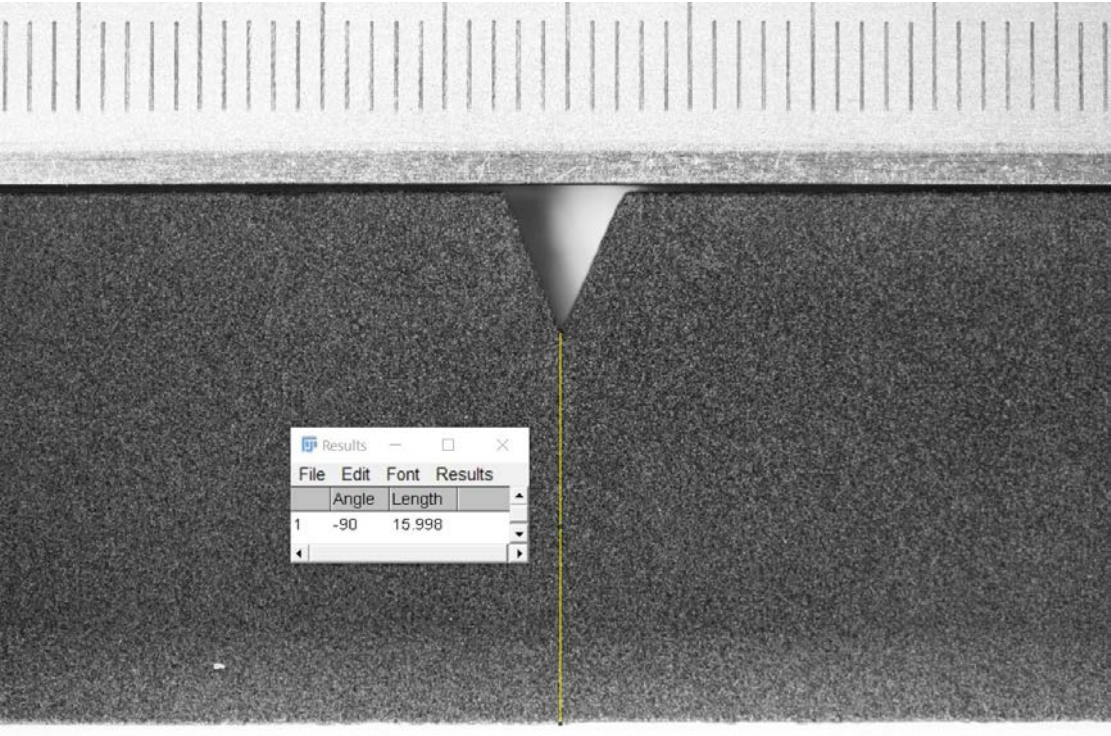


Figure G.1: Measure of the net width of the 0VR0PA12\_-1\_1 specimen.

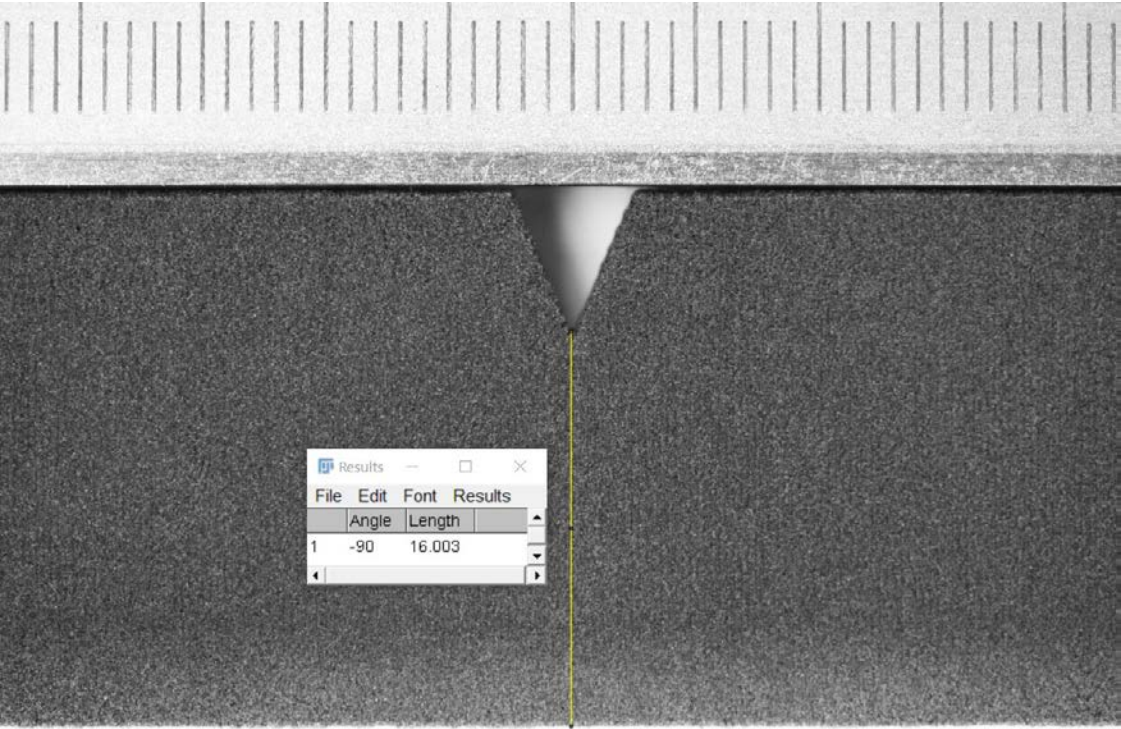


Figure G.2: Measure of the net width of the 0VR0PA12\_-1\_2 specimen.



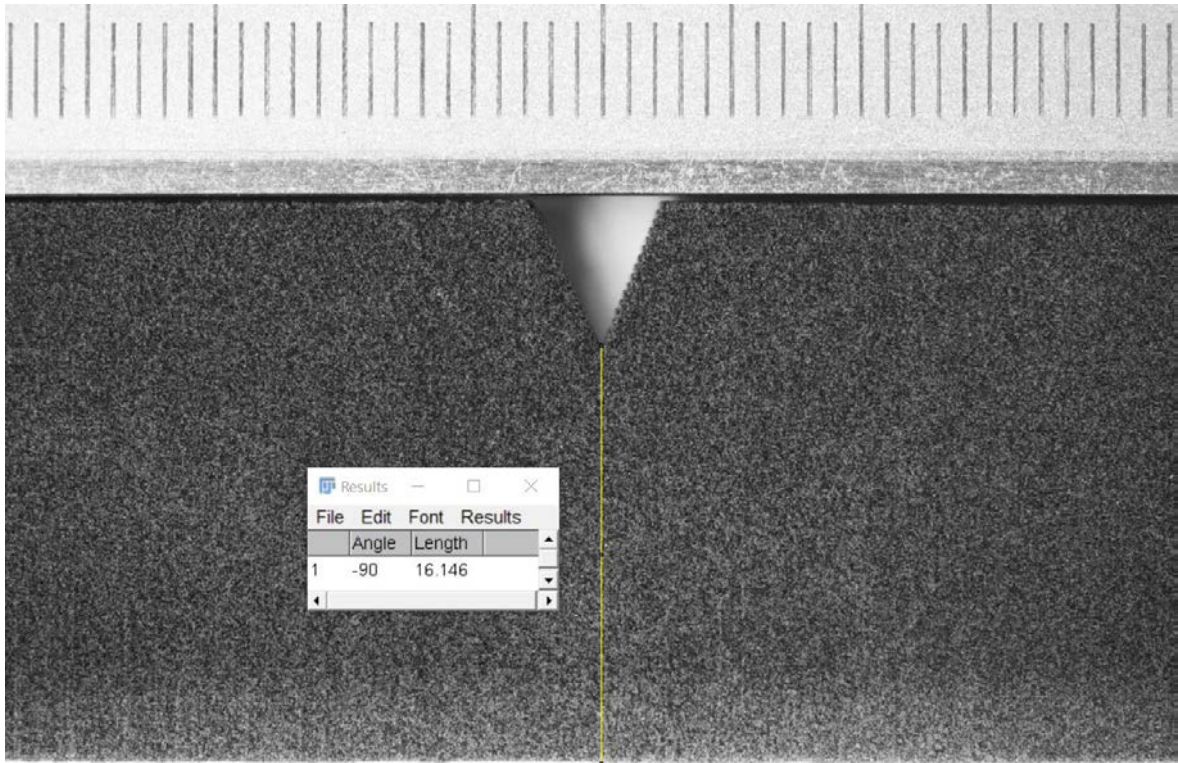


Figure G.3: Measure of the net width of the 0VR0PA12\_-1\_3 specimen.

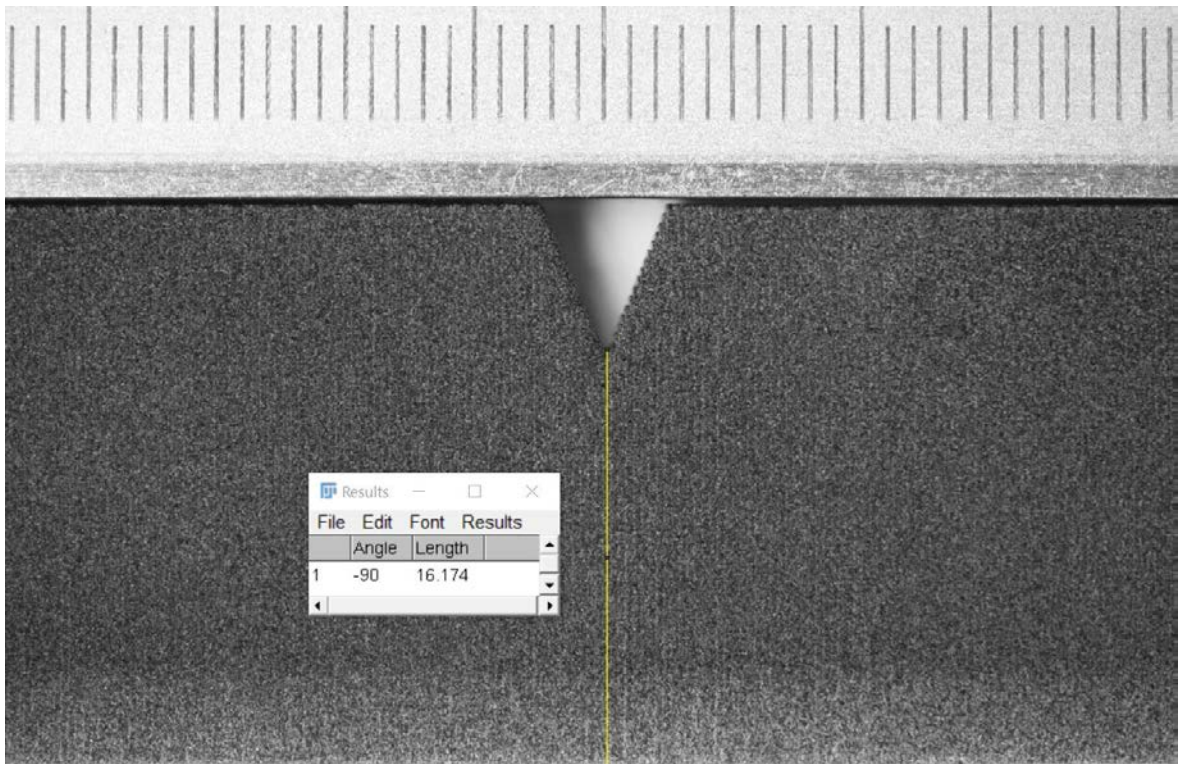


Figure G.4: Measure of the net width of the 0VR0PA12\_-1\_4 specimen.



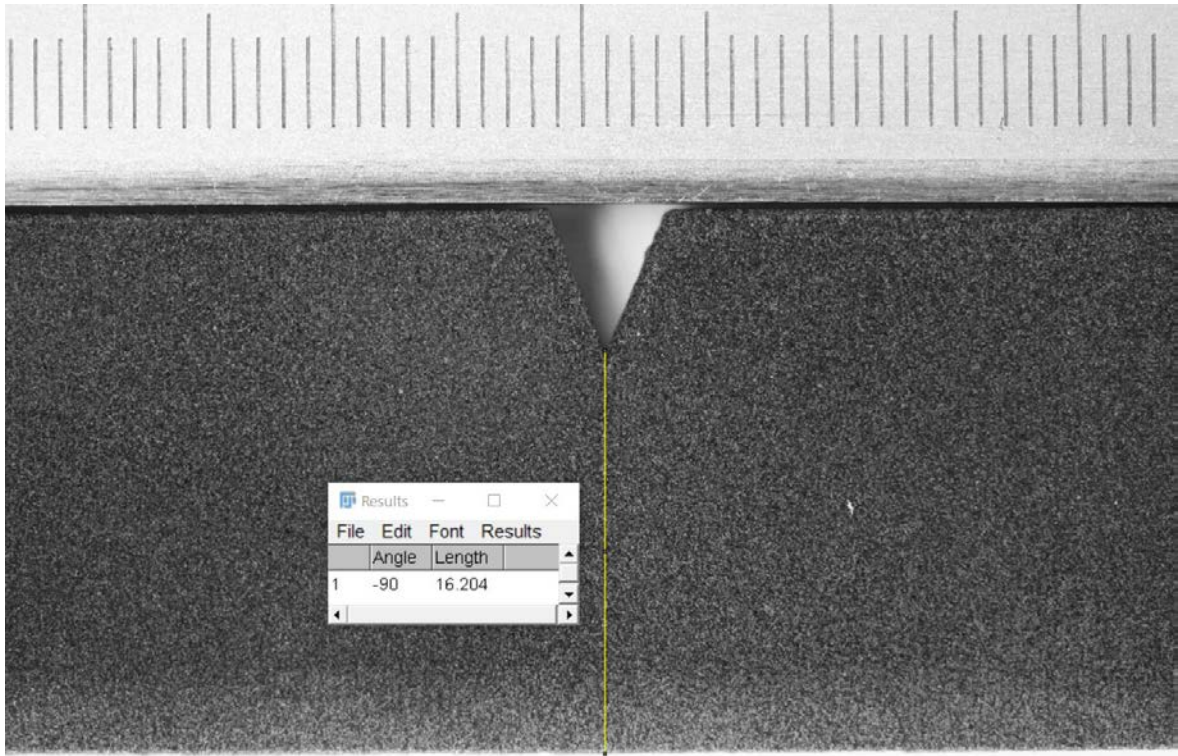


Figure G.5: Measure of the net width of the 0VR0PA12\_-1\_5 specimen.

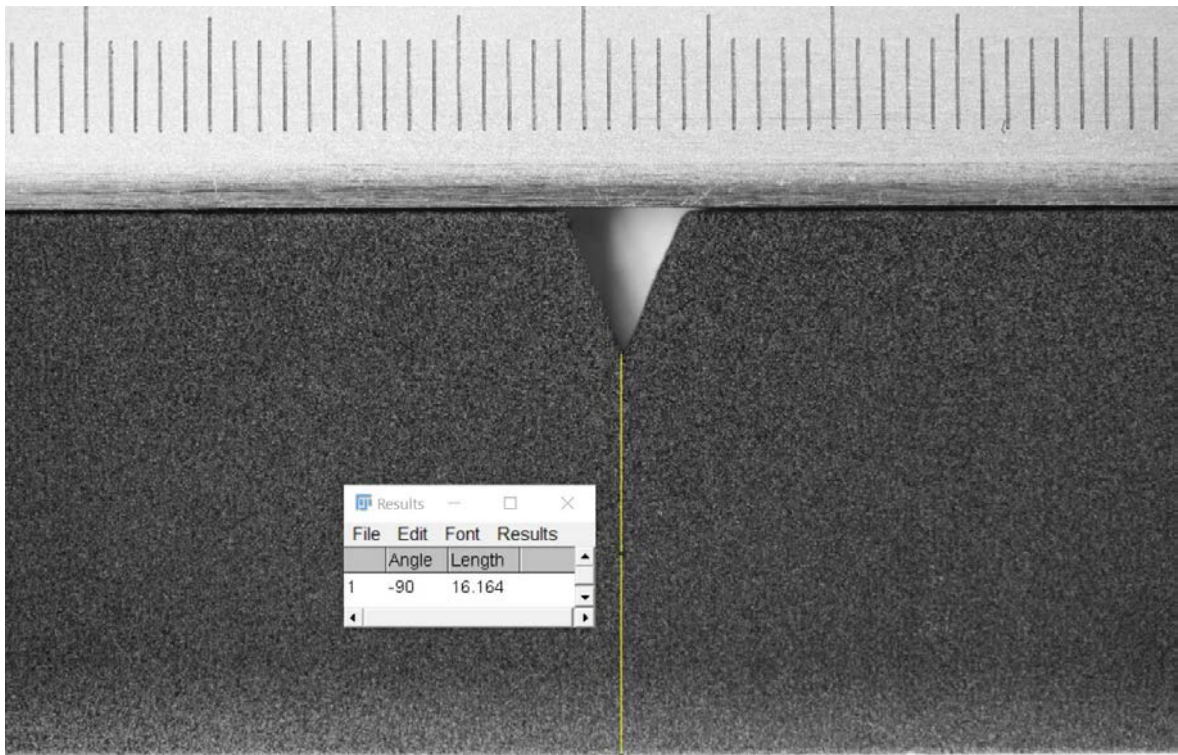


Figure G.6: Measure of the net width of the 0VR0PA12\_-1\_6 specimen.

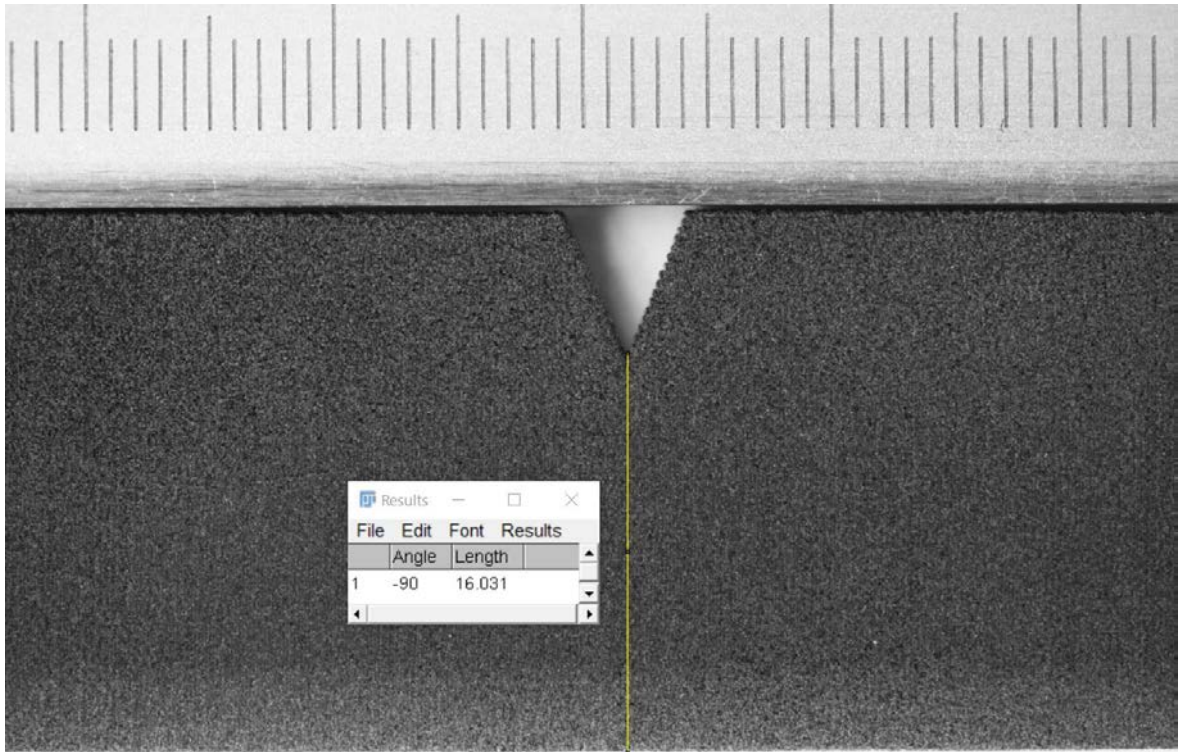


Figure G.7: Measure of the net width of the 0VR0PA12\_-1\_7 specimen.

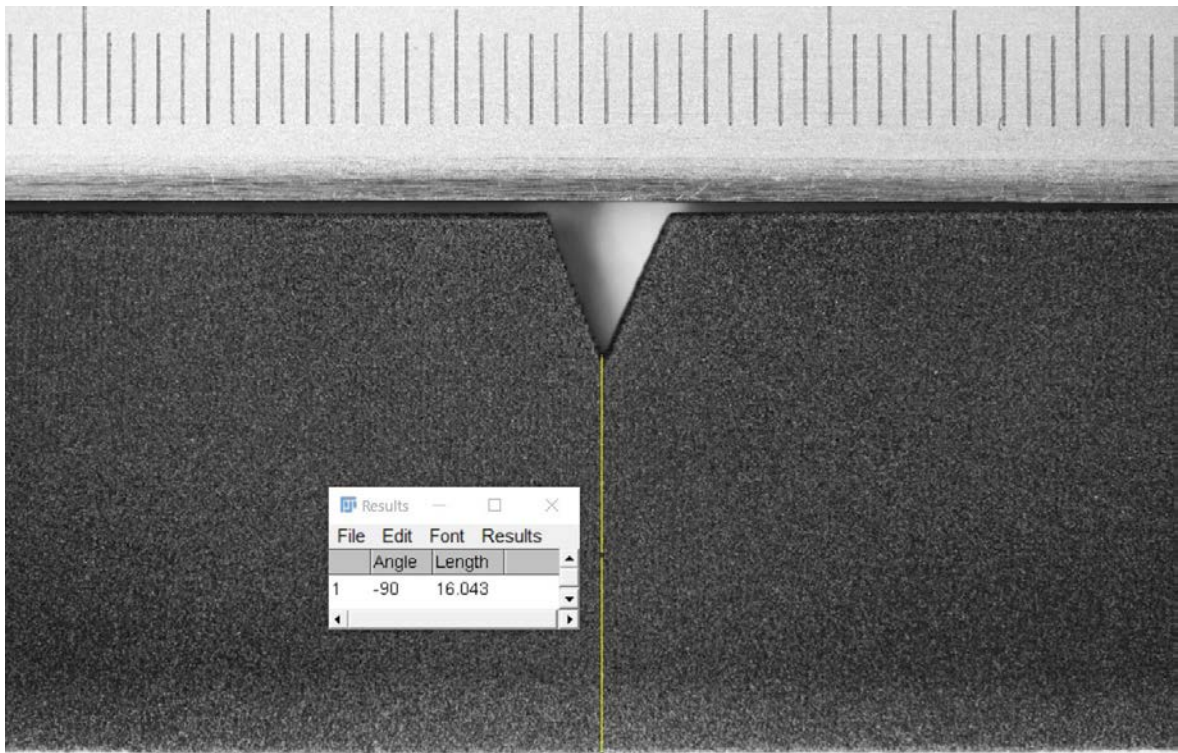


Figure G.8: Measure of the net width of the 0VR0PA12\_-1\_8 specimen.



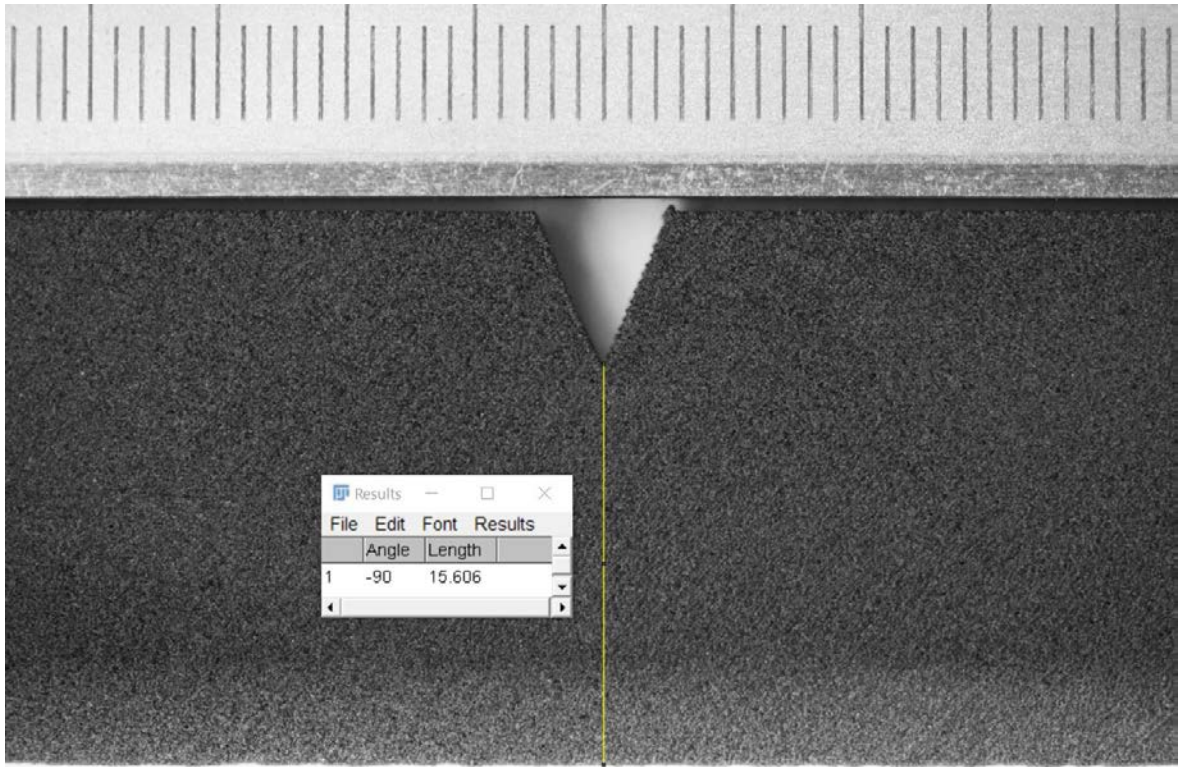


Figure G.9: Measure of the net width of the 45VR0PA12\_-1\_1 specimen.

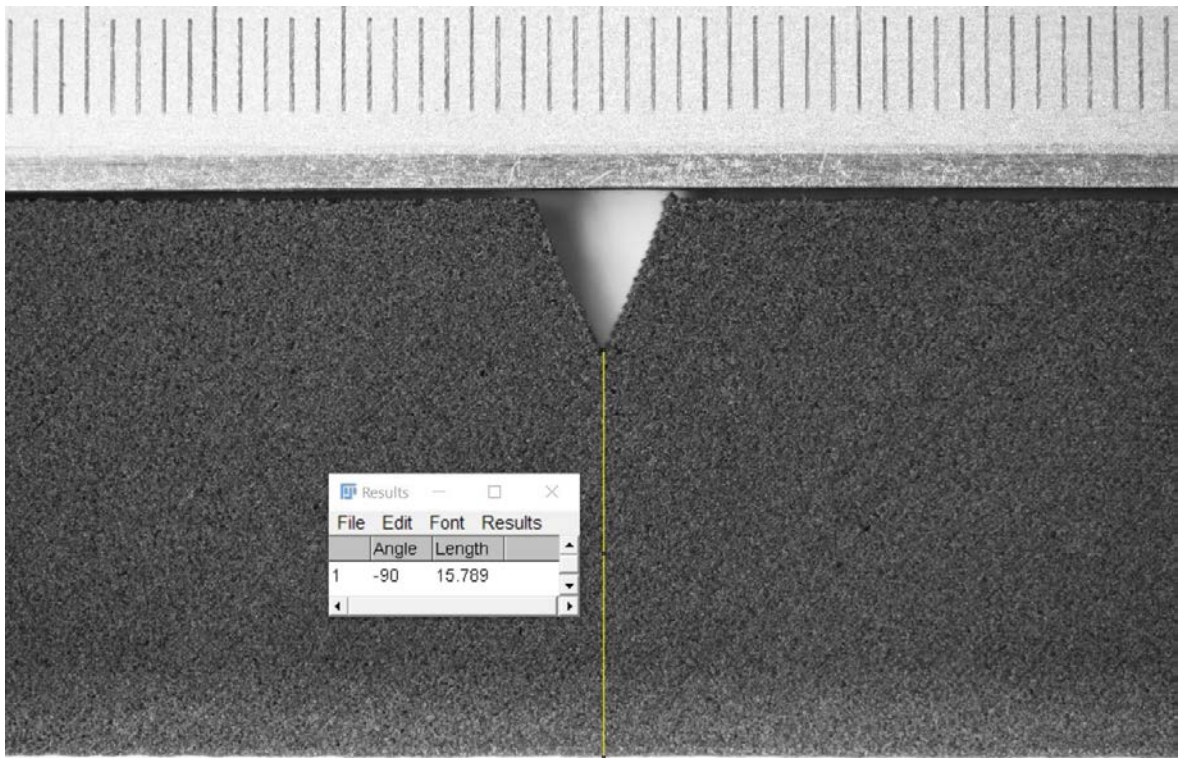


Figure G.10: Measure of the net width of the 45VR0PA12\_-1\_2 specimen.

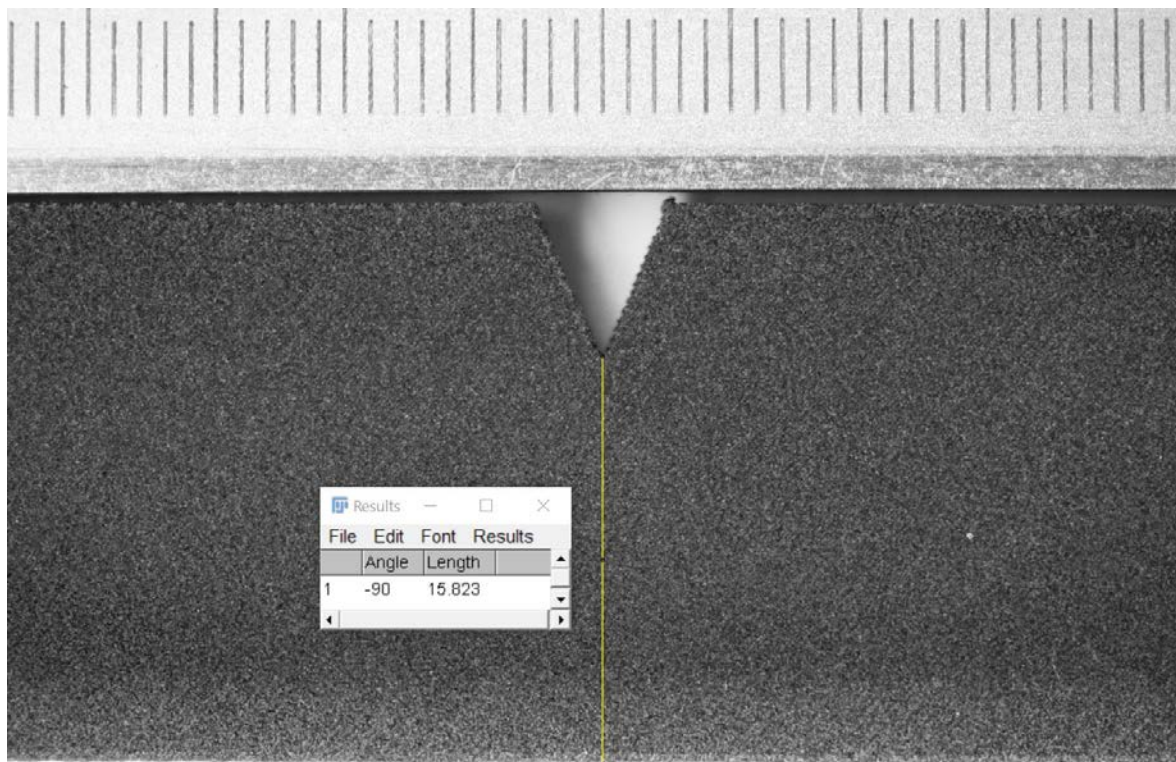


Figure G.11: Measure of the net width of the 45VR0PA12\_-1\_3 specimen.

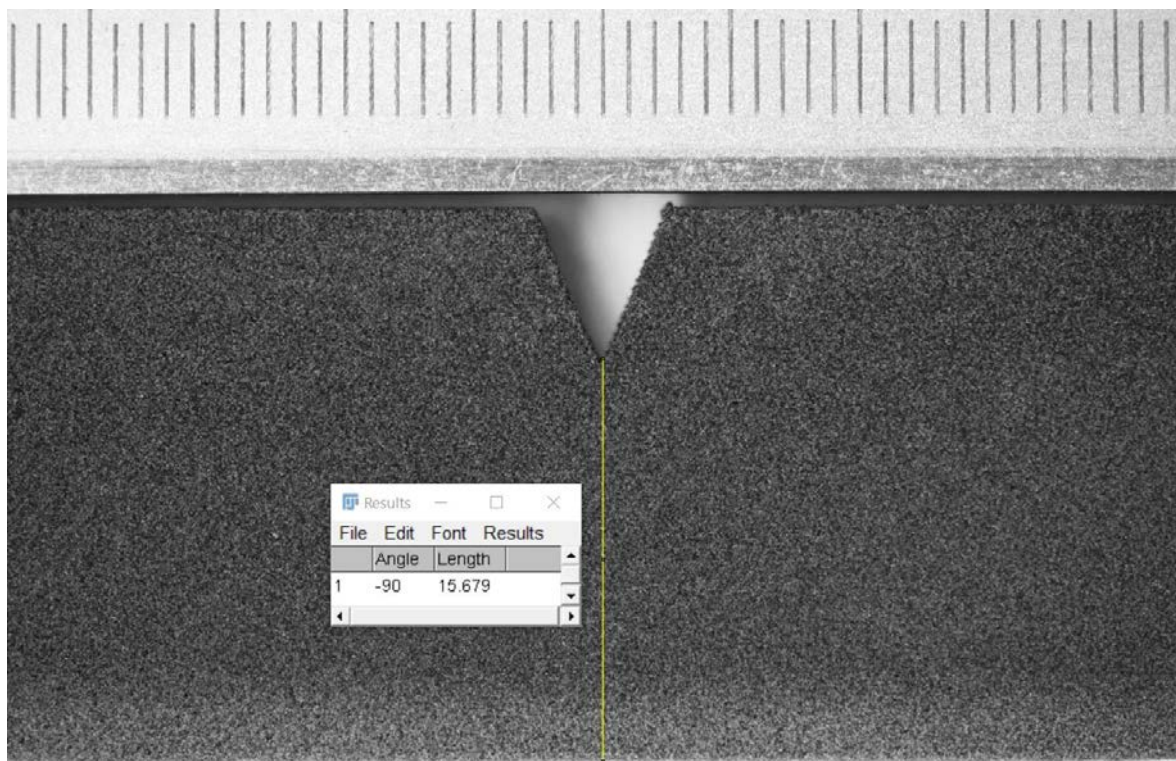


Figure G.12: Measure of the net width of the 45VR0PA12\_-1\_4 specimen.



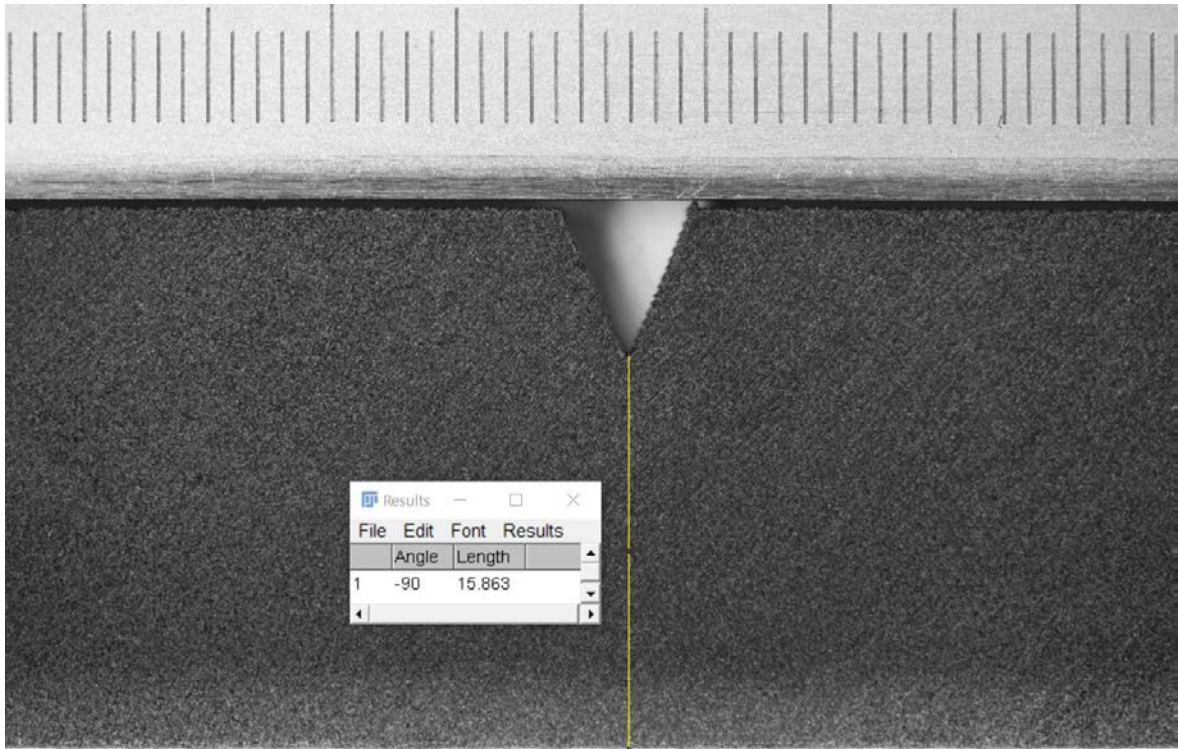


Figure G.13: Measure of the net width of the 45VR0PA12\_-1\_5 specimen.

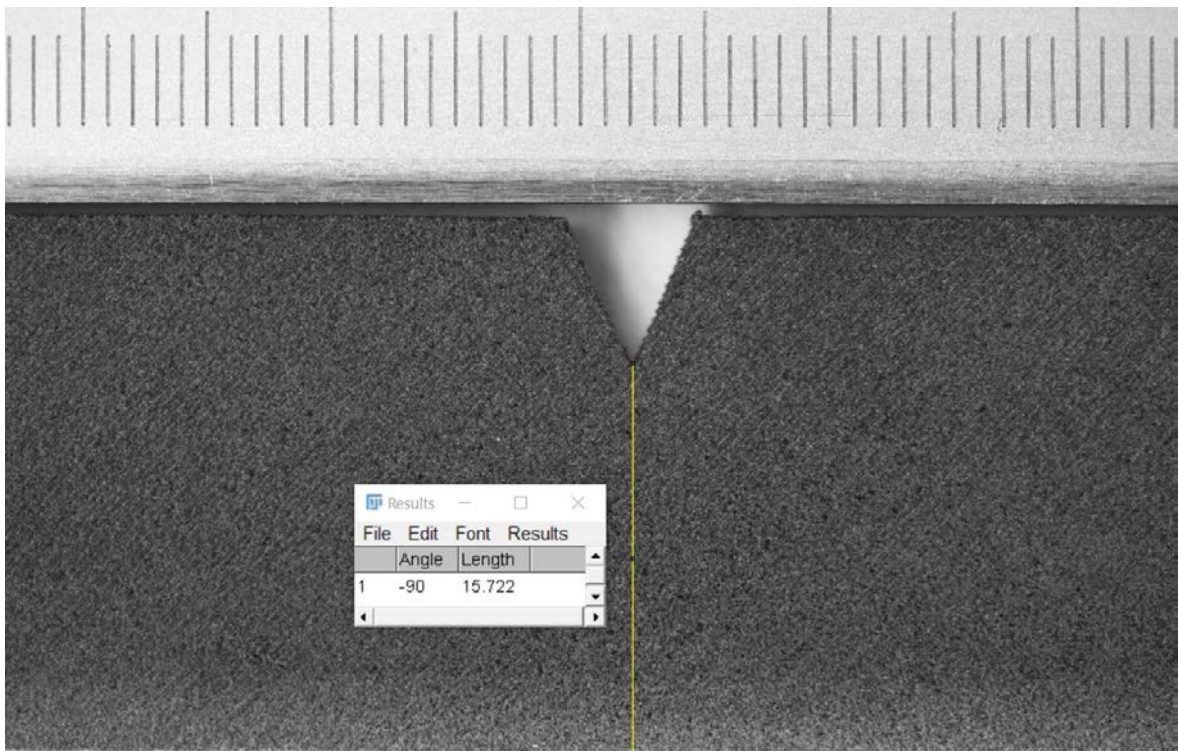


Figure G.14: Measure of the net width of the 45VR0PA12\_-1\_6 specimen.

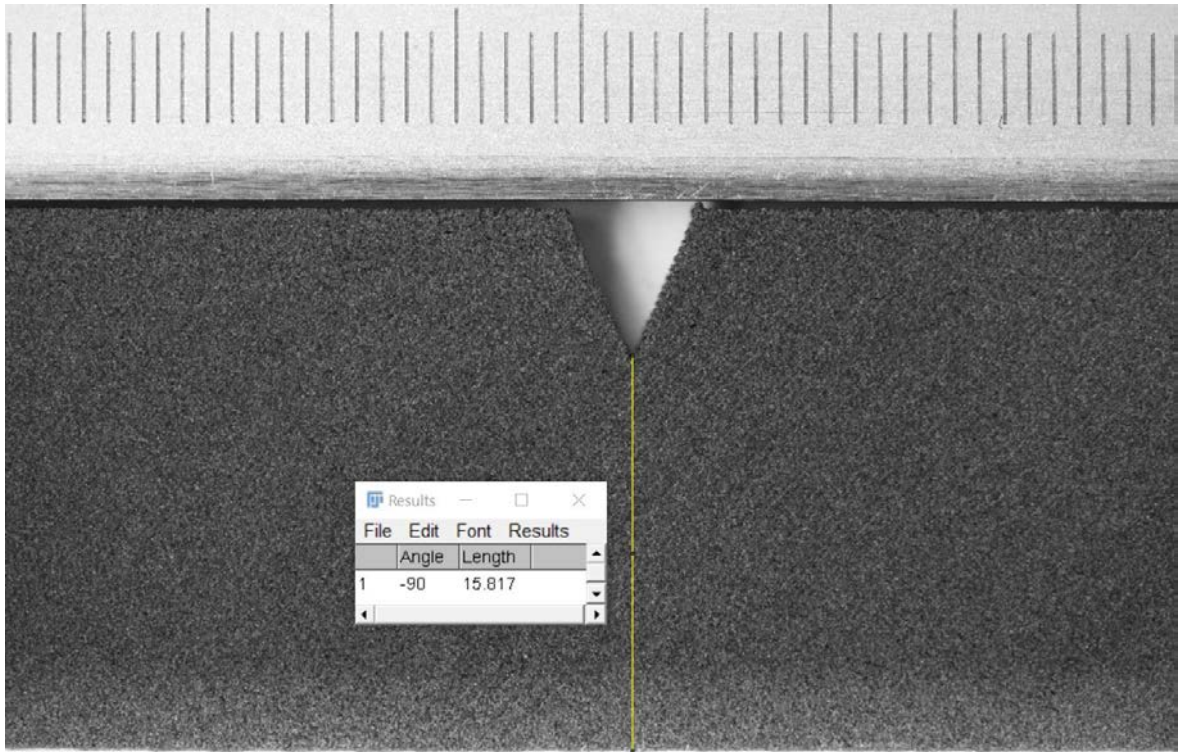


Figure G.15: Measure of the net width of the 45VR0PA12\_-1\_7 specimen.

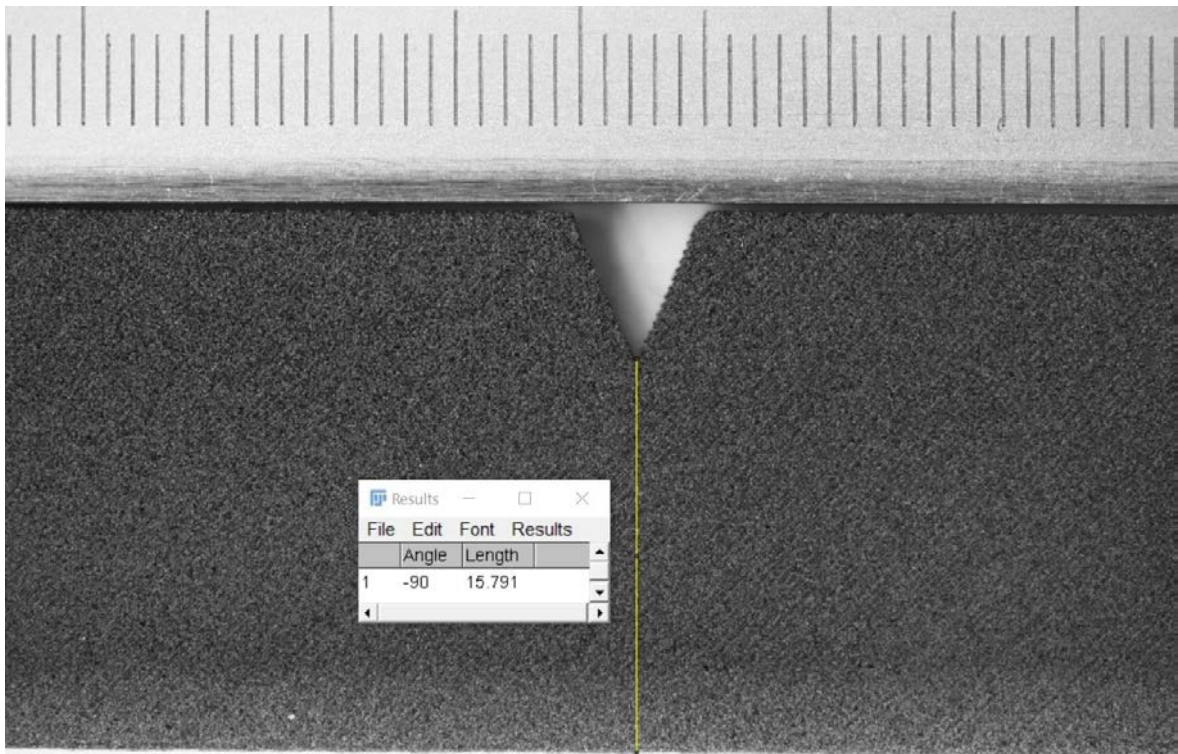


Figure G.16: Measure of the net width of the 45VR0PA12\_-1\_8 specimen.





Figure G.17: Measure of the net width of the 90VR0PA12\_-1\_1 specimen.



Figure G.18: Measure of the net width of the 90VR0PA12\_-1\_1BIS specimen.



Figure G.19: Measure of the net width of the 90VR0PA12\_-1\_2 specimen.

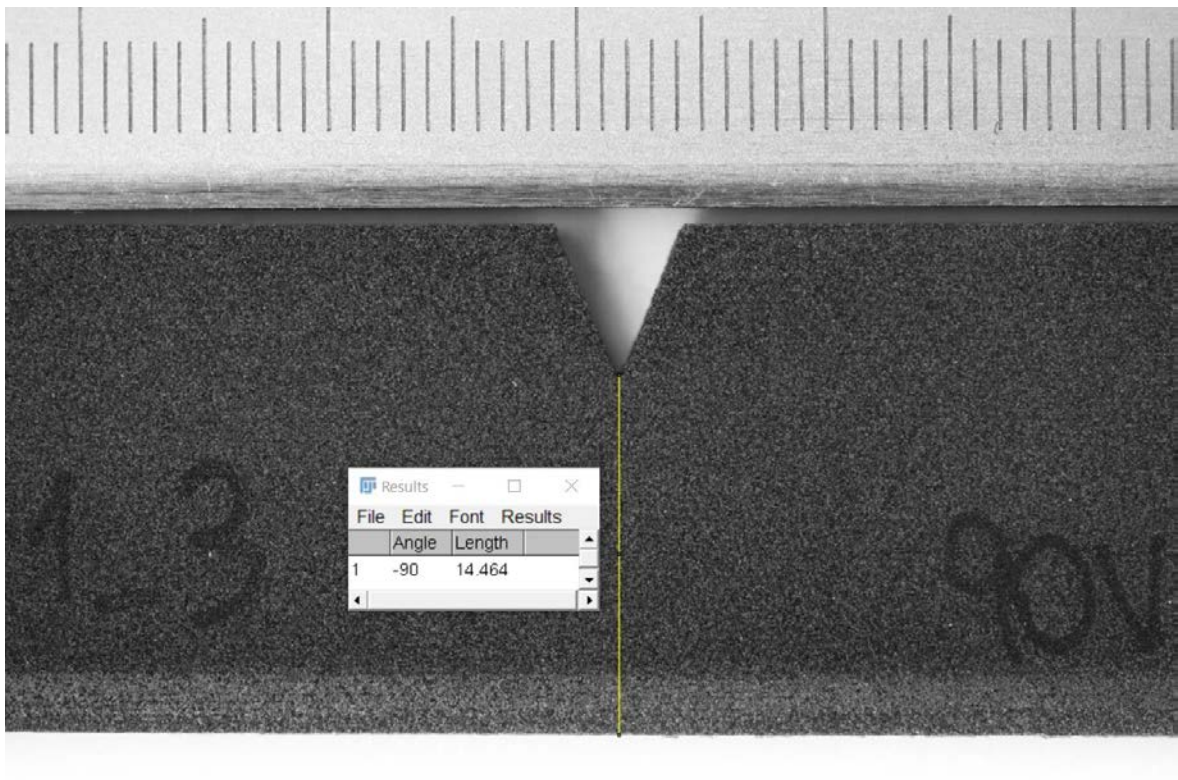


Figure G.20: Measure of the net width of the 90VR0PA12\_-1\_3 specimen.



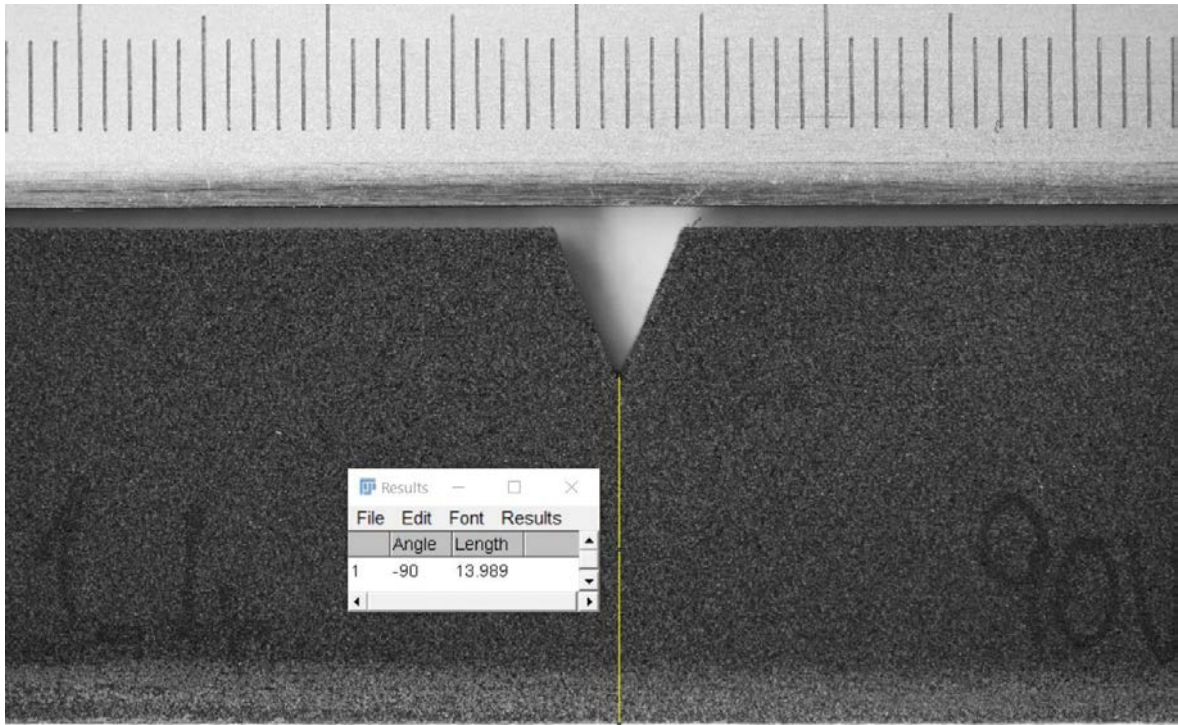


Figure G.21: Measure of the net width of the 90VR0PA12\_-1\_4 specimen.

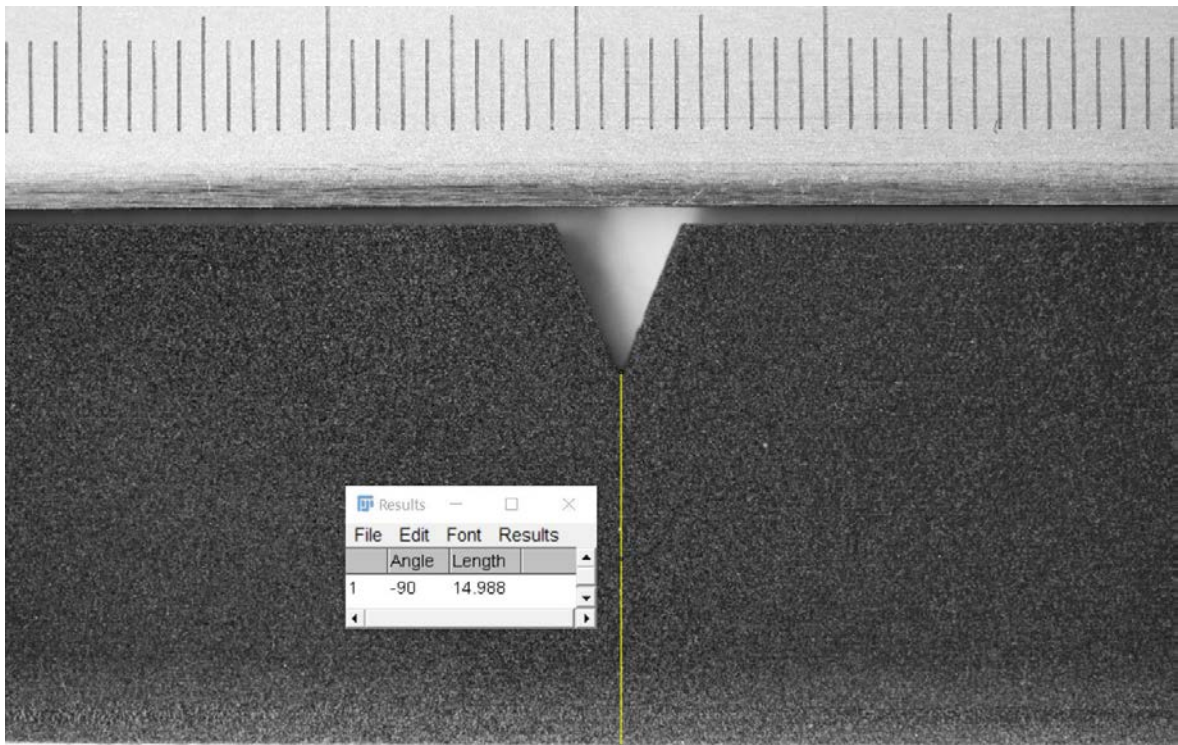


Figure G.22: Measure of the net width of the 90VR0PA12\_-1\_5 specimen.



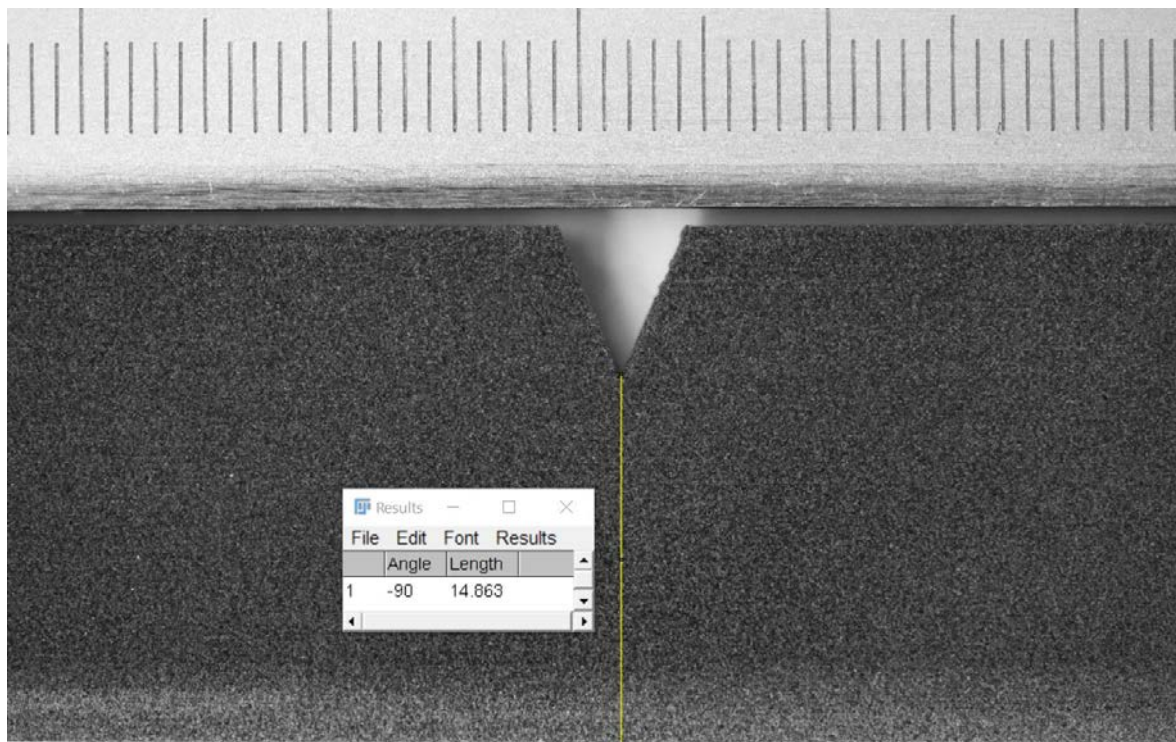


Figure G.23: Measure of the net width of the 90VR0PA12\_-1\_6 specimen.

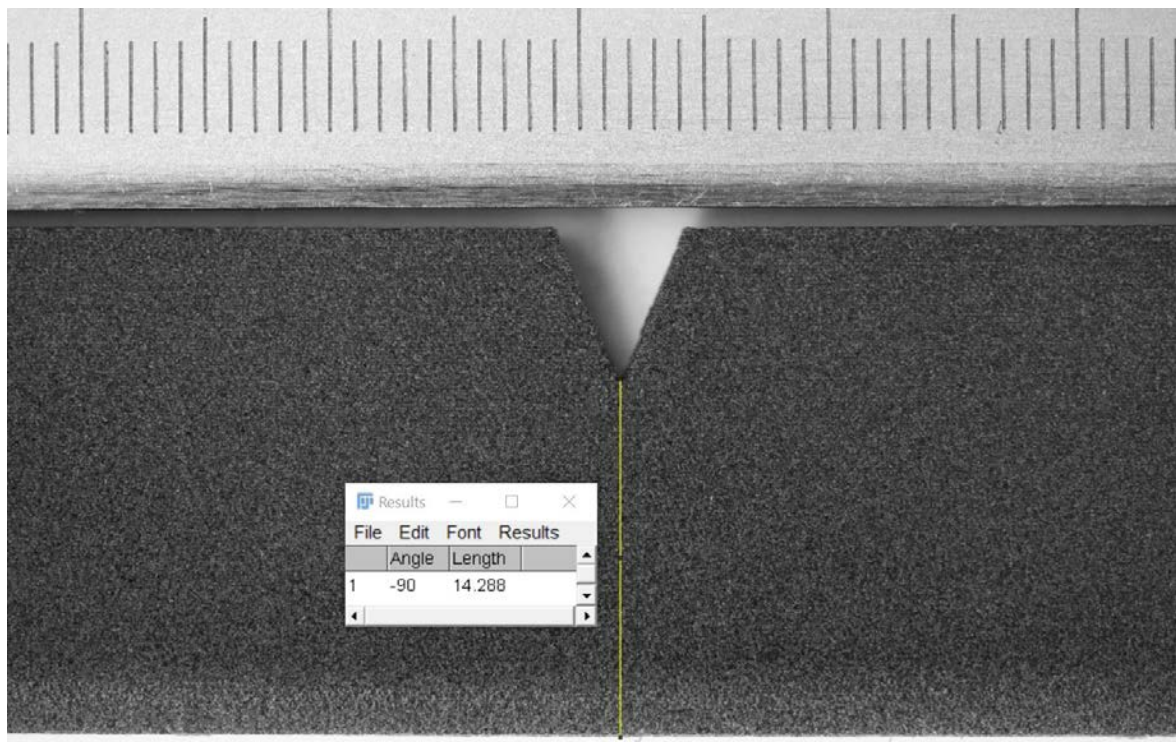


Figure G.24: Measure of the net width of the 90VR0PA12\_-1\_7 specimen.

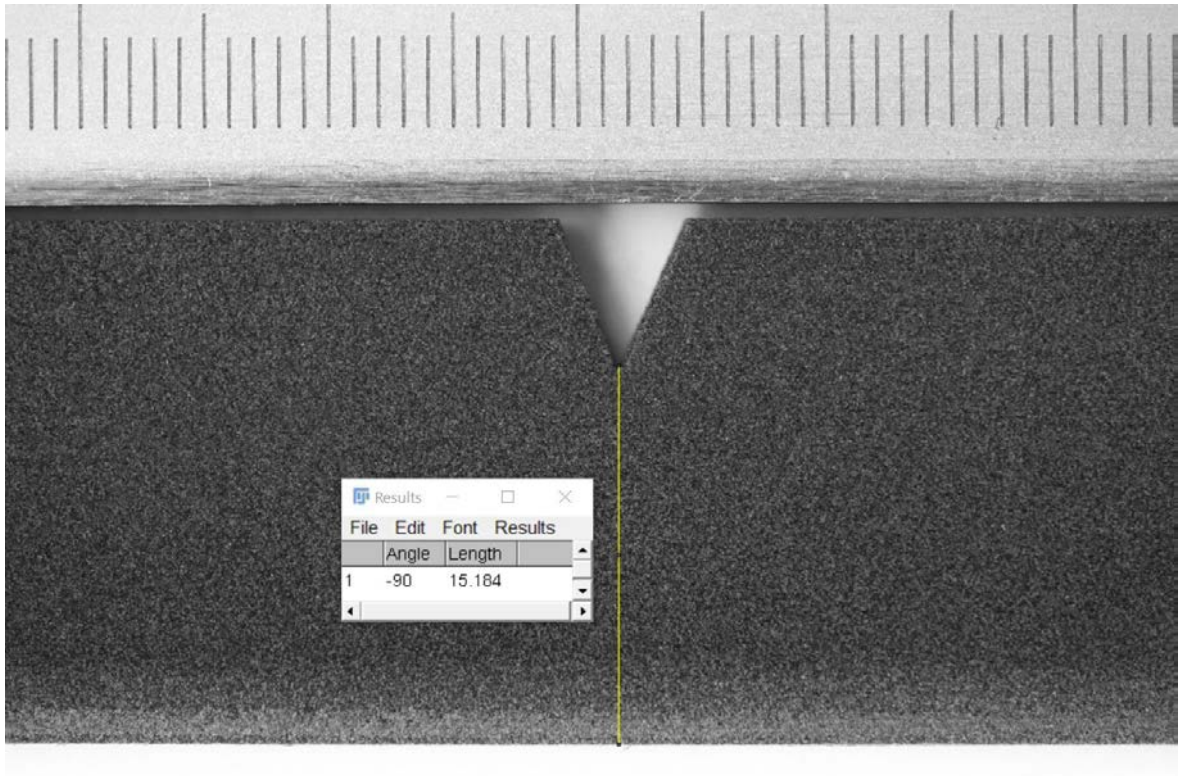


Figure G.25: Measure of the net width of the 90VR0PA12\_-1\_8 specimen.